THÈSE

Pour obtenir le grade de

Docteur

Délivré par ECOLE NATIONALE SUPERIEURE DE CHIMIE DE MONTPELLIER

Préparée au sein de l'école doctorale Sciences Chimiques Balard
Et de l'unité de recherche UMR 5253 CNRS-UM-ENSCM

Spécialité : Chimie et Physico Chimie de Matériaux

Présentée par ANDRÉS FELIPE SIERRA SALAZAR

WATERBORNE CATALYTIC MATERIALS WITH ORIGINAL DESIGN

Soutenue le 15 novembre 2017 devant le jury composé de

Mme Stefania ALBONETTI, Professeur, University of Bologna	Rapporteur
Mme Pilar ARANDA, Docteur, Materials Science Institute of the National Research Council of Spain	Rapporteur
Mme Corine GERARDIN, Directeur de Recherche CNRS, ENSCM	Président du jury
M. Tony CHAVE, Chargé de Recherche CNRS, CEA Marcoule	Examinateur
M. Salvatore ABATE, Docteur, University of Messina	Examinateur
M. Patrick LACROIX-DESMAZES, Directeur de Recherche CNRS, ENSCM	Directeur de thèse
Mme Siglinda PERATHONER, Professeur, University of Messina	Co-Directeur de thèse
M. André AYRAL, Professeur, Université Montpellier - IEM	Invité
M. Vasile HULEA, Professeur, ENSCM	Invité

UNIVERSITA DEGLI STUDI DI MESSINA

Joint Research Doctorate Course SINCHEM – Sustainable and Industrial Chemistry – Erasmus Mundus

Dottorato di XXX ciclo in

Ingegneria e Chimica dei Materiali e delle Costruzioni

Coordinatori: Prof.ssa Siglinda Perathoner

Prof. Signorino Galvagno

SSD CHIM04

WATERBORNE CATALYTIC MATERIALS WITH ORIGINAL DESIGN

Tesi di: Dott. Andrés Felipe Sierra Salazar

Tutori: Dott. Patrick Lacroix-Desmazes (ENSCM)

Prof.ssa Siglinda Perathoner (UNIME)

Anno Accademico 2016 – 2017

SIERRA SALAZAR, Andrés Felipe

afsierrasa@gmail.com

Materials Chemist and Chemical Engineer

● Research ● Development ● Entrepreneurship ●

Professional skills:

→ Project management
→ Effective communication
→ Ability to anticipate
→ Adaptability
→ Polyglot: English, French, Spanish, Italian

Strengths:

→ International team work
→ Commitment
→ Loyalty
→ Integrity
→ Proactivity

Work Experience

October 2014 to September 2017 (expected) — **PhD candidate in Erasmus+ European Program on Sustainable Industrial Chemistry (SINCHEM)**

25 months at Ecole Nationale Supérieure de Chimie de Montpellier, France
8 months at Università degli Studi di Messina, Italy
3 months at CEA Marcoule, France

Project leader in collaborative work between 7 laboratories on catalysts development with original design

- Catalysts (Pt, Pd, CeO_2, SiO_2) preparation, characterisation and testing in batch and semi-continuous modes
- Supplementary skills in polymer chemistry, sonochemistry, sol-gel science and supercritical CO_2 processes

Feburary 2014 to July 2014 — **Internship in chemistry (Master 2)**– Ipsen Innovation, Les Ulis, France

- Solid phase peptides synthesis and bio-conjugation techniques
- Skills in immunochemistry tests and other characterisation techniques

January 2011 to January 2013 — **Junior Researcher** – Universidad Nacional de Colombia, Medellin, Colombia

Project on innovative biofuels via catalytic biomass valorisation

Awarded with two *competitive scholarships* by the Colombian Department for Science, Technology and Research (COLCIENCIAS)

January 2011 to January 2012 — **Entrepreneur BIOREFINING SAS – Start Up**

Business project based on the results of the Research Group on Bioprocesses and Reactive Flows of the Universidad Nacional de Colombia.

Awarded second place in contest for *venture capital* run by the CREAME Business Incubator (NERI - Colombia)

January 2010 to January 2011 — **New Products Designer** - COLTABACO S.A. – *A Philip Morris International affiliate*, Medellin, Colombia

- Product development for Andean cluster
- Planning and monitoring of prototype, pilot and industrial trials with new materials

March 2009 to March 2010 — **Volunteer as Trainee Service Coordinator** – AIESEC, Escuela de Ingeniería de Antioquia, Colombia

- Local sales and young leadership development (leader of a 10-person team)
- Help international trainees with integration and legal procedures for stay and housing

Education

October 2014 to September 2017 (expected)
PhD in Chemistry and Physical chemistry of Materials – Ecole Nationale Supérieure de Chimie de Montpellier
PhD in Engineering and Chemistry of Materials – Università degli Studi di Messina, Italy
Double degree in the European doctoral programme on Sustainable Industrial Chemistry (SINCHEM)
Erasmus Mundus Scholarship by the European Commission (FPA2013-037) : Ranked 1 / 157 candidates
Thesis title: *Waterborne catalytic materials with original design*

September 2012 to July 2014
Master's Degree in Chemistry – First-class honours, Université Paris Sud, France
Master's Degree in Chemistry, Universidade do Porto, Portugal
Master's Degree in Materials Science and Engeneering – Cum Lode, Università degli Studi di Genova, Italy
Multiple degrees in the European Master's course SERP-Chem (Surface, Electro, Radiation and Photo Chemistry)
Training focused on nanoscience and catalysis
Erasmus Mundus Scholarship by the European Commission (worldwide competition)

October 2011 to December 2011
Training on Technology and Innovation Management, Universidad Nacional de Colombia, Colombia
Project proposals, innovation and intellectual property, including patents

January 2005 to July 2010
Chemical Engineer, Universidad Nacional de Colombia, Colombia
Ranked 1 / 13 in the promotion (GPA : 4.5 / 5.0)
Thermodynamics, Operation units, Process control, Projects evaluation
Options : Waste water biological treatment, Industrial fermentation processes, Marketing management

Certification in Environmental management system - ISO 14001:04
Certification in Quality management systems - ISO 9001:00 et ISO 19011

Other Skills

Languages

Spanish	Native	**Italian**	Fluent
English (TOEFL)	Bilingual	**Portuguese**	Intermediate level
French (DELF)	Bilingual	**Chinese-Mandarin**	Beginner

Computer skills
Technology intelligence: Reaxys, SciFinder, ScienceDirect
Programming: Visual Basic, PHP, MySQL
Software: Microsoft Office (Word, Excel, PowerPoint, Outlook, Access, Visio), ChemDraw, ChemCad, Solid Edge, MATLAB, Macromedia Flash, Fireworks, Macromedia Dreamweaver Mx.

Personal Interests

Traveling, sharing and experiencing different cultures.
Sports: swimming, running and gym training.

Scientific Contributions

Several oral presentations at international conferences in The United States of America, Spain, Colombia, Germany, Italy and France

Written contributions:

- Andrés Felipe Sierra Salazar, et al. "*Engineering of silica-supported platinum catalysts with hierarchical porosity combining latex synthesis, sonochemistry and sol-gel process – II. Catalytic performance*", Microporous Mesoporous Mater. 256 (2018) 227–234. DOI : 10.1016/j.micromeso.2017.08.016
- Andrés Felipe Sierra Salazar, et al. "*Engineering of silica-supported platinum catalysts with hierarchical porosity combining latex synthesis, sonochemistry and sol-gel process – I. Material preparation*", Microporous Mesoporous Mater. 234 (2016) 207–214. DOI: 10.1016/j.micromeso.2016.07.009
- Andrés Felipe Sierra-Salazar, et al. "*Hierarchically porous Pd/SiO2 catalyst by combination of miniemulsion polymerisation and sol-gel method for the direct synthesis of H_2O_2*", Catal. Today. In press (2016). DOI: 10.1016/j.cattod.2016.12.021.
- Book chapter: *"Biomasa lignocelulósica en Colombia, pretratamientos y productos de valor agregado", "Aprovechamiento de biomasa lignocelulósica: algunas experiencias de investigación en Colombia"* Editor: Universidad de Bogotá Jorge Tadeo Lozano (2014).

List of scientific contributions issued from this research project

Papers:

- A.F. Sierra-Salazar, V. Hulea, A. Ayral, T. Chave, S.I. Nikitenko, P.J. Kooyman, F.D. Tichelaar, S. Abate, S. Perathoner, P. Lacroix-Desmazes, "*Engineeringof silica-supported platinum catalysts with hierarchical porosity combining latex synthesis, sonochemistry and sol-gel process – II. Catalytic performance*" Microporous Mesoporous Mater. 256 (2018) 227–234. DOI: 10.1016/j.micromeso.2017.08.016

- A.F. Sierra-Salazar, W.S.J. Li, M. Bathfield, A. Ayral, S. Abate, T. Chave, S.I. Nikitenko, V. Hulea, S. Perathoner, P. Lacroix-Desmazes, "*Hierarchically porous Pd/SiO_2 catalyst by combination of miniemulsion polymerisation and sol-gel method for the direct synthesis of H_2O_2*", Catal. Today. In press (2016). DOI:10.1016/j.cattod.2016.12.021.

- A.F. Sierra-Salazar, T. Chave, A. Ayral, S.I. Nikitenko, V. Hulea, P.J. Kooyman, F.D. Tichelaar, S. Perathoner, P. Lacroix-Desmazes, "*Engineering of silica-supported platinum catalysts with hierarchical porosity combining latex synthesis, sonochemistry and sol-gel process – I. Material preparation*", Microporous Mesoporous Mater. 234 (2016) 207–214. DOI:10.1016/j.micromeso.2016.07.009.

Oral presentations:

- "*Pt and Pd-based catalysts with hierarchical porosity prepared by a combination of latex synthesis, sonochemistry and sol-gel process*"" A.F. Sierra-Salazar, W.S.J. Li, M. Bathfield, T. Chave, A. Ayral, S.I. Nikitenko, V. Hulea, P. J. Kooyman, F.D. Tichelaar, S. Abate, S. Perathoner, P. Lacroix-Desmazes, Proceeedings Europacat 2017, 27th-31st August 2017, Florence (Italy)

- "*Réduction sonochimique de métaux nobles en présence de latex pour la préparation de catalyseurs à designs originaux*" A. F. Sierra Salazar, T. Chave, S. I. Nikitenko, A. Ayral, V. Hulea, P. J. Kooyman, F.D. Tichelaar, S. Abate, S. Perathoner, P. Lacroix-Desmazes. Proceeedings Journées Scientifiques Ultrasons et Procédés - 4ème édition, 4th-5th July 2017, Toulouse (France)

- "*Sonochemical deposition of noble metal on latex beads for the preparation of hierarchically porous silica supported catalysts*", A.F. Sierra Salazar, T. Chave, S. Nikitenko, A. Ayral, V. Hulea, P.J. Kooyman, F.D. Tichelaar, S. Perathoner, P. Lacroix-Desmazes. Proceeedings 5th International Symposium on Green Chemistry (ISGC-5), 16th-19th May 2017, La Rochelle (France)

- "*Direct synthesis of hydrogen peroxide from oxygen and hydrogen using hierarchically porous Pd/SiO_2 catalysts*" A.F. Sierra-Salazar, W.S.J. Li, M. Bathfield, A. Ayral, S. Abate, T. Chave, S.I. Nikitenko, V. Hulea, S. Perathoner, P. Lacroix-Desmazes, Proceeedings workshop on Activation and Valuation of Small Molecules, 30th November 2016, Lyon (France)

- "*Combinaison de la polymérisation en émulsion, de la sonochimie et du procédé sol-gel pour la synthèse de catalyseur supporté Pt/SiO_2 à porosité hiérarchique*", A.F. Sierra Salazar, T. Chave, A. Ayral, S. Nikitenko, V. Hulea, P.J. Kooyman, F.D. Tichelaar, W.S.J. Li, S. Perathoner, P. Lacroix-Desmazes, Proceeedings 45ème Colloque National du Groupe Français d'études et d'applications des Polymères (GFP), 15th-18th November 2016, Marseille (France)

- "*Hierarchically porous Pt/SiO_2 by sol-gel process with a sonochemically decorated latex template*", A.F. Sierra Salazar, T. Chave, A. Ayral, S. Nikitenko, V.Hulea, P.J. Kooyman, F.D. Tichelaar, S. Abate, S. Perathoner, P. Lacroix-Desmazes, Proceeedings First workshop on rational design for improved functionalities of porous inorganic materials - Saint-Gobain CREE, 7th-9th November 2016, Cavaillon (France)

- "*Silica-supported platinum catalysts with hierarchical porosity prepared by innovative coupling of various synthesis routes*" A.F. Sierra Salazar, T. Chave, S.Nikitenko, V. Hulea, A. Ayral, P.J. Kooyman, S. Abate, S. Perathoner, P. Lacroix-Desmazes Proceeedings Gordon Research Seminar on Green Chemistry, 30th-31st July 2016, Stowe VT (United States)

- "*Sonochemical approach for the synthesis of porous materials*" T. Chave, A.F. Sierra Salazar, C. Cau , A. Ayral, Y. Guari, V. Hulea, P. Lacroix-Desmazes,S.I. Nikitenko. Proceeedings Energy Materials Nanotechnology (EMN) Meeting on Mesoporous Materials 13th-17th June 2016, Prague (Czech Republic)

- "*Waterborne hierarchically porous silica-supported platinum catalyst by sol-gel synthesis with a sonochemically decorated latex template*" A.F. Sierra Salazar, T. Chave, S. Nikitenko, A.Ayral, V. Hulea, S. Perathoner, P.J. Kooyman, P. Lacroix-Desmazes. Proceeedings French Conference on Catalysis, 23rd-27th May 2016, Fréjus (France)

- "*Hierarchically porous silica supporting platinum catalytic nanoparticles by innovative coupling of various synthesis routes*" A.F. Sierra Salazar, T. Chave, A.Ayral, V. Hulea, S. Nikitenko, P.J. Kooyman, S. Perathoner, P. Lacroix-Desmazes Proceeedings Balard Chemistry Conferences: Prospects in porous materials, 5th-8th April 2016, Montpellier (France).

- "*Combination of polymer latexes, sonochemistry and sol-gel route for the preparation of silica supported catalysts*" A.F. Sierra-Salazar, T. Chave, S.Nikitenko, V. Hulea, A. Ayral, S. Perathoner, P.J. Kooyman, P. Lacroix-Desmazes Proceeedings 3rd International Conference of the Cluster of Excelence "Talor-Made fuels from biomass", 23rd-25th June 2015, Aachen (Germany).

Flash Oral - Poster Presentation:

- "*Silica-supported platinum catalysts with hierarchical porosity prepared by a combination of latex synthesis, sonochemistry and sol-gel process*" A.F. Sierra Salazar, T. Chave, S. Nikitenko, V. Hulea, A. Ayral, S. Perathoner, P.J. Kooyman, P. Lacroix-Desmazes Proceeedings 5th International Conference on Structured Catalysts and Reactors, 21st-24th June 2016, Donostia-San Sebastián (Spain)

Posters:

- "*Silica-supported Pt catalysts with hierarchical porosity prepared by a combination of latex synthesis, sonochemistry and sol-gel process*" A.F. Sierra Salazar, T. Chave, S. Nikitenko, A. Ayral , S. Perathoner, P.J. Kooyman, F.D. Tichelaar, P. Lacroix-Desmazes, V. Hulea. Proceeedings 8th International Syposium Nanoporous Materials (NANO-8), 9th - 12th July 2017, Ottawa (Canada)

- "*Preparation of supported catalysts with hierarchical porosity: removal of the polymer template by supercritical carbon dioxide extraction*", W.S.J. Li, A.F. Sierra-Salazar, A. Ayral, T. Chave, P. Lacroix-Desmazes, Proceeedings 16th European Meeting on Supercritical Fluids (EMSF), 25th-28th April 2017, Lisbon (Portugal)

- "*Silica-supported platinum catalysts with hierarchical porosity prepared by a combination of latex synthesis, sonochemistry and sol-gel process*" A.F. Sierra Salazar, T. Chave, S. Nikitenko, V. Hulea, A. Ayral, S. Perathoner, P.J. Kooyman, P. Lacroix-Desmazes Proceeedings 33e Club Emulsion, 3rd-4th October 2016, Castres (France)

- "*Silica-supported platinum catalysts with hierarchical porosity prepared by innovative coupling of various synthesis routes*" A.F. Sierra Salazar, T. Chave, S.Nikitenko, V. Hulea, A. Ayral, P.J. Kooyman, S. Abate, S. Perathoner, P. Lacroix-Desmazes Proceeedings Gordon Research Conference on Green Chemistry, 31st July – 5th August 2016, Stowe VT (United States)

- "*Silica-supported platinum catalysts with hierarchical porosity prepared by a combination of latex synthesis, sonochemistry and sol-gel process*" A.F. Sierra Salazar, T. Chave, S. Nikitenko, V. Hulea, A. Ayral, S. Perathoner, P.J. Kooyman, P. Lacroix-Desmazes Proceeedings The 16th International Congress on Catalysis, 3rd-8th July 2016, Beijing (China)

- "*Combination of polymer latexes, sonochemistry and sol-gel route for the preparation of silica supported catalysts*" A.F. Sierra-Salazar, T. Chave, V. Hulea, A. Ayral, P. Lacroix-Desmazes Proceeedings 14èmes journées du Groupe Français des Polymères – Section Méditerranée, 22nd-23rd October 2015, Nice (France)

- "*Combination of polymer latexes, sonochemistry and sol-gel route for the preparation of silica supported catalysts*" A.F. Sierra-Salazar, T. Chave, V. Hulea, A. Ayral, P. Lacroix-Desmazes Proceeedings Colloque National GFP, 23rd-26th November 2015, Luxembourg (Luxembourg)

- "*Combination of polymer latexes, sonochemistry and sol-gel route for the elaboration of silica supported catalysts*" A.F. Sierra-Salazar, T. Chave, V. Hulea, A. Ayral, P. Lacroix-Desmazes Proceeedings 3rd International Symposium on Green Chemistry, 3rd-7th May 2015, La Rochelle (France)

This work was funded by SINCHEM Joint Doctorate Programme-Erasmus Mundus Action (framework agreement N°2013-0037; specific grant agreement n°2014-0679).

ACKNOWLEDGMENTS

This work was funded by SINCHEM Joint Doctorate Programme-Erasmus Mundus Action (framework agreement N°2013-0037; specific grant agreement n°2014-0679 for PhD thesis of A. F. Sierra Salazar) and ARPE project n°2015-004515 of the Languedoc Roussillon Region, now Region Occitanie, France (for the contribution of Maël Bathfield and Jennifer Li). The research leading to these results has received funding from the European Union Seventh Framework Programme under Grant Agreement 312483 – ESTEEM2 (Integrated Infrastructure Initiative – I3) for TEM measurements.

Special acknowledgments:

To the reviewers and members of the jury that accepted to evaluate my PhD thesis: Prof. STEFANIA ALBONETTI, Dr. PILAR ARANDA, Prof. MARCO ZECCA, Prof. ALESSANDRO SCARSO and Dr. CORINE GERARDIN.

To my supervisors that guided me through my PhD training, providing continuous support and encouragement to overcome the scientific challenges related to my research project:

- Dr. PATRICK LACROIX-DESMAZES (Ecole Nationale Supérieure de Chimie de Montpellier, ENSCM, France. Laboratory "Ingénierie et Architectures Macromoléculaires", IAM)
- Prof. ANDRE AYRAL (Institut Européen de Membranes - IEM)
- Prof. VASILE HULEA (Ecole Nationale Supérieure de Chimie de Montpellier, ENSCM, France. Laboratory "Matériaux Avancés pour la Catalyse et la Santé", MACS)
- Dr. TONY CHAVE (CEA, Marcoule, France)
- Dr. SERGUEI NIKITENKO (CEA, Marcoule, France)
- Prof. SIGLINDA PERATHONER (University of Messina, Unime, Italy)
- Dr. SALVATORE ABATE (University of Messina, Unime, Italy)
- Prof. PATRICIA J. KOOYMAN (University of Cape Town, South Africa)
- Dr. FRANS D. TICHELAAR (Delft University of Technology, TU Delft).

To the members of the "*comités de suivi de thèse*" for the annual evaluation of my research: Dr. BENJAMIN NOTTELET, Dr. FRÉDÉRIC LAMATY, Dr. DAMIEN QUEMENER and Dr. JEAN-JACQUES ROBIN.

To my colleagues that were involved in my research project: Dr. MAËL BATHFIELD for the preparation of the hybrid Pd-containing polystyrene latex template by miniemulsion polymerisation and to W.S. JENNIFER LI for the preparation of the Pd/SiO_2 catalyst derived thereof. To DIDIER COT for the SEM images (Institut Européen des Membranes, France).VÉRONIQUE VIGUIER for TEM sample preparation, FRANCK GODIARD for TEM images (Pôle Chimie Balard, Common Service of Electron Microscopy, France). ABDESLAM EL-MANSOURI for mercury porosimetry and nitrogen adsorption (Institut Européen des Membranes, France). Dr. VALERIE FLAUD for some XPS analyses (Pôle Chimie Balard, Université de Monpellier, France). Dr. RADU-DORIN ANDREI and Dr. OLINDA GIMELLO for training on gas chromatography (Institut Charles Gerhardt, MACS team, France). Dr. PASCALE GUIFFREY for

access to the calcination equipment (Institut Charles Gerhardt, AM2N team, France). Prof. FRANÇOIS FIGUERAS for the valuable discussions.

To the SINCHEM consortium members that made possible this European PhD framework. A special acknowledgment to the selection committee that permitted me to join this programme, in particular to Prof. FRANCESCO DI RENZO, who interviewed me. I also want to thank the professors that have made this programme possible and those who have given me feedback during the SINCHEM meetings, including: Prof. GABRIELE CENTI, Prof. STEFANIA ALBONETTI , Prof. FABRIZIO CAVANI, Prof. REGINA PALKOVITS, Prof. WALTER LEITNER, Prof. ALESSANDRA QUADRELLI, Prof. CHLOE THIEULEUX and Prof. STEVE HOWDLE.

To my SINCHEM colleagues that are always striving for excellence. Thank you for the feedback, support and help: AISHA MATAYEVA, PAYAL BAHETI, KRISTINE TOLOD, SHIMING CHEN, POOJA GAVAL, MATILDE SOLMI, DANILO BONINCONTRO, IQRA ZUBAIR AWAN, HO PHUOC HOANG, ERWIN FERNANDEZ, TAPISH SABOO, CHALACHEW MEBRAHTU, ALBA CASTAÑÓN RODRÍGUEZ, TAHRIZI ANDANA, BHANU CHANDRA MAREPALLY, GIULIANA RUBULOTTA, MARIA GYNGAZOVA, ASJA PETTIGNANO, EMILIA SOFIA STRENG, ATIF EMRE DEMET, OLENA VOZNIUK, YU ZHANG, DANIEL ANTONIO AGUILERA BULLA, SONIA AGUILERA SEGURA, QUANG NGUYEN TRAN, VALERIA MASLOVA, AKASH KAITHAL, RAVI SRIVASTAVA, MARCELO ALVES FAVARO, ULISSE MONTANARI, SAMANTHA MOLINA GUTIERREZ, FERENC MARTINOVIC, RISMA YULISTIANA, HUA WEI, ANA PATRICIA ALVES COSTA PACHECO, MEDET ZHUKUSH, PAOLA BLAIR VASQUEZ, STEFANIE MERSMANN and CLEMENT CAMP.

To the permanent staff at IAM Lab for their help and support, including: Dr. CLAIRE NEGRELL, Dr. SYLVAIN CAILLOL, Dr. CÉCILE BOUILHAC, Dr. JULIEN PINAUD, JOEL COUVE, Dr. BRUNO AMEDURI, Dr. CHRISTINE JOLY-DUHAMEL, Dr. VINCENT LADMIRAL, Dr. BERNARD BOUTEVIN, Dr. GHISLAIN DAVID, Dr. REMI AUVERGNE, and ABDELATIF MANSERI.

To my colleagues at IAM Lab for their support, feedback and help, including: CORALIE PHILIPPE, SANDY GOSSET, Dr. GUILLAUME COUTURE, VALENTIN HETIER, Dr. ELENA MAZZON, Dr. ADRIEN CORNILLE, Dr. THIBAUT SOULESTIN, Dr. MARINE BLAIN, ANNE-SOPHIE MORA, Dr. MARC GUERRE, MARC-ADRIEN TRONCHE, Dr. MELANIE DECOSTANZI, ANTHONY PHIMPHACHANH, Dr. VINCENT FROIDEVAUX, AGATHE BOUVET-MARCHAND, Dr. MAXENCE FACHE, SANJIB BANERJEE, EMELINE PLACET, Dr. GABRIEL FOYER, Dr. ETIENNE LABALME, Dr. EMILIE DARROMAN, CLÉMENT COQUERY, ROMAIN TAVERNIER, Dr. FANNY JAILLET, Dr. BENJAMIN CAMPAGNE, Dr. RAPHAEL MENARD, Dr. FATOUMATA CAMARA, BENOIT BRIOU, Dr. GERALD LOPEZ, Dr. FEIFEI NG, LUCAS JEGO, Dr. ELENA DOLCI, Dr. IBRAHIMA FAYE, YVAN ECOCHARD, JULIETTE LOMEGE, AXEL TRAMAUX, CÉLINE BONNEAUD, RENAUD JEANNIN, ELINE LAURENT, Dr. LAETITIA KORCHIA, NADIA HAMMAMI, CHLOÉ PRUVOST, FLORENT FANGET, ADRIEN SEVILLA, BENJAMIN LAMAUD and all PhD students, post-docs and trainees in these three years that I might have not listed here.

To the professors, staff and colleagues at MACS Lab for their help and support, including: Dr. NATHALIE TANCHOUX, Dr. ANNE GALARNEAU, Dr. CLAUDIA CAMMARANO, JÉREMY RODRIGUEZ, GÉRALDINE LAYRAC, Dr. GWENDOLINE GRAVÉ, LAURA VAUGON, Dr. ELODIE WAN, MELODY MATHONNAT and Dr. EMILIE MOLINA.

To the people that gave me some training in France: CEDRIC TOTEE and Dr. GILLES SILLY for training on NMR, RAY HORN for training on effective and speed reading and Dr. JULIEN HAINES for training on XRD.

To the administrative staff at ENSCM, including: CHRISTINE EUZET, JOSEPHA THIEVET, GAËLLE AMMELOOT, MARIE-NOELLE NTSAME-NGUEMA, MARIE-JOSÉE MARTIN, MARIE-CHRISTINE BORIE, HÉLÈNE DRÔME, ISABELLE LEGROS, LAURE RABESON and GREGORY THEROND. Also to CLAUDINE SOUDAIS for her help concerning legal procedures in Europe.

To all the personnel and colleagues at CEA of Marcoule, including: DOMINIQUE ALPE CONCHY, Dr. RACHEL PFLIEGER, Dr. MATTHIEU VIROT, ELODIE DALODIÈRE, REN JI, Dr. TEMIM OUERHANI, Dr. FLORENCE NOUAILLE, MATHILDE DIAS, HÉLÈNE MARTIN and VAININA RUSSELLO.

To all my colleagues at Unime for their help and training on science and Italian culture: Dr. KATIA BARBERA, Dr. GIANFRANCO GIORGIANNI, Dr. GIORGIA PAPANIKOLAOU, SERENA GENTILUOMO, Dr. PAOLA LANZAFAME, Dr. CHIARA GENOVESE, FRANCESCO TAVELLA, Dr. ROSALBA PASSALACQUA, LEONE FRUSTERI, Dr. CLAUDIO AMPELLI, ANNA MARIA CASELLA, LAYLA FILICIOTTO and ROBERTO DI CHIO.

To my master's professors at SERP-Chem Erasmus Mundus programme who accepted me to join the master's programme and opened me the door to study in Europe. Additionally, their courses were very valuable during this PhD research project. I thank them all, notably: Prof. SANDRINE LACOMBE, Prof. NICOLAS RABASSO and Prof. PEDRO DE OLIVEIRA at Université Paris-Sud, Prof. MARIO ROCCA, Prof. GUIDO BUSCA, Prof. GABRIELLA BORZONE and Prof. ANDREA BASSO at Università di Genova, Prof. MARIA DAS DORES, Prof. EDUARDO F. MARQUES, Prof. AGOSTINHA MATOS, Prof. CARLOS MELO PEREIRA and Prof. JOÃO MONTE at Universidade do Porto. I also want to thank Dr. SERGE AUVIN, Dr. OLIVIER LAVERGNE and PAUL HUMBRECHT for the knowledge transmitted during my internship at Ipsen.

To my tutor since my first semester at Universidad Nacional de Colombia and still today: Prof. ANGELA ADRIANA RUIZ COLORADO, for her continuous support and professional guidance. Also to my language teachers who helped me make this personal project a reality, specially: JOANNA TAMAYO and MARIA ELENA VALENCIA.

To all my friends all around the globe that have encouraged me throughout these years. Finally, to my family in Colombia and in France. Here some word to them:

Mis agradecimientos muy especiales para mis abuelos: GABRIELA MARGARITA GARCÍA GARCÍA, PABLO EMILIO SIERRA SIERRA, ANA BEIBA CARMONA BARRERA y JESÚS ANTONIO SALAZAR TOBÓN, a mis padres: FABIOLA DE JESÚS SALAZAR CARMONA y LUIS EMILIO SIERRA GARCÍA, y a mis padrinos: IRMA SIERRA GARCÍA, LEONARDO MANRIQUE GÓMEZ y DIANA MARÍA SIERRA GARCÍA, a quienes debo la persona que soy hoy. Ellos fueron quienes me criaron y me inculcaron con su ejemplo los valores que me definen como persona. Igualmente agradezco a mis hermanos: GLORIA PATRICIA, JUAN CAMILO y MARÍA PAULINA, a mis sobrinos: SAMANTHA, STEFANY y JERÓNIMO, y a todos mis familiares (tanto Sierra como Salazar) por su incondicional apoyo. También quiero resaltar mis agradecimientos para la delegación de mi familia en Europa: mis

primos GLORIA FRANCO SIERRA, EDGAR VALENCIA e hijos: JUAN y SANTIAGO, por su apoyo incondicional durante mi experiencia en el exterior.

Mes remerciements les plus sincères à PIERRE, JOCELYNE, FRANCIS, AMANDINE et FRANCK MONTANARI pour leur soutien toutes ces années.

CONTENTS

ABSTRACT – VULGARISATION

Catalysis is one of the pillars for developing sustainable processes and products, since it permits to use fewer resources by accelerating chemical reactions by means of a catalyst (a substance that accelerates a reaction without being consumed). To provide more performant catalysts based on precious metals (e.g. Pt, Pd), this study proposes a novel preparation method for controlling the distribution of metal nanoparticles within a material with pores of various sizes. It starts by the preparation of polymer beads, followed by the formation of metal nanoparticles on the polymer beads surface, using ultrasound. Then, these decorated polymer beads are embedded into silica; all steps being carried out in environmentally-friendly water. The organic polymer template is removed by calcination, which results in a hierarchically porous silica containing the metal nanoparticles. These catalysts are used for the *p*-chloronitrobenzene hydrogenation and for the direct synthesis of hydrogen peroxide.

RESUME - VULGARISATION

La catalyse est l'un des piliers pour le développement de procédés durables, car elle permet d'utiliser moins de ressources en accélérant les réactions chimiques grâce à un catalyseur (une substance qui accélère la réaction sans être consommée). Pour préparer des catalyseurs plus performants à base de métaux précieux (ex. Pt, Pd), cette étude propose une nouvelle méthode qui permet le contrôle de la distribution de nanoparticules métalliques dans un matériau poreux. D'abord, des billes de polymère sont préparées. Ensuite, des nanoparticules métalliques sont formées sur la surface du polymère en utilisant des ultrasons. Enfin, ces billes décorées sont incorporées dans de la silice (toutes ces étapes sont menées dans l'eau). Les billes de polymère sont éliminées par calcination, ce qui conduit à une silice hiérarchiquement poreuse avec des nanoparticules métalliques. Ces catalyseurs sont utilisés pour l'hydrogénation du *p*-chloronitrobenzene et la synthèse directe du peroxyde d'hydrogène.

RIASSUNTO - VOLGARIZZAZIONE

La catalisi è uno dei pilastri per lo sviluppo di processi sostenibili perché permette di utilizzare meno risorse accelerando le reazioni chimiche attraverso un catalizzatore (una sostanza che accelera la reazione senza essere consumata). Al fine di preparare dei catalizzatori più efficienti basati su metalli preziosi (es. Pt, Pd), questo studio propone un nuovo metodo che consente di controllare la distribuzione delle nanoparticelle metalliche in un materiale poroso. In primo luogo, vengono preparate perline di polimero. Successivamente, delle nanoparticelle metalliche vengono formate sulla superficie del polimero utilizzando ultrasuoni. Poi, queste perline decorate vengono incorporate all'interno della silice (tutte queste fasi vengono eseguite in acqua). Infine, il polimero viene rimosso mediante calcinazione, portando ad una silice gerarchicamente porosa con nanoparticelle metalliche. Questi catalizzatori vengono utilizzati per l'idrogenazione di *p*-cloronitrobenzene e la sintesi diretta di acqua ossigenata.

ABSTRACT

Catalysis is one of the Green Chemistry Principles given its importance for limiting environmental impacts and improving current processes, as well as for developing new sustainable processes and products. Today, catalytic processes are present in about 90% of all industrial chemical transformations. In order to provide more performant catalysts, rational design approaches should be privileged. Unfortunately, the routes to control the spatial distribution of individual functions within porous solids are limited. In order to address such a challenge, this study provides a novel waterborne preparation method for controlling the distribution of metal nanoparticles within hierarchically meso- and macroporous catalysts. It consists of the combination of latex synthesis, sonochemistry and sol-gel process. All these steps can be carried out in water, reducing environmental impact.

The first step is the synthesis of latex, typically polystyrene. The second step is the sonochemical synthesis and deposition of noble metal nanoparticles on the surface of the latex polymer. The third step is the synthesis of the support by sol-gel process using tetraethyl orthosilicate under controlled conditions to modulate the porosity of the final silica matrix. As a result, this method permits to preferentially locate the active sites within the macropores, which are surrounded by a mesoporous matrix.

Using this approach, it was possible to synthesise a monodisperse polystyrene latex with particle size of ca. 130 nm by emulsion polymerisation. Then, the latex was decorated with platinum nanoparticles of ca. 2.3 nm by sonochemical reduction of sodium tetrachloroplatinate. The mesoporous silica support was prepared by a two-step acid-base catalysed sol-gel synthesis in the presence of the decorated latex. After calcination, the organic template left behind macropores with the noble metal nanoparticles within the generated macropores. Mesopores (2-15 nm) connecting these macropores (110-400 nm) are tuned by varying the synthesis conditions. Typically, it was possible to obtain specific surface areas and total pore volumes as high as 615 m^2/g and 0.74 cm^3/g, respectively.

In a first case study, hierarchically porous Pt/SiO_2 catalysts were evaluated in the selective hydrogenation of *p*-chloronitrobenzene (*p*-CNB) to produce *p*-chloroaniline. They exhibited activities up to 91.7 ± 2.9 $mol_{CNB}/(min\ mol_{Pt})$ and selectivity values up to 100 ± 2% at 80% of conversion, in comparison with 47.7 ± 2.9 $mol_{CNB}/(min\ mol_{Pt})$ and 91 ± 2%, respectively, obtained with a commercial catalyst under the same conditions.

Moreover, in a second case study, it was possible to demonstrate the versatility of this technique to bring different functionalities to the porous support. Polystyrene or CeO_2-containing hybrid latexes produced by emulsion polymerisation were successfully decorated with Pd or bimetallic Pt-Pd nanoparticles via sonochemical reduction. Alternatively, Pd-containing hybrid latexes were prepared by miniemulsion polymerisation. Subsequently, the latexes were used in sol-gel chemistry to prepare silica-supported Pd, Pd-Pt and $Pd\text{-}CeO_2$ catalysts with hierarchical porosity (meso and macro). These materials were tested in the direct synthesis of hydrogen peroxide from hydrogen and oxygen. The best productivity of H_2O_2 was obtained with the bimetallic Pd-Pt catalyst with 32500 $mol_{H_2O_2}/(h\ mol_{metal})$ in batch, and the best selectivity was obtained with $Pd\text{-}CeO_2/SiO_2$ catalyst (63 ± 2%) in semi-batch.

In summary, this thesis proposes a new waterborne preparation method for hierarchically porous functional materials by the combination of latex synthesis, sonochemical reduction and sol-gel process. It has been demonstrated that this preparation technique provides a very powerful and versatile toolbox for catalyst tailoring and optimisation. Further perspectives to achieve improved morphologies and controlled active sites distribution are also proposed.

RESUME

La catalyse est l'un des piliers pour le développement de procédés durables, car elle permet d'utiliser moins de ressources en accélérant les réactions chimiques. Afin de fournir des catalyseurs plus performants, les approches de conception rationnelle doivent être privilégiées. Malheureusement, les voies pour contrôler la répartition spatiale des sites actifs dans des solides poreux sont limitées. Cette étude propose alors une nouvelle méthode de préparation de catalyseurs pour contrôler la distribution de nanoparticules métalliques au sein des catalyseurs hiérarchiquement poreux (méso et macro) en combinant la synthèse de latex, la réduction sonochimique et le procédé sol-gel.

La première étape est la synthèse d'une empreinte porogène de billes de polystyrène (latex) obtenues par polymérisation en émulsion aqueuse. La deuxième étape est la synthèse et le dépôt de nanoparticules de métaux nobles sur la surface des billes de polymère par voie sonochimique dans l'eau. La troisième étape est la synthèse du support catalytique par un procédé sol-gel en milieu aqueux en utilisant le latex décoré et l'orthosilicate de tétraéthyle (TEOS) dans des conditions contrôlées pour moduler la porosité finale de la matrice de silice (mésoporeuse). Toutes les étapes de cette approche sont effectuées dans l'eau, ce qui limite les impacts environnementaux de la préparation du catalyseur. L'élimination du porogène organique (latex) par calcination génère les macropores. Le matériau résultant possède alors une morphologie inédite pour un catalyseur, avec des macropores fonctionnalisés par des nanoparticules métalliques, dans une matrice de silice mésoporeuse.

Ainsi, il a été possible de synthétiser un latex monodisperse de polystyrène (~130 nm), lequel a été décoré avec des nanoparticules de platine (~2.3 nm) par réduction sonochimique. Le matériau final de silice a présenté des mésopores (2-15 nm) reliant les macropores (110-400 nm) contenant les nanoparticules de Pt. Il a été possible d'obtenir des surfaces spécifiques et des volumes poreux totaux de 615 m^2/g et 0,74 cm^3/g, respectivement.

Dans un premier cas d'étude, des catalyseurs de Pt/SiO_2 à porosité hiérarchique ont été évalués dans l'hydrogénation sélective du *p*-chloronitrobenzene (*p*-CNB) pour produire la *p*-chloroaniline. Ils ont présenté des activités catalytiques allant jusqu'à 91,7 ± 2,9 $mol_{CNB}/(min\ mol_{Pt})$ et des sélectivités jusqu'à 100 ± 2% à 80% de conversion, par rapport à 47,7 ± 2,9 $mol_{CNB}/(min\ mol_{Pt})$ et 91 ± 2%, respectivement, obtenus dans les mêmes conditions avec un catalyseur commercial.

Dans un deuxième cas d'étude, des latex de polystyrène seuls ou hybrides (contenant du CeO_2) ont été préparés par polymérisation en émulsion. Ils ont été décorés avec des nanoparticules de Pd ou bimétalliques de Pt-Pd par réduction sonochimique. Une variante a consisté à préparer des latex hybrides contenant du Pd par polymérisation en miniémulsion. Par la suite, ces latex ont été utilisés dans le procédé sol-gel pour préparer des catalyseurs à base de Pd, Pd-Pt et Pd-CeO_2 supportés sur de la silice à porosité hiérarchique. Ces matériaux ont été testés dans la synthèse directe du peroxyde d'hydrogène à partir d'hydrogène et d'oxygène. La meilleure productivité a été obtenue avec le catalyseur bimétallique Pd-Pt avec 32500 $mol_{H_2O_2}/(h\ mol_{métal})$ en batch, et la meilleure sélectivité a été obtenue avec le catalyseur Pd-CeO_2/SiO_2 (63 ± 2%) en semi-continu.

En résumé, cette thèse propose une nouvelle méthode de préparation dans l’eau de matériaux fonctionnels à porosité hiérarchique en combinant la synthèse de latex, la réduction sonochimique et le procédé sol-gel. Il a été démontré que cette technique de préparation fournit une boîte à outils très puissante et polyvalente pour la préparation et l'optimisation des catalyseurs. Des perspectives pour améliorer davantage les morphologies et la distribution contrôlée des sites actifs sont également proposées.

RIASSUNTO

La catalisi è uno dei pilastri per lo sviluppo di processi sostenibili in quanto consente di utilizzare meno risorse, accelerarando le reazioni chimiche. Al fine di fornire catalizzatori più efficienti, si dovrebbero privilegiare degli approcci di disegno razionali. Purtroppo, i modi per controllare la distribuzione spaziale delle singole funzioni chimique nei solidi porosi sono limitati. Questo studio propone un metodo innovativo per la preparazione di catalizzatori al fine di controllare la distribuzione delle nanoparticelle metalliche all'interno di catalizzatori gerarchicamente porosi (meso e macro) combinando la sintesi di lattice, la riduzione sonochimica e il processo sol-gel.

Il primo passo è la sintesi di una sagoma di perline di polistirene (lattice) ottenute mediante la polimerizzazione in emulsione acquosa. Il secondo passo consiste nella sintesi e la deposizione sonochimica delle nanoparticelle di metallo nobile sulla superficie delle perline di polimero. Infine, il terzo passo si basa sulla sintesi del supporto mediante un processo sol-gel in mezzo acquoso usando il lattice decorato e ortosilicato tetraetilico (TEOS) in condizioni controllate per modulare la porosità finale della matrice di silice (mesoporosa). Tutte le fasi di questo approccio sono effettuate in acqua, limitando gli impatti ambientali della preparazione del catalizzatore. La rimozione della sagoma (lattice) mediante calcinazione genera i macropori. Il materiale risultante è un catalizzatore con una nuova morfologia: dei macropori all'interno di una matrice di silice mesoporosa funzionalizzati da nanoparticelle metalliche.

In questo modo è stato possibile sintetizzare un lattice monodisperso di polistirene (~ 130 nm), il quale è stato decorato con delle nanoparticelle di platino (~ 2.3 nm) via riduzione sonochimica. Il materiale di silice finale ha mostrato dei mesopori (2-15 nm) che collegano i macropori (110-400 nm) contenenti le nanoparticelle di Pt. In generale, è stato possibile ottenere delle superfici e dei volumi totali dei pori di 615 m^2/g e 0,74 cm^3/g, rispettivamente.

In un primo caso di studio, i catalizzatori Pt/SiO_2 con porosità gerarchica sono stati testati nella idrogenazione selettiva di *p*-cloronitrobenzene (*p*-CNB) per produrre *p*-cloroanilina. Hanno mostrato delle attività catalitiche fino a 91,7 ± 2,9 $mol_{CNB}/(mol_{Pt}$ min) e delle selettività fino a 100 ± 2% al 80% di conversione, rispetto a 47,7 ± 2 9 $mol_{CNB}/(mol_{Pt}$ min) e 91 ± 2%, rispettivamente, ottenuti con un catalizzatore commerciale nelle stesse condizioni.

In un secondo caso di studio dei lattici, sia di polistirene solo oppure ibrido contenente CeO_2, sono stati preparati mediante polimerizzazione in emulsione. Questi lattici sono stati decorati con delle nanoparticelle di Pd o bimetalliche di Pt-Pd mediante riduzione sonochimica. In alternativa, un lattice ibrido contenente Pd è stato preparato mediante polimerizzazione in mini-emulsione. Successivamente, questi lattici sono stati utilizzati nel processo sol-gel per la preparazione di catalizzatori a base di Pd, di Pt-Pd e di $Pd-CeO_2$ supportati sulla silice con porosità gerarchica. Questi materiali sono stati testati nella sintesi diretta del perossido di idrogeno dall'idrogeno e dall'ossigeno. La migliore produttività è stata ottenuta con il catalizzatore bimetallico Pd-Pt con 32500 $mol_{H_2O_2}/(h\ mol_{metallo})$ in batch, e la migliore selettività è stata ottenuta con il catalizzatore $Pd-CeO_2/SiO_2$ (63 ± 2 %) in semi-continuo.

In sintesi, questa tesi di dottorato propone un nuovo metodo per la preparazione in acqua di materiali funzionali con porosità gerarchica mediante la combinazione della sintesi di lattice,

della riduzione sonochimica e del processo sol-gel. È stato dimostrato che questa tecnica di preparazione fornisce uno strumentario molto potente e versatile per la preparazione e l'ottimizzazione dei catalizzatori. Sono inoltre proposte altre prospettive per migliorare le morfologie e la distribuzione controllata dei siti attivi.

I. INTRODUCTION

Catalytic processes are of capital importance in the industrial development of the society as we know it today [1]. Indeed, current catalytic processes represent about 90% of all industrial chemical transformations [2]. Among them, catalytic processes involving supported nanoparticles of precious metals such as platinum, palladium and gold are currently used for producing fuels and other molecules of industrial interest [3,4]. Additionally, catalysis is one of the 12 Principles of Green Chemistry [5] because of its potential to contribute to the development of more sustainable chemicals, products and processes , for a sustainable future. Particularly, heterogeneous catalysis is commonly preferred over homogeneous catalysis due to the ease of removal of solid catalysts from the reaction media, so they can be recycled and reused several times prior to deactivation [6]. Nevertheless, there is still the need for developing more performant heterogeneous catalytic materials for current and new processes.

Rational catalyst design is a topic that has been actively discussed in the field as an opportunity to accelerate the development of tailor-made materials based on specific needs, reducing trial-and-error testing and establishing structure-property relationships [7]. Thus, from the experimental perspective, tools for the modulation of the catalyst texture (internal porosity and pore interconnectivity) and the tailoring of active sites are crucial for the preparation of rationalised catalysts. However, currently, there is limited availability of methods for controlling the spatial distribution of metal active sites within porous materials [8].

The aim of this work is to develop a new synthesis method for catalyst preparation in order to improve the active sites (noble metals) distribution at low loadings while controlling the hierarchical porosity of the support material. A catalyst structure with hierarchical porosity combines pores of different sizes (micropores: < 2 nm, mesopores: 2-50 nm, and macropores: > 50 nm). The importance of hierarchical porosity in catalysis is that the interconnected pores of different sizes allow the reagents and products to go through the porous matrix and reach all active sites [9].

The proposed method consists of the synthesis of a template decorated with metal nanoparticles and their transfer to sol-gel-derived mesoporous silica matrix. A schematic representation is given in Figure 1. The first step is the synthesis of a polystyrene latex template by emulsion polymerisation. The second step is the sonochemical synthesis and deposition of noble metal nanoparticles on the surface of the polymer latex. The third step is the synthesis of the support by sol-gel processes using the decorated latex template and tetraethyl orthosilicate (TEOS) under controlled conditions to modulate the porosity of the final silica matrix (mesoporous). The elimination of the organic template (latex) by calcination finally generates the macropores. The resulting material possesses a novel catalyst morphology based on macropores functionalised with metal nanoparticles, within a mesoporous silica matrix. Importantly, this approach is waterborne, which limits the environmental impacts of the catalyst preparation.

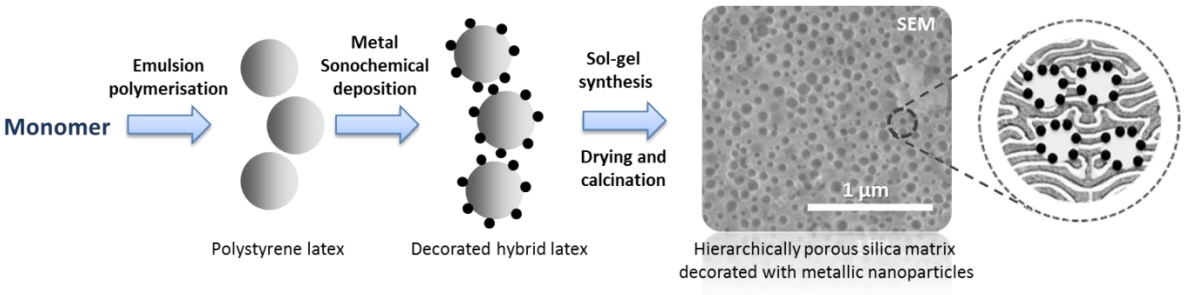

Figure 1 Supported catalyst synthesis by combining emulsion polymerisation, sonochemistry and sol-gel route.

Additionally, this technique offers a versatile toolbox for catalyst tailoring. Indeed, for example, it is possible to consider the macropores decoration with bimetallic nanoparticles prepared sonochemically (Figure 2.a.). Furthermore, the material can also be made of a mixture of empty and decorated macropores by using non-decorated and decorated latex templates to decouple the level of macroporosity and the metal loading (Figure 2.b.). Many other combinations are also possible by playing with the experimental conditions at each step of synthesis reported in Figure 1.

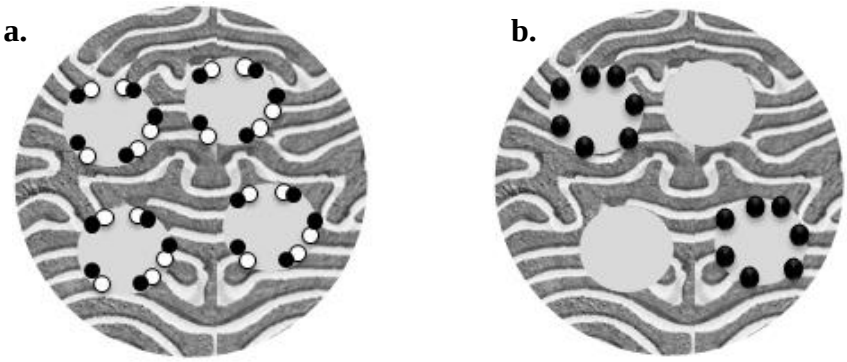

Figure 2. Examples of hierarchically porous materials with: a. Macropores decorated with bimetallic nanoparticles and b. A mixture of empty and decorated macropores.

The strategy to carry out this research project was based on the Research Question: "Is it possible to vary the morphology and catalytic performance of waterborne catalytic materials prepared by the combination of emulsion polymerisation, sonochemistry and sol-gel route by modifying the conditions of any of the preparation step?"

In order to answer this Research Question, the General Objective for this PhD work was to investigate in detail the effect of each preparation step: polymer latex synthesis, sonochemistry and sol-gel, on the catalysts final morphology and the catalytic performances. This general objective was addressed according to three specific objectives based on two selected reactions given their industrial relevance:

- ✓ Synthesise silica-supported platinum catalysts and evaluate them for the selective hydrogenation of *p*-chloronitrobenzene to *p*-chloroaniline.
- ✓ Synthesise silica-supported palladium catalysts and evaluate them for the direct synthesis of hydrogen peroxide from oxygen and hydrogen.
- ✓ Identify relationships between activity and catalyst structure.

Aligned with these objectives, the discussion presented in this manuscript is composed of 5 chapters:

II. State of the art. It includes an overview of the available synthesis pathways for the modulation of the support porosity and catalyst functionalisation.

III. Platinum-based catalysts preparation. This chapter details the catalyst preparation and the effect of several experimental parameters (such as sonochemical reduction conditions, template amount during the sol-gel synthesis and calcination temperature) on the catalyst morphology.

IV. Platinum-based catalysts performance. It presents the catalytic performance of the materials described in Chapter III for the selective hydrogenation of *p*-chloronitrobenzene to *p*-chloroaniline. It discusses the effects of the operation conditions, of the catalyst pre-treatment and of the variation of the macro- and mesoporosity on the catalytic performance.

V. Palladium-based catalysts preparation. It explores the versatility of this synthesis method for tailoring active sites of different nature. So it describes the preparation of hierarchically porous Pd/SiO_2, $Pd\text{-}Pt/SiO_2$ and $Pd\text{-}CeO_2/SiO_2$ materials.

VI. Palladium-based catalysts performance. This chapter presents the catalytic performance of the materials described in Chapter V for the direct synthesis of hydrogen peroxide from oxygen and hydrogen. It discusses the effect of the different type of active sites on the catalyst performance.

VII. General conclusion and perspectives. This concluding section highlights the main findings of this research and proposes new approaches for the continuous improvement of the catalysts performance.

This research project was possible thanks to the participation of several collaborators in 7 laboratories in 4 countries:

- In France :
  - Dr. Patrick Lacroix-Desmazes, MSc. Jennifer Li and Dr. Maël Bathfield at the laboratory "*Ingénierie et Architectures Macromoléculaires*" - *Institut Charles Gerhardt Montpellier*,
  - Prof. André Ayral at the *Institut Européen de Membranes*,
  - Dr. Tony Chave and Dr. Sergey Nikitenko at the *Institut de Chimie Séparative de Marcoule – CEA*, and
  - Prof. Vasile Hulea at the laboratory "*Matériaux Avancés pour la Catalyse et la Santé*" - *Institut Charles Gerhardt Montpellier*.
- In Italy : Prof. Siglinda Perathoner and Dr. Salvatore Abate at *Università di Messina*
- In South Africa : Prof. Patricia J. Kooyman at *University of Cape Town*
- In The Netherlands : Dr. Frans D. Tichelaar at *Delft University of Technology*

Such collaboration was within a European framework of the Sustainable Industrial Chemistry Doctoral Programme (SINCHEM) financed by the European Commission (http://www.sinchem.eu/).

References

[1] S. George, Introduction: heterogeneous catalysis, Chem. Rev. 95 (1995) 475–476. http://pubs.acs.org/doi/abs/10.1021/cr00035a001 (accessed January 15, 2015).

[2] American Chemical Society, Technology Vision 2020 The U.S. Chemical Industry, Washington, DC, 1996. https://energy.gov/sites/prod/files/2013/11/f4/chem_vision.pdf.

[3] C.H. Bartholomew, R.J. Farrauto, Fundamentals of Industrial Catalytic Processes, John Wiley & Sons, Inc., Hoboken, NJ, USA, 2005. doi:10.1002/9780471730071.

[4] T. Muroi, Role of Precious Metal Catalysts, Noble Metals, InTech, 2012.

[5] P.T. Anastas, J.C. Warner, Green Chemistry: Theory and Practice, Oxford University Press, New York, 1998.

[6] M.-O. Coppens, G. Wang, Optimal Design of Hierarchically Structured Porous Catalysts, in: U.S. Ozkan (Ed.), Des. Heterog. Catal., Wiley-VCH Verlag GmbH & Co. KGaA, Weinheim, Germany, 2009: pp. 25–58. doi:10.1002/9783527625321.

[7] 2013 AIChE Annual Meeting, Rational Catalyst Design, (2013). https://aiche.confex.com/aiche/2013/webprogram/Session24747.html (accessed November 15, 2014).

[8] C.M.A. Parlett, M.A. Isaacs, S.K. Beaumont, L.M. Bingham, N.S. Hondow, K. Wilson, A.F. Lee, Spatially orthogonal chemical functionalization of a hierarchical pore network for catalytic cascade reactions, Nat. Mater. 15 (2016) 178–182. doi:10.1038/nmat4478.

[9] A. Corma, From microporous to mesoporous molecular sieve materials and their use in catalysis, Chem. Rev. 97 (1997) 2373–2420. doi:10.1021/cr960406n.

II. STATE OF THE ART

Content

II.1- Introduction

As a pillar of green chemistry, catalysis should keep striving for improving performance, notably by reducing waste (i.e. improving selectivity) and using less resources (i.e. enhancing catalytic activity). However, in addition to developing greener catalytic processes, the preparation of the required catalytic materials should also be itself as green as possible. For

instance, waterborne routes offer an option to reduce environmental impact during the catalysts preparation by avoiding the use of volatile organic compounds (VOCs).

In the search for improving catalytic performances, approaches towards original catalyst design with hierarchically porous structures appear as a promising option to address some of the current challenges that the chemical industry faces. In order to understand such challenges, this chapter will start by giving a quick look at the history of catalysis, followed by a brief overview of current challenges in catalysis and how hierarchically porous materials could be beneficial. Subsequently, the state of the art for porosity modulation will be presented, followed by conventional and advanced techniques for catalyst functionalisation.

II.2- Catalysis, once upon a time…

Without taking into account wine and beer production, the first catalytic process ever developed was the sulfuric acid production catalysed by a lead chamber in 1746 [1]. Nevertheless, the first descriptions of the concept of catalysis were made at the end of the XVIII century by Elizabeth Fulhame in her book "An essay on combustion (…)" in 1794 [2,3]. A few years later, in 1835, Jöns Jakos Berzelius used the term *catalysis* to describe the acceleration of a reaction by a substance that remained unchanged at the end [4]. Since then, the growth of the chemical industry has been strongly related to the development of catalytic processes, being present today in about 90% of all chemical industrial processes [5].

Currently, catalysis is defined by The International Union of Pure and Applied Chemistry (IUPAC) as the process in which a substance (the catalyst) increases the rate of the reaction without modifying the overall standard Gibbs energy change in the reaction. It is important to note that the catalyst is both a reactant and product of the reaction, meaning that the catalyst is restored after each catalytic cycle. IUPAC also classifies catalysis within two categories: homogeneous catalysis, in which only one phase is involved; and heterogeneous catalysis, in which the reaction occurs at or near an interface between phases (*e.g.* solid-liquid). Notably, heterogeneous systems with solid catalysts present several advantages over homogeneous catalysts, such as the ease of catalyst separation from the reaction medium, recyclability and stability [6].

The practical basis for heterogeneous catalyst design started with the development of catalytic processes for the production of sulphuric acid and ammonia. Regarding the ammonia synthesis, it is the result of the theoretical and experimental work of Haber, Ostwald and Nernst, whose research allowed the thermodynamic understanding of the reaction and permitted the development of its catalytic production at the industrial scale. In 1910, Haber started to collaborate with Carl Bosch at BASF, who implemented a comprehensive catalyst testing program leading to *ca.* 20.000 catalytic tests and several industrial plants operating by 1922. Such theoretical and experimental effort set a precedent for catalyst development [7].

Regarding the history of the contact process for sulfuric acid synthesis, it accounts with the protection of several developments by a number of inventors: in 1831, Peregrine Philips patented a process to produce sulphur trioxide with a platinum catalyst [8], in 1846, Jullion claimed an asbestos-supported platinum catalyst for this and other reactions [9] and in 1853, Hunt patented the use of silica as a catalyst support [10]. Later, in 1898, BASF developed

platinised asbestos by impregnation, and since then other platinum- and vanadium-based catalysts have been developed in the research of overcoming several challenges such as catalyst activity, poisoning, pressure drop increase due to catalyst disintegration, catalyst operation life and cost [7].

All these studies in catalysis were somehow influenced by the boom of formal discoveries of new elements at the end of the XVIII and during the XIX centuries. Platinum traces have been found in Egyptian artefacts and enriched-platinum alloys have been discovered in the ancient Incas' territories in Ecuador [11]. Nevertheless, platinum metal was first formally described in 1748 by Antonio de Ulloa in his report of voyage to South America [12]. When passing by Popayán (a city in the south of Colombia), he learnt about the existence of a metallic impurity in gold, which was very abundant in the gold mines of Chocó (currently a Colombian province limiting with Panamá). He named it *Platina*. Its extraction was forbidden by the Spanish government since it was used to falsify coins due to its difficult isolation form gold. In 1749, W. Watson and W. Brownrigg published their very early studies on the properties of this element very much unknown at that time [13]. In 1786, Pierre-François Cabaneau - a French chemist - developed a method for purifying platinum that encouraged the Spanish monarchy to establish a monopoly for platinum extraction. With analytical techniques to identify illegal platinum alloys, scientists then dedicated some attention to study the properties of this new metal [14]. In 1802, William Hyde Wollaston discovered palladium when trying to purify platinum from an ore coming from South Africa. This new metal exhibited similar chemical properties as platinum, but with lower melting point and lower density. Based on these observations, the Irish chemist Richard Chenevix questioned the discovery by saying that it was just an alloy of platinum and mercury. However, after some controversy, it was proven that palladium was correctly a new element [15]. In 1817, Humphry Davy discovered the catalytic use of platinum and palladium when experimenting with the combustion of gaseous mixtures [16,17].

At the end of the XIX century, most of the developments in catalysis were based on empirical discoveries, like the alkali-enhancement of vanadium pentoxide catalysts reported by Slama and Wolf [18]. Nevertheless, rational catalyst design can be tracked back to 1868 with the Deacon process that included the development of copper chloride catalyst especially selected for the production of chlorine [19]. It constitutes an early example of logical catalyst selection instead of empirical discovery [7]. Nowadays, it is well understood that humankind needs to develop more sustainable catalytic processes to keep delivering comfort, but being responsible with the environment. In 1998, P. Anastas and J. Warner developed the 12 Principles of Green Chemistry as an early conception of what would make a greener chemical, process, or product [20]. Later, P. Anastas and J. Zimmerman also presented the 12 Principles of Green Engineering outlining what would make a greener chemical process or product [21]. In those principles, catalysis is an important axis to reduce waste, energy consumption, use of resources, etc. And several of the challenges that arise nowadays in terms of economy, energy and environment protection are expected to be overcome with further developments in catalysis, but not with trial-and-error approaches; instead rational thinking has been adopted to design performant catalysts and optimise processes [22,23].

II.3- Current challenges in catalysis

The development of sustainable catalytic processes must keep the link with the market needs. In this sense, new approaches to do applied research like information mining will undoubtedly be useful to tackle scientific challenges in synergy between industry and academia [24]. In this section, a short market analysis with the opportunities and scientific challenges in catalysis is given.

II.3.1- Market analysis and perspectives of development

Regarding macroeconomics trends, the global catalyst market reached USD 23.2 billion and nearly USD 24.6 billion in 2013 and 2014, respectively. It is forecast to reach USD 29.9 billion by 2019 [25] and USD 34.3 billion by 2024 [26]. Within this market, four segments can be differentiated depending on the industrial application: environment, petroleum refining, petrochemicals and polymers, and chemical synthesis (Figure 3) [27]. Particularly, catalysts for environmental applications are expected to witness the fastest volume growth at 4.4% annual from 2016 to 2024. Such forecast is due to the increasing adoption of catalysts for environmental remediation processes including industrial and municipal waste treatment and vehicle emission control systems [26].

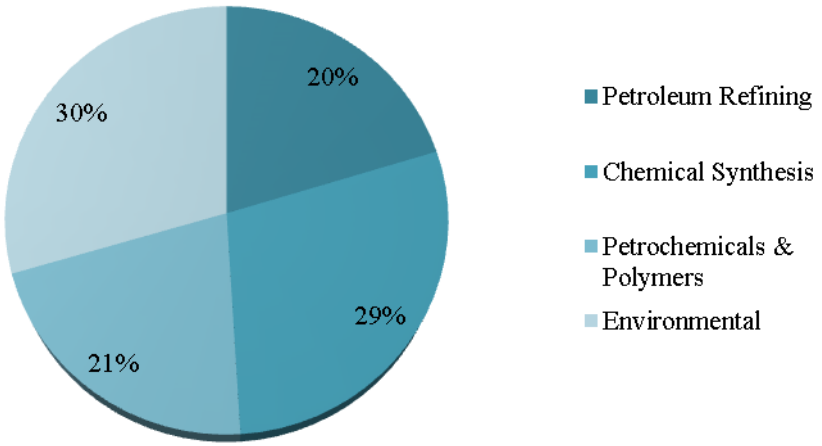

Figure 3. Catalyst market segments in 2015. Based on [28]

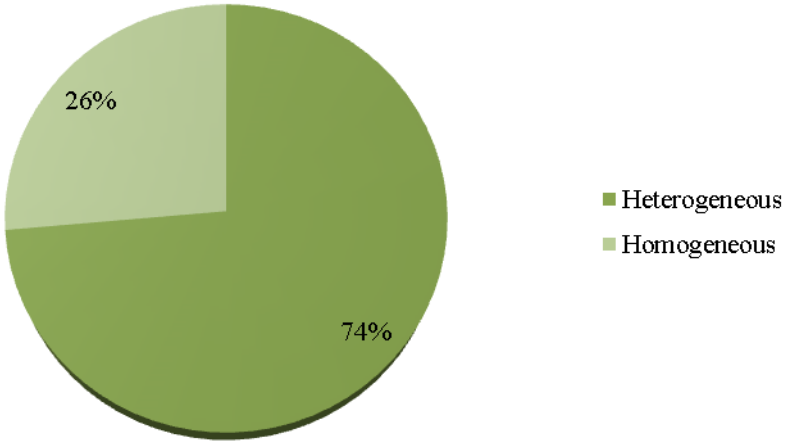

Figure 4. Global market demand by catalyst type in 2015. Based on [28]

In 2015, heterogeneous catalysts were used extensively accounting for 73.6% of the global market volume (Figure 4). Low price and easy market access of heterogeneous products are expected to remain favourable factors over the next seven years. In particular, the metal catalysts demand was 1,568.4 kilo tons in 2015 and is expected to grow in light of its increasing application in the organic synthesis of chemicals commodities including ammonia. Other relevant applications of metal catalysts (based on Ni, Cu, Cr, Mb, Pd, Pt, Au, Ru, Rh) are chemical processing, refining, and polymer production. The demand of zeolite-based catalysts is also expected to increase on account of its properties such as high porosity and adjustable acidity [26].

Some of the key global catalyst producers are Zeolyst International, Inc, W.R Grace & Co-Conn, UOP LLC, Johnson Matthey PLC, INEOS Group Limited, E.I. du Pont de Nemours & Company, Evonik Industries AG, Exxon Mobil Corporation, Eka Chemicals AB, Clariant International Ltd, Chevron, BASF SE, Arkema Group, AXENS/IFPEN, Albemarle Corporation and Air Products and Chemicals Incorporated [29].

In industry, the use of catalysts is economically attractive because it costs much less than 1% of the sales revenue from the products which they help create [27,30], and also because the implementation of catalytic processes and the improvement of current catalysts can significantly reduce energy consumption and greenhouse gas emissions [31]. Some of the top opportunities for sustainable catalytic processes are:

- Sustainable energy sources as well as storage and efficient use of energy: as an example, hydrogen is a promising clean fuel [32]. However, it is mainly produced by catalytic steam reforming, which coproduces CO_2. So other economically competitive and efficient catalytic developments are imperative [33,34]. Photocatalysis is a promising option to make hydrogen out of water, but efficient catalysts must be developed yet [35,36]. The hydrogen storage is another aspect that requires further developments [37]. Biofuels produced from biomass transformation are another possibility of renewable energy source. However, the catalytic transformation of the raw feedstock into useful chemicals is still challenging [38–40].
- Environment preservation: some of the challenges are solid and liquid waste reduction and treatment, reduction of environmental impact of the use and disposal of catalysts,

development of more energy-efficient processes pointing to reduce greenhouse gases release, control of indoor pollution and reduction of the environmental impact of transport [41]. For the later, the automobile exhaust catalysts is a successful example of catalyst development for environmental remediation [42].

- Valorisation of carbon dioxide: CO_2 can be captured and transformed into synthesis gas (syngas), methanol [43] or other high value chemicals [44]. However the limitation is based on the thermodynamics stability of CO_2, that in principle could be overcome by kinetics [23].
- Speciality chemicals: most of them are currently produced in homogenous systems, but they constitute a big area of interest for heterogeneous processes with solid catalysts, due to the ease of handling and reuse of such catalytic materials. The challenge is the selectivity, because for instance, chemicals for pharmaceutical applications require very often enantioselectivity that is not easily achievable with solid catalysts. However, hybrid systems, including anchored organic moieties on inorganic supports could offer a suitable solution [23,45].
- These new challenges appear in addition to old catalytic processes still requiring further development. For instance, the production of chemical commodities like ammonia and hydrogen peroxide must be priority in the agenda: ammonia production is currently the industrial process that consumes more energy (2.5 EJ in 2010) and releases more greenhouse gases (350 $MtCO_2$-eq in 2010) than any other large volume chemicals [31] and hydrogen peroxide production process has low efficiency, high energy consumption and produces considerable amounts of waste [46]. Epoxidation reactions for olefins other than ethylene [47] or the selective partial oxidation of hydrocarbons [48] are also processes with great potential for new developments. Additionally, well-established catalytic reactions are still object of research to improve the catalysts and therefor the process performances, some of them are hydrogenation, hydrocracking, reforming of hydrocarbons, fuels synthesis, nitrogen processing and fixation [23].

II.3.2- Heterogeneous catalyst: a challenge in itself

The ultimate challenge in heterogeneous catalysis is to understand the fundamental basis of the molecular interactions of the reaction medium (liquid or gas) with the solid catalyst, and then use the available synthesis techniques to design and prepare the catalyst architectures in order to drive the reactions to form selectively the desired product [45]. Indeed, heterogeneous catalysis is a complex process that involves several phenomena: mass transport, sorption and chemical reaction. Each one of them provides an opportunity to improve the catalyst performance. Considering a porous solid catalyst, nine stages can be recognised in a catalytic process as shown in Figure 5 [49,50]:

1. Reactants mass transport towards the solid: the reagents have to arrive from the bulk to the solid boundary layer.
2. Reactants diffusion from the fluid phase (liquid or gas) through the boundary layer adjacent to the external surface of the catalyst.
3. Reactants diffusion through the pores within the catalyst from the outer surface towards the active sites.

4. Reactants adsorption on the inner surface.
5. Chemical reaction at the active sites.
6. Desorption of the reaction products from the inner surface.
7. Products diffusion through the pores towards the outer surface of the solid.
8. Products diffusion through the boundary layer into the bulk fluid phase.
9. Product transport within the reaction medium.

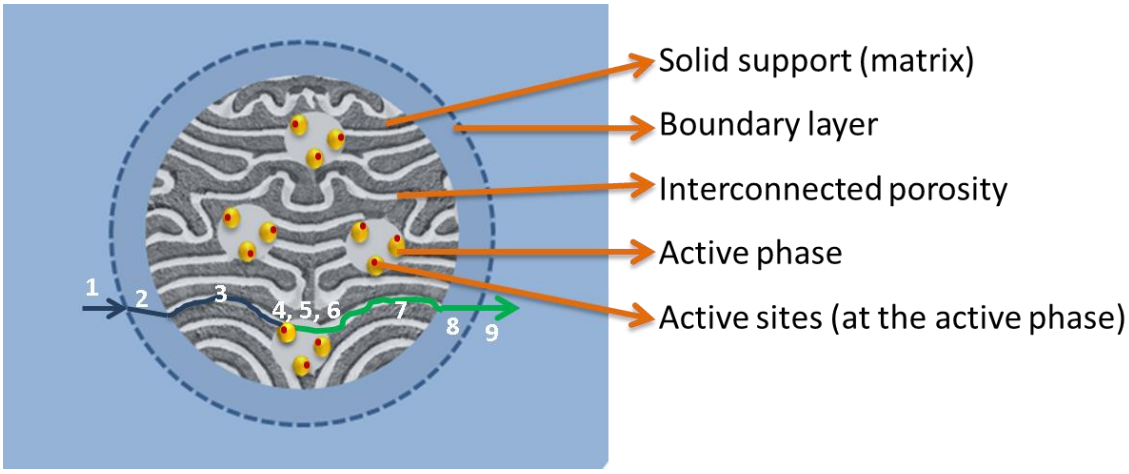

Figure 5. Main steps involved in heterogeneous catalysis

It is also important to consider that heterogeneous catalysis takes place in a multiscale process, since the chemical transformations occur at the nanometric scale, but the catalyst grains and shaped structures range from micrometres to centimetres, and still the reactor size can reach a few meters in size. All this complexity motivates the catalyst development from a rational design perspective directed to achieve better selectivity, enhance productivity and operate at milder conditions. To do so from the point of view of the catalyst preparation, several tools have become available including active particle size, shape tuning, inclusion of multiple catalytic functionalities and three-dimensional porous support architecture.

Typically, heterogeneous catalysts are based on oxides of transition metal or lanthanides with multiple valences, noble metals, nickel, cobalt, iron, silico-aluminates or alkaline earth mixed oxides [27]. In general, two main routes for the catalysts preparation can be distinguished: the first is when the catalytically active phase is generated as a new solid phase (by precipitation or a decomposition reaction), and the second is when the active phase is introduced and fixed onto a pre-existing solid (by impregnation, for instance)[51].

From the macroscopic point of view, the shaping procedure for a support or an intrinsically active catalyst depends on the set-up where it will be used. In that regard, four types of reactors can be highlighted: fixed-bed, moving-bed, fluidised-bed and monolithic (Figure 6). In the fixed-bed, grains, balls or other shapes of few millimetres or centimetres are immobilised, while the reaction medium flows through (very small particles can lead to high-pressure drop). Moving-beds require millimetric beads of a homogenous size in order guarantee a homogeneous counter-current flow of catalyst particles against the reaction medium that goes through the bed.

Fluidised-beds use porous grains of sub-millimetric size, and takes advantage of vigorous fluid-solid contact favoured by the use of small catalyst particles [27,52]. Finally, the monolithic reactor has contacting patterns such as honeycomb or sponge-like that lead to low-pressure drop and high flow rates[53].

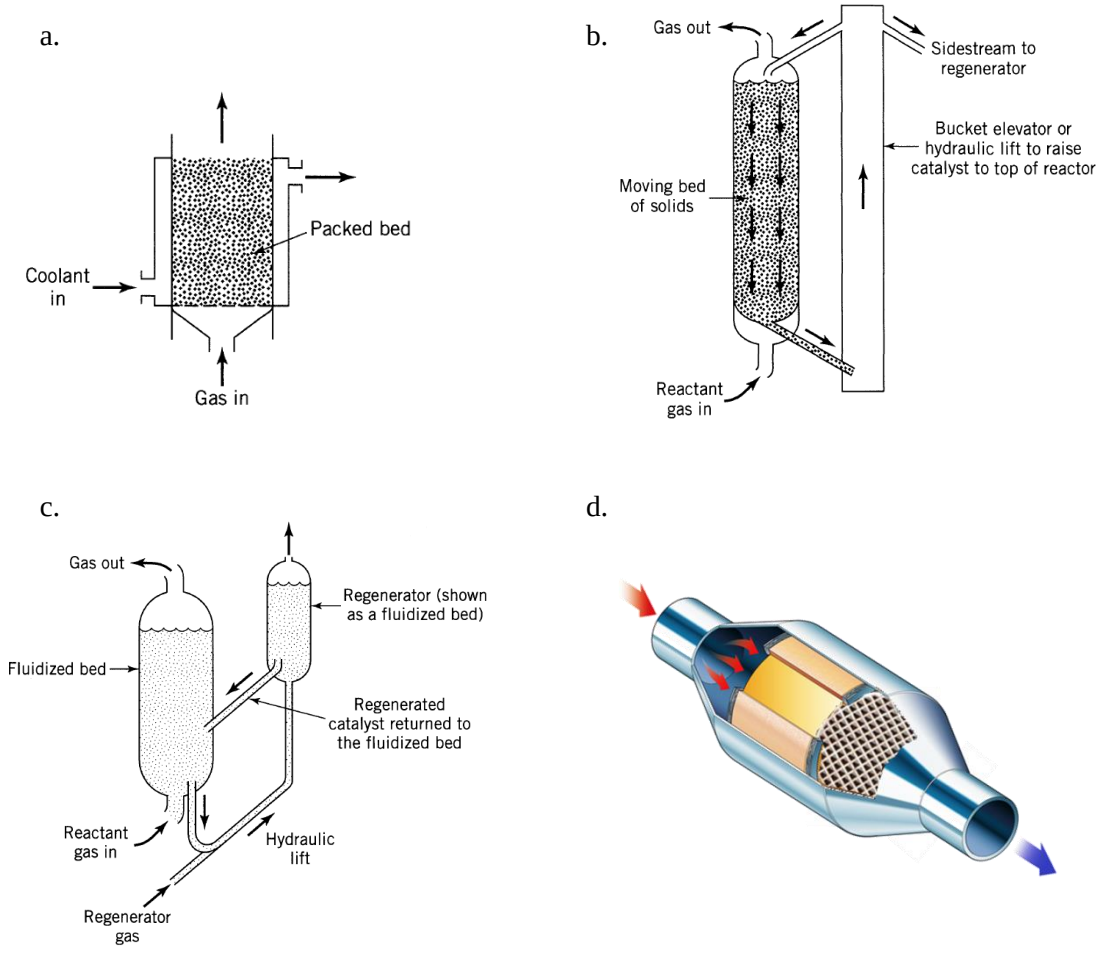

Figure 6. Representation of: a. Fixed-bed reactor, b. Moving-bed reactor, c. Fluidised-bed reactor [52]. and d. Monolithic reactor (based on [54]).

In general, porous grains of sub-millimetric size can be prepared by pulverisation of sols and subsequent thermal or chemical gelification. Millimetric beads of a homogenous size can be prepared by drop-coagulation of a sol suspended in another liquid phase. Larger grains can be prepared by granulation that consists of the agglomeration of wet powders. Other specific shapes can be achieved via pelletizing by compressing a dry powder. Extrusion of mineral pastes can also be used for the preparation of monoliths or cylindrical shapes [27,55].

From the microscopic point of view, the architecture of the catalyst structure should also be carefully considered, since the catalyst porosity and active sites distribution have important effects on the catalyst performance. For instance, zeolites have the advantage of possessing small pores that act as molecular sieves for reactant selection before reaching the active site. As a consequence, the small pore size enhances the selectivity [45], but it also limits the mass transfer, reducing the catalyst performance [56,57]. Moreover, larger pores than those obtained with zeolites are also important for applications with larger molecules like cellulose or proteins [58]. In order to conciliate selectivity, optimal mass transfer phenomena and overall catalyst performance, a hierarchically porous structured material is proposed to offer the optimal catalyst structure required for a given reaction.

In general, a catalyst structure with hierarchical porosity combines pores of different sizes (micropores smaller than 2.0 nm, mesopores between 2.0 and 50.0 nm and macropores larger than 50.0 nm, according to IUPAC classification). The homogeneous distribution of such pores within the material is also a key parameter in order to obtain better diffusion within the catalyst [22]. In fact, when the diffusion is the controlling step of the overall reaction, improvements at the active sites would not significantly increase the catalyst performance. Instead, the mass transport within the material becomes of major concern for catalyst improvement. This is where the modulation of internal porosity and pore interconnectivity plays an important role in catalyst design.

II.4- Synthesis pathways for preparing catalysts with specific/innovative/original designs

Hierarchical structured porous materials have a large range of applications including life science for biomaterials and drug delivery, energy for sensors, fuel cells, supercapacitors and batteries, separation and adsorption used for instance in bioreactors and DNA purifiers and catalysis and photocatalysis [59,60].

Rational design of hierarchical porosity of catalytic material has been studied for achieving a specific tailoring based on the application requirements [61]. Concerning the porosity, especially in silica-based materials, sol-gel methods are suitable for obtaining micro- and mesoporous materials [62,63]. Such technique could also be environmentally friendly since water can be used without co-solvent as reaction medium along the preparation steps [64]. Nevertheless, in the last three decades, there has been a large development of other approaches that allow achieving tailored hierarchically porous materials.

II.4.1- Modulation of the support porosity

Regarding the development of mesoporous materials, in the early 90's, the Mobile Company marked an important step in the preparation of ceramic materials with controlled porosity when they reported the family of MCM (Mobile Composition of Matters) [65,66]. Even though, at

that time, there were already some methods to obtained disordered mesoporous structures like silica under controlled sol-gel processes [67] or modified layered materials [68], that development was a breakthrough because it presented the preparation of ordered mesoporous materials by polymerising a silica source around an organic liquid crystal template of quaternary ammonium surfactants. Since then, a large interest has grown in the preparation of a variety of structures using a diversity of preparation techniques giving rise to porous channels or entrapped pores [69].

Porous channels act as highways for the transport of molecules from the solution towards the active sites within the solid, or out of it in the case of products [22]. On the other hand, in the presence of entrapped pores, the cut-off of the material is determined by the porosity of the oxide walls [70]. Nevertheless, they increase the material's permeability, reducing the mass transport resistance throughout the solid. Rigby and co-workers demonstrated that empty macropores can reduce the total mass transport resistance by about half compared to only mesoporous material [71]. They proposed a simple unit cell model for mass transport resistance in a macroporous structure, as shown in Figure 7, where R is the resistance to diffusive flux through the mesoporous wall from the neighboring cell to the macropore, r it the resistance to diffusive flux through the macropore, and the resistance for going through the mesoporous material around the macropore is also of size R. The total resistance R_{Tot} is then given by:

$$R_{Tot} = R + \left[\left(\frac{1}{R}\right) + \left(\frac{1}{r}\right)\right]^{-1}$$

So in the limiting case that the resistance through the macropore is zero ($r = 0$), $R_{Tot} = R$. But in a second limiting case, if an infinite resistance through the macropore is supposed ($r = \infty$), $R_{Tot} = 2R$, which means that the flux would only go through the mesoporous material. The reality is very close to the first limiting case, since the macropore is empty, meaning that the presence of macropores strongly reduces the resistance to diffusive flux through the material in comparison with an only-mesoporous matrix.

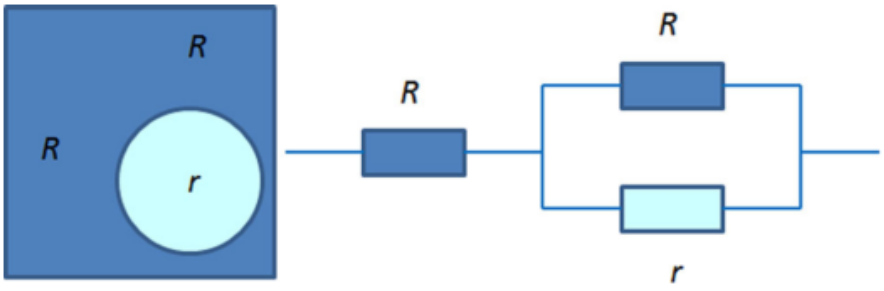

Figure 7. Simple unit cell model for mass transport resistance in a macroporous structure. Light shade circle corresponds to a macropore and dark-shaded area corresponds to the mesoporous support [71].

Nanoporous materials can be classified in three categories depending on the framework building blocks: purely inorganic, purely organic and hybrid organic-inorganic. The purely inorganic materials include pure and metal-doped silica, metal oxides, mixed oxides, metal phosphates and porous carbons. The purely organic classification comprises materials such as organic porous polymers. And the hybrid organic-inorganic category is formed by materials such as periodic mesoporous organosilica (PMO), metal oxophenylphosphate and metal organic frameworks (MOF) [72]. Even though there are general preparation methods, each nanoporous material is prepared by specific synthesis protocols [72,73]. The following subsections will focus on the preparation of inorganic materials by various techniques. Additionally, some examples of nanoporous materials with catalysis application will be described.

II.4.1.1- Matrix porosity tailoring by sol-gel synthesis

Typically, the sol-gel method consists of the polymerisation of monomeric alkoxide precursors, for instance tetraethylorthosilicate (TEOS) is used in the preparation of silica. Initially, a sol is formed (homogeneous dispersion of polymeric clusters or suspension of solid nanoparticles in the reaction medium) and then it becomes a gel by intricate linkage between the clusters of nanoparticles. When using alkoxide precursor, especially silicon alkoxides, two distinctive reactions are observed in such polymerisation: hydrolysis and condensation (Figure 8). The hydrolysis is characterised by the nucleophilic attack of the oxygen atom of a water molecule releasing an alcohol and forming a silanol group (-SiOH). On the other hand, condensation can be of two types: oxolation (or water condensation) and alkoxolation (or alcohol condensation). In the first, the reaction between two silanols (-SiOH) leads to siloxane bridges (Si-O-Si) releasing a water molecule, and in the second, the reaction between a silanol (-SiOH) and an alkoxysilane (-SiOR) leads to siloxane bridges releasing an alcohol molecule.

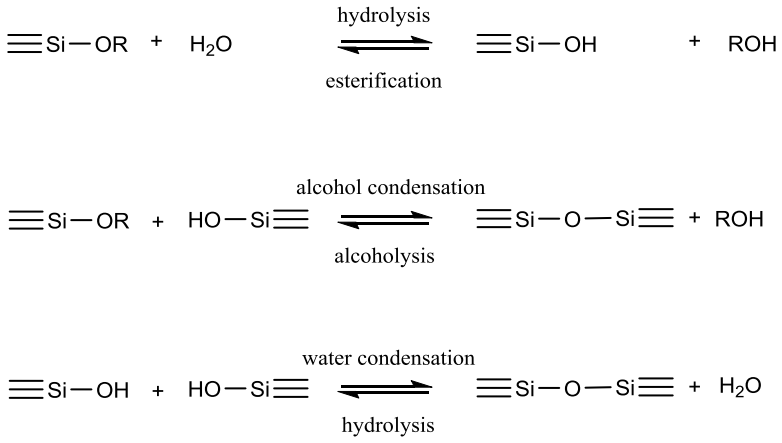

Figure 8. Silicon alkoxide hydrolysis and condensation reactions [74].

Regarding the mechanisms of these reactions, they depend on whether the reactions are acid- or base-catalysed, as follows [74,75]:

Acid-catalysed hydrolysis:

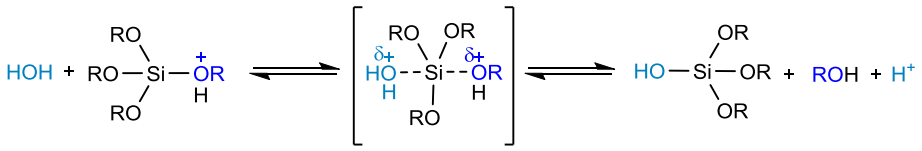

Acid-catalysed condensation:

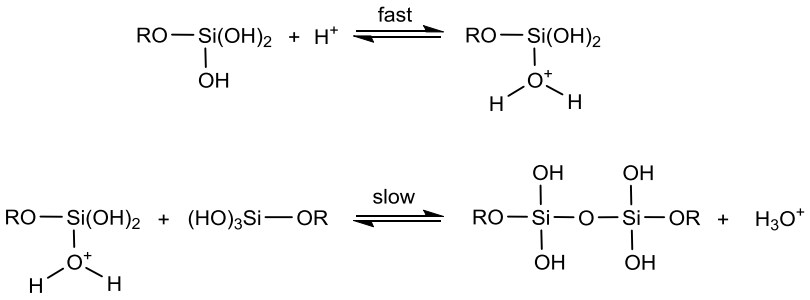

Base-catalysed hydrolysis:

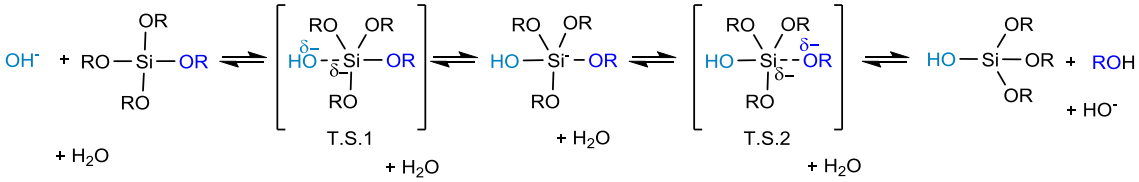

Base-catalysed condensation:

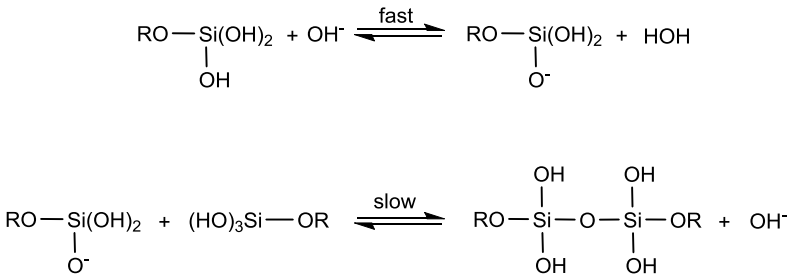

Figure 9. Hydrolysis and condensation reaction mechanisms depending on pH

In addition to a distinctive reaction mechanism, the morphology of the material also changes depending on the pH [74]. As shown in Figure 10, at acidic pH, the network growth is favoured by the formation of linear molecules occasionally cross-linked. On the other hand, at basic pH (Figure 11), the polymerisation of highly branched clusters is favoured, which are then linked to form a gel [75]. After solvent removal by evaporation, the resulting material is called a xerogel.

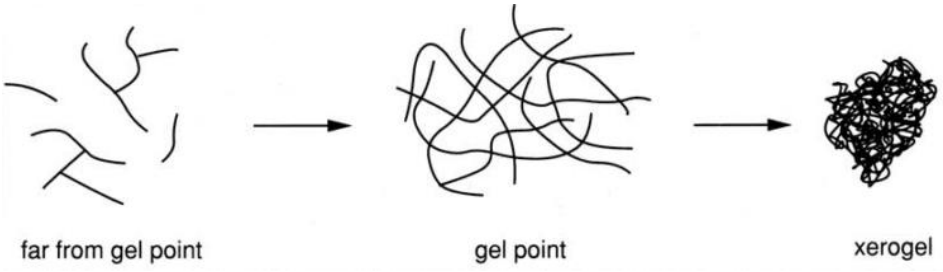

Figure 10. Typical structure at acidic hydrolysis conditions [75].

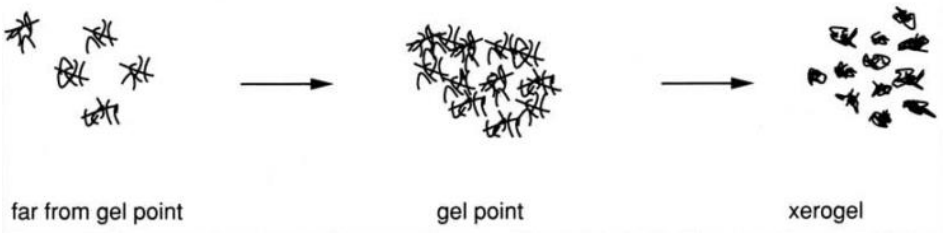

Figure 11. Typical structure at basic hydrolysis conditions [75].

Furthermore, the hydrolysis ratio *h* (water/alkoxide molar ration) also defines the morphology of the final material. For low values of *h*, linear polymers are favoured, while at high values of *h*, dense clusters are formed, as shown on Figure 12 [76]. Thus weakly cross-linked polymeric networks are favoured at acidic pH and low *h* values, while highly branched colloidal particles are favoured at basic pH and high *h* values [74].

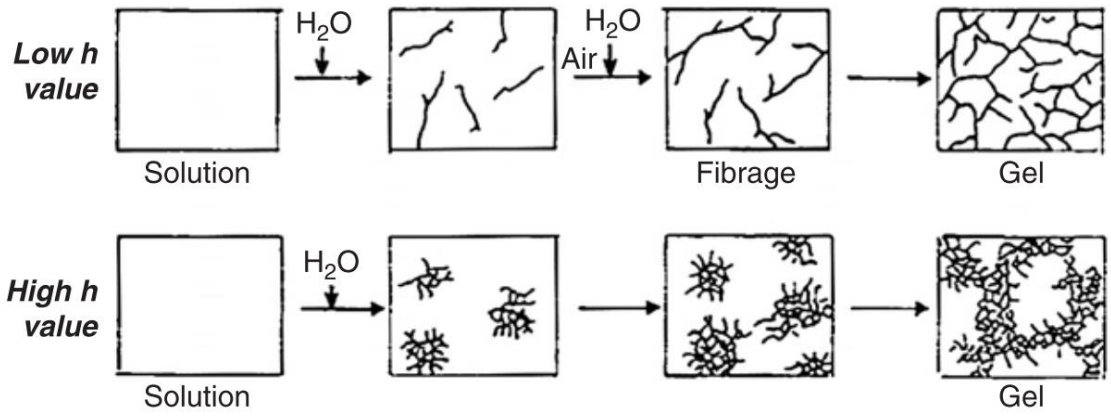

Figure 12. Effect of the hydrolysis ratio on the gel structure [76].

The corresponding xerogels are the resulting solids after solvent evaporation, which are compressed by the effect of capillary forces during solvent removal. The resulting porosity

depends on the strength of the gel network to resist the compressive forces of surface tension. The porosity can be reinforced by selecting appropriate sol-gel conditions that lead to a reinforced network. Table 1 presents the texture characteristics of xerogels prepared by varying the *h* and/or the pH in one or two steps. The two-step acid-base catalysed sol-gel synthesis has been reported to lead to mesoporous silica with pore diameters between 1 and 10 nm. It consisted of an initial stage at low pH and low *h* to favour the TEOS hydrolysis forming a low cross-linked polymeric network and then, the pH was increased in order to favour the condensation of the reinforcement of the silica by favouring the branching of the initial network. Even though, the resulting material was amorphous and the porosity was not ordered, this kind of material exhibited high porosity and large surface areas as shown in Table 1.

Table 1. Textural characterisation of xerogels using different sol-gel conditions [67].

Sol-gel method	$h_{\text{first step}}$	$h_{\text{second step}}$	Porosity (%)	Pore diameter (nm)	Specific surface area (m^2/g)
One-step base catalysed	2.3	-	70	1-20	515
Two-step acid catalysed	1.1	5.0	54	1-5	740
Two-step acid-base catalysed	1.1	3.8	67	1-10	910

In order to avoid the capillary effects of solvent evaporation on the structure, supercritical drying and freeze drying are some of the alternatives. In the case of supercritical drying, the wet gel is put into a high-pressure vessel that is then loaded with a supercritical fluid like carbon dioxide. The reactor is then flushed at a supercritical condition in such a way and for long enough time that the initial solvent is completely removed from the material. Finally, the supercritical fluid is changed to gas phase without passing by the liquid phase, so the solid-liquid interfaces that generate the capillary shrinkage are avoided. The resulting material is called an aerogel. In the case of freeze-drying, once the gel is formed, it is cooled down, for instance with liquid nitrogen or a cooling bath like isopropanol plus solid carbon dioxide. Then, it is put under vacuum. The solvent that at that moment is in solid form will sublimate without generating capillary forces due to the suppression of solid-liquid interfaces. Unlike supercritical drying, monoliths are not possible with this method, since the solvent crystals formed during the cooling down step fracture the gel. Only flake-like structures can be obtained [67].

II.4.1.2- Matrix porosity tailoring by template-based methods

Template is the term to refer to a pattern used in sewing or graphic arts to replicate shapes or designs. In material science, the word template denotes a material used to generate porosity within a matrix. During its formation, the matrix nucleates and grows embedding the template. Subsequently, the template is removed, revealing in the matrix the porosity induced by the geometry of the templating structure. In the case of ceramic matrices produced by sol-gel processes, their porosity can be controlled by two approaches: either the precursors are compounds with alkoxide-like structure containing a templating molecule, or the templating

molecule or nanoparticle (not chemically bonded to the sol-gel precursors) is enclosed during the sol-gel synthesis [76]. This study will focus on the latter, which also has two types: soft and hard templating. The soft templating (also known as endotemplate method) refers to supramolecular entities like self-assembled arrangements of structure directing molecules like surfactants. The hard templating (also known as exotemplate method) implies the use of a solid material such as polymers, silica and carbon [72].

II.4.1.2.i- Soft templating

The preparation of mesoporous materials by the soft templating approach includes the use of molecules known as structure directing agents (SDA), typically in the form of lyotropic liquid crystals. Liquid-crystal state is a mesomorphous state and it is considered the fourth phase state of the matter that takes place in between the crystalline and the liquid states. Liquid crystals can be of two types: thermotropic and lyotropic. The first corresponds to substances that transit to the liquid-crystal state when increasing the temperature. The second corresponds to substances that form a liquid-crystal phase when dissolved in water or other solvents within a certain range of concentration. The characteristic of liquid crystals is that the molecules arrange in an anisotropic manner, forming diverse structures [77].

Typically, lyotropic liquid crystal phases are formed by amphiphilic molecules, which are compounds with both hydrophobic and hydrophilic regions within the same molecule. In water, such molecules migrate to the interphase water-air and arrange in such a way that the polar part of the molecule interacts with the water and the non-polar part faces the air. As a consequence, these molecules reduce the surface tension by reducing the number of water molecules at the interface that are otherwise subject of unbalanced cohesive forces. This is why these compounds are known as surfactants or "surface-active" molecules. When the surface (water-air) is crowded with surfactant molecules and more surfactant is added to the system, the extra molecules must self-assemble in micelles. This concentration is known as Critical Micelle Concentration (CMC). Micelles are clusters in which the hydrophilic part faces the water and the hydrophobic part faces the interior of the cluster. Depending on the concentration of surfactant in the medium, they can form diverse structures as shown in Figure 13 [72,78].

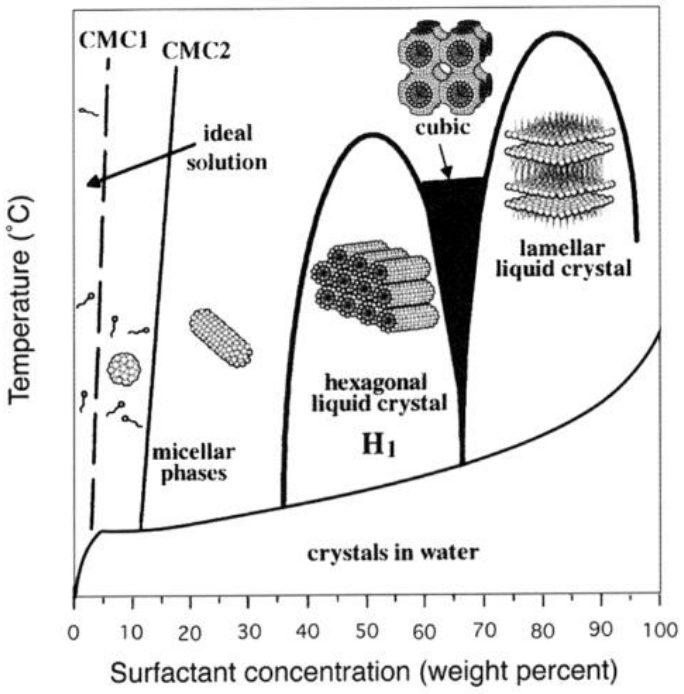

Figure 13. Schematic phase diagram of cetyltrimethylammonium bromide (CTAB) in water [78].

At high surfactant concentration, the water can be entrapped within reverse micelles (with the hydrophobic part facing out of the micelle). Other structures like reverse bicontinuous cubic structures have also been observed experimentally, as illustrated in Figure 14.

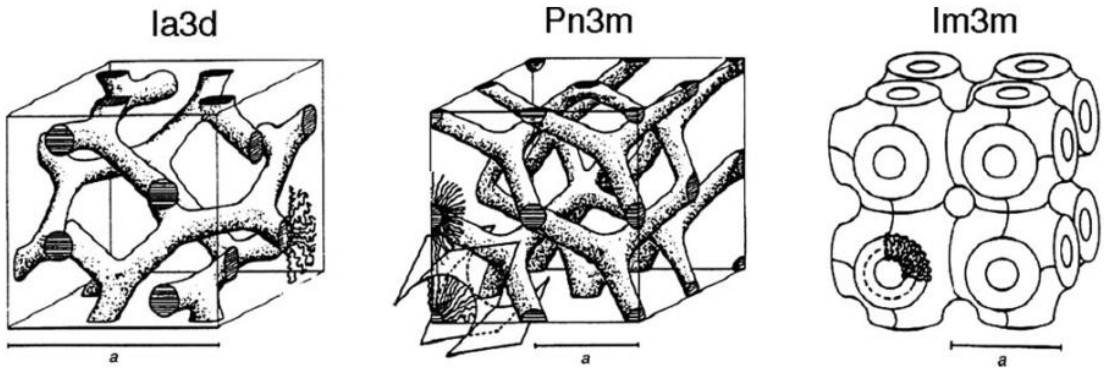

Figure 14. Reversed bicontinuous cubic phases [79].

The liquid crystal phase can also be influenced by the surfactant molecular structure in such a way that the preferred self-assembled structure would be spheres, cylinders, bilayers or inversed structures [80]. It is rationalised using the critical packing parameter as a geometrical

relationship between the hydrophobic and the hydrophilic regions ($CPP = v / a_0 l_c$, being v the volume of the molecule, a_0 the area of the head and l_c the length of the tail) [81,82]. The effect of CPP on the preferred structure is summarised in Figure 15. The liquid crystal engineering by tailoring the amphiphilic molecule geometry has been reviewed [83], reporting the achievement of a controlled and wide variety of normal and reversed phases in the mesophase structures.

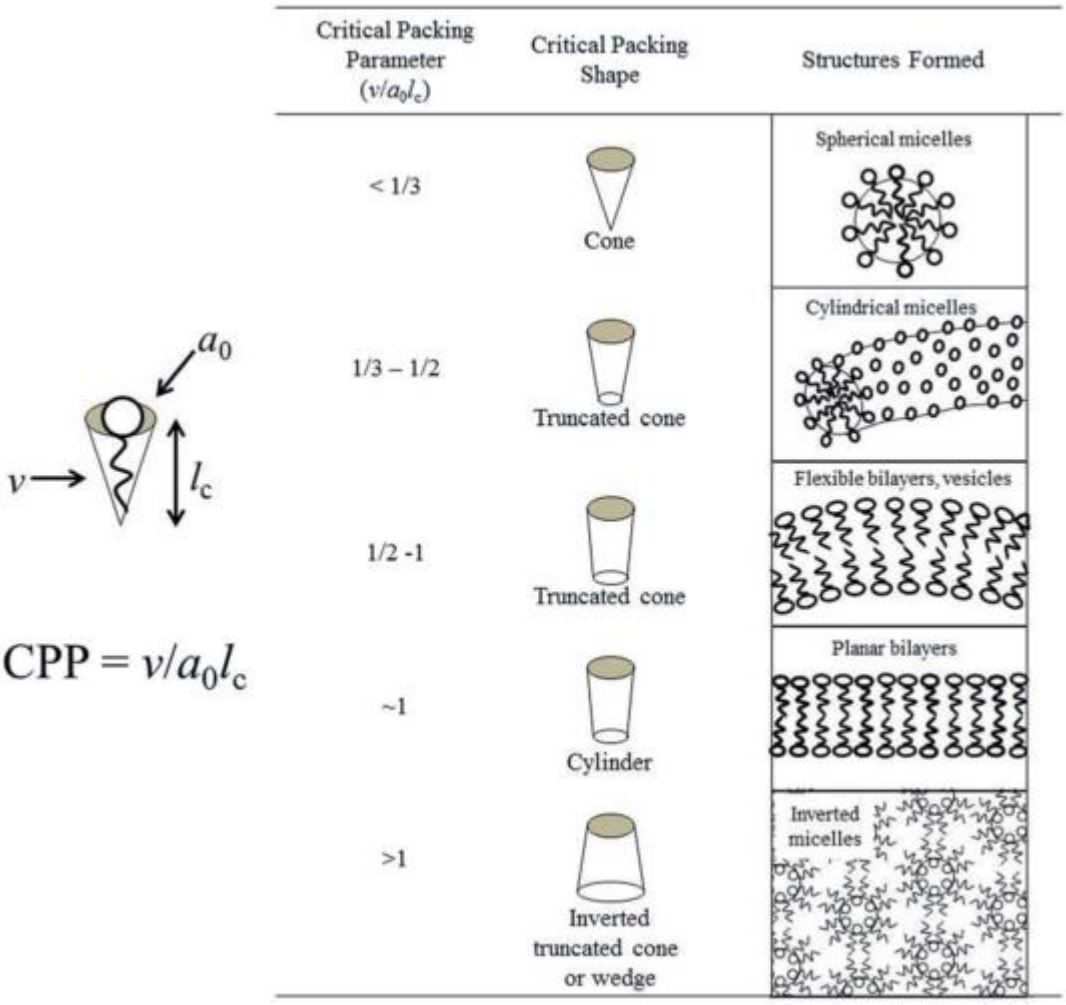

Figure 15. Effect of the critical packing parameter on the mesomorphous structure [84].

In terms of chemical structure, surfactants can be classified as non-ionic, anionic, cationic and amphoteric (or zwitterionic) [72]. The non-ionic surfactants contain a hydrophilic part that does not ionise in water like alcohol, ether, ester, amide, etc. A common example is Pluronic P123, which is a tri-block copolymer surfactant formed by two blocks of poly(ethylene oxide) as hydrophilic part and one block of poly(propylene oxide) as hydrophobic part, as depicted in Figure 16 [85]. Anionic surfactants are amphiphilic molecules in which the hydrophilic part in an anion, which dissociates from its cation in water. The hydrophilic anion can include function groups such as carboxylates (RCO_2^-), sulphates (RSO_4^-), sulfonates (RSO_3^-) and phosphates

($R_1PO_4^-$ R_2). On the other hand, the corresponding cation is usually potassium, sodium or quaternary ammonium ion. Sodium dodecyl sulphate (SDS) and sodium dodecylbenzene sulfonate (SDBS) are examples of widely used anionic surfactants [72,86,87]. Contrarily, cationic surfactants have a cation as hydrophilic part of the amphiphilic molecule, which dissociates from the corresponding anion in solution. Typically, amines or quaternary ammonium ions (RNH_3^+) belong to this category. Cetylpyridinium chloride (CPC) and cetyltrimethylammonium bromide (CTAB) are common examples of cationic surfactants [72,88,89]. Finally, amphoteric also known as zwitterionic surfactants have a hydrophilic part containing both dissociated cation and anion. Natural amino acids and phospholipids belong to this category [90]. Lauryl betaines and dodecyl betaines are a few common examples of amphoteric surfactants [63,72,91].

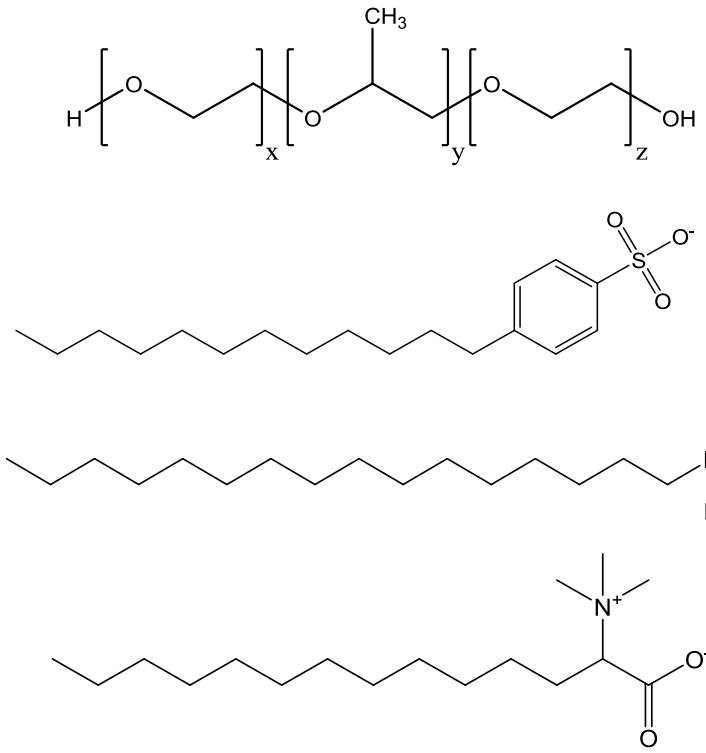

Non-ionic surfactant: Pluronic® P-123. IUPAC name: Poly(ethylene glycol)-*block*-poly(propylene glycol)-*block*- poly(ethylene glycol).

Anionic surfactant: sodium dodecylbenzene sulfonate (SDBS).

Cationic surfactant: cetyltrimethylammonium bromide (CTAB)

Amphoteric surfactant: lauryl betaine

Figure 16. Examples of the different types of surfactant.

There is another type of structure directing agents that are not surfactants, i.e. which do not reduce the surface tension of the liquid when they are in solution. They can be of three types [72]: single molecule without self-assembly ability like tetrapropylammonium hydroxide (TPA) that has been used in the nucleation and growth of zeolites [92], small molecules with low molecular weight that induce self-assembled arrangements such as urea [93,94] and sodium salicylate [95,96], or supramolecules, large molecules that do not form micelles like dendrimers [97–99].

The flexibility of surfactant templates to lead to different arrangements by changing their chemical structure, geometry and concentration has attired great interest for the preparation of

mesoporous materials. The use of soft templates became a trending topic after the development made by the Mobile Company. In particular, they used liquid crystals of alkyltrimethylammonium bromide (C_n-TAB) or chloride (C_n-TAC), in which the silicate material formed solid walls between the ordered surfactant micelles [65,73]. Depending on the type of surfactant, the morphology of the channels varied. For instance, MCM-41 consisted of hexagonal channels, while MCM-48 and MCM-50 had bicontinuous cubic and lamellar mesostructures, respectively [73,100]. The mechanism starts by the formation of surfactant micelles that self-assemble in arrays depending on the concentration and the type of surfactant (hexagonal array exemplified in Figure 17). Then, the silicate material starts to condensate around the surfactant assembly, leading to the formation of a solid-surfactant composite. Subsequently, the surfactant can be removed by calcination or extraction, leading to the porous material [100].

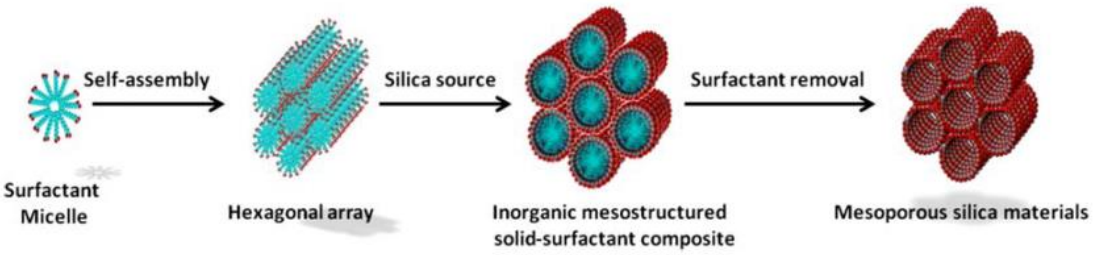

Figure 17. Ordered mesoporous silica formation by liquid-crystal templating [100].

Several micellar templated structures have been developed since, such as M41S, FSM-16, HMS, MSU-x and SBA-x [69]. For example, MSU-1 (Michigan State University) material was prepared with poly(ethylene oxide)-based surfactants leading to disordered channel structures with uniform diameters ranging from 2.0 to 5.8 nm [101]. Another example is the SBA-x (Santa Barbara Amorphous) family of ordered mesoporous silica with pore sizes ranging between 2 nm and 30 nm that were prepared with non-ionic alkyl poly(ethylene oxide) (PEO) oligomeric surfactant and poly(alkylene oxide) block copolymer templates in acidic medium. The pores were orderly arranged with cubic (*Im*$\bar{3}$*m* or *Pm*$\bar{3}$*m*), three dimensional hexagonal (*P*6_3/*mmc*), honeycomb hexagonal (*p*6*mm*) and lamellar (L_α) structures. Particularly, SBA-15 is a hexagonal mesoporous silica prepared with a template of poly(alkylene oxide) triblock copolymer surfactant species such as Pluronic® P-123 (poly(ethylene oxide)-*block*-poly(propylene oxide)-*block*-poly(ethylene oxide), $EO_{20}PO_{70}EO_{20}$). Its pores are ranging from 4.6 to 30 nm and the silica walls have a thickness ranging from 3.1 to 6.4 nm [102].

Other works have led to the preparation of plugged hexagonal templated silica (PHTS), which is a structured material consisting, of a honeycomb hexagonal structure with pores of 6-8 nm diameter and *ca*. 4 nm wall thicknesses. These pores contain internal microporous silica nanocapsules (as depicted in Figure 18) that are formed by a large excess of the silica precursor that is rapidly hydrolysed at the very low pH used during the synthesis. Such a material exhibited much more hydrothermal and mechanical stability than conventional micellar templated structures. Such a performance has been attributed to the wall thickness in comparison with other silica like MCM-48 that has walls of only *ca*. 1 nm [69].

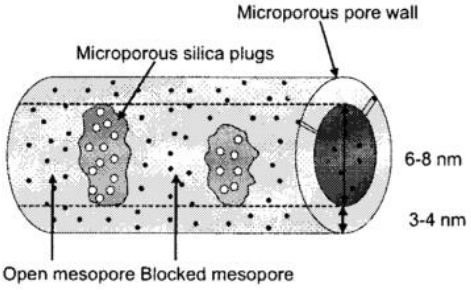

Figure 18. Plugged hexagonal templated silica [69].

Table 2 summarises the mesopore size that is achievable with diverse soft templates. Notably, the combination of surfactants with swelling agents (such as 1,3,5-trimethyl benzene, TMB) can lead to larger pore sizes by increasing the template micelle size [103]. For instance, a combination of food grade emulsifier polyglycerol esters of fatty acids (PGEFA) and *n*-decane, as soft-template and swelling agent, respectively, have been used in the preparation of mesoporous silica with pore size in the interval 2 - 14 nm [104].

Table 2. Mesoporosity tailoring with soft templates (based on [105]).

Pore size (nm)	**Method**
2 – 5	Surfactants with diverse chain lengths Long chain quaternary cationic salts Neutral organoamines
5 – 8	Charged surfactants combined with organic swelling agents
2 – 8	Non-ionic surfactants
4 – 20	Triblock-copolymer-based surfactants
10 – 30	High molecular weight block-copolymers Triblock-copolymers combined with swelling agents

Dual surfactant templating is another approach to prepare hierarchical mesoporous materials. The idea is to form a template of mixture of micelles with different sizes. The challenge is to find the balance in the surfactants interaction, because on the one hand, phase separation or segregation of the surfactant species can occur, and on the other hand, mixed micelles could be formed. In both cases no hierarchical structure would be formed [59]. For instance, dual – mesoporous silica spheres have been prepared with a core-shell structure. The shell porosity was tailored with CTAB leading to pores of 2 nm. The core was templated with polystyrene-*bock*-poly(acrylic acid) (PS-*b*-PAA) and CTAB, leading to pores between 12.8 and 18.5 nm [106]. Figure 19 presents a sample with 2.0 and 14.3 nm dual mesopores prepared with CTAB and PS_{100}-*b*-PAA_{16}. Other core/shell structures with spherical and ellipsoidal morphologies have been prepared with cetyltrimethylammonium bromide (C_{16}TAB), tetraethyl orthosilicate (TEOS) and octadecyltrimethoxysilane (C_{18}TMS). Such materials with double mesoporous silica shells with average pore size: 2.4 nm and 3.8 nm were explored in drug delivery applications exhibiting high biocompatibility [107].

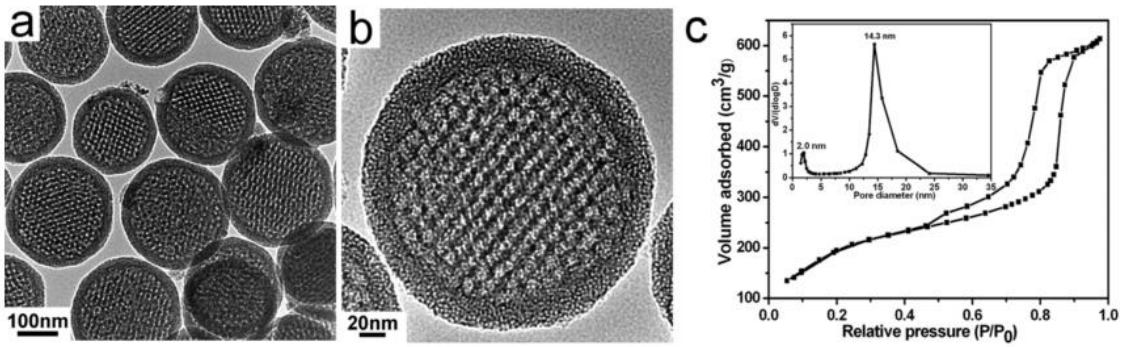

Figure 19. Dual-mesoporous silica spheres: a. and b. TEM images, c. N_2-physisorption isotherms with insert of BJH pore diameter distribution from the adsorption branch.

The use of surfactant mixtures has also permitted the synthesis of yolk/shell structures. Lauryl sulfonate betaine (LSB), sodium dodecyl benzenesulfonate (SDBS) and 3-amino-propyltriethoxysilane (APS) were used to form vesicles with movable nanoparticles cores (SiO_2, Au or Fe_2O_3). The silica shells were then prepared by a sol-gel process via the hydrolysis of APS and tetraethyl orthosilicate (TEOS), as shown in Figure 20 [87].

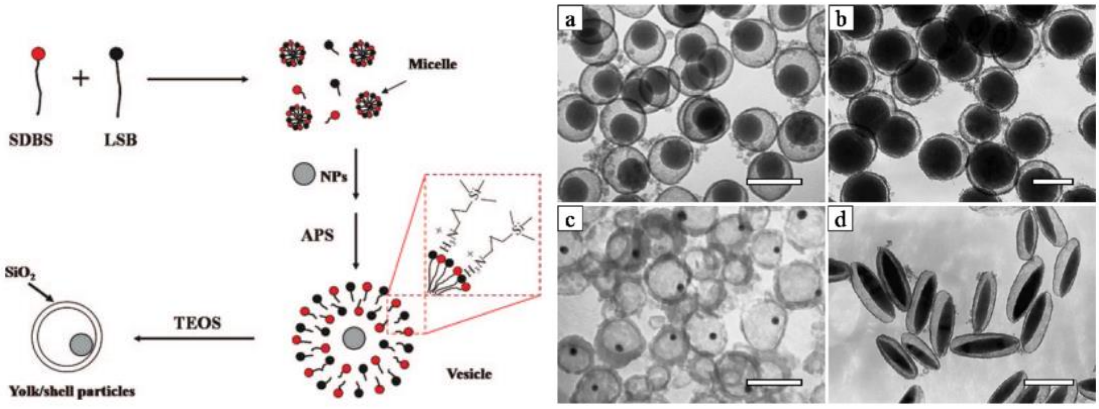

Figure 20. Schematic synthesis method for yolk/shell particles synthesis (left). TEM images of silica shells with cores of: a. and b. SiO_2, c. Au, d. Fe_2O_3 (right). Scale bars: 200 nm, except in d.: 100nm [87].

II.4.1.2.ii- Hard templating

This approach involves a hard or rigid material as template, whose structure determines the morphology of the desired product. Mesostructured silica, polymer spheres, porous membranes, foams, ion exchange resins and carbon fibres are some examples of hard templates [108]. Because numerous examples of hard templating routes published in the literature involve the use of polymer latexes and also because such latexes have been used in our experimental work, in the first part of this section general principles for the synthesis of polymer latexes by the most common way, i.e. emulsion polymerisation [109] will be recalled.

a) Synthesis of polymer latexes by emulsion polymerisation

An emulsion is a liquid-liquid dispersion that is thermodynamically unstable. Surfactants are then used in order to make kinetically stable droplets dispersed within the continuous medium. The droplets size typically range between 1 and 20 µm [110]. The emulsion polymerisation takes its name from the starting system, which in the simplest case is an emulsion made of water, a low water-soluble monomer (e.g. styrene), a water-soluble initiator (e.g. persulfate) and a surfactant [109]. In the case of styrene polymerised with a persulfate initiator, the polymerisation takes place following a free radical mechanism consisting of three steps: initiation, propagation and termination, as shown in Figure 21. The initiation is the attack of the initiator radical to the monomer creating a covalent bond and a new radical. The propagation is the subsequent radical attacks to other monomer molecules while making a chain of covalently bound monomer molecules (polymer chain). The termination takes place when two radicals combine (or disproportionate, for instance in the case of methyl methacrylate polymerisation), producing a dead chain (or two dead chains if disproportionation occurs) that cannot continue to polymerise [111].

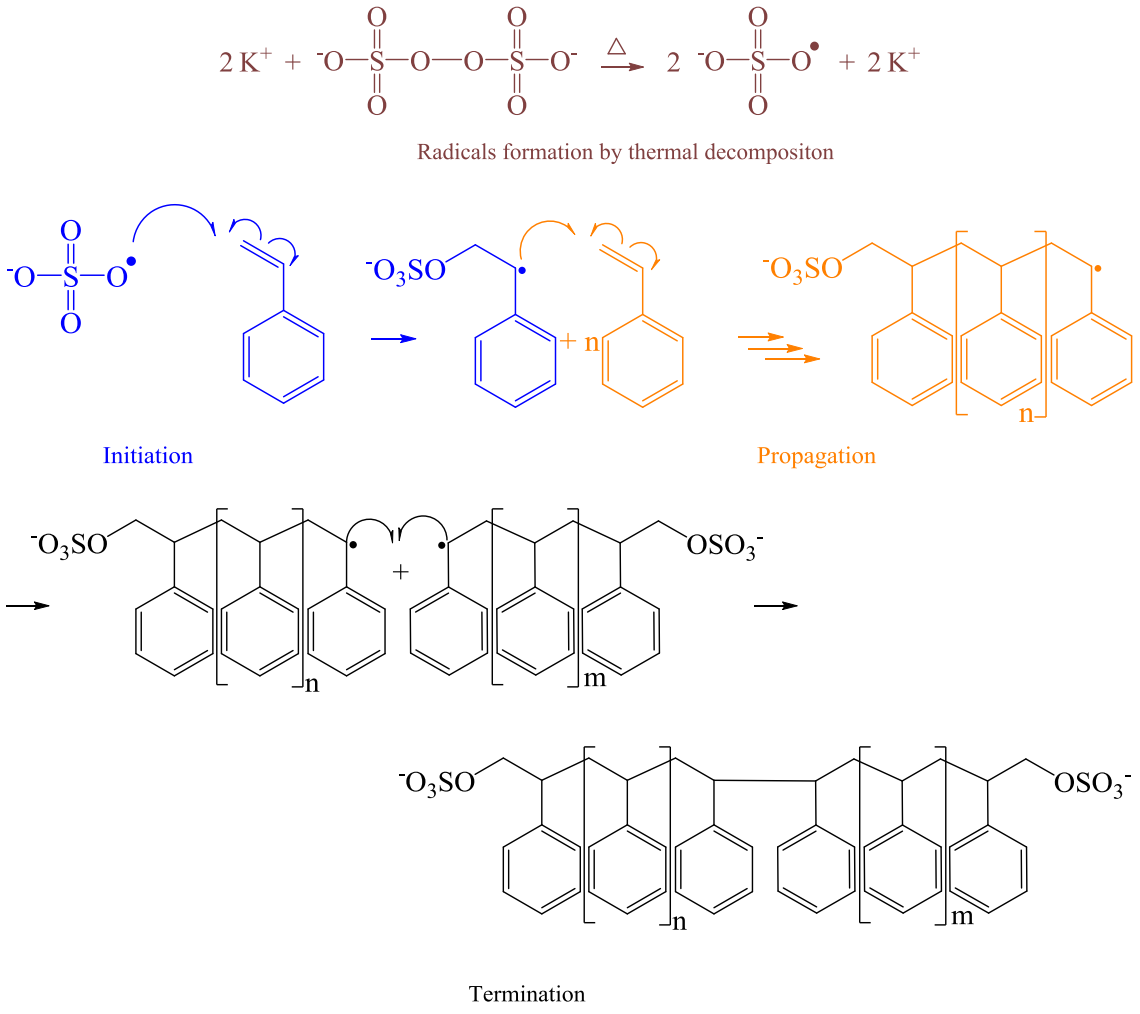

Figure 21. Styrene free radical polymerisation mechanism with potassium persulfate initiator.

Emulsion polymerisation is a widely used technique due to some advantages such as the use of water dispersion medium (which is more environmentally friendly than volatile organic solvents), it permits excellent heat dispersion during the synthesis and the emulsion low viscosity allows reaching high weight fractions of polymer. Nevertheless, the mechanism of polymer particles formation and growth is quite complex, and has only been understood in details recently [109]. In a typical batch polymerisation, three intervals are recognisable, as represented in Figure 22. Interval I: the particle nucleation takes place forming precursor particles. Monomer droplets and surfactant (surfactant forming micelles if above the critical micelle concentration) are present. Interval II: Only mature particles (colloidally stable particles) and monomer droplets are present. The particles keep growing and the monomer droplets act as reservoirs by keeping the monomer concentration within the particles essentially constant (monomer diffusion is faster than polymerisation). Interval III: the monomer droplets are exhausted and the remaining monomer within the particles is polymerised [109]. It is important to keep in mind that living radicals are required to permit particle growth. However, radicals are dynamic and can terminate, exit or enter the particles as depicted in Figure 23. As a consequence of this complex dynamics, many polymer chains are present within a latex particle.

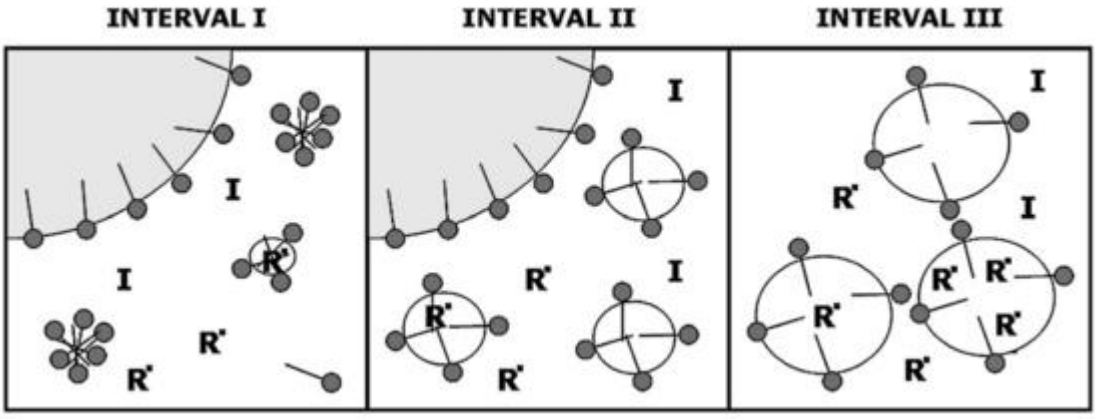

Figure 22. Typical emulsion polymerisation intervals. The grey circles represent the monomer droplets, stabilised by surfactant molecules. Micelles are represented by clusters of surfactant molecules in Interval I. R• are radicals and I are initiator molecules. White circles are surfactant-stabilised latex particles [112].

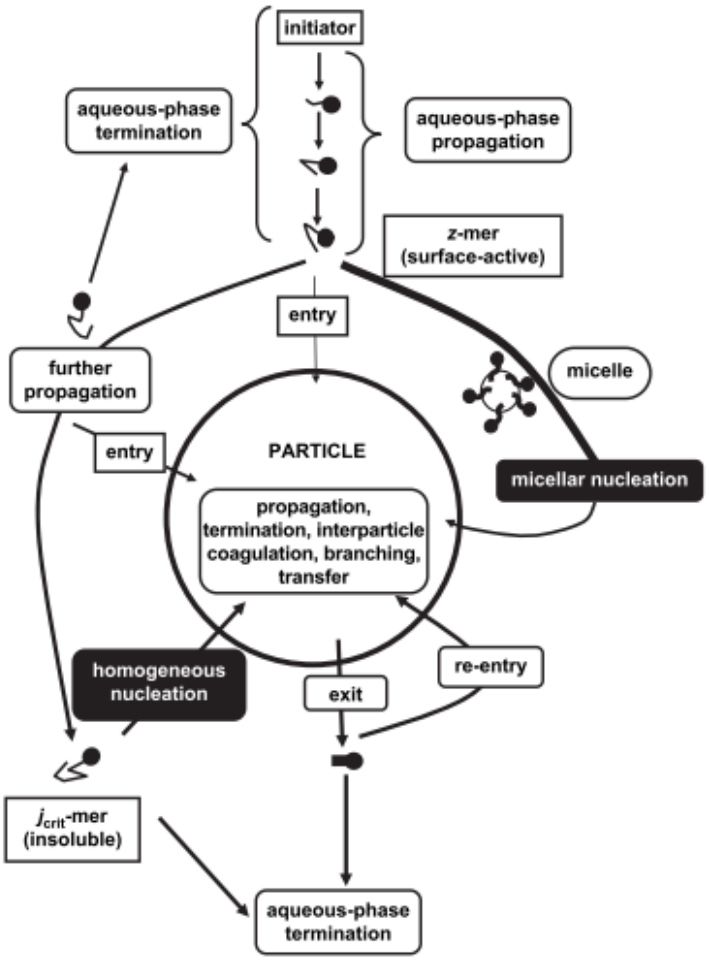

Figure 23. Kinetic processes during a typical emulsion polymerisation reaction. The head-tailed structures represent living radical polymer chains. The *z*-mer is a water-soluble initiator head with a long enough polymer chain to act as a surfactant being able to form micelles. The j_{crit}-mer is a water-soluble initiator head with such a long polymer chain that it is not soluble anymore forming a particle [109].

There are several ways to tune the functional groups present in the polymer chain, for instance by changing the initiator, the monomer, the surfactant or using a mixture. For instance, potassium persulfate, sodium bisulphite and ferric ammonium sulphate as initiators, and sodium dodecyl sulphate and sodium dodecyl sulfonate as surfactants have been used in different proportions to prepare polystyrene latexes with either sulphate, sulfonate or both functional groups at the surface of the polymer beads [113]. Carboxylic groups have also been brought to the surface of polystyrene beads using 4,4′-azobis(4-cyanovaleric acid) as initiator [114]. In terms of monomer, polystyrene nanoparticles have been prepared with styrene and divinyl benzene with oleic acid as comonomer, giving carboxyl group functionalities to the nanoparticles [115]. Another polymer has been functionalised using a mixture of styrene and sodium styrene sulfonate to prepare poly[styrene-*co*-(sodium styrene sulfonate)] by emulsion polymerisation [116]. In addition to effects on the polymer's chemical structure, variations of the latex formulation can also influence the particle size of the beads in suspension. For example, the nucleation stage of the styrene polymerisation in emulsion has been enhanced by the addition of sodium styrene sulfonate, leading to a number of particles (N_p) of the order of

10^{17} particles/cm^3 water, which is two orders of magnitude larger than in the case of styrene alone [117]. Considering that for a given amount of monomer, the volume of a particle is inversely proportional to the number of particles nucleated during the Interval I, a larger N_p corresponds to a smaller particle size.

Other alternative polymerisation techniques are summarised in Table 3. A couple of differentiating features are worth been briefly commented: in the inversed systems, the monomer is water-soluble and forms droplets within an organic continuous phase [118]. Both precipitation and dispersion polymerisations start from a homogenous medium, in which the monomer is soluble, but not the polymer, so as the reaction proceeds, the polymer creates non soluble particles. The main difference between these two types of polymerisation is that in the dispersion one, a stabiliser is added to control the colloidal stability of the dispersed phase formed during the polymerisation.

With the exception of dispersion and precipitation polymerisations, these methods are made of two non-miscible liquids that are kinetically stabilised, notably, with surfactants. The only remarkable exception in stability is the microemulsion, which is thermodynamically stable due to the addition of large amounts of surfactant and cosurfactant (like an alcohol: ex. n- pentanol) [119,120]. In such a case, instead of being a milky suspension, it is transparent and it is formed spontaneously with small and narrow particle size distribution. However, the microemulsion polymerisation is a complex heterogeneous process and the stability of the system can be affected as the polymerisation takes place [121,122].

Regarding miniemulsion polymerisation, in order to achieve small droplets, high energy shear is required (Figure 24), which is generally done by ultrasonication at low frequencies (e.g. 20 kHz) [123–129], static mixers [130,131], rotor-stators [132] or high pressure homogenisers [133,134]. Since the polymerisation is desired to only occur within the droplets, a hydrophobic agent is required to limit the diffusion of the monomer towards the continuous phase by building up an osmotic pressure in the droplets (it is therefore also called an osmotic pressure agents) counteracting the Laplace pressure [123].

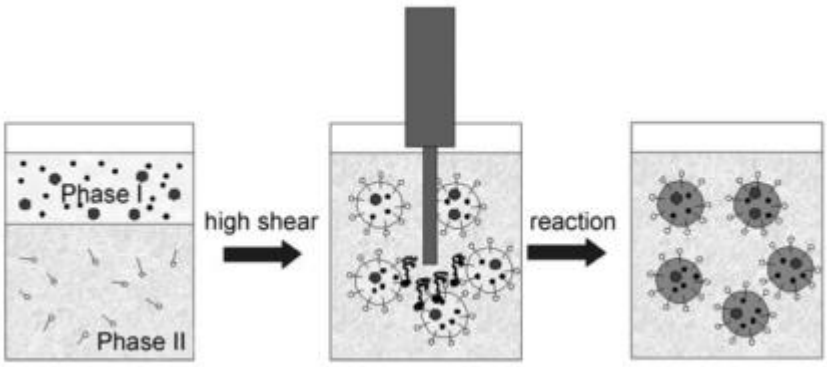

Figure 24. Miniemulsion process: Two immiscible phases (I: monomer, hydrophobic agent and initiator, and II: water and surfactant) are subjected to high shear, forming small, homogeneous, and narrowly distributed nanodroplets. In a subsequent polymerisation reaction, ideally no change of the droplets/particles size is observed [123].

Table 3. Polymerisation techniques in dispersed media (based on [110,111])

Polymerisation	Droplets size	Continuous phase	Monomer	Initiator	Polymer particle size	Comments
Suspension	50 µm – 10 mm	Aqueous	Oil-soluble	Oil-soluble	50 – 10 mm	Particles formed by polymerisation within the droplets.
Emulsion	1 – 20 µm	Aqueous	Low water-soluble	Water-soluble	50 – 500 nm	Particles formed by nucleation within the aqueous phase.
Precipitation	No droplets. Homogeneous starting phase	Aqueous (or organic)	Water-soluble (or oil-soluble)	Water-soluble (or oil-soluble)	Variable	The polymerisation mainly occurs in the continuous phase. The final system is not colloidally stable.
Dispersion	No droplets. Homogeneous starting phase	Organic (or aqueous)	Oil-soluble (or aqueous)	Oil-soluble (or aqueous)	0.5 – 20 µm	A stabiliser is added to ensure colloidal stability of the formed particles. The polymerisation occurs in the continuous phase and in the formed particles (if swollen by monomer).
Microsuspension	0.2 – 20 µm	Aqueous	Oil-soluble	Oil-soluble	0.2 – 20 µm	Larger amount of surfactant (or steric stabiliser) is required than in suspension. The polymerisation occurs within the droplets.
Miniemulsion	50 – 300 nm	Aqueous	Oil-soluble	Water- or Oil-soluble	50 – 300 nm	A hydrophobic agent is required to avoid Ostwald ripening. The polymerisation occurs within the droplets.
Microemulsion	10 – 20 nm	Aqueous	Oil-soluble	Water-soluble	10 – 50 nm	A cosurfactant is required (ex. n-pentanol). Thermodynamic stability could be affected by the polymerisation.
Inversed-suspension	50 µm – 10 mm	Organic	Water-soluble	Water-soluble	50 – 10 mm	Particles formed by polymerisation within the droplets.
Inversed-emulsion	0.5 – 20 µm	Organic	Low oil-soluble	Oil-soluble	50 – 500 nm	Particles formed by nucleation within the organic phase.
Inversed-miniemulsion	50 – 300 nm	Organic	Water-soluble	Oil-soluble	50 – 300 nm	Lipophobic additive is required to avoid Ostwald ripening.
Inversed-microemulsion	10 – 20 nm	Organic	Water-soluble	Oil-soluble	10 – 50 nm	Thermodynamic stability could be affected by the polymerisation.

b) Examples of hard templating implementation

A typical example is the preparation of carbon using a silica template, as schematised in Figure 25. First, mesoporous silica templates are tailored by surfactant self-assembly approaches, and then their pores are loaded with carbon sources such as sucrose. Such composite materials are then carbonised by H_2SO_4 or by heat treatments. Subsequently, the silica template is removed by HF or NaOH leading to the mesoporous carbon with the negative morphology of the starting silica template [105,135–137].

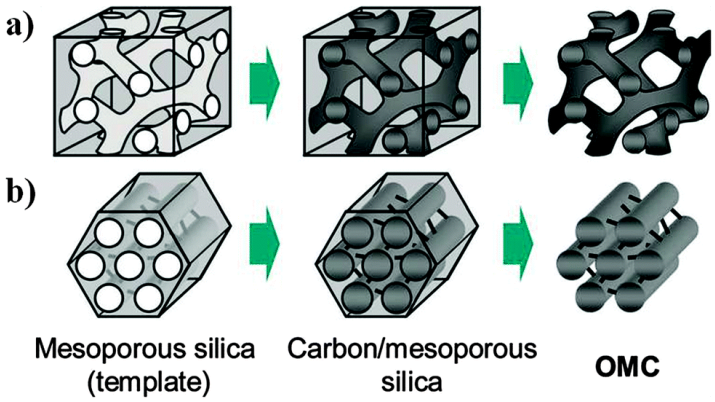

Figure 25. Ordered mesoporous carbons (OMC) preparation with mesoporous silica templates: a. MCM-48, b. SBA-15.

A colloidal suspension of polymer spheres – known as latex – can also be used as a template in order to define spherical pores within the final material [59]. Similarly to the case of sacrificial silica template, the polymer beads are removed from the composite material, typically by thermal treatment. This approach has allowed the preparation of continuous porous materials such as sponge-like materials[138], films and membranes [139] or discrete particles with tailored porosity such as hollow spheres and core/shell structures [140,141].

For example, highly ordered and uniform films and particles with hierarchical pore systems were obtained with polystyrene templates using dip-coating and spray-drying methods [142]. Using centrifugal forces, highly ordered porous monolayers were generated with polystyrene and silica nanoparticles [143]. TiO_2 anatase-based membranes have also been prepared exhibiting hierarchical porosity by using polystyrene latex, titania hydrosol and non-ionic triblock copolymer [144]. With catalytic applications in mind, a tin oxide material has also been prepared using polystyrene nanoparticles of 500 nm as template by electrophoretic deposition. After removal of the template by calcination at 600°C, the SnO_2 exhibited an inverse opal structure as shown in Figure 28 [145]. Other materials based on TiO_2 and ZrO_2 [146], as well as hierarchically porous SiO_2 membranes [70], have been successfully obtained using the latex templating method.

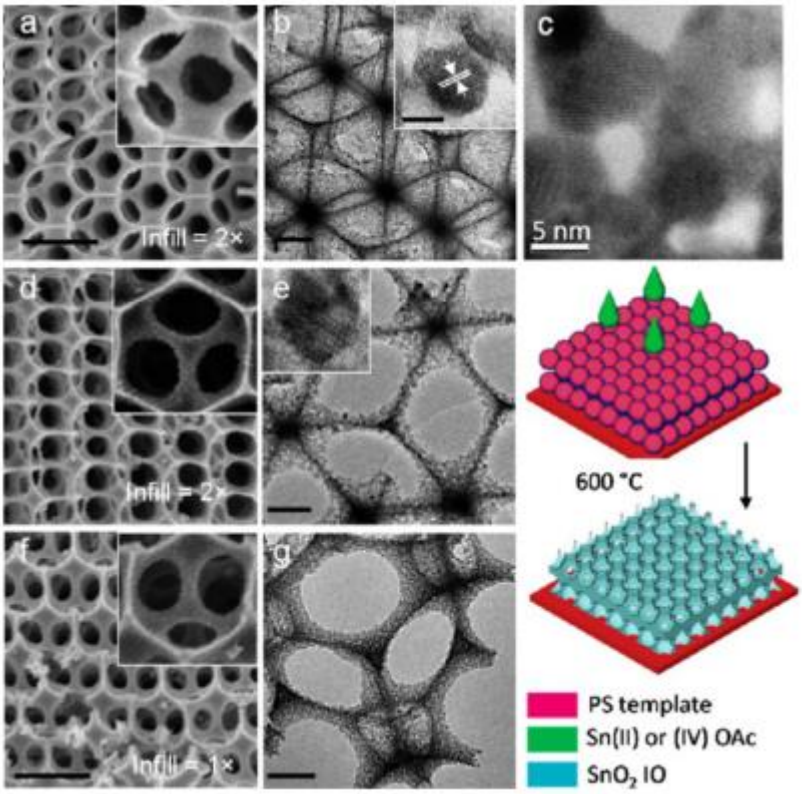

Figure 26. SnO_2 inverse opals by electrophoretic impregnation of a polystyrene template. Scale bars represent 100 nm [145].

Regarding discrete structures with controlled porosity, several examples with varied applications have been reported [140]. For instance, hollow titania spheres have been obtained by polystyrene templating. The positively charged polystyrene was prepared by dispersion polymerisation, and then coated via sol-gel process of tetra-*n*-butyl titanate. The organic polymer was then removed by dissolution with ammonia, leading to hollow titania spheres [147]. The same approach was used to prepare hollow silica spheres, which were subsequently decorated with Ag nanoparticle by electrostatic interaction. This material exhibited excellent antibacterial activity [88].

Moreover, monodisperse spherical hollow particles with ordered mesoporous silica shells have been prepared by dual latex/surfactant templating using polystyrene beads and CTAB in ethanol/water medium. Non-aggregated hollow silica nanoparticles were obtained with 200 nm average diameter with hollow cores ranging between 60 and 90 nm and shell mesopores of *ca*. 2 nm, as shown in Figure 27. The structure could be finely tuned by varying the synthesis conditions [148].

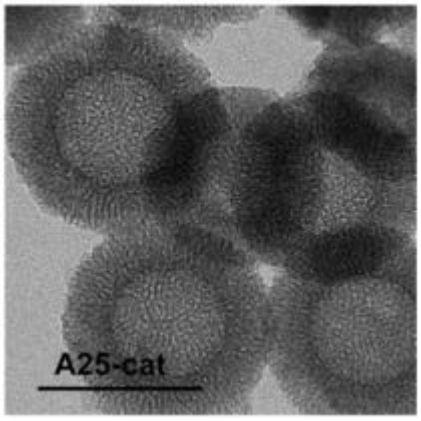

Figure 27. Silica hollow spheres by dual latex/surfactant templating. Scale bar: 100 nm [148].

Another example is the combination of polymer colloids (polystyrene or polymethyl methacrylate latexes) with micelles of ionic liquids or block copolymers reported for the preparation of hierarchical porous materials with controlled pore sizes ranging from pores of 2-3 nm (with ionic liquid micelles) and 6-22 nm (with copolymer surfactants) to 90-1000 nm (with the polymer latexes). As shown in Figure 28, the macropores are surrounded by ordered mesoporous walls [149].

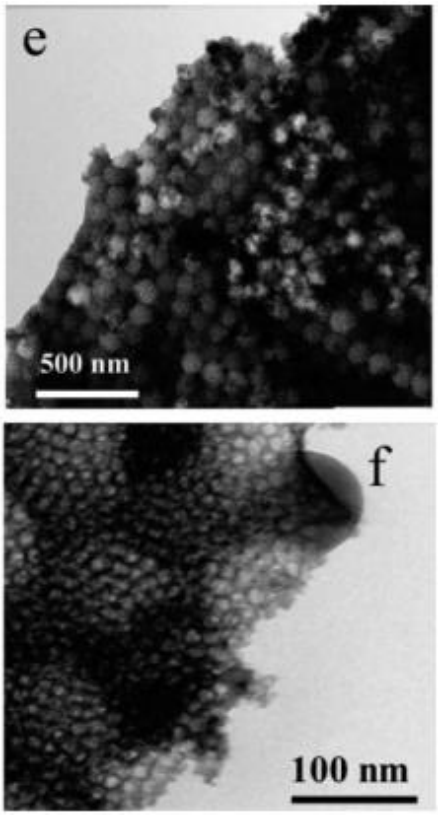

Figure 28. TEM images at different magnifications of hierarchically ordered silica prepared with polymethyl methacrylate latex (PMMA), (poly(ω-hydroxypoly(ethylene-co-butylene)-co-poly(ethylene oxide))) (KLE) and ionic liquid 1-hexadecyl-3-methylimidazolium chloride (C_{16}-mimCl). Spherical macropores (top) and ordered mesoporous walls (bottom) can be observed [149].

The combination of two polymer templates has also been used in the nanomasking approach to prepare dual-porous hollow nanoparticles. As shown in Figure 29, a mixed template of amine-functionalised polystyrene beads of 500 nm and carboxy-functionalised polystyrene nanoparticles of 100 nm (denoted nanomasks) aggregate due to electrostatic interaction. Then, the shell was formed by sol-gel synthesis by adding silica precursors that polycondensed on the template surface. The template was then removed by calcination generating synthetic hollow mesoporous spheres (SHMS). These structures were successfully used in drug delivery applications in vivo [150].

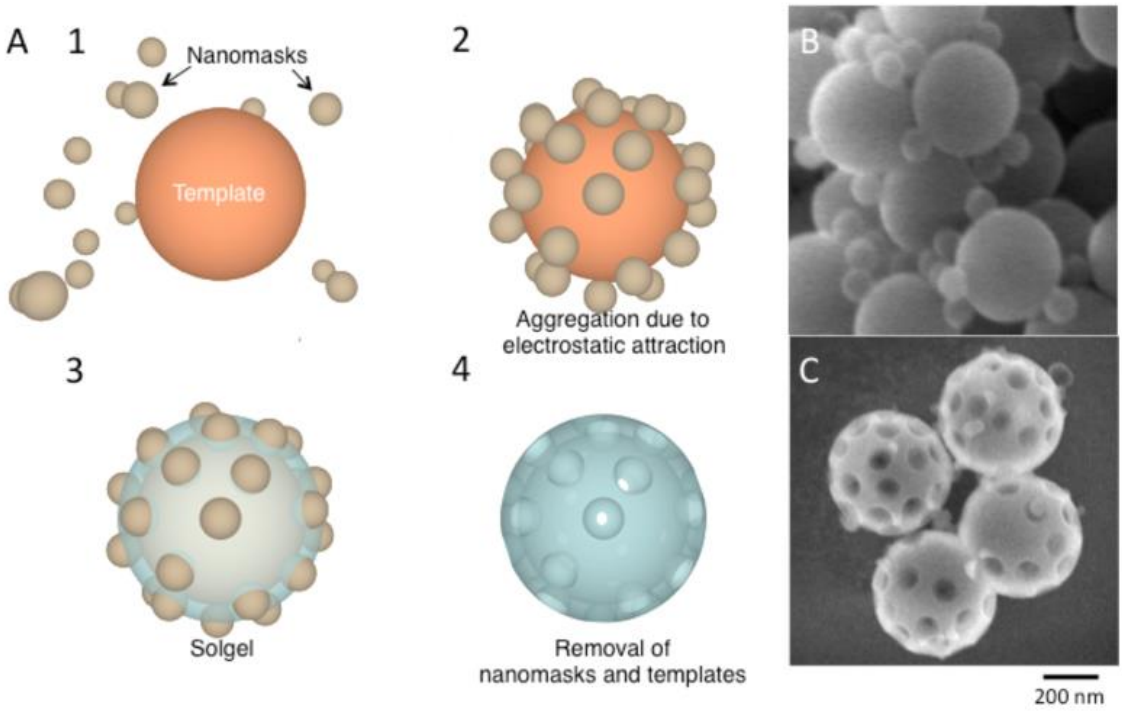

Figure 29. Nanomasking method: A. synthesis steps, B. templates interaction, C. final hollow nanoparticles [150].

Hierarchical templates for multimodal porous materials have also been prepared by covalently bounding large polystyrene particles with smaller ones, forming a core and shell like structure. These templates allow the interconnection of large macropores through meso- or small macropores, as depicted in Figure 30. Several templates were prepared by combining particles of 1500, 1200, 450 and 340 nm in the core and 110, 80 and 29 nm on the shell. To do so, two coupling reactions were used: carbodiimide-assisted coupling of carboxylic with amine groups and base-assisted coupling of epoxy with amine groups. Using such template, silica materials with interconnected hierarchically porous material were obtained as shown in Figure 30 [151].

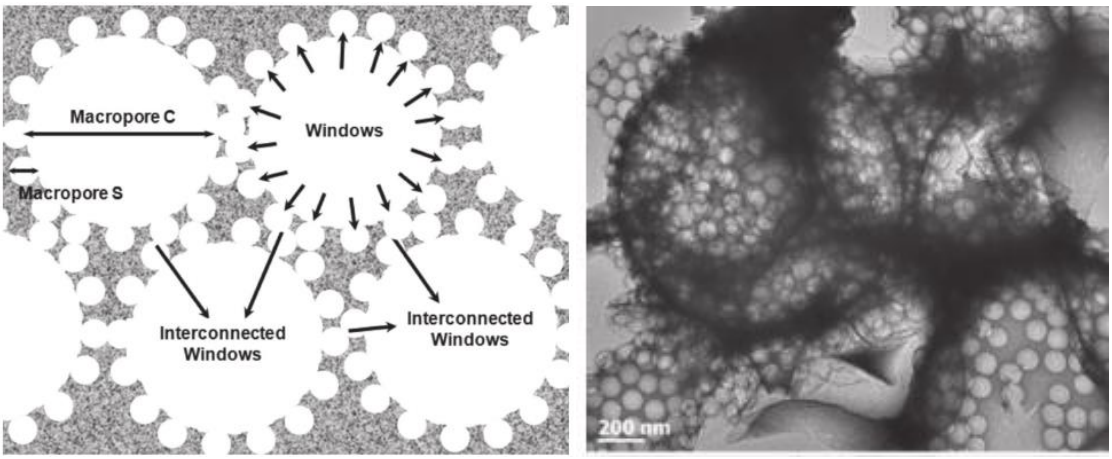

Figure 30. Schematic cross-section of multimodal silica (left). Multimodal porous silica prepared with 1500/110 nm hierarchical template (right) [151].

In the previous examples, the control of interactions between the template and the desired material are very important in order to avoid segregation. In addition to electrostatic Coulombic forces, hydrogen, coordination and covalent bonds should also be taken into consideration to synthesize mesostructured materials [105]. In the case of silica, the surface charge can be varied depending on the pH. Its zero point of charge is at pH = 2, so below this value (pH < 2), the silica charge is positive and above (pH > 2), the charge is negative [72]. As a consequence, the silica/template interaction can be modulated based on the pH, from the silica point of view. However, in the case of polymer latex templates, the surface charge of the beads depends on the functional groups present at the surface, which can be tuned during the latex synthesis.

As perspectives in the sustainable catalyst preparation with templates, greener approaches could be considered such as the use of recyclable templates [152] and bio-degradable or bio-sourced surfactants and polymers [153].

II.4.1.3- Other techniques for matrix porosity tailoring

Emulsion templating requires the use of surfactants to create diverse structuring arrangements like microemulsions, emulsions or bicontinous systems. MCF (Meso Cellular Foam) materials have been prepared by using oil in water microemulsions stabilised with triblock copolymer surfactants [154]. Porous carbon materials have been prepared by emulsion templating, which consists of a starting emulsion of solvent droplets in a continuous phase of carbon-rich monomers and initiators. The polymerisation takes place forming a matrix around the solvent droplets. After solvent removal and polymer carbonisation, a structured porous carbon is obtained (Figure 31). This approach has been used starting from a styrene-containing continuous phase, which after polymerisation and pyrolysis at 700 °C leads to a highly porous carbon as shown in Figure 32.

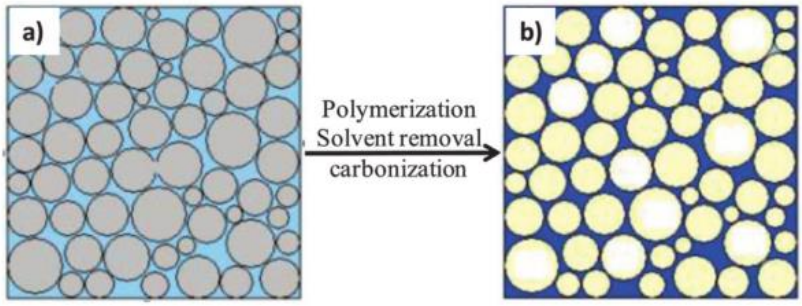

Figure 31. Porous carbon preparation by emulsion-templating [136].

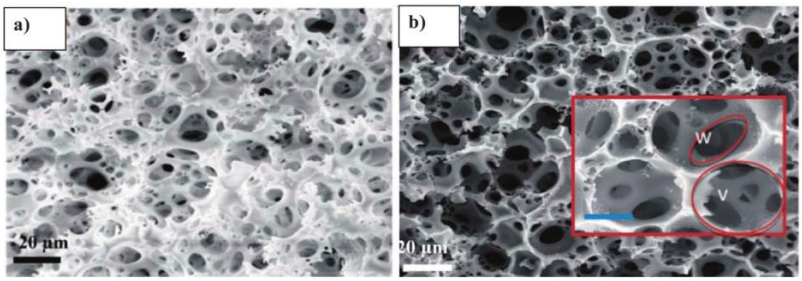

Figure 32. SEM images of: a. high internal phase emulsion (HIPE) polymer based on polystyrene, b. carbonaceous structure after pyrolysis. Scale bar in the insert corresponds to 10 nm [155].

Bicontinuous microemulsion templates have been prepared for the synthesis of mesostructured materials. The synthesis approach consisted of ternary blends of two homopolymers and a diblock copolymer that self-assemble in three-dimensional continuous networks. Particularly, polyethylene (PE), poly(ethylene-*alt*-propylene) (PEP) and poly(ethylene-*b*-ethylene-*alt*-propylene) were mixed at 127 °C for 2 h, then quenched in liquid nitrogen. Subsequently, PEP was removed by extraction with tetrahydrofuran. The resulting material exhibited macropores of *ca*. 100 nm. This material could then be used as template in the nanocasting process, as presented in Figure 33 [156].

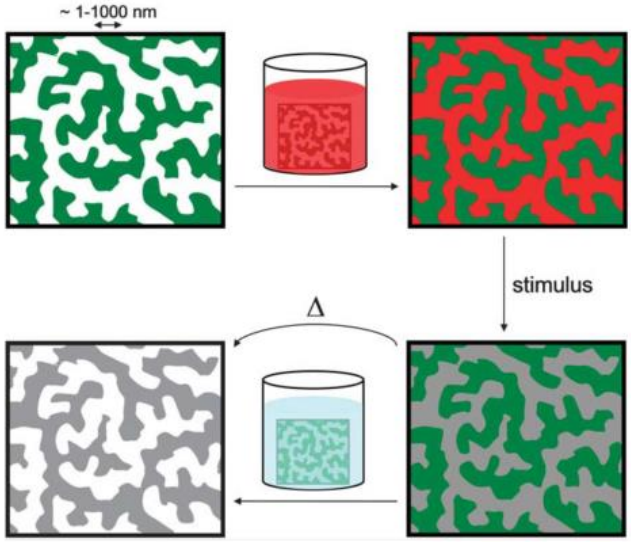

Figure 33. General nanocasting process: a template is infiltrated with a liquid precursor (red), which, after an external stimulus, produces the desired product, leading to a composite material/template. Subsequently, the template is removed with a selective reagent (blue), leading to the porous material [156].

In the 1992, Nakanishi proposed an alternative to nanocasting in order to prepare macroporous silica monoliths. It consisted of a simultaneous phase separation (spinodal decomposition) and a sol-gel transition. The starting point is a single phase including acid, an alkoxide such as TEOS, a solvent such as water and an organic polymer such as polyethylene oxides (PEO). While the alkoxide polymerises, it induces a phase separation leading to bicontinuous silica-rich and water-rich phases. The structure is then fixed by the sol-gel transition. The macroporous structure is revealed after removal of the water-rich phase [157,158]. A second step in basic medium can be used to generate disordered mesoporosity by dissolution-reprecipitation of the silica and Ostwald ripening processes. However, if that second step is carried out in the presence of structure directing agents like CTAB, ordered mesoporosity can be achieved, as shown in Figure 34 [159]. Additionally, via pseudomorphic transformation [160], it is also possible to transform the amorphous silica walls into zeolites, leading to monolithic zeolites with hierarchical porosity [161].

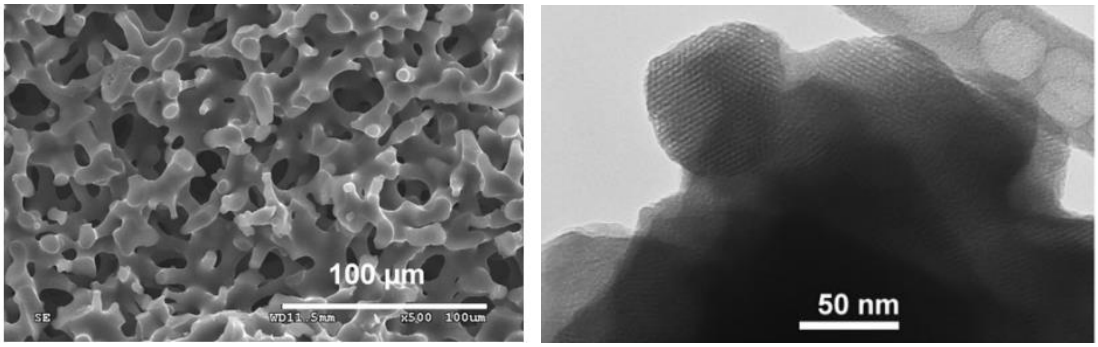

Figure 34. SEM image of silica monolith by simultaneous spinodal decomposition and sol-gel transition (left), and TEM image of the ordered mesoporosity achieved (right) [159].

In addition to sol-gel controlling and soft and hard templating, there are other techniques that can be used to prepare hierarchical porous materials such as gas foaming, ice templating, supercritical fluids methods (such as foaming upon $scCO_2$ depressurisation or CO_2/water emulsion templating[162]), and selective leaching (by dissolution of one of the phases that constitute a starting composite material made of two immiscible phases in intimate contact, *e.g.* NiO and ZnO, of which only ZnO is soluble in alkali solutions [59]).

Silica materials have been prepared by a nanofoaming method consisting of the hydrolysis of tetraethyl orthosilicate (TEOS) at pH= 5 and *h* ratio= 10, for 1 h. Then the sol was instantaneously heated above 500 °C, leading to solid silica with closed pores between 1 and 10 nm, as observed in Figure 35. Such small porosity is due to the simultaneous instantaneous hardening of the silica by condensation of the residual hydroxyl functions and the water vaporisation that forms enclosed bubbles [163].

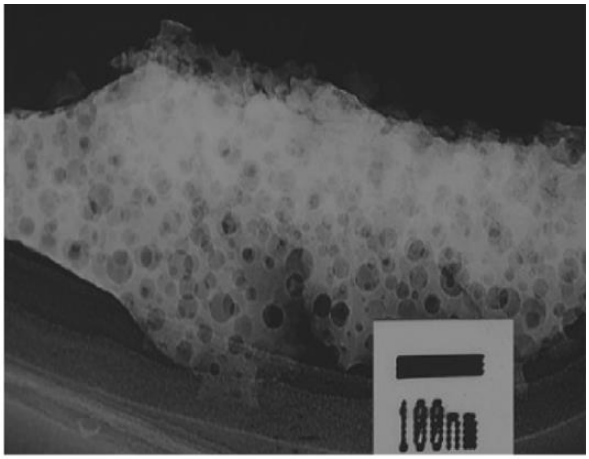

Figure 35. Porous silica by nanofoaming [163].

Ice templating is another method based on a controlled freeze-drying approach. It consists of ceramic slurry that is put into a mould and then frozen, forming solvent crystals that act as porogens. Subsequently, the material is freeze-dried in order to remove the solvent by sublimation, avoiding shrinkage and fractures due to capillary forces. Then, the material is sintered to improve its strength and to modulate the desired microstructure [59,164,165]. The control of ice crystals formation can lead to preferential orientations as depicted in Figure 36. After removal of the template, aligned structures are obtained [166].

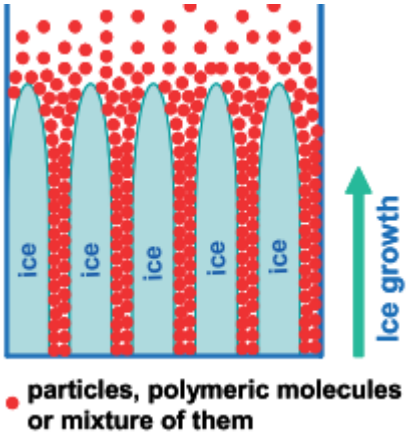

Figure 36. Schematic representation of the directional freeze-drying process. The particles are excluded from the ice crystals, which are formed from de the bottom to the top [166].

Macroporous silica gels with microhoneycomb structure have been prepared using micrometer-sized ice crystals of *tert*-butanol as a template. The macropores size could be controlled between 2 and 40 µm by varying the immersion rate into the cold bath and the freezing temperature. The micro- and mesoporosity of their honeycomb walls was also modified with a hydrothermal treatment in basic aqueous solutions reaching pores up to 45 nm [167]. Other works have been reported using a combination of micellar and ice templating, permitting the synthesis of silica monoliths with hierarchical meso- and macroporosity. The micelles were made of Pluronic P123 and the final structure exhibited a hexagonal ordered mesoporosity of 5.5–7.8 nm, and a bundle-like structure with macropores of 50–200 nm, as observed in Figure 37 [168].

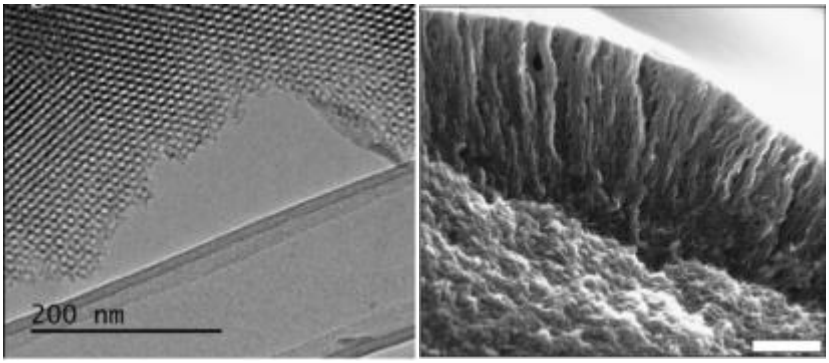

Figure 37. Hierarchically porous silica by combining ice- and micellar templating. Scale bar on the left: 500 nm [168].

II.4.1.4- Hierarchically porous materials for catalysis

The combination of different pore sizes have been claimed to have a beneficial effect on the catalyst performance. For instance, the combination of micro- and mesoporosity has been reported to lead stronger catalyst resistance to deactivation [169]. Much effort has been put on the structuration of aluminophosphates, clays, hydroxides, metal organic frameworks and zeolites in order to improve their catalytic properties (described in more detail in Annex I). For

example, it has been observed that the vapour-phase benzene alkylation with ethylene to ethylbenzene was faster and more selective using mesoporous zeolite crystals than purely microporous analogues. Such a better selectivity was due to a shorter diffusion path length that reduced the resident time of the product within the micropores, consequently, it limited successive alkylation reactions of the desired ethylbenzene to polyalkylbezenes [170].

Nevertheless, it is important to keep in mind that the catalytic activity of zeolites, as well as their shape-selective character, is due to the crystalline framework [171], which is inevitably microporous. So the existence of micropores in hierarchical zeolites is a must. However, when the catalytically active function has another origin, for instance supported metals or grafted organic moieties, a hierarchically porous structure with meso- and macropores is a more promising design to enhance the catalyst performance [172]. The first hierarchical meso- and macroporous materials were reported by Yang *et al.* in 1998, who prepared porous silica, niobia, and titania with three-dimensional structures using templates of polystyrene spheres and amphiphilic triblock copolymers [173]. Recently, the use of catalysts or catalyst supports based on hierarchically porous materials have gained much attention within a wide range of applications, such as photocatalysis [174], biomass valorisation [175], pollution abatement [176], fuel and organic chemistry [177].

In particular, supported metal catalysts have been reported to be more performant in a variety of reactions when the support exhibited hierarchical porosity. Such performance is typically explained by enhanced internal mass and heat transfer and by a better active site dispersion and accessibility. For instance, cobalt and ruthenium supported on hierarchically porous nano-fibrous alumina (with pores of 16 nm and 240 nm) have been reported to be more selective in the syngas (H_2 and CO) conversion to hydrocarbons *via* Fischer-Tropsch synthesis, in comparison with only mesoporous alumina supports [178]. For the same reaction, an excellent performance has also been reported with cobalt on bimodal meso-macroporous silica, in comparison with Co on an only-macroporous support [179].

Regarding fuel cell applications, improved performance has been reported for methanol oxidation using a Pt-Ru alloy supported on a hierarchically porous carbon (with pores of 10 nm and 300 nm), compared with commercial carbon supports. Such support was prepared by template replication of aggregates of small silica particles, which were themselves templated by a self-assembled lattice of larger monodisperse polystyrene beads. The metal alloy was prepared by impregnation and chemical reduction with $NaBH_4$ [180]. Another example is a carbon support with sea urchin morphology that has been prepared via carbon nanotube growth onto hollow mesoporous carbon shells using chemical vapour deposition. Pt deposited on such support exhibited higher methanol electro-oxidation rates than when using commercial carbon, hollow mesoporous carbon shells or carbon nanotubes supports, independently [181]. Pd nanoparticles homogeneously dispersed on a hierarchical meso- and macroporous SnO_2 support (with pores of 12 nm and *ca*. 500 nm) has also exhibited a superior performance in electrocatalytic oxidation reactions compared to commercial Pd/C [145].

Organic transformations have also been proven to take advantage of hierarchically porous catalysts. For instance, Pt supported on commercial hyper-cross-linked polystyrene with meso- and macroporosity (most pores in the range 20-100 nm) has outperformed an equivalent Pt catalyst supported on microporous polymer in the direct oxidation of $_L$-sorbose to 2-keto-$_L$-

gulonic acid [182]. Regarding hydrogenation, a macro- and mesostructured Pd/TiO_2 material (mesopores of 4.8 nm and macropores of 2–3 µm) has exhibited higher catalytic activity than an equivalent non-structured catalyst for the selective hydrogenation of styrene (reaction used in the stabilisation of petrol blending compounds) [183].

Hierarchically porous catalysts have also been successfully used in environment remediation. For instance, Pt nanoparticles supported on γ-alumina with hierarchically ordered mesopores (4 nm) and macropores (500 nm) have outperformed commercial $Pt/\gamma\text{-}Al_2O_3$ in the selective oxidation of CO [184]. Pt supported on meso- (3-14 nm) and macroporous (200-250 nm) titania have also exhibited better performance than a commercial catalyst in this same reaction [185]. In addition to hierarchical porosity, chemical synergies can be also used to improve catalytic performances. For instance, a hierarchically porous silica support has been used to prepare an $Au/CeO_2/SiO_2$ composite material, which exhibited excellent catalytic performance in the CO oxidation in comparison with only mesoporous silica supports. Thus the combination of hierarchical porosity and $Au\text{-}CeO_2$ interactions boosted the catalytic performance in such a way that the temperature required for complete conversion was reduced by half [186].

The next section includes further examples of functionalised hierarchical porous materials, giving special attention to their preparation.

II.4.2- Catalyst functionalisation

In heterogeneous catalysis, the general idea is to optimise processes by reducing the catalyst cost and increasing its performance [1]. Current challenges in the catalysis field motivate a deep research on catalysts preparation based on the understanding of how they work. For reactions that require some chirality in the active sites, anchoring specific ligands [187,188] and organometallic complexes [189,190] is a promising approach. Such materials could even have further applications like controlled drug-release [191]. For reactions where noble metals are still the catalyst of choice, it is important to reduce their cost by improving their dispersion on the support and by reducing their mass loading on the final catalytic material [192]. The main motivation to reduce the amount of noble metals in catalysts is their commercial price in the commodities market: for example, in June 2017, a troy ounce (31.1034768 g) of platinum and palladium cost *ca*. 960 U$ and *ca*. 860 U$, respectively [193]. In the following pages, conventional methods to prepare supported metal catalysts as well as recent remarkable approaches will be described.

II.4.2.1- Supported catalyst synthesis by conventional methods

The goal of conventional methods for the synthesis of supported catalysts is to maximise the active surface area per weight unit of the active phase. These methods can be summarised in a few techniques [50,194,195]:

- Co-precipitation
  This method consists of precipitating simultaneously the metal and the support. However, the interference of the metallic precursor with the support polymerisation chemistry might lead to undesirable catalyst textural properties such as less defined pore size and shape [196]. Pd/SiO_2 materials have been prepared by this method, leading to Pd nanoparticles of about 5 nm, but with a limited catalytic performance [197].

- Deposition-precipitation
  Unlike for co-precipitation, in this method the solid support is already formed and the desired particles are deposited on it (Figure 38). The metal precursor is a highly soluble salt, e.g. nitrate, sulphate. It precipitates as a hydroxide or carbonate on the support surface when the pH is increased. It is important to guarantee a rapid mixing to favour the nucleation on the support surface and avoid it in the bulk solution. Subsequently, an additional step of reduction/activation is required before use. Platinum has been deposited on carbon nanofibers using homogeneous deposition precipitation with $Pt(NH_3)_4(NO_3)_2$ as precursor. Metal nanoparticles of 1-3 nm were obtained with this method [198].

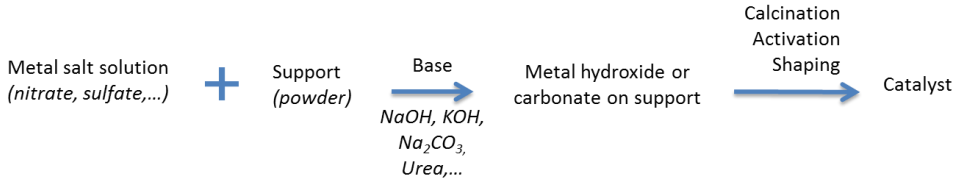

Figure 38. Deposition-precipitation method.

- Impregnation
  This method has two variants: Incipient wetness impregnation and wet impregnation. The first variant is also known as dry impregnation or pore volume impregnation (Figure 39). It consists of preparing a solution of the metal precursor in a volume that is equal to or slightly lower than the support pore volume. The solution is dropped on the support and due to capillary forces, it enters into the pores. After a heat treatment, the metal is distributed within the support. The second variant follows the same principle, but the only difference is that the volume of precursor solution is larger than the support pore volume.

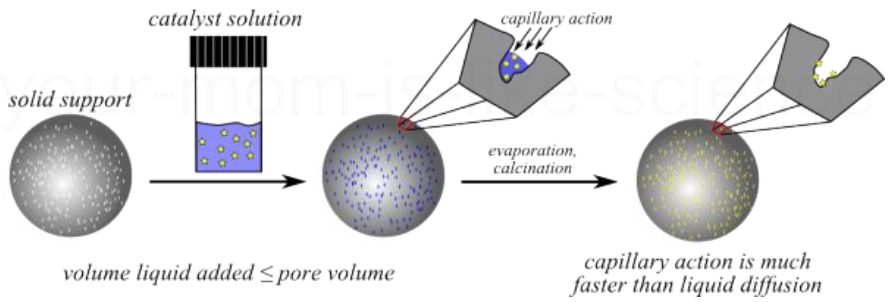

Figure 39. Dry or pore volume impregnation method [199].

These two methods are commonly used for catalyst preparation [200,201]. For instance, silica and alumina supports, including mesoporous SBA-15 (porosity ranging from 5 to 30 nm), have been functionalised via wet impregnation technique with Ni, Ce, Zr, Mo and B for methane steam reforming, for which the SBA-15 supported catalyst exhibited the best performance [202]. Incipient wetness impregnation technique has also been used for preparing platinum and palladium based catalyst on silica and alumina as support. For this purpose, solutions of tetraammineplatinum nitrate and tetraamminepalladium nitrate have been used [192]. But despite the ease of using this method, it often leads to broad nanoparticle size distributions and the control on the particle size and dispersion is difficult [196].

In an attempt to control the particle size, an approach with metal nanoclusters has been explored for the production of heterogeneous catalyst. In general, they include two main steps: metal nanocluster synthesis and deposition on a support [203]. The metal nanoclusters are produced by reduction of metal salts such as ammonium tetrachlorplatinate (II) ($(NH_4)_2PtCl_4$) and stabilized by ligands like polyvinylpyrrolidone or by solvents and anions [204]. However, the removal of the ligands can lead to changes in the nanoparticles size and morphology [205] and the limitation in the control of the homogeneous dispersion within the support still remains as it is related to the impregnation phenomena: capillary filling or diffusional loading of the pores [50]. Nevertheless, hierarchical porosity could remediate this limitation by allowing easier access to the porous network. Indeed, a three-dimensionally ordered hierarchically porous SnO_2 was decorated by wet impregnation with a colloidal suspension of Pd nanoparticles [145]. Another material, a hierarchical porous silica has been decorated with Pt and Pd nanoparticles by incipient wetness impregnation in such a way that the mesopores were decorated with Pt nanoparticles of 2.2 nm and the macropores were decorated with Pd nanoparticles of 5.6 nm. The strategy consisted of using a polystyrene template and a Pluronic P123 block-copolymer template to induce macro- and mesoporosity within the silica material, respectively (Figure 40). The polystyrene template was removed by toluene reflux extraction, keeping the Pluronic P123 within the mesopores. The macropores were then hydrophobised with triethoxy(octyl)silane. Subsequently P123 was extracted by methanol reflux. In this way, the mesopores were hydrophilic and the macropores, hydrophobic. The mesopores were initially decorated by incipient wetness impregnation with an aqueous solution of H_2PtCl_6 and the macropores were decorated with a colloidal suspension of oleylamine-capped Pd nanoparticles in hexane. This material exhibited an outstanding performance in the two-steps cascade oxidation reaction to produce cinnamic acid form cinnamyl alcohol [206].

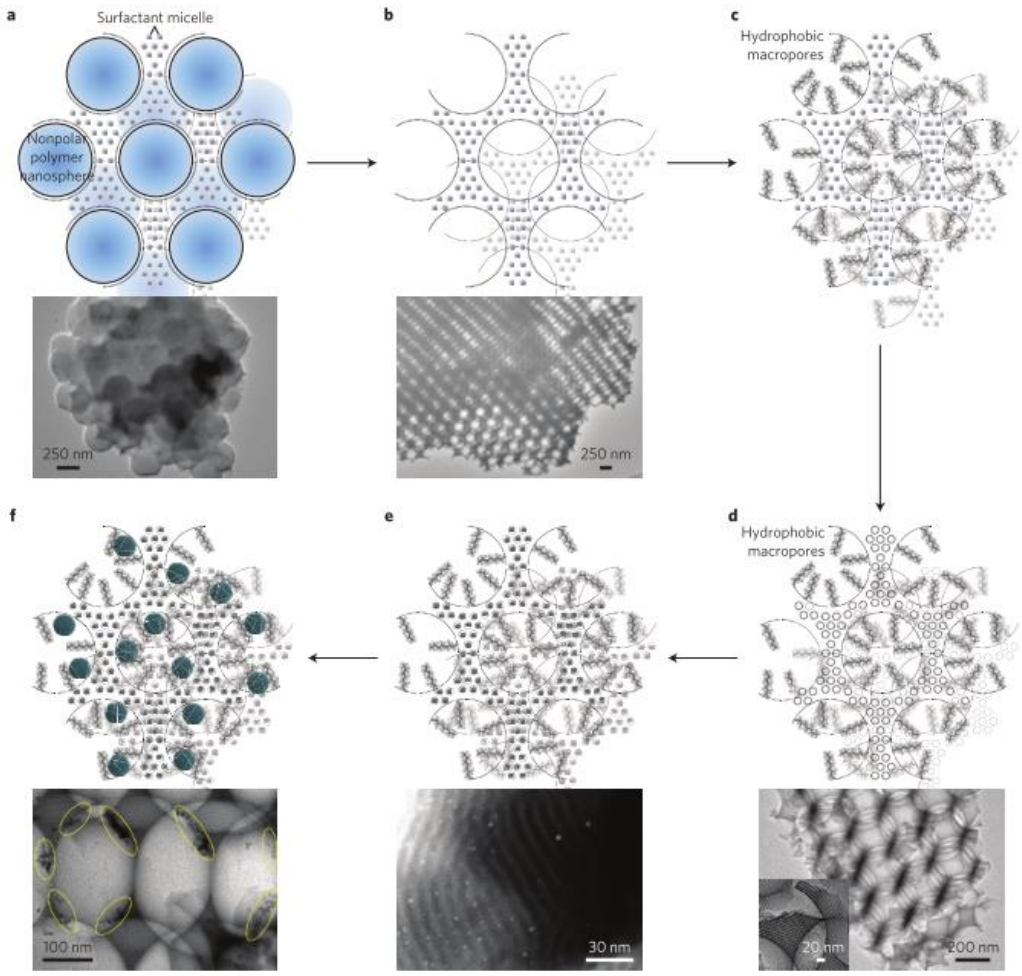

Figure 40. Orthogonal functionalisation of hierarchically porous silica: a. Polystyrene and Plurionic P123 templated silica, b. Silica after polystyrene extraction from the macropores, c. Hydrophobation of the macropores with triethoxy(octyl)silane, d. P123 extracted-material by methanol reflux, e. Selective decoration of mesopores with Pt nanoparticles, f. Selective decoration of macropores with Pd nanoparticles [206].

- Adsorption

  In this method, the support is immersed in a solution containing the metal salt precursor, so it adsorbs the metal ions due to favourable electrostatic interactions. The support is dried after removing the liquid phase, which is different to wet impregnation where the solid is dried with presence of the excess liquid. As a result, a uniform deposition of small amounts of metal can be achieved [50]. Pt-based catalysts have been prepared by this method when contacting carbon [207] and silica [208] supports with H_2PtCl_6 aqueous solutions.

- Ion exchange
  A support containing low valence ions is immersed in a metal salt solution. These low valence ions in the support exchange with higher valence ions in the solution. This method can be also applied for the separation of palladium from rhodium, iridium and platinum [209] or for the recovery of platinum from chloride solutions [210]:

$$2\overline{RCl} + [PtCl_6]^{2-} \leftrightarrow \overline{R_2[PtCl_6]} + 2Cl^-$$

  For both adsorption and ion exchange, a reduction step is required before using the catalyst. In some cases, chemical reduction would involve the use of an excess of additional reagents such $NaBH_4$ or hydrazine, which must be removed prior to catalytic applications [196].

II.4.2.2- Supported catalyst synthesis by advanced methods

In the search for more performant catalysts, several approaches have been explored, including physical, chemical or physico-chemical routes. Some of the more remarkable are briefly described in this section.

- Chemical vapour deposition (CVD) or atomic layer deposition (ALD)
  This technique allows coating surfaces of complex shapes with a high quality material, such as thin films. For catalyst preparation, gaseous precursors of the active phase are required. They enter into contact with the support at high temperatures and a solid-gas reaction takes place generating an atomic layer at each pulse. After several cycles, the material grows as a thin film on the support. With this method, highly dispersed and active supported metal and oxide catalysts can be prepared. Using atomic layer deposition with platinum (II) acetylacetonate as precursor, platinum has been successfully deposited on carbon nanofibers. Nanoparticles of 2-6 nm were obtained on this materials [211]. A wide range of elements, oxides, nitrides, sulphides and others can be deposited by this method. However, the main drawback of this technique is the limited choice of effective reaction pathways, so it is not yet possible to grow every material using ALD [212].

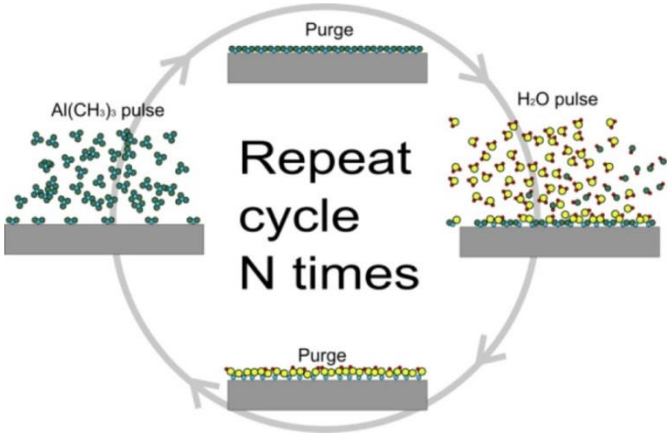

Figure 41. Atomic layer deposition (ALD) [213].

- Electrochemical reduction
  The metal precursor, initially as a salt aqueous solution, is reduced by applying an electrical potential. Pt nanoparticles have been deposited on carbon electrode supports by electrochemical reduction, starting from hexachloroplatinic acid [214]. Such technique can also be used to prepare alloys by electrochemical co-reduction of two-metal species [73]. The limitation is the requirement of conductive supports to be used as electrodes. This is the reason why this technique has been mostly used to decorate carbonaceous materials [196].

- Flame spray pyrolysis
  Similarly to the co-precipitation method, this synthesis starts from a solution of metal and support precursors. It is then injected in the form of a fine spray into a flame, leading to the final catalyst. A material of 2.5 wt.% Pd supported on La_2O_3/Al_2O_3 has been prepared starting from a solution of aluminium(III) *sec*-butoxide, lanthanum isopropoxide and palladium acetylacetonate dissolved in xylene. It was then treated in a flame of methane-oxygen, leading to a highly thermally stable material with Pd nanoparticles of less than 5 nm [215]. Unfortunately, due to the nature of this technique, it is not possible to finely tailor the support structure.

- Pulsed laser ablation
  In this technique, a solid surface (precursor) is irradiated with a laser, which locally provides enough energy to heat and ionise the irradiated area, leading to the ejection of material in the form of plasma, which is then cooled down and deposited on a support as nanoparticles. Using this technique, Rh, bimetallic Rh/Pt and trimetallic Rh/Pt/Au nanoparticles have been supported on Al_2O_3, TiO_2 and CeO_2. However, similarly to atomic layer deposition, this technique can only decorate the external surfaces of the support [216].

- Chemical, thermal and microwave assisted reduction
  Reducing agents like sodium borohydride or hydrazine can reduce metals cations (M^{m+}) in solution to their elemental state (M^0), according to the equations [217]:

$$M^{m+} + m\,BH_4^- + 3m\,H_2O \longrightarrow M^0 + m\,B(OH)_3 + 3.5m\,H_2$$

$$M^{m+} + \frac{m}{4}\,N_2H_4 \longrightarrow M^0 + \frac{m}{4}\,N_2 + mH^+$$

$$M^{m+} + m\,N_2H_4 + m\,OH^- \longrightarrow M^0 + \frac{m}{2}\,N_2 + mNH_3 + m\,H_2O$$

Figure 42. Metals cations reduction with borohydride (top) or hydrazine (middle and bottom) compounds [217]

This kind of chemical reduction requires the presence of stabilising agents such as ethylene glycol and glycerol for the reduced structures. In this way, Ag, Pd, Cu, Ni, and Bi porous structures with sponge-like morphology have been prepared at room temperature [218]. Ag nanoparticles have also been prepared using polyvinylpyrrolidone (PVP) as a capping agent [219].

Thermally activated reduction methods are also possible using alcohols or polyols. In the first case, the metal ions are reduced while alcohols with an α-hydrogen atom are oxidised to the corresponding carbonyl group (e.g. formaldehyde in the case of methanol) [220]. Using this method, $RuCl_3$, $PdCl_2$ and H_2PtCl_6 have been reduced in the presence of PVP as stabiliser under a reflux of ethanol/water (1/1, v/v) at 95-100 °C for 2 h. Colloidal dispersions of Ru, Pd and Pt were obtained with nanoparticles of 2.8, 4.2 and 1.4 nm, respectively [221].

The second case is the polyol method, in which a polyol like ethylene glycol is thermally dehydrated, forming acetaldehyde as a reductant. Subsequently, it reacts with the metal ions to form metallic nanoparticles and diacetyl [222], as follow:

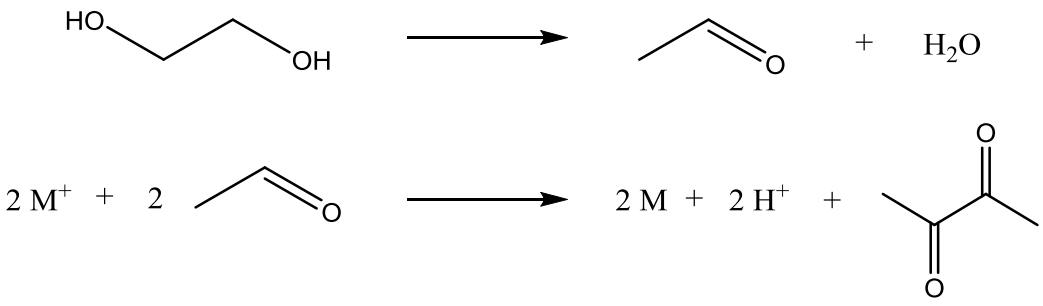

Figure 43. Polyol reduction method [222].

However, at temperatures above 140 °C in the presence of oxygen, ethylene glycol produces glycolaldehyde, which acts as reducing agent in that case [222].

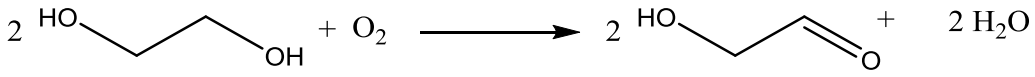

Figure 44. Glycolaldehyde formation above 140 °C [222].

Using the polyol method at 160 °C, it has been possible to prepare Pd nanoparticles stabilized with PVP, exhibiting controlled shapes: octahedrons (24 nm), cubes (20 nm) and tetrahedrons (22 nm, up to 120 nm) [223].

Microwaves assisted methods permit reduced preparation times compared to thermal methods and allow the preparation of small particles with narrow size distribution. For instance, metal salts like $HAuCl_4$ or $Pd(NO_3)_2$ were mixed with either $Ce(NO_3)_4$, $Zn(NO_3)_2$, or $Cu(NO_3)_2$ ethylic solutions and adjusted to pH 10 dropwise with NaOH. The mixtures were irradiated with microwaves for 10 minutes with cycles of 10 s on and 20 s off. PVP was also used as capping agent for the noble metal nanoparticles. Such procedure led to Au or Pd nanoparticles supported on either CeO_2, CuO, or ZnO nanoparticles of a few nanometres [224]. The polyol method has also been used with microwave assistance, for which 2 mL of a H_2PtCl_6 solution was mixed with 25 mL of ethylene glycol and irradiated for 60 s at a maximum temperature of 170 °C. The colloidal solution was then stabilised with 1-dodecanethiol, leading to Pt nanoparticles ranging between 1.9 and 7.4 nm depending on the synthesis conditions. Using this method, Pt and bimetallic Pt-Ru nanoparticles were prepared and supported on Vulcan or carbon nanotubes. The latter with bimetallic particles exhibited the best performance in the room temperature electrooxidation of methanol [225]. Stable mono-metallic [226] and bi-metallic [227] colloids have also been prepared via microwave heating using water as solvent, glucose as a mild and non-toxic reducer and PVP as the chelating agent. Such colloids have been used in the preparation of Au/Cu and Au/Pd bimetallic catalysts supported on titania and ceria exhibiting an increase of selectivity in the liquid phase oxidation of 5-hydroxymethylfufural (HMF) to 2,5-furandicarboxylic acid (FDCA) [227].

Au, Ag, Pd have been deposited on mesoporous silica SBA-12 (prepared beforehand by soft-templating) using a microwave-assisted protocol with ethanol and acetone–water as both, solvent and reducing agents. The nanoparticles size ranged between 2 and 80 nm depending on the metal loading and microwave irradiation time. This method permitted the synthesis of extremely active catalysts in the oxidation of styrene [228]. Microwaves have also been used in the preparation of hierarchically porous materials with Pt nanoparticles. A silica sol was prepared in the presence of two templates: a polystyrene latex template to achieve macropores and a non-ionic triblock copolymer (Pluronic F_{68}: $(EO)_{80}(PO)_{30}(EO)_{80}$) to lead to ordered mesopores. Additionally, a solution of H_2PtCl_6 in ethylene glycol was added to the sol, which was then treated with microwaves to carry out the Pt reduction. The sol was used to prepare films by dip-coating, in which the final hierarchical porosity was composed of micropores (<2 nm), ordered mesopores (ca. 4 nm) and macropores (ca. 70 nm), and the Pt nanoparticles of about 4 nm were located within the mesopores, as shown in Figure 45 [229].

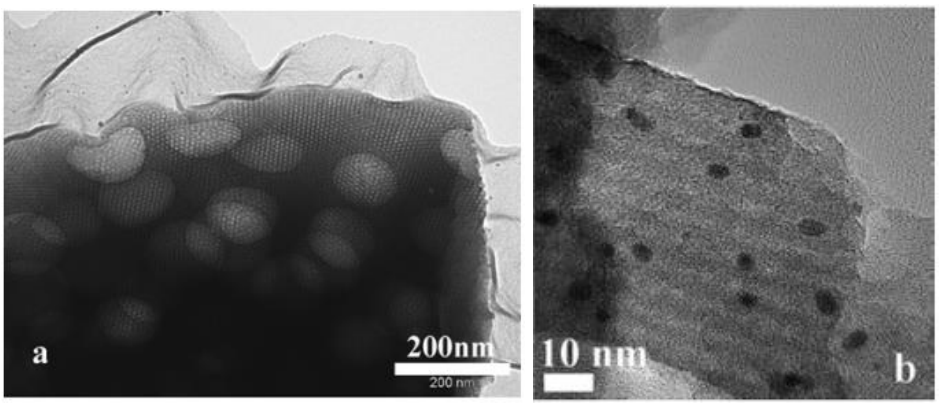

Figure 45. Two different magnifications of a hierarchically porous silica with Pt nanoparticles prepared by microwave-assisted method [229].

- Supercritical fluids

  This method requires the dissolution of a metal precursor in a supercritical fluid, which is then contacted with a support. Subsequent reduction under supercritical conditions or after depressurisation is required, which can be either thermal or with reducing agents (e.g. hydrogen). Chemical reduction under supercritical conditions is known as Supercritical Fluid Reactive Deposition (SFRD). CO_2 is the most used solvent under supercritical conditions since it is abundant, non-flammable, non-toxic and relatively cheap. This technique resembles the impregnation one, but with improved features: it reduces the production of waste-water by using supercritical CO_2 as solvent, the lower surface tension of the fluid enables better penetration and the collapse of the support porosity is also overcome by avoiding liquid-gas interfaces. The challenges of this technique are related to the limited solubility of many metal precursors in $scCO_2$ and the cost of the equipment to operate at the required conditions of temperature and pressure [230,231]. Using this method, it has been possible to obtain Pt particles as small as 1.8 nm supported on TiO_2, Al_2O_3 and MCM-41 starting form dimethyl-(1,5-cyclooctadiene)-platinum ($Pt(COD)Me_2$) or fluorinated organometallic Pt precursors [232]. Pt/Al_2O_3 prepared by the SFRD method has exhibited a better performance in the CO oxidation compared to catalysts prepared by conventional impregnation [233]. Other catalysts based on Pt, Ru and Ni and supported on graphene have been prepared and evaluated for the selective partial hydrogenation of limonene. Such materials exhibited nanoparticles ranging between 2 and 15 nm with very good catalytic performance [234]. Ni has also been supported on mesoporous silica SBA-15 [235]. Another wide-scope approach has been proposed, comprising the preparation of a copolymer/Pd(II) supramolecular complex purposely prepared from palladium acetate by ligand exchange with poly(1,1,2,2-tetrahydroperfluorodecylacrylate-*co*-acetoacetoxyethylmethacrylate) (poly(FDA-*co*-AAEMA)). The resulting poly(FDA- *co*-AAEMA)-Pd(II) supramolecular complex was used to impregnate a mesostructured commercial silica (MSU-H) in $scCO_2$. After reduction in hydrogen, the material exhibited Pd nanoparticles (2–9 nm) evenly distributed on the silica matrix with good catalytic activity in the Heck reaction (formation of a substituted alkene from an unsaturated halide with an alkene) [236].

- Sonochemistry

  This technique uses sound waves with frequencies above 18 kHz (ultrasound), particularly between tens of kHz to a few MHz. In general, the sound is transmitted as a pressure wave, and so an oscillation of compression and expansion cycles is created in the liquid medium. During this oscillation, some bubbles are formed in the expansion stage. They continue oscillating with the ultrasound wave and growing until they reach a size that is no longer stable, so they suddenly collapse (within a few μs). This phenomenon is known as acoustic cavitation and it is schematised in Figure 46. These very fast implosions lead to very extreme local conditions (of the order of 10^3 °C and 10^2 bars) that create non-equilibrium plasma inside the cavitation bubble [237,238].

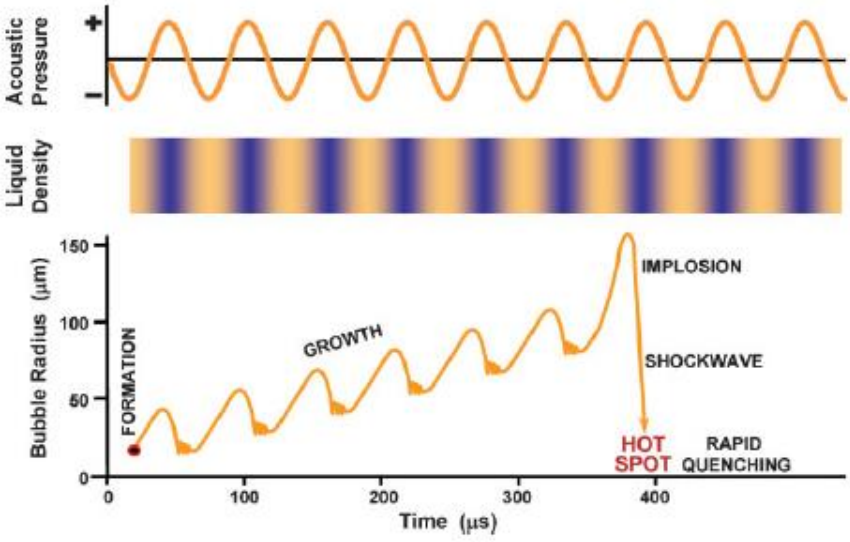

Figure 46. Schematic acoustic cavitation phenomenon [238].

Depending on the operation conditions, the acoustic cavitation phenomenon can lead to chemical or physical effects (see Annex II for further details). Regarding the chemical effects, they occur at high ultrasound frequencies (of the order of 10^2 kHz). At such conditions, water molecules can be split into $H^\bullet$ and $OH^\bullet$ radicals within the cavitation bubble [239,240]. Hydrogen, H_2, generated by the recombination of $H^\bullet$ radicals within these bubbles, reacts with the metal ions to reduce them to metallic nanoparticles [241–244]. Carbon monoxide can be added to the reaction medium in order to enhance the metal reduction under ultrasonic irradiation by increasing the formation of H_2 [239]. Indeed, CO scavenges $OH^\bullet$ radicals produced in the water splitting within the cavitation bubble, to yield more $H^\bullet$ [241]:

$$CO + OH^\bullet \xrightarrow{)))} CO_2 + H^\bullet$$

In addition to this, CO is also a reducing species that can react with metal ions at the cavitation bubble interface. These two effects simultaneously increase the metal reduction rate.

For example, the sonochemical reduction of Pt(II) ions under an Ar atmosphere at room temperature takes place according to the reaction [241]:

$$PtCl_4^{2-} + H_2 \xrightarrow{)))} Pt^0 + 2H^+ + 4Cl^-$$

But under CO/Ar and at room temperature, the Pt(II) ions can also be reduced following the reaction [241]:

$$PtCl_4^{2-} + CO + H_2O \xrightarrow{)))} Pt^0 + CO_2 + 2H^+ + 4Cl^-$$

A schematic representation of the chemical phenomena is presented in Figure 47.

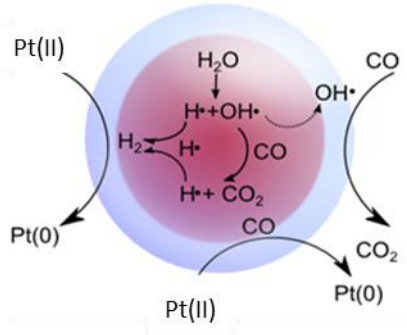

Figure 47. Schematic representation of the sonochemical reduction of Pt. Based on [241].

Even though the homolytic water splitting under ultrasound could be enough to account for producing hydrogen for metallic ions reduction, there are reports of using formic acid [241], hydrogen gas and polyols [245] in combination with ultrasonic irradiation. This is particularly interesting when the reactive species produced sonochemically are present in limited amounts, requiring the optimisation of the operation conditions or the coupling with other redox systems.

Gold nanoparticles (2–2.5 nm) have been synthesised and supported on mesoporous materials (TiO_2 and Fe_2O_3) by a sonochemical method using $HAuCl_4$ precursor, 20 kHz, ethanol as solvent and a 95% Ar - 5% H_2 atmosphere (interestingly, the supports were also prepared via sonochemical synthesis [246–248]). Such materials were tested for the CO oxidation reaction, being able to achieve a complete CO conversion at a low temperature (170 °C) [249].

H_2PtCl_6 has been reduced under sonochemical irradiation at 20 kHz in the presence of formic acid 1M under Ar atmosphere or in water under 90% Ar - 10% CO atmosphere, leading to Pt nanoparticles of 3–5 nm, which were deposited *in-situ* on polystyrene latex of ca. 100 nm. This decorated latex was used as template for the preparation of macroporous silica [250]. This study demonstrated the feasibility of decorated polymer

templates as porogens and Pt nanoparticles carrier as a first step in the structuration of silica-supported catalysts.

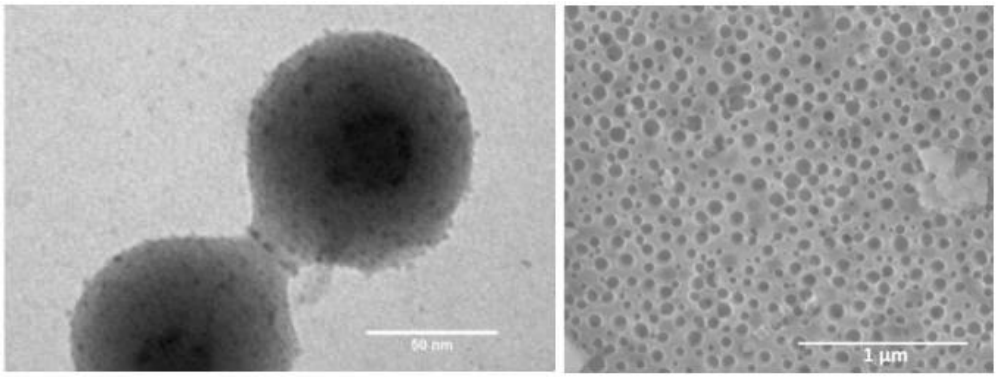

Figure 48. Pt-decorated polystyrene latex (left) and macroporous silica-supported Pt catalyst after template removal (right) [250].

Interestingly, sonochemistry can be used in combination with other techniques to enhance processes. For instance, electrochemical reduction (in case of conductive support) coupled with ultrasound irradiation improves the mass transport of the reducible species by decreasing the diffusion layer thickness [251]. $LiNi_{0.8}Co_{0.2}O_2$/PANI composites have also been prepared using an ultrasound treatment leading to homogeneous materials containing a large amount of the metal oxide particles of small size. Such treatment resulted to be more effective than conventional methods such as magnetic stirring [252]. In polymerisation chemistry, the radicals generated during the water molecule cleavage by sonochemical effects have been used as radical initiators [111], being first described for the polymerisation of butyl acrylate and vinyl acetate [112].

II.5- Summary of the literature review and presentation of the experimental project

Catalysis is by itself a green chemistry pillar and it provides high potential to address current and future challenges in the chemical industry. In addition to being listed as one of the 12 Principles of green chemistry, catalysis contributes from several fronts to the design of more sustainable chemicals, processes and products. Even though, catalytic processes have been widely adopted – being present today in about 90% of all industrial chemical transformations – there is a huge opportunity for developing new processes and improving catalytic materials performance.

The catalyst market is forecast to be USD 34.3 billion by 2024; and even though it is a large figure, it only represents less than 1% of the sales revenue from the products created using catalytic processes. In 2015, heterogeneous catalysts were used extensively accounting for 73.6% of the global market volume due to their ease of handling, low price and easy market access. Such important market participation motivates the focus of this work on heterogeneous catalytic materials, and more specifically on supported metal catalysts, whose demand was 1,568.4 kilo tons in 2015 and is expected to grow in light of its increasing application in the organic synthesis of chemicals commodities.

In the efforts for developing more performant catalytic processes, materials with original designs, notably with hierarchical porosity, have been proven to exhibit superior performances than only micro- or mesoporous catalysts. Some important applications where hierarchically porous materials have shown excellent results are photocatalysis, fuel chemistry (e.g. fuel cells, Fischer-Tropsch and catalytic cracking reactions), selective organic reactions (e.g. oxidation, epoxidation, hydrogenation, isomerisation, C-C bond forming), biomass valorisation and pollution abatement. Remarkable features on this kind of materials that make them outperform non-structured catalysts are enhanced internal mass and heat transfer, higher active site accessibility and higher metal dispersion [177].

In regard of the high potential of hierarchical porosity, this research project will focus on the preparation of metal catalysts deposited on a meso- and macroporous silica support. The choice of silica is made upon the well stablished state of the art on silicon-alkoxides chemistry for the tailored silica synthesis via controlled sol-gel conditions. Additionally, several templating approaches have been proposed to achieve silica-based hierarchically porous materials.

The understanding of structure-function relations is also very important in order to make rational designs of structured catalysts. To do so, it is important to guarantee experimental techniques that allow fine tuning catalyst morphologies and active sites homogeneous dispersion. Furthermore, structured catalysts preparation should also be green. To do so, waterborne approaches are desired over methods based on organic solvents. This point valorises the combination of controlled sol-gel synthesis with aqueous suspensions of polymer templates for meso- and macropores tailoring, respectively. Additionally, a procedure for catalyst functionalisation based on homolytic water splitting using sonochemistry is attractive, since it reduces the use of chemicals that are generally hazardous; and it is at the same time more atom-economical and prevents further steps of purification. Based on these aspects, the catalyst synthesis proposed herein is based on the combination of polymer synthesis, sonochemical

decoration and sol-gel process. This approach aims for achieving materials with regular distribution of metal decorated macropores and controlled support structure with hierarchical porosity.

Two case studies are proposed. The first is the preparation of Pt/SiO_2 catalysts for the selective hydrogenation of chloronitrobenzene to produce chloroaniline. This reaction has been selected considering that haloanilines are important building blocks in the synthesis of a large variety of nitrogen-containing industrial products such as fertilizers, polymers, dyes and drugs [253]. Accordingly, Chapter III is focused on the preparation of silica-supported platinum catalysts with hierarchical porosity and Chapter IV discusses the effect of the hierarchical porosity on the catalytic performance of such materials.

The second case study is the preparation of Pd-based catalysts for the hydrogen peroxide direct synthesis from oxygen and hydrogen. Hydrogen peroxide is a very important chemical commodity, but currently, it is produced by an anthraquinone-based process, which is highly energy consuming and large-volume waste producing. The direct synthesis of hydrogen peroxide was selected since it is a promising alternative to the current process [46], being the selectivity the main challenge to overcome [254]. Accordingly, Chapter V explores the versatility of the proposed catalyst preparation method to make Pd/SiO_2, bimetallic $Pd\text{-}Pt/SiO_2$ and $Pd\text{-}CeO_2/SiO_2$ catalysts with hierarchical porosity. The alternative preparation of Pd-containing hybrid latex template via miniemulsion polymerisation is also proposed. Finally, Chapter VI presents the comparison of the catalytic performances of these Pd-based materials.

The international collaboration as well as the implication of scientists with different expertise and horizons, such as in the frame of the Sustainable Industrial Chemistry Doctoral Programme (SINCHEM), is a prerequisite to perform this type of study. Indeed, the final optimisation of catalytic materials will require the close collaboration between chemists, material scientists, chemical engineers and molecular simulation experts [177].

II.6- References

[1] I. Fechete, Y. Wang, J.C. Védrine, The past, present and future of heterogeneous catalysis, Catal. Today. 189 (2012) 2–27. doi:10.1016/j.cattod.2012.04.003.

[2] E. Fulhame, An essay on combustion, with a view to a new art of dying and painting wherein the phlogistic and antiphlogistic hypotheses are proved erroneous, Jonhson, R, London, 1794.

[3] J.F. Coindet, Extrait de l'ouvrage de Mme. Fulhame, Ann. Chim. 26 (1798) 58.

[4] J.J. Berzelius, Årsberättelsen om framsteg i fysik och kemi [Annual report on progress in physics and chemistry], Royal Swedish Academy of Sciences, Stockholm, 1835.

[5] American Chemical Society, Technology Vision 2020 The U.S. Chemical Industry, Washington, DC, 1996. https://energy.gov/sites/prod/files/2013/11/f4/chem_vision.pdf.

[6] G.A. Kraus, Heterogeneous Catalysis for Today's Challenges: Synthesis, Characterization and Applications, Royal Society of Chemistry, Cambridge, 2015. doi:10.1039/9781849737494.

[7] L. Lloyd, Handbook of Industrial Catalysts, Springer US, Boston, MA, 2011. doi:10.1007/978-0-387-49962-8.

[8] Phillips, British Patent 6096, 1831.

[9] Jullion, British Patent 11425, 1846.

[10] Hunt, British Patent 1919, 1853.

[11] D. McDonald, L.B. Hunt, A History of Platinum and Its Allied Metals, Johnson Matthey, London, 1982.

[12] J.J. y Santacilia, A. de Ulloa, Relacion historica del viage a la America meridional hecho de orden de S. Mag., 1748.

[13] W. Watson, W. Brownrigg, Several Papers concerning a New Semi-Metal, Called Platina; Communicated to the Royal Society by Mr. Wm. Watson F. R. S., Philos. Trans. R. Soc. London. 46 (1749) 584–596. doi:10.1098/rstl.1749.0110.

[14] Guyton, Examen de quelques propriétés du Platine, Ann. Chim. 25 (1794) 3–20.

[15] M.C. Usselman, The Wollaston/Chenevix controversy over the elemental nature of palladium: A curious episode in the history of chemistry, Ann. Sci. 35 (1978) 551–579. doi:10.1080/00033797800200431.

[16] H. Davy, Some New Experiments and Observations on the Combustion of Gaseous Mixtures, with an Account of a Method of Preserving a Continued Light in Mixtures of Inflammable Gases and Air without Flame, Philos. Trans. R. Soc. London. 107 (1817) 77–85. doi:10.1098/rstl.1817.0009.

[17] A.B. Robertson, The Early History of Catalysis, Platin. Met. Rev. 19 (1975) 64–69. doi:10.1007/BF03214875.

[18] F. Slama, H. Wolf, Oxidation of sulfur dioxid and catalyst therefor, US1371004, 1921.

[19] H. Deacon, British Patent 1403, 1868.

[20] P.T. Anastas, J.C. Warner, Green Chemistry: Theory and Practice, Oxford University Press, New York, 1998.

[21] P.T. Anastas, J.B. Zimmerman, Peer Reviewed: Design Through the 12 Principles of Green Engineering, Environ. Sci. Technol. 37 (2003) 94A–101A. doi:10.1021/es032373g.

[22] M.-O. Coppens, G. Wang, Optimal Design of Hierarchically Structured Porous Catalysts, in: U.S. Ozkan (Ed.), Des. Heterog. Catal., Wiley-VCH Verlag GmbH & Co. KGaA, Weinheim, Germany, 2009: pp. 25–58. doi:10.1002/9783527625321.

[23] F. Zaera, New challenges in heterogeneous catalysis for the 21st century, Catal. Letters. 142 (2012) 501–516. doi:10.1007/s10562-012-0801-9.

[24] S. Deville, A.J. Stevenson, Mapping Ceramics Research and Its Evolution, J. Am. Ceram. Soc. 98 (2015) 2324–2332. doi:10.1111/jace.13699.

[25] BCC Research, Global Markets for Catalysts, (2015).

[26] Grand View Research Inc., Catalyst Market Size Expected To Reach $34.3 Billion By 2024, (2016). http://www.grandviewresearch.com/press-release/catalyst-market-analysis (accessed June 20, 2017).

[27] A. Ayral, A. Julbe, D. Dhaler, P. Euzen, J.-P. Joulin, J. Lopez, Les ceramiques pour la filtration, la catalyse et l'environnement, in: G. Fantozzi, J.-C. Niepce, G. Bonnefont (Eds.), Les Céramiques Ind. Propriétés, Mise En Forme Appl., 2013: p. 512.

[28] Grand View Research Inc., Catalyst Market Size, Share & Trends | Global Industry Report, 2016. http://www.grandviewresearch.com/industry-analysis/catalyst-market.

[29] Grand View Research Inc., Catalyst Market Analysis By Product (Heterogeneous, Homogenous), By Material (Zeolites, Metals, Chemical Compounds), By Application (Refinery, Chemical Synthesis, Polymer, Environment) And Segment Forecasts To 2020, (2014). http://www.prweb.com/releases/global-catalyst-market/industry-trend-forecast/prweb12101227.htm (accessed June 20, 2017).

[30] C. Adams, Educational Archives - North American Catalysis Society, (2012). http://nacatsoc.org/category/educational/ (accessed June 20, 2017).

[31] M. van der Van, Y. Kobayashi, R. Diercks, Technology Roadmap: Energy and GHG Reductions in the Chemical Industry via Catalytic Processes, Energy Technol. Perspect. (2013) 1–60.

[32] M. Balat, Potential importance of hydrogen as a future solution to environmental and transportation problems, Int. J. Hydrogen Energy. 33 (2008) 4013–4029. doi:10.1016/j.ijhydene.2008.05.047.

[33] J.N. Armor, The multiple roles for catalysis in the production of H2, Appl. Catal. A Gen. 176 (1999) 159–176. doi:10.1016/S0926-860X(98)00244-0.

[34] R.M. Navarro, M.A. Peña, J.L.G. Fierro, Hydrogen production reactions from carbon feedstocks: Fossil fuels and biomass, Chem. Rev. 107 (2007) 3952–3991. doi:10.1021/cr0501994.

[35] P. V. Kamat, Meeting the clean energy demand: Nanoestructure Architectures for Solar Energy Conversion, Phys. Chem. 392 (2007) 2834–2860. doi:10.1002/adma.200902096.

[36] K. Maeda, K. Domen, Photocatalytic water splitting: Recent progress and future challenges, J. Phys. Chem. Lett. 1 (2010) 2655–2661. doi:10.1021/jz1007966.

[37] J. Pérez-Carvajal, P. Aranda, A. Berenguer-Murcia, D. Cazorla-Amorós, J. Coronas, E. Ruiz-Hitzky, Nanoarchitectures based on layered titanosilicates supported on glass fibers: Application to hydrogen storage, Langmuir. 29 (2013) 7449–7455. doi:10.1021/la304519a.

[38] S. Zinoviev, F. Müller-Langer, P. Das, N. Bertero, P. Fornasiero, M. Kaltschmitt, G. Centi, S. Miertus, Next-generation biofuels: Survey of emerging technologies and sustainability issues, ChemSusChem. 3 (2010) 1106–1133. doi:10.1002/cssc.201000052.

[39] M.R.G. Klaas, H. Schöne, Direct, high-yield conversions of cellulose into biofuel and

platform chemicals - On the way to a sustainable biobased economy, ChemSusChem. 2 (2009) 127–128. doi:10.1002/cssc.200800186.

[40] J.N. Chheda, G.W. Huber, J.A. Dumesic, Liquid-phase catalytic processing of biomass-derived oxygenated hydrocarbons to fuels and chemicals, Angew. Chemie - Int. Ed. 46 (2007) 7164–7183. doi:10.1002/anie.200604274.

[41] G. Centi, P. Ciambelli, S. Perathoner, P. Russo, Environmental catalysis: Trends and outlook, Catal. Today. 75 (2002) 3–15. doi:10.1016/S0920-5861(02)00037-8.

[42] R.M. Heck, R.J. Farrauto, Automobile exhaust catalysts, Appl. Catal. A Gen. 221 (2001) 443–457. doi:10.1016/S0926-860X(01)00818-3.

[43] R. Raudaskoski, E. Turpeinen, R. Lenkkeri, E. Pongrácz, R.L. Keiski, Catalytic activation of CO2: Use of secondary CO2 for the production of synthesis gas and for methanol synthesis over copper-based zirconia-containing catalysts, Catal. Today. 144 (2009) 318–323. doi:10.1016/j.cattod.2008.11.026.

[44] V. Havran, M.P. Duduković, C.S. Lo, Conversion of methane and carbon dioxide to higher value products, Ind. Eng. Chem. Res. 50 (2011) 7089–7100. doi:10.1021/ie2000192.

[45] A. Corma, Heterogeneous catalysis: Understanding for designing, and designing for applications, Angew. Chemie - Int. Ed. 55 (2016) 6112–6113. doi:10.1002/anie.201601231.

[46] G. Centi, S. Perathoner, S. Abate, Direct Synthesis of Hydrogen Peroxide: Recent Advances, in: Mod. Heterog. Oxid. Catal., Wiley-VCH Verlag GmbH & Co. KGaA, 2009: pp. 253–287. doi:10.1002/9783527627547.ch8.

[47] Q.H. Xia, H.Q. Ge, C.P. Ye, Z.M. Liu, K.X. Su, Advances in Homogeneous and Heterogeneous Catalytic Asymmetric Epoxidation, Chem. Rev. 105 (2005) 1603–1662. doi:10.1021/cr0406458.

[48] F. Cavani, J.H. Teles, Sustainability in catalytic oxidation: An alternative approach or a structural evolution?, ChemSusChem. 2 (2009) 508–534. doi:10.1002/cssc.200900020.

[49] V. Hulea, Matériaux et Procédés Catalytiques: lecture, (2014).

[50] G. Ertl, H. Knözinger, J. Weitkamp, Handbook of heterogeneous catalysis, Wiley-VCH Verlagsgesellschaft mbH, 1997.

[51] J.A. Schwarz, C. Contescu, A. Contescu, Methods for Preparation of Catalytic Materials, Chem. Rev. 95 (1995) 477–510. doi:10.1021/cr00035a002.

[52] O. Levenspiel, Chemical reaction engineering, Ind. Eng. Chem. Res. 38 (1999) 4140 – 4143. doi:10.1021/ie990488g.

[53] P. Avila, M. Montes, E.E. Miró, Monolithic reactors for environmental applications, Chem. Eng. J. 109 (2005) 11–36. doi:10.1016/j.cej.2005.02.025.

[54] Johnson Matthey, AUTOCATALYST, (2005). http://www.technology.matthey.com/article/56/3/165-176/ (accessed November 2, 2016).

[55] J.F.L. Page, Applied heterogeneous catalysis: design, manufacture, use of solid catalysts, 1987. https://books.google.com/books?id=DcBTAAAAMAAJ.

[56] P.S. Metkar, V. Balakotaiah, M.P. Harold, Experimental study of mass transfer limitations in Fe- and Cu-zeolite-based NH3-SCR monolithic catalysts, Chem. Eng. Sci. 66 (2011) 5192–5203. doi:10.1016/j.ces.2011.07.014.

[57] J. Pérez-Ramírez, C.H. Christensen, K. Egeblad, C.H. Christensen, J.C. Groen, Hierarchical zeolites: Enhanced Utilisation of Microporous Crystals in Catalysis by Advances in Materials Design., Chem. Soc. Rev. 37 (2008) 2530–2542. doi:10.1039/b809030k.

[58] K.C.-W. Wu, Chapter 1. Synthesis of Multi-functionalized Mesoporous Silica Nanoparticles for Cellulosic Biomass Conversion, in: Heterog. Catal. Today's Challenges Synth. Charact. Appl., 2015: pp. 1–27. doi:10.1039/9781849737494-00001.

[59] X.-Y. Yang, L.-H. Chen, Y. Li, J.C. Rooke, C. Sanchez, B.-L. Su, Hierarchically porous materials: synthesis strategies and structure design, Chem. Soc. Rev. 46 (2017) 481–558. doi:10.1039/C6CS00829A.

[60] Y. Wan, D. Zhao, On the controllable soft-templating approach to mesoporous silicates., Chem. Rev. 107 (2007) 2821–60. doi:10.1021/cr068020s.

[61] B. Louis, G. Laugel, P. Pale, M.M. Pereira, Rational design of microporous and mesoporous solids for catalysis: from the molecule to the reactor, ChemCatChem. 3 (2011) 1263–1272. doi:10.1002/cctc.201100110.

[62] N. Tanchoux, S. Pariente, P. Trens, F. Fajula, Confinement and curvature effects as a tool for selectivity orientation in heterogeneous catalysis: Isomerisation of n-hexene over MCM-41-type catalysts, J. Mol. Catal. A Chem. 305 (2009) 8–15. doi:10.1016/j.molcata.2008.11.017.

[63] D. Zhao, Y. Wan, W. Zhou, Ordered mesoporous materials, Wiley-VCH Verlag GmbH

& Co. KGaA, Weinheim, Germany, 2013. doi:10.1002/9783527647866.

[64] D. Avnir, V.R. Kaufman, Alcohol is an unnecessary additive in the silicon alkoxide sol-gel process, J. Non. Cryst. Solids. 192 (1987) 180–182. doi:10.1016/S0022-3093(87)80368-X.

[65] C.T. Kresge, M.E. Leonowicz, W.J. Roth, J.C. Vartuli, J.S. Beck, Ordered mesoporous molecular sieves synthesized by a liquid-crystal template mechanism, Nature. 359 (1992) 710–712. doi:10.1038/359710a0.

[66] J.S. Beck, J.C. Vartuli, W.J. Roth, M.E. Leonowicz, C.T. Kresge, K.D. Schmitt, C.T.-W. Chu, D.H. Olson, E.W. Sheppard, S.B. McCullen, J.B. Higgins, J.L. Schlenkert, A New Family of Mesoporous Molecular Sieves Prepared with Liquid Crystal Templates, J. Am. Chem. Soc. (1992) 10834–10843. doi:10.1021/ja00053a020.

[67] C.J. Brinker, G.W. Scherer, Sol–Gel Science: The physics and chemistry of sol-gel processing, Elsevier, London, 1990.

[68] R.M. Tindwa, D.K. Ellis, G.-Z. Peng, A. Clearfield, Intercalation of n-alkylamines by α-zirconium phosphate, J. Chem. Soc. Faraday Trans. 1 Phys. Chem. Condens. Phases. 81 (1985) 545. doi:10.1039/f19858100545.

[69] P. Van Der Voort, P.I. Ravikovitch, K.P. De Jong, M. Benjelloun, E. Van Bavel, A.H. Janssen, A. V. Neimark, B.M. Weckhuysen, E.F. Vansant, A new templated ordered structure with combined micro- and mesopores and internal silica nanocapsules, J. Phys. Chem. B. 106 (2002) 5873–5877. doi:10.1021/jp025642i.

[70] A. Ayral, A. Julbe, C. Guizard, Ceramic Membrane Processing: New Approaches in Design and Applications, in: B. Lee, S. Komarneni (Eds.), Chem. Process. Ceram. Second Ed., CRC Press, New York, 2005: pp. 629–666.

[71] A. Nepryahin, R.S. Fletcher, E.M. Holt, S.P. Rigby, Techniques for direct experimental evaluation of structure–transport relationships in disordered porous solids, Adsorption. 22 (2016) 993–1000. doi:10.1007/s10450-016-9806-9.

[72] N. Pal, A. Bhaumik, Soft templating strategies for the synthesis of mesoporous materials: Inorganic, organic-inorganic hybrid and purely organic solids, Adv. Colloid Interface Sci. 189-190 (2013) 21–41. doi:10.1016/j.cis.2012.12.002.

[73] K. Ariga, A. Vinu, Y. Yamauchi, Q. Ji, J.P. Hill, Nanoarchitectonics for Mesoporous Materials, Bull. Chem. Soc. Jpn. 85 (2012) 1–32. doi:10.1246/bcsj.20110162.

[74] C.J. Brinker, Hydrolysis and condensation of silicates: Effects on structure, J. Non. Cryst. Solids. 100 (1988) 31–50. doi:10.1016/0022-3093(88)90005-1.

[75] M.J. Buckley, A.M.; Greenblatt, Sol-Gel Preparation of Silica Gels, J. Chem. Ed. 71 (1994) 599. doi:10.1007/BF02745295.

[76] A. Ayral, A. Julbe, V. Rouessac, S. Roualdes, J. Durand, Microporous silica membrane: basic principles and recent advances, in: R. Mallada, M. Menendez (Eds.), Inorg. Membr. Synth. Charact. Appl., Elsevier, Amsterdam, 2008: pp. 33–74.

[77] S. Ermakov, A. Beletskii, O. Eismont, V. Nikolaev, Brief Review of Liquid Crystals, in: Liq. Cryst. Biotribology, 2016: pp. 37–56. doi:10.1007/978-3-319-20349-2_2.

[78] N.K. Raman, M.T. Anderson, C.J. Brinker, Template-Based Approaches to the Preparation of Amorphous, Nanoporous Silicas, Chem. Mater. 8 (1996) 1682–1701. doi:10.1021/cm960138+.

[79] T. Kaasgaard, C.J. Drummond, Ordered 2-D and 3-D nanostructured amphiphile self-assembly materials stable in excess solvent, Phys. Chem. Chem. Phys. 8 (2006) 4957. doi:10.1039/b609510k.

[80] J.M. Seddon, Structure of the inverted hexagonal (HII) phase, and non-lamellar phase transitions of lipids, BBA - Rev. Biomembr. 1031 (1990) 1–69. doi:10.1016/0304-4157(90)90002-T.

[81] J. Israelachvili, The science and applications of emulsions — an overview, Colloids Surfaces A Physicochem. Eng. Asp. 91 (1994) 1–8. doi:10.1016/0927-7757(94)02743-9.

[82] J.N. Israelachvili, D.J. Mitchell, B.W. Ninham, Theory of self-assembly of hydrocarbon amphiphiles into micelles and bilayers, J. Chem. Soc. Faraday Trans. 2. 72 (1976) 1525. doi:10.1039/f29767201525.

[83] C. Tschierske, Liquid crystal engineering – new complex mesophase structures and their relations to polymer morphologies, nanoscale patterning and crystal engineering, Chem. Soc. Rev. 36 (2007) 1930. doi:10.1039/b615517k.

[84] M. Salim, H. Minamikawa, A. Sugimura, R. Hashim, Amphiphilic designer nano-carriers for controlled release: from drug delivery to diagnostics, Med. Chem. Commun. 5 (2014) 1602–1618. doi:10.1039/C4MD00085D.

[85] G. Wanka, H. Hoffmann, W. Ulbricht, Phase Diagrams and Aggregation Behavior of Poly(oxyethylene)-Poly(oxypropylene)-Poly(oxyethylene) Triblock Copolymers in Aqueous Solutions, Macromolecules. 27 (1994) 4145–4159. doi:10.1021/ma00093a016.

[86] S. Šegota, S. Heimer, Đ. Težak, New catanionic mixtures of dodecyldimethylammonium bromide/sodium dodecylbenzenesulphonate/water, Colloids Surfaces A Physicochem.

Eng. Asp. 274 (2006) 91–99. doi:10.1016/j.colsurfa.2005.08.051.

[87] X.-J. Wu, D. Xu, Formation of Yolk/SiO(2) shell structures using surfactant mixtures as template., J. Am. Chem. Soc. 131 (2009) 2774–2775. doi:10.1021/ja808452r.

[88] G. Gu, J. Xu, Y. Wu, M. Chen, L. Wu, Synthesis and antibacterial property of hollow SiO2/Ag nanocomposite spheres, J. Colloid Interface Sci. 359 (2011) 327–333. doi:10.1016/j.jcis.2011.04.002.

[89] M.F. Ottaviani, A. Moscatelli, D. Desplantier-Giscard, F. Di Renzo, P.J. Kooyman, B. Alonso, A. Galarneau, Synthesis of micelle-templated silicas from cetyltrimethylammonium bromide/1,3,5-trimethylbenzene micelles, J. Phys. Chem. B. 108 (2004) 12123–12129. doi:10.1021/jp049032p.

[90] C.M.C. Faustino, A.R.T. Calado, L. Garcia-Rio, Mixed micelle formation between amino acid-based surfactants and phospholipids, J. Colloid Interface Sci. 359 (2011) 493–498. doi:10.1016/j.jcis.2011.04.016.

[91] Z. Zhang, X. Yan, B. Tian, C. Yu, B. Tu, G. Zhu, S. Qiu, D. Zhao, Synthesis of ordered small pore mesoporous silicates with tailorable pore structures and sizes by polyoxyethylene alkyl amine surfactant, Microporous Mesoporous Mater. 90 (2006) 23–31. doi:10.1016/j.micromeso.2005.10.026.

[92] S. Shirani Lapari, Z. Ramli, S. Triwahyono, Effect of Different Templates on the Synthesis of Mesoporous Sodalite, J. Chem. 2015 (2015) 1–6. doi:10.1155/2015/272613.

[93] P. Howlader, P. Das, E. Zangrando, P.S. Mukherjee, Urea-Functionalized Self-Assembled Molecular Prism for Heterogeneous Catalysis in Water, J. Am. Chem. Soc. 138 (2016) 1668–1676. doi:10.1021/jacs.5b12237.

[94] J.-Y. Zheng, J.-B. Pang, K.-Y. Qiu, Y. Wei, Synthesis of mesoporous titanium dioxide materials by using a mixture of organic compounds as a non-surfactant template, J. Mater. Chem. 11 (2001) 3367–3372. doi:10.1039/b105907f.

[95] A. V. Sangwai, R. Sureshkumar, Coarse-Grained Molecular Dynamics Simulations of the Sphere to Rod Transition in Surfactant Micelles, Langmuir. 27 (2011) 6628–6638. doi:10.1021/la2006315.

[96] A. Sambasivam, A. V. Sangwai, R. Sureshkumar, Self-Assembly of Nanoparticle–Surfactant Complexes with Rodlike Micelles: A Molecular Dynamics Study, Langmuir. 32 (2016) 1214–1219. doi:10.1021/acs.langmuir.5b03689.

[97] Y.H. Kim, D.K. Yoon, H.-T. Jung, Recent advances in the fabrication of nanotemplates from supramolecular self-organization, J. Mater. Chem. 19 (2009) 9091–9102.

doi:10.1039/b910496h.

[98] B.J. Auten, H. Lang, B.D. Chandler, Dendrimer templates for heterogeneous catalysts: Bimetallic Pt–Au nanoparticles on oxide supports, Appl. Catal. B Environ. 81 (2008) 225–235. doi:10.1016/j.apcatb.2007.12.012.

[99] M.A. Albiter, R. Morales, F. Zaera, Dendrimer-based synthesis of Pt catalysts for hydrocarbon conversion, Appl. Catal. A Gen. 391 (2011) 386–393. doi:10.1016/j.apcata.2010.05.045.

[100] P. Kunal, B.G. Trewyn, Chapter 2. Mesoporous Silica Supported Single-site Catalysis, in: Heterog. Catal. Today's Challenges Synth. Charact. Appl., 2015: pp. 28–60. doi:10.1039/9781849737494-00028.

[101] S.A. Bagshaw, E. Prouzet, T.J. Pinnavaia, Templating of Mesoporous Molecular Sieves by Nonionic Polyethylene Oxide Surfactants, Science. 269 (1995) 1242–1244. doi:10.1126/science.269.5228.1242.

[102] D. Zhao, Q. Huo, J. Feng, B.F. Chmelka, G.D. Stucky, Nonionic Triblock and Star Diblock Copolymer and Oligomeric Surfactant Syntheses of Highly Ordered, Hydrothermally Stable, Mesoporous Silica Structures, J. Am. Chem. Soc. 120 (1998) 6024–6036. doi:10.1021/ja974025i.

[103] Y. Shi, B. Li, P. Wang, R. Dua, D. Zhao, Micelle swelling agent derived cavities for increasing hydrophobic organic compound removal efficiency by mesoporous micelle@silica hybrid materials, Microporous Mesoporous Mater. 155 (2012) 252–257. doi:10.1016/j.micromeso.2012.02.002.

[104] M.P. Kapoor, A. Vinu, W. Fujii, T. Kimura, Q. Yang, Y. Kasama, M. Yanagi, L.R. Juneja, Self-assembly of mesoporous silicas hollow microspheres via food grade emulsifiers for delivery systems, Microporous Mesoporous Mater. 128 (2010) 187–193. doi:10.1016/j.micromeso.2009.08.019.

[105] D. Zhao, Y. Wan, W. Zhou, Ordered Mesoporous Materials, Wiley-VCH Verlag GmbH & Co. KGaA, Weinheim, Germany, 2013. doi:10.1002/9783527647866.

[106] D. Niu, Z. Ma, Y. Li, J. Shi, Synthesis of core−shell structured dual-mesoporous silica spheres with tunable pore size and controllable shell thickness, J. Am. Chem. Soc. 132 (2010) 15144–15147. doi:10.1021/ja1070653.

[107] Y. Chen, H. Chen, M. Ma, F. Chen, L. Guo, L. Zhang, J. Shi, Double mesoporous silica shelled spherical/ellipsoidal nanostructures: Synthesis and hydrophilic/hydrophobic anticancer drug delivery, J. Mater. Chem. 21 (2011) 5290. doi:10.1039/c0jm04024j.

[108] Y. Xie, D. Kocaefe, C. Chen, Y. Kocaefe, Review of Research on Template Methods in Preparation of Nanomaterials, J. Nanomater. 2016 (2016) 1–10. doi:10.1155/2016/2302595.

[109] S.C. Thickett, R.G. Gilbert, Emulsion polymerization: State of the art in kinetics and mechanisms, Polymer (Guildf). 48 (2007) 6965–6991. doi:10.1016/j.polymer.2007.09.031.

[110] P. Lacroix-Desmazes, Polymérisations en milieux dispersés, in: Chim. Procédés Polymérisation, Groupe Français d'études et d'applications des Polymères, 2010: pp. 93–120. http://hal.archives-ouvertes.fr/hal-00630371/ (accessed June 20, 2014).

[111] K. Matyjaszewski, T.P. Davis, eds., Handbook of Radical Polymerization, John Wiley & Sons, Inc., Hoboken, NJ, USA, 2002. doi:10.1002/0471220450.

[112] G. Cooper, F. Grieser, S. Biggs, Butyl Acrylate/Vinyl Acetate Copolymer Latex Synthesis Using Ultrasound As an Initiator, J. Colloid Interface Sci. 184 (1996) 52–63. doi:10.1006/jcis.1996.0596.

[113] R.M. Fitch, W.T. McCarvill, Surface chemistry of polystyrene colloids prepared by mixed initiator/surfactant systems, J. Colloid Interface Sci. 66 (1978) 20–25. doi:10.1016/0021-9797(78)90179-0.

[114] A.Y. Menshikova, T.G. Evseeva, Y.O. Skurkis, T.B. Tennikova, S.S. Ivanchev, Monodisperse carboxylated polystyrene particles: synthesis, electrokinetic and adsorptive properties, Polymer (Guildf). 46 (2005) 1417–1425. doi:10.1016/j.polymer.2004.11.071.

[115] G. Liu, P. Liu, Preparation of carboxyl-coated polystyrene nanoparticles using oleic acid, IET Nanobiotechnology. 3 (2009) 23. doi:10.1049/iet-nbt.2008.0009.

[116] D. Arunbabu, Z. Sanga, K.M. Seenimeera, T. Jana, Emulsion copolymerization of styrene and sodium styrene sulfonate: Kinetics, monomer reactivity ratios and copolymer properties, Polym. Int. 58 (2009) 88–96. doi:10.1002/pi.2497.

[117] L. Farias-Cepeda, J. Herrera-Ordonez, A.R. Hernandez-Martinez, M. Estevez, L. Rosales-Marines, Super-enhanced particle nucleation in styrene emulsion polymerization in the presence of sodium styrene sulfonate, J. Colloid Interface Sci. 500 (2017) 126–132. doi:10.1016/j.jcis.2017.04.015.

[118] M. Pabon, J.-M. Corpart, J. Selb, F. Candau, Synthesis in inverse emulsion and properties of water-soluble associating polymers, J. Appl. Polym. Sci. 84 (2002) 1418–1430. doi:10.1002/app.10337.

[119] F. Candau, Polymerization in Inverse Emulsions and Microemulsions, in: An Introd. to Polym. Colloids, Springer Netherlands, Dordrecht, 1990: pp. 73–96. doi:10.1007/978-94-009-0521-4_3.

[120] M.A. Malik, M.Y. Wani, M.A. Hashim, Microemulsion method: A novel route to synthesize organic and inorganic nanomaterials, Arab. J. Chem. 5 (2012) 397–417. doi:10.1016/j.arabjc.2010.09.027.

[121] V.M. Ovando-Medina, E. Mendizábal, R.D. Peralta, Kinetics modeling of microemulsion copolymerization, Polym. Bull. 54 (2005) 129–140. doi:10.1007/s00289-005-0369-2.

[122] F. Candau, M. Pabon, J.-Y. Anquetil, Polymerizable microemulsions: some criteria to achieve an optimal formulation, Colloids Surfaces A Physicochem. Eng. Asp. 153 (1999) 47–59. doi:10.1016/S0927-7757(98)00425-7.

[123] K. Landfester, Miniemulsion polymerization and the structure of polymer and hybrid nanoparticles, Angew. Chemie - Int. Ed. 48 (2009) 4488–4508. doi:10.1002/anie.200900723.

[124] J. Hu, M. Chen, L. Wu, Organic-inorganic nanocomposites synthesized via miniemulsion polymerization, Polym. Chem. 2 (2011) 760. doi:10.1039/c0py00284d.

[125] E. Schreiber, U. Ziener, A. Manzke, A. Plettl, P. Ziemann, K. Landfester, Preparation of narrowly size distributed metal-containing polymer latexes by miniemulsion and other emulsion techniques: Applications for nanolithography, Chem. Mater. 21 (2009) 1750–1760. doi:10.1021/cm802796y.

[126] A. Manzke, C. Pfahler, O. Dubbers, A. Plettl, P. Ziemann, D. Crespy, E. Schreiber, U. Ziener, K. Landfester, Etching masks based on miniemulsions: A novel route towards ordered arrays of surface nanostructures, Adv. Mater. 19 (2007) 1337–1341. doi:10.1002/adma.200601945.

[127] E. Pouget, J. Tonnar, C. Eloy, P. Lacroix-Desmazes, B. Boutevin, Synthesis of Poly(styrene)- b -poly(dimethylsiloxane)- b -poly(styrene) Triblock Copolymers by Iodine Transfer Polymerization in Miniemulsion, Macromolecules. 39 (2006) 6009–6016. doi:10.1021/ma060416i.

[128] J. Tonnar, E. Pouget, P. Lacroix-Desmazes, B. Boutevin, Synthesis of poly(vinyl acetate)-blockpoly(dimethylsiloxane)-block- poly(vinyl acetate) copolymers by iodine transfer photopolymerization in miniemulsion, Macromol. Symp. 281 (2009) 20–30. doi:10.1002/masy.200950703.

[129] J. Tonnar, P. Lacroix-Desmazes, Controlled radical polymerization of butyl acrylate and methyl methacrylate by reverse iodine transfer polymerization (RITP) in miniemulsion:

Use of hydrogen peroxide as oxidant, ACS Symp. Ser. 1024 (2009) 65–79. doi:10.1021/bk-2009-1024.ch005.

[130] R. Rahme, C. Graillat, G. Farzi, T.F.L. McKenna, T. Hamaide, Miniemulsion Polymerizations Using Static Mixers: Towards High Biocompatible Hydrophobe Contents, Macromol. Chem. Phys. 211 (2010) 2331–2338. doi:10.1002/macp.201000302.

[131] G.A. Farzi, E. Bourgeat-Lami, T.F.L. McKenna, Miniemulsions using static mixers: Part 2. Co-emulsification and composite materials using SMX static mixers, Can. J. Chem. Eng. 89 (2011) 1434–1440. doi:10.1002/cjce.20514.

[132] A. López, A. Chemtob, J.L. Milton, M. Manea, M. Paulis, M.J. Barandiaran, S. Theisinger, K. Landfester, W.D. Hergeth, R. Udagama, T. McKenna, F. Simal, J.M. Asua, Miniemulsification of monomer-resin hybrid systems, Ind. Eng. Chem. Res. 47 (2008) 6289–6297. doi:10.1021/ie701768z.

[133] M. Manea, A. Chemtob, M. Paulis, J.C. de la Cal, M.J. Barandiaran, J.M. Asua, Miniemulsification in high-pressure homogenizers, AIChE J. 54 (2008) 289–297. doi:10.1002/aic.11367.

[134] A. Lopez, Y. Reyes, E. Degrandi-Contraires, E. Canetta, C. Creton, J.L. Keddie, J.M. Asua, Simultaneous Free-Radical and Addition Miniemulsion Polymerization: Effect of the Chain Transfer Agent on the Microstructure of Polyurethane-Acrylic Pressure-Sensitive Adhesives, Macromol. Mater. Eng. 298 (2013) 53–66. doi:10.1002/mame.201100390.

[135] H. Nishihara, T. Kyotani, Templated Nanocarbons for Energy Storage, Adv. Mater. 24 (2012) 4473–4498. doi:10.1002/adma.201201715.

[136] A.D. Roberts, X. Li, H. Zhang, Porous carbon spheres and monoliths: morphology control, pore size tuning and their applications as Li-ion battery anode materials., Chem. Soc. Rev. 43 (2014) 4341–56. doi:10.1039/c4cs00071d.

[137] C. Yu, J. Fan, B. Tian, D. Zhao, G.D. Stucky, High-yield synthesis of periodic mesoporous silica rods and their replication to mesoporous carbon rods, Adv. Mater. 14 (2002) 1742–1745. doi:10.1002/1521-4095(20021203)14:23<1742::AID-ADMA1742>3.0.CO;2-3.

[138] K.A. Sashkina, N.A. Rudina, A.I. Lysikov, A.B. Ayupov, E. V. Parkhomchuk, Hierarchically porous materials built of Fe–silicalite nanobeads, J. Mater. Chem. A. 2 (2014) 16061–16070. doi:10.1039/C4TA02904F.

[139] A. Walcarius, Mesoporous materials and electrochemistry, Chem. Soc. Rev. 42 (2013) 4098. doi:10.1039/c2cs35322a.

[140] M. Pérez-Page, E. Yu, J. Li, M. Rahman, D.M. Dryden, R. Vidu, P. Stroeve, Template-based syntheses for shape controlled nanostructures, Adv. Colloid Interface Sci. 234 (2016) 51–79. doi:10.1016/j.cis.2016.04.001.

[141] B. Jung, P. Theato, Organic/Inorganic Composite Latexes: TheMarriage of Emulsion Polymerization and Inorganic Chemistry, Adv. Polym. Sci. (2012) 1–34. doi:10.1007/12.

[142] A.B.D. Nandiyanto, N. Hagura, F. Iskandar, K. Okuyama, Design of a highly ordered and uniform porous structure with multisized pores in film and particle forms using a template-driven self-assembly technique, Acta Mater. 58 (2010) 282–289. doi:10.1016/j.actamat.2009.09.004.

[143] A.B.D. Nandiyanto, T. Ogi, F. Iskandar, K. Okuyama, Highly ordered porous monolayer generation by dual-speed spin-coating with colloidal templates, Chem. Eng. J. 167 (2011) 409–415. doi:10.1016/j.cej.2010.11.077.

[144] F. Bosc, P. Lacroix-Desmazes, A. Ayral, TiO2 anatase-based membranes with hierarchical porosity and photocatalytic properties, J. Colloid Interface Sci. 304 (2006) 545–8. doi:10.1016/j.jcis.2006.09.064.

[145] G. Collins, M. Blömker, M. Osiak, J.D. Holmes, M. Bredol, C. O'Dwyer, Three-Dimensionally Ordered Hierarchically Porous Tin Dioxide Inverse Opals and Immobilization of Palladium Nanoparticles for Catalytic Applications, Chem. Mater. 25 (2013) 4312–4320. doi:10.1021/cm402458v.

[146] C. Verissimo, O.L. Alves, Microstructural modifications in macroporous oxides prepared via latex templating: synthesis and thermal stability of porous microstructure, J. Am. Ceram. Soc. 89 (2006) 2226–2231. doi:10.1111/j.1551-2916.2006.00996.x.

[147] X. Cheng, M. Chen, L. Wu, G. Gu, Novel and Facile Method for the Preparation of Monodispersed Titania Hollow Spheres, Langmuir. 22 (2006) 3858–3863. doi:10.1021/la0534221.

[148] H. Blas, M. Save, P. Pasetto, C. Boissière, C. Sanchez, B. Charleux, Elaboration of monodisperse spherical hollow particles with ordered mesoporous silica shells via dual latex/surfactant templating: Radial orientation of mesopore channels, Langmuir. 24 (2008) 13132–13137. doi:10.1021/la801897k.

[149] O. Sel, D. Kuang, M. Thommes, B. Smarsly, Principles of Hierarchical Meso- and Macropore Architectures by Liquid Crystalline and Polymer Colloid Templating, Langmuir. 22 (2006) 2311–2322. doi:10.1021/la0520841.

[150] I. Ortac, D. Simberg, Y. Yeh, J. Yang, B. Messmer, W.C. Trogler, R.Y. Tsien, S. Esener,

Dual-Porosity Hollow Nanoparticles for the Immunoprotection and Delivery of Nonhuman Enzymes, Nano Lett. 14 (2014) 3023–3032. doi:10.1021/nl404360k.

[151] B. Zhao, M.M. Collinson, Well-Defined Hierarchical Templates for Multimodal Porous Material Fabrication, Chem. Mater. 22 (2010) 4312–4319. doi:10.1021/cm101146n.

[152] M. Bathfield, J. Warnant, C. Gérardin, P. Lacroix-Desmazes, Asymmetric neutral, cationic and anionic PEO-based double-hydrophilic block copolymers (DHBCs): synthesis and reversible micellization triggered by temperature or pH, Polym. Chem. 6 (2015) 1339–1349. doi:10.1039/C4PY01502A.

[153] C. Gérardin, J. Reboul, M. Bonne, B. Lebeau, Ecodesign of ordered mesoporous silica materials, Chem. Soc. Rev. 42 (2013) 4217. doi:10.1039/c3cs35451b.

[154] P. Schmidt-Winkel, W.W. Lukens, D. Zhao, P. Yang, B.F. Chmelka, G.D. Stucky, Mesocellular Siliceous Foams with Uniformly Sized Cells and Windows, J. Am. Chem. Soc. 121 (1999) 254–255. doi:10.1021/ja983218i.

[155] H.D. Asfaw, M. Roberts, R. Younesi, K. Edström, Emulsion-templated bicontinuous carbon network electrodes for use in 3D microstructured batteries, J. Mater. Chem. A. 1 (2013) 13750. doi:10.1039/c3ta12680c.

[156] B.H. Jones, T.P. Lodge, Nanocasting nanoporous inorganic and organic materials from polymeric bicontinuous microemulsion templates, Polym. J. 44 (2012) 131–146. doi:10.1038/pj.2011.136.

[157] K. Nakanishi, N. Soga, Phase separation in silica sol-gel system containing polyacrylic acid I. Gel formaation behavior and effect of solvent composition, J. Non. Cryst. Solids. 139 (1992) 1–13. doi:10.1016/S0022-3093(05)80800-2.

[158] K. Nakanishi, Pore Structure Control of Silica Gels Based on Phase Separation, J. Porous Mater. 4 (1997) 67–112. doi:10.1023/A:1009627216939.

[159] J. Babin, J. Iapichella, B. Lefèvre, C. Biolley, J.-P. Bellat, F. Fajula, A. Galarneau, MCM-41 silica monoliths with independent control of meso- and macroporosity, New J. Chem. 31 (2007) 1907. doi:10.1039/b711544j.

[160] A. Galarneau, J. Iapichella, K. Bonhomme, F. De Renzo, P. Kooyman, O. Terasaki, F. Fajula, Controlling the morphology of mesostructured silicas by pseudomorphic transformation: A route towards applications, Adv. Funct. Mater. 16 (2006) 1657–1667. doi:10.1002/adfm.200500825.

[161] Y. Tong, T. Zhao, F. Li, Y. Wang, Synthesis of Monolithic Zeolite Beta with Hierarchical Porosity Using Carbon as a Transitional Template, Chem. Mater. 18 (2006)

4218–4220. doi:10.1021/cm060035j.

[162] R. Butler, I. Hopkinson, A.I. Cooper, Synthesis of Porous Emulsion-Templated Polymers Using High Internal Phase CO 2 -in-Water Emulsions, J. Am. Chem. Soc. 125 (2003) 14473–14481. doi:10.1021/ja037570u.

[163] K. Kurumada, Instantaneous nanofoaming method for fabrication of closed-porosity silica particle, in: Nanoparticle Technol. Handb., Elsevier, 2012: pp. 583–588. doi:10.1016/B978-0-444-56336-1.50052-7.

[164] S. Deville, S. Meille, J. Seuba, A meta-analysis of the mechanical properties of ice-templated ceramics and metals, Sci. Technol. Adv. Mater. 16 (2015) 043501. doi:10.1088/1468-6996/16/4/043501.

[165] S. Deville, Ice-templating, freeze casting: Beyond materials processing, J. Mater. Res. 28 (2013) 2202–2219. doi:10.1557/jmr.2013.105.

[166] H. Zhang, A.I. Cooper, Aligned Porous Structures by Directional Freezing, Adv. Mater. 19 (2007) 1529–1533. doi:10.1002/adma.200700154.

[167] H. Nishihara, S.R. Mukai, D. Yamashita, H. Tamon, Ordered macroporous silica by ice templating, Chem. Mater. 17 (2005) 683–689. doi:10.1021/cm048725f.

[168] J. Dhainaut, G. Piana, S. Deville, C. Guizard, M. Klotz, Freezing-induced ordering of block copolymer micelles, Chem. Commun. 50 (2014) 12572–12574. doi:10.1039/C4CC05556J.

[169] J. Lee, Y. Park, P. Kim, H. Kim, J. Yi, Preparation of NaCl-incorporated plugged mesoporous silica using a cost-effective precursor and applications to the hydrodechlorination of chlorinated hydrocarbons, J. Mater. Chem. 14 (2004) 1050. doi:10.1039/b309991a.

[170] C.H. Christensen, K. Johannsen, I. Schmidt, C.H. Christensen, Catalytic Benzene Alkylation over Mesoporous Zeolite Single Crystals: Improving Activity and Selectivity with a New Family of Porous Materials, J. Am. Chem. Soc. 125 (2003) 13370–13371. doi:10.1021/ja037063c.

[171] A. Corma, From microporous to mesoporous molecular sieve materials and their use in catalysis, Chem. Rev. 97 (1997) 2373–2420. doi:10.1021/cr960406n.

[172] Z.-Y. Yuan, B.-L. Su, Insights into hierarchically meso–macroporous structured materials, J. Mater. Chem. 16 (2006) 663–677. doi:10.1039/B512304F.

[173] P. Yang, T. Deng, D. Zhao, P. Feng, D. Pine, B.F. Chmelka, G.M. Whitesides, G.D.

Stucky, Hierarchically Ordered Oxides, Science. 282 (1998) 2244–2246. doi:10.1126/science.282.5397.2244.

[174] J. Pérez-Carvajal, P. Aranda, S. Obregón, G. Colón, E. Ruiz-Hitzky, TiO2-clay based nanoarchitectures for enhanced photocatalytic hydrogen production, Microporous Mesoporous Mater. 222 (2016) 120–127. doi:10.1016/j.micromeso.2015.10.007.

[175] A. Lolli, R. Amadori, C. Lucarelli, M.G. Cutrufello, E. Rombi, F. Cavani, S. Albonetti, Hard-template preparation of Au/CeO2 mesostructured catalysts and their activity for the selective oxidation of 5-hydroxymethylfurfural to 2,5-furandicarboxylic acid, Microporous Mesoporous Mater. 226 (2016) 466–475. doi:10.1016/j.micromeso.2016.02.014.

[176] M. Mureseanu, A. Reiss, I. Stefanescu, E. David, V. Parvulescu, G. Renard, V. Hulea, Modified SBA-15 mesoporous silica for heavy metal ions remediation, Chemosphere. 73 (2008) 1499–1504. doi:10.1016/j.chemosphere.2008.07.039.

[177] C.M.A. Parlett, K. Wilson, A.F. Lee, Hierarchical porous materials: catalytic applications, Chem. Soc. Rev. 42 (2013) 3876–3893. doi:10.1039/c2cs35378d.

[178] A. Martinez, G. Prieto, J. Rollan, Nanofibrous γ-Al2O3 as support for Co-based Fischer–Tropsch catalysts: Pondering the relevance of diffusional and dispersion effects on catalytic performance, J. Catal. 263 (2009) 292–305. doi:10.1016/j.jcat.2009.02.021.

[179] Noritatsu Tsubaki, Y. Zhang, S. Sun, H. Mori, Y. Yoneyama, X. Li, K. Fujimoto, A new method of bimodal support preparation and its application in Fischer–Tropsch synthesis, Catal. Commun. 2 (2001) 311–315. doi:10.1016/S1566-7367(01)00055-3.

[180] G.S. Chai, I.S. Shin, J.-S. Yu, Synthesis of Ordered, Uniform, Macroporous Carbons with Mesoporous Walls Templated by Aggregates of Polystyrene Spheres and Silica Particles for Use as Catalyst Supports in Direct Methanol Fuel Cells, Adv. Mater. 16 (2004) 2057–2061. doi:10.1002/adma.200400283.

[181] Y. Piao, K. An, J. Kim, T. Yu, T. Hyeon, Sea urchin shaped carbon nanostructured materials: carbon nanotubes immobilized on hollow carbon spheres, J. Mater. Chem. 16 (2006) 2984. doi:10.1039/b601684g.

[182] L.M. Bronstein, G. Goerigk, M. Kostylev, M. Pink, I.A. Khotina, P.M. Valetsky, V.G. Matveeva, E.M. Sulman, M.G. Sulman, A. V. Bykov, N. V. Lakina, R.J. Spontak, Structure and Catalytic Properties of Pt-Modified Hyper-Cross-Linked Polystyrene Exhibiting Hierarchical Porosity, J. Phys. Chem. B. 108 (2004) 18234–18242. doi:10.1021/jp046459n.

[183] T.-Y. Zeng, Z.-M. Zhou, J. Zhu, Z.-M. Cheng, P.-Q. Yuan, W.-K. Yuan, Palladium supported on hierarchically macro–mesoporous titania for styrene hydrogenation, Catal.

Today. 147 (2009) S41–S45. doi:10.1016/j.cattod.2009.07.029.

[184] S.-W. Bian, Y.-L. Zhang, H.-L. Li, Y. Yu, Y.-L. Song, W.-G. Song, γ-Alumina with hierarchically ordered mesopore/macropore from dual templates, Microporous Mesoporous Mater. 131 (2010) 289–293. doi:10.1016/j.micromeso.2010.01.004.

[185] J. Sarkar, V.T. John, J. He, C. Brooks, D. Gandhi, A. Nunes, G. Ramanath, A. Bose, Surfactant-Templated Synthesis and Catalytic Properties of Patterned Nanoporous Titania Supports Loaded with Platinum Nanoparticles, Chem. Mater. 20 (2008) 5301–5306. doi:10.1021/cm8014034.

[186] L.-H. Ren, H.-L. Zhang, A.-H. Lu, Y. Hao, W.-C. Li, Porous silica as supports for controlled fabrication of Au/CeO2/SiO2 catalysts for CO oxidation: Influence of the silica nanostructures, Microporous Mesoporous Mater. 158 (2012) 7–12. doi:10.1016/j.micromeso.2012.03.010.

[187] T. Kang, Y. Park, K. Choi, J.S. Lee, J. Yi, Ordered mesoporous silica (SBA-15) derivatized with imidazole-containing functionalities as a selective adsorbent of precious metal ions, J. Mater. Chem. 14 (2004) 1043. doi:10.1039/b315829b.

[188] Y. Han, H.V. Huynh, Pyrazolin-4-ylidenes: a new class of intriguing ligands., Dalton Trans. 40 (2011) 2141–2147. doi:10.1039/c0dt01037e.

[189] M. Tada, T. Sasaki, Y. Iwasawa, Design of a novel molecular-imprinted Rh-amine complex on SiO2 and its shape-selective catalysis for alpha-methylstyrene hydrogenation, J. Phys. Chem. B. 108 (2004) 2918–2930. doi:10.1021/jp036421v.

[190] Y. Yang, Z. Weng, S. Muratsugu, N. Ishiguro, S.-I. Ohkoshi, M. Tada, Preparation and Catalytic Performances of a Molecularly Imprinted Ru-Complex Catalyst with an NH(2) Binding Site on a SiO(2) Surface., Chemistry. (2011) 1142–1153. doi:10.1002/chem.201100529.

[191] E. Molina, J. Warnant, M. Mathonnat, M. Bathfield, M. In, D. Laurencin, C. Jérôme, P. Lacroix-Desmazes, N. Marcotte, C. Gérardin, Drug–Polymer Electrostatic Complexes as New Structuring Agents for the Formation of Drug-Loaded Ordered Mesoporous Silica, Langmuir. 31 (2015) 12839–12844. doi:10.1021/acs.langmuir.5b03221.

[192] S.A. Kishore Kumar, M. John, S.M. Pai, Y. Niwate, B.L. Newalkar, Low temperature hydrogenation of aromatics over Pt–Pd/SiO2–Al2O3 catalyst, Fuel Process. Technol. 128 (2014) 303–309. doi:10.1016/j.fuproc.2014.07.028.

[193] Thomson Reuters, CNBC, (2017). http://www.cnbc.com/ (accessed June 7, 2017).

[194] S. Airaksinen, Preparation of solid catalysts, (2008).

http://books.google.com/books?hl=en&lr=&id=ev47CMLmM2sC&oi=fnd&pg=PP2&dq=Preparation+of+solid+catalysts&ots=IqeO96o8Y-&sig=Xim6IZQW-iWP70OUxXM411aCb7A (accessed January 15, 2015).

[195] A. Taguchi, F. Schüth, Ordered mesoporous materials in catalysis, Microporous Mesoporous Mater. 77 (2005) 1–45. doi:10.1016/j.micromeso.2004.06.030.

[196] R.J. White, R. Luque, V.L. Budarin, J.H. Clark, D.J. Macquarrie, Supported metal nanoparticles on porous materials. Methods and applications., Chem. Soc. Rev. 38 (2009) 481–494. doi:10.1039/b802654h.

[197] A. Barau, V. Budarin, A. Caragheorgheopol, R. Luque, D.J. Macquarrie, A. Prelle, V.S. Teodorescu, M. Zaharescu, A Simple and Efficient Route to Active and Dispersed Silica Supported Palladium Nanoparticles, Catal. Letters. 124 (2008) 204–214. doi:10.1007/s10562-008-9465-x.

[198] M. Toebes, Y. Zhang, J. Hájek, T.A. Nijhuis, J.H. Bitter, A.J. Dillen, D.Y. Murzin, D.C. Koningsberger, K.. de Jong, Support effects in the hydrogenation of cinnamaldehyde over carbon nanofiber-supported platinum catalysts: characterization and catalysis, J. Catal. 226 (2004) 215–225. doi:10.1016/j.jcat.2004.05.026.

[199] B. Average, (...) Heterogeneous catalyst solid support, (2013). https://yourmomislike.wordpress.com/tag/wetness/ (accessed July 7, 2017).

[200] J. Scalbert, C. Daniel, Y. Schuurman, C. Thomas, F.C. Meunier, Rational design of a CO2-resistant toluene hydrogenation catalyst based on FT-IR spectroscopy studies, J. Catal. 318 (2014) 61–66. doi:10.1016/j.jcat.2014.07.013.

[201] L. Villegas, F. Masset, N. Guilhaume, Wet impregnation of alumina-washcoated monoliths: Effect of the drying procedure on Ni distribution and on autothermal reforming activity, Appl. Catal. A Gen. 320 (2007) 43–55. doi:10.1016/j.apcata.2006.12.011.

[202] V. Arcotumapathy, D.-V.N. Vo, D. Chesterfield, C.T. Tin, A. Siahvashi, F.P. Lucien, A.A. Adesina, Catalyst design for methane steam reforming, Appl. Catal. A Gen. 479 (2014) 87–102. doi:10.1016/j.apcata.2014.04.020.

[203] Y. Wang, J. Zhang, X. Wang, J. Ren, B. Zuo, Y. Tang, Metal nanoclusters stabilized with simple ions and solvents—promising building blocks for future catalysts, Top. Catal. 35 (2005) 35–41. doi:10.1021/cm0000853.

[204] Z. Jiang, W. Shangguan, Rational removal of stabilizer-ligands from platinum nanoparticles supported on photocatalysts by self-photocatalysis degradation, Catal. Today. 242 (2015) 372–380. doi:10.1016/j.cattod.2014.07.037.

[205] S. Tsubota, T. Nakamura, K. Tanaka, M. Haruta, Effect of calcination temperature on the catalytic activity of Au colloids mechanically mixed with TiO2 powder for CO oxidation, Catal. Letters. 56 (1998) 131–135. doi:10.1023/A:1019069315071.

[206] C.M.A. Parlett, M.A. Isaacs, S.K. Beaumont, L.M. Bingham, N.S. Hondow, K. Wilson, A.F. Lee, Spatially orthogonal chemical functionalization of a hierarchical pore network for catalytic cascade reactions, Nat. Mater. 15 (2016) 178–182. doi:10.1038/nmat4478.

[207] L.B. Okhlopkova, Properties of Pt/C catalysts prepared by adsorption of anionic precursor and reduction with hydrogen. Influence of acidity of solution, Appl. Catal. A Gen. 355 (2009) 115–122. doi:10.1016/j.apcata.2008.12.006.

[208] S. Boujday, Evolution of transition metal speciation in the preparation of supported catalysts: halogenoplatinate(IV) on silica, Catal. Letters. 88 (2003) 23–30. doi:10.1023/A:1023526614460.

[209] W.M. MacNevin, W.B. Crummett, Bahavior of Platinum Group Metals toward Ion Exchange Resins, Anal. Chem. 25 (1953) 1628–1630. doi:10.1021/ac60083a014.

[210] O.N. Kononova, T.A. Leyman, A.M. Melnikov, D.M. Kashirin, M.M. Tselukovskaya, Ion exchange recovery of platinum from chloride solutions, Hydrometallurgy. 100 (2010) 161–167. doi:10.1016/j.hydromet.2009.11.011.

[211] A.J. Plomp, H. Vuori, A.O.I. Krause, K.P. de Jong, J.H. Bitter, Particle size effects for carbon nanofiber supported platinum and ruthenium catalysts for the selective hydrogenation of cinnamaldehyde, Appl. Catal. A Gen. 351 (2008) 9–15. doi:10.1016/j.apcata.2008.08.018.

[212] R.W. Johnson, A. Hultqvist, S.F. Bent, A brief review of atomic layer deposition: from fundamentals to applications, Mater. Today. 17 (2014) 236–246. doi:10.1016/j.mattod.2014.04.026.

[213] A. Säynätjoki, Atomic-layer-deposited thin films for silicon nanophotonics, SPIE Newsroom. (2012) 6–8. doi:10.1117/2.1201204.004218.

[214] S. Domínguez-Domínguez, J. Arias-Pardilla, Á. Berenguer-Murcia, E. Morallón, D. Cazorla-Amorós, Electrochemical deposition of platinum nanoparticles on different carbon supports and conducting polymers, J. Appl. Electrochem. 38 (2008) 259–268. doi:10.1007/s10800-007-9435-9.

[215] R. Strobel, S.E. Pratsinis, A. Baiker, Flame-made Pd/La2O3/Al2O3 nanoparticles: thermal stability and catalytic behavior in methane combustion, J. Mater. Chem. 15 (2005) 605. doi:10.1039/b413198c.

[216] S. Senkan, M. Kahn, S. Duan, A. Ly, C. Leidholm, High-throughput metal nanoparticle catalysis by pulsed laser ablation, Catal. Today. 117 (2006) 291–296. doi:10.1016/j.cattod.2006.05.051.

[217] J.P. Chen, L.. Lim, Key factors in chemical reduction by hydrazine for recovery of precious metals, Chemosphere. 49 (2002) 363–370. doi:10.1016/S0045-6535(02)00305-3.

[218] Y. Wang, Y.-F. Shi, Y.-B. Chen, L.-M. Wu, Hydrazine reduction of metal ions to porous submicro-structures of Ag, Pd, Cu, Ni, and Bi, J. Solid State Chem. 191 (2012) 19–26. doi:10.1016/j.jssc.2012.02.059.

[219] B. Khodashenas, H.R. Ghorbani, Synthesis of silver nanoparticles with different shapes, Arab. J. Chem. (2015). doi:10.1016/j.arabjc.2014.12.014.

[220] B. Zhou, S. Hermans, G.A. Somorjai, eds., Nanotechnology in Catalysis, 1st ed., Springer US, New York, 2004. https://books.google.fr/books?id=epTLkvLL6-sC&pg=PA55&lpg=PA55&dq=nanoparticles+alcohol+reduction+pathway&source=bl&ots=luhLYLL0tJ&sig=SfqyIy7TX8pw7s4KcQUlz6jq-As&hl=en&sa=X&ved=0ahUKEwivyOXE463UAhWHwBQKHQpkDrMQ6AEIKTAA#v=onepage&q=nanoparticles alcohol r.

[221] N. Toshima, Y. Yamaji, T. Teranishi, T. Yonezawa, Photosensitized Reduction of Carbon Dioxide in Solution Using Noble-Metal Clusters for Electron Transfer, Zeitschrift Für Naturforsch. A. 50 (1995) 283–291. doi:10.1515/zna-1995-2-321.

[222] S.E. Skrabalak, B.J. Wiley, M. Kim, E. V. Formo, Y. Xia, On the Polyol Synthesis of Silver Nanostructures: Glycolaldehyde as a Reducing Agent, Nano Lett. 8 (2008) 2077–2081. doi:10.1021/nl800910d.

[223] V.L. Nguyen, D.C. Nguyen, H. Hirata, M. Ohtaki, T. Hayakawa, M. Nogami, Chemical synthesis and characterization of palladium nanoparticles, Adv. Nat. Sci. Nanosci. Nanotechnol. 1 (2010) 035012. doi:10.1088/2043-6262/1/3/035012.

[224] G. Glaspell, L. Fuoco, M.S. El-Shall, Microwave Synthesis of Supported Au and Pd Nanoparticle Catalysts for CO Oxidation, J. Phys. Chem. B. 109 (2005) 17350–17355. doi:10.1021/jp0526849.

[225] Z. Liu, X.Y. Ling, B. Guo, L. Hong, J.Y. Lee, Pt and PtRu nanoparticles deposited on single-wall carbon nanotubes for methanol electro-oxidation, J. Power Sources. 167 (2007) 272–280. doi:10.1016/j.jpowsour.2007.02.044.

[226] M. Blosi, S. Albonetti, S. Ortelli, A.L. Costa, L. Ortolani, M. Dondi, Green and easily scalable microwave synthesis of noble metal nanosols (Au, Ag, Cu, Pd) usable as catalysts, New J. Chem. 38 (2014) 1401–1409. doi:10.1039/C3NJ00894K.

[227] M. Blosi, S. Ortelli, A. Costa, M. Dondi, A. Lolli, S. Andreoli, P. Benito, S. Albonetti, Bimetallic Nanoparticles as Efficient Catalysts: Facile and Green Microwave Synthesis, Materials (Basel). 9 (2016) 550. doi:10.3390/ma9070550.

[228] J.M. Campelo, T.D. Conesa, M.J. Gracia, M.J. Jurado, R. Luque, J.M. Marinas, A.A. Romero, Microwave facile preparation of highly active and dispersed SBA-12 supported metal nanoparticles, Green Chem. 10 (2008) 853. doi:10.1039/b801754a.

[229] C. Yacou, M.-L. Fontaine, A. Ayral, P. Lacroix-Desmazes, P.-A. Albouy, A. Julbe, One pot synthesis of hierarchical porous silica membrane material with dispersed Pt nanoparticles using a microwave-assisted sol–gel route, J. Mater. Chem. 18 (2008) 4274–4279. doi:10.1039/b807029f.

[230] Y. Zhang, C. Erkey, Preparation of supported metallic nanoparticles using supercritical fluids: A review, J. Supercrit. Fluids. 38 (2006) 252–267. doi:10.1016/j.supflu.2006.03.021.

[231] S.E. Bozbağ, C. Erkey, Supercritical deposition: Current status and perspectives for the preparation of supported metal nanostructures, J. Supercrit. Fluids. 96 (2015) 298–312. doi:10.1016/j.supflu.2014.09.036.

[232] S. Wolff, M. Crone, T. Muller, M. Enders, S. Bräse, M. Türk, Preparation of supported Pt nanoparticles by supercritical fluid reactive deposition: Influence of precursor, substrate and pressure on product properties, J. Supercrit. Fluids. 95 (2014) 588–596. doi:10.1016/j.supflu.2014.08.034.

[233] M. Casapu, A. Fischer, A.M. Gänzler, R. Popescu, M. Crone, D. Gerthsen, M. Türk, J.-D. Grunwaldt, Origin of the Normal and Inverse Hysteresis Behavior during CO Oxidation over Pt/Al2O3, ACS Catal. 7 (2017) 343–355. doi:10.1021/acscatal.6b02709.

[234] J. Morère, E. Sánchez-Miguel, M.J. Tenorio, C. Pando, A. Cabañas, Supercritical fluid preparation of Pt, Ru and Ni/graphene nanocomposites and their application as selective catalysts in the partial hydrogenation of limonene, J. Supercrit. Fluids. 120 (2017) 7–17. doi:10.1016/j.supflu.2016.10.007.

[235] J. Morère, S. Royuela, G. Asensio, P. Palomino, E. Enciso, C. Pando, A. Cabañas, Deposition of Ni nanoparticles onto porous supports using supercritical CO2 : effect of the precursor and reduction methodology, Philos. Trans. R. Soc. A Math. Phys. Eng. Sci. 373 (2015) 20150014. doi:10.1098/rsta.2015.0014.

[236] F. Gasc, S. Clerc, E. Gayon, J.-M. Campagne, P. Lacroix-Desmazes, Supercritical CO2-mediated design of Pd supported catalysts using an amphiphilic functional copolymer, J. Supercrit. Fluids. 105 (2015) 136–145. doi:10.1016/j.supflu.2015.01.003.

[237] S.I. Nikitenko, R. Pflieger, Toward a new paradigm for sonochemistry: Short review on nonequilibrium plasma observations by means of MBSL spectroscopy in aqueous solutions, Ultrason. Sonochem. (2016). doi:10.1016/j.ultsonch.2016.02.003.

[238] K.S. Suslick, Sonochemistry, Science. 247 (1990) 1439–1445. doi:10.1126/science.247.4949.1439.

[239] A.A. Ndiaye, R. Pflieger, B. Siboulet, J. Molina, J.-F. Dufrêche, S.I. Nikitenko, Nonequilibrium vibrational excitation of OH radicals generated during multibubble cavitation in water., J. Phys. Chem. A. 116 (2012) 4860–7. doi:10.1021/jp301989b.

[240] J.H. Bang, K.S. Suslick, Applications of Ultrasound to the Synthesis of Nanostructured Materials, Adv. Mater. 22 (2010) 1039–1059. doi:10.1002/adma.200904093.

[241] T. Chave, N.M. Navarro, S. Nitsche, S.I. Nikitenko, Mechanism of Pt(IV) sonochemical reduction in formic acid media and pure water, Chem. - A Eur. J. 18 (2012) 3879–85. doi:10.1002/chem.201102355.

[242] Y. Mizukoshi, E. Takagi, H. Okuno, R. Oshima, Y. Maeda, Y. Nagata, Preparation of platinum nanoparticles by sonochemical reduction of the Pt(IV) ions: Role of surfactants, Ultrason. Sonochem. 8 (2001) 1–6. doi:10.1016/S1350-4177(00)00027-4.

[243] Y. Mizukoshi, R. Oshima, Y. Maeda, Y. Nagata, Preparation of platinum nanoparticles by sonochemical reduction of the Pt(II) ion, Langmuir. 15 (1999) 2733–2737. doi:10.1021/la9812121.

[244] T. Sakai, H. Enomoto, K. Torigoe, H. Sakai, M. Abe, Surfactant- and reducer-free synthesis of gold nanoparticles in aqueous solutions, Colloids Surfaces A Physicochem. Eng. Asp. 347 (2009) 18–26. doi:10.1016/j.colsurfa.2008.10.037.

[245] N. Perkas, Z. Zhong, L. Chen, M. Besson, A. Gedanken, Sonochemically Prepared high Dispersed Ru/TiO2 Mesoporous Catalyst for Partial Oxidation of Methane to Syngas, Catal. Letters. 103 (2005) 9–14. doi:10.1007/s10562-005-6496-4.

[246] Y. Wang, X. Tang, L. Yin, W. Huang, Y. Rosenfeld Hacohen, A. Gedanken, Sonochemical Synthesis of Mesoporous Titanium Oxide with Wormhole-like Framework Structures, Adv. Mater. 12 (2000) 1183–1186. doi:10.1002/1521-4095(200008)12:16<1183::AID-ADMA1183>3.0.CO;2-X.

[247] D.N. Srivastava, N. Perkas, A. Gedanken, I. Felner, Sonochemical Synthesis of Mesoporous Iron Oxide and Accounts of Its Magnetic and Catalytic Properties, J. Phys. Chem. B. 106 (2002) 1878–1883. doi:10.1021/jp015532w.

[248] N. Perkas, O. Palchik, I. Brukental, I. Nowik, Y. Gofer, A Mesoporous Iron-Titanium

Oxide Composite Prepared Sonochemically, J. Phys. Chem. B. 107 (2003) 8772–8778. doi:10.1021/jp022447v.

[249] N. Perkas, Z. Zhong, J. Grinblat, A. Gedanken, Deposition of Gold Particles on Mesoporous Catalyst Supports by Sonochemical Method, and their Catalytic Performance for CO Oxidation, Catal. Letters. 120 (2008) 19–24. doi:10.1007/s10562-007-9257-8.

[250] T. Chave, A. Grunenwald, A. Ayral, P. Lacroix-Desmazes, S.I. Nikitenko, Sonochemical deposition of platinum nanoparticles on polymer beads and their transfer on the pore surface of a silica matrix, J. Colloid Interface Sci. 395 (2013) 81–84. doi:10.1016/j.jcis.2012.12.029.

[251] R.G. Compton, J.C. Eklund, F. Marken, Sonoelectrochemical processes: A review, Electroanalysis. 9 (1997) 509–522. doi:10.1002/elan.1140090702.

[252] Y. Mosqueda, E. Pérez-Cappe, J. Arana, E. Longo, A. Ries, M. Cilense, P.A.P. Nascente, P. Aranda, E. Ruiz-Hitzky, Preparation and characterization of LiNi0.8Co0.2O2/PANI microcomposite electrode materials under assisted ultrasonic irradiation, J. Solid State Chem. 179 (2006) 308–314. doi:10.1016/j.jssc.2005.09.030.

[253] P. Serna, A. Corma, Transforming Nano Metal Nonselective Particulates into Chemoselective Catalysts for Hydrogenation of Substituted Nitrobenzenes, ACS Catal. 5 (2015) 7114–7121. doi:10.1021/acscatal.5b01846.

[254] S. Abate, G. Centi, S. Perathoner, S. Melada, F. Pinna, G. Strukul, The issue of selectivity in the direct synthesis of H2O2 from H2 and O2: the role of the catalyst in relation to the kinetics of reaction, Top. Catal. 38 (2006) 181–193. doi:10.1007/s11244-006-0083-9.

III. PLATINUM-BASED CATALYSTS PREPARATION

Contents

Some of the results described in this chapter have been published:

> A.F. Sierra Salazar, T. Chave, A. Ayral, S. Nikitenko, V. Hulea, P. Kooyman, F.D. Tichelaar, S. Perathoner, P. Lacroix-Desmazes. "Engineering of silica-supported platinum catalysts with hierarchical porosity combining latex synthesis, sonochemistry and sol-gel process – I. Material preparation". *Microporous and Mesoporous Materials*, 234 (2016), 207–214. DOI:10.1016/j.micromeso.2016.07.009

III.1- Introduction

Rational catalyst design is a topic that has been actively discussed as an opportunity to accelerate the development of tailor-made materials based on specific needs, reducing trial-and-error testing and establishing structure-property relationships [1]. In general, a reaction in heterogeneous catalysis includes several steps of mass transport, sorption and chemical reaction – each of them providing an opportunity to improve the catalyst performance [2]. At a molecular level, the catalyst performance may be improved by a proper catalyst design that considers morphology effects (porous structure), physical effects (dispersion and electrostatic interactions) and chemical effects (electron arrangement) [3]. However, when the diffusion is the controlling step of the overall reaction, improvement of the active phase would not significantly increase the catalyst performance. Instead, the mass transport within the material becomes of major concern for catalyst improvement [4]. This is where the modulation of internal porosity and pore interconnectivity plays an important role in catalyst design. For instance, to improve mass transport phenomena, the catalyst can be conceived to have hierarchical porosity by combining pores of different sizes (micropores – smaller than 2 nm, mesopores – between 2 and 50 nm, and macropores – bigger than 50 nm, according to IUPAC classification) [5].

Rational design of the hierarchical porosity and the appropriate chemical composition of catalytic materials has been studied for achieving a specific tailoring based on the application requirements [6–8]. Generally, the sol-gel process, especially of silicon-based materials, is well described concerning the synthesis of hierarchically porous materials with micro- and mesopores [9–11]. In addition, this method is environmentally friendly since water can be used as reaction medium without co-solvent along the different preparation steps [12]. The sol-gel

synthesis of mesoporous silica is achievable by controlling the hydrolysis and condensation conditions: acid or basic catalysis in one or two steps [13–15]. Templating is another useful tool for the synthesis of meso- and macroporous materials. Templates such as self-assembling molecules, also called structure-directing agents (e.g. surfactants), and polymer nanoparticles have been used in the preparation of porous materials based on silica [16–21] and other oxides [22–24].

Catalytic processes involving supported noble metals such as platinum, palladium and gold are currently used for producing fuels and other compounds of industrial interest [25–28]. Platinum nanoparticles supported on hierarchically porous silica have been prepared by using various techniques, including impregnation, precipitation, ion-exchange and colloidal deposition [28, 29]. Some of the authors of the present study proposed original methods consisting of a polystyrene latex template and platinum nanoparticles prepared by microwave-assisted synthesis [31] or by sonochemical deposition [32]. The advantage of the sonochemical method is that the platinum forms nanoparticles upon reduction by the hydrogen generated *in-situ* under ultrasonic irradiation, limiting the requirement of additional reagents in the process [33].

The aim of this work is to integrate the engineering of an optimised hierarchically porous (meso- and macropores) catalyst support with the synthesis and transfer of a sonochemically decorated polymer template. Herein, we describe a rational design procedure for achieving the desired specifications (hierarchical porosity of the support and Pt nanoparticle distribution within the support). The silica-supported platinum catalysts with hierarchical porosity were synthesised following the stages depicted in Figure 49. The first step is the synthesis of the polystyrene (PS) latex template by emulsion polymerisation. The second step is the sonochemical synthesis and deposition of platinum nanoparticles on the surface of the polymer latex. The third step is the synthesis of the support by sol-gel processes using tetraethyl orthosilicate (TEOS) under controlled conditions to modulate the porosity of the final silica matrix (micro- and/or mesopores). Interestingly, all these steps can be carried out in water, reducing environmental impacts.

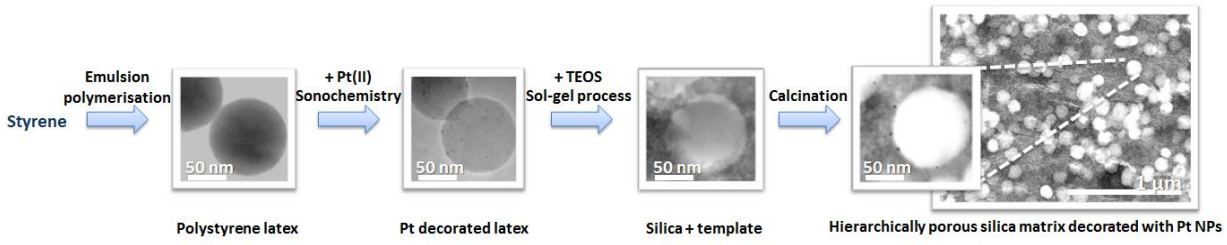

Figure 49. Supported catalyst synthesis by combining emulsion polymerisation, sonochemistry and sol-gel route.

III.2- Experimental

III.2.1- Materials

Potassium persulfate ($K_2S_2O_8$, KPS, 99%, Sigma Aldrich), sodium metabisulfite ($Na_2S_2O_5$, SMBS, 97%, Sigma Aldrich), sodium dodecylbenzenesulfonate ($C_{12}H_{25}C_6H_4SO_3Na$, SDBS, 99%, Sigma Aldrich), sodium tetrachloroplatinate (Na_2PtCl_4, 42.6% Pt, Strem), hexachloroplatinic acid ($H_2PtCl_6.6H_2O$, 37.7% Pt, Strem), tetraethyl orthosilicate ($Si(OC_2H_5)_4$, TEOS, 98%, Sigma Aldrich), absolute ethanol (C_2H_5OH, >99.8%, Sigma Aldrich) and 1 wt.% Pt/SiO_2 (Sigma Aldrich, referred to as 0.7REF) were used as received. Hydrochloric acid (HCl, 37%, Sigma Aldrich) and ammonium hydroxide (NH_4OH, 28%, Sigma Aldrich) were used to prepare acidic and basic solutions with deionised water (1 microS/cm, D8 ion exchange demineraliser A2E Affinage de L'Eau or 18.2 MΩ·cm at 25 °C, Milli-Q). Styrene (99.0%, Sigma Aldrich) was distilled in order to remove its stabiliser: 4-tert-butylcatechol.

III.2.2- Polystyrene (PS) latex template synthesis

The polystyrene (PS) latex template was prepared by emulsion polymerisation of styrene using a redox initiator system: KPS as oxidiser and SMBS as reducer. SDBS was used as surfactant. The polymerisation was carried out under argon atmosphere with a molar ratio styrene : water : KPS : SMBS : SDBS = 1 : 50 : 5×10^{-3} : 3.2×10^{-3} : 6.6×10^{-4}, in a 350 mL double-walled glass reactor with a glass stirring blade operating at 250 rpm. The temperature was regulated as follows: 1 h at 65 °C, 2 h at 72 °C and 3 h at 85 °C.

III.2.3- Template functionalisation using sonochemistry

The latex template was functionalised with platinum nanoparticles formed *in-situ* by reducing sodium tetrachloroplatinate or hexachloroplatinic acid under ultrasonic irradiation. Typically, the reaction was carried out in a reactor consisting of a 150 mL glass flask introduced in a deionised water bath contained in a double-walled glass reactor mounted on the top of a high-frequency piezoelectric transducer with a 25 cm² irradiation surface (ELAC Nautik, Figure 50). The transducer was supplied by a generator with a maximum electrical power of 125 W (T & C Power Conversion, Inc.). The acoustic power supplied in the whole system was 0.14 W/mL at 205 kHz for 12 h, determined by calorimetry (see Annex II). The sonochemical activity under the conditions used was estimated to be 0.32 µmol/min at 20 °C in water under argon atmosphere by measuring the hydrogen peroxide formation rate within the inner reaction vessel, as described elsewhere [34]. The temperature of the system was regulated at 20 °C. 90 mL of polystyrene latex were used with 9 mL of 10 g Pt/L sodium tetrachloroplatinate solution (for a latex at ca. 1 wt.% Pt/polystyrene, or when specified at 5 g Pt/L sodium tetrachloroplatinate solution for a latex at ca. 0.5 wt.% Pt/polystyrene). Prior to sonication, Ar was bubbled for about 15 minutes from the bottom of the latex-containing flask at ca. 130 mL/min. Then, the Ar bubbling was set at the liquid-gas interphase and the reaction medium homogeneity was ensured

using a 3-blade glass stirrer. Other experiments were carried out as described above but under an atmosphere of 10 vol. % CO/Ar, instead of pure Ar. In such a case, the platinum precursor solution was added just after starting the ultrasound irradiation in order to avoid the formation of platinum carbonyls [33].

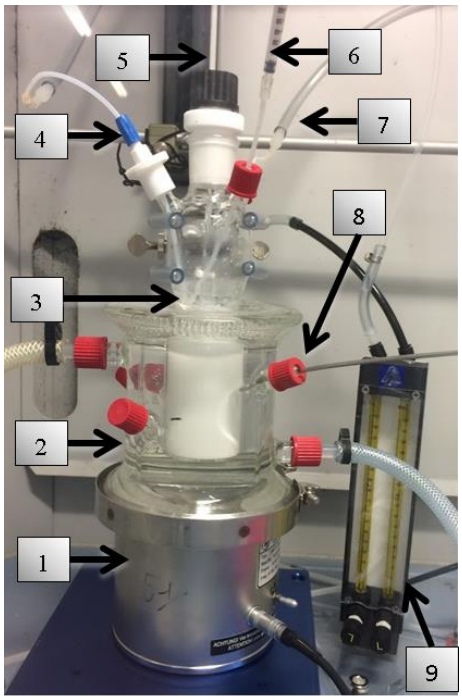

Figure 50. Experimental set-up for sonochemistry with non-direct contact: (1) Elac Nautik transducer supplied by a 125 W maximal electric power generator, (2) 350 mL thermostated double-walled glass reactor, (3) 150 mL inner reaction vessel, (4) gas inlet, (5) glass rod, (6) sample outlet, (7) gas outlet, (8) thermocouple, (9) flowmeter.

The experiment carried out at 343 kHz was performed as described above, only changing the high-frequency piezoelectric transducer, which also had a 25 cm² irradiation surface (ELAC Nautik). The set-up was identical to that shown in Figure 50. The sonochemical activity under the conditions used was estimated to be 0.16 µmol/min at 20 °C in water under argon atmosphere by measuring the hydrogen peroxide formation rate within the inner reaction vessel, as described elsewhere [34].

The experiments carried out at 100 kHz were performed in a reactor with direct contact between the reaction medium and the surface of the high-frequency piezoelectric transducer, as shown in Figure 51 (the transducer was polished after every use to remove any deposit of Pt). The sonochemical activity under the conditions used was estimated to be 0.38 µmol H_2O_2/min at 20 °C in water under argon atmosphere [34]. Typically, the temperature of the system was regulated at 20 °C. 200 mL of polystyrene latex were used with 19 mL of 10 mg Pt/mL sodium tetrachloroplatinate solution (for a latex at ca. 1 wt. % Pt/polystyrene, or when specified at 10 mL of solution for a latex at ca. 0.5 wt. % Pt/polystyrene). Prior to sonication, Ar was bubbled

for about 15 minutes from the bottom of the latex-containing flask at ca. 130 mL/min. Then, the Ar bubbling was set at the liquid-gas interphase and the reaction medium homogeneity was ensured using a 3-blade glass stirrer.

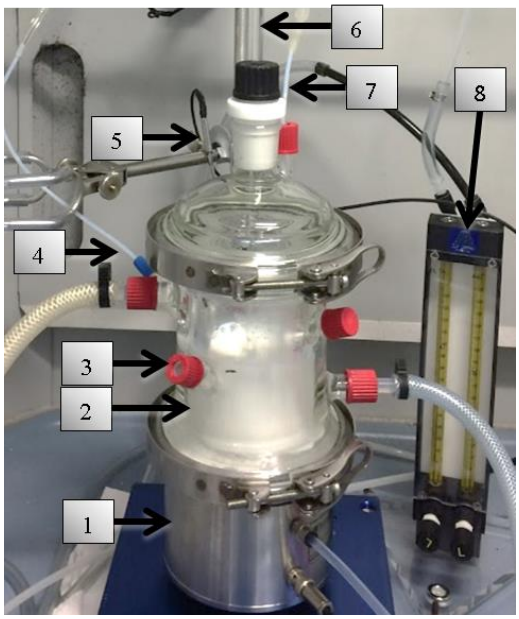

Figure 51. Experimental set-up for sonochemistry with direct contact: (1) Elac Nautik transducer supplied by a 125 W maximal electric power generator, (2) 350 mL thermostated double-walled glass reactor, (3) sample outlet, (4) gas inlet, (5) thermocouple, (6) glass rod, (7) gas outlet, (8) flowmeter.

The experiments carried out at 20 kHz were performed under 10 vol.% CO/Ar atmosphere using either hexachloroplatinic acid or sodium tetrachloroplatinate. The set-up consisted of a tightly closed thermostated glass reactor equipped with a 1 cm^2 titanium probe and piezoelectric transducer supplied by a 20 kHz generator (750 W Sonics), as shown in Figure 52. The acoustic power provided at 30% amplitude was 0.35 W/mL. The temperature was controlled at 21 °C. The total reaction mixture consisted of 47 mL of deionised water, 2.5 mL of latex at 10 wt.% solids, 0.5 mL of Pt precursor solution at 5 g Pt/L. Prior to sonication, 10 vol.% CO/Ar was bubbled for about 15 minutes from the bottom of the latex-containing flask at ca. 130 mL/min. Then, the gas bubbling was set at the liquid-gas interphase.

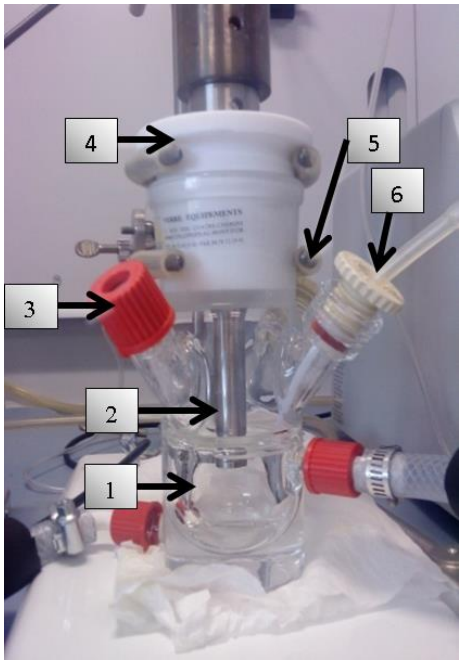

Figure 52. Image of the 20 kHz experimental set-up: (1) 50 mL thermostated double-walled glass reactor, (2) titanium probe supplied by a 750W maximal electric power generator, (3) sample outlet, (4) closing joint, (5) gas outlet, (6) gas inlet. Generator, thermocouple and flowmeter are not visible in the picture

III.2.4- Silica matrix via sol-gel synthesis

The silica matrix was synthesised by a sol-gel technique using three procedures (see nomenclature in Table 6). The first one (A40 and A60) was an acid catalysed sol-gel synthesis using 10.3 mL of tetraethyl orthosilicate and 22.5 mL of HCl solution at 10^{-2} M. The synthesis was carried out either at 20, 40 or 60 °C. The gelation time was recorded in each case. The second procedure (B40 and B60) was a two-step acid-base catalysed sol-gel synthesis. The difference with procedure A is that 9 mL of NH_4OH solution at 5×10^{-2} M were added at one third of the gelation time as observed in the acid catalysed synthesis. Once all samples reached the gel point, they were dried at 80 °C for at least 24 h. The third procedure (C40 and C60) was the same as the second one, but using 25 mL of latex (at 10 wt. % solids) instead of 22.5 mL of HCl solution at 10^{-2} M. Samples $B40_{cal}$, $B60_{cal}$, C40 and C60 where calcined under an air flow of ca. 50 mL/min in a Heraeus® RO tube furnace (Kendro) at 650 °C with a temperature profile of 5 °C/min up to 250 °C, then 0.5 °C/min up to 300 °C, a plateau at 300 °C for 2 h and then 0.5 °C/min up to 650 °C, and kept at 650 °C for 2 h prior to natural cooling.

All Pt-containing silica materials were prepared with Pt-decorated latex templates following the same procedure as for C40: the reaction mixture (consisting of TEOS, latex and HCl solution as detailed in Table 4) was stirred at 40 °C for 23.3 h in a glass round-bottomed flask. Then, the amount of 5×10^{-2} M NH_4OH solution specified in Table 4 was added in one shot. Once the samples reached the gel point, they were dried at 80 °C for at least 24 h. Then, the catalysts were calcined under air flow at a rate of ca. 50 mL/min in a Heraeus® RO tube furnace

(Kendro) at the temperature specified in Table 4. The temperature profile for calcination at 450 °C consisted of 5 °C/min up to 270 °C, then 1 h at 270 °C, then 0.33 °C/min up to 450 °C, and kept at 450 °C for 2 h prior to natural cooling. The temperature profile for calcination at 650 °C consisted of 5 °C/min up to 250 °C, then 0.5 °C/min up to 300 °C, a plateau at 300 °C for 2 h and then 0.5 °C/min up to 650 °C, and kept at 650 °C for 2 h prior to natural cooling.

The catalysts are named based on their Pt loading and calcination temperature, e.g. 0.7cal450 for a catalyst at 0.7 wt. % Pt/SiO_2 and calcined at 450 °C. However, when a relevant feature in the catalyst preparation is under study, it is added at the end of the catalyst name after a hyphen. Thus, for a material with 12.5% of macroporosity, it is called: 0.2cal450-12.5%, or when the material was prepared at 343 kHz, it is called 0.3cal450-343kHz (note: when not specified, the default value for macroporosity is 50% and for the ultrasound frequency is 205 kHz).

Table 4. Reaction mixture for the two-step acid-base catalysed sol-gel synthesis

Sample	TEOS (mL)	Pt-decorated latex (mL)	Non-decorated latex (mL)	0.01 M HCl solution[a] (mL)	5×10^{-2} M NH_4OH solution[b] (mL)	Calcination temperature (°C)
0.7cal450	10.3	25.0	-	-	7.0	450
0.7cal650	10.3	25.0	-	-	7.0	650
0.8cal450-50%	7.5	19.0	-	-	5.1	450
0.4cal450-33.3%	7.5	9.5	-	8.6	5.1	450
0.3cal450-25%	7.5	6.3	-	11.4	5.1	450
0.2cal450-12.5%	7.5	2.7	-	14.7	5.1	450
0.4cal650-25/25%	7.5	9.5	9.5	-	5.1	650
0.3cal450-100kHz	7.5	19.0	-	-	5.1	450
0.3cal450-205kHz	10.3	25.0	-	-	7.0	450
0.3cal450-343kHz	7.5	19.0	-	-	6.2	450
1cal650-50%-IWI	10.3	-	25.0	-	5.3	650

[a] An amount of 0.01 M HCl solution was added in some reactions in order to keep a constant water/TEOS molar ratio of 28.
[b] The amount of base varied depending on the requirement of the latex to reach a pH 9.6.

The silica matrix corresponding to 1cal650-50%-IWI was impregnated drop-wise with a solution of Na_2PtCl_4 at 10 g/L while stirring manually (for 1 g of silica, 1 mL of solution was used, in agreement with a pore volume of 1.1 mL/g measured in the silica matrix by mercury porosimetry). Subsequently, it was dried overnight at 80 °C and then it was treated under a hydrogen flow at ca. 40 mL/min in a vertical stainless steel tubular reactor within a temperature-controlled tubular furnace following a temperature profile of 3 °C/min up to 300 °C and a plateau for 2 h at 300 °C, after which it was let cool down naturally (the catalyst was kept in place with quartz wool on the top and on the bottom of the reactor). A commercially available 1 wt. % Pt/SiO_2 material (referred to as 0.7REF) was characterised as received.

III.2.5- Characterisation

After polystyrene latex synthesis, pH (PHM210 standard pH meter, Radiometer Analytical) and percentage of solids (MLS moisture analyser, KERN) were measured. The latex particle size was determined by dynamic light scattering (DLS) with a Vasco-3 particle size analyser (Cordouan Technologies) and by scanning electron microscopy (SEM) with a high resolution microscope S-4800 (Hitachi) operating at 2 kV. Typically, the samples for DLS measurements were prepared by diluting 5 µL of latex at 10 % solids in 5 mL of deionised water. Latex samples for SEM were dried overnight in a vacuum Raypa® drying oven (Espinar S. L.) at 40 °C and 0.01 mbar; the resulting powders were attached to sample holder stubs using carbon conductive adhesive tape. Then, the samples were sputtered with platinum.

The zeta potential of latex was measured with a Wallis zeta potential analyser (Cordouan Technologies) or a Zetasizer Nano ZS (Malvern). Inductively coupled plasma optical emission spectrometry (ICP-OES) measurements were carried out with a Spectro Arcos ICP-OES (Ametek). It was used to follow the Pt reduction during the sonochemical reactions by quantifying the residual Pt ions in solution. Polystyrene and reduced Pt nanoparticles were removed from the samples by filtration using two PTFE 0.2 µm 13 mm filters in a series, as previously reported [32]. The clear phase was then diluted 100 times with 0.3 M nitric acid, prior to injection in the ICP-OES. ICP calibration curves were recorded using SCP Science platinum standard solutions. The estimated experimental uncertainty for concentrations measurements by ICP was 5%.

A sample of polystyrene functionalised with Pt at 20 kHz was dried overnight in a vacuum Raypa® drying oven (Espinar S. L.) at 40 °C and 0.01 mbar; the resulting powder was attached to sample holder stubs using carbon conductive adhesive tape (no metal sputtering in this case). Then it was analysed by SEM in a Hitachi S4500 FEG (Hitachi) and energy dispersive X-ray (EDX) spectra were acquired using AZtecEnergy (Oxford Instruments). Functionalised latexes and silica matrices before and after template removal were studied with transmission electron microscopy (TEM) using a 2200FS – 200 kV TEM (Jeol), a Tecnai F20ST/STEM monochromated TEM (FEI) or a Titan 80-300 kV cubed Cs-corrected TEM (FEI). Latex samples for TEM were prepared by diluting 10 µL of latex in 3 mL of absolute ethanol, depositing a drop on a formvar/carbon-coated 300 mesh Cu TEM grid followed by drying in ambient air. Silica samples were ground in a mortar, and then a few milligrams were encapsulated in an EMbed 812 resin before a section of 70 nm thick was cut and deposited on a Cu TEM grid, using an ultramicrotome Ultracut UCT (Leica Microsystems) equipped with a DiATOME ultra diamond knife. High resolution TEM (HR-TEM) analyses, including annular dark-field (ADF) images and energy-dispersive X-ray (EDX) spectroscopy, were performed in a Titan 80/300 kV cubed Cs-corrected TEM (FEI). For those analyses, a specimen of silica-supported Pt catalyst was ground and ultrasonically shaken in ethanol, and then a drop was casted in air from the coloured dispersion onto a 200 mesh Cu grid with a holey carbon support foil (Quantifoil).The TEM images were analysed manually using ImageJ software (USA National Institutes of Health).

Thermal gravimetric analyses (TGA) for latex decomposition in artificial air were carried out in a Q50 thermal gravimetric analyser (TA Instruments), using a heating rate of 10 °C/min up to 700 °C. Additional TGA and differential scanning calorimetry (DSC) were carried out in

artificial air in a Simultaneous Thermal Analyser (STA 6000, PerkinElmer), using a heating rate of 10 °C/min up to 900 °C. The silica matrix surface area and mesopore size distribution were determined by nitrogen adsorption-desorption using an ASAP-2020 physisorption analyser (Micromeritics), with an estimated experimental uncertainty of 6% [35]. Mesopore size distributions were based on the Barrett-Joyner-Halenda (BJH) method on the adsorption branch. The macropore size distribution was characterised by mercury porosimetry using an AutoPore IV 9500 (Micromeritics).

The X-ray photoelectron spectroscopy (XPS) analyses were carried out using an ESCALAB 250 (Thermo Electron), using a monochromatic excitation source: Al Kα (1486.6 eV). The analysed surface was of 400 µm diameter and the charge was compensated by an electron beam (-2 eV). XPS binding energies were referred to the Si-O component of silicon $Si2p_{3/2}$ at 103.2 eV. Temperature-programmed reduction (TPR) was carried out on an Autochem II (Micromeritics). The hierarchically porous materials were analysed after calcination at either 450 °C or 650 °C. In all cases, a 1 h *in-situ* pre-treatment at 120 °C in argon flow was carried out. Then, the TPR experiments were carried out between -50 °C and 350 °C, with a temperature ramp of 10 °C/min in 5% H_2/Ar flow.

All Pt/SiO_2 samples were studied by elemental analysis by ICP-OES. They were prepared by grinding 50 mg of catalyst with 250 mg of Na_2O_2. Then, the mixture was placed in a zirconium crucible at 480 °C for 1 hour in static air. After natural cooling, 180 mL of water were added to the mixture. Then, 20 mL of 6 M HCl solution were added under stirring and heating at ca. 50 °C and water was added to obtain a total of 250 mL. Then, 1.2 mL of the catalyst solution were added to 4.8 mL of a 0.3 M HNO_3 solution prior to ICP measurement. The experimental uncertainty for metal loadings was estimated to 5% of the reported value.

III.3- Results

The desired catalyst morphology was specified to consist of a meso- and macroporous silica matrix with Pt nanoparticles of a few nanometres in diameter mainly located in the macropores. To achieve such a material, a polystyrene latex template was first prepared and decorated with Pt nanoparticles. Then, the silica matrix was optimised to have about 50% of mesoporosity. Finally, a material with hierarchical porosity and Pt nanoparticles mainly on the macropore surfaces was obtained.

III.3.1- Synthesis and functionalisation of the PS latex template

III.3.1.1- PS latex template

Typically, the latex obtained with the described procedure had a pH of 2 and a solids content of ca. 10 wt. %. This protocol worked well to produce stable latexes (more than 10 months shelf-life). The latex dispersity (Đ) was calculated as the ratio of the weight-average diameter (D_w) over the number-average diameter (D_n). For a typical latex, the particle size characterisation revealed a D_n of 134 nm, a D_w of 140 nm, and a Đ of 1.04. It was observed that for this PS latex, the Đ was very close to 1, which corresponds to a uniform distribution of the PS particle size. In Figure 53, it can also be noticed that the particles are randomly close packed after drying the sample for SEM imaging. This phenomenon is expected after drying of a stable dispersion of monodisperse particles.

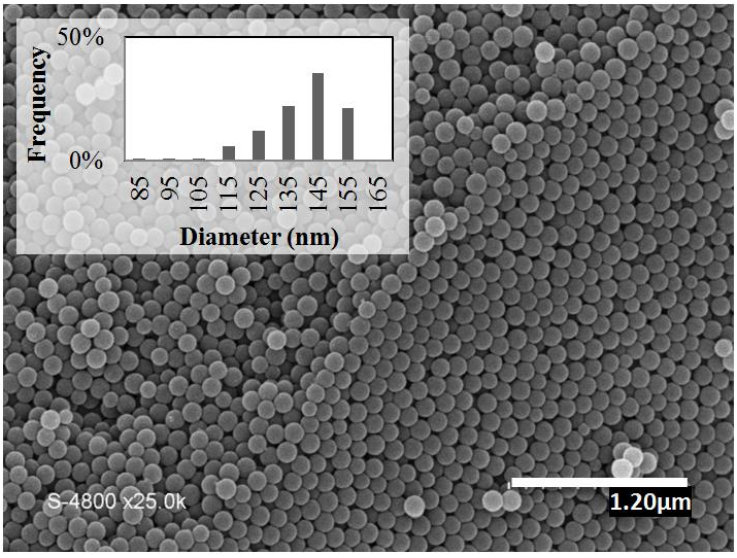

Figure 53. SEM images of PS latex template. Particle size distribution histogram in the inset.

III.3.1.2- Sonochemical decoration

The PS template was then decorated with Pt nanoparticles under ultrasonic irradiation. As described in Chapter II, the sonochemical reduction is achieved due to the acoustic cavitation that occurs in the liquid medium when exposed to ultrasound (between tens of kHz to a few MHz). Within the cavitation bubble, water molecules can be split into H• and OH• radicals [35, 36]. Hydrogen, H_2, generated by the recombination of H• radicals within these bubbles, reacts with the platinum ions to reduce them to metallic platinum nanoparticles [33]. Carbon monoxide can also be added to the reaction medium in order to enhance the platinum reduction under ultrasonic irradiation [36].

III.3.1.2.i- Template decoration at 20 kHz

Two Pt precursors were evaluated for the preparation of Pt nanoparticles at the surface of polystyrene beads: a Pt(IV) salt - hexachloroplatinic acid - and a Pt(II) salt - sodium tetrachloroplatinate. They were tested at 0.05 g Pt/L (equivalent to ca. 0.002 g Pt) at 20 kHz under a 10 vol. % CO/Ar atmosphere. As shown in Figure 54, the Pt decoration was successful and the nanoparticle size was not dependent on the precursor that was used (ca. 2 nm in both cases). However, the time required to reduce 99 % of the Pt in the case of hexachloroplatinic acid was 5 h, compared with 3.4 h required for sodium tetrachloroplatinate. This difference in time stands on the fact the in the case of hexachloroplatinic acid, the Pt has to be reduced from an oxidation state +4 to +2 and finally to 0. In the case of sodium tetrachloroplatinate, it is already starting on a +2 oxidation state.

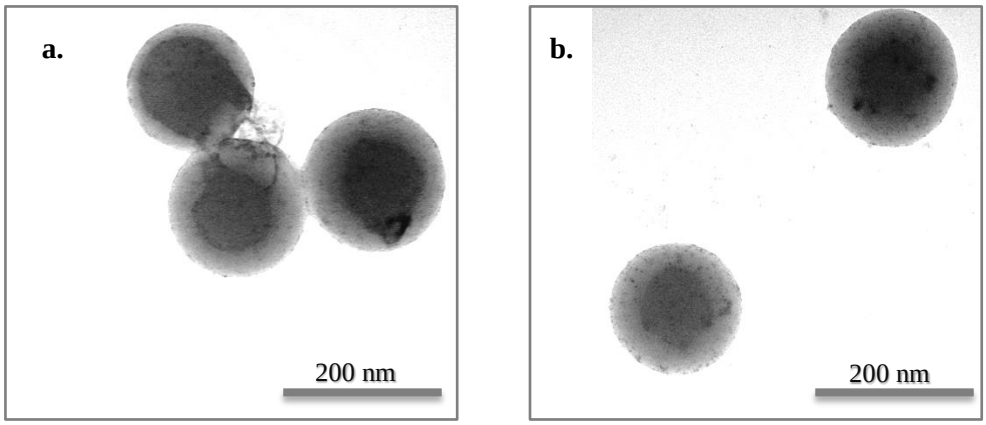

Figure 54. TEM images for Pt reduction at 20 kHz under 10 vol. % CO/Ar, using: a. Hexachloroplatinic acid (Pt NPs: D_n: 1.8 nm, Đ: 1.12). b. Sodium tetrachloroplatinate (Pt NPs: D_n: 1.9 nm, Đ: 1.22).

Additionally, due to the nature of the ultrasound at 20 kHz, important mechanic effects take place, eroding the sonotrode after every use. As a consequence, since the sonotrode was in direct contact with the reaction medium, the latex was polluted with sediments of Ti and Al

coming from the alloy of which the sonotrode is made of, as shown in the EDX spectrum in Figure 55.

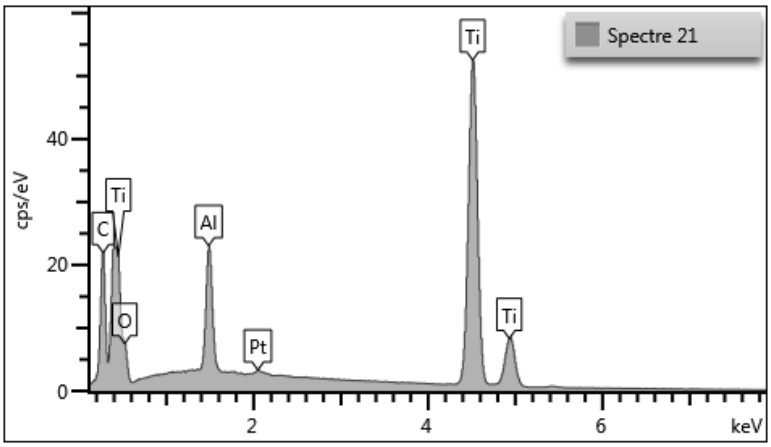

Figure 55. EDX spectrum of dry Pt-decorated polystyrene

Considering the sample pollution issue by sonotrode erosion and the low concentrations required to operate at 20 kHz, it was not possible to use such decorated latexes in the preparation of hierarchically porous Pt/SiO_2 materials. Furthermore, since no significant particle size difference was observed when using hexachloroplatinic acid (H_2PtCl_6) or sodium tetrachloroplatinate (Na_2PtCl_4), it is advantageous to use the Pt(II) precursor for the next experiments in regard of the faster kinetics (3.4 h with Na_2PtCl_4 versus 5 h with H_2PtCl_6 for reducing ca. 0.002 g Pt).

III.3.1.2.ii- Template decoration at 205 kHz

These experiments at 205 kHz were carried out with a Pt concentration of ca. 1 g Pt/L, which was much higher than the 0.05 g Pt/L used for the experiments at 20 kHz (equivalent to ca. 0.1 g Pt at 205 kHz versus ca. 0.002 g at 20 kHz). This higher metal concentration made possible to obtain ca. 1 wt. % Pt/polystyrene using a latex at ca. 10 wt.% solids required for the following steps in the catalyst preparation (it is important to note that a latex with low amount of solids would require an additional step to concentrate it. In order to avoid such additional step, it is desired to carry out the latex decoration at ca. 10 wt. % solids).

After the sonochemical reduction, the platinum nanoparticles were confirmed to be at the surface of the polymer template. Indeed, annular dark field (ADF) and energy dispersive X-ray spectroscopy (EDX) analyses in STEM mode were carried out to observe if the spots on the PS beads actually correspond to Pt nanoparticles. As shown in Figure 56, it is confirmed that these particles contain Pt. Furthermore, some particles were also observed on the sample holder carbon film. However, these particles did not contain Pt, but mainly S and Ca, elements that are present at low concentration due to the latex formulation.

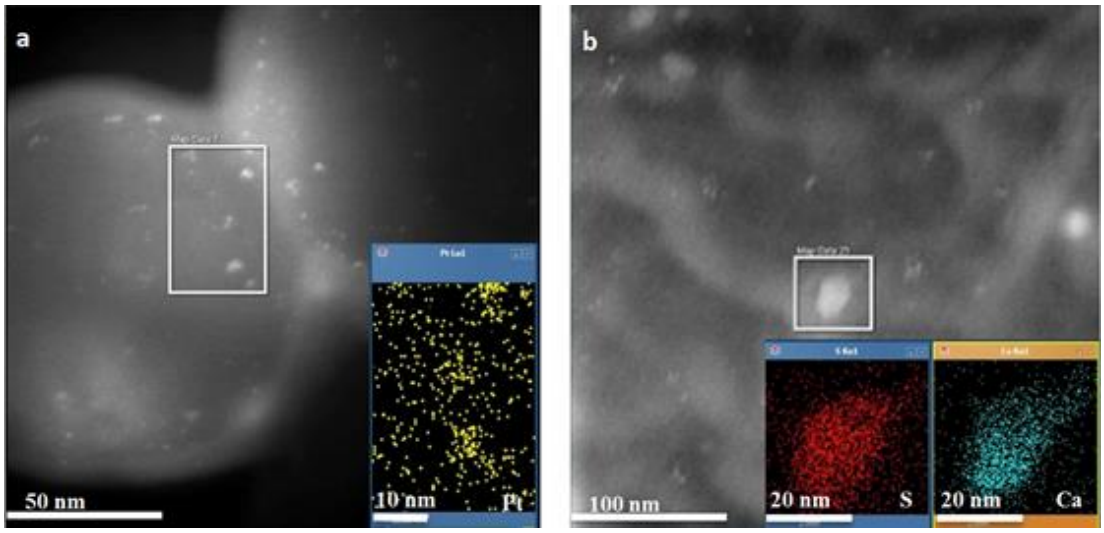

Figure 56. ADF in STEM mode images of Pt nanoparticles reduced at 20 °C, 205 kHz, in presence of PS beads under 10 vol.% CO/Ar: a. The polymer beads, insert of Pt EDX mapping, b. The sample holder carbon film, insert of S and Ca EDX mapping.

Furthermore, by analysing the images shown in Figure 57, lattice spacings consistent with Pt (111) and (200) planes were observed. Specifically in Figure 57b, a lattice spacing of 2.3 ± 0.1 Å was measured, corresponding to {111} facets in platinum (0.2265 nm). This confirmed that the particles observed on the latex as dark spots correspond to Pt nanoparticles.

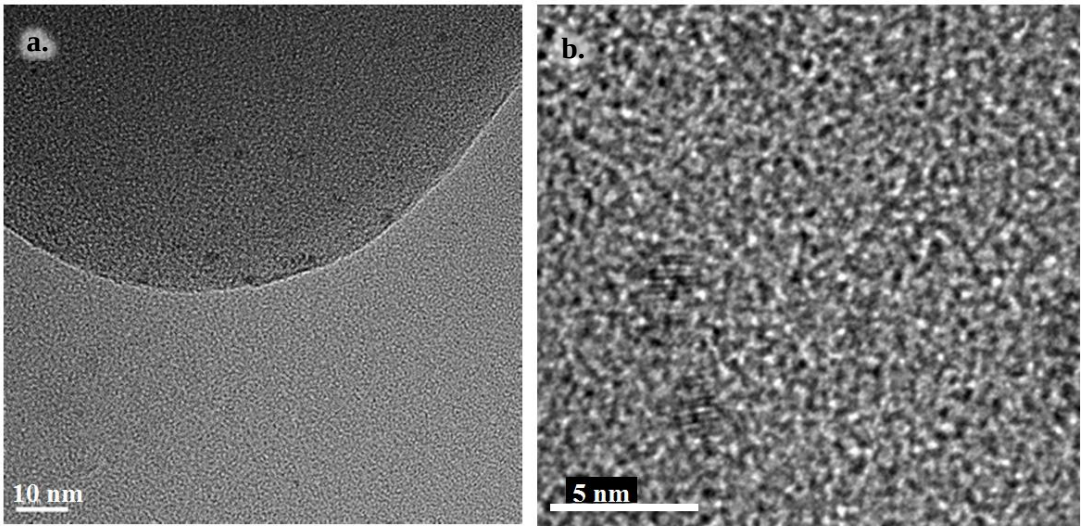

Figure 57. TEM imaging of a Pt-decorated PS latex template prepared at 20 °C, 205 kHz in 10 vol. % CO/Ar atmosphere on: a. Tecnai F20ST/STEM monochromated microscope, b. Titan 80-300 kV cubed Cs-corrected microscope.

Electrostatic charge could be considered as a first attempt to explain the Pt-PS interaction. However, this is not the case since Pt(II) ions (from Na_2PtCl_4), Pt nanoparticles and PS beads are negatively charged. The zeta potential for the PS beads was −49 ± 7 mV and for the Pt nanoparticles was −17 ± 7 mV (the zeta potential of Pt nanoparticles was measured in a sample of Pt ions sonochemically reduced in the absence of latex). A more plausible explanation for the Pt-polymer bead interaction is the attachment of Pt nanoparticles to sulfonate groups at the surface of the PS beads, as has been reported elsewhere [38]. In the present case, sulfonate groups are certainly present at the polymer bead surface not only due to the SDBS used as surfactant in the latex formulation, but also due to sulfonate radicals generated by the redox initiation couple used in the latex polymerisation: KPS and SMBS [39,40]. Moreover, during the sonochemical reduction, the cavitation phenomenon is favoured at the interface between water and hydrophobic materials by decreasing the energy required for forming a bubble of vapour [41]. In the case of the PS bead template, the surface is mostly hydrophobic, so it is likely to have more cavitation bubbles at the PS surface-liquid interface than in the homogeneous medium, favouring the Pt reduction at the polymer surface.

Moreover, the sonochemical reduction was carried out either under Ar or under 10 vol. % CO/Ar. Considering the high amount of platinum engaged in the system (ca. 1 g/L, equivalent to 0.1 g of Pt), ultrasonic treatments of at least 14 h were expected to achieve a complete reduction of the noble metal, so the reactions were carried out on two days with a stop during the night for safety reasons. As expected, the Pt reduction was faster at the beginning of the reaction in the presence of CO (first 500 min in Figure 58) [33]. It has two causes. First, the ability of CO to directly reduce Pt ions at the interface of the cavitation bubble, according to the equation:

$$PtCl_4^{2-} + CO + H_2O \xrightarrow{)))} Pt^0 + CO_2 + 2H^+ + 4Cl^-$$

Second, the ability of CO to enhance the hydrogen formation: CO is a scavenger of OH• radicals generated during the water molecule splitting process under ultrasonic irradiation. This reaction leads to a higher formation rate of H_2 which is a reducing agent for platinum in the system [33].

$$CO + OH^\bullet \xrightarrow{)))} CO_2 + H^\bullet$$

$$2H^\bullet \xrightarrow{)))} H_2$$

$$PtCl_4^{2-} + H_2 \xrightarrow{)))} Pt^0 + 2H^+ + 4Cl^-$$

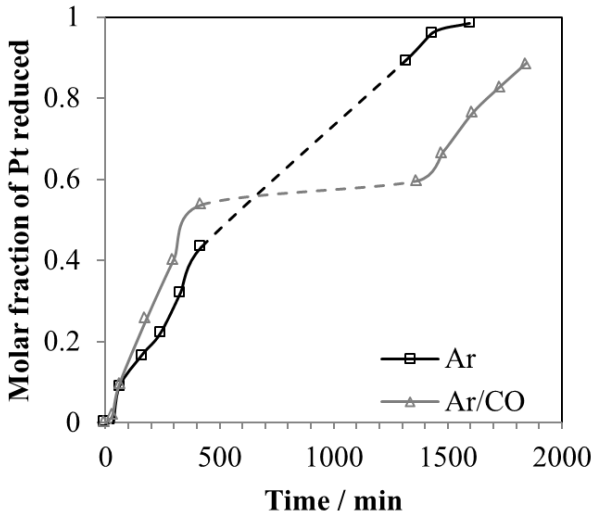

Figure 58. Monitoring of Pt(II) reduction under Ar and 10 vol. % CO/Ar at 205 kHz and 20 °C, in presence of polystyrene beads at 9 wt. % solids. Plain lines for the duration of the ultrasound irradiation. No gas bubbling during silent period. Experimental uncertainty estimated to 5%.

Interestingly, only the sample that was being reduced under Ar continued evolving overnight (Figure 58). It is because, when CO/Ar is used, as soon as the ultrasonic irradiation is turned off, there are no more radicals or other species that could reduce the Pt. On the other hand, when only Ar is used, the OH• radicals can be scavenged by other molecules in the vicinity of cavitation bubbles like surfactants (SDBS in this case) [42], leading to the formation and accumulation in solution of reducing species that would continue the Pt reduction even after stopping the ultrasonic irradiation.

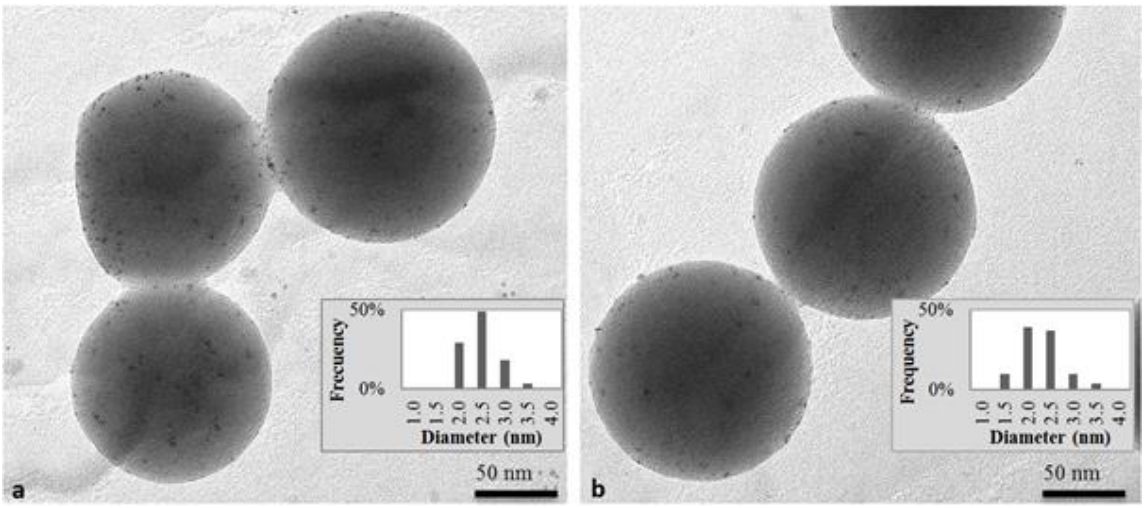

Figure 59. TEM images of Pt nanoparticles reduced at 20 °C, 205 kHz in presence of PS beads under: a. Ar atmosphere and b. 10 vol. % CO/Ar atmosphere. Particle size distribution histogram is shown in the insert.

From a morphological point of view, no major effect of the gas atmosphere was observed on the particle size of the Pt nanoparticles (Figure 59). In Ar, the Pt average particle diameter was Dn = 2.3 nm, Dw = 2.5 nm, Đ = 1.10. Similarly, in CO/Ar, the average particle diameter was Dn = 2.1 nm, Dw = 2.4 nm, Đ = 1.15. So, from the morphological perspective, it is not necessary to use CO for the successful PS template decoration.

It is possible to conclude that the latex decoration at 205 kHz was successful, leading to ca. 1 wt. % Pt/polystyrene using a latex at ca. 10 wt.% solids (as required for the next steps in the catalyst preparation). Furthermore, the Pt nanoparticles were of about 2 nm regardless of the use of an atmosphere of Ar or 10 vol. % CO/Ar.

III.3.1.2.iii- Template decoration using alternative sonochemical set-ups

Due to technical problems, the set-up operating at 205 kHz was no longer available. In order to find other alternatives for the Pt reduction, two other reaction set-ups were evaluated. The first alternative was a reactor operating at 100 kHz, in which the reaction medium was in direct contact with the ultrasound-generating surface, as detailed in the experimental section. The choice of a reactor with or without direct contact between the transducer and the reaction medium is related to the possibility of the transducer surface to be cleaned after every use (only the transducer at 100 kHz could be polished after every use). Ideally, the best configuration would be with direct contact, in order to improve the sonochemical effects in the reaction medium. In the non-direct contact reactor, the ultrasounds must go through the glass-walls of the inner reactor leading to energy loss. However, the sonochemical activity measured by the H_2O_2 formation was still similar at 100 kHz and at 205 kHz: 0.38 µmol H_2O_2/min and 0.32 µmol H_2O_2/min, respectively.

The second alternative was a reactor operating at 343 kHz. This set-up was similar to the one at 205 kHz (without direct-contact), but with a transducer working at a different frequency (343 kHz). Both systems at 343 kHz and at 205 kHz absorbed the same acoustic power: 0.14 W/mL. However, the set-up at 343 kHz exhibited a lower sonochemical activity (0.16 µmol H_2O_2/min) than at 205 kHz (0.32 µmol H_2O_2/min) due to a more important energy loss at 343 kHz than at 205 kHz.

Latexes decorated at 100 kHz and at 343 kHz were compared to a latex decorated at 205 kHz. The three of them were prepared by reduction of sodium tetrachloroplatinate at 0.5 g Pt/L under Ar atmosphere at 20 °C, using a polystyrene latex at ca. 10 wt. % solids (leading to 0.5 wt.% Pt/polystyrene). Table 5 gives the Pt particle size obtained in each case, as well as some experimental information. Figure 60 presents TEM images of the Pt-decorated latexes and corresponding sonochemical reduction profiles. The average particle size did not show any significant variation with the different set-ups. However, the particle size distribution was narrower and with a smaller standard deviation, when using the set-up at higher ultrasound frequency.

Table 5. Pt particle size versus ultrasound frequency

Frequency (kHz)	Reactor type	Amount of Pt in the system (g)	Absorbed acoustic power (W/mL)	H_2O_2 formation rate[34] (µmol/min)	Particle size (nm)	Đ
100	Direct contact	0.10	0.21 ± 0.02	0.38 ± 0.04	2.9 ± 0.8	1.38
205	Non-direct contact	0.05	0.14 ± 0.01	0.32 ± 0.03	2.4 ± 0.7	1.29
343	Non-direct contact	0.05	0.14 ± 0.01	0.16 ± 0.02	2.1 ± 0.4	1.12

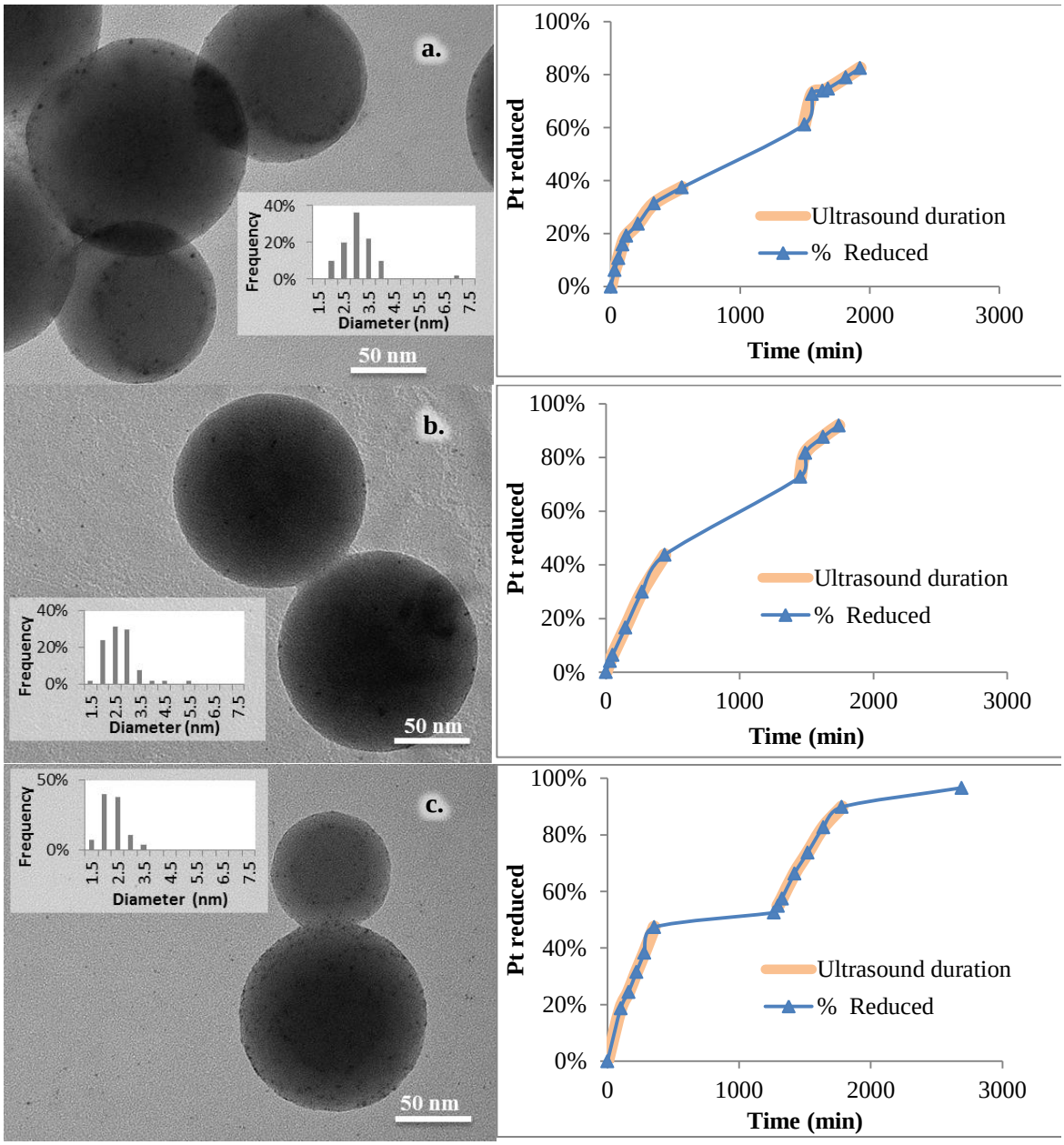

Figure 60. TEM images of Pt-decorated latex (left) and Pt reduction profiles (right) at: a. 100 kHz, b. 205 kHz and c. 343 kHz. Bold lines correspond to the duration of the ultrasound irradiation. Thin lines correspond to silent periods.

Despite of the differences of sonochemical activity in the evaluated set-ups, the reduction of 90% of the Pt took, in all cases, two days with an overnight silent period. However, as observed in Figure 60.c, only the sample reduced at 343 kHz did not evolve significantly overnight, probably due to a lower generation rate of radicals (related to a lower sonochemical activity) that decreased the formation of reducing species that could keep reducing Pt in the absence of ultrasound.

Although, the alternative reaction set-ups (operating at 100 kHz and 343 kHz) worked at slightly different operation conditions compared with the set-up at 205 kHz, as detailed in Table 5 (frequency, sonochemical activity, direct or non-direct liquid-transducer contact, etc.), it was possible to successfully decorate polystyrene latexes with Pt nanoparticles of similar sizes: 2.9 ± 0.8 nm, 2.4 ± 0.7 nm and 2.1 ± 0.4 nm in the set-up at 100, 205 and 343 kHz, respectively. These latexes were prepared at ca. 0.5 wt. % Pt/polystyrene and ca. 10 wt. % solids.

III.3.2- Optimisation of the silica matrix

The idea is to prepare a macroporous silica by polymer templating. Such macropores are desired to be surrounded by a mesoporous silica matrix, obtained by optimised sol-gel conditions. The strategy starts by the preparation of a silica matrix with a desired mesoporosity of 50% (without macropores at this stage), given by:

$$\frac{Vol_{mesopores}}{Vol_{SiO_{2,mesoporous}}} \times 100 = \frac{Vol_{mesopores}}{Vol_{mesopores} + Vol_{SiO_{2,dense}}} \times 100$$

Where $Vol_{mesopores}$ is the volume of mesopores, $Vol_{SiO_{2,dense}}$ is the volume of the dense silica skeleton and $Vol_{SiO_{2,mesoporous}}$ is the volume of mesoporous silica. Note that in this case, the mesoporosity is equal to the total porosity of the material.

Subsequently, it is desired to include enough polymer beads within the mesoporous silica in order to obtain a macropore volume of 50% with respect to the total volume (macroporosity), given by:

$$\frac{Vol_{macropores}}{Vol_{SiO_{2,macro+\,mesoporous}}} \times 100 = \frac{Vol_{macropores}}{Vol_{macropores} + Vol_{SiO_{2,mesoporous}}} \times 100$$

Where $Vol_{macropores}$ is the volume of macropores, $Vol_{SiO_{2,mesoporous}}$ is the volume of the mesoporous silica skeleton and $Vol_{SiO_{2,macro+\,mesoporous}}$ is the total volume of macroporous and mesoporous silica. The total porosity of this hierarchically porous material is given by the volume of meso and macropores divided by the total volume of material.

Having these specifications in mind, it is possible to calculate the required amounts of latex template and silica precursor (tetraethyl orthosilicate - TEOS) to prepare 1 g of hierarchically porous silica. Given that the density of dense silica is 2.2 g/mL, the density of polystyrene is approximatively 1 g/mL and the polystyrene content in the latex is ca. 10 wt. %, the required amount of latex to prepare 1 g of mesoporous silica with 50% macroporosity is:

$$1\ g_{SiO_{2,dense}} \times \frac{1\ mL_{SiO_{2,dense}}}{2.2\ g_{SiO_{2,dense}}} \times \frac{2\ mL_{SiO_{2,mesoporous}}}{1\ mL_{SiO_{2,dense}}} \times \frac{1\ mL_{macropores}}{1\ mL_{SiO_{2,mesoporous}}} \times \frac{1\ mL_{polystyrene}}{1\ mL_{macropores}}$$
$$\times \frac{1\ g_{polystyrene}}{1\ mL_{polystyrene}} \times \frac{100\ g_{latex}}{10\ g_{polystyrene}} \times \frac{1\ ml_{latex}}{1\ g_{latex}} = \mathbf{9.1\ ml_{latex}}$$

And the required amount of TEOS is:

$$1\ g_{SiO_{2,dense}} \times \frac{1\ mol_{SiO_2}}{60.08\ g_{SiO_{2,dense}}} \times \frac{1\ mol_{TEOS}}{1\ mol_{SiO_2}} \times \frac{208.33\ g_{TEOS}}{1\ mol_{TEOS}} \times \frac{1\ ml_{TEOS}}{0.93\ g_{TEOS}} = \mathbf{3.7\ ml_{TEOS}}$$

Considering the amount of water in the latex, the corresponding water/TEOS molar ratio is 27.

Having this information, it is possible to start by the optimisation of the mesoporous silica matrix. Three temperatures were evaluated for the synthesis of the silica matrix: 20, 40 and 60 °C. However, at 20 °C, the hydrolysis and condensation reactions were so slow that several weeks were required to achieve the gelation point (576 h). Thus, only temperatures of 40 and 60 °C were considered further in this study.

Table 6 shows the textural characteristics of the materials at each of the steps taken for engineering a mesoporous silica matrix. Experiments A and B were carried out without template, but with an HCl solution (pH = 2) that mimics the pH of the latex template. With one-step acid catalysed sol-gel synthesis (A40 and A60), the material was only microporous (according to the *t*-plot method, employing the Halsey equation adapted to silica by Cranston and Inkley [43,44]) and the porosity was below the initial specification (32% and 41% compared with a target of 50%). This microporosity is expected for syntheses in such acidic conditions where weakly-branched structures are favoured [13]. Nevertheless, this step was important to determine the gelation time of the medium at the pH of the latex template with the given water/TEOS ratio. With this information, it was possible to set up a procedure for a two-step acid-base catalysed sol-gel synthesis (B40 and B60): a base was added at one third of the gelation time required under acidic conditions, increasing the pH from 2 to 9.6. Such an increase in pH, after partial acid hydrolysis, speeds up the condensation reactions and allows branched structures to rearrange in such a way that larger pores and a more crosslinked silica network are formed. Consequently, the maximum capillary pressure is reduced, and the mechanical resistance of the network is increased so the shrinkage during solvent evaporation is limited. As a result, a large total porosity is obtained in the resulting structure [13]. Using this technique, mesoporous silica materials were prepared with the desired mesoporosity (> 50%): 54 % and 51% for the syntheses at 40 °C and 60 °C, respectively.

Table 6. Textural characterisation of silica materials without Pt.

Sample	Description	Sol-gel synthesis temp. (°C)	Gelation time - tg (h)	BET surface area (m^2/g)	Total pore volume (by N_2-ads/des.) (cm^3/g)	Total pore volume (by Hg-poro.) (cm^3/g)	Micropore volume (cm^3/g)	Mesopore volume (cm^3/g)	Macropore volume (cm^3/g)	Total porosity (%)	BJH Adsorp. average mesopore diameter (nm)	BJH Desorp. average mesopore diameter (nm)	Mesopore range (nm)	Average macropore diameter (nm)	Macropore range (nm)
A40	One-step acid catalysed sol-gel synthesis w/o latex	40	72.0	434	0.21	-	0.21	-	-	32	-	-	-	-	-
B40	Two-step acid-base catalysed sol-gel synthesis w/o latex	40	25.0	620	0.54	-	-	0.54	-	54	3.8	3.8	2-15	-	-
$B40_{cal}$	B40 calcined at 650 °C	-	-	557	0.48	-	-	0.48	-	51	3.7	3.8	2-15	-	-
C40	Two-step acid-base catalysed sol-gel synthesis with latex. Calcination at 650 °C	40	23.7	615	0.74	0.71	-	0.48	0.26	62	5.8	3.8	2-11	134	110-170
A60	One-step acid catalysed sol-gel synthesis w/o latex	60	14.0	640	0.32	-	0.32	-	-	41	-	-	-	-	-
B60	Two-step acid-base catalysed sol-gel synthesis w/o latex	60	5.0	707	0.47	-	-	0.47	-	51	3.2	3.8	2-11	-	-
$B60_{cal}$	B60 calcined at 650 °C	-	-	652	0.43	-	-	0.43	-	49	3.1	3.8	2-11	-	-
C60	Two-step acid-base catalysed sol-gel synthesis with latex. Calcination at 650 °C	60	2.3	572	0.61	0.66	-	0.48	0.18	59	4.9	3.8	2-15	128	110-170

After calcination at 650 °C, the total pore volume decreased in both materials (B40 and B60) and a loss of specific surface area was observed: B40 decreased from 620 m²/g to 557 m²/g and B60 decreased from 707 m²/g to 652 m²/g. As discussed in detail by Brinker and Scherer [13], structural changes occur during heating of silica gels. In the temperature range from 150 °C to 550 °C these changes are mainly associated with the removal of residual alkoxy groups, condensation reactions and structural relaxation, while at higher temperatures sintering processes are activated. Due to our strategy of two-step acid-base catalysed hydrolysis giving rise to a mesoporous silica matrix, structural changes are limited below 800 °C [13]. This is experimentally confirmed by the rather limited decrease of specific surface area and final values of silica matrix porosity, remaining within the targeted range of ca. 50 %.

The next step was the silica matrix synthesis in the presence of the polystyrene latex template (procedure C). Figure 61 shows that both materials, C40 and C60, synthesised at 40 and 60 °C, respectively, exhibit mesopores, mostly ranging from 2 to 10 nm. And contrary to what has been obtained without template (procedure B), the specific surface area at 40 °C (615 m²/g) is larger than at 60 °C (572 m²/g). The pore equivalent diameter distribution (mainly in the mesopore range) was obtained by plotting the first derivative of the adsorbed volume with respect to the pores equivalent diameter given by the BJH method and the average pore diameter is given by:

$$\frac{4 \times \text{“BJH cumulative adsorption or desorption pore volume”}}{\text{“pore area” (cylindrical pores)}}$$

The total pore volumes by nitrogen physisorption were found to be 0.74 cm³/g and 0.61 cm³/g for C40 and C60, respectively. Of which, 0.48 cm³/g was due to the mesoporosity in both cases, as measured in the adsorption branch up to an equivalent pore diameter of 50 nm. The difference, 0.26 cm³/g and 0.13 cm³/g for C40 and C60, respectively, would correspond to the macroporosity.

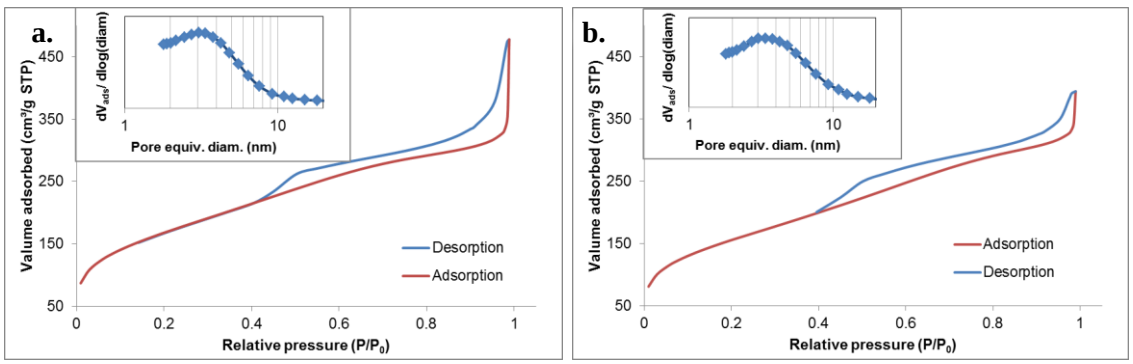

Figure 61. Nitrogen adsorption-desorption isotherms of silica with hierarchical porosity: a. Sample C40, b. Sample C60. Pore equivalent diameter distributions are presented in the insets.

However, it is expected that nitrogen capillary condensation might not be complete in the macropores, so mercury porosimetry was used instead trying to obtain more reliable information on the macropores. Figure 62 shows the mercury porosimetry results for these two materials (C40, C60) after removing the latex template at 650 °C. It is important to note that the first slope of cumulative intrusion corresponds to the mercury filling of the boundaries between grains of the material and not yet to the intrusion into the material. In addition, a marked hysteresis can be noticed; this is because during the intrusion, the mesopores must be filled before the macropores, since the matrix that contains the macropores is mesoporous. So it is during the extrusion that it is possible to obtain information about the macroporosity of the material. The macropore equivalent diameter distribution was obtained by plotting the first derivative of the extruded mercury volume with respect to the pores equivalent diameter. These results show that the macropore size distribution corresponds approximately to the size distribution of the PS template. In terms of average values, the macropores obtained by synthesis at 40 °C and 60 °C were 134 nm and 128 nm, respectively, compared to 134 nm of the PS beads in the latex template. The total pore volumes found by mercury porosimetry at maximum intrusion were 0.71 cm^3/g and 0.66 cm^3/g for C40 and C60, respectively. These values are similar to those obtained by nitrogen physisorption.

The mercury porosimetry presents some limitations, mainly by a maximum applied pressure of 60.000 psia that correspond to the mercury intrusion into pores as small as 3.6 nm. So pore volumes within micro- and mesopores below 3.6 nm are not quantified by this technique. However, in this specific case, it was possible to obtain similar pore volume values to that in nitrogen physisorption because the average mesopore diameters were larger: 5.8 nm and 4.9 nm for C40 and C60, respectively, as calculated with the BJH method in the adsorption branch (please note that differences with the desorption branch (see Table 6) result from discrepancies between adsorbent porosity and the applied BJH model assuming open-ended cylindrical capillaries).

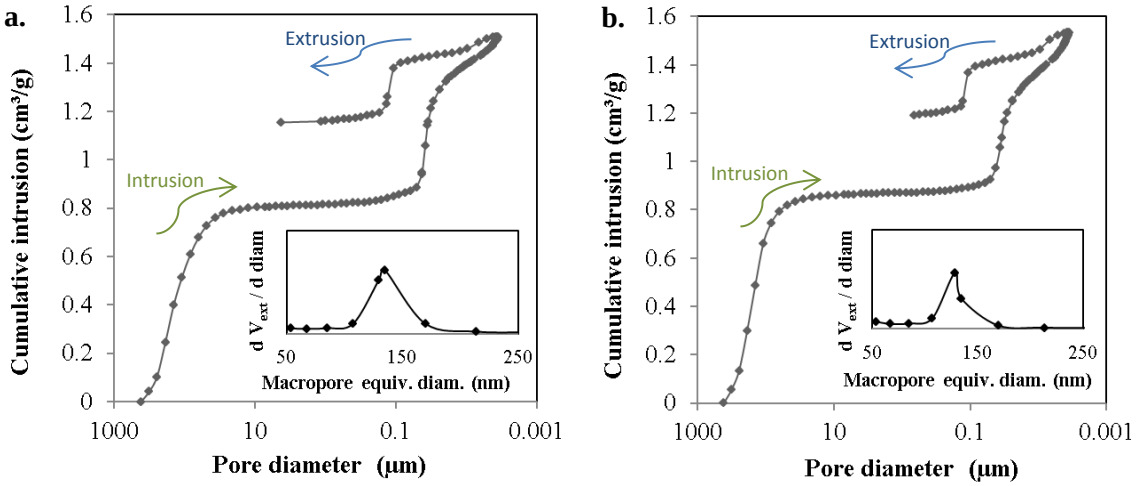

Figure 62. Mercury porosimetry of silica with hierarchical porosity: a. Sample C40, b. Sample C60. Macropore equivalent diameter distribution is presented in the insets.

The proposed two-step acid-base catalysed sol-gel syntheses in the presence of a polystyrene latex template permitted to obtain a hierarchically porous structure with mesopore sizes from 2 nm up to 15 nm and macropores of 110-170 nm. However, at this point, one of the sol-gel procedures (at 40 °C or 60 °C) needs to be chosen for the next step using the Pt-decorated template. From the results given above, it can be concluded that the matrix synthesised at 40 °C has the largest specific surface area and total pore volume (respectively: 615 m^2/g and 0.74 cm^3/g at 40 °C versus 572 m^2/g and 0.66 cm^3/g at 60 °C). In addition, the gelation time at 60 °C is very short (2.3 h versus 23.7 h at 40 °C), implying larger relative error on the addition time of the second hydrolysis solution (base-catalysed hydrolysis step at one third of the gelation time), which results in larger variability between batches with small variations in time. For these reasons, the temperature of 40 °C has been selected for the sol-gel synthesis in the presence of the Pt-decorated latex.

III.3.3- Characterisation of the final materials

After the preparation of silica materials with Pt-decorated latex by the two-step acid-base catalysed sol-gel synthesis at 40 °C, the procedure for template removal by calcination was defined based on thermogravimetric analyses. The resulting materials after template removal were characterised in terms of matrix pore texture and Pt particle size and oxidation state.

III.3.3.1- Template removal

Thermogravimetric analyses (TGA) were carried out on the starting latex template and on the samples immediately after the sol-gel synthesis. It was observed that for the polymer alone the thermal degradation was complete above 425 °C (Figure 63), in agreement with Pfaffli et al. [45]. However, for the silica matrix with polystyrene template without Pt, at least 610 °C were required for complete polymer degradation (Figure 64.a). That higher temperature is required because the silica matrix constrains the template removal [46].

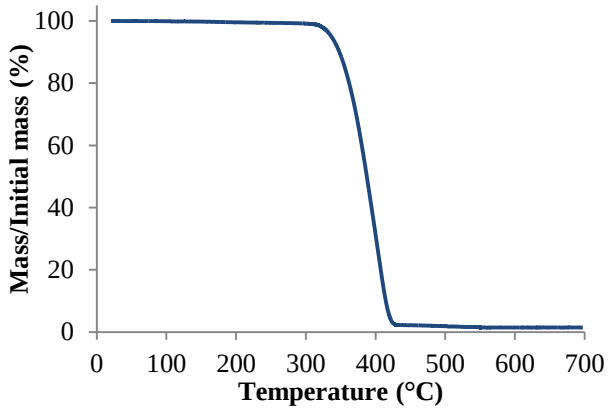

Figure 63. Thermogravimetric profile of dry polystyrene beads under air at 10 °C/min.

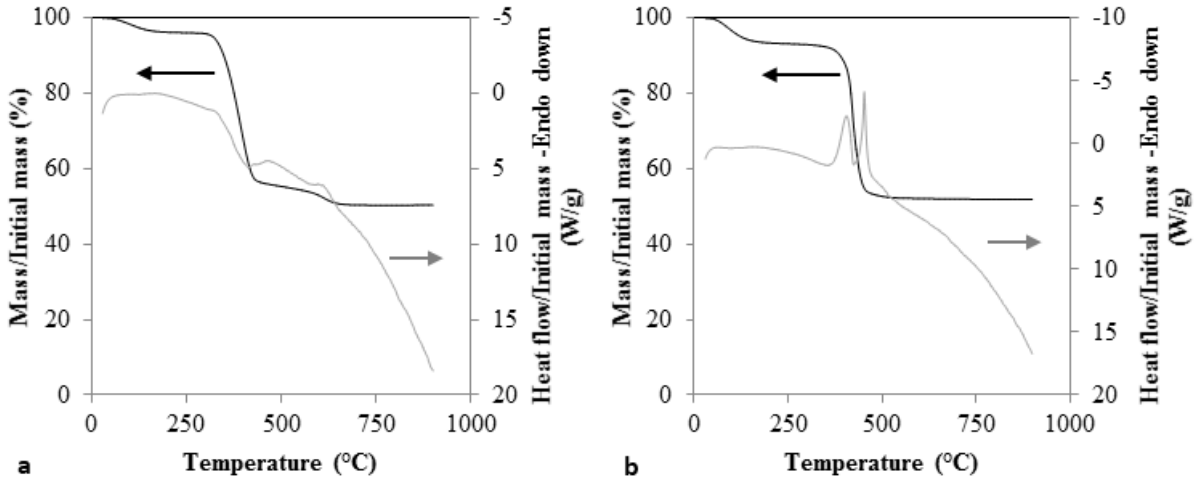

Figure 64. Differential scanning calorimetric (gray lines) and thermogravimetric analyses (black lines): a. SiO_2 with polystyrene template, b. SiO_2 with 1 wt.% Pt-decorated polystyrene template. (Please note that the complete latex removal in the silica composite material corresponds to *a.* 50 wt.% of total mass loss)

On the other hand, when the Pt nanoparticles are present in the material, the complete polymer removal occurs at 450 °C (Figure 64.b); there is no further weight loss, nor any other exo- or endothermic effects above this temperature. This difference in temperature is due to Pt-assisted template removal, which is confirmed by the DSC profiles: when Pt is absent, the template degradation is mainly endothermic (Figure 64.a), in which case the template removal mainly occurs by the polymer breaking down into volatile species [45,47]. The exothermic peak observed at 610 °C might correspond to the spontaneous ignition of the remaining polymer still trapped within the silica [48]. When Pt is present, the template removal is only an exothermic process (Figure 64.b) because the Pt acts as an oxidation catalyst [49].

In conclusion, 650 °C is the required temperature for polystyrene template removal from the silica matrix by calcination. However, in the presence of Pt, which acts as an oxidation catalyst, the calcination temperature can be decreased down to 450 °C.

III.3.3.2- Pt nanoparticles characterisation

The materials were calcined either at 450 °C (referred to as 0.7cal450) or 650 °C (referred to as 0.7cal650). Figure 65 shows that, after template removal by calcination, the Pt nanoparticles are correctly transferred to the silica matrix, being positioned at the macropore surfaces. However, the Pt has sintered after calcination at 650 °C, as shown in Figure 65.b: D_n = 6.5 nm, D_w = 8.9 nm, Đ = 1.36, to be compared with D_n = 2.3 nm for the initial Pt nanoparticles decorating the latex template. This is caused by coalescence and Ostwald ripening of the Pt particles [50,51]. In contrast, when the material was calcined at a lower temperature (450 °C), it reduced sintering of the Pt nanoparticles as shown in Figure 65.a: D_n = 4.6 nm, D_w = 5.9 nm, Đ = 1.28.

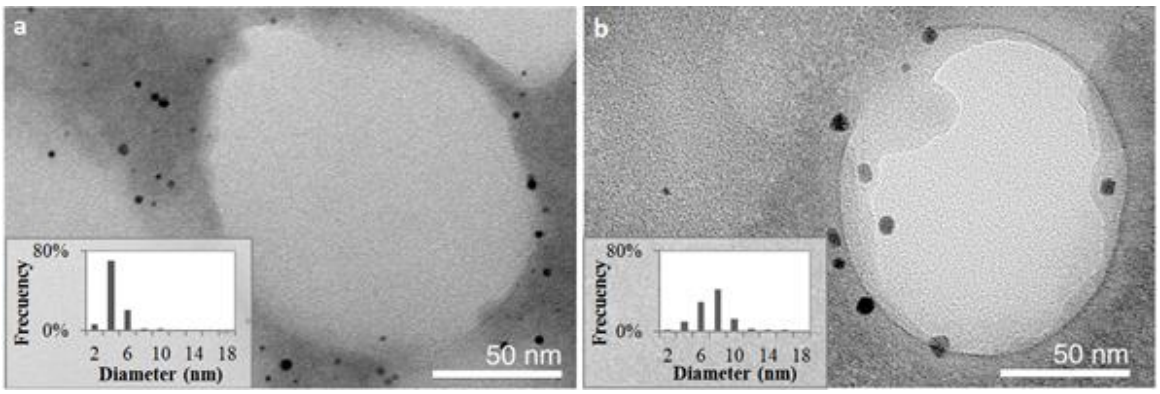

Figure 65. TEM images of 0.7 wt.% Pt on silica after calcination: a. At 450 °C –0.7cal450, b. At 650 °C – 0.7cal650. Corresponding particle size distribution histograms in the insets.

In order to study the Pt nanoparticles in more detail, high resolution transmission electron microscopy (HRTEM) images were collected for catalysts 0.7cal450 and 0.7cal650. Figure 66 shows selected Pt nanoparticles present in those materials. Lattice spacings of 2.3 ± 0.1 Å were

found, corresponding to Pt(111). Additionally, energy-dispersive X-ray spectroscopy (EDX) maps were recorded for several Pt nanoparticles (Figure 67). Only trace amounts of carbon were found in the 27 maps of both samples: 0.7cal650 and 0.7cal450, so it was not possible to quantify it. In most cases (20 out of 27), no correlation between C and Pt was seen, *i.e.* C presence was equal on the NP and the supporting SiO_2 (Figure 67.a). Sometimes the C content on the Pt particles was higher than on the support, but this can hardly be judged as significant in view of the ever present C contamination. This permits to conclude that no significant carbon residues remained at the Pt nanoparticle surface after calcination both at 450 °C and at 650 °C.

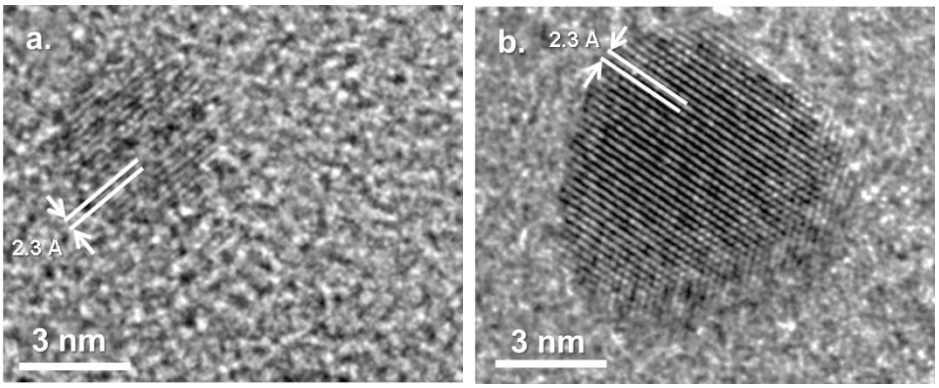

Figure 66. Pt nanoparticle HRTEM images: a. 0.7cal450 and b. 0.7cal650.

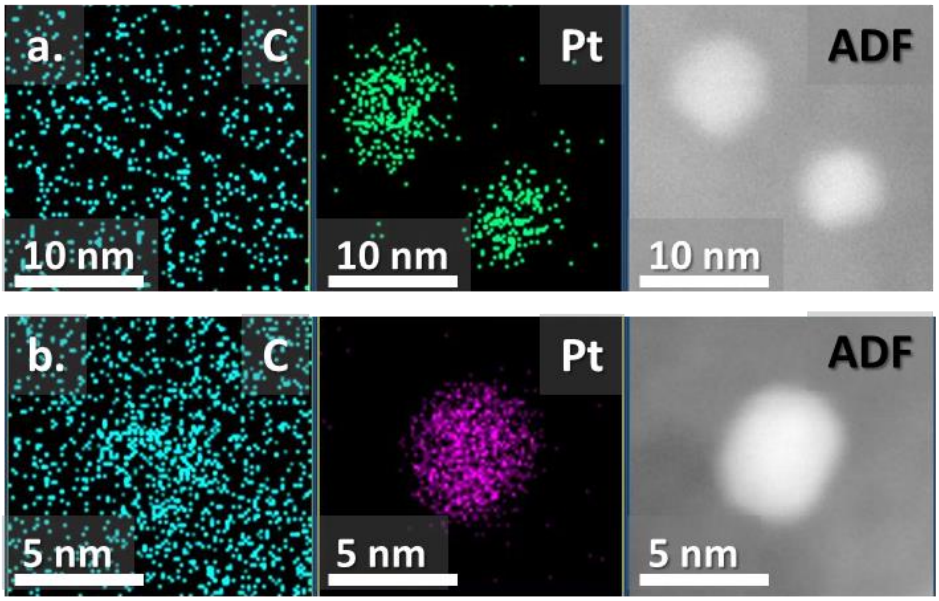

Figure 67. Carbon and platinum EDX mapping and annular dark field (ADF) STEM images of: a. 0.7cal450 and b. 0.7cal650.

Both calcination procedures at 450 °C and at 650 °C were efficient for the removal of the organic template. However, the calcination at 450 °C limited the nanoparticles sintering from 2.3 nm in the starting decorated latex to 4.6 nm after calcination at 450 °C (compared with 6.5 nm after calcination at 650 °C). In both cases, the Pt nanoparticles exhibited (111) planes.

III.3.3.3- Oxidation state and chemical environment of Pt

In order to characterise the oxidation state of the Pt nanoparticles, X-Ray photoelectron spectroscopy (XPS) was used on the Pt-containing hybrid latex prepared under Ar at 205 kHz, the subsequent composite material prepared by sol-gel synthesis and the final material after being calcined at 450 °C (0.7cal450). Figure 68 presents the corresponding XPS spectra. Unfortunately, given the low Pt content on these samples, the spectra were poorly resolved and reliable deconvolution for qualitative analysis was not possible. Nevertheless, a qualitative analysis was still conceivable. Figure 68.a shows that the Pt on the decorated hybrid latex was present in a mixture or oxidation states, mainly Pt(0) and Pt(II). However, after the sol-gel synthesis (Figure 68.b), the Pt signals shifted to higher binding energies (Pt oxide species region), which can be due to the strong metal-support interaction that takes place between Pt and silica when the catalyst is prepared by the sol-gel method [52,53]. After calcination, this interaction was less marked, so a larger component of Pt(0) was observed again (Figure 68.c). It is important to note that no difference in the Pt oxidation state is expected between 0.7cal450 and 0.7cal650 [54].

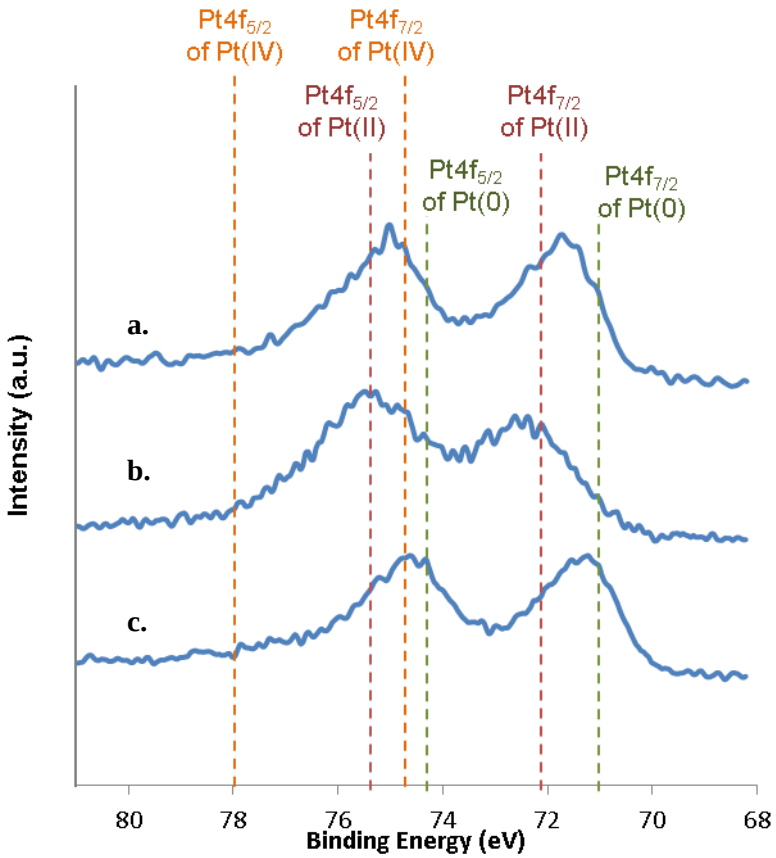

Figure 68. XPS spectra of Pt4f core level of: a. Polystyrene template decorated with Pt under ultrasound under Ar, b. Silica composite with Pt-containing-polymer template, c. Silica material in b. after calcination at 450 °C (0.7cal450).

Hydrogen temperature programmed reduction (H_2-TPR) was also used to characterise the Pt surface oxidation state of within the catalysts 0.7cal450 and 0.7cal650, as shown in Figure 69. For the sake of comparison, the silica support prepared with a non-decorated latex template and calcined at 650 °C (C40) was also studied. The silica support did not show any special pattern in the H_2-TPR profile, as expected [55]. Typically, peaks at ca. 100 °C correspond to the reduction of platinum species at the surface [56]. In this case, 0.7cal450 and 0.7cal650 did not show any pattern either, so no reducible Pt oxide species were observed at the Pt surface.

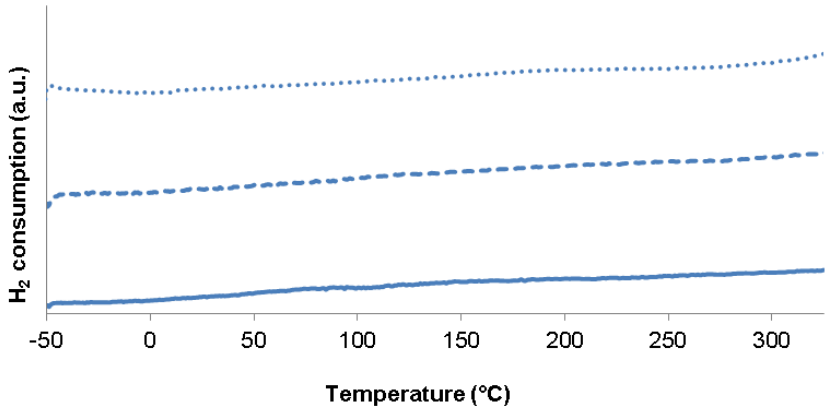

Figure 69. H_2-TPR profiles of: (• • • •) hierarchically porous 0.7cal450, (- - -) hierarchically porous 0.7cal650, (——) and hierarchically porous SiO_2 matrix calcined at 650 °C.

After calcination for template removal, the Pt nanoparticles exhibited a mixture of Pt(0) and Pt(II) oxidation states, according to the XPS characterisation. However, no reducible Pt oxide species were observed at the Pt surface (below 325 °C), according to the H_2-TPR analyses.

III.3.3.4- Pore texture characterisation

The nitrogen adsorption-desorption isotherms and Hg porosimetry profiles of 0.7cal450 and 0.7cal650 are presented in Figure 70 and Figure 71, respectively. The main characteristics of these catalysts are summarised in Table 7, including Pt loading and particle size, as well as pore texture details.

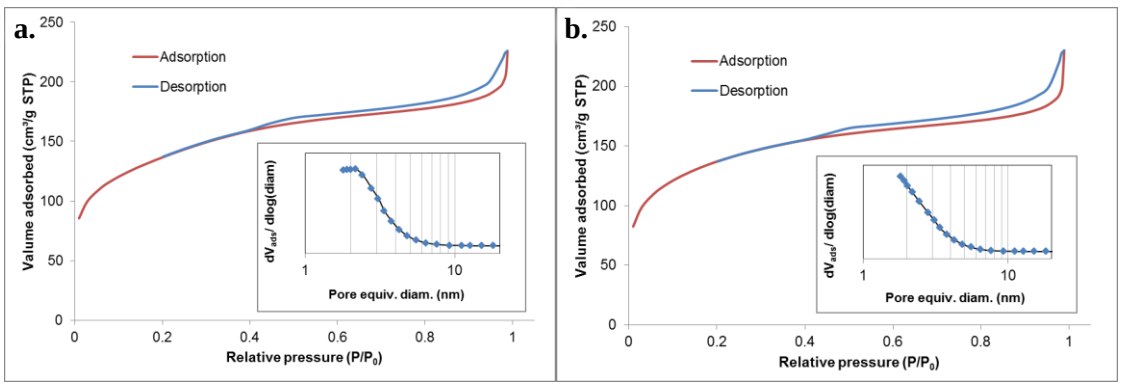

Figure 70. Nitrogen adsorption-desorption isotherms of catalyst: a. 0.7cal450 and b. 0.7cal650. Mesopore equivalent diameter distributions are presented in the insets.

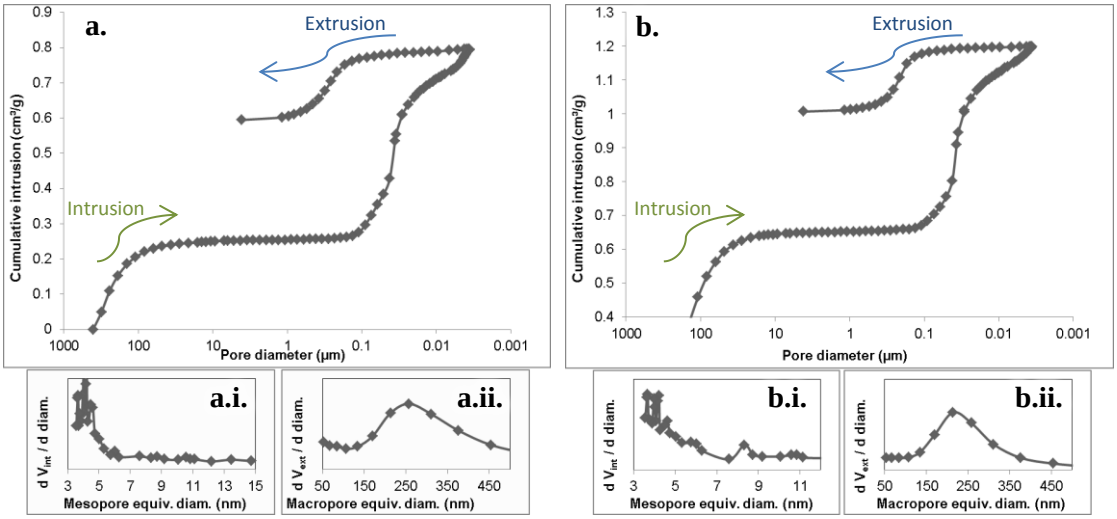

Figure 71. Mercury porosimetry of catalyst a. 0.7cal450 (a.i. and a.ii. are the corresponding meso- and macropores equivalent diameter distribution, respectively) and b. 0.7cal650 (b.i. and b.ii. are the corresponding meso- and macropores equivalent diameter distribution, respectively).

Table 7. Characterisation of catalysts 0.7cal450 and 0.7cal650.

Characteristics		0.7cal450	0.7cal650
Pt loading[a] (wt.%)		0.7	0.7
Pt NPs size[b]	D_n (nm)	4.6 ± 1.1	6.5 ± 2.2
	Đ[b]	1.28	1.36
Total BET surface area[c] (m^2/g)		490	490
Mesopore average size in adsorption branch[c] (nm)		4.2	4.7
Mesopore average size in desorption branch[c] (nm)		4.0	4.5
Mesopore size range[c] (nm)		2-7	2-7
Macropore size range[d] (nm)		110-400	110-400
Total pore volume (by N_2 physisorption)[c] (cm^3/g)		0.35	0.36
Total pore volume (by Hg porosimetry)[d] (cm^3/g)		0.54	0.55
Total pore volume (using both techniques)[e] (cm^3/g)		0.77	0.77
Total porosity (%)		63	63

[a] Determined by elemental analysis by ICP-OES
[b] Determined by HRTEM. Dispersity Đ=D_w/D_n, D_w being weight-average diameter and D_n being number-average diameter.
[c] Determined using nitrogen physisorption
[d] Determined using mercury porosimetry.
[e] The total pore volume was calculated as the maximum Hg intrusion from 1 µm down to 3.5 nm plus the volume of nitrogen adsorbed up to 3.5 nm equivalent diameter by BJH method in the adsorption branch.

Comparing the texture of the Pt-containing catalysts (0.7cal450 and 0.7cal650) with the non-decorated silica (C40, Table 6), it is possible to see some differences in the pore texture of these materials. Such differences are due to chemical modification of the latex template during the sonochemical decoration with Pt nanoparticles (this is further discussed in in Section III.3.5-*Pt-catalysts derived from latexes decorated in alternative sonochemical set-ups at 100 and 343 kHz*). Notably, the mesopore size distribution was slightly narrower (2-7 nm in 0.7cal450 and 0.7cal650 instead of 2-11 nm in C40). However, mesopores up to 11 nm could still be seen by intrusion of Hg (Figure 71.a.i and Figure 71.b.i). Additionally, the macropores exhibited a slightly larger size which corresponds to the aggregation of about 3 or 4 polymer beads. This results in a smaller specific surface area (490 m^2/g versus 615 m^2/g without Pt). Nevertheless, the total pore volumes and total porosities of 0.7cal450 and 0.7cal650 were very similar to the non-decorated silica. This leads to a total porosity of 63% for both Pt-decorated silica catalysts and 62% for the non-decorated silica. However, given the large difference in pore volumes obtained by N_2 physisorption and Hg porosimetry, it was not possible to obtained reliable meso- and macropore volumes. This might be due to incomplete nitrogen capillary condensation within large macropores and mercury intrusion constriction by small mesopores.

The materials prepared with ca. 1 wt. % Pt/polystyrene latex template decorated at 205 kHz exhibited the desired hierarchically porous structure with similar total porosities to the material prepared with non-decorated latex (63% and 62%, respectively), despite of having slightly smaller mesopores (2-7 nm versus 2-11 nm with non-decorated template) and slightly larger macropores (110-400 nm versus 110-170 nm with non-decorated template).

At this point, it is possible to say that this novel preparation method, which combines polystyrene latex template preparation by emulsion polymerisation, template decoration with Pt nanoparticles by sonochemistry and silica matrix preparation by two-step acid-base catalysed sol-gel synthesis, permits to obtain hierarchically porous silica-supported Pt catalysts with mesopores of 2-7 nm and macropores of 110-400 nm. The variation of the calcination temperature permitted to obtain Pt nanoparticles of different size: 4.6 nm at 450 °C and 6.5 nm at 650 °C, without noticeable silica structure modification. Additionally, the use of a latex template for generating macropores that has been beforehand decorated with Pt nanoparticles permits to control the spatial distribution of the Pt nanoparticles throughout the support, selectively in the macropores. This tool is valuable considering the limited availability of methods for controlling the spatial distribution of active sites within porous materials [57]. The possibility of tailoring the catalyst texture and controlling the noble metal particle size and spatial distribution allows the optimisation of important aspects in heterogeneous catalysis such as heat and mass transport phenomena inside the material. The two next sections will focus on the effect of changes of latex content and sonication conditions on the properties of the resulting catalysts.

III.3.4- Effect of latex template amount on the material morphology

Based on the methodology described above, a family of hierarchically porous materials was prepared with theoretical macroporosity (volume of macropores/total volume of material) ranging between 12.5% and 50%. For this, the first step was the preparation of a Pt-decorated template under ultrasounds at 205 kHz under Ar atmosphere (Figure 72). The average Pt particle diameter on the polymer beads was D_n = 2.5 nm, D_w = 5.1 nm, Đ = 1.98.

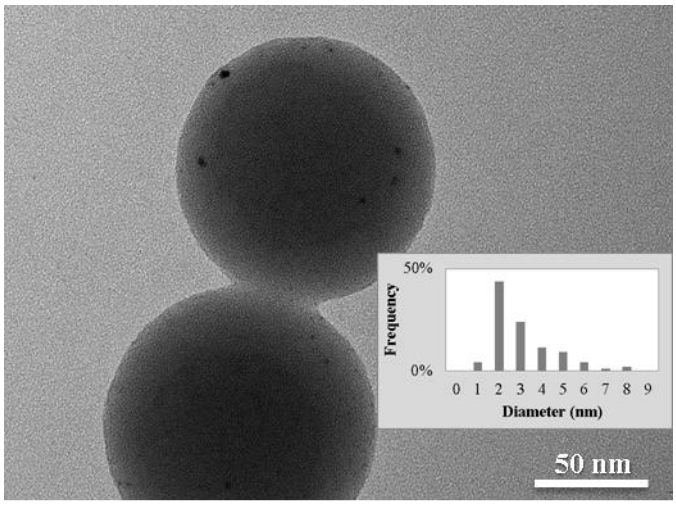

Figure 72. TEM image of Pt nanoparticles reduced at 20 °C, 205 kHz in presence of PS beads under Ar atmosphere. Particle size distribution histogram is shown in the insert.

The silica matrix studied in Section III.3.2-*Optimisation of the silica matrix*, was prepared with a volume of polymer beads to obtain a theoretical macro-porosity of 50%. Varying the amount of decorated polymer template, it was possible to prepare materials targeting macroporosity of 50, 33, 25 and 12.5%. After calcination at 450 °C, these materials were named 0.8cal450-50%, 0.4cal450-33%, 0.3cal450-25% and 0.2cal450-12.5%, respectively. Additionally, by mixing decorated and non-decorated latexes, another target was possible: a total 50% macroporosity, with half of it as non-decorated macropores. After calcination at 650 °C, this material was called 0.4cal650-25/25%. The reason for a higher calcination temperature in the latter was the absence of Pt in some macropores, so the catalysed polymer removal at lower temperature could not take place homogeneously throughout the material. Figure 73 shows the TEM and SEM images of these materials. It is important to note that the diagonal stripes observed on the TEM images are due to the shear forces during the microtome sample preparation and they are not features related to the materials, as confirmed on the SEM images, where such stripes are absent.

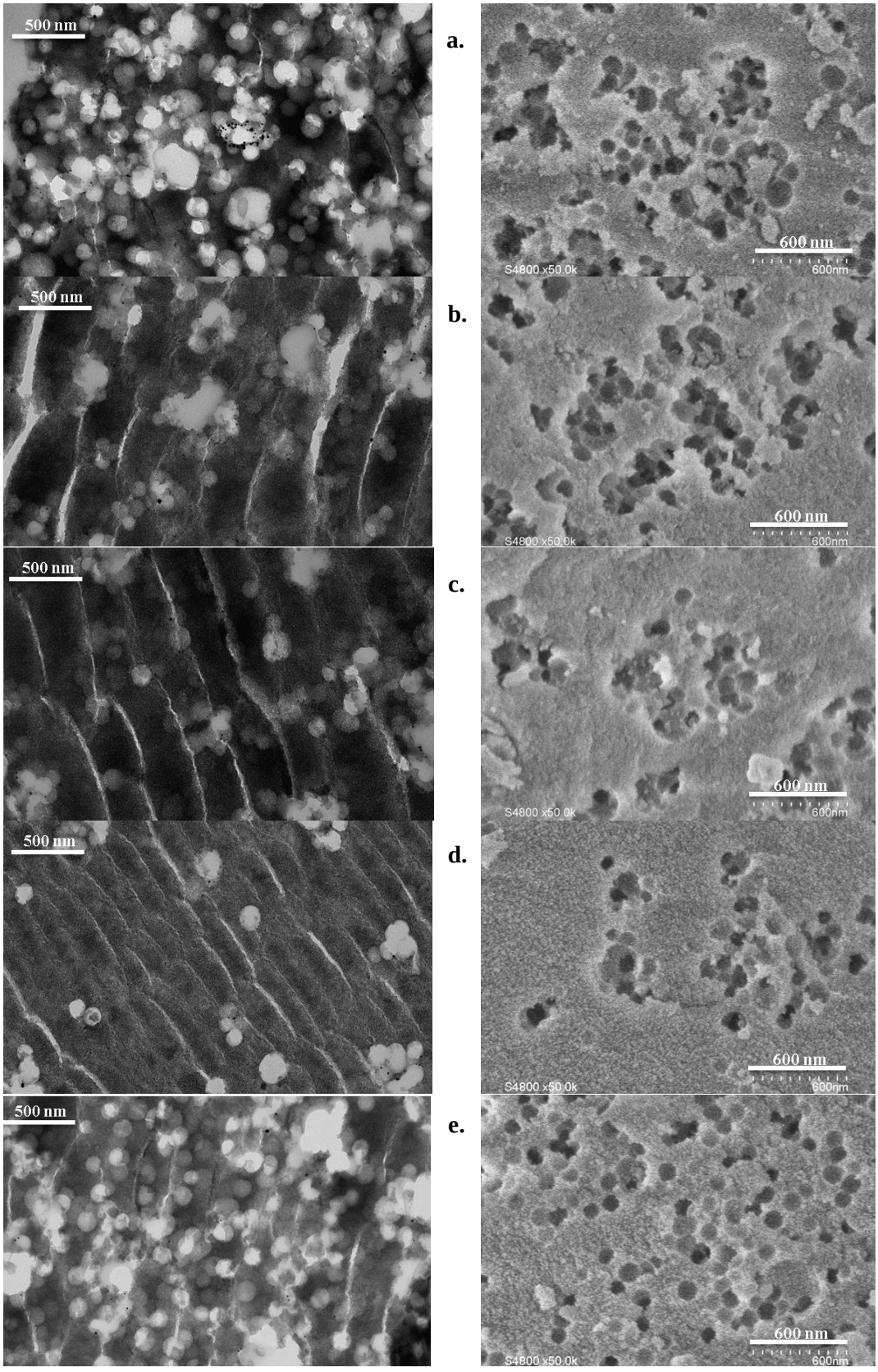

Figure 73. TEM (left) and SEM (right) images of: a. 0.8cal450-50%, b. 0.4cal450-33%, c. 0.3cal450-25%, d. 0.2cal450-12.5% and e. 0.4cal650-25/25%.

In Figure 73, it can be seen that in 0.8cal450-50%, 0.4cal450-33%, 0.3cal450-25% and 0.2cal450-12.5% a few polymer beads formed small aggregates within the silica matrix, leading to larger macropores than expected. In contrast, 0.4cal650-25/25% showed a better polymer distribution, but some aggregates could still be observed. This can be attributed to a slight decrease on the polymer colloidal stability due to the presence of Pt on the surface of the beads that screens somehow the electrostatic repulsion between polymer particles (zeta potential discussion in Section III.3.5-*Pt-catalysts derived from latexes decorated in alternative sonochemical set-ups at 100 and 343 kHz*).

Table 8 presents the catalysts textural characterisation of these materials as well as Pt loadings and nanoparticle sizes. Figure 74 shows the corresponding nitrogen physisorption isotherms and mercury porosimetry profiles.

Regarding the Pt loading, it followed the expected trend with respect to the amount of Pt-decorated template used in the preparation of each sample. 0.4cal650-25/25% exhibited the larger particle size given the higher calcination temperature. 0.8cal450-50% had a larger particle size than 0.7cal450 (8.6 ± 3.6 vs. 4.6 ± 1.1 nm), due to a slightly higher Pt content, but also probably due to a larger amount of directly connected macropores in 0.8cal450-50% (related to polymer beads aggregates). Furthermore, it was expected that decreasing the amount of decorated template, the Pt nanoparticles sintering would have been limited (by increasing the distance between macropores within the mesoporous matrix). However, due to the macropores direct connection as a result of small aggregates of polymer beads, the Pt sintering did not decrease significantly (8.6 ± 3.6 nm for 0.8cal450-50%, compared to 6.7 ± 3.1 nm for 0.2cal450-12.5%).

Regarding the nitrogen physisorption characterisation, it can be noticed that the BET specific surface area decreases with the amount of decorated template. This could be due to a slightly more acidic pH in the decorated template after the sonochemical reduction, that could be unnoticed, but that is important in terms of acid concentration. For instance, the concentration of $[H_3O^+]$ is 10% higher in a latex at pH 1.96 than at pH 2.00. This is important because the acid catalyses the TEOS reactions. Indeed, it has been shown that slight changes in pH could modify the TEOS condensation reaction rates [13], which leads to slightly different microstructures. This would also explain a slightly smaller average pore size in these materials (between 3.5 and 4.1 nm, based on the adsorption branch) than in non-decorated hierarchically porous silica, C40 (5.8 nm, based on the adsorption branch). Nevertheless, the mesoporous structure was still obtained with mesopore size ranges between 2 and 9 nm in most cases. Additionally, the nitrogen capillary condensation within the macropores was not complete, probably due to larger macropores generated by small polymer aggregates. This explains smaller total pore volumes by N_2 physisorption in these materials (between 0.56 and 0.65 cm^3/g) than in C40 (0.74 cm^3/g).

Table 8. Characterisation of catalysts 0.8cal450-50%, 0.4cal450-33.3%, 0.3cal450-25%, 0.2cal450-12.5% and 0.4cal650-25/25%.

Characteristics		0.8cal450-50%	0.4cal450-33.3%	0.3cal450-25%	0.2cal450-12.5%	0.4cal650-25/25%
Pt loading[a] (wt.%)		0.8	0.4	0.3	0.2	0.4
Pt NPs size[b]	D_n (nm)	8.6 ± 3.6	7.6 ± 3.4	8.2 ± 3.7	6.7 ± 3.1	10.2 ± 3.9
	Đ[b]	1.54	1.79	1.76	1.68	1.46
Total BET surface area[c] (m^2/g)		759	729	718	694	674
Mesopore average size in adsorption branch[c] (nm)		3.6	3.5	3.6	3.6	4.1
Mesopore average size in desorption branch[c] (nm)		3.5	3.4	3.4	3.3	3.9
Mesopore size range in adsorption branch[c] (nm)		2-7	2-9	2-9	2-9	2-9
Total pore volume (by N_2 physisorption)[c] (cm^3/g)		0.56	0.59	0.60	0.60	0.65
Total porosity (by N_2 physisorption)[c] (%)		55	57	57	57	59
Pore size at the beginning of Hg intrusion[d] (nm)		60	29	24	20	35
Macropore size range in extrusion branch[d] (nm)		110-400	N/A	N/A	N/A	90-310
Total pore volume (by Hg intrusion)[d] (cm^3/g)		0.47	0.40	0.26	0.16	0.63
Total porosity (by Hg intrusion)[d] (%)		51	47	37	26	58
Total pore volume (using both techniques)[e] (cm^3/g)		0.82	0.70	0.58	0.57	0.89
Total porosity (using both techniques)[e] (%)		64	61	56	56	66

[a] Determined by elemental analysis by ICP-OES
[b] Determined by TEM. Dispersity $Đ=D_w/D_n$, D_w being weight-average diameter and D_n being number-average diameter.
[c] Determined using nitrogen physisorption. Equivalent pore diameters calculated by BJH method.
[d] Determined using mercury porosimetry.
[e] The total pore volume was calculated as the maximum Hg intrusion from 1 µm down to 3.5 nm plus the volume of nitrogen adsorbed up to 3.5 nm equivalent diameter by BJH method in the adsorption branch.
N/A: non-available

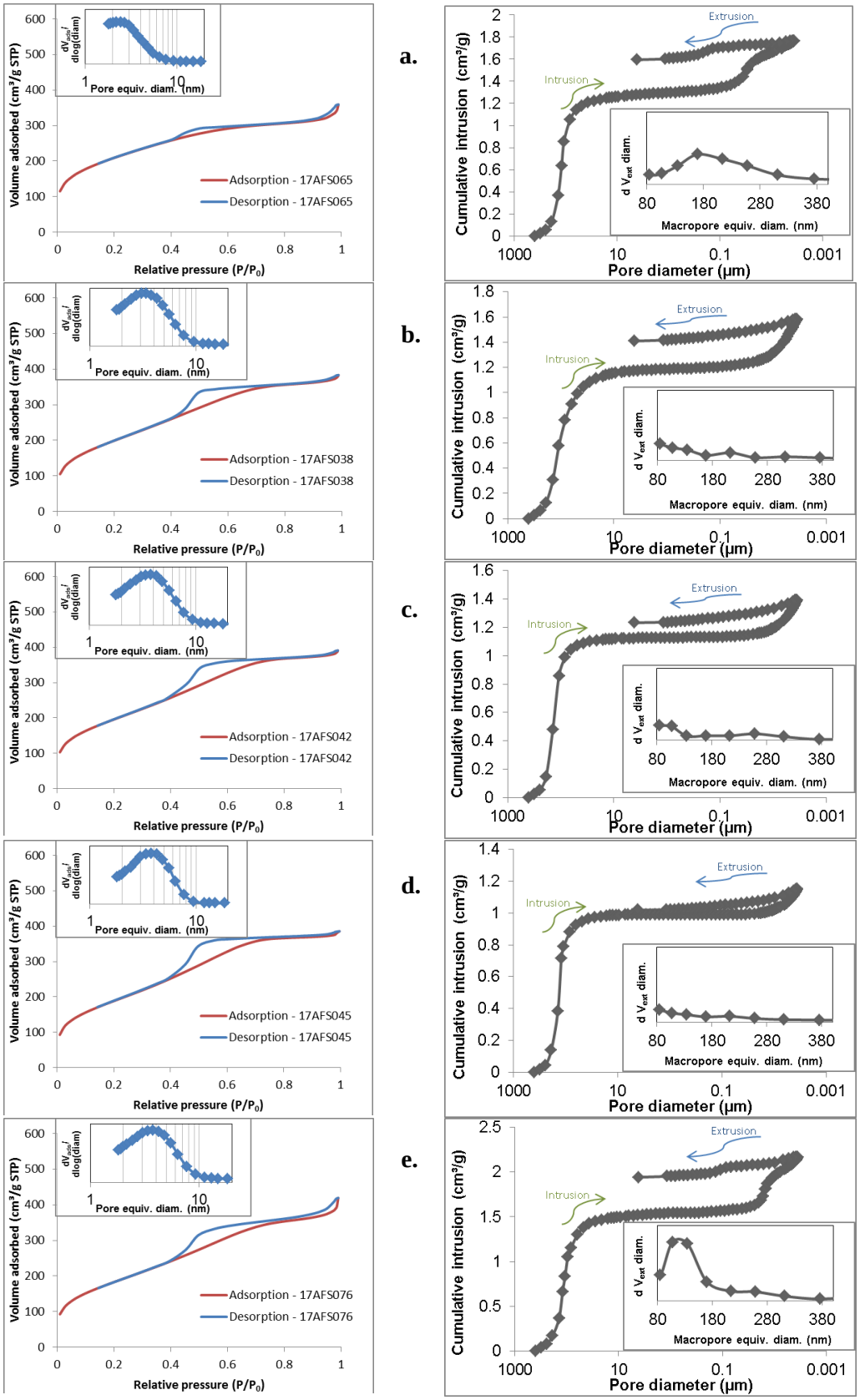

Figure 74. N_2 physisorption isotherms (left) and Hg porosimetry profiles (right) of: a. 0.8cal450-50%, b. 0.4cal450-33%, c. 0.3cal450-25%, d. 0.2cal450-12.5% and e. 0.4cal650-25/25%.

From the mercury porosimetry profiles, it can be understood that the macroporosity characterisation was not complete due to incomplete mercury intrusion, especially when the amount of macropores was below 33%. So no information about the macropores in these samples was obtained. Nevertheless, valuable information could be extracted from the intrusion profiles. For instance, the pore size at which mercury intrusion began decreased with the amount of macropores, which means that the macropores form channels by direct connection of several macropores (Figure 75). Such channels are shorter to be noticeable when the amount of polymer beads decrease. So that, for the materials 0.4cal450-33%, 0.3cal450-25% and 0.2cal450-12.5%, the mercury intrusion took place exclusively by the mesoporous network, limiting the accessibility to the macropores. As a result, some macropores could not be filled with mercury to be measured.

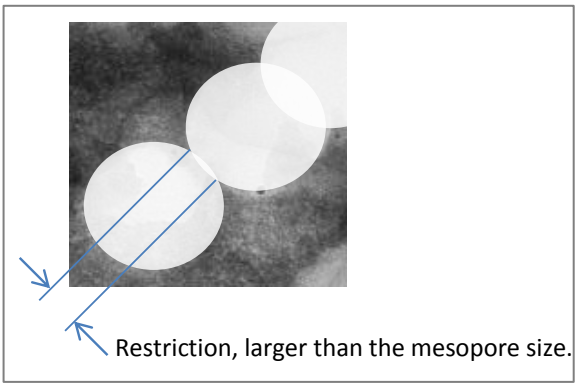

Figure 75. Highlighted feature of directly connected macropores on a 0.8cal450-50% TEM image. Macropores diameter of ca. 140 nm.

Directly connected macropores are not surprising. It has been demonstrated by computational calculations of the percolation threshold of disordered packed spheres that the critical volume of spheres at which long-range interconnections occur is 19.9% [58]. This explains why the macropore size distribution in the extrusion branch for 0.2cal450-12.5% was flat (Figure 74.d).

Table 8 reports a total pore volume based on a combination of nitrogen physisorption and mercury porosimetry. It adds the maximum mercury intrusion up to 3.5 nm and the volume of nitrogen adsorbed up to 3.5 nm equivalent diameter by BJH method in the adsorption branch. This calculation is closer to the real value, but it assumes total intrusion within the macropores, which is not the case as already discussed. So the total pore volume is still underestimated. These results put in evidence the need of other techniques for the reliable characterisation of hierarchically porous materials. Fortunately, new techniques on this area are under development such the characterisation of porous materials using Positron Annihilation Lifetime Spectroscopy (PALS) giving information on pores accessibility and connectivity [59].

It can be concluded that it is possible to vary the amount of polymer template in order to tailor the amount of macroporosity within the catalyst. Additionally, the amount of Pt within the catalyst can be modified by changing the amount of decorated template, which can also be successfully combined with non-decorated template for additional macroporosity. Surprisingly, the Pt sintering did not decrease significantly when decreasing the amount of decorated macropores in the material (8.6 ± 3.6 nm for 0.8cal450-50%, compared to 6.7 ± 3.1 nm for 0.2cal450-12.5%), which was due to the formation of small polymer aggregates that define the amount of Pt within the resulting macropore. Moreover, the variation of the amount of decorated template had a limited influence on the mesopore size distribution (going from 2-9 nm to 2-7 nm with 12.5% and 50% of decorated macropores, respectively) due to very slight pH differences during the sol-gel syntheses. However, the hierarchical meso- and macroporous structure was guaranteed in all materials. Unfortunately, the measurement of total pore volumes of these hierarchically porous materials was not reliable since the macropores are too large for nitrogen physisorption and the mesopores are too small for mercury porosimetry.

III.3.5- Pt-catalysts derived from latexes decorated in alternative sonochemical set-ups at 100 and 343 kHz

In agreement with the previous sections where polystyrene latexes were successfully decorated with Pt using sodium tetrachloroplatinate at 1 g Pt/L (equivalent to 0.1 g Pt) and 205 kHz, the same concentration of Pt precursor was tried to be reduced at 100 kHz. However, although the Pt reduction was successful in the set-up at 100 kHz, the latex colloidal stability was affected. The latex was more viscous after Pt reduction, which indicates a significant modification of the electrical double layer around the polymer beads [60]. Additionally, it segregated during the sol-gel synthesis, leading to very fragile and non-homogeneous materials. A dilution in ethanol during the sol-gel synthesis was also tried, which led to a macroscopically homogeneous material. Unfortunately, it was very fragile after calcination and it was not microscopically homogeneous since the ethanol enhanced the Pt nanoparticles mobility while the silica matrix was still under formation. Nevertheless, it was possible to prepare silica materials with the expected morphology when decreasing by half the amount of Pt on the latex (ca. 0.5 wt. % Pt/polystyrene using a latex at ca. 10 wt. % solids). Thus, this section presents the characteristics of silica materials derived from the latexes decorated in alternative sonochemical conditions at 100 and 343 kHz (at ca. 0.5 wt. % Pt/polystyrene and ca. 10 wt. % solids), and they are compared to a silica material prepared from a latex prepared at 205 kHz with the same Pt loading. The sonochemical decoration of such latexes was discussed in Section III.3.1.2.iii-*Template decoration using alternative sonochemical set-ups*.

Silica materials with theoretical 50% of macroporosity were prepared with the latexes decorated at 100, 205 and 343 kHz using the two-step acid-base catalysed sol-gel synthesis already described. They were named 0.3cal450-100kHz, 0.3cal450-205kHz and 0.3cal450-343kHz, accordingly. The three materials exhibited the expected morphology with spherical macropores distributed within the silica matrix, as shown in Figure 76.

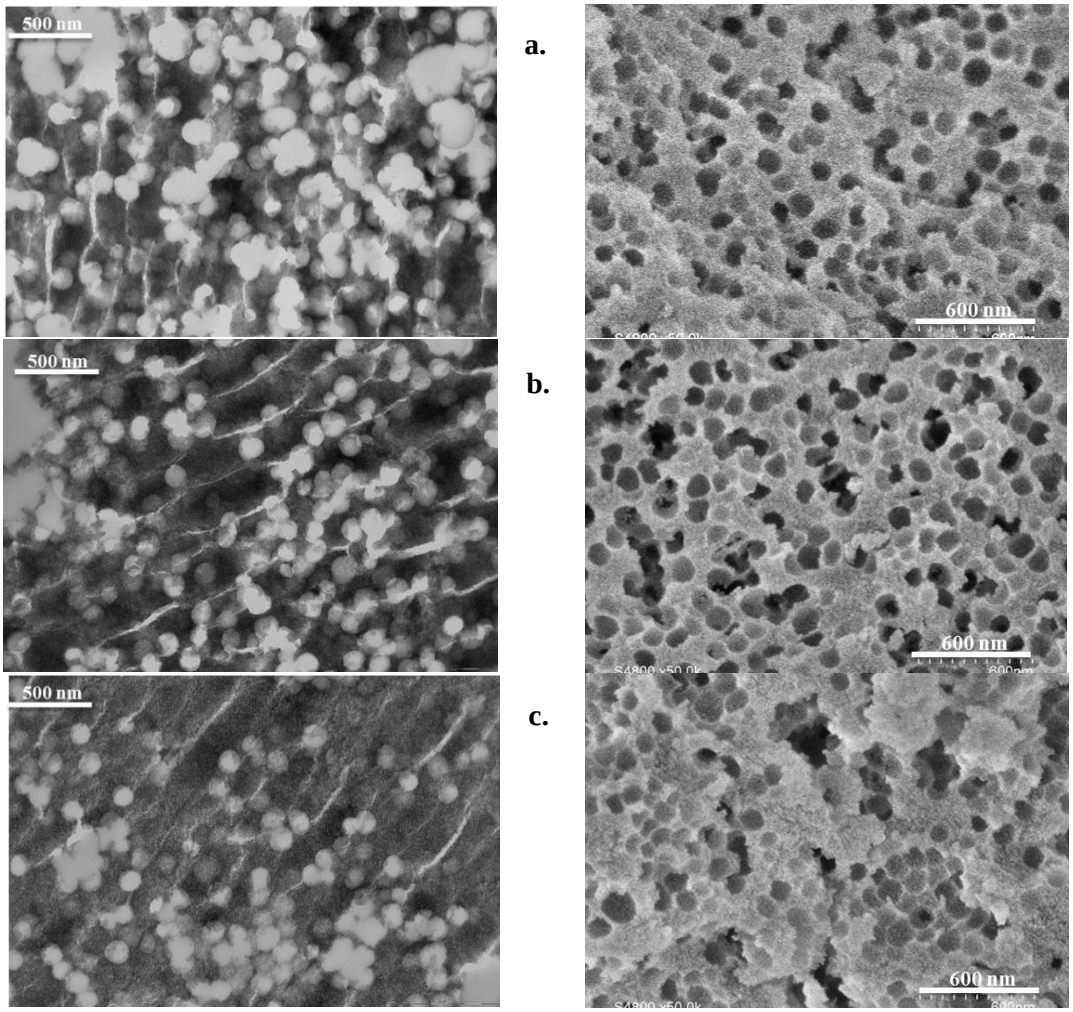

Figure 76. TEM (left) and SEM (right) images of: a. 0.3cal450-100kHz, b. 0.3cal450-205kHz and c. 0.3cal450-343kHz

Table 9 summarises the structural characterisation of these materials and Figure 77 presents the corresponding N_2 physisorption isotherms and Hg porosimetry profiles.

Regarding the Pt nanoparticles size on the final materials, it followed the same trend as on the polymer template, being slightly smaller when using the set-up at higher ultrasound frequency. This means that the particle size on the decorated template has an influence on the particle size in the final material after calcination. Additionally, it can be noticed that the Pt particle sizes were smaller in 0.3cal450-100kHz, 0.3cal450-205kHz and 0.3cal450-343kHz, which were prepared with a template at 0.5 wt.% Pt/polymer in comparison with 0.8cal450-50% (8.6 ± 3.6 nm) and 0.3cal450-25% (8.2 ± 3.7 nm) that were prepared with a hybrid template at ca. 1 wt.% Pt/polymer. This means that reducing the Pt loading on the template, the Pt particle size in the final material decreases.

Table 9. Characterisation of catalysts 0.3cal450-100kHz, 0.3cal450-205kHz and 0.3cal450-343kHz

Characteristics		0.3cal450-100kHz	0.3cal450-205kHz	0.3cal450-343kHz
Pt loading[a] (wt.%)		0.3	0.3	0.3
Pt NPs size[b]	D_n (nm)	4.7 ± 1.3	4.5 ± 1.1	3.9 ± 1.0
	Đ[b]	1.21	1.18	1.15
Total BET surface area[c] (m^2/g)		744	632	617
Mesopore average size in adsorption branch[c] (nm)		3.6	4.2	5.0
Mesopore average size in desorption branch[c] (nm)		3.5	4.1	4.6
Mesopore size range in adsorption branch[c] (nm)		2-9	2-13	2-15
Total pore volume (by N_2 physisorption)[c] (cm^3/g)		0.55	0.64	0.77
Total porosity (by N_2 physisorption)[c] (%)		55	59	63
Pore size at the beginning of Hg intrusion[d] (nm)		130	60	60
Macropore size range in extrusion branch[d] (nm)		130-310	130-310	110-260
Total pore volume (by Hg intrusion)[d] (cm^3/g)		0.61	0.73	0.92
Total porosity (by Hg intrusion)[d] (%)		57	62	67
Total pore volume (using both techniques)[e] (cm^3/g)		0.95	1.00	1.08
Total porosity (using both techniques)[e] (%)		68	69	70

[a] Determined by elemental analysis by ICP-OES
[b] Determined by TEM. Dispersity $Đ=D_w/D_n$, D_w being weight-average diameter and D_n being number-average diameter.
[c] Determined using nitrogen physisorption. Equivalent pore diameters calculated by BJH method.
[d] Determined using mercury porosimetry.
[e] The total pore volume was calculated as the maximum Hg intrusion from 1 µm down to 3.5 nm plus the volume of nitrogen adsorbed up to 3.5 nm equivalent diameter by BJH method in the adsorption branch.
N/A: non-available

Comparing the texture characteristics of 0.3cal450-100kHz, 0.3cal450-205kHz and 0.3cal450-343kHz against the material prepared with non-decorated latex: C40 (Table 6), it can be seen that 0.3cal450-343kHz is the one that resembles it the most with a specific surface area of 617 m^2/g versus 615 m^2/g for C40. The total porosities by nitrogen physisorption were measured to be 63% and 62 % for 0.3cal450-343kHz and C40, respectively. However, the mesopore average diameter in the adsorption branch was slightly smaller in the Pt-decorated material: 5.0 nm versus 5.8 nm for C40, although the mesopore size range was slightly larger: 2 to 15 nm, while 2 to 11 nm for C40.

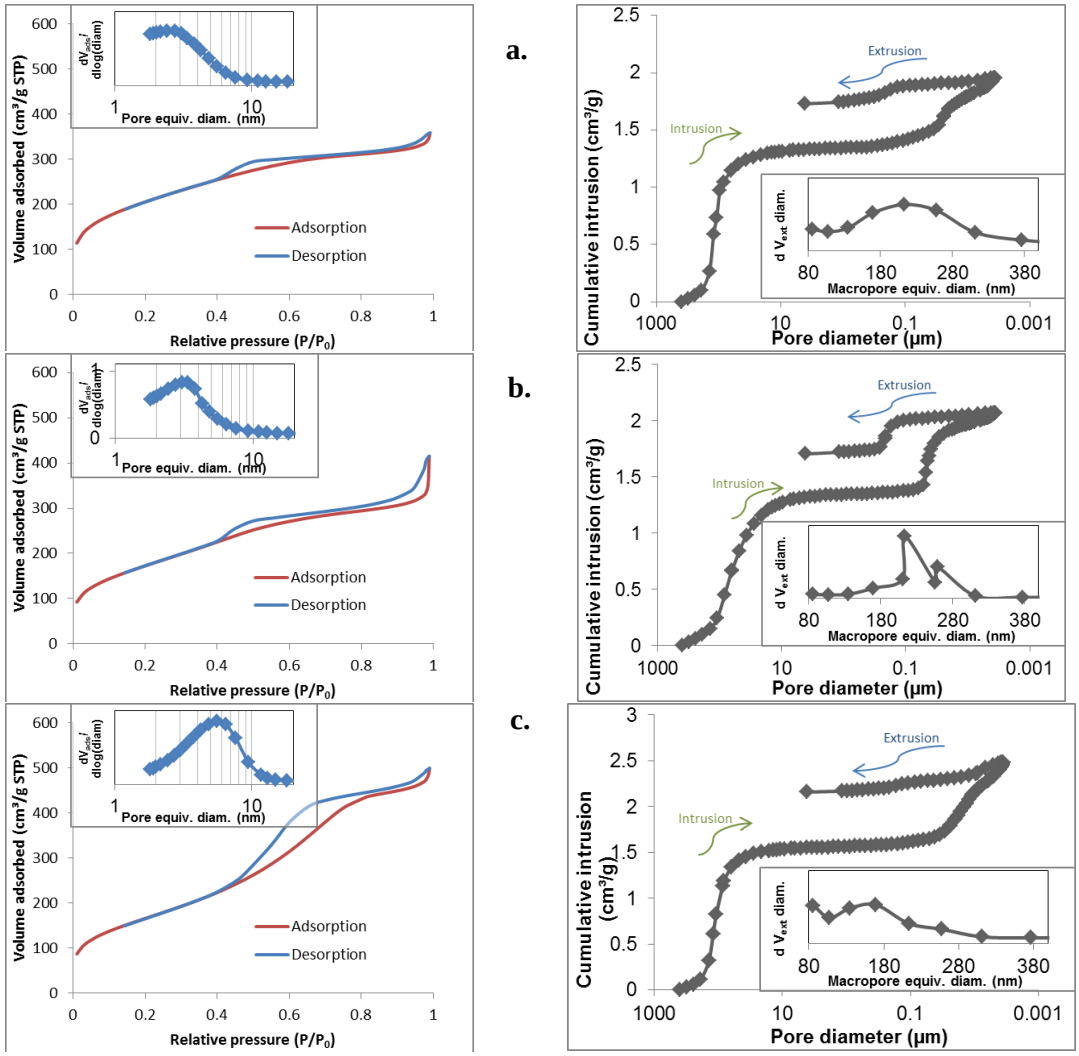

Figure 77. N_2 physisorption isotherms (left) and Hg porosimetry profiles (right) of: a. 0.3cal450-100kHz, b. 0.3cal450-205kHz and c. 0.3cal450-343kHz

Regarding the mercury porosimetry characterisation, the mercury intrusion volume was larger than the total nitrogen adsorption, meaning that the capillary condensation of nitrogen within the macropores was incomplete. Additionally, it can be noticed that the macropore size range is larger in 0.3cal450-343kHz (110-260 nm) than in C40 (110-170 nm), which means that still some aggregates of polymer beads are formed (as observed in Figure 76c). However, 0.3cal450-343kHz shows the smallest macropores sizes in comparison with all other Pt-decorated silica material prepared by this method (usually up to 400 nm). This means that the latex decorated at 343 kHz was the least disturbed colloidal system during the sonochemical decoration in terms of template colloidal stability, leading to the largest amount of individual macropores. Contrarily, 0.3cal450-100kHz exhibited the smallest mesopore size distribution and exhibited the lowest porosity. Additionally, the mercury intrusion in this sample started at a larger macropores size (130 nm) in comparison with the other two samples (60 nm), meaning that the phenomenon of polymer beads aggregation during the sol-gel synthesis was more important with the latex treated sonochemically at 100 kHz. These observations are in agreement with a higher

sonochemical activity in the set-up at 100 kHz than at 205 or 343 kHz: 0.38 ± 0.04, 0.32 ± 0.03 and 0.16 ± 0.02 µmol H_2O_2/min, respectively, which seems to indicate that a high sonochemical activity could reduce the latex colloidal stability by partially degrading the polymer beads surface.

It is important to recall that the polystyrene latex template used in these experiments is stabilised by electrostatic repulsion between the polymer beads. Such repulsion is originated by the negatively charged surface groups at the polymer beads surface: sulfonates and sulphates. When the latex was decorated with Pt at ca. 0.5 wt. % Pt/polystyrene at 343 kHz, the polymer beads zeta-potential went from -54.4 ± 0.9 eV in the starting latex to -48.4 ± 0.9 eV after sonochemical decoration, evidencing that even in this latex that exhibited the best colloidal stability during the sol-gel synthesis, the Pt decoration decreased its colloidal stability by reducing the strength of the polymer beads repulsion, since the Pt nanoparticles interact with the sulfonate groups at the polymer beads [38].

Consequently, the sonochemical conditions for the template decoration with Pt nanoparticles have an effect on the resulting hierarchically porous silica material prepared by the two-step acid-base catalysed sol-gel synthesis. The best sonochemical reduction conditions seem to be at low metal content in order to limit the latex destabilisation by screening of stabilising functional groups at the surface. Additionally, a low sonochemical activity could limit the degradation of the polymer beads surface, leading to a better polymer colloidal stability. Indeed, it was found that the silica material prepared in the set-up with the lowest sonochemical activity (0.16 µmol H_2O_2/min at 343 kHz versus 0.38 and 0.32 µmol H_2O_2/min at 100 and 205 kHz, respectively), exhibited the closest structural characteristics to an equivalent silica prepared with non-decorated latex: specific surface area and the total porosity of 617 m^2/g and 63% versus 615 m^2/g and 62 % without Pt. Interestingly, the variation of the sonochemical conditions permitted to obtain materials with different mesopore size distribution: 2-9, 2-11 and 2-15 nm in the set-up at 100, 205 and 343 kHz, respectively.

III.3.6- Characterisation of other Pt/SiO_2 catalysts

For comparison reasons, a material was prepared as C40 (with non-decorated latex). Subsequently, it was impregnated with a solution of sodium tetrachloroplatinate (the same precursor used to prepare the decorated templates by sonochemical reduction) and it was reduced at 300 °C (referred to as 1cal650-50%-IWI). Additionally, a commercial Pt/SiO_2 catalyst was characterised (referred to as 0.7REF). Figure 78 presents their corresponding electron microscopy images. In Figure 78a, it can be seen that 1cal650-50%-IWI has the desired hierarchical porosity. Additionally, a large Pt nanoparticle can be observed in the same image, which is due to the lack of control on the Pt dispersion throughout the material by standard incipient wetness impregnation.

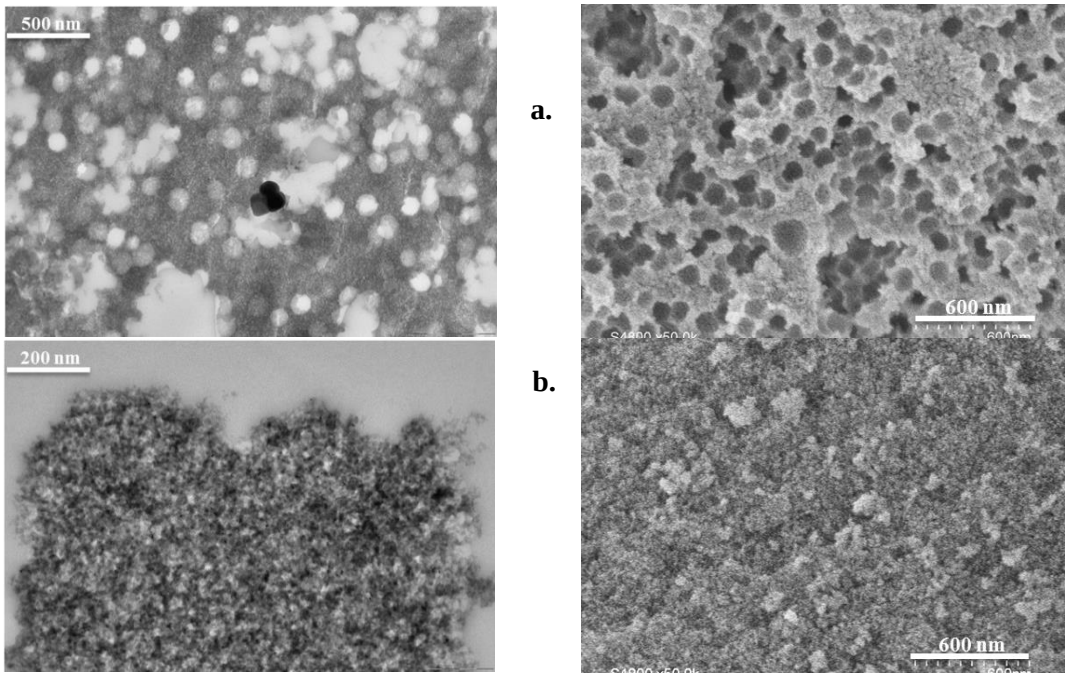

Figure 78. TEM (left) and SEM (right) images of: a. 1cal650-50%-IWI and b. 0.7REF

Table 10 summarises the textural characteristics of these catalysts and Figure 79 presents the corresponding nitrogen physisorption isotherms and mercury porosimetry profiles. The most remarkable observation is the large Pt particle size and board size distribution in 1cal650-50%-IWI (29.7 nm, [3-200] nm). On the other hand, the commercial catalyst exhibited small Pt nanoparticles (2.9 ± 1.2 nm) in the sample as received, which are slightly smaller than those obtained in 0.3cal450-343kHz (3.9 ± 1.0 nm). Larger particles are usually obtained within the hierarchically porous materials described herein due to the calcination step required for template removal.

0.7REF exhibited only a mesoporous structure with pores within the range: 11 to 28 nm. It was possible to completely characterise this material by nitrogen physisorption, since complete capillary condensation was possible within this pore range (as observed in the adsorption isotherm in Figure 79b), so that, the total porosity of this material was measured to be 71 %.

Table 10. Characterisation of catalysts a. 1cal650-50%-IWI and 0.7REF

Characteristics		1cal650-50%-IWI	0.7REF
Pt loading[a] (wt.%)		1	0.7
Pt NPs size[b]	D_n (nm)	29.7 [3-200 nm]	2.9 ± 1.2
	Đ[b]	6.16	1.62
Total BET surface area[c] (m^2/g)		575	260
Mesopore average size in adsorption branch[c] (nm)		5.2	18.0
Mesopore average size in desorption branch[c] (nm)		5.9	13.0
Mesopore size range in adsorption branch[c] (nm)		2-15	11-28
Total pore volume (by N_2 physisorption)[c] (cm^3/g)		0.77	1.09
Total porosity (by N_2 physisorption)[c] (%)		63	71
Pore size at the beginning of Hg intrusion[d] (nm)		60	29
Macropore size range in extrusion branch[d] (nm)		110-170	-
Total pore volume (by Hg intrusion)[d] (cm^3/g)		1.11	0.95
Total porosity (by Hg intrusion)[d] (%)		71	68
Total pore volume (using both techniques)[e] (cm^3/g)		1.25	0.96
Total porosity (using both techniques)[e] (%)		73	68

[a] Determined by elemental analysis by ICP-OES
[b] Determined by TEM. Dispersity $Đ=D_w/D_n$, D_w being weight-average diameter and D_n being number-average diameter.
[c] Determined using nitrogen physisorption. Equivalent pore diameters calculated by BJH method.
[d] Determined using mercury porosimetry.
[e] The total pore volume was calculated as the maximum Hg intrusion from 1 µm down to 3.5 nm plus the volume of nitrogen adsorbed up to 3.5 nm equivalent diameter by BJH method in the adsorption branch.
N/A: non-available

The characteristics of 1cal650-50%-IWI were very similar to that of C40 (Table 6), with slightly lower specific surface area (575 m^2/g versus 615 m^2/g for C40), but the same total pore volume by nitrogen physisorption (0.77 cm^3/g). However, the mercury porosimetry profile in Figure 79.a did not show any macropores during the extrusion branch. This might be due to the collapse of the structure at the very high pressure during the intrusion (up to 60 000 psia, corresponding to a pore diameter of 3.5 nm). So decreasing the maximum intrusion pressure up to 20 000 psia (which corresponds to an equivalent pore diameter of 10 nm), it was possible to observe a macropore size range of 110-170 nm. The corresponding mercury porosimetry profile is presented in Figure 80.

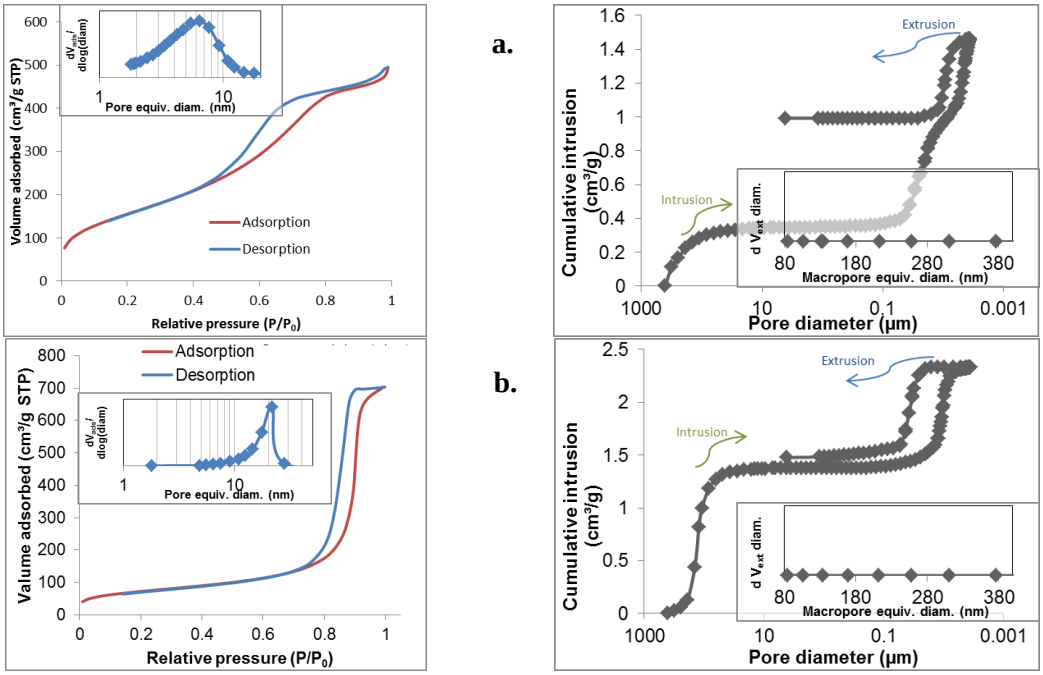

Figure 79. N_2 physisorption isotherms (left) and Hg porosimetry profiles (right) of: a. 1cal650-50%-IWI and b. 0.7REF

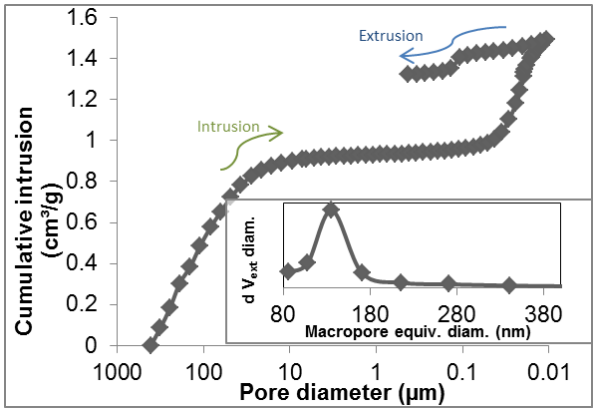

Figure 80. Hg porosimetry profile of 1cal650-50%-IWI at a maximum pressure of 20.000 psia (equivalent pore diameter: 10 nm)

Despite of being prepared under the same conditions with the same amount of latex template to obtain 50% macroporosity, 1cal650-50%-IWI and C40 exhibited different maximum mercury intrusion volumes: 1.11 cm^3/g, and 0.71 cm^3/g, respectively. The larger mercury intrusion volume in 1cal650-50%-IWI might be related to the silica structure collapse (of 1cal650-50%-IWI) at the high pressure used for the mercury porosimetry (up to 60 000 psia), indicating that the volume of mercury displaced by squeezing the silica structure was larger than the volume of mercury displaced by pores filling (i.e. not all macropores of C40 are filled with mercury at the highest mercury intrusion pressure). This confirms that the mercury porosimetry is not reliable

to completely characterise the pore volume of the hierarchically porous materials prepared in this work, since the macropores filling is incomplete due to the small mesopores of the matrix that surrounds the macropores.

Furthermore, considering a total pore volume for 1cal650-50%-IWI calculated as the maximum mercury intrusion up to 3.5 nm plus the volume of nitrogen adsorbed up to 3.5 nm (equivalent diameter by BJH method in the adsorption branch), it was possible to obtain a total porosity of 73%, which is very close to the initial target set for the synthesis of this hierarchically porous material: 75% of total porosity given by 50% macroporosity within a matrix with 50% of mesoporosity.

It is possible to prepare hierarchically porous silica supports (with mesopores of 2-15 nm and macropores of 110-170 nm) and impregnate them with a metal precursor by incipient wetness impregnation. However, in such a case, there is a lack of control of the metal particle size. Indeed, the silica support impregnated with 1 wt. % Pt/SiO_2 exhibited very large Pt nanoparticles with a board size distribution (29.7 nm, [3-200] nm). Furthermore, it was confirmed the requirement of reliable techniques for characterising of the total pore volume in this kind of hierarchically porous materials. Nevertheless, a total porosity of 73% could be measured in this material, which is very close to the total porosity of 75% initially targeted.

Moreover, a commercial catalyst was also characterised, which only exhibited mesopores of 11-28 nm and Pt nanoparticles of 2.9 ± 1.2 nm. Such nanoparticles are just slightly smaller than those that can be obtained in hierarchically porous catalysts with a sonochemically decorated template (3.9 ± 1.0 nm, for 0.3cal450-343kHz).

III.4- Conclusions

It was possible to synthesise a polystyrene latex with a particle size around 130 nm by emulsion polymerisation. Subsequently, the latex was successfully decorated with ca. 2 nm Pt nanoparticles. This decorated latex was used as template for the preparation of a silica-supported platinum catalyst with hierarchical porosity (meso- and macropores). The hierarchical porosity was tuned by varying the sol-gel synthesis conditions. Preferential location of the Pt nanoparticles in the macropores was also achieved. After template removal, the Pt oxidation state was mainly Pt(0) and no significant amounts of carbon residues were observed on the Pt nanoparticles.

The atmosphere: Ar or 10 vol. % CO/Ar, did not have any significant influence on the Pt particle size after sonochemical reduction. However, four parameters were found to have an effect on the Pt particle size: calcination temperature, template loading, particle size on the decorated template and macropores aggregation. The best arrangement to limit Pt nanoparticles sintering is using the lowest calcination temperature as possible, reducing the amount of Pt in the macropore by reducing the Pt loading on the template (e.g. 0.3cal450-343kHz with Pt nanoparticles of 3.9 ± 1.0 nm). In this sense, it is also important to use stable latexes that decrease the amount of small aggregates of polymer beads. This was the issue found with the series of materials at different porosities: a decrease on the amount of decorated macroporosity from 50% to 12.5% did not significantly decrease the Pt particle size (8.6 ± 3.6 for 0.8cal450-50% versus 6.7 ± 3.1 nm for 0.2cal450-12.5%), due to the formation of small aggregates. The Pt nanoparticles sintering by mobility from one macropore to another through the mesoporosity is less likely. For instance, the catalyst 0.3cal450-343kHz exhibited the smallest Pt nanoparticles (3.9 ± 1.0 nm), despite of having a large average mesopore diameter (5.0 nm, with mesopore range 2-15 nm). Finally, a small starting particle size on the template could also lead to smaller particles on the final material after calcination.

Regarding the silica matrix microstructure, the materials typically exhibited surface areas ranging between 500 and 750 m^2/g, depending on the decorated latex. Indeed, it was found that the sonochemical decoration of the latex had an influence on the catalyst macropore size due to polymer beads aggregation by two effects: screening of stabilising functional groups at the surface by the Pt nanoparticles and polymer beads surface degradation at high sonochemical activity (e.g. 0.38 µmol H_2O_2/min). The sample that resembled the most the silica matrix with non-decorated latex (C40) was 0.3cal450-343kHz, since the sonochemical activity at 343 kHz was low enough to limit the latex degradation (0.16 µmol H_2O_2/min) and the low metal content limited the latex destabilisation by screening of stabilising functional groups at the polymer surface. Nevertheless, all samples exhibited the meso- and macroporous hierarchical structure, with mesopores ranging at least between 2-7 nm and up to 2-15 nm.

It was not possible to reliably establish the meso- and the macroporous volumes since the mercury intrusion and the nitrogen adsorption gave different values. However, given that 1cal650-50%-IWI had very similar characteristics to C40 by nitrogen physisorption, it can be thought that even when those values are similar, it is possible that the mercury intrusion is incomplete and the nitrogen condensation does not fill all macropores. So this calls in question the reliability of the meso- and the macroporous volumes established for C40 and C60 in Table 6. So there is a need of a reliable technique to characterise the porosity of this kind of

hierarchically porous materials. Nonetheless, by the collapse of 1cal650-50%-IWI during mercury intrusion, it was possible to obtain a total porosity of 73%, which is very close to the initial target set for the synthesis of this hierarchically porous material: 75% of total porosity given by 50% macroporosity within a matrix with 50% of mesoporosity.

As a conclusion, the novel preparation method described in this chapter combines polystyrene latex template preparation by emulsion polymerisation, template decoration with Pt nanoparticles by sonochemistry and silica matrix preparation by two-step acid-base catalysed sol-gel synthesis (all steps performed in water). Such method allowed fulfilling the requirements of the initial specifications for the desired catalytic material (50% macroporosity with a mesoporous silica matrix and Pt nanoparticles preferentially within the macropores). This catalyst preparation method can be adapted to catalysts with other active phases (e.g. Pd, as it will be discussed in Chapter V), and at the same time it allows the optimisation of catalytic materials for reactions with larger molecules that might require texture tailoring, for instance in the low temperature Fischer-Tropsch waxes hydrocracking [61]. The next chapter will be focused on the catalytic evaluation of these materials in the selective hydrogenation of *p*-chloronitrobenzene to *p*-chloroaniline, including the comparison with a commercially available Pt/SiO_2 catalyst (0.7REF).

III.5- References

[1] Z. Wang, P. Hu, Towards rational catalyst design: a general optimization framework, Philos. Trans. R. Soc. A. 374 (2016) 20150078. doi:10.1098/rsta.2015.0078.

[2] G. Ertl, H. Knözinger, J. Weitkamp, Handbook of heterogeneous catalysis, Wiley-VCH Verlagsgesellschaft mbH, 1997.

[3] E.E. Santiso, M.K. Kostov, A.M. George, M.B. Nardelli, K.E. Gubbins, Confinement effects on chemical reactions-Toward an integrated rational catalyst design, Appl. Surf. Sci. 253 (2007) 5570–5579. doi:10.1016/j.apsusc.2006.12.121.

[4] M.E. Davis, R.J. Davis, Fundamentals of chemical reaction engineering, McGraw-Hill, New York, 2003. doi:10.1021/ed043pA758.1.

[5] C.M.A. Parlett, K. Wilson, A.F. Lee, Hierarchical porous materials: catalytic applications, Chem. Soc. Rev. 42 (2013) 3876–3893. doi:10.1039/c2cs35378d.

[6] G. Wang, M.O. Coppens, Rational design of hierarchically structured porous catalysts for autothermal reforming of methane, Chem. Eng. Sci. 65 (2010) 2344–2351. doi:10.1016/j.ces.2009.09.079.

[7] B. Louis, G. Laugel, P. Pale, M.M. Pereira, Rational design of microporous and mesoporous solids for catalysis: from the molecule to the reactor, ChemCatChem. 3 (2011) 1263–1272. doi:10.1002/cctc.201100110.

[8] B.-L. Su, C. Sanchez, X.-Y. Yang, eds., Hierarchically structured porous materials: from nanoscience to catalysis, separation, optics, energy, and life science, Wiley-VCH Verlag GmbH & Co. KGaA, 2012.

[9] M.-O. Coppens, J. Sun, T. Maschmeyer, Synthesis of hierarchical porous silicas with a controlled pore size distribution at various length scales, Catal. Today. 69 (2001) 331–335. doi:10.1016/S0920-5861(01)00386-8.

[10] N. Tanchoux, S. Pariente, P. Trens, F. Fajula, Confinement and curvature effects as a tool for selectivity orientation in heterogeneous catalysis: Isomerisation of n-hexene over MCM-41-type catalysts, J. Mol. Catal. A Chem. 305 (2009) 8–15. doi:10.1016/j.molcata.2008.11.017.

[11] D. Zhao, Y. Wan, W. Zhou, Ordered mesoporous materials, Wiley-VCH Verlag GmbH & Co. KGaA, Weinheim, Germany, 2013. doi:10.1002/9783527647866.

[12] D. Avnir, V.R. Kaufman, Alcohol is an unnecessary additive in the silicon alkoxide sol-gel process, J. Non. Cryst. Solids. 192 (1987) 180–182. doi:10.1016/S0022-3093(87)80368-X.

[13] C.J. Brinker, G.W. Scherer, Sol–Gel Science: The physics and chemistry of sol-gel processing, Elsevier, London, 1990.

[14] A. Ayral, A. Julbe, V. Rouessac, S. Roualdes, J. Durand, Microporous silica membrane: basic principles and recent advances, in: R. Mallada, M. Menendez (Eds.), Inorg. Membr. Synth. Charact. Appl., Elsevier, Amsterdam, 2008: pp. 33–74.

[15] C.J. Brinker, K.D. Keefer, D.W. Schaefer, C.S. Ashley, Sol-gel transition in simple silicates, J. Non. Cryst. Solids. 48 (1982) 47–64. doi:10.1016/0022-3093(86)90119-5.

[16] D. Niu, Z. Ma, Y. Li, J. Shi, Synthesis of core−shell structured dual-mesoporous silica spheres with tunable pore size and controllable shell thickness, J. Am. Chem. Soc. 132 (2010) 15144–15147. doi:10.1021/ja1070653.

[17] A.B.D. Nandiyanto, N. Hagura, F. Iskandar, K. Okuyama, Design of a highly ordered and uniform porous structure with multisized pores in film and particle forms using a template-driven self-assembly technique, Acta Mater. 58 (2010) 282–289. doi:10.1016/j.actamat.2009.09.004.

[18] A.B.D. Nandiyanto, T. Ogi, F. Iskandar, K. Okuyama, Highly ordered porous monolayer generation by dual-speed spin-coating with colloidal templates, Chem. Eng. J. 167 (2011) 409–415. doi:10.1016/j.cej.2010.11.077.

[19] R. Balgis, T. Ogi, A.F. Arif, G.M. Anilkumar, T. Mori, K. Okuyama, Morphology control of hierarchical porous carbon particles from phenolic resin and polystyrene latex template via aerosol process, Carbon N. Y. 84 (2015) 281–289. doi:10.1016/j.carbon.2014.12.010.

[20] A.B.D. Nandiyanto, S.-G. Kim, F. Iskandar, K. Okuyama, Synthesis of spherical mesoporous silica nanoparticles with nanometer-size controllable pores and outer diameters, Microporous Mesoporous Mater. 120 (2009) 447–453. doi:10.1016/j.micromeso.2008.12.019.

[21] M. Bathfield, J. Warnant, C. Gérardin, P. Lacroix-Desmazes, Asymmetric neutral, cationic and anionic PEO-based double-hydrophilic block copolymers (DHBCs): synthesis and reversible micellization triggered by temperature or pH, Polym. Chem. 6 (2015) 1339–1349. doi:10.1039/C4PY01502A.

[22] C. Verissimo, O.L. Alves, Microstructural modifications in macroporous oxides prepared via latex templating: synthesis and thermal stability of porous microstructure, J. Am. Ceram. Soc. 89 (2006) 2226–2231. doi:10.1111/j.1551-2916.2006.00996.x.

[23] F. Bosc, P. Lacroix-Desmazes, A. Ayral, TiO2 anatase-based membranes with hierarchical porosity and photocatalytic properties, J. Colloid Interface Sci. 304 (2006) 545–8. doi:10.1016/j.jcis.2006.09.064.

[24] X. Meng, L. Duan, H. Qin, X. Xie, A. Umar, H. Wang, Q. Wang, A novel synthesis and characterization of ordered meso/macroporous alumina with hierarchical and adjustable pore size, J. Nanosci. Nanotechnol. 14 (2014) 7340–7344(5). doi:http://dx.doi.org/10.1166/jnn.2014.9216.

[25] T. Muroi, Role of Precious Metal Catalysts, Noble Metals, InTech, 2012.

[26] R. Rendon, S.K. Rendon-Lara, A.L. Fernandez-Osorio, V.M. Ugalde-Saldivar, Aerobic synthesis of palladium nanoparticles, Rev. Adv. Mater. Sci. 27 (2011) 31–42.

[27] M. Haruta, M. Daté, Advances in the catalysis of Au nanoparticles, Appl. Catal. A Gen. 222 (2001) 427–437. doi:10.1016/S0926-860X(01)00847-X.

[28] J.K. Edwards, J. Pritchard, L. Lu, M. Piccinini, G. Shaw, A.F. Carley, D.J. Morgan, C.J. Kiely, G.J. Hutchings, The direct synthesis of hydrogen peroxide using platinum-promoted gold–palladium catalysts, Angew. Chemie (International Ed. (2014) 2381 – 2384. doi:10.1002/anie.201308067.

[29] G. Lee, Y. Jeong, B.G. Kim, J.S. Han, H. Jeong, H. Bin Na, J.C. Jung, Hydrogen production by catalytic decalin dehydrogenation over carbon-supported platinum catalyst: Effect of catalyst preparation method, Catal. Commun. 67 (2015) 40–44. doi:10.1016/j.catcom.2015.04.002.

[30] R.J. White, R. Luque, V.L. Budarin, J.H. Clark, D.J. Macquarrie, Supported metal nanoparticles on porous materials. Methods and applications., Chem. Soc. Rev. 38 (2009) 481–494. doi:10.1039/b802654h.

[31] C. Yacou, M.-L. Fontaine, A. Ayral, P. Lacroix-Desmazes, P.-A. Albouy, A. Julbe, One pot synthesis of hierarchical porous silica membrane material with dispersed Pt nanoparticles using a microwave-assisted sol–gel route, J. Mater. Chem. 18 (2008) 4274–4279. doi:10.1039/b807029f.

[32] T. Chave, A. Grunenwald, A. Ayral, P. Lacroix-Desmazes, S.I. Nikitenko, Sonochemical deposition of platinum nanoparticles on polymer beads and their transfer on the pore surface of a silica matrix, J. Colloid Interface Sci. 395 (2013) 81–84. doi:10.1016/j.jcis.2012.12.029.

[33] T. Chave, N.M. Navarro, S. Nitsche, S.I. Nikitenko, Mechanism of Pt(IV) sonochemical reduction in formic acid media and pure water, Chem. - A Eur. J. 18 (2012) 3879–85.

doi:10.1002/chem.201102355.

[34] R. Pflieger, T. Chave, G. Vite, L. Jouve, S.I. Nikitenko, Effect of operational conditions on sonoluminescence and kinetics of H2O2 formation during the sonolysis of water in the presence of Ar/O2 gas mixture, Ultrason. Sonochem. 26 (2015) 169–175. doi:10.1016/j.ultsonch.2015.02.005.

[35] A. Badalyan, P. Pendleton, Analysis of Uncertainties in Manometric Gas-Adsorption Measurements. I: Propagation of Uncertainties in BET Analyses, Langmuir. 19 (2003) 7919–7928. doi:10.1021/la020985t.

[36] A.A. Ndiaye, R. Pflieger, B. Siboulet, J. Molina, J.-F. Dufrêche, S.I. Nikitenko, Nonequilibrium vibrational excitation of OH radicals generated during multibubble cavitation in water., J. Phys. Chem. A. 116 (2012) 4860–7. doi:10.1021/jp301989b.

[37] J.H. Bang, K.S. Suslick, Applications of Ultrasound to the Synthesis of Nanostructured Materials, Adv. Mater. 22 (2010) 1039–1059. doi:10.1002/adma.200904093.

[38] D.W. Kim, J.M. Lee, C. Oh, D.S. Kim, S.G. Oh, A novel preparation route for platinum-polystyrene heterogeneous nanocomposite particles using alcohol-reduction method, J. Colloid Interface Sci. 297 (2006) 365–369. doi:10.1016/j.jcis.2005.09.067.

[39] J. Garnier, P.-E. Dufils, J. Vinas, Y. Vanderveken, A. van Herk, P. Lacroix-Desmazes, Synthesis of poly(vinylidene chloride)-based composite latexes by emulsion polymerization from epoxy functional seeds for improved thermal stability, Polym. Degrad. Stab. 97 (2012) 170–177. doi:10.1016/j.polymdegradstab.2011.10.019.

[40] C. Graillat, C. Pichot, A. Guyot, Preparation and characterization of low size polystyrene latex particles with various strong acid surface charges, Colloids and Surfaces. 56 (1991) 189–200. doi:10.1016/0166-6622(91)80120-D.

[41] F. Caupin, E. Herbert, Cavitation in water: a review, Comptes Rendus Phys. 7 (2006) 1000–1017. doi:10.1016/j.crhy.2006.10.015.

[42] J.Z. Sostaric, P. Riesz, Sonochemistry of surfactants in aqueous solutions: an EPR spin-trapping study., J. Am. Chem. Soc. 123 (2001) 11010–9. doi:10.1021/ja010857b.

[43] R.W. Cranston, F.A. Inkley, Advances in Catalysis and Related Subjects, Academic Press, New York, 1955.

[44] P.A. Albouy, A. Ayral, Coupling x-ray scattering and nitrogen adsorption: An interesting approach for the characterization of ordered mesoporous materials. Application to hexagonal silica, Chem. Mater. 14 (2002) 3391–3397. doi:10.1021/cm0211453.

[45] P. Pfaffli, A. Zitting, H. Vainio, Thermal degradation products of homopolymer polystyrene in air, Scand. J. Work. Environ. Heal. 4 (1978) 22–27. doi:10.5271/sjweh.2744.

[46] M.A. Ver Meer, B. Narasimhan, B.H. Shanks, S.K. Mallapragada, Effect of mesoporosity on thermal and mechanical properties of polystyrene/silica composites, ACS Appl. Mater. Interfaces. 2 (2010) 41–47. doi:10.1021/am900540x.

[47] O. Bera, B. Pilić, J. Pavličević, M. Jovičić, B. Holló, K.M. Szécsényi, M. Špirkova, Preparation and thermal properties of polystyrene/silica nanocomposites, Thermochim. Acta. 515 (2011) 1–5. doi:10.1016/j.tca.2010.12.006.

[48] J.L. Gurman, L. Baier, B.C. Levin, Polystyrenes: A review of the literature on the products of thermal decomposition and toxicity, Fire Mater. 11 (1987) 109–130. doi:10.1002/fam.810110302.

[49] J.G. Firth, S.J. Gentry, A. Jones, Oxidation reactions on platinum catalysts, J. Catal. 34 (1974) 159–161. doi:10.1016/0021-9517(74)90023-2.

[50] K. Kayhani, K. Mirabbaszadeh, P. Nayebi, A. Mohandesi, Surface effect on the coalescence of Pt clusters: A molecular dynamics study, Appl. Surf. Sci. 256 (2010) 6982–6985. doi:10.1016/j.apsusc.2010.05.010.

[51] S.B. Simonsen, I. Chorkendorff, S. Dahl, M. Skoglundh, J. Sehested, S. Helveg, Ostwald ripening in a Pt/SiO2 model catalyst studied by in situ TEM, J. Catal. 281 (2011) 147–155. doi:10.1016/j.jcat.2011.04.011.

[52] W. Tang, X. Wu, Y. Chen, Catalytic removal of gaseous benzene over Pt / SBA-15 catalyst : the effect of the preparation method, React. Kinet. Mech. Catal. 114 (2015) 711–723. doi:10.1007/s11144-014-0817-9.

[53] R.D. Gonzalez, T. Lopez, R. Gomez, Sol—Gel preparation of supported metal catalysts, Catal. Today. 35 (1997) 293–317. doi:10.1016/S0920-5861(96)00162-9.

[54] D. Sellick, D. Morgan, S. Taylor, Silica Supported Platinum Catalysts for Total Oxidation of the Polyaromatic Hydrocarbon Naphthalene: An Investigation of Metal Loading and Calcination Temperature, Catalysts. 5 (2015) 690–702. doi:10.3390/catal5020690.

[55] A.G.M. Da Silva, P.A. Robles-Dutenhefner, A. Dias, H. V. Fajardo, A.S.P. Lovón, J.J. Lovón-Quintana, G.P. Valença, Gold, palladium and gold-palladium supported on silica catalysts prepared by sol-gel method: Synthesis, characterization and catalytic behavior in the ethanol steam reforming, J. Sol-Gel Sci. Technol. 67 (2013) 273–281. doi:10.1007/s10971-013-3076-8.

[56] N. Boufaden, R. Akkari, B. Pawelec, J.L.G. Fierro, M.S. Zina, A. Ghorbel, Dehydrogenation of methylcyclohexane to toluene over partially reduced silica-supported Pt-Mo catalysts, J. Mol. Catal. A Chem. 420 (2016) 96–106. doi:10.1016/j.molcata.2016.04.011.

[57] C.M.A. Parlett, M.A. Isaacs, S.K. Beaumont, L.M. Bingham, N.S. Hondow, K. Wilson, A.F. Lee, Spatially orthogonal chemical functionalization of a hierarchical pore network for catalytic cascade reactions, Nat. Mater. 15 (2016) 178–182. doi:10.1038/nmat4478.

[58] R.M. Ziff, S. Torquato, Percolation of disordered jammed sphere packings, J. Phys. A Math. Theor. 50 (2017) 085001. doi:10.1088/1751-8121/aa5664.

[59] H.K.M. Tanaka, Y. Yamauchi, T. Kurihara, Y. Sakka, K. Kuroda, A.P. Mills, Exploration of a standing mesochannel system with antimatter/matter atomic probes, Adv. Mater. 20 (2008) 4728–4733. doi:10.1002/adma.200800395.

[60] D. Megías-Alguacil, F.J. Arroyo, F. Carrique, a. V. Delgado, The electroviscous effect in ethylcellulose latex suspensions. Effect of ionic strength and correlation between theory and experiments, Colloid Polym. Sci. 278 (2000) 647–653. doi:10.1007/s003960000299.

[61] C. Bouchy, G. Hastoy, E. Guillon, J.A. Martens, Fischer-Tropsch Waxes Upgrading via Hydrocracking and Selective Hydroisomerization, Oil Gas Sci. Technol. - Rev. l'IFP. 64 (2009) 91–112. doi:10.2516/ogst/2008047.

IV. PLATINUM-BASED CATALYSTS PERFORMANCE IN THE SELECTIVE HYDROGENATION OF P-CHLORONITROBENZENE

Contents

Some of the results described in this chapter have been published:

> A.F. Sierra Salazar, V. Hulea, A. Ayral, T. Chave, S. Nikitenko, P. Kooyman, F.D. Tichelaar, S. Abate, S. Perathoner, P. Lacroix-Desmazes. "Engineering of silica-supported platinum catalysts with hierarchical porosity combining latex synthesis, sonochemistry and sol-gel process - II. Catalytic performance". *Microporous and Mesoporus Materials* 256 (2018) 227–234. DOI:10.1016/j.micromeso.2017.08.016.

IV.1- Introduction

Designing catalysts using a rational approach requires the possibility to control the architecture of the material at all scales, from lengths of a few nanometers up to several centimeters. Notably, a multi-scale hierarchical porosity plays an important role in the catalyst activity, selectivity and deactivation prevention [1]. Chapter III describes the preparation of platinum catalysts with hierarchical porosity by the combination of latex synthesis, sonochemistry and sol-gel process, which is a waterborne approach. In short, it starts from the preparation of a polystyrene latex by emulsion polymerisation (Figure 49, Chapter III). Then, the latex is decorated with Pt nanoparticles by sonochemical reduction of a water-soluble Pt precursor. Subsequently, the Pt-containing hybrid latex is used as template in the two-step acid-base catalysed sol-gel synthesis of a mesoporous silica matrix. This composite material is then calcined to remove the organic polymer template, leaving behind macropores decorated with Pt nanoparticles [2]. In this chapter, the catalytic performance of these materials is evaluated in the production of *p*-chloroaniline (*p*-CAN).

In view of its industrial importance, the selective hydrogenation of *p*-chloronitrobenzene (*p*-CNB) to *p*-CAN has been chosen to study the catalytic performance of tailored Pt-based catalysts with hierarchical porosity. Haloanilines such as *p*-CAN are important building blocks in the synthesis of a large variety of nitrogen-containing industrial products such as fertilizers, polymers, dyes and drugs [3]. Conventionally, they are produced from the corresponding halonitrobenzene (e.g. *p*-CNB) with stoichiometric reductants or hydride reagents. In line with green chemistry principles, notably the principle of atom economy [4], the most efficient method for large-scale halogenated aniline production is the heterogeneously catalytic hydrogenation of halogenated nitroarenes with H_2. Due to the discovery of promising catalytic systems for this reaction, based on platinum, palladium, rhodium, ruthenium, nickel, gold, iridium, etc. [3,5–12], it has received more and more attention recently.

The major drawback of heterogeneous catalysts is the hydrodehalogenation of the aromatic haloaniline by hydrogenolysis of the carbon–halogen bond [5,13,14]. Other side products can

also be formed as shown in Figure 81. From the selectivity enhancement point of view, the choice of the catalyst is very important to reduce the side reactions, particularly the hydrogenolysis of the halogen atom. Table 11 presents some of the selectivity values reported in the literature for different catalysts. Among them, platinum-based catalysts have received much attention for minimising dehalogenation. Several strategies have been employed to improve selectivity such as metal alloying [14–18], tuning the metal/support interaction [19] or adding promoters or inhibitors [20]. Particularly, alloying has been very effective. For instance, the selectivity towards *p*-CAN went from 82% with Pt/Al_2O_3 to 98% with a bimetallic $Pt\text{-}Sn/Al_2O_3$ catalyst [14]. Other systems such as Pt(0) nanoparticles entrapped within a nano-hybrid sol-gel matrix have been studied in the selective hydrogenation of nitro compounds in the presence of different functionalities such as reducible carbonyl, amide, ester, amine and halide groups, achieving selectivity values between 50 and 100% [21].

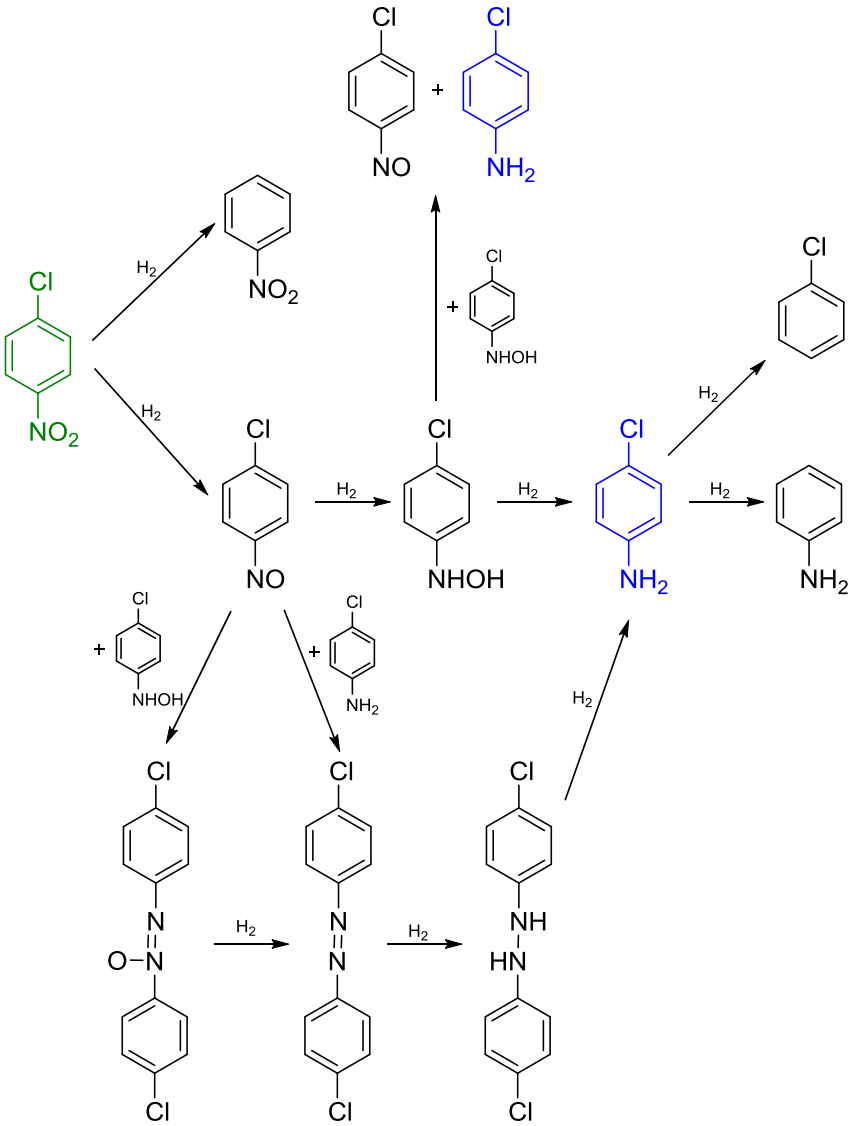

Figure 81. Possible reaction pathways in the hydrogenation of *p*-chloronitrobenzene (*p*-CNB) to produce *p*-chloroaniline (*p*-CAN) [22].

Table 11. Selectivity values reported for the hydrogenation of *p*-CNB to *p*-CAN

Catalyst	Selectivity towards *p*-CAN (%)	Conversion (%)	Temp. (°C)	Pressure (bars)	Ref.
Pt/SiO_2	35	100	40	1	[18]
$PtZn/SiO_2$	>99	100	40	1	[18]
Pt/Al_2O_3	82	>99	30	1	[14]
$PtSn/Al_2O_3$	98	>99	30	1	[14]
Pt/CNT	74	>99	30	1	[16]
PtMn/CNT	99	>99	30	1	[16]
Pt/Al_2O_3	85	>98	30	1	[19]
Pt/TiO_2	99	>98	30	1	[19]
Pt/TiO_2	93	>99	30	1	[15]
$PtFe/TiO_2$	98	>99	30	1	[15]
Ru/SiO_2	80	99	100	10	[23]
Pt/CeO_2	99	99	60	30	[24]
$Pd_{0.01}Ru_{0.01}Ce_{0.98}O_{2-\delta}$	100	100	35	1	[17]
Pt/C	71	88	35	40	[25]
Pd/P-doped carbon layers	>99	100	90	10	[12]
Au/SiO_2	100	100	140	40	[26]
Au/hybrid poly(4-vinyl-benzyl trimethylammonium chloride) – Al_2O_3	>99	80	25	20	[27]
Pt-Sm anchored with poly(vinylpyrrolidone)	96	100	30	1	[20]
Pt-Ce anchored with poly(vinylpyrrolidone)	98	100	30	1	[20]
Pt/Organosilica matrix	87	100	25	1	[21]

The selectivity of the catalytic hydrogenation reactions is also influenced by many other factors, including temperature, pressure, stirring, as well as the catalyst support. Typically, the catalysts for the selective hydrogenation of *p*-CNB have been evaluated in batch conditions at temperatures ranging between 30 and 140 °C, with hydrogen pressures between 10 and 40 bars and stirring speed between 700 and 1200 rpm [6,12,23–26,28–32]. Furthermore, suitable carriers such as carbon, alumina, barium carbonate, barium sulphate, calcium carbonate, kieselguhr, silica and titania have been reported for the preparation of supported platinum catalysts for the hydrogenation of chloronitrobenzene [15,16,19]. However, these approaches have not focused on the development of catalytic systems taking into account a three-dimensional multiscale architecture. Particularly, hierarchical porosity in catalytic materials is important in developing catalysts with high surface areas, large pore volumes, and efficient mass transport [33,34].

As mentioned, given the industrial relevance of the selective hydrogenation of *p*-CNB to *p*-CAN, this reaction has been chosen for the evaluation of hierarchically porous Pt/SiO_2 catalysts. Such catalysts provide Pt active sites within a tailored textural environment that could be advantageous for the reaction, the selectivity being the most relevant point. The catalytic study consists of some distinct steps. First, different operation conditions are studied. Subsequently, the effect of the catalyst pre-treatment conditions such as calcination temperature and pre-reduction under hydrogen flow are considered. Such performances are compared against that of a commercially available catalyst. Afterwards, the catalyst stability is discussed. Finally, given

the versatility of this technique to tailor the catalyst hierarchical porosity, the effect of further textural modifications on the catalyst macro- and mesoporosity is also discussed.

IV.2- Experimental

IV.2.1- Reagents and catalysts

p-Chloronitrobenzene ($ClC_6H_4NO_2$, *p*-CNB, 99%, Sigma Aldrich), *p*-chloroaniline ($ClC_6H_4NH_2$, *p*-CAN, 99%, Sigma Aldrich), octanol ($C_8H_{17}OH$, 99.5%, TCI), absolute ethanol (C_2H_5OH, 99.8%, Sigma Aldrich), 1 wt.% Pt/SiO_2 (Sigma Aldrich, referred to as 0.7REF) were used as received.

The preparation of hierarchically porous Pt/SiO_2 catalysts was described in Chapter III. The characteristics of such materials are reminded in Table 12. The catalysts are named based on their Pt loading and calcination temperature, e.g. 0.7cal450 for a catalyst at 0.7 wt. % Pt/SiO_2 and calcined at 450 °C. However, when a relevant feature in the catalyst preparation is under study, it is added at the end of the catalyst name after a hyphen. Thus, for a material with 12.5% of macroporosity, it is called: 0.2cal450-12.5%, or when the material was prepared at 343 kHz, it is called 0.3cal450-343kHz (note: when not specified, the default value for macroporosity is 50% and for the ultrasound frequency is 205 kHz).

Typically, the catalytic experiments were performed directly after catalyst calcination. Catalyst 0.7cal450 was also evaluated after a pre-treatment for 2 h at 300 °C (referred to as 0.7cal450-red300) or at 450°C (referred to as 0.7cal450-red450) under hydrogen flow at *ca*. 10 mL/min in a vertical glass reactor within a temperature-controlled tubular furnace. The behaviour of the commercial catalyst 0.7REF was evaluated under the same catalytic conditions as a reference catalyst. 0.7REF after hydrogen treatment at 300 °C is referred to as 0.7REF-red300.

Table 12. Characteristics of the hydrogenation catalysts according to Chapter III

Characteristics		**0.7cal450**	**0.7cal650**	**0.8cal450-50%**	**0.4cal450-33.3%**	**0.3cal450-25%**	**0.2cal450-12.5%**	**0.4cal650-25/25%**
Pt loading[a] (wt.%)		0.7	0.7	0.8	0.4	0.3	0.2	0.4
Pt NPs size[b]	D_n (nm)	4.6 ± 1.1	6.5 ± 2.2	8.6 ± 3.6	7.6 ± 3.4	8.2 ± 3.7	6.7 ± 3.1	10.2 ± 3.9
	Đ[b]	1.28	1.36	1.54	1.79	1.76	1.68	1.46
Total BET surface area[c] (m^2/g)		490	490	759	729	718	694	674
Mesopore average size in adsorption branch[c] (nm)		4.2	4.7	3.6	3.5	3.6	3.6	4.1
Mesopore average size in desorption branch[c] (nm)		4.0	4.5	3.5	3.4	3.4	3.3	3.9
Mesopore size range in adsorption branch[c] (nm)		2-7	2-7	2-7	2-9	2-9	2-9	2-9
Total pore volume (by N_2 physisorption)[c] (cm^3/g)		0.35	0.36	0.56	0.59	0.60	0.60	0.65
Pore size at the beginning of Hg intrusion[d] (nm)		130	130	60	29	24	20	35
Macropore size range in extrusion branch[d] (nm)		110-400	110-400	110-400	N/A	N/A	N/A	90-310
Total pore volume (by Hg intrusion)[d] (cm^3/g)		0.54	0.55	0.47	0.40	0.26	0.16	0.63
Total pore volume (using both techniques)[e] (cm^3/g)		0.77	0.77	0.82	0.70	0.58	0.57	0.89
Total porosity (using both techniques)[e] (%)		63	63	64	61	56	56	66

Table 12 (continuation)

Characteristics		0.7REF	1cal650-50%-IWI	0.3cal450-100kHz	0.3cal450-205kHz	0.3cal450-343kHz
Pt loading[a] (wt.%)		0.7	1	0.3	0.3	0.3
Pt NPs size[b]	D_n (nm)	2.9 ± 1.2	29.7 [3-200 nm]	4.7 ± 1.3	4.5 ± 1.1	3.9 ± 1.0
	Đ[b]	1.62	6.16	1.21	1.18	1.15
Total BET surface area[c] (m^2/g)		260	575	744	632	617
Mesopore average size in adsorption branch[c] (nm)		18.0	5.2	3.6	4.2	5.0
Mesopore average size in desorption branch[c] (nm)		13.0	5.9	3.5	4.1	4.6
Mesopore size range in adsorption branch[c] (nm)		11-28	2-15	2-9	2-13	2-15
Total pore volume (by N_2 physisorption)[c] (cm^3/g)		1.09	0.77	0.55	0.64	0.77
Pore size at the beginning of Hg intrusion[d] (nm)		29	60	130	60	60
Macropore size range in extrusion branch[d] (nm)		-	110-170	130-310	130-310	110-260
Total pore volume (by Hg intrusion)[d] (cm^3/g)		0.95	1.11	0.61	0.73	0.92
Total pore volume (using both techniques)[e] (cm^3/g)		0.96	1.25	0.95	1.00	1.08
Total porosity (using both techniques)[e] (%)		68	73	68	69	70

[a] Determined by elemental analysis by ICP-OES
[b] Determined by TEM. Dispersity $Đ=D_w/D_n$, D_w being weight-average diameter and D_n being number-average diameter.
[c] Determined using nitrogen physisorption. Equivalent pore diameters calculated by BJH method.
[d] Determined using mercury porosimetry.
[e] The total pore volume was calculated as the maximum Hg intrusion from 1 µm down to 3.5 nm plus the volume of nitrogen adsorbed up to 3.5 nm equivalent diameter by BJH method in the adsorption branch.
N/A: non-available

IV.2.2- Catalytic experiments

The catalytic hydrogenation reactions were carried out in a 0.3 L well-mixed gas-slurry reactor Parr autoclave with titanium vessel, operating in batch mode. The reactor was equipped with a 4838 Temperature and Stirring Controller (Parr Instrument Company, Figure 82). In a typical catalytic experiment, the reactor was loaded with 1 g of *p*-CNB (6.3 mmol), 100 mL of ethanol as solvent, 0.2 g of catalyst and 0.6 g of octanol as internal standard. The reactor was closed and flushed 3 times with nitrogen. Then, the temperature was set at the desired temperature, under constant agitation (*ca*. 1000 rpm) and the pressure was raised to the operating level by hydrogen feeding (9 bars, or 2 bars when specified). During the experiment, hydrogen was continuously fed, so that the total pressure was maintained constant in the reactor. 2 mL-samples were withdrawn periodically from the reactor. At the end of the reaction, the reactor was cooled down naturally and the pressure was released.

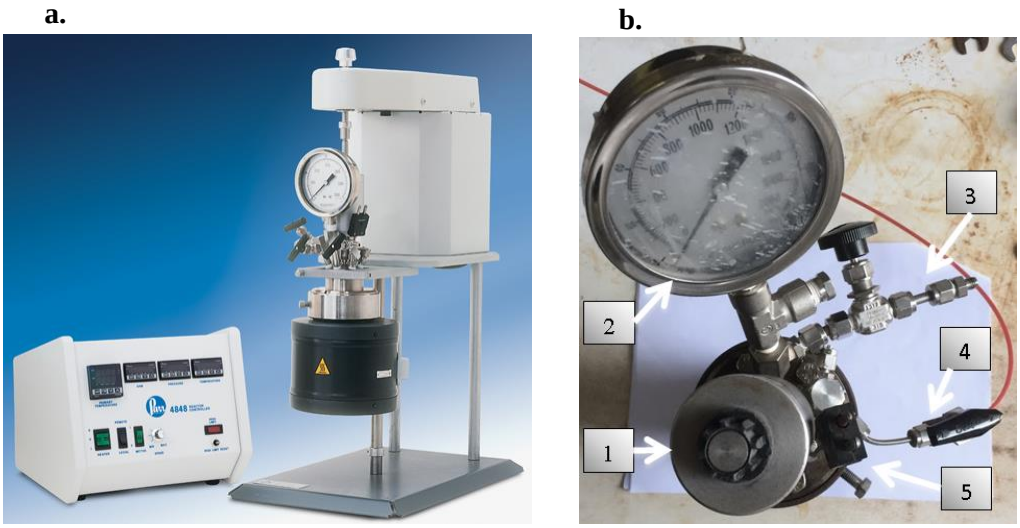

Figure 82. Image of the experimental set-up: a. Parr reactor equipped with a 4838 Temperature and Stirring Controller, b. Reactor head with: 1. Magnetic drive, 2. Manometer, 3. H_2 inlet line equipped with a valve, 4. Outlet line equipped with a valve and 5. Thermocouple.

The products were analysed by gas chromatography (GC) on a Varian 3900 chromatograph equipped with a flame ionization detector (FID) and a DB-1 capillary column (30 m x 0.32 mm, 3 µm film thicknesses, Agilent). Samples of 0.5 µL were injected manually with a 1 µL glass syringe. The chromatograph temperatures were set as follows: injector at 250 °C, FID at 280 °C, column initial and final temperatures: 40 °C and 220 °C respectively, heating at a rate of 15 °C/min. *p*-CNB, *p*-CAN and aniline were quantified using calibration curves based on the product/octanol molar ratio versus the corresponding product/octanol peak areas ratio in the experimental chromatographs.

Additionally, all reaction products were identified by GC (GC-2010 Plus, Shimadzu) with a quadripole mass spectrometry (MS) detector (GCMS-QP2010 SE) equipped with a SLB^{TM}-5ms capillary column (30 m × 0.25 mm, 0.25 µm film thicknesses, Supelco). The detector and the

injector temperatures were 200 °C and 280 °C, respectively. The column initial and final temperatures were 40 °C and 220 °C respectively, with a heating rate of 15 °C/min.

Some of the reaction products were also analysed by Nuclear Magnetic Resonance (NMR) spectroscopy. The NMR spectra were recorded on a Bruker AC 400 instrument, using deuterated benzene, deuterated chloroform or deuterium oxide as solvents. The recording experimental conditions were 4 s of acquisition time, 1 s of pulse delay and 8 scans for ^{1}H NMR and 2 s of acquisition time, 2 s of pulse delay and 256 scans for ^{13}C NMR.

Recycling test. After reaction the spent catalyst was filtered, rinsed with 96 vol. % ethanol and dried overnight at 80 °C. The recyclability experiments were carried out at 70 °C and 9 bars of hydrogen pressure with the recovered catalyst 0.6cal650 (prepared following the same procedure than for 0.7cal650). In these runs, the reaction time was 80 min and the amount of catalyst was 200.9, 197.4, 191.6, 187.1 and 184.9 mg in the first, second, third, fourth and fifth cycles, respectively (a very limited catalyst loss was observed after every catalyst recovery procedure probably due to adhesion of some grains to the filter or to the reactor vessel and lines. Some catalyst loss during sampling was also possible).

Leaching test. Retention of the active Pt nanoparticles on the support was verified by removing the filterable catalyst (0.6cal650) after 50% conversion had been reached. The resulting reaction mixture did not show additional conversion under the same reaction conditions (70 °C and 9 bars), indicating no Pt active species are present in solution when the catalyst is removed.

Blank test. A blank run was also carried out by mixing the reactants in the absence of catalyst. No conversion was observed after 120 minutes.

The catalyst performance was evaluated based on the selectivity and initial reaction rate of each reaction. The selectivity towards *p*-CAN was calculated either at 50% or 80% conversion of *p*-CNB. Given that *p*-CAN and aniline were the only products in quantifiable amounts, the selectivity was calculated by:

$$Selectivity = \frac{[p-CAN]}{[p-CAN]+[aniline]} \times 100$$

Where the concentrations of *p*-CAN and aniline are expressed in molarity. The initial reaction rate ($mol_{CNB}/min\ mol_{Pt}$) was calculated as the difference of the number of moles of *p*-CNB at 0 min ($n_{p-\mathrm{CNB},0}$) and after 15 min of reaction ($n_{p-\mathrm{CNB},15\mathrm{min}}$), divided by 15 min and the number of moles of Pt (n_{Pt}) in the reactor, as follows:

$$Initial\ reaction\ rate = \frac{n_{p-\mathrm{CNB},0} - n_{p-\mathrm{CNB},15\mathrm{min}}}{15\ min \times n_{Pt}}$$

IV.2.3- Materials characterisation

The catalyst evaluated in this chapter were characterised as described in Chapter III. The only additional characterisation is the XPS analysis of 0.7cal450 and 0.7cal450-red450, which was carried out at the University of Messina in a PHI VersaProbe II analyser (Physical Electronics), using a monochromatic excitation source: Al Kα (1486.6 eV). The analysed surface was of 300

μm diameter. Position of XPS binding energies were referred to silver foil, whose binding energy was taken equal to 368.2 eV for $Ag3d_{5/2}$.

IV.3- Results and discussion

Silica-supported Pt catalysts with hierarchical meso- and macroporosity were evaluated for the selective hydrogenation of *p*-CNB to *p*-CAN in the liquid phase. Such materials were prepared by the combination of latex synthesis, sonochemistry and sol-gel synthesis leading to materials with Pt nanoparticles mainly located on the macropores, as described in Chapter III.

IV.3.1- Hydrogenation of *p*-CNB – reaction products

As previously reported, various products, including *p*-CAN, aniline, chlorobenzene, *p*-chloronitrosobenzene, nitrobenzene, *p*-chlorophenylhydroxylamine, etc., can be obtained during this reaction [14]. In our study, the only products appearing in significant amounts were *p*-CAN and aniline. In most of tests, only traces of other products (such as *p*-chloronitrosobenzene and *p*-chlorophenylhydroxylamine) were observed. Typical GC-FID chromatograms of the reaction medium along the reaction time are presented in Figure 83, from which it is possible to obtain a kinetic profile for the reaction, as shown in Figure 84.

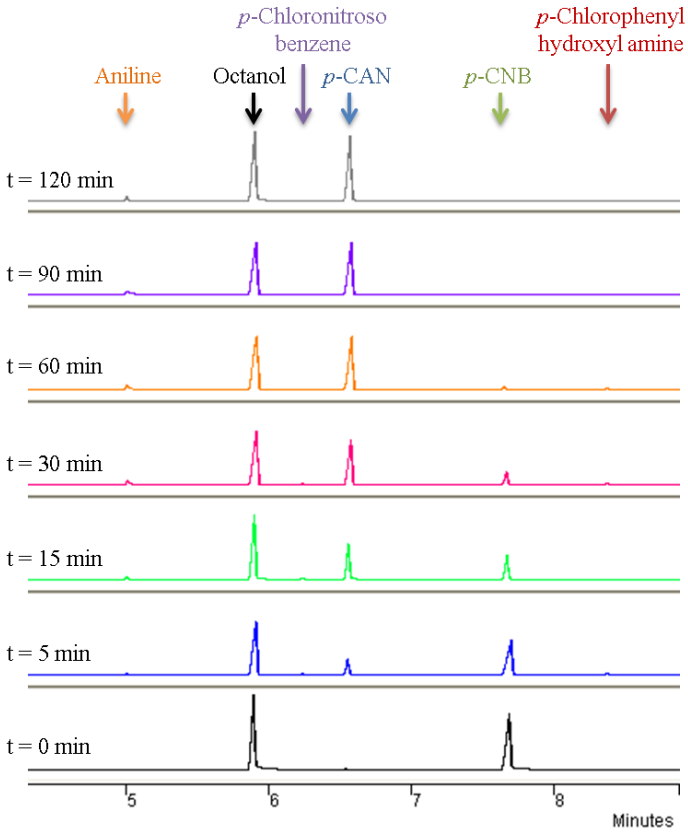

Figure 83. GC-FID chromatograms (at different reaction time) for the reaction products of the hydrogenation of *p*-CNB with hierarchically porous silica-supported catalyst 0.7cal450. Conditions: 70 °C and 9 bars.

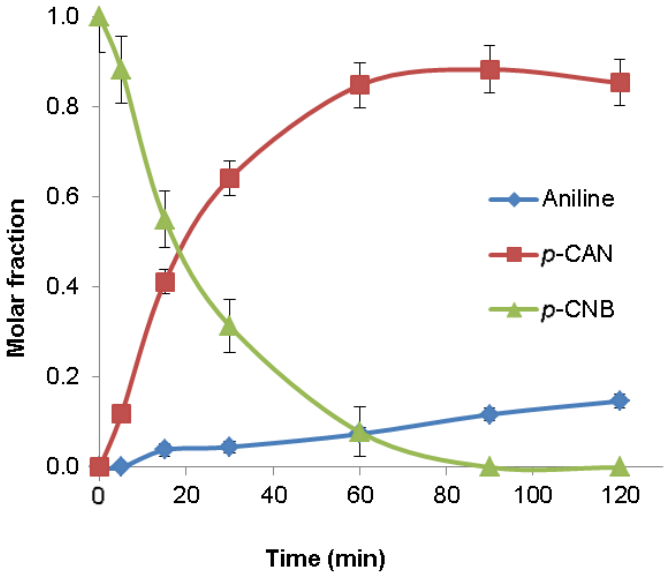

Figure 84. Typical kinetic profiles by GC-FID for the *p*-CNB hydrogenation over 0.7cal450 catalyst. Conditions: 70 °C and 9 bars.

According to the kinetic profiles presented in Figure 84, the initial product is *p*-CAN, but as the reaction goes on, aniline is produced and its concentration increases constantly. After 90 min, the conversion of *p*-CNB is complete and the concentration of aniline increases at the expense of *p*-CAN. This explains why the selectivity at 50% conversion was always higher than at 80% conversion, as shown in Table 13 and Table 14 (the selectivity being defined by [*p*-CAN]/([*p*-CAN]+[aniline])). These results confirm a reaction in series towards aniline, with *p*-CAN being an intermediate product. The main reaction pathway is summarised in Figure 85. Similar reaction pathways have been previously proposed by Cárdenas-Lizana et al.[35] and Jiang et al. [36].

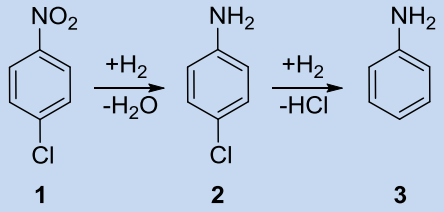

Figure 85. Simplified reaction pathway of the hydrogenation of *p*-CNB (1: *p*-CNB, 2: *p*-CAN, 3: Aniline).

The following sections discuss the effect of the operation conditions, the catalyst pre-treatment and the variation of the macro- and mesoporosity on the selectivity towards *p*-CAN and on the activity in terms of initial reaction rate.

IV.3.2- Effect of the operation conditions on the catalytic performance

In order to define appropriate reaction conditions for the following catalytic tests, a screening of different hydrogen pressures and temperatures was carried out using the catalyst 0.7cal450.

IV.3.2.1- Effect of the hydrogen pressure

These experiments with catalyst 0.7cal450 were carried out at 60 °C and 2 or 9 bars of hydrogen pressure. The corresponding catalytic performances are presented in Table 13. As expected, by increasing the hydrogen pressure, the catalytic activity increased, which is related to the higher hydrogen concentration in the liquid medium [37]. Additionally, the selectivity at 80% conversion also increased: 75.5% at 2 bars, and 91.5% at 9 bars. This can be explained by a longer reaction time to reach 80% conversion: 106 min at 2 bars versus 58 min at 9 bars, increasing the probability of a *p*-CAN molecule being readsorbed and hydrogenated to aniline. So at a hydrogen pressure of 9 bars, the production of *p*-CAN is favoured.

Table 13. Catalyst 0.7cal450 performance at different hydrogen pressures.

Temp. (°C)	Pressure (bar)	Initial reaction rate[a] (mol_{CNB}/min mol_{Pt})	Selectivity at 50 % conversion[b] (%)	Selectivity at 80 % conversion[c] (%)
60	2	17.9	85.0	75.5
60	9	22.6	97.7	91.5

[a] ± 2.9 mol_{CNB}/min mol_{Pt}. [b] Selectivity to *p*-CAN ± 0.6%. [c] Selectivity to *p*-CAN ± 1.8%. Reactions carried out with 0.2 g of catalyst, 1 g of *p*-CNB and 100 mL of ethanol as solvent.

IV.3.2.2- Effect of the temperature

The catalyst 0.7cal450 was evaluated at three different temperatures: 50, 60 and 70 °C, at a constant hydrogen pressure of 9 bars. Table 14 presents the corresponding catalytic performances. The selectivity did not change significantly in this temperature range. However, the catalytic activity increased with the temperature, in agreement with Arrhenius' law.

Table 14. Catalyst 0.7cal450 performance at different temperatures.

Temp. (°C)	Pressure (bar)	Initial reaction rate[a] (mol_{CNB}/min mol_{Pt})	Selectivity at 50 % conversion[b] (%)	Selectivity at 80 % conversion[c] (%)
50	9	6.2	95.8	94.1
60	9	22.6	97.7	91.5
70	9	33.7	97.0	92.7

[a] ± 2.9 mol_{CNB}/min mol_{Pt}. [b] Selectivity to *p*-CAN ± 0.6%. [c] Selectivity to *p*-CAN ± 1.8%. Reactions carried out with 0.2 g of catalyst, 1 g of *p*-CNB and 100 mL of ethanol as solvent.

Taking into account a constant hydrogen pressure, the equation of a pseudo-first order reaction rate can be written as:

$$-\frac{d[CNB]}{dt} = k'[CNB]$$

Where *k'* is the apparent reaction rate constant, *t* is time and [*CNB*] is the concentration of *p*-CNB at any time. By solving the differential equation, it is transformed into:

$$ln[CNB] = -k'.t + ln\,[CNB]_0$$

Where $[CNB]_0$ is the initial concentration of *p*-CNB. So, by plotting the *ln*[*CNB*] versus time, it is possible to obtain *k'*. Figure 86 shows the plot corresponding to 70 °C and 9 bars. Since it is a straight line, it validates the assumption of a first order reaction with respect to the concentration of *p*-CNB.

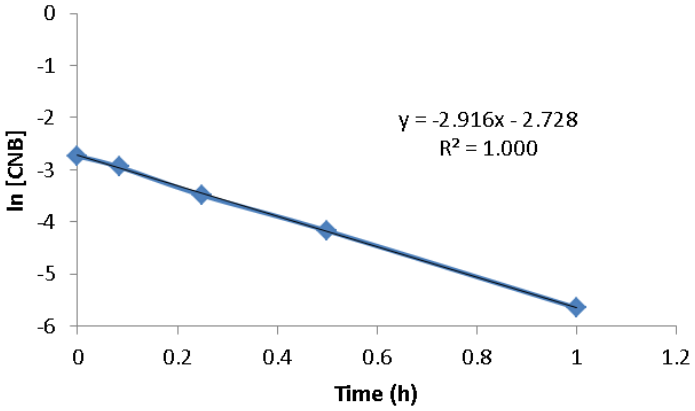

Figure 86. Validation of first order reaction with respect to *p*-CNB. Conditions: 70 °C and 9 bars.

For the reactions performed at 50, 60 and 70 °C with catalyst 0.7cal450, the obtained values of *k'* were: 1.6, 2.0 and 2.9 h^{-1}, respectively.

The Arrhenius equation can be written as:

$$ln(k') = ln(A) - \frac{E_a}{R}\left(\frac{1}{T}\right)$$

Where *A* is the collision frequency factor, E_a is the activation energy, *R* is the universal gas constant and *T* is the absolute temperature. So by plotting the *ln*(*k'*) versus (*1/T*), it is possible to obtain the activation energy (Figure 87). In this case, it was 27.5 ± 7.8 kJ/mol, which is in agreement with 25.1 ± 2.1 kJ/mol reported for Pt nanoparticles of ca. 4 nm supported on alumina [22].

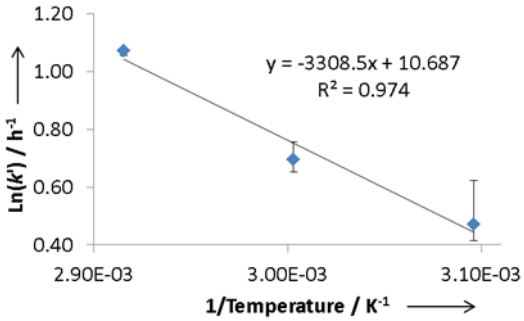

Figure 87. Arrhenius plot for the hydrogenation of *p*-CNB at 50, 60 and 70 °C.

On account of this operation conditions screening, temperature of 70 °C and hydrogen pressure of 9 bars were chosen for the following catalytic experiments, given the high catalyst activity (initial rate: 33.7 mol_{CNB}/min mol_{Pt}) at elevated selectivity (97% selectivity at 50% conversion of *p*-CNB) obtained at these conditions.

IV.3.3- Effect of the catalyst pre-treatment conditions on the catalytic performance

As described in Chapter III, the polymer template that leads to macropores is removed by calcination at temperatures above 450 °C in the presence of Pt. In this section, the effect of that calcination temperature on the catalytic performance is assessed. Furthermore, the effect of a subsequent reduction pre-treatment before reaction is also evaluated.

IV.3.3.1- Effect of the calcination temperature

As shown in Chapter III, the Pt particle size increased with the calcination temperature. In order to evaluate the influence of such calcination step on the catalytic performance, catalysts 0.7cal450 and 0.7cal650 (calcined at 450 °C or 650 °C, respectively) were evaluated for the hydrogenation of *p*-CNB at 70 °C and 9 bars. Additionally, a commercial material was also tested (0.7REF).

In order to have enough elements for the discussion, X-ray photoelectron spectroscopy (XPS) analyses were performed on the fresh catalysts (0.7cal450, 0.7cal650 and 0.7REF) and on 0.7cal650 and 0.7REF after being used in the catalytic reaction. Figure 88 shows the corresponding XPS spectra. Unfortunately, given the low Pt content of these samples, the collected XPS spectra were not resolved enough, so a deconvolution for quantitative analysis would not be reliable. Nevertheless, a useful qualitative analysis is still possible. 0.7REF as-received was mainly oxidised (Figure 88a), since almost no signal was observed in the binding energy (BE) region of Pt(0) (i.e. 70.8 eV). However, it was strongly reduced *in-situ* under the reaction conditions, exhibiting a narrow full width at half maximum (FWHM) in the region of Pt(0) after being used in the reaction (Figure 88b). This can be explained by the fact that the reaction temperature was 70 °C, which falls in the temperature range of the reduction peak observed for 0.7REF by H_2-TPR between 25 °C and 150 °C, as shown in Figure 89. Indeed, such reduction profile is in agreement with H_2-TPR patterns of Pt/SiO_2 prepared by wet impregnation and calcined at 500 °C: the peak around 100 °C corresponds to the reduction of platinum species at the surface [38].

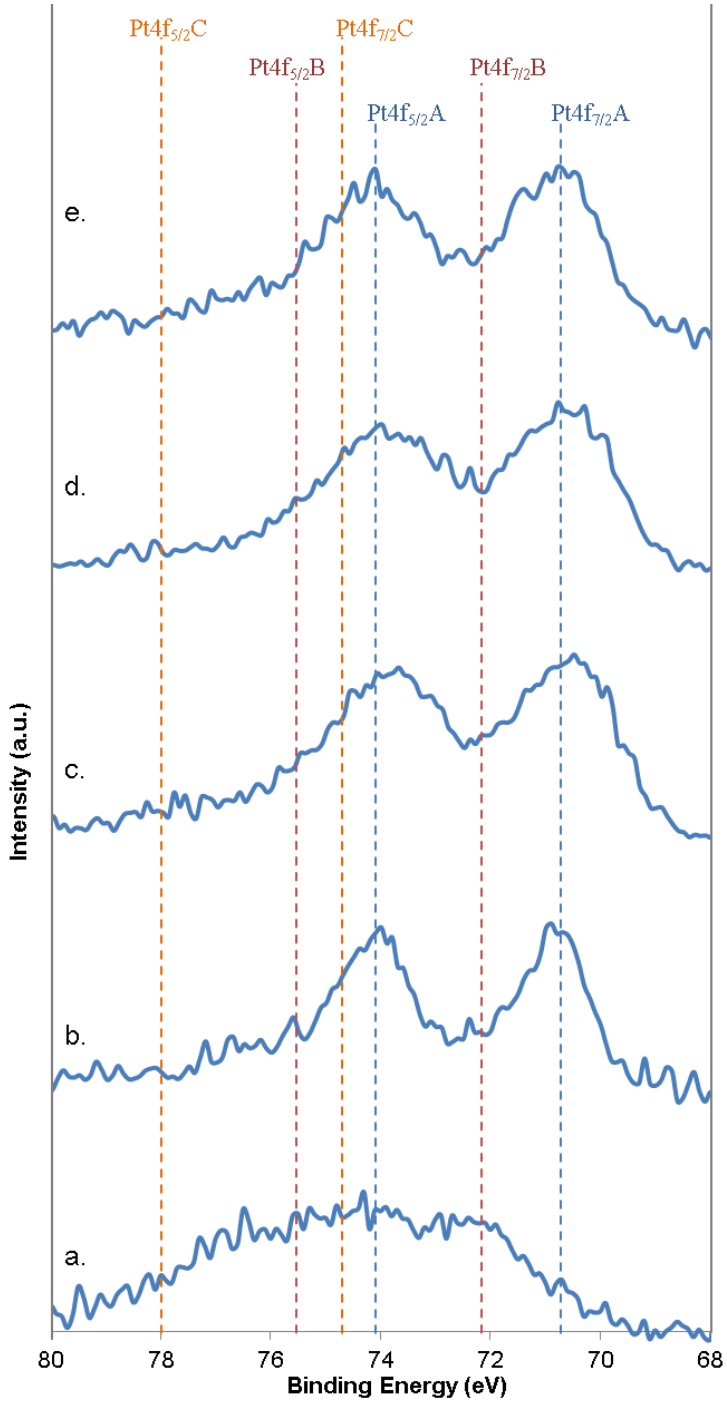

Figure 88. Pt4f core level XPS signals for: a. 0.7REF, fresh, b. 0.7REF, used, c. 0.7cal450, fresh,
d. 0.7cal650, fresh, and e. 0.7cal650, used. Characteristic binding energies for Pt(0): $Pt4f_{7/2}A$ and $Pt4f_{5/2}A$, 70.8 and 74.1 eV, respectively, for Pt(II): $Pt4f_{7/2}B$ and $Pt4f_{5/2}B$, 72.2 and 75.5 eV, respectively, and for Pt(IV): $Pt4f_{7/2}C$ and $Pt4f_{5/2}C$, 74.7 and 78.0 eV, respectively [39–41].

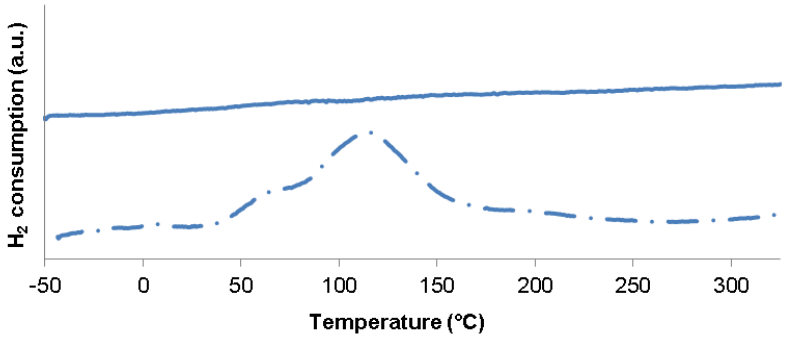

Figure 89. H_2-TPR profiles of Pt-free silica matrix (—) and 0.7REF(— •).

The fresh hierarchically porous catalysts (0.7cal450, 0.7cal650 fresh catalysts) mainly contained Pt(0) (Figure 88c and d). This means that even after the calcination step, the sonochemically prepared Pt NPs remained stable mainly in their metallic oxidation state Pt(0). It can also be observed that the 0.7cal650 used catalyst (Figure 88e) exhibited a spectrum very similar to the 0.7cal650 fresh catalyst (Figure 88d), meaning that no significant change of the oxidation state occurred at the reaction conditions. This observation was in agreement with the H_2-TPR profile for 0.7cal650 fresh catalyst that showed no evident peak of hydrogen consumption below 150 °C, as discussed in Chapter III.

The catalytic performances of 0.7cal450, 0.7cal650 and 0.7REF in the hydrogenation of *p*-CNB are presented in Table 15. A clear trend can be observed for the selectivity: it increases while the catalytic activity (initial reaction rate) decreases, which is a common trend in agreement with the literature [3]. Besides this, on one hand, as larger particles have smaller specific surface area (i.e. less Pt available at the nanoparticle surface for the reaction), a lower reaction rate on a total Pt basis is to be expected. On the other hand, it has been reported that the specific reaction rate expressed on a surface Pt atom basis increases with a larger particle size, which has been explained by large Pt particles being better at stabilising a transition state with weak negative charge derived from the adsorbed *p*-CNB [22]. In this case, the expected improved surface reaction rate due to larger particles was probably counterbalanced by a smaller specific surface area, eventually leading to an almost constant initial reaction rate (Table 15, samples 0.7cal450 and 0.7cal650). Additionally, it has been shown that the selectivity of Pt in this specific reaction increases with the particle size, since the product *p*-CAN is adsorbed less strongly on large particles in comparison with the reactant *p*-CNB, decreasing the likelihood of *p*-CAN to be hydrogenated further towards aniline [19]. And indeed, the sample calcined at 650 °C (0.7cal650) that had a larger average particle size of 6.5 nm showed a better selectivity of 96.7% compared to the other two catalysts (0.7cal450 and 0.7REF).

Table 15. Effect of the calcination temperature on the catalytic performance.

Sample	Calcination Temp. (°C)	Pt NPs size		Initial reaction rate[b] (mol_{CNB}/ min mol_{Pt})	Selectivity at 50 % conversion[c] (%)	Selectivity at 80 % conversion[d] (%)
		D_n (nm)	Đ[a]			
0.7cal450	450	4.6	1.28	33.7	97.0	92.7
0.7cal650	650	6.5	1.36	31.9	100	96.7
0.7REF	N/A	2.9	1.60	47.7	95.7	90.8

[a] Dispersity Đ=D_w/D_n, D_w being weight-average diameter and D_n being number-average diameter, determined by TEM. [b] ± 2.9 mol_{CNB}/min mol_{Pt}. [c] Selectivity to *p*-CAN ± 0.6%. [d] Selectivity to *p*-CAN ± 1.8%. N/A: non-available. Reactions carried out at 70 °C, 9 bars of H_2 with 0.2 g of catalyst, 1 g of *p*-CNB and 100 mL of ethanol as solvent.

Conversely, 0.7REF exhibited a higher initial reaction rate compared to the other two catalysts (0.7cal450 and 0.7cal650), which can be explained by a larger active surface area as a result of the smaller particle size and a larger amount of Pt(0) formed *in-situ* (probably at the beginning of the reaction). Indeed, the narrower FWHM observed in the XPS spectrum of this sample after reaction (Figure 88b), in comparison with the other catalysts, indicates qualitatively that this sample contained less oxide species than the other catalysts.

Consequently, it could be concluded that a higher calcination temperature (650 °C for 0.7cal650 compared to 450°C for 0.7cal450) leading to larger Pt nanoparticles (6.5 nm compared to 4.6 nm) improves the selectivity of these hierarchically porous catalysts towards *p*-CAN: 96.7 % selectivity compared to 92.7% selectivity at 80% conversion of *p*-CNB. Regarding the commercial catalyst (0.7REF), it exhibited lower selectivity (up to 95.7% selectivity) than the hierarchically porous catalyst 0.7cal650 (up to 100% selectivity), but it was more active (initial rate: 47.7 mol_{CNB}/min mol_{Pt} compared to 31.9 mol_{CNB}/min mol_{Pt}) probably due to its larger amount of easily reducible Pt species (reduction *in situ*), as well as its smaller particle size (2.9 nm compared to 6.5 nm).

IV.3.3.2- Effect of the hydrogen pre-treatment

The catalytic performance was also evaluated after a pre-treatment under hydrogen flow. The experimental results are summarised in Table 16. The reference catalyst was reduced for 2 h at 300 °C (Table 16, sample 0.7REF-red300). With such pre-treatment, the Pt particles sintered to 6.1 nm average diameter, which is more than double their initial value without pre-treatment (2.9 nm) (Table 15, sample 0.7REF). This pre-treatment did not significantly modify the activity (47.7 ± 2.9 and 47.4 ± 2.9 mol_{CNB}/min mol_{Pt}, without and with pre-treatment, respectively), probably because the larger proportion of reduced Pt species, as active catalyst, is partially counterbalanced by the lower specific surface area of the resulting Pt nanoparticles. In addition, the selectivity is high in both cases and increased only slightly (within the statistical uncertainty) despite the larger particle size after reduction.

Table 16. Effect of the hydrogen pre-treatment on the catalytic performance.

Sample	Reduction Temp. (°C)	Pt NPs size		Initial reaction rate[b] (mol_{CNB}/ min mol_{Pt})	Selectivity at 50 % conversion[c] (%)	Selectivity at 80 % conversion[d] (%)
		D_n (nm)	Đ[a]			
0.7cal450-red300	300	4.6	1.18	28.4	99.3	95.2
0.7cal450-red450	450	5.4	1.26	20.2	100.0	100.0
0.7REF-red300	300	6.1	1.89	47.4	95.2	92.5

[a] Dispersity $Đ=D_w/D_n$, D_w being weight-average diameter and D_n being number-average diameter, determined by TEM. [b] ± 2.9 mol_{CNB}/min mol_{Pt}. [c] Selectivity to *p*-CAN ± 0.6%. [d] Selectivity to *p*-CAN ± 1.8%. N/A: non-available. Reactions carried out at 70 °C, 9 bars of H_2 with 0.2 g of catalyst, 1 g of *p*-CNB and 100 mL of ethanol as solvent.

The catalyst calcined at 450 °C (0.7cal450) was pre-treated in under hydrogen flow at two different temperatures: 300 °C (as for the reference catalyst) and 450 °C (as the temperature of calcination). The former treated under H_2 at 300 °C (0.7cal450-red300) did not show any significant difference with respect to the catalyst without any pre-treatment (Table 15, sample 0.7cal450). It was not surprising since, as discussed in Chapter III, it was observed on the H_2-TPR profile that no reduction occurred below 300 °C, so there are no additional Pt(0) species available for the reaction. In addition, the particle size did not increase, since the material was already stabilised by calcination at a higher temperature (450 °C), so no significant effect on the selectivity was observed. On the other hand, the latter treated under H_2 at 450 °C (0.7cal450-red450) increased the particle size from 4.6 nm to 5.4 nm, without any further Pt reduction taking place, as observed by XPS analysis (Figure 90), leading to an increase of the selectivity up to 100% and a decrease of the activity.

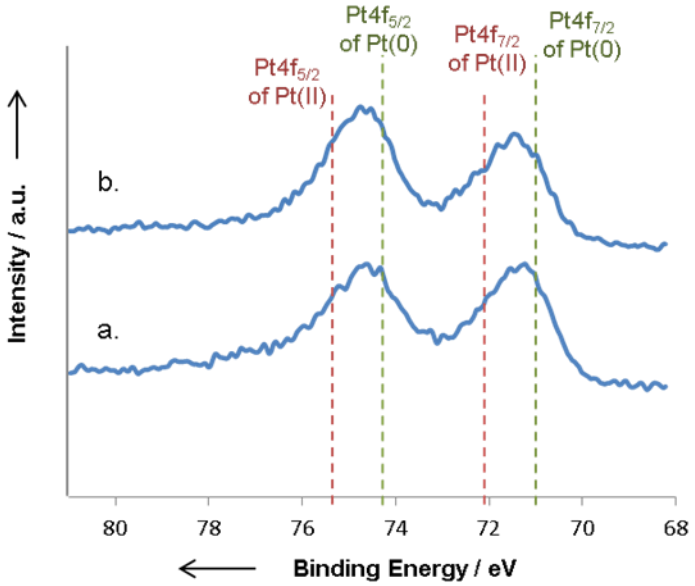

Figure 90. XPS spectra of: a. Hierarchically porous 0.7cal450 calcined at 450 °C and b. Hierarchically porous 0.7cal450-red450 calcined at 450 °C and reduced at 450 °C.

Therefore, given that the Pt catalyst with hierarchical porosity (0.7cal450) was already active directly after calcination, a pre-treatment in hydrogen at 300 °C (0.7cal450-red300) or at 450 °C (0.7cal450-red450) was unnecessary. It was even counterproductive in terms of activity since for 0.7cal450-red450 the initial rate was 20.2 mol_{CNB}/min mol_{Pt}, compared to 33.7 mol_{CNB}/min mol_{Pt} without pre-treatment (0.7cal450), which was due to a decrease of active surface related to an increase of Pt nanoparticle size by sintering at 450 °C (5.4 nm compared to 4.6 nm before pre-treatment). Furthermore, at these reaction conditions (70 °C and 9 bars of hydrogen pressure), reduction pre-treatment was also not required for the reference catalyst (0.7REF) due to an efficient *in situ* reduction at this temperature. However, in case of decreasing the operating temperature below 50 °C, the *in-situ* reduction of 0.7REF would not be as effective as at 70 °C according to its corresponding H_2-TPR (Figure 89).

IV.3.4- Catalyst stability

The catalyst stability was assessed considering the chemical (oxidation state) and structural stability, as well as the performance upon recycling.

As mentioned in the previous section, 0.7cal450 and 0.7cal650 did not require any pre-treatment to be active catalysts. Indeed, the sonochemical synthesis was enough to reduce the Pt precursor and form Pt nanoparticles that were chemically stable mainly in Pt(0) oxidation state, even after a strong oxidation treatment for template removal at temperatures up to 650 °C. More importantly, the stability of our hierarchical catalyst at the catalytic reaction conditions was also evidenced by the XPS results after reaction, where the oxidation state of the used catalyst 0.7cal650 (Figure 88e) was very close to that of the fresh catalyst (Figure 88d).

Regarding the catalyst structural stability, the textural characteristics of 0.7cal450 after reaction showed that the catalyst structure was stable under the evaluated reaction conditions. Notably the specific surface area was determined to be 510 ± 30 m^2/g, which was not significantly different [42] from the initial specific surface area (490 ± 30 m^2/g). Furthermore, additional to the Pt nanoparticles retention test (retention of the active Pt species in the silica support, as reported in the experimental part), elemental analysis of Pt by ICP-OES indicated a stable Pt content in the catalyst, confirming non-detectable Pt leaching from the used catalyst.

In order to evaluate the recyclability of these hierarchically porous materials, another batch of catalyst, namely 0.6cal650 catalyst, was prepared (following the same procedure as described for 0.7cal650) (remark: larger Pt nanoparticle size was obtained for this batch: 11.8 ± 4.2 nm for the batch 0.6cal650 compared to 6.5 ± 2.2 nm nm for the batch 0.7cal650). It was used in five consecutive reaction cycles (each cycle until ca. 50% conversion). No significant Pt leaching was detected after the five cycles (loss of Pt < 3%, which is below the uncertainty of 5%). Figure 91 shows the kinetic profiles for the *p*-CNB hydrogenation over 0.6cal650 catalyst. Figure 91.a shows that the consumption of *p*-CNB becomes slower after the first and second cycles. The initial reaction rate goes from 20.2 ± 2.9 $mol_{CNB}/min\ mol_{Pt}$, in the first use, to 16.3 and 9.2 ± 2.9 $mol_{CNB}/min\ mol_{Pt}$ for the second and third cycles, respectively. However, after the third cycle, the initial reaction rate was almost constant: 9.2, 11.6 and 11.2 ± 2.9 $mol_{CNB}/min\ mol_{Pt}$ for the third, fourth and fifth cycles, respectively (Figure 91.b). Furthermore, no aniline was detected in these experiments (indicating 100% selectivity towards *p*-CAN at ca. 50% conversion of *p*-CNB).

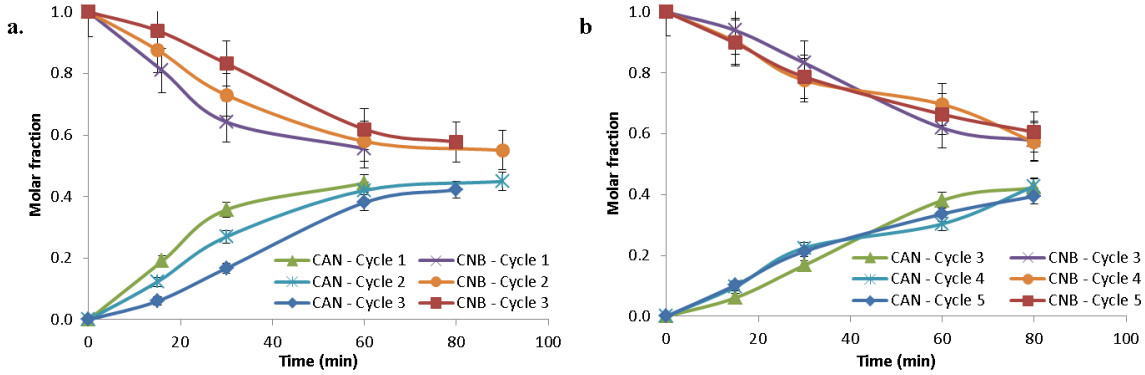

Figure 91. Kinetic profiles for the *p*-CNB hydrogenation over 0.6cal650 catalyst. Conditions: 70 °C and 9 bars.

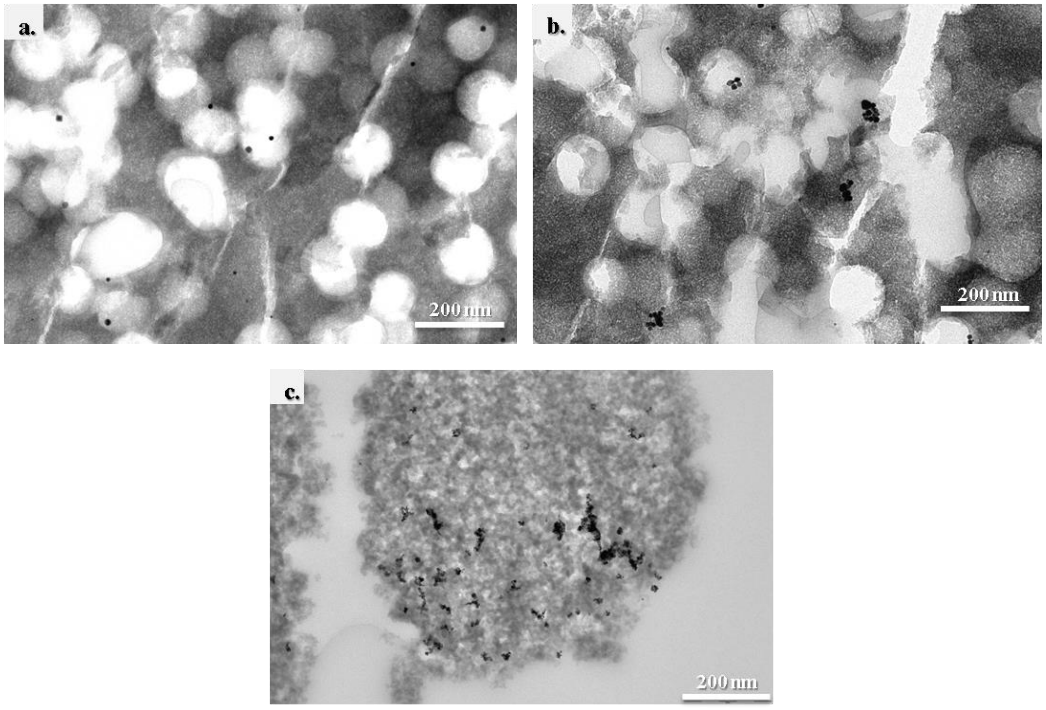

Figure 92. TEM images of porous silica-supported catalysts: a. 0.6cal650, fresh catalyst, b. 0.6cal650 after five catalytic cycles, c. 0.7REF after one catalytic cycle.

The decrease of activity in the three first cycles can be explained by the aggregation of the Pt nanoparticles during the reaction (Figure 92). Indeed, the initial nanoparticles of D_n = 11.8 ± 4.2 nm (Đ = 1.30) (Figure 92.a) formed aggregates of D_n = 20.0 ± 10.4 nm (Đ = 1.66) during the catalytic experiments (Figure 92.b). Such an aggregation did not continue after the third reaction cycle because the mesoporous walls (mesopore size range ca. 2-7 nm) hindered further movement of large Pt aggregates. The aggregation of the Pt nanoparticles was also noticed for the reference mesoporous catalyst (0.7REF, Figure 92.c), which exhibited aggregates of D_n = 14.1 ± 9.6 nm (Đ = 3.76), starting from Pt nanoparticles of 2.9 ± 1.2 nm (Đ = 1.60). Such an aggregation (up to 5 times the initial particle size after one single reaction) took place due to the large mesopore size range in 0.7REF (11-28 nm).

In summary, the hierarchically porous Pt/SiO_2 catalysts exhibited similar textural characteristics before and after being used in the hydrogenation of *p*-CNB (70 °C and 9 bars), evidencing the catalyst structure stability. Elemental analysis of Pt by ICP-OES indicated a stable Pt content in the catalyst, confirming non-detectable Pt leaching from the used catalyst. Furthermore, the Pt nanoparticles were chemically stable mainly in Pt(0) oxidation state, even after a strong oxidation treatment for template removal (up to 650 °C). Nonetheless, given the weak metal-support interaction of Pt and silica [43], the Pt nanoparticles can move within the support. Consequently, when a Pt nanoparticle contacts other Pt particles, they form larger aggregates, which are kept together by cohesive forces. For instance, in catalyst 0.6cal650 (with mesopores of 2-7 nm), the Pt NPs (11.8 ± 4.2 nm) doubled in size by forming aggregates of 20.0 ± 10.4 nm after recycling the catalyst 5 times. This aggregation issue was even more noticeable in the commercial catalyst: after one single use, the aggregates were 5-fold the initial particle size (Pt NPs of 2.9 ± 1.2 nm formed aggregates of 14.1 ± 9.6 nm), which is attributed to its larger mesopores (11-28 nm).

The aggregation of the Pt nanoparticles within the hierarchically porous silica matrix could be limited by decreasing the Pt loading on the polymer template, which would lead to less Pt nanoparticles within a single macropore. Another option would be to use a more diluted hybrid latex template, so that less polymer beads would lead to fewer macropores. This would decrease the probability of several macropores to be in direct contact, hindering the mobility of the Pt nanoparticles out of a single macropore. These two strategies will be discussed in the next two sections.

IV.3.5- Effect of the catalyst macroporosity and of the macropore connectivity on the catalytic performance

In order to study the effect of macropore connectivity on the catalyst performance, including the Pt nanoparticles aggregation during reaction, several samples were prepared varying the amount of macropores in the material and they were evaluated for the selective hydrogenation of *p*-CNB to *p*-CAN.

In four samples, the amount of Pt-decorated macropores (% of macropore volume related to the total catalyst volume) was varied (by using less and less hybrid latex in the formulation): 50%, 33.3%, 25% and 12.5% (0.8cal450-50%, 0.4cal450-33.3%, 0.3cal450-25% and 0.2cal450-12.5%, respectively). A fifth sample was prepared to have 25% of Pt-decorated macroporosity (Pt-polystyrene hybrid latex) and 25% of Pt-free macroporosity (polystyrene latex without Pt nanoparticles) (0.4cal650-25/25%). The sixth sample was prepared with 50% macroporosity (using polystyrene latex without Pt nanoparticles), but the Pt was brought to the material by incipient wetness impregnation and reduction in H_2 at 300 °C for 2 h (1cal650-50%-IWI), instead of sonochemical decoration of the latex template as in the other hierarchically porous materials. These materials are schematised in Figure 93 and Figure 94.

IV.3.5.1- Catalytic performance

The corresponding catalytic performances of the materials described above are presented in Table 17. In the first four rows (0.8cal450-50%, 0.4cal450-33.3%, 0.3cal450-25% and 0.2cal450-12.5%), it can be seen that the initial Pt particle size was not significantly different. A smaller Pt particle size was expected when designing these experiments using less amount of decorated template. Indeed, it was expected that decreasing the amount of decorated template, the Pt nanoparticles sintering would have been limited (by increasing the distance between macropores within the mesoporous matrix). However, as discussed in Chapter III, due to the macropores direct connection as a result of small aggregates of polymer beads, the Pt sintering did not decrease significantly (8.6 ± 3.6 nm for 0.8cal450-50%, compared to 6.7 ± 3.1 nm for 0.2cal450-12.5%). After reaction, those particles formed aggregates that increased the particle size and the standard deviation. Additionally, the aggregates size after reaction did not significantly varied with the percentage of macroporosity (14.0 ± 10.4 nm for 0.8cal450-50%, compared to 12.4 ± 9.2 nm for 0.2cal450-12.5%), which indicates that the aggregation and Pt particle growth is mainly limited by the metal present within a given macropore. Thus, the aggregation of the Pt nanoparticles does not proceed by Pt nanoparticles transfer between macropores through the mesoporous structure (otherwise 0.2cal450-12.5% would have exhibited smaller Pt aggregates). 0.4cal650-25/25% exhibited larger initial particle size before reaction (10.2 ± 3.9 nm) than the previous four samples due to its higher calcination temperature during the synthesis (650 °C instead of 450 °C). Congruently, the aggregates after reaction were also slightly larger (17.0 ± 9.5 nm). Finally, 1cal650-50%-IWI exhibited nanoparticles with large size variation (Đ = 6.16, compared to Đ = 1.46 for 0.4cal650-25/25%), illustrating the lack of control for a spatially homogeneous Pt deposition via incipient wetness impregnation. Indeed, it exhibited an average particle size of 29.7 nm, but with a large variation range between 3 nm and 200 nm. Additionally, it can be noticed that the particle size measured after reaction is

smaller (6.9 nm [2-46 nm]) than before reaction, which might be an artefact given the poor homogeneity of the Pt on the material prepared by impregnation.

Table 17. Effect of the macroporosity on the catalytic performance.

Sample	Theor. macro-porosity (%)	NPs size before reaction D_n (nm) Đ[a]	NPs size after reaction D_n (nm) Đ[a]	Initial reaction rate[b] (mol_{CNB}/ min mol_{Pt})	Apparent Initial reaction rate[c] ($\times 10^{-5}$ mol_{CNB}/ min)	Selectivity at 50 % conversion[d] (%)	Selectivity at 80 % conversion[e] (%)
0.8cal450-50%	50.0	8.6 ± 3.6 (Đ = 1.54)	14.0 ± 10.4 (Đ = 2.34)	21.0	16	93.9	94.5
0.4cal450-33.3%	33.3	7.6 ± 3.4 (Đ = 1.79)	12.2 ± 9.1 (Đ = 2.54)	26.7	11	96.8	97.4
0.3cal450-25%	25.0	8.2 ± 3.7 (Đ = 1.76)	11.8 ± 10.0 (Đ = 3.43)	31.9	10	99.1	97.8
0.2cal450-12.5%	12.5	6.7 ± 3.1 (Đ = 1.68)	12.4 ± 9.2 (Đ = 2.58)	43.5	7	100.0	100.0
0.4cal650-25/25%	50.0	10.2 ± 3.9 (Đ = 1.46)	17.0 ± 9.5 (Đ = 1.90)	31.0	12	100.0	100.0
1cal650-50%-IWI	50.0	29.7 [3-200 nm] (Đ = 6.16)	6.9 [2-46 nm] (Đ = 5.19)	35.9	37	49.4	54.8

[a] Dispersity $Đ=D_w/D_n$, D_w being weight-average diameter and D_n being number-average diameter, determined by TEM. [b] ± 2.9 mol_{CNB}/min mol_{Pt}. [c] ± 1 mol_{CNB}/min. [d] Selectivity to *p*-CAN ± 0.6%. [e] Selectivity to *p*-CAN ± 1.8%. N/A: non-available. Reactions carried out at 70 °C, 9 bars of H_2 with 0.2 g of catalyst, 1 g of *p*-CNB and 100 mL of ethanol as solvent. The catalyst grain size was carefully controlled between 250 and 425 µm in these experiments.

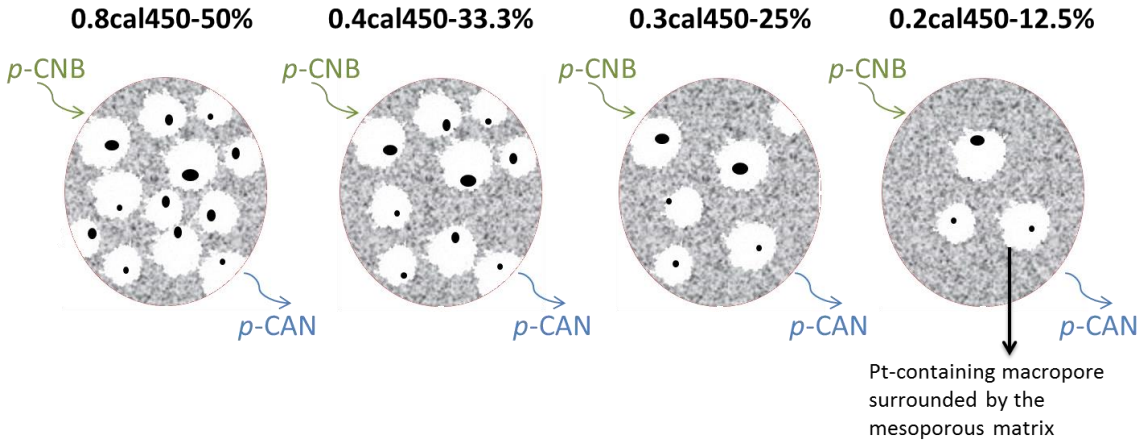

Figure 93. Schematic representation of the variation of active sites when decreasing the amount of decorated macropores.

As shown in Figure 93, the Pt loading in 0.8cal450-50%, 0.4cal450-33.3%, 0.3cal450-25% and 0.2cal450-12.5% decreased when the amount of decorated macroporosity decreased. So when decreasing the amount of Pt, the number of active sites also decreased since the particle size in

these samples was very similar. As a result, a slower apparent initial reaction rate was obtained for the catalysts with lower Pt loadings, as shown in Table 17 (e.g. 16×10^{-5} mol_{CNB}/min for 0.8cal450-50% versus 7×10^{-5} mol_{CNB}/min for 0.2cal450-12.5%). Consequently, as the overall reaction proceeds more slowly, the selectivity is enhanced, as already reported for this reaction [17]. For example, 0.2cal450-12.5% exhibited 100% selectivity towards *p*-CAN at 80% conversion of *p*-CNB, compared with 0.8cal450-50% that only achieved 94.5% selectivity at the same conversion.

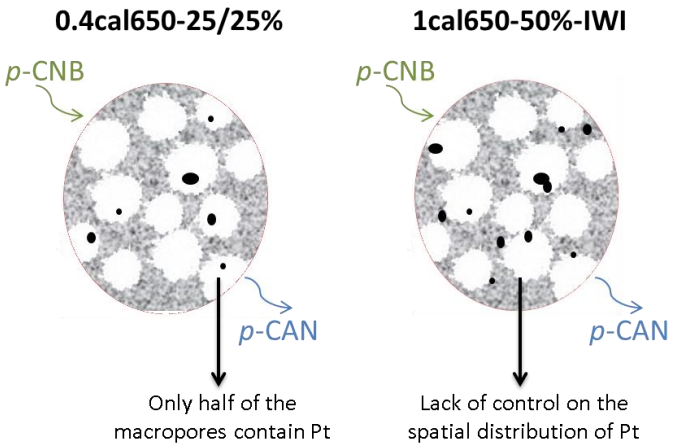

Figure 94. Schematic representation of 0.4cal650-25/25% with half Pt-decorated and half empty macropores (left) and 1cal650-50%-IWI decorated by incipient wetness impregnation (right).

By comparison of two samples with the same amount of Pt, it can be seen that when increasing the total macroporosity with empty macropores, the initial reaction rate was enhanced: 0.4cal450-33.3% (33.3% of total macroporosity) exhibited 26.7 ± 2.9 mol_{CNB}/min mol_{Pt}, versus 0.4cal650-25/25% (50% of total macroporosity) that exhibited 31.0 ± 2.9 mol_{CNB}/min mol_{Pt}. This was observed despite the fact that 0.4cal650-25/25% had less active Pt surface area due to a larger particle size (10.2 ± 3.9 nm), in comparison with 0.4cal450-33.3% (7.6 ± 3.4 nm). Such an improvement can be attributed to the presence of more interconnected networks at 50% macroporosity that enhanced the internal diffusion of products and reactants (the critical volume of spheres at which long-range interconnections occur is 19.9% [44]).

Regarding 1cal650-50%-IWI, it presented a large initial reaction rate (37×10^{-5} mol_{CNB}/min), but in this case, it might be due to large amount of active sites given the fact that this was the only sample reduced *ex-situ* as required after the impregnation. However, it also presented the lowest selectivity (54.8% selectivity at 80% conversion) due to the formation of cyclohexylammonium chloride (as discussed in Annex IV).

With respect to the texture stability after reaction, all used catalysts presented almost constant total BET surface areas and total pore volumes, as shown in Table 18. Only 0.8cal450-50% and 1cal650-50%-IWI presented a slight decrease of surface area (going from 759 m^2/g to 700 m^2/g and from 575 m^2/g to 525 m^2/g, respectively) and porosity (losing 2 and 3% respectively).

Table 18. Texture characterisation before and after reaction by nitrogen physisorption.

	Before reaction			After reaction		
	Total BET Surface Area (m^2/g)	Total pore volume (cm^3/g)	Porosity (%)	Total BET Surface Area (m^2/g)	Total pore volume (cm^3/g)	Porosity (%)
0.8cal450-50%	759	0.56	55	700	0.51	53
0.4cal450-33.3%	729	0.59	57	722	0.64	58
0.3cal450-25%	718	0.60	57	703	0.61	57
0.2cal450-12.5%	694	0.60	57	681	0.58	56
0.4cal650-25/25%	674	0.65	59	668	0.68	60
1cal650-50%-IWI	575	0.77	63	525	0.68	60

Concerning the initial reaction rate in a Pt molar basis, it was observed that when decreasing the amount of decorated macropores, the initial reaction rate increased (e.g. 21.0 $mol_{CNB}/min\ mol_{Pt}$ for 0.8cal450-50% versus 43.5 $mol_{CNB}/min\ mol_{Pt}$ for 0.2cal450-12.5%). A plausible explanation to this unexpected behaviour will be further discussed below.

Up to here, it could be thought that in order to have the same overall activity of 1 g of 0.8cal450-50% with 0.2cal450-12.5%, it would be required almost 2-fold the amount of catalyst:

$$\frac{21.0\,\frac{mol_{CNB}}{min\ mol_{Pt}} \times 0.8\,\% \frac{g_{Pt}}{g_{0.8\text{cal}450-50\%}} \times 1\ g_{0.8\text{cal}450-50\%}}{43.5\,\frac{mol_{CNB}}{min\ mol_{Pt}} \times 0.2\,\% \frac{g_{Pt}}{g_{0.2\text{cal}450-12.5\%}}} = \mathbf{1.93}\ \boldsymbol{g_{0.2\text{cal}450-12.5\%}}$$

However, it represents ca. 50% less Pt and 100% selectivity, instead of 94.5% in the case of 0.8cal450-50%. Moreover, additional empty macropores would further improve the catalytic performance by favouring more interconnected networks as observed for 0.4cal650-25/25% (50% of total macroporosity) that exhibited 31.0 ± 2.9 $mol_{CNB}/min\ mol_{Pt}$ versus 0.4cal450-33.3% (33.3% of total macroporosity) that exhibited 26.7 ± 2.9 $mol_{CNB}/min\ mol_{Pt}$.

IV.3.5.1.i- Initial reaction rate in a Pt molar basis

In order to explain the variations of initial reaction rate in a Pt molar basis, it is important to know if there are any diffusional limitations. It is possible to predict empirically when the diffusion is the controlling step in overall reaction using the Thiele modulus (Φ), which quantifies the ratio of the reaction rate to the diffusion rate in the pellet [45]. For a first-order reaction, the Thiele modulus is given by:

$$\Phi = L\sqrt{\frac{k}{D_e}}$$

Where k is the apparent reaction rate constant, D_e is the effective diffusivity of the reactant and L is a characteristic length scale (e.g. half the thickness of a catalytic slab, or one-third the radius of a spherical catalyst particle). Using the Thiele modulus, it is possible to determine the effectiveness factor (η), which is the ratio between the actual reaction rate and the ideal reaction rate in the absence of any diffusional resistance [45,46]. So when the diffusion limitations are important, η is smaller than the unity. For the first-order reaction in spherical pellets, the effectiveness factor is given by:

$$\eta = \frac{1}{\Phi}\left[\frac{1}{\tanh 3\Phi} - \frac{1}{3\Phi}\right]$$

In a porous medium, the effective diffusivity can be calculated by:

$$D_e = \frac{D_m \varepsilon}{\tau}$$

Where D_m is the bulk diffusivity, ε is the catalyst porosity and τ is the tortuosity factor (which for random networks is equal to 4) [1]. The bulk diffusivity of *p*-CNB in ethanol has not been reported in the literature to my knowledge. So it can be either measured experimentally or predicted using models based on experimental Abraham descriptors [47]. For *p*-CNB, the predicted Abraham descriptors are E =1.297, S=0.251, A=0.000, B=0.254, V=1.548. Using these values in the model created by Hills *et al*. [47], it is possible to calculate the diffusion coefficient of *p*-CNB in ethanol at 298 K:

$$logD_{12} = 0.29 - 0.34A - 0.16B - 0.11V = 0.07908$$

$$D_{12} = (1.20 \pm 0.04) \times 10^{-5} cm^2/s$$

Which is close to the values reported for chlorobenzene and nitrobenzene in ethanol at the same temperature: 1.61×10^{-5} cm^2/s and 1.44×10^{-5} cm^2/s, respectively [47]. It is also larger than the value reported for *p*-CNB in water at 293 K: 0.76×10^{-5} cm^2/s [48].

So the effective diffusion coefficient of *p*-CNB within the catalyst 0.8cal450-50%, which has 64% of porosity, is:

$$D_e = \frac{D_m \varepsilon}{\tau} = \frac{1.20 \times 10^{-5} cm^2/s \times 0.64}{4} = 1.92 \times 10^{-6} cm^2/s = 1.92 \times 10^{-10} m^2/s$$

This value is five orders of magnitude larger than the experimental effective diffusion coefficient for *p*-CNB within HZSM-5 zeolite: 6×10^{-15} m^2/s, in water at 300 K [49].

In order to calculate the effective diffusivity at the temperature of the reaction (70 °C = 343 K), the Stokes-Einstein equation can be used:

$$\frac{D_{T1}}{D_{T2}} = \frac{T1}{T2}\frac{\mu_{T2}}{\mu_{T1}}$$

Where T corresponds to the absolute temperature and μ is the dynamic viscosity of the solvent.

So the effective diffusivity of *p*-CNB in ethanol within the porous catalyst at 343 K is:

$$D_{343\,K} = D_{298\,K}\frac{343\,K}{298\,K}\frac{1.2040\,mPa\,s}{0.4730\,mPa\,s} = 5.62\times10^{-10}m^2/s$$

Using this information, it is possible to calculate the Thiele modulus and the effectiveness factor for each reaction. The results are presented in Table 19. The porosity values are taken from the characterisation presented in Table 12 and the apparent reaction rate constant were calculated as explained in Section IV.3.2.1-*Effect of the hydrogen pressure*. The diameter of catalyst grain size was taken as 450 µm.

Table 19. Thiele moduli and the effectiveness factors for catalysts with different macroporosity

Sample	Pt loading (%)	τ	ε	k (s^{-1})	D_e m^2/s	Φ	η
0.8cal450-50%	0.8	4	0.64	5.58×10^{-4}	5.62×10^{-10}	0.075	0.997
0.4cal450-33.3%	0.4	4	0.61	4.02×10^{-4}	5.36×10^{-10}	0.065	0.997
0.3cal450-25%	0.3	4	0.56	3.15×10^{-4}	4.92×10^{-10}	0.060	0.998
0.2cal450-12.5%	0.2	4	0.56	2.05×10^{-4}	4.92×10^{-10}	0.048	0.999
0.4cal650-25/25%	0.4	4	0.66	4.90×10^{-4}	5.80×10^{-10}	0.069	0.997
1cal650-50%-IWI	1.0	4	0.73	2.19×10^{-3}	6.41×10^{-10}	0.138	0.989

In Table 19, it can be seen that the effective diffusion coefficients did not largely change with the variation of porosity; additionally, the effectiveness factors are close to the unity, meaning that there are not diffusional limitations for this reaction with a grain size of 450 µm. Contrarily, if the calculations were made with the effective diffusion coefficient reported for *p*-CNB within HZSM-5 zeolite (6×10^{-15} m^2/s at 300 K, equivalent to 1.76×10^{-15} m^2/s at 343 K) [49], the Thiele moduli would be as large as 26 and the effectiveness factors, as small as 0.04, confirming that a microporous matrix would largely constrain the reaction by diffusion limitations.

So, keeping in mind the absence of diffusional limitations, the increase of initial reaction rate per mole of Pt as the amount of Pt-decorated macroporosity decreased (Table 17, going from 21.0 ± 2.9 $mol_{CNB}/min\ mol_{Pt}$ using 0.8cal450-50%, to 43.5 ± 2.9 $mol_{CNB}/min\ mol_{Pt}$ using 0.2cal450-12.5%) must be due to an enhanced diffusive flux of product out of the catalyst grain when the Pt loading decreases given by a larger concentration gradient within the catalyst grain when the active sites are more dispersed (*e.g.* 0.2cal450-12.5%). Such enhanced diffusive flux of product would also favour the product desorption from the active sites, which would be readily available for adsorbing a new reactant molecule. A schematic representation of the product gradient is presented in Figure 95. This can be seen by the Fick's first law that relates the diffusive flux (J) to the concentration gradient in space:

$$J = -D\frac{d\varphi}{dx}$$

Where φ is the concentration and D is the diffusion coefficient. So, for a constant diffusion coefficient, when the concentration gradient is large, the diffusive flux is also large.

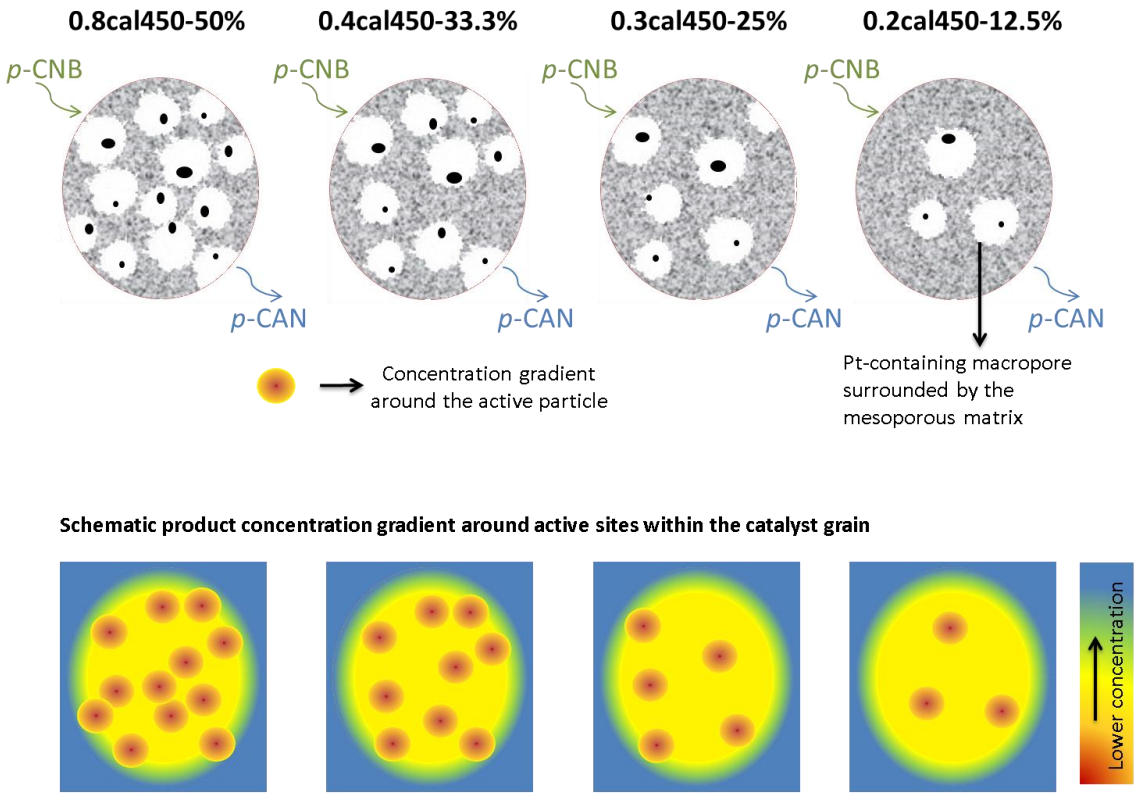

Figure 95. Schematic representation of the variation of product concentration around the Pt nanoparticles within a porous catalyst grain.

Given that in the previous discussion it was concluded that the effective diffusion coefficient does not vary significantly within the four materials represented in Figure 95, the diffusive flux only depends on the concentration gradient. When the Pt particles are more spaced in the whole volume, the concentration gradient between the active site and the immediate vicinity is higher, so the diffusive flux out of the catalyst grain is also higher, improving the catalyst activity in a Pt basis. This is in agreement with the trend observed for the initial reaction rate: 21.0, 26.7, 31.9 and 43.5 ± 2.9 $mol_{CNB}/min\ mol_{Pt}$ for 0.8cal450-50%, 0.4cal450-33.3%, 0.3cal450-25% and 0.2cal450-12.5%, respectively. Also, 0.4cal650-25/25% and 0.3cal450-25% exhibited very similar initial reaction rates of 31.0 and 31.9 ± 2.9 $mol_{CNB}/min\ mol_{Pt}$, respectively, which could be due to a similar distribution of the active sites throughout the catalyst.

These experimental results indicate that in the absence of diffusional limitations, locating the Pt particles far from each other enhances the initial reaction rate per mole of Pt by leading to larger local concentration gradients. However, the limitation of this analysis is that the dimensionless values presented in Table 19 are based on predicted diffusion coefficients. The tortuosity factors could depend on the Thiele modulus [1] and the porosity values measured for these catalysts could be underestimated as discussed in Chapter III. Nevertheless, even if the tortuosity value increased to 10 or the porosity decreased to 0.5, the effective diffusion value would remain within the same order of magnitude. For example, the effective diffusion coefficient for 0.8cal450-50% would change from 5.62×10^{-10} m^2/s to 1.8×10^{-10} m^2/s and the effectiveness

factors in Table 19 would still be close to the unity (0.997 versus 0.989, in this example). In any case, it is strongly recommended to carry out a set of experiments keeping constant the total amount of macroporosity, while decreasing the amount of decorated macropores. This would avoid any interference of the variation of the total porosity. Additionally, it is recommended to measure experimentally the effective diffusion coefficients for these catalysts, so that more reliable effectiveness factors would be obtained.

From this part, it can be concluded that even though no major diffusional limitations were observed by theoretical calculation of the Thiele modulus, for a given Pt loading, an increase in the macroporosity with empty macropores enhances the initial reaction rate (going from 26.7 ± 2.9 mol_{CNB}/min mol_{Pt} with 0.4cal450-33.3% (33.3% macroporosity, all decorated with Pt) to 31.0 ± 2.9 mol_{CNB}/min mol_{Pt} with 0.4cal650-25/25% (50% of total macroporosity, of which only half contains Pt)). Moreover catalysts with lower Pt loading, but similar Pt particle size exhibits higher selectivity and higher initial reaction rate. For instance, 0.2cal450-12.5% exhibited 43.5 ± 2.9 mol_{CNB}/min mol_{Pt} as initial reaction rate and 100% selectivity at 80% conversion, while 0.8cal450-50% exhibited 21.0 ± 2.9 mol_{CNB}/min mol_{Pt} and 94.5% selectivity at the same conversion. Finally, the hierarchically porous materials prepared by sonochemistry were more selective towards *p*-CAN (up to 100%) than an equivalent catalyst prepared by impregnation (1cal650-50%-IWI), which only exhibited 54.8% selectivity at 80% conversion.

IV.3.6- Effect of the catalyst mesoporosity on the catalytic performance

As described in Chapter III, three materials at the same Pt loading were prepared from polystyrene latex templates decorated by sonochemistry with Pt nanoparticles in different reaction set-ups, either at 100, 205 or 343 kHz. This led to materials with slightly different mesopore size ranges, being larger for the catalyst prepared in the reactor at 343 kHz (2-15 nm), followed in order by the one at 205 kHz (2-13 nm) and at 100 kHz (2-9 nm). Additionally, the Pt particle size in these materials slightly decreased when using the set-up at higher ultrasound frequency. The catalytic performances of these materials for the hydrogenation of *p*-CNB are presented in Table 20.

Table 20. Effect of the sonochemical set-ups on the catalytic performance

Sample	Meso-pore size range (nm)	NPs size before reaction D_n (nm) Đ[a]	NPs size after reaction D_n (nm) Đ[a]	Initial reaction rate[b] (mol_{CNB}/ min mol_{Pt})	Selectivity at 50 % conversion[c] (%)	Selectivity at 80 % conversion[d] (%)
0.3cal450-100kHz	2-9	4.7 ± 1.3 (Đ = 1.21)	8.6 ± 6.6 (Đ = 3.03)	57.8	91.9	92.0
0.3cal450-205kHz	2-13	4.5 ± 1.1 (Đ = 1.18)	8.4 ± 7.6 (Đ = 3.11)	74.0	91.5	91.8
0.3cal450-343kHz	2-15	3.9 ± 1.0 (Đ = 1.15)	8.8 ± 7.8 (Đ = 3.26)	91.7	92.1	92.1

[a] Dispersity $Đ=D_w/D_n$, D_w being weight-average diameter and D_n being number-average diameter, determined by TEM. [b] ± 2.9 mol_{CNB}/min mol_{Pt}. [c] Selectivity to *p*-CAN ± 0.6%. [d] Selectivity to *p*-CAN ± 1.8%. N/A: non-available. Reactions carried out at 70 °C, 9 bars of H_2 with 0.2 g of catalyst, 1 g of *p*-CNB and 100 mL of ethanol as solvent. The catalyst grain size was carefully controlled between 250 and 425 µm in these experiments.

As discussed in Chapter III, these three materials had homogeneous distribution of Pt nanoparticles within the material and their macroporous structures exhibited hierarchical meso- and macroporous structures. However, as summarised in Table 20, their mesopore size range was slightly different: 2-9, 2-13 and 2-15 nm for 0.3cal450-100kHz, 0.3cal450-205kHz and 0.3cal450-343kHz, respectively. It enhanced the effective diffusion within the catalyst, increasing the catalyst activity: 57.8, 74.0 and 91.7 ± 2.9 mol_{CNB}/min mol_{Pt} for 0.3cal450-100kHz, 0.3cal450-205kHz and 0.3cal450-343kHz, respectively. Furthermore, the selectivity values towards *p*-CAN obtained with 0.3cal450-100kHz, 0.3cal450-205kHz and 0.3cal450-343kHz were the very similar (92.0%, 91.8% and 92.1%, respectively, at 80 % conversion) because their particle sizes were also alike (4.7 nm, 4.5 nm and 3.9 nm, respectively).

Regarding the Pt aggregates after reaction, it can be seen that they were of about the same size (8.6 nm, 8.4 nm and 8.8 nm for 0.3cal450-100kHz, 0.3cal450-205kHz and 0.3cal450-343kHz, respectively), independently of the mesopore size range. For instance, 0.3cal450-343kHz exhibited the smallest Pt particles (3.9 nm) with the largest mesopore size range (2-15 nm), and the Pt aggregate size (8.8 nm) was about the same as in the other two materials. This supports

the previous observation when evaluating the macroporosity effect on the aggregation of Pt nanoparticles: the aggregation of nanoparticles within this type of hierarchically porous catalysts is limited by the amount of Pt within a given macropore and less by the migration of Pt nanoparticles through the mesoporosity.

Finally, we can compare 0.3cal450-100kHz, 0.3cal450-205kHz and 0.3cal450-343kHz against the best performance of the commercial catalyst: an initial reaction rate of 47.4 ± 2.9 mol_{CNB}/min mol_{Pt} and a selectivity of 92.5 ± 1.8% at 80 % conversion of *p*-CNB (0.7REF-red300, Table 16). It is possible to see that these hierarchically porous catalyst performed much better than the reference commercial material in terms of initial reaction rate (up to 91.7 ± 2.9 mol_{CNB}/min mol_{Pt}) for about the same selectivity (92.1 ± 1.8% at 80 % conversion of *p*-CNB) without the need of any reduction pre-treatment (while the commercial catalyst is *in situ* reduced, provided that the reaction temperature is high enough, i.e. 70 °C). Additionally, the Pt particles aggregation in the commercial catalyst (0.7REF) was more marked (2.9 ± 1.2 nm aggregated up to 14.1 ± 9.6 nm) than for these materials (e.g. for 0.3cal450-343kHz it went from 3.9 ± 1.0 nm to 8.8 ± 7.8 nm). Such an aggregation (up to 5 times the initial particle size after one single reaction) in the case of the commercial catalyst took place due to much larger mesopore size range (11-28 nm).

Regarding the textural characteristics of these hierarchically porous materials, they did not change significantly. Even for the catalyst prepared at 100 kHz with the latex that was the least stable, the specific surface area after reaction was 743 m^2/g compared to 742 m^2/g before reaction. Similarly, 0.3cal450-343kHz went from 610 m^2/g before reaction to 617 m^2/g after reaction.

In conclusion, a larger mesopore size range permitted to enhance the catalyst activity regarding the initial reaction rate since it went from 57.8 ± 2.9 mol_{CNB}/min mol_{Pt} to 91.7 ± 2.9 mol_{CNB}/min mol_{Pt} when the mesopore size range went from 2-9 nm to 2-15 nm. Additionally, since these mesopores were not as large as those in the commercial catalyst (11-28 nm), the Pt nanoparticles aggregation was limited to 8.8 ± 7.8 nm (with a mesopores between 2-15 nm), instead of 14.1 ± 9.6 nm with the commercial catalyst. Finally, with about the same selectivity (ca. 92% at 80% conversion) 0.3cal450-343kHz almost doubled the initial reaction rate of the commercial catalyst (91.7 ± 2.9 mol_{CNB}/min mol_{Pt} versus 47.4 ± 2.9 mol_{CNB}/min mol_{Pt}) which could be attributed to the hierarchical porosity in 0.3cal450-343kHz.

IV.4- Conclusions

The combination of latex synthesis, sonochemistry and sol-gel process allowed preparing waterborne Pt-based materials that showed to be active catalysts in the selective hydrogenation of *p*-CNB to produce *p*-CAN without requiring any catalyst reduction pre-treatment nor *in-situ* reduction. Additionally, their micro-structure was stable under the reaction conditions. The catalytic performance of these materials was assessed in terms of the selectivity towards *p*-CAN, the initial reaction rate, as well as the stability.

In a general manner, these hierarchically porous materials can be considered efficient catalysts for this reaction. It is important to note that they exhibited better selectivity (up to 100% at 80% conversion) than a commercially-available reference catalyst (up to 92.5% at 80% conversion). The main parameter that permitted to enhance the selectivity was the Pt particle size. The best size seemed to be ca. 7 nm. On these large metal particles the product *p*-CAN is adsorbed less strongly in comparison with the reactant *p*-CNB, decreasing the likelihood of *p*-CAN to be hydrogenated further towards aniline [19]. Such particle size was achieved either by calcination at high temperature (650 °C) or by increasing the Pt loading on the hybrid polymer template (ca. 1 wt. % Pt/polystyrene). Catalysts with lower Pt loading, but similar Pt particle size (obtained by using less amount of Pt decorated latex template) also showed enhanced selectivity. For example, the sample 0.2cal450-12.5% (with 0.2 wt. % Pt/SiO_2 and particles of 6.7 ± 3.1 nm) exhibited 100% selectivity at 80% conversion.

A hierarchically porous matrix decorated with Pt by incipient wetness impregnation and subsequent reduction under hydrogen flow was also prepared and evaluated in the hydrogenation reaction of *p*-CNB. Under similar conditions, it exhibited very poor selectivity towards *p*-CAN (54.8% at 80% conversion). Important amount of by-products, including aniline and cyclohexylammonium chloride, were formed with this catalyst. This behaviour was attributed to the lack of control to achieve narrow Pt particle size distributions (e.g. 1cal650-50%-IWI exhibited Pt particles of size between 3 and 200 nm).

In terms of catalytic activity, the hierarchically porous catalysts have also been superior to the commercial catalyst. For instance, the sample 0.3cal450-343kHz exhibited an initial reaction rate of 91.7 ± 2.9 $mol_{CNB}/min\ mol_{Pt}$, much higher than that obtained with the commercial catalyst (47.4 ± 2.9 $mol_{CNB}/min\ mol_{Pt}$). Such an improvement was attributed to the hierarchical porosity with a large mesoporous size (2-15 nm) obtained by preparing the decorated template in the sonochemical set-up at 343 kHz (with moderate sonochemical activity). Nevertheless, very large mesoporosity could promote the Pt nanoparticles aggregation as in the case of the commercial catalyst, in which the mesopores of 11-28 nm permitted the aggregation of initial Pt particles of 2.9 ± 1.2 nm up to 14.1 ± 9.6 nm, compared with 0.3cal450-343kHz (with mesopores of 2-15 nm), in which the initial Pt particles of 3.9 ± 1.0 nm only aggregated up to 8.8 ± 7.8 nm.

In general, no major diffusional limitations were observed in the hierarchically porous materials by calculation of the Thiele modulus and effectiveness factors. However, it was observed that for a given Pt loading, an increase in the macroporosity slightly enhanced the initial reaction rate: 0.4cal650-25/25% (50% of total macroporosity) exhibited 31.0 ± 2.9 $mol_{CNB}/min\ mol_{Pt}$

versus 0.4cal450-33.3% (33.3% of total macroporosity) that exhibited 26.7 ± 2.9 mol_{CNB}/min mol_{Pt}, this was observed despite the fact that 0.4cal650-25/25% had less active Pt surface area due to a larger particle size (10.2 ± 3.9 nm), in comparison with 0.4cal450-33.3% (7.6 ± 3.4 nm). Such an improvement was attributed to the presence of more interconnected macropores at 50% of total macroporosity that enhanced the internal diffusion of products and reactants.

IV.4.1- Perspectives

In order to study more in detail the effect of the Pt loading on the selectivity, it is recommended to carry out a set of experiments keeping constant the total amount of macroporosity, while decreasing the amount of decorated macropores. This would avoid any interference of the variation of the total porosity. Additionally, it is recommended to measure experimentally the effective diffusion coefficients for these catalysts, so that more reliable effectiveness factors would be obtained.

Regarding the possibilities for catalyst rational design by this combination of latex synthesis, sonochemistry and sol-gel process, the smallest Pt particle size achievable at a given Pt loading is limited by the calcination temperature required for removing the polystyrene template (at least
450 °C in the presence of Pt). For instance, at 0.7 wt. % Pt/SiO_2, the smallest particle size was 4.6 nm ± 1.1 nm (0.7cal450). This opens the possibilities to optimise this catalyst preparation method by using, for instance, polymer latex templates with lower degradation temperature so that they could be removed in milder conditions. Alternatively, it would be worth investigating polymers soluble in green solvents like supercritical carbon dioxide for template removal by supercritical extraction at temperature less than 100 °C [50].

The strategy explored in this work is part of a larger catalyst engineering approach for the preparation of silica-supported materials with hierarchical porosity. It is important to have in mind that the catalytic tests discussed herein were carried out in batch conditions, at which there are not marked mass transport limitations. Contrarily, catalytic tests in dynamic flow conditions through a porous monolithic contactor would take advantage of the hierarchical porous characteristics of these materials, considering the higher mass transport limitations that a continuous-flow operation requires to overcome. For such operation conditions, this waterborne catalyst preparation method is versatile enough to allow the preparation by dip-coating of monolithic pieces such as honeycombs structures or solid foams, maintaining the hierarchical micro-structure described herein. Moreover, this technique permits to optimise the catalyst effectiveness since it is possible to modify the effective diffusion within the catalyst by modifying the catalyst meso- and macroporosity, and simultaneously adjust the selectivity and intrinsic reaction rate by controlling the distribution of active sites within the catalyst and modifying the particle size by varying the metal loading and the calcination temperature. Another possible improvement is to modify the amorphous silica matrix into a zeolite more stable phase by pseudomorphic transformation [51]. Furthermore, based on this catalyst preparation method, other metals and/or metal oxides (e.g. Pd or CeO_2) could be incorporated within the support, as it will be discussed in Chapter V and VI.

IV.5- References

[1] M.-O. Coppens, G. Wang, Optimal Design of Hierarchically Structured Porous Catalysts, in: U.S. Ozkan (Ed.), Des. Heterog. Catal., Wiley-VCH Verlag GmbH & Co. KGaA, Weinheim, Germany, 2009: pp. 25–58. doi:10.1002/9783527625321.

[2] A.F. Sierra Salazar, T. Chave, A. Ayral, S.I. Nikitenko, V. Hulea, P.J. Kooyman, F.D. Tichelaar, S. Perathoner, P. Lacroix-Desmazes, Engineering of silica-supported platinum catalysts with hierarchical porosity combining latex synthesis, sonochemistry and sol-gel process – I. Material preparation, Microporous Mesoporous Mater. (2016) 207–214. doi:10.1016/j.micromeso.2016.07.009.

[3] P. Serna, A. Corma, Transforming Nano Metal Nonselective Particulates into Chemoselective Catalysts for Hydrogenation of Substituted Nitrobenzenes, ACS Catal. 5 (2015) 7114–7121. doi:10.1021/acscatal.5b01846.

[4] P.T. Anastas, J.C. Warner, Green Chemistry: Theory and Practice, Oxford University Press, New York, 1998.

[5] X. Wang, M. Liang, J. Zhang, Y. Wang, Selective Hydrogenation of Aromatic Chloronitro Compounds, Curr. Org. Chem. 11 (2007) 299–314. doi:10.2174/138527207779940856.

[6] G.Y. Fan, L. Zhang, H.Y. Fu, M.L. Yuan, R.X. Li, H. Chen, X.J. Li, Hydrous zirconia supported iridium nanoparticles: An excellent catalyst for the hydrogenation of haloaromatic nitro compounds, Catal. Commun. 11 (2010) 451–455. doi:10.1016/j.catcom.2009.11.021.

[7] M. Oubenali, G. Vanucci, B. Machado, M. Kacimi, M. Ziyad, J. Faria, A. Raspolli-Galetti, P. Serp, Hydrogenation of p-chloronitrobenzene over nanostructured-carbon-supported ruthenium catalysts, ChemSusChem. 4 (2011) 950–956. doi:10.1002/cssc.201000335.

[8] K. Layek, M.L. Kantam, M. Shirai, D. Nishio-Hamane, T. Sasaki, H. Maheswaran, Gold nanoparticles stabilized on nanocrystalline magnesium oxide as an active catalyst for reduction of nitroarenes in aqueous medium at room temperature, Green Chem. 14 (2012) 3164–3174. doi:10.1039/c2gc35917k.

[9] Y. Wang, Z. Rong, Y. Wang, P. Zhang, Y. Wang, J. Qu, Ruthenium nanoparticles loaded on multiwalled carbon nanotubes for liquid-phase hydrogenation of fine chemicals: An exploration of confinement effect, J. Catal. 329 (2015) 95–106. doi:10.1016/j.jcat.2015.04.034.

[10] F. Li, R. Ma, B. Cao, H. Song, J. Liang, H. Song, Effect of loading method on selective

hydrogenation of chloronitrobenzenes over amorphous Ni-B/CNTs catalysts, Catal. Commun. 80 (2016) 1–4. doi:10.1016/j.catcom.2016.03.009.

[11] A.B. Dongil, L. Pastor-Pérez, J.L.G. Fierro, N. Escalona, A. Sepúlveda-Escribano, Synthesis of palladium nanoparticles over graphite oxide and carbon nanotubes by reduction in ethylene glycol and their catalytic performance on the chemoselective hydrogenation of para-chloronitrobenzene, Appl. Catal. A Gen. 513 (2016) 89–97. doi:10.1016/j.apcata.2015.11.048.

[12] C. Lu, M. Wang, Z. Feng, Y. Qi, F. Feng, L. Ma, Q. Zhang, X. Li, A phosphorus–carbon framework over activated carbon supported palladium nanoparticles for the chemoselective hydrogenation of para-chloronitrobenzene, Catal. Sci. Technol. 7 (2017) 1581–1589. doi:10.1039/C7CY00157F.

[13] R. Baltzly, A.P. Phillips, The catalytic hydrogenolysis of halogen compounds, J. Am. Chem. Soc. 68 (1946) 261–265. doi:10.1021/ja01206a034.

[14] B. Coq, A. Tijani, F. Figuéras, Influence of alloying platinum for the hydrogenation of p-chloronitrobenzene over PtM/Al2O3 catalysts with M=Sn, Pb, Ge, Al, Zn, J. Mol. Catal. 71 (1992) 317–333. doi:10.1016/0304-5102(92)85022-8.

[15] X. Han, R. Zhou, G. Lai, X. Zheng, Influence of support and transition metal (Cr, Mn, Fe, Co, Ni and Cu) on the hydrogenation of p-chloronitrobenzene over supported platinum catalysts, Catal. Today. 93-95 (2004) 433–437. doi:10.1016/j.cattod.2004.06.053.

[16] X.X. Han, Q. Chen, R.X. Zhou, Study on the hydrogenation of p-chloronitrobenzene over carbon nanotubes supported platinum catalysts modified by Mn, Fe, Co, Ni and Cu, J. Mol. Catal. A Chem. 277 (2007) 210–214. doi:10.1016/j.molcata.2007.07.052.

[17] R. Mistri, J. Llorca, B.C. Ray, A. Gayen, Pd0.01Ru0.01Ce0.98O2-δ: A highly active and selective catalyst for the liquid phase hydrogenation of p-chloronitrobenzene under ambient conditions, J. Mol. Catal. A Chem. 376 (2013) 111–119. doi:10.1016/j.molcata.2013.04.018.

[18] S. Iihama, S. Furukawa, T. Komatsu, Efficient catalytic system for chemoselective hydrogenation of halonitrobenzene to haloaniline using PtZn intermetallic compound, ACS Catal. 6 (2016) 742–746. doi:10.1021/acscatal.5b02464.

[19] B. Coq, A. Tijani, R. Dutartre, F. Figuéras, Influence of support and metallic precursor on the hydrogenation of p-chloronitrobenzene over supported platinum catalysts, J. Mol. Catal. 79 (1993) 253–264. doi:10.1016/0304-5102(93)85106-4.

[20] X. Han, R. Zhou, X.M. Zheng, H. Jiang, Effect of rare earths on the hydrogenation properties of p- chloronitrobenzene over polymer-anchored platinum catalysts, J. Mol.

Catal. A Chem. 193 (2003) 103–108. doi:10.1016/S1381-1169(02)00178-4.

[21] V. Pandarus, R. Ciriminna, F. Béland, M. Pagliaro, A new class of heterogeneous platinum catalysts for the chemoselective hydrogenation of nitroarenes, Adv. Synth. Catal. 353 (2011) 1306–1316. doi:10.1002/adsc.201000945.

[22] B. Coq, A. Tijani, F. Figuéras, Particle size effect on the kinetics of p-chloronitrobenzene hydrogenation over platinum/alumina catalysts, J. Mol. Catal. 68 (1991) 331–345. doi:10.1016/0304-5102(91)80091-G.

[23] J. Ning, J. Xu, J. Liu, H. Miao, H. Ma, C. Chen, X. Li, L. Zhou, W. Yu, A remarkable promoting effect of water addition on selective hydrogenation of p-chloronitrobenzene in ethanol, Catal. Commun. (2007). doi:10.1016/j.catcom.2007.01.032.

[24] Z. Sun, H. Zhang, G. An, G. Yang, Z. Liu, Supercritical CO2-facilitating large-scale synthesis of CeO2 nanowires and their application for solvent-free selective hydrogenation of nitroarenes, J. Mater. Chem. (2010). doi:10.1039/b921510g.

[25] H. Cheng, X. Meng, Y. Yu, F. Zhao, The effect of water on the hydrogenation of o-chloronitrobenzene in ethanol, n-heptane and compressed carbon dioxide, Appl. Catal. A Gen. (2013). doi:10.1016/j.apcata.2013.01.028.

[26] Y.Y. Chen, J.S. Qiu, X.K. Wang, J.H. Xiu, Preparation and application of highly dispersed gold nanoparticles supported on silica for catalytic hydrogenation of aromatic nitro compounds, J. Catal. (2006). doi:10.1016/j.jcat.2006.05.028.

[27] C.H. Campos, B.F. Urbano, C.C. Torres, J.A. Alderete, A Novel Synthesis of Gold Nanoparticles Supported on Hybrid Polymer/Metal Oxide as Catalysts for p-Chloronitrobenzene Hydrogenation, J. Chem. 2017 (2017) 1–9. doi:10.1155/2017/7941853.

[28] C. Lian, H. Liu, C. Xiao, W. Yang, K. Zhang, Y. Liu, Y. Wang, Solvent-free selective hydrogenation of chloronitrobenzene to chloroaniline over a robust Pt/Fe3O4 catalyst, Chem. Commun. (2012). doi:10.1039/c2cc16620h.

[29] M. Liu, X. Mo, Y. Liu, H. Xiao, Y. Zhang, J. Jing, V.L. Colvin, W.W. Yu, Selective hydrogenation of o-chloronitrobenzene using supported platinum nanoparticles without solvent, Appl. Catal. A Gen. 439-440 (2012) 192–196. doi:10.1016/j.apcata.2012.07.006.

[30] Y. Wang, Y. Yang, Y. Li, J. Lai, K. Sun, A green synthesis route of ortho-chloroaniline: Solvent-free selective hydrogenation of ortho-chloronitrobenzene over Pt–Ru/Fe3O4/C catalyst, Catal. Commun. 19 (2012) 110–114. doi:10.1016/j.catcom.2011.12.014.

[31] B. Zuo, Y. Wang, Q. Wang, J. Zhang, N. Wu, L. Peng, L. Gui, X. Wang, R. Wang, D. Yu, An efficient ruthenium catalyst for selective hydrogenation of ortho-chloronitrobenzene prepared via assembling ruthenium and tin oxide nanoparticles, J. Catal. (2004). doi:10.1016/j.jcat.2003.12.007.

[32] V. Kratky, M. Kralik, M. Mecarova, M. Stolcova, L. Zalibera, M. Hronec, Effect of catalyst and substituents on the hydrogenation of chloronitrobenzenes, Appl. Catal. A Gen. 235 (2002) 225–231. doi:10.1016/S0926-860X(02)00274-0.

[33] C.M.A. Parlett, K. Wilson, A.F. Lee, Hierarchical porous materials: catalytic applications, Chem. Soc. Rev. 42 (2013) 3876–3893. doi:10.1039/c2cs35378d.

[34] G. Wang, M.O. Coppens, Rational design of hierarchically structured porous catalysts for autothermal reforming of methane, Chem. Eng. Sci. 65 (2010) 2344–2351. doi:10.1016/j.ces.2009.09.079.

[35] F. Cárdenas-Lizana, Y. Hao, M. Crespo-Quesada, I. Yuranov, X. Wang, M. a Keane, L. Kiwi-Minsker, Selective Gas Phase Hydrogenation of p -Chloronitrobenzene over Pd Catalysts: Role of the Support, ACS Catal. 3 (2013) 1386–1396. doi:10.1021/cs4001943.

[36] L. Jiang, H. Gu, X. Xu, X. Yan, Selective hydrogenation of o-chloronitrobenzene (o-CNB) over supported Pt and Pd catalysts obtained by laser vaporization deposition of bulk metals, J. Mol. Catal. A Chem. 310 (2009) 144–149. doi:10.1016/j.molcata.2009.06.009.

[37] R.B. Mane, A.S. Potdar, J.M. Nadgeri, N.S. Biradar, C. V. Rode, Selectivity tuning options in hydrogenation of m-chloronitrobenzene to m -chloroaniline over mono- and bimetallic supported Pt catalysts, Ind. Eng. Chem. Res. 51 (2012) 15564–15572. doi:10.1021/ie301363x.

[38] N. Boufaden, R. Akkari, B. Pawelec, J.L.G. Fierro, M.S. Zina, A. Ghorbel, Dehydrogenation of methylcyclohexane to toluene over partially reduced silica-supported Pt-Mo catalysts, J. Mol. Catal. A Chem. 420 (2016) 96–106. doi:10.1016/j.molcata.2016.04.011.

[39] J.F. Moulder, W.F. Stickle, P.E. Sobol, K.D. Bomben, Handbook of X-ray photoelectron spectroscopy: a reference book of standard spectra for identification and interpretation of XPS data, Physical Electronics Division, Perkin-Elmer Corporation, 1992.

[40] F. Coloma, A. Sepulveda-Escribano, J.L.G. Fierro, F. Rodriguez-Reinso, Preparation of Platinum Supported on Pregraphitized Carbon Blacks, Langmuir. 10 (1994) 750–755. doi:10.1021/la00015a025.

[41] K.N. Han, C.A. Li, M.-P.N. Bui, X.-H. Pham, B.S. Kim, Y.H. Choa, G.H. Seong, Development of Pt/TiO2 nanohybrids-modified SWCNT electrode for sensitive

hydrogen peroxide detection, Sensors Actuators B Chem. 174 (2012) 406–413. doi:10.1016/j.snb.2012.08.066.

[42] A. Badalyan, P. Pendleton, Analysis of Uncertainties in Manometric Gas-Adsorption Measurements. I: Propagation of Uncertainties in BET Analyses, Langmuir. 19 (2003) 7919–7928. doi:10.1021/la020985t.

[43] D. Sellick, D. Morgan, S. Taylor, Silica Supported Platinum Catalysts for Total Oxidation of the Polyaromatic Hydrocarbon Naphthalene: An Investigation of Metal Loading and Calcination Temperature, Catalysts. 5 (2015) 690–702. doi:10.3390/catal5020690.

[44] R.M. Ziff, S. Torquato, Percolation of disordered jammed sphere packings, J. Phys. A Math. Theor. 50 (2017) 085001. doi:10.1088/1751-8121/aa5664.

[45] E.L. Cussler, Diffusion - Mass Transfer in Fluid Systems, 1997.

[46] N. Gemo, P. Biasi, P. Canu, T.O. Salmi, Mass transfer and kinetics of H2O2 direct synthesis in a batch slurry reactor, Chem. Eng. J. 207-208 (2012) 539–551. doi:10.1016/j.cej.2012.07.015.

[47] E.E. Hills, M.H. Abraham, A. Hersey, C.D. Bevan, Diffusion coefficients in ethanol and in water at 298K: Linear free energy relationships, Fluid Phase Equilib. 303 (2011) 45–55. doi:10.1016/j.fluid.2011.01.002.

[48] J.H. Montgomery, Groundwater Chemicals Desk Reference, Fourth Edition, (2007) 1752. doi:10.1201/9781420009132.

[49] Z. Guo, S. Zheng, Z. Zheng, F. Jiang, W. Hu, L. Ni, Selective adsorption of p-chloronitrobenzene from aqueous mixture of p-chloronitrobenzene and o-chloronitrobenzene using HZSM-5 zeolite, Water Res. 39 (2005) 1174–1182. doi:10.1016/j.watres.2004.12.031.

[50] Z. Ma, P. Lacroix-Desmazes, Synthesis of hydrophilic/CO2-philic poly(ethylene oxide)-b-poly(1,1,2,2-tetrahydroperfluorodecyl acrylate) block copolymers via controlled/living radical polymerizations and their properties in liquid and supercritical CO2, J. Polym. Sci. Part A Polym. Chem. 42 (2004) 2405–2415. doi:10.1002/pola.20117.

[51] M. Mańko, J. Vittenet, J. Rodriguez, D. Cot, J. Mendret, S. Brosillon, W. Makowski, A. Galarneau, Synthesis of binderless zeolite aggregates (SOD, LTA, FAU) beads of 10, 70µm and 1mm by direct pseudomorphic transformation, Microporous Mesoporous Mater. 176 (2013) 145–154. doi:10.1016/j.micromeso.2013.04.006.

V. PALLADIUM-BASED CATALYSTS PREPARATION

Contents

Some of the results described in this chapter have been published:

> A.F. Sierra Salazar, W.S.J. Li, M. Bathfield, A. Ayral, S. Abate, T. Chave, S. Nikitenko, V. Hulea, S. Perathoner, P. Lacroix-Desmazes. "Hierarchically porous Pd/SiO2 catalyst by combination of miniemulsion polymerisation and sol-gel method for the direct synthesis of H_2O_2". *Catalysis Today* (2016), DOI: 10.1016/j.cattod.2016.12.021.

V.1- Introduction

Metal catalysts are important in organic synthesis. Particularly, for industrial applications, they should be economical exhibiting high activity at low loadings [1–3]. Palladium-based catalysts are important materials for a wide variety of reactions, so they have been considered as promising catalysts to carry out reactions under mild conditions in the efforts to develop greener processes [4]. Being slightly cheaper than platinum, this metal exhibits different catalytic behavior [5]. So for certain reactions, palladium leads to better selectivity, which motivates the tailoring of even more performant Pd-based catalysts. For instance, palladium is the metal of choice for most catalyst formulations for the direct synthesis of H_2O_2 from H_2 and O_2 [6]. In order to develop more performing catalysts, superior preparation techniques are required in order to control homogeneous metal dispersion within the support, while keeping small metal particles [7]. Additionally, a support with a hierarchically porous structure is desired in order to avoid mass transport limitations [8].

This chapter is dedicated to the preparation of silica-supported Pd catalysts based on the methodology previously described in Chapter III. Four approaches were investigated exploiting the versatility of the different preparation steps in order to lead to materials with hierarchical porosity having low Pd loadings, exhibiting nanoparticles of different nature such as monometallic Pd, bimetallic Pt-Pd and mixed metallic-metal oxide Pd-CeO_2.

The first approach is the preparation of Pd-based catalysts by a combination of polystyrene latex synthesis by emulsion polymerisation, functionalisation using sonochemistry and silica matrix

synthesis by sol-gel method (Figure 96.a.). The second one utilises the versatility of the sonochemical technique to create Pt-Pd bimetallic nanoparticles by a subsequent functionalisation of the polystyrene beads (Figure 96.b.). The third one comprises the synthesis of a hybrid latex template containing CeO_2 nanoparticles at the surface of the polymer beads. The template is then functionalised with Pd by sonochemical reduction and subsequently, the silica matrix is prepared via sol-gel method (Figure 96.c.). The last approach is the preparation of hybrid Pd/polystyrene latex template via miniemulsion polymerisation (Figure 96.d.). All these approaches are waterborne, which contributes to a sustainable catalyst design.

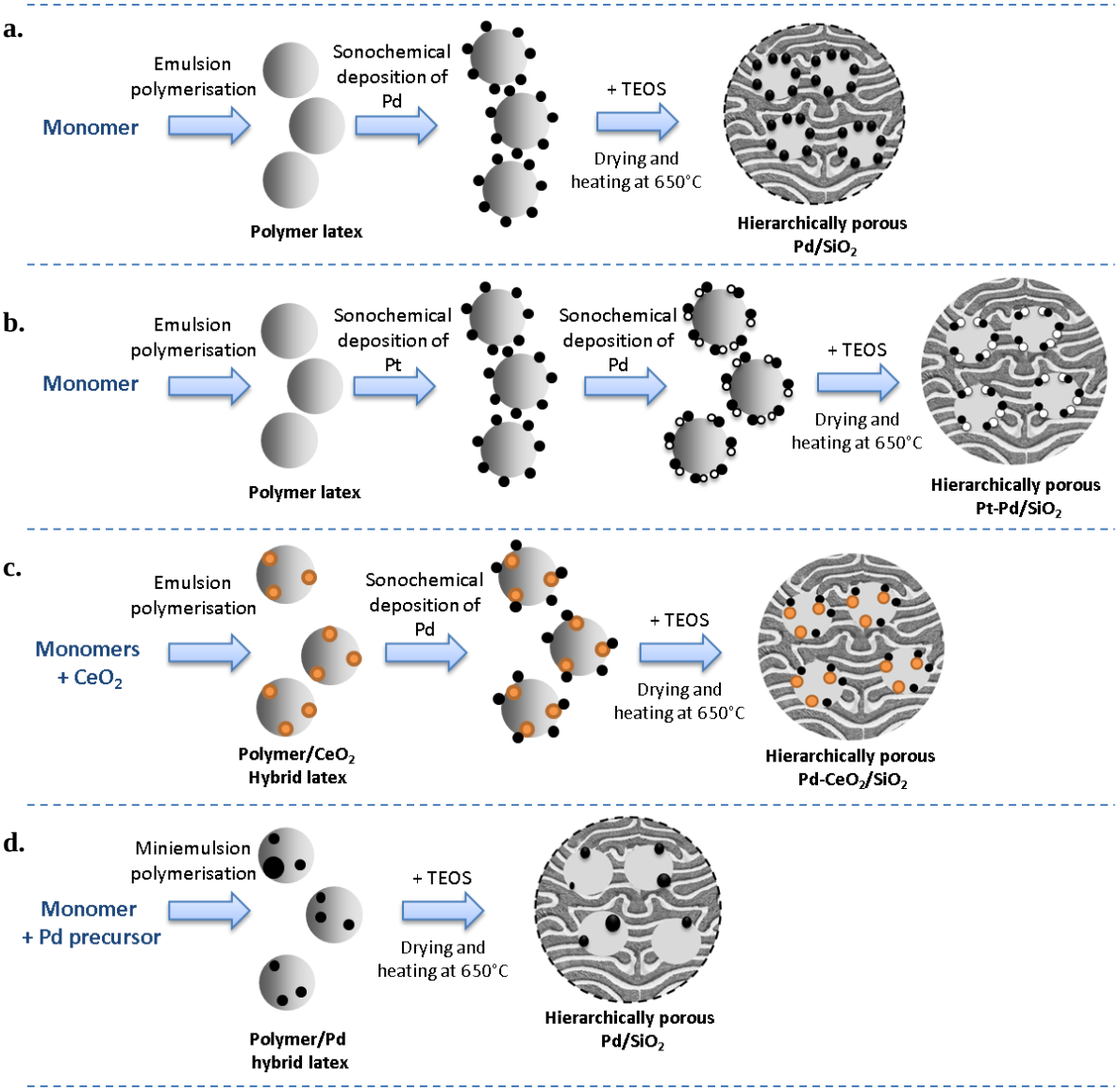

Figure 96. Strategies for the preparation of hierarchically porous Pd-based catalysts: a. Pd/SiO_2 via sol-gel synthesis with sonochemically decorated latex template, b. $Pt\text{-}Pd/SiO_2$ via sol-gel synthesis with sonochemically decorated latex template, c. $Pd\text{-}CeO_2/SiO_2$ via sol-gel synthesis with sonochemically decorated hybrid latex template and d.Pd/SiO_2 via sol-gel synthesis with hybrid latex template.

V.2- Experimental

V.2.1- Materials

Potassium persulfate ($K_2S_2O_8$, KPS, 99%, Sigma Aldrich), sodium metabisulfite ($Na_2S_2O_5$, SMBS, 97%, Sigma Aldrich), ammonium persulfate ($(NH_4)_2S_2O_8$, APS, 98%, Sigma Aldrich), sodium dodecylbenzenesulfonate (SDBS, 99%, Sigma Aldrich), sodium tetrachloroplatinate (Na_2PtCl_4, 84%, Strem), sodium tetrachloropalladate (Na_2PdCl_4, 99.9%, Sigma Aldrich), palladium (II) acetylacetonate ($Pd(acac)_2$, 99%, Sigma Aldrich), tetraethyl orthosilicate (TEOS, 98%, Sigma Aldrich), n-hexadecane (99%, Acros), 1,4-dioxane (99%, Merck), commercial cerium oxide aqueous dispersion (Nanobyk-3810, 18 wt.%, Byk Chemie) were used as received. 2,2'-Azobis(2-methylpropionitrile) (AIBN, 98%, Sigma Aldrich) was purified by recrystallization in methanol. Styrene (99%, Sigma Aldrich), methyl acrylate (99%, Alfa Aesar), butyl acrylate (BA, Aldrich, 99%) and acrylic acid (AA, Aldrich, 99%) were purified by distillation. Hydrochloric acid (HCl, 37%, Sigma Aldrich), sodium hydroxide (NaOH, 98%, Sigma Aldrich) and ammonium hydroxide (NH_4OH, 28%, Sigma Aldrich) were used to prepare acidic and basic solutions with deionised water (1 microS/cm, D8 ion exchange demineraliser from A2E Affinage de L'Eau, or 18.2 MΩ·cm at 25 °C, Milli-Q). Dibenzyl trithiocarbonate (DBTTC) was synthesised as described in the literature [9].

V.2.2- Polystyrene latex template synthesis

The polystyrene latex template was prepared by emulsion polymerisation of styrene using a redox initiator system: KPS and SMBS, as described in Chapter III. Briefly, the polymerisation was carried out with a molar ratio styrene : water : KPS : MBSS : SDBS = 1 : 50 : 5×10^{-3} : 3.2×10^{-3} : 6.6×10^{-4}, in a 350 mL double-walled glass reactor with a glass stirring blade at 250 rpm, under Ar atmosphere. The temperature was regulated as follows: 1 h at 65 °C, 2 h at 72 °C and 3 h at 85 °C. The latex pH (PHM210 standard pH meter, Radiometer Analytical, France) and percentage of solids (MLS moisture analyser, KERN, Germany) were then measured. The latex particle size was determined by dynamic light scattering (DLS) with a Vasco particle size analyser (Cordouan Technologies, France) and by scanning electron microscopy (SEM) with a high resolution SEM Hitachi S-4800 (Hitachi, Japan). The polydispersity index (PDI) was obtained from the cumulants analysis of the DLS intensity correlation [10]. Typically, the samples for DLS measurements were prepared by diluting 5 µL of latex at 10 % solids in 5 mL of deionised water. Latex samples for SEM were dried overnight in a vacuum Raypa® drying oven (Espinar S. L., Spain) at 40 °C and 0.01 mbar. The SEM images were analysed manually using ImageJ software (USA National Institutes of Health). The latex dispersity ($Đ$) was calculated as the ratio of the weight-average diameter (D_w) over the number-average diameter (D_n). For a typical polystyrene latex, the pH was 2.0 and the particle size characterisation revealed a D_n of 134 nm, a D_w of 140 nm, and a $Đ$ of 1.04.

V.2.3- Hybrid CeO_2-containing poly(styrene-*co*-methyl acrylate) latex template synthesis

This latex was prepared by emulsion polymerisation following a procedure adapted from previous works described somewhere else [11,12]. Briefly, a macro-RAFT agent constituted of amphipathic oligomers of poly(BA_5-*co*-AA_5) was prepared by copolymerisation of butyl acrylate (10.60 g) and acrylic acid (6.03 g) in 1,4-dioxane (24.95 g) at 70 °C, using AIBN (0.24 g) as initiator and DBTTC (4.80 g) as RAFT agent (DBTTC: AIBN molar ratio=11). The macro-RAFT agent was dried overnight in a vacuum oven at 50°C [11].

Subsequently, styrene and methyl acrylate (styrene: methyl acrylate = 90:10 mass ratio) were copolymerised by emulsion polymerisation in the presence of the amphipathic RAFT oligomers and the dialysed cerium oxide nanoparticles. First, the macro-RAFT agent (0.12 g) was dissolved in water (49 g) and the pH was adjusted to 7 with 0.1 M NaOH solution (using a PHM210 Standard pH meter from MeterLab). Then, the cerium oxide dispersion (1.57 g) and the initiator (0.042 g APS) were added. This solution was introduced in a 4 neck double-walled 100 ml glass reactor, surmounted by a condenser and equipped with a mechanical glass anchor stirrer, at room temperature. The aqueous medium and the monomers mixture (5.88 g, composed of 5.27 g of styrene and 0.61 g of methyl acrylate) were bubbled separately with Ar for 30 min. Subsequently, the glass reactor was regulated to 70°C with a continuous flow of thermostated water/ethylene glycol fluid delivered by a Lauda E200 circulating pump and the reaction medium was stirred at 250 rpm with a magnetic stirrer. The monomers mixture was be fed at 27 µL/min into the reactor during 4 h (Braun Perfusor Compact syringe pump). The reactor was then left for 2 h more at the same temperature and stirring conditions. The reactor was under Ar atmosphere at all times. The monomer conversion was measured to be 91%, leading to a hybrid CeO_2-poly(styrene-*co*-methyl acrylate) latex at 10 wt.% solids (4.8 wt.% CeO_2 based on polymer) with a final pH = 6.9.

V.2.4- Template functionalisation via sonochemical reduction

The latex template was functionalised with palladium nanoparticles formed *in-situ* by reducing Na_2PdCl_4 under ultrasonic irradiation. The reaction was carried out in a reactor consisting of a 200 mL glass flask introduced in a deionised water bath contained in a double-walled glass reactor with a sonotrode on the bottom, as shown in Figure 97. The acoustic power supplied was 0.14 W/mL at 205 kHz for 12 h. Under these conditions, the hydrogen peroxide formation rate was measured to be 0.973 µmol/min in water under Ar atmosphere [13]. The temperature of the system was regulated at 20 °C. 90 mL of polystyrene latex (at 9.2 wt.% solids) were used with 9 mL of Na_2PdCl_4 solution in water at 10 mg Pd/mL. Prior to Pd addition and sonication, Ar (or 10 vol.% CO/Ar) was bubbled at a flow rate of *c.a.* 120 mL/min for about 15 minutes from the bottom of the latex containing flask. Then, the Ar (or 10 vol.% CO/Ar) bubbling was set at the liquid-gas interphase, the Pd solution was added and the reaction medium was stirred with a glass blade. Subsequently, the ultrasound irradiation was started. The CeO_2-containing poly(styrene-*co*-methyl acrylate) hybrid latex was decorated with Pd using the same procedure

with Ar bubbling, except that 40 mL of latex (at 10 wt.% solids) and 10 mL of Na_2PdCl_4 solution at 0.7 mg Pd/mL were used in that case.

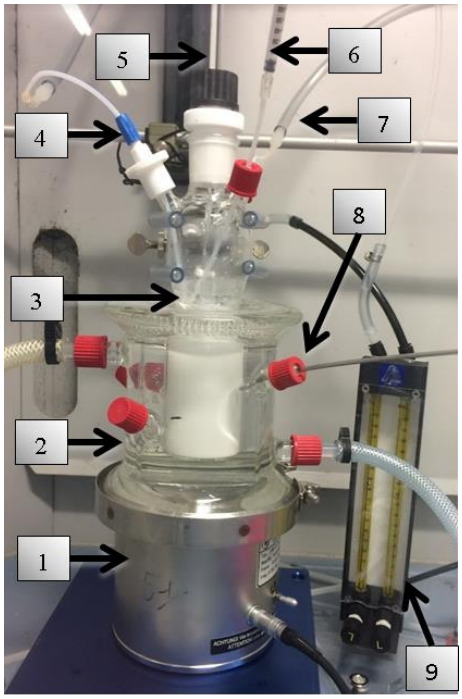

Figure 97. Experimental set-up for sonochemistry: (1) Elac Nautik transducer supplied by a 120 W maximal electric power generator, (2) 350 mL thermostated double-walled glass reactor, (3) 150 mL glass flask, (4) gas inlet, (5) glass rod, (6) sample outlet, (7) gas outlet, (8) thermocouple, (9) flowmeter.

To prepare the polystyrene latex template decorated with bimetallic Pt-Pd nanoparticles, the same experimental set-up was used. The temperature of the system was regulated at 20 °C. Prior to sonication, 90 mL of polystyrene latex (at 9.0 wt.% solids) were bubbled with a 10 vol.% CO/Ar gas mixture during 15 minutes from the bottom of the latex containing flask. Then, the 10 vol.% CO/Ar bubbling was set at the liquid-gas interphase, the reaction medium was stirred with a glass blade and 5 mL of Na_2PtCl_4 solution at 5 mg Pt/mL were added. Subsequently, the ultrasound irradiation was started. After 63 % of Pt reduction (after 8 h of ultrasound irradiation at 205 kHz), 5 mL of Na_2PdCl_4 solution at 3.2 mg Pd/mL were added. The reaction continued until complete metal reduction. The overall Pt/Pd molar ratio was 0.9. Inductively coupled plasma optical emission spectrometry (ICP-OES) measurements were carried out in a SPECTRO ARCOS ICP-OES (Ametek, France). It was used to follow the Pt and Pd reduction during the sonochemical reactions by quantifying the residual Pt or Pd ions in solution. Polystyrene and reduced Pt and/or Pd nanoparticles were removed from the aliquots by filtrating with two PTFE 0.2 µm 26 mm filters in series. The clear phase was then diluted 100 times with nitric acid 0.3 M, prior injection in the ICP-OES.

V.2.5- Hybrid Pd-containing polystyrene latex template synthesis by miniemulsion polymerisation

The palladium-containing polystyrene latex template was prepared by miniemulsion polymerisation with styrene (6 g), hexadecane as hydrophobic agent (0.32 g), SDBS (0.13 g), deionised water (57 g), AIBN (0.06 g), and $Pd(acac)_2$ (0.04 g). Deionised water and SDBS were combined in a 250 mL beaker and purged with Ar for 30 minutes. Styrene, hexadecane, $Pd(acac)_2$, and AIBN were combined to form the organic phase and purged with argon for 15 minutes. Meanwhile, a 150 mL double-walled glass reactor equipped with a U-shaped glass stirring rod was heated to 75 °C and filled with argon. The organic phase was then added to the SDBS aqueous solution under vigorous mixing (magnetic stir bar) for 30 minutes under argon bubbling in an ice bath to form a macroemulsion. The macroemulsion (tens of microns to millimeter droplet size) was sonicated to form a miniemulsion (tens of nanometers droplet size) by using a BioBlock Scientific Vibracell 75043 equipped with a CV33 probe (13 mm diameter) at 750 W, 20 kHz and 60% amplitude for 3 minutes. This was performed in an ice bath to avoid premature polymerisation at this stage [14]. The miniemulsion was subsequently transferred to the heated double-walled glass reactor to start the polymerisation. The reaction proceeded for 2.5 hours with aliquots withdrawn periodically.

V.2.6- Sol-gel synthesis

The silica matrix was prepared by a two-step acid-base catalysed sol-gel synthesis, as described in Chapter III. In a typical procedure for styrene homopolymer templates, 10 mL of polymer latex was adjusted to pH 2 using a 0.5 M HCl solution when required. The acidic latex was then added to a 25 mL round-bottom flask with a magnetic stir bar and immersed in a 40 °C oil bath. Then, 4.1 mL of TEOS were added to the latex under magnetic stirring. The round-bottom flask was then sealed with a septum and kept under agitation at 40 °C until a third of the gelation time in acidic conditions was attained. At this time, 3.6 mL of a solution of 0.05 M NH_4OH (quantity predetermined based on titration of latex at pH 2) was added in one shot to the mixture to increase the pH to pH=9.6 and complete the gel formation process. For the material prepared with the hybrid CeO_2-containing poly(styrene-*co*-methyl acrylate) latex template, the same experimental set-up was used but the procedure was slightly modified since the template colloidal stability was not guaranteed at pH 2. In that case, 8 mL of TEOS were hydrolysed at 60 °C with 2.7 mL of 0.01 M HCl solution for 2 h. Then 22.5 mL of hybrid latex and 2.3 mL of 0.05 M NH_4OH were added and left reacting until gel formation. All gelled materials were dried in a ventilated oven at 80 °C overnight, and then calcined in a Heraeus® RO tube furnace (Kendro) at 650 °C in air, according to the temperature profile: 5 °C/min up to 250 °C, then 0.5 °C/min up to 300 °C, a plateau at 300 °C for 2 h and then 0.5 °C/min up to 650 °C. The materials were kept at this temperature for 1 h prior to natural cooling of the oven. After calcination at 650 °C, the materials were treated in hydrogen at 40 mL/min and 300 °C for 2 h in a vertical quartz tubular reactor. When specified, the calcination at 450 °C took place with the following temperature profile: 5 °C/min up to 270 °C, then 1 h at 270 °C and then 0.33 °C/min up to 450 °C. The material was kept at this temperature for 2 h prior to natural cooling down of the oven.

V.2.7- Characterisation

The silica matrix textural properties were determined by nitrogen adsorption-desorption using an Autosorb® iQ automated gas sorption analyser (Quantachrome Instruments) with an estimated experimental uncertainty of 6% [15]. Samples were degassed at 200 °C for at least 3 h before analysis. Mesopore size distributions were based on the Barrett-Joyner-Halenda (BJH) method on the desorption branch. In all samples, no microporosity was observed according to the t-plot method, employing the Halsey equation adapted to silica by Cranston and Inkley [16,17]. Total pore volumes were calculated from the total adsorbed volume at a relative pressure of 0.987 (P/P_0). Thermal gravimetric analyses (TGA) for latex decomposition under air or oxygen were carried out in a Q50 thermal gravimetric analyser (TA Instruments) or in a Thermogravimetric analyser (STA-MS, Perkin-Elmer) at a heating rate of 10 °C/min from room temperature until 900 °C (unless other specified). The calcined catalysts were analysed by hydrogen temperature-programmed reduction (H_2-TPR) in an Autochem II Chemisorption Analyser (Micromeritics). Typically, the sample was heated to 120 °C for 90 minutes under 50 mL/min of argon for removal of absorbed water. Then the sample was cooled down to -60 °C under argon. Once the temperature was stable, the analysis gas was changed to 5 vol.% H_2/Ar at 50 mL/min. When the signal of the thermal conductivity detector (TDC) was stable, the temperature ramp started at 10 °C/min up to 950 °C.

Functionalised latexes and catalysts after template removal were observed by transmission electron microscopy (TEM) using a 2200FS – 200 kV TEM (Jeol). Latex samples for TEM were prepared by diluting 10 µL of latex in 3 mL of deionised water, depositing a drop on a Formvar/carbon-coated 300 mesh Cu TEM grid followed by drying under ambient air. Silica samples were ground in a mortar, and encapsulated in an EMbed 812 resin before a section of 70 nm thick was cut and deposited on a Cu TEM grid, using an ultramicrotome Ultracut UCT (Leica Microsystems) equipped with a DiATOME ultra diamond knife. High resolution TEM (HR-TEM) analyses, including annular dark-field (ADF) images and energy-dispersive X-ray (EDX) spectroscopy, were performed in a Titan 80/300 kV cubed Cs-corrected TEM (FEI). For those analyses, a specimen of silica-supported Pt-Pd catalyst was ground and ultrasonically shaken in ethanol, and then a drop was casted in air from the coloured dispersion onto a 200 mesh Cu grid with a holey carbon support foil (Quantifoil). A specimen of silica-supported Pd-CeO_2 catalyst powder was crushed under hexane, ultrasonically shaken and drop casted on the foil. The TEM images were analysed manually using ImageJ software (USA National Institutes of Health).

The X-ray photoelectron spectroscopy (XPS) analyses were carried out using a PHI VersaProbe II analyser (Physical Electronics). Pd3d, Ce3d, Pt4f, C1s, O1s, and Si1s binding energies (BE) were recorded using Al K_α (1486.6 eV) as excitation source and a pass energy of 23.5 eV. For the survey acquisition, the pass energy was 117 eV. The X-ray settings were 100 µm beam size at 100 W and 20 kV HP. Position of XPS peaks of the corresponding elements was referred to silver foil, whose energy was taken equal to 368.2 eV for $Ag3d_{5/2}$.

Solid samples for elemental analysis by ICP-OES were prepared by grinding 50 mg of silica-supported catalyst with 250 mg of Na_2O_2. Then the mixture was placed in a zirconium crucible at 480 °C for 1 hour in static air. After natural cooling, 180 mL of water were added to the mixture. Then, 20 mL of 6 M HCl solution were added under heating and stirring and water was

added to obtain a total of 250 mL. Then, 1.2 mL of the catalyst solution were added to 4.8 mL of a 0.3 M HNO_3 solution prior to ICP measurement.

V.3- Results

One of the biggest challenges of this project has been the sonochemical reduction of Pd controlling the morphology of the nanoparticles and their interaction with the polymer latex template. The difficulty stands on the several palladium species that can be formed in solution. According to Pourbaix diagrams, species such as $Pd^{[2+]}$, $PdOH^{[+]}$, $PdO_{(aq)}$, $Pd_{(s)}$, $PdO_{(s)}$, $Pd(OH)_{2(s)}$ can be present [18]. Their appearance depends on the pH, but also on other additives that could be found in the medium, for instance, complexing agents such as ammonia, chlorides, bromides and carbonates [18,19]. In order to overcome this challenge, several approaches exploring different reaction conditions were tested.

V.3.1- Hierarchically porous Pd/SiO_2 catalyst via sol-gel synthesis with sonochemically decorated polystyrene latex template

In line with the strategy for preparing silica-supported Pt catalysts presented in the previous chapters, the idea was to prepare a polystyrene latex by emulsion polymerisation, decorate it with Pd nanoparticles by sonochemical means, and then, use this decorated latex as template for the sol-gel process to obtain a hierarchically porous catalyst, as depicted in Figure 96.a.

V.3.1.1- Sonochemical reduction of Pd on polystyrene latex

The polystyrene latex template was prepared as mentioned in the experimental description. During the sonochemical reduction of Na_2PdCl_4, at high Pd concentration (ca. 1 g Pd /L, so ca. 0.1 g Pd in 100 mL required for ca. 1 wt.% Pd/polystyrene using a 10 wt.% polystyrene latex), a black precipitate was observed at the bottom of the flask (Figure 98). When Ar was used during the ultrasound irradiation at 205 kHz, Pd was not observed at the surface of the polymer beads (Figure 99.a.). On the other hand, when CO/Ar (10 vol.%) was used, it was possible to obtain the desired hybrid latex with Pd nanoparticles of (D_n =) 6.7 ± 2.7 nm (D_w =10.6 nm, Đ =1.59, Figure 99.b.), but a fine black precipitate was still observed at the bottom of the flask, even though it could be easily redispersed by vigorous shaking. Another difference was that under 10 vol.% CO/Ar atmosphere, no Pd ions were detected in solution after 90 min of ultrasonic irradiation, while under Ar atmosphere, it took 360 min to consume all Pd ions.

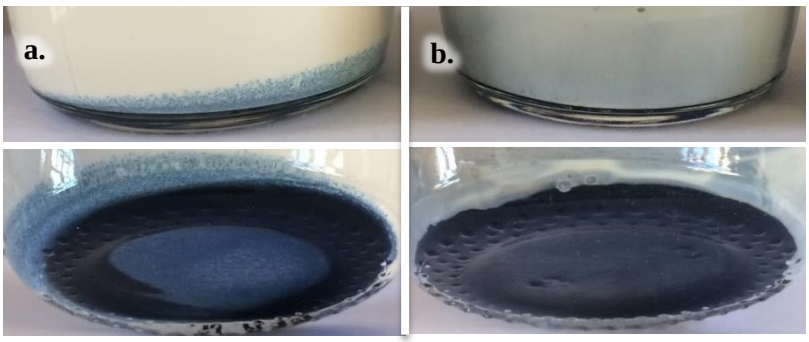

Figure 98. Pictures of 10 wt.% polystyrene latex (top) and bottom of recipient (bottom) containing 1 wt.% Pd/polystyrene, reduced under ultrasound in: a. Ar and b. 10 % vol. CO/Ar.

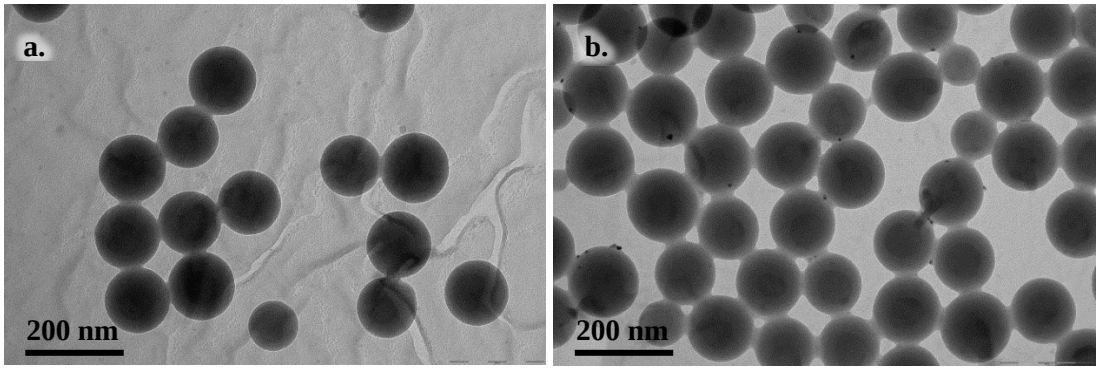

Figure 99. TEM images of 10 wt.% polystyrene latex containing 1 wt.% Pd/polystyrene, reduced under ultrasound in: a. Ar and b. 10 vol.% CO/Ar.

In an attempt to understand the polystyrene-Pd interaction during ultrasonic reduction under Ar atmosphere, the reaction medium was diluted by a factor of 10 (ca. 0.1 g Pd /L and ca. 1 wt.% polystyrene). In such conditions, it was possible to obtain a Pd-decorated latex, but with some free Pd nanoparticles, as observed in Figure 100.a. Additionally, such latex was very diluted to be used as template in the following steps. Another experiment was carried out with 10 wt.% polystyrene latex containing 0.1 wt.% Pd/polystyrene under Ar, expecting that providing a larger polymer surface, the Pd would only be on the polymer beads. Unfortunately, some Pd nanoparticles were still observed standing alone on the TEM grid (Figure 100.b.).

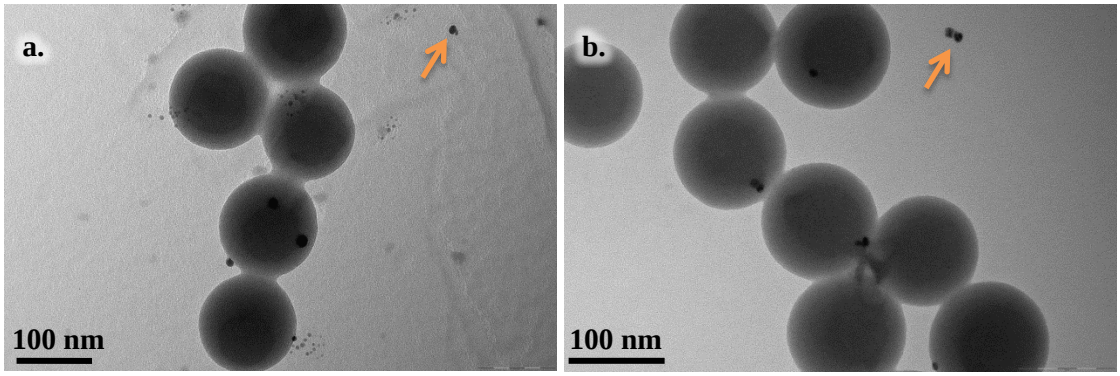

Figure 100. TEM images of Pd sonochemically reduced in Ar: a. 1 wt.% polystyrene latex containing 1 wt.% Pd/polystyrene, b. 10 wt.% polystyrene latex containing 0.1 wt.% Pd/polystyrene. Orange arrows highlighting free Pd particles.

So a poor polymer-Pd interaction was evidenced when the sonochemical reduction was carried out under Ar atmosphere. Conversely, as shown in Figure 99, a 10 vol.% CO/Ar atmosphere favoured the decoration of the polystyrene beads. This could be explained by an enhancing effect of CO in the nucleation of small Pd particles that could be easily stabilised at the surface of the polymer. While in the case of Ar, the particles growth was favoured, leading to large colloidally unstable Pd particles at high Pd concentration, which settled as large particles as clearly observed on Figure 98.a.

V.3.1.2- Catalyst preparation and characterisation

In agreement with the results obtained during the Pd sonochemical reduction, the latex at 1 wt.% Pd/polystyrene reduced under 10 vol.% CO/Ar atmosphere was chosen for the preparation of a hierarchically porous Pd/SiO_2. The silica support was prepared by a two-step acid-base catalysed sol-gel synthesis in order to obtain a mesoporous matrix, as already described in Chapter III. For the sake of comparison, another material was also prepared with non-decorated latex.

Thermogravimetric analyses were carried out in order to define the calcination conditions for the template removal. In a first stage the non-decorated latex was studied alone. It was observed that above 425 °C in air, 97 wt.% of the polymer degraded at a heating rate of 10 °C/min and 99 wt.% at 5 °C/min, in agreement with Pfaffli *et al*. [20]. Secondly, the silica matrix with non-decorated latex was studied at a heating rate of 10 °C/min in air. It could be observed that at least 610 °C were required for complete polymer degradation, since the matrix constrained the template removal, thus requiring a higher calcination temperature than the polymer alone [21]. Figure 101 presents the comparison of the polystyrene template thermal degradation in air, before and after being included in the silica matrix. It is important to note that the complete latex removal in the silica composite material corresponds to approximatively 50 wt.% of total mass loss.

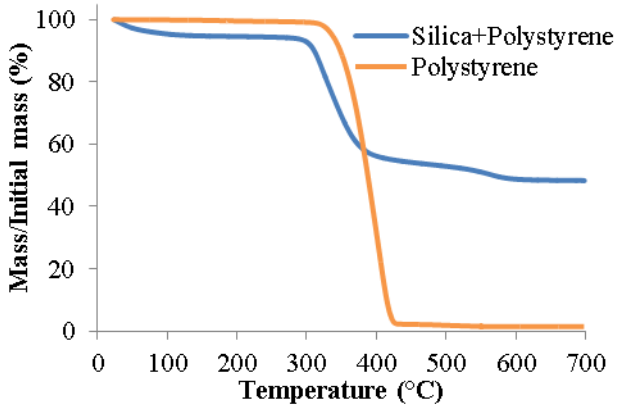

Figure 101. Thermogravimetric analyses in air at a heating rate of 10 °C/min of non-decorated polystyrene latex and composite material of SiO_2 and non-decorated polystyrene template.

Regarding the DSC profile of the non-decorated latex within the silica material (Figure 102.a.), the template degradation was mainly endothermic, in which case the template removal mainly occurred by the polymer breaking down into volatile species [20,22]. The exothermic peak observed at 610 °C might correspond to the spontaneous ignition of the remaining polymer still trapped within the silica [23]. On the other hand, when Pd was present in the material, the first mass loss was related to an endothermic process (Figure 102.b.), corresponding to a thermal degradation of the polymer. However, the DSC profile showed a second signal with an exothermic maximum at 472 °C. It was related to an oxidation reaction catalysed by the Pd present in the material, similarly to the polymer oxidation catalysed by the Pt [24]. However, it was still required to calcine up to 650 °C in order to guarantee a complete polymer removal.

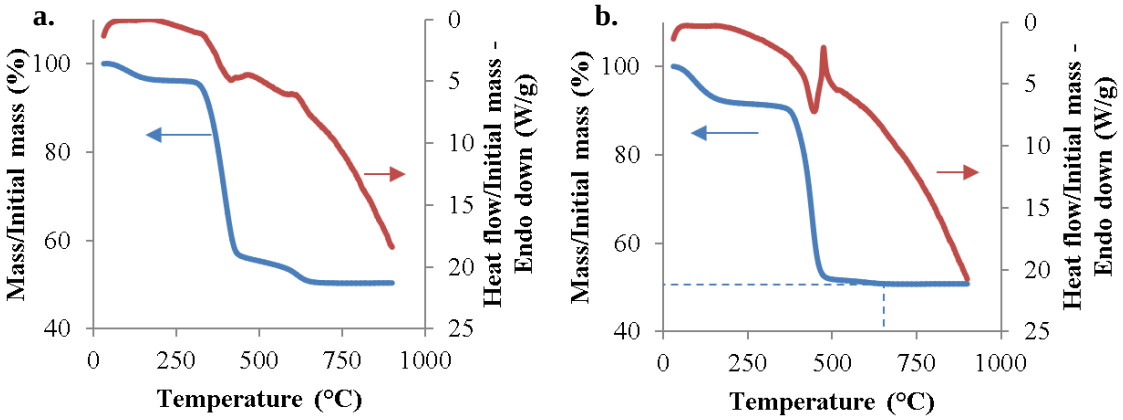

Figure 102. Differential scanning calorimetric (red lines) and thermogravimetric analyses (blue lines) in air at a heating rate of 10 °C/min: (a) SiO_2 with polystyrene template, (b) SiO_2 with 0.7 wt.% Pd/polystyrene template.

Subsequently, the material was calcined at 650 °C in air, revealing the morphology desired with macropores of *ca*. 140 nm as expected from the polystyrene template (Figure 103). In the TEM images, the Pd nanoparticles were measured to have a number-average diameter D_n of 16.2 ± 4.6 nm (D_w =19.9 nm, Đ =1.23), which represents an important Pd nanoparticles sintering at 650 °C, since the starting template had 6.7 ± 2.7 nm Pd nanoparticles. Unfortunately, as observed in the thermogravimetric analyses, the calcination at high temperature of 650 °C was required for a complete template removal.

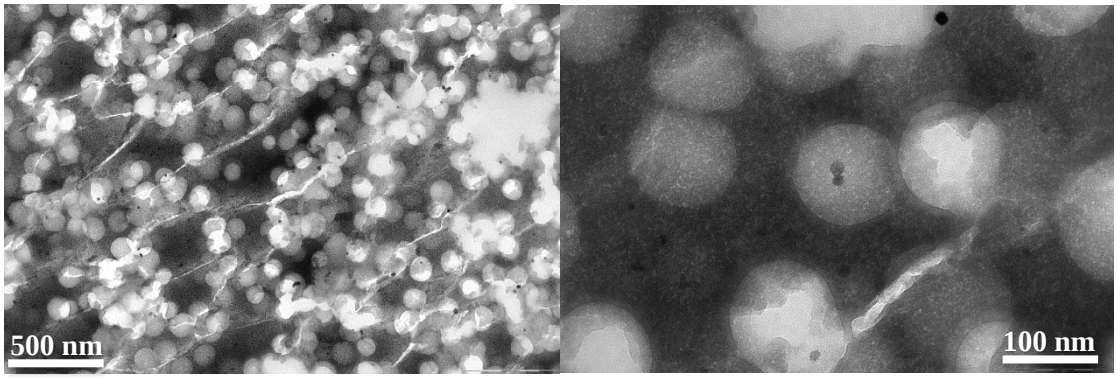

Figure 103. TEM images of 0.7 wt.% Pd/SiO_2, calcined at 650 °C.Please note that the diagonal stripes are due to the shear stress by microtome sample preparation.

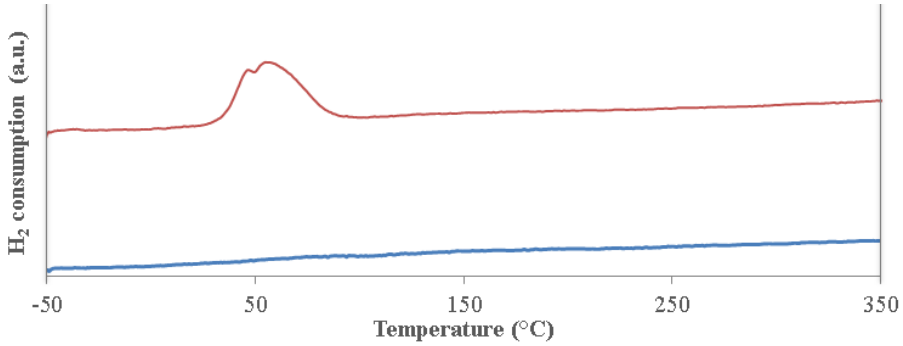

Figure 104. H_2-TPR profiles of: 0.7 wt.% Pd/SiO_2 calcined at 650 °C (red, top) and Pd-free SiO_2 (blue, bottom).

H_2-TPR analysis confirmed that after calcination at 650 °C (Figure 104), the material required to be reduced since non-metallic Pd species were present in the sample (reduction peak centered at 52 °C). So a reduction treatment under hydrogen flow was carried out at 300 °C. The nitrogen physisorption isotherm (Figure 106) of the final material 0.7 wt.% Pd/SiO_2 after reduction revealed a characteristic hysteresis of a macro-mesoporous network with a mesoporous diameter size distribution up to ca. 5 nm. The catalyst exhibited a surface area of 425 m^2/g and a total pore volume of 0.47 cm^3/g. These values were below the expected characteristic observed on the silica matrix previously prepared under the same conditions: 615 m^2/g surface area and 0.74 cm^3/g total pore volume (Chapter III). This could be due to non-reduced Pd species (as observed by XPS, discussed below) that could interact with TEOS or with the ethanol produced *in-situ* during the sol-gel process, interfering with the formation of branched silica chains that are important to obtain a porous material. Indeed, some experiments, non-detailed here, showed that Pd ions have an effect on the sol-gel process: sol-gel syntheses were tried with a Pd-containing latex with only 33% Pd reduced, so 67% of the Pd was in the medium as chloropalladate ions. In such a case, the gelation time was reduced (typically from 72h to 21h) and the gel obtained was not homogeneous: polymer template and silica segregated. Such segregation occurs because the ethanol formed *in-situ* during the hydrolysis of TEOS is required to have a homogenous mixture, otherwise the latex and TEOS phases do not mix during the silica matrix formation [25], leading to segregation of the polymer beads. So in the presence of Pd(II) species in solution, they could be reduced with ethanol, forming acetaldehyde [26], which could keep reducing more Pd(II) [27], decreasing the pH of the medium and reducing the latex colloidal stability.

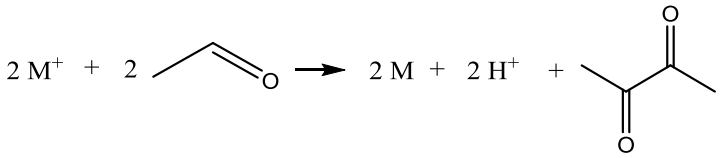

Figure 105. Acetaldehyde as a reducing agent for metal (M) ions [27].

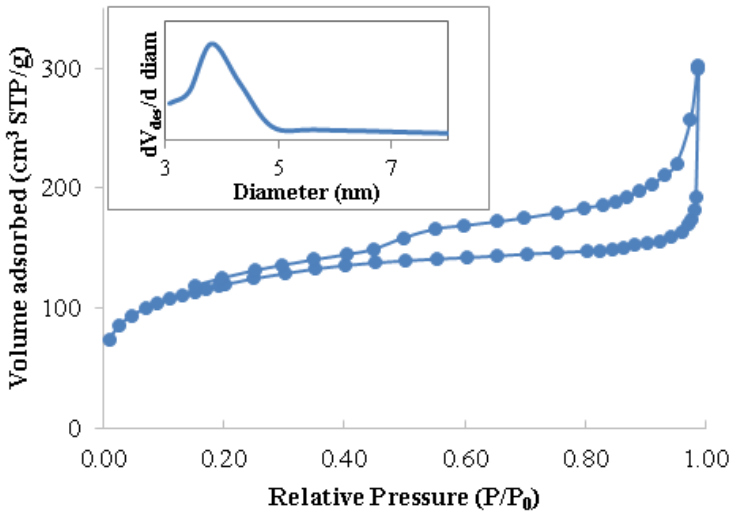

Figure 106. Nitrogen adsorption-desorption isotherms of the calcined and reduced 0.7 wt.% Pd/SiO_2 catalyst. Mesopore size distribution is shown in the inset.

In order to study the oxidation state of Pd along the preparation steps, XPS analyses were carried out. The corresponding spectra are presented in Figure 107. It was observed that the XPS spectra of both latexes after decoration with Pd, either in Ar or in 10 vol.% CO/Ar, exhibited very similar profiles (Figure 107.a. and b.). However, in those hybrid latexes, the Pd was in a mixture of Pd(0) and Pd(II) oxidations states, showing that the ultrasonic reduction was not complete. After the sol-gel synthesis with the Pd-decorated latex under 10 vol.% CO/Ar, the composite material exhibited mostly oxidised species of Pd (Figure 107.c.), which could correspond to Pd complexes formed during the sol-gel process, as binding energies at 338 eV have been reported to correspond to Pd complexes grafted on silica [28]. After calcination of this material at 650 °C, the main species observed was PdO (Figure 107.d.), which implies that such heat treatment (required for the template removal) strongly oxidises the Pd, in agreement with the H_2-TPR analysis. However, after a reduction treatment under hydrogen at 300 °C, mainly Pd(0) was found (Figure 107.e.) within the hierarchically porous material.

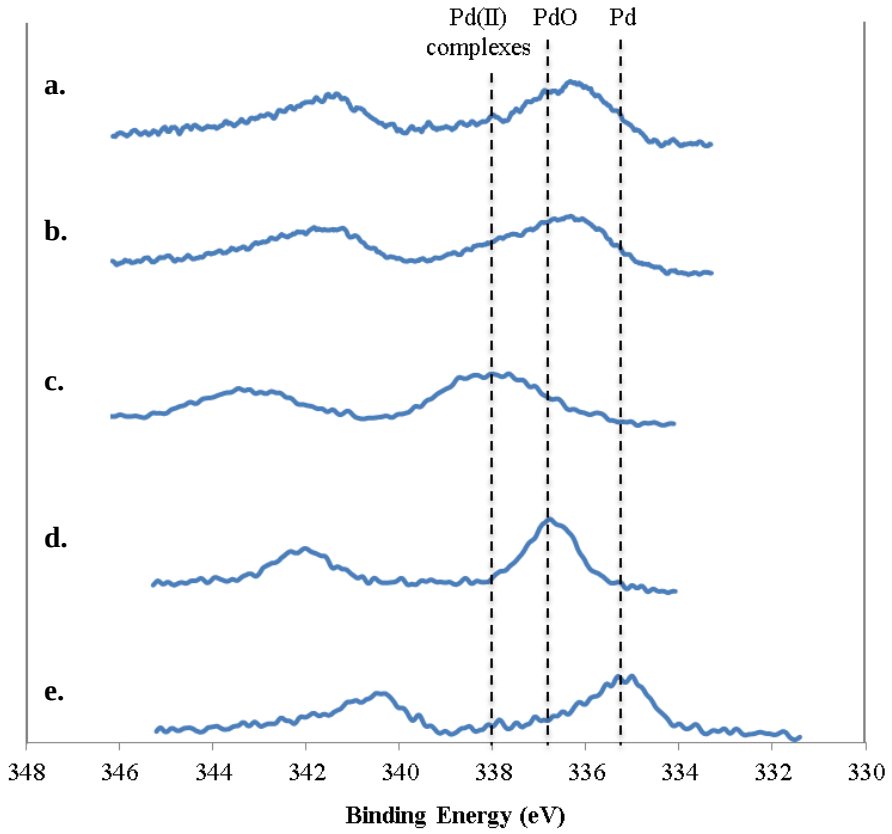

Figure 107. XPS spectra of Pd3d core level of: a. Polystyrene template decorated with Pd under ultrasound in Ar, b. Polystyrene template decorated with Pd under ultrasound in 10 vol. % CO/Ar, c. Silica composite with polymer template in b., d. Silica material in c. after calcination at 650 °C, e. Silica material in c. after calcination at 650 °C and reduction at 300 °C.

So the sonochemical decorated template prepared under 10 vol. % CO/Ar atmosphere was successfully used in the preparation of a hierarchically porous Pd/SiO_2 material with Pd nanoparticles of 16.2 ± 4.6 nm. Such nanoparticles were mainly composed of Pd(II) after the template removal by calcination at 650 °C, but they were reduced to Pd(0) under hydrogen at 300 °C.

V.3.2- Hierarchically porous Pt-Pd/SiO_2 catalyst by combination of latex synthesis, sonochemistry and sol-gel process

This approach takes advantage of the flexibility of the sonochemical technique to reduce several metals in series or in parallel. It starts by the preparation of polystyrene latex by emulsion polymerisation, then, a Pt seed is prepared by sonochemical reduction and, then the Pd precursor is added to form bimetallic nanoparticles under ultrasound. Such hybrid latex is used as template for the sol-gel process in order to obtain a hierarchically porous catalyst, as depicted in Figure 96.b.

V.3.2.1- Pt-Pd nanoparticles synthesis by sonochemistry

In Chapter III, it was observed that the Pt was preferentially located at the polystyrene beads surface. So we decided to set an experiment starting with a Pt precursor reduction, in order to form Pt nanoparticles as a seed for the following Pd precursor reduction. The desired metal loadings were 0.3 wt.% Pt and 0.2 wt.% Pd, in order to have a atomic ratio Pt/Pd close to 1. The Pd solution was added at 63 % of Pt reduction (after 8 h of ultrasound irradiation at 205 kHz). Then, the Pd and Pt reduction occurred very fast: all Pd and Pt were completely reduced in only 20 minutes, showing a synergistic reduction effect of the two metals. The nanoparticles were only observed at the polystyrene surface, no free particles were observed (Figure 108). They were measured to have a number-average diameter D_n of 3.6 ± 1.3 nm (D_w =5.0 nm, Đ =1.39).

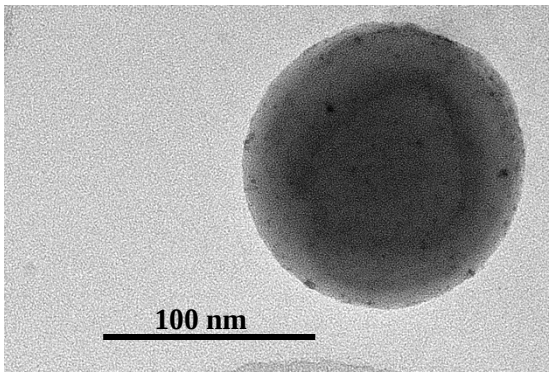

Figure 108. TEM images of 10 wt. % polystyrene latex containing 0.3 wt. % Pt/polystyrene and 0.2 wt. % Pd/polystyrene, reduced under ultrasound at 205 kHz in 10 vol. % CO/Ar at 20 °C.

V.3.2.1- Catalyst preparation and characterisation

The Pt-Pd decorated latex was used as template for the preparation of a hierarchically porous silica material by sol-gel method, using a two-step acid-base catalysed sol-gel synthesis as already described in Chapter III. Thermogravimetric analyses were then carried out. Figure 109 shows the TGA and DSC profiles for a composite material with Pt and Pd. In that case, only exothermic effects were observed. The first one was probably governed by the oxidation reaction catalysed by Pt and the second one by a mixture of both metals. The maximum temperature for the second exothermic peak was 462 °C, which lies in between the values obtained individually for the Pt and the Pd composite materials. Even though, the two metals

catalysed the polymer oxidation, their low loadings were not enough to achieve a complete template removal at 450 °C (as observed in Chapter III with Pt at 0.7 wt.%), leading to only 88.3 wt. % of polymer removed in this case. So a heat treatment in air at 650 °C was still required for a 99.4 wt. % template removal.

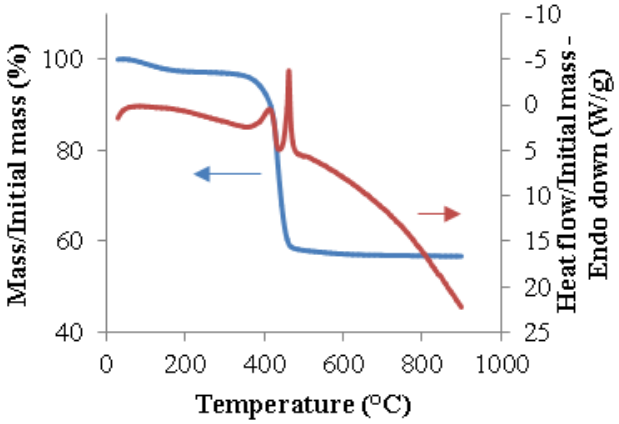

Figure 109. Differential scanning calorimetric (red line) and thermogravimetric analyses (blue line) in air at a heating rate of 10 °C/min SiO_2 with 0.3 wt.% Pt and 0.2 wt.% Pd/polystyrene template.

After polymer removal upon calcination at 650 °C, a H_2-TPR profile was recorded. Surprisingly, no evident reductions peaks were observed probably due to the low metal content (Figure 110). However, the XPS analyses confirmed that after calcination, the main oxidation states were Pt(II) and Pd(II). So a reduction treatment under hydrogen flow at 300 °C was carried out, as in the previous case. After such treatment, the oxidation number of the two elements was mainly equal to zero (Figure 111).

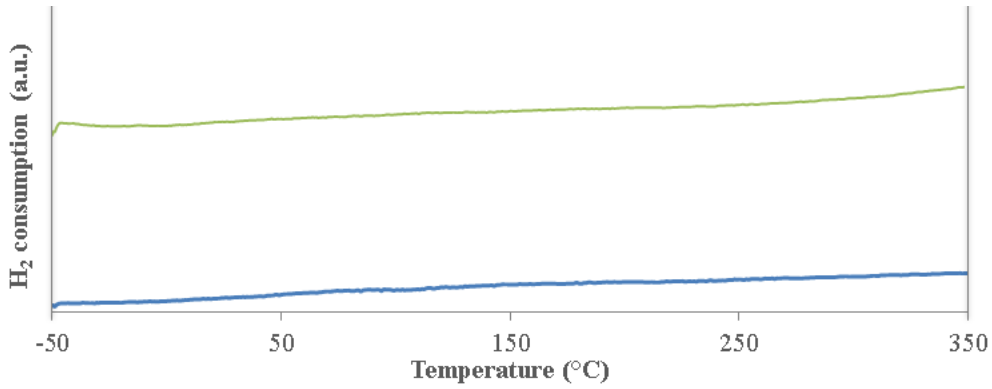

Figure 110. H_2-TPR profiles of: 0.3 wt.% Pt and 0.2 wt.% Pd/SiO_2 calcined at 650 °C (green, top) and SiO_2 (blue, bottom).

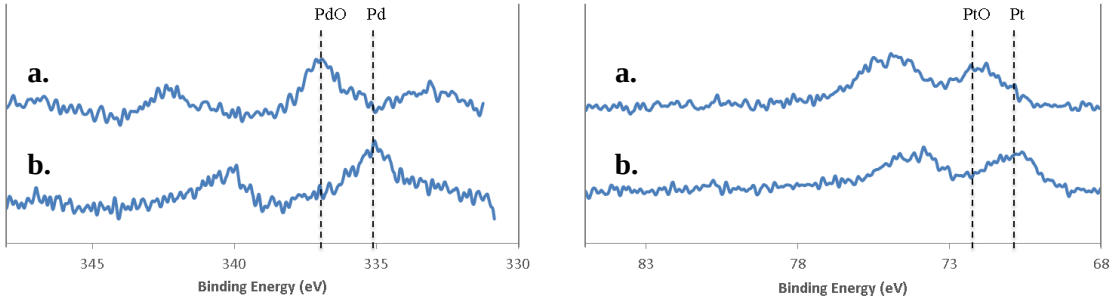

Figure 111. XPS spectra of Pd3d (left) and Pt4f (right) core level of: a. Silica material prepared with Pt-Pd-decorated latex template after calcination at 650 °C, b. Silica material in a. after reduction at 300 °C.

After calcination at 650 °C and hydrogen treatment at 300 °C, the catalyst exhibited the morphology desired with macropores with diameter of ca. 130 nm, in agreement with the latex template used (Figure 112). The particle size was D_n of 3.8 ± 1.4 nm (D_w =5.9 nm, Đ =1.54), which is not significantly different to the particle size measured in the hybrid latex (D_n = 3.6 ± 1.3 nm), so no significant metal sintering occurred. However, it was observed that in terms of composition, two different groups could be identified: small particles (ca. 4 nm) with 73 ± 5 at. % Pd and 27 ± 5 at. % Pt, and larger particles (> 6 nm) with 28 ± 3 at. % Pd and 72 ± 3 at.% Pt. Nevertheless, the overall composition was 57 ± 5 at.% Pd and 43 ± 5 at.% Pt, which is in agreement with expected atomic ratio Pt/Pd of 0.9. In Figure 113.a., lattice fringes of 2.2 ± 1 Å were measured, corresponding to Pt and Pd (111) planes [29,30]. In Figure 113.b, it can be seen that Pd and Pt are distributed homogeneously within one particle, which is proof of a bimetallic interaction that could be due to the synergistic reduction of the Pt and Pd ions during the sonochemical reduction.

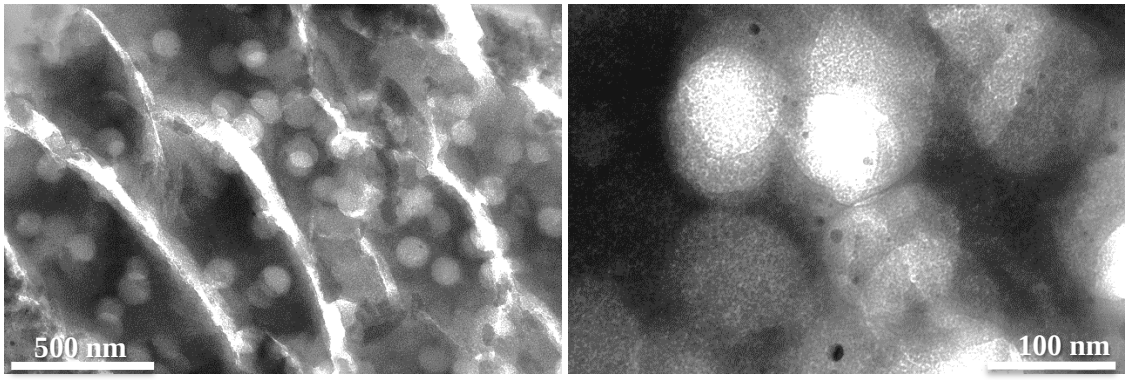

Figure 112. TEM images of 0.3 wt.% Pt - 0.2 wt.% Pd/SiO_2, calcined at 650 °C and reduced at 300 °C. Please note that the diagonal stripes are due to the shear stress by microtome sample preparation.

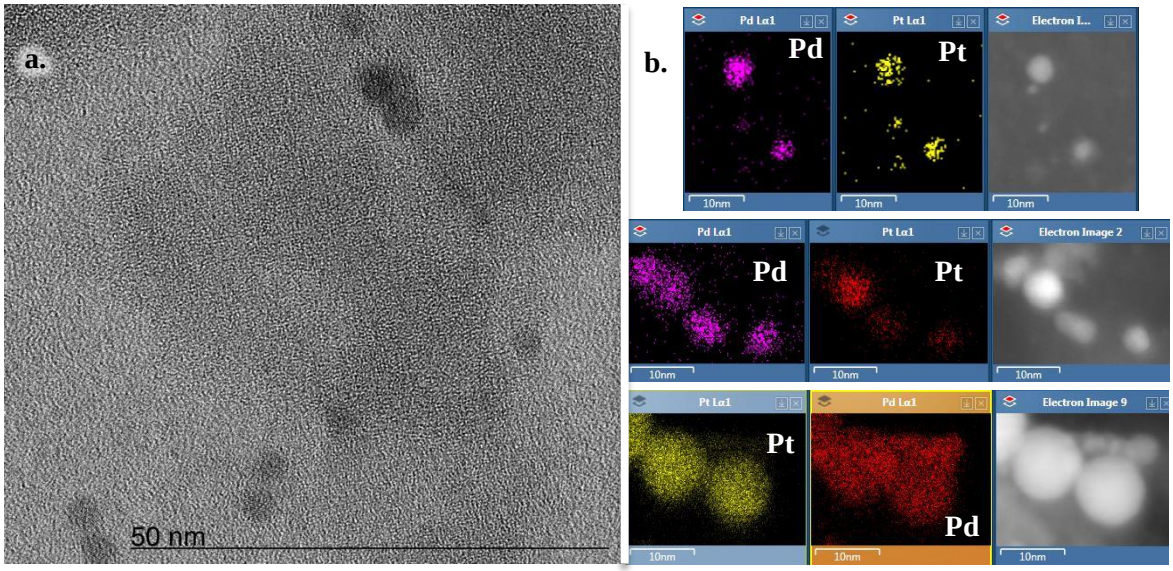

Figure 113. 0.3 wt.% Pt - 0.2 wt.% Pd/SiO_2, calcined at 650 °C and reduced at 300 °C: a. HRTEM image and b. EDX images for Pt and Pd in few particles.

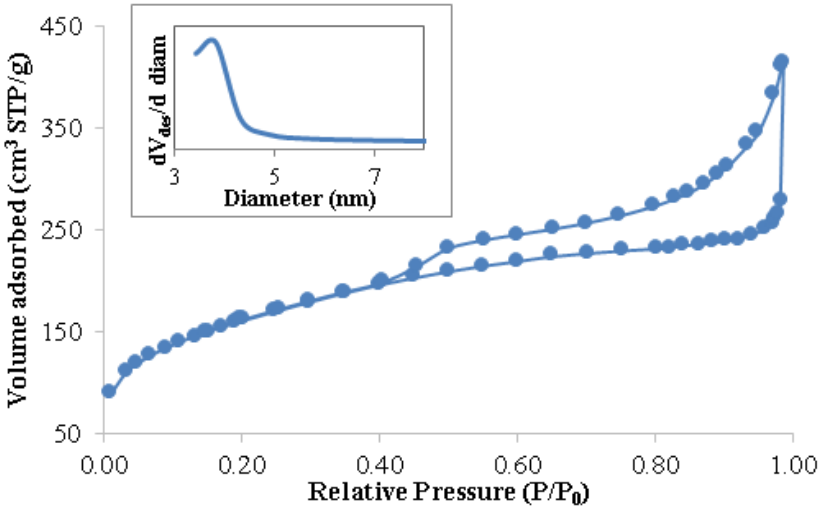

Figure 114. Nitrogen adsorption-desorption isotherms of the calcined and reduced 0.3 wt.% Pt - 0.2 wt.% Pd/SiO_2 catalyst. Mesopore size distribution is shown in the inset.

Figure 114 shows the nitrogen physisorption isotherms for the catalyst after being calcined and reduced. The hysteresis observed in this sample was typical of an interconnected network of meso- and macropores. The mesopores size distribution was observed to be up to ca. 5 nm. The specific surface area and the total pore volume were measured to be 581 ± 35 m^2/g and 0.64 ± 0.04 cm^3/g, respectively. These values were similar to those observed for Pt-based catalysts prepared using the same method (632 ± 38 m^2/g and 0.64 ± 0.04 cm^3/g, 0.3cal450-205kHz characterised in Chapter III).

In summary, it was possible to prepare a 0.3 wt. % Pt - 0.2 wt. % Pd/polystyrene latex template by sonochemical reduction of Na_2PtCl_4 and Na_2PdCl_4 at 205 kHz under 10 vol. % CO/Ar at 20 °C. Such template was successfully used in the preparation of a hierarchically porous Pt-Pd/SiO_2 material with bimetallic Pt-Pd nanoparticles of 3.8 ± 1.4 nm. Such nanoparticles were mainly composed of Pt (II) and Pd(II) species after the template removal by calcination at 650 °C, but they were reduced to Pt(0) and Pd(0) under hydrogen at 300 °C.

V.3.3- Hierarchically porous Pd-CeO_2/SiO_2 catalyst by combination of latex synthesis, sonochemistry and sol-gel process

This approach takes advantage of the versatility of the latex synthesis technique to prepare hybrid materials, to be used as the initial template. It starts by the preparation of a hybrid latex containing CeO_2 nanoparticles by emulsion polymerisation [11], then, this latex is decorated with Pd nanoparticles by sonochemical reduction. Finally, the Pd-decorated hybrid latex is used as template for the sol-gel process to obtain a hierarchically porous catalyst, as depicted in Figure 96.c.

V.3.3.1- Sonochemical preparation of Pd nanoparticles on hybrid CeO_2-containig latex

As already described in the experimental details, the hybrid latex used in this procedure was a statistically copolymer of styrene and methyl acrylate prepared by emulsion polymerisation in the presence of CeO_2 nanoparticles (constituted of a few crystallites of ca. 3 nm) and a macro RAFT agent (poly(BA_5-co-AA_5), BA stands for butyl acrylate and AA, for acrylic acid). The CeO_2/polymer ratio was 4.8 wt. %. In the TEM images, the polymer beads were measured to have an average particle size D_n of 100 ± 20 nm (D_w =112 nm, Đ =1.13).

In general, using sonochemistry at low Pd concentrations, it was possible to prepare Pd-containing latexes with the desired morphology and macroscopic stability, as previously discussed in Section V.3.1.1-*Sonochemical reduction of Pd on polystyrene latex*. Keeping that in mind, it was decided to develop other materials by reducing 0.2 wt. % Pd/polymer on a 10 wt. % hybrid latex containing CeO_2 nanoparticles. After the sonochemical reduction, no large Pd particles were observed (Figure 115.b.), unlike the Pd sonochemical reduction on polystyrene latex. A very few number of free particles were observed, but it could be CeO_2, by comparison with the TEM images of the hybrid polymer before the sonochemical treatment (Figure 115.a.). No evidence of Pd and CeO_2 segregation was observed.

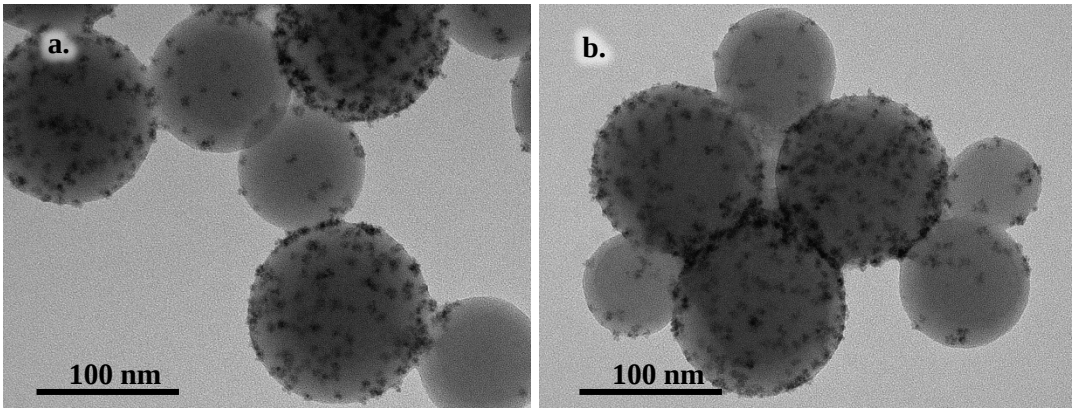

Figure 115. TEM images of 10 wt.% CeO_2 hybrid latex: **a.** before Pd decoration and b. containing 0.2 wt.% Pd/polymer reduced under ultrasound at 205 kHz under Ar at 20 °C.

V.3.3.2- Catalyst preparation and characterisation

The Pd-CeO_2 hybrid latex was used as template for the preparation of a hierarchically porous silica material using a modified version of the two-step acid-base catalysed sol-gel synthesis used for styrene homopolymer templates, as described in the experimental section. Such modification was required because the stability of this hybrid latex was not guaranteed at pH 2, since no surfactant was used in this formulation and the polymer beads were only stabilised by carboxylic functional groups (pKa ~ 5) from the macro-RAF agent and sulphate functional groups (pKa ~ 2) derived from the initiators. So a pre-hydrolysis of the silica precursor was required before the latex addition.

After calcination of the composite material at 450 °C, it was possible to observe macropores corresponding to the empty space left by the removed template, in agreement with the desired morphology (Figure 116), giving good evidence that the silica matrix had embedded the latex template. However, TGA and DSC analyses permitted to conclude that at 450 °C, only 84 wt.% of the polymer was removed (Figure 117). A treatment at 650 °C was required for a complete polymer removal. DSC profile only had two exothermic peaks, meaning that the polymer was removed by catalytic oxidation due to the presence of Pd and CeO_2.

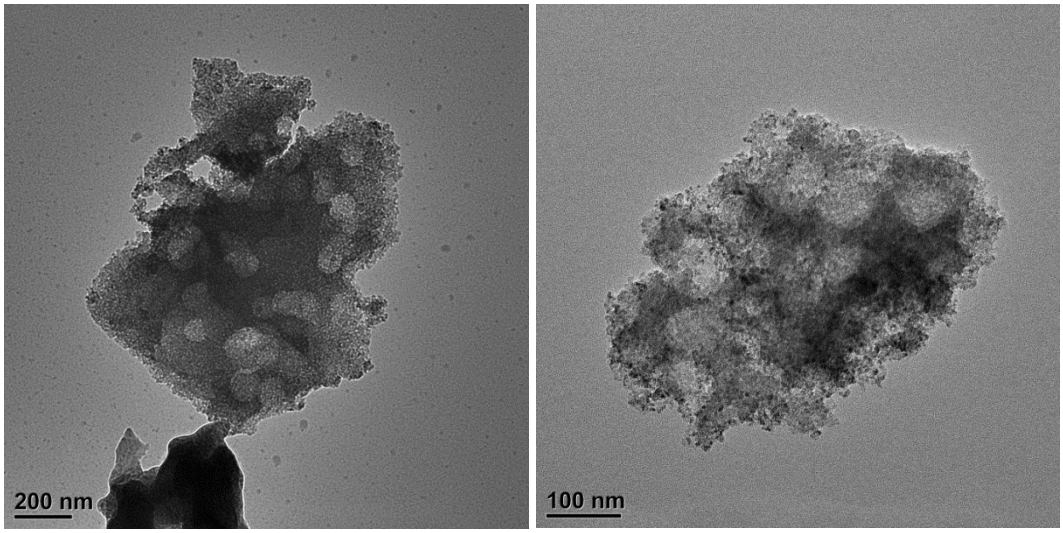

Figure 116. TEM images of 0.2 wt.% Pd-3.8 wt.% CeO_2 /SiO_2 calcined at 450 °C, ground sample.

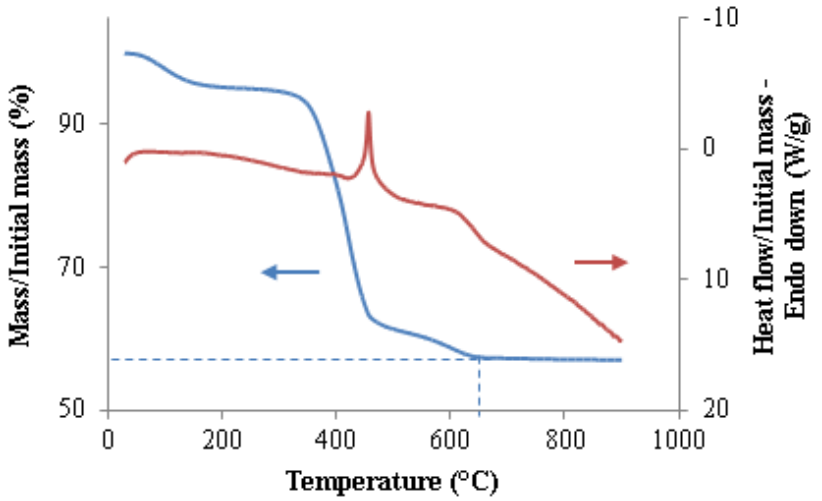

Figure 117. Differential scanning calorimetric (red line) and thermogravimetric analyses (blue line) in air at a heating rate of 10 °C/min of silica composite material with Pd-CeO_2 hybrid latex.

A H_2-TPR profile was recorded for the sample calcined at 650 °C. Four features can be observed in Figure 118. A small peak around 50 °C corresponding to Pd reduction, as previously observed in Figure 104. Another peak between 170 °C and 270 °C, which can be attributed to the reduction of PdO_y-CeO_{2-x} species [31], since it has been demonstrated that transition metals (e.g. Pt or Pd) can lower the reduction temperature of metal oxides via hydrogen spillover [32]. A third peak centred at 450 °C can be attributed to the reaction between hydrogen and the ceria that was not in direct contact with Pd species [31]. Finally, the large peak centred at 650 °C can be attributed to signal in the thermal conductivity detector (TDC) originated by residues of the template left on the silica after calcination at 650 °C or by-products of further condensation reactions within the silica support. A similar profile could be observed on the silica sample prepared with non-decorate polystyrene template (blue curve in Figure 118).

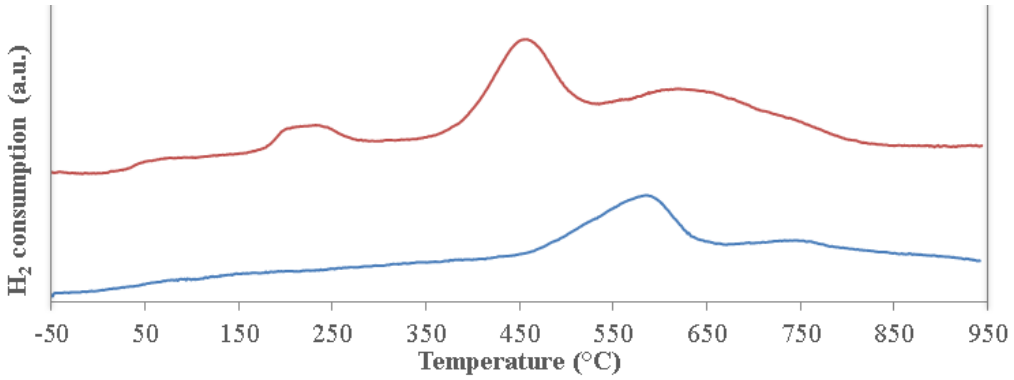

Figure 118. H_2-TPR profiles of 0.2 wt.% Pd-3.8 wt.% CeO_2 /SiO_2 (red, top) and Pd-free templated SiO_2 (blue, bottom), both calcined at 650 °C.

XPS analyses confirmed a reduction of Pd species after a hydrogen treatment at 300 °C, while the Ce spectra remained practically unchanged as shown in Figure 119. It is interesting to note that unlike the material with only Pd/SiO_2, where mainly Pd(0) was observed after reduction at 300 °C (Figure 107), in this case the Pd is present in a broad range of oxidation states, mainly related to the interactions with the ceria nanoparticles [31].

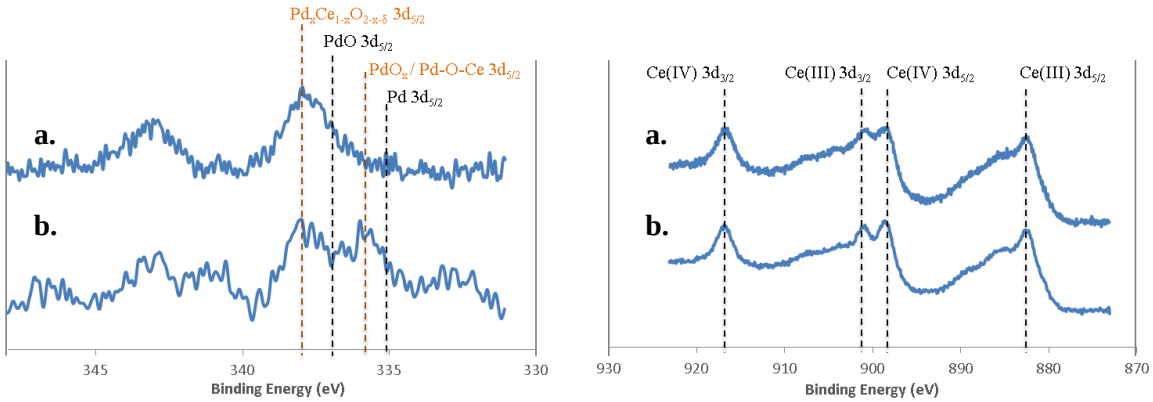

Figure 119. XPS spectra of Pd3d (left) and Ce3d (right) core level of: a. 0.2 wt.% Pd-3.8 wt.% CeO_2 /SiO_2 after calcination at 650 °C, b. Silica material in a. after reduction at 300 °C.

HRTEM observations and EDX analyses were also carried out to confirm the Pd-CeO_2 interaction. The particle average size was found to be Dn of 4.8 ± 0.9 nm (Dw =5.3 nm, Đ =1.11). In Figure 120, lattice fringes of 2.4 ± 0.2 Å and 3.4 ± 0.2 Å were measured, corresponding to Pd plane (111) [29] and CeO_2 plane (111) [33], respectively.

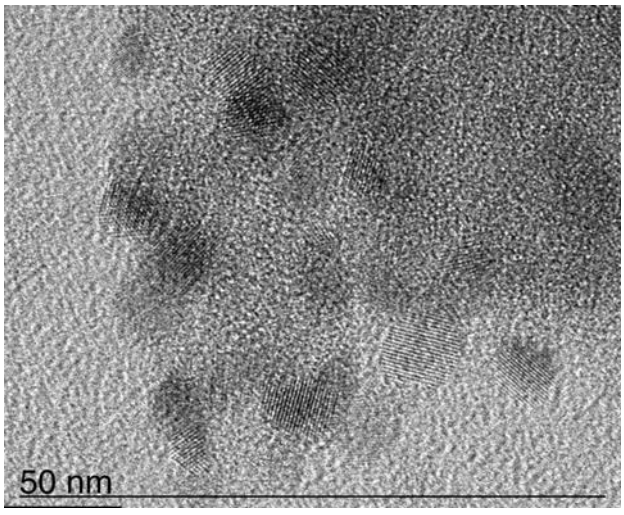

Figure 120. HRTEM image of 0.2 wt.% Pd-3.8 wt.% CeO_2 /SiO_2 calcined at 650 °C and reduced at 300 °C

Regarding the EDX mapping, it was carried out using a normal counting speed in order to avoid excessive C contamination (C was present from the grid film) and bending of the sample. However, due to the low Pd content, its corresponding signal was not very intense, as shown in Figure 121. Even, in some large clusters, the detected Pd content was almost zero. Nevertheless,

it was possible to quantify Pd and Ce on several nanoparticles, having Pd/Ce atomic ratios close to the expected 7% (Figure 122).

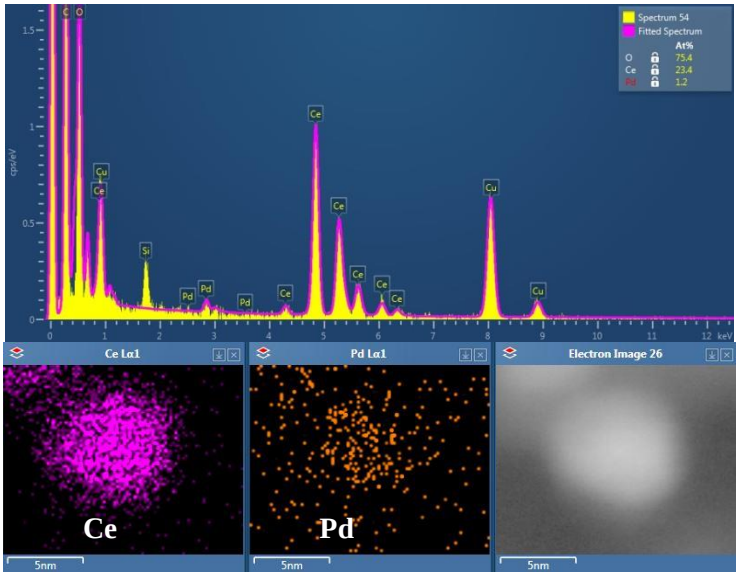

Figure 121. EDX spectrum, Ce and Pd mapping and ADF image of 0.2 wt.% Pd-3.8 wt.% CeO_2 /SiO_2 calcined at 650 °C and reduced at 300 °C.

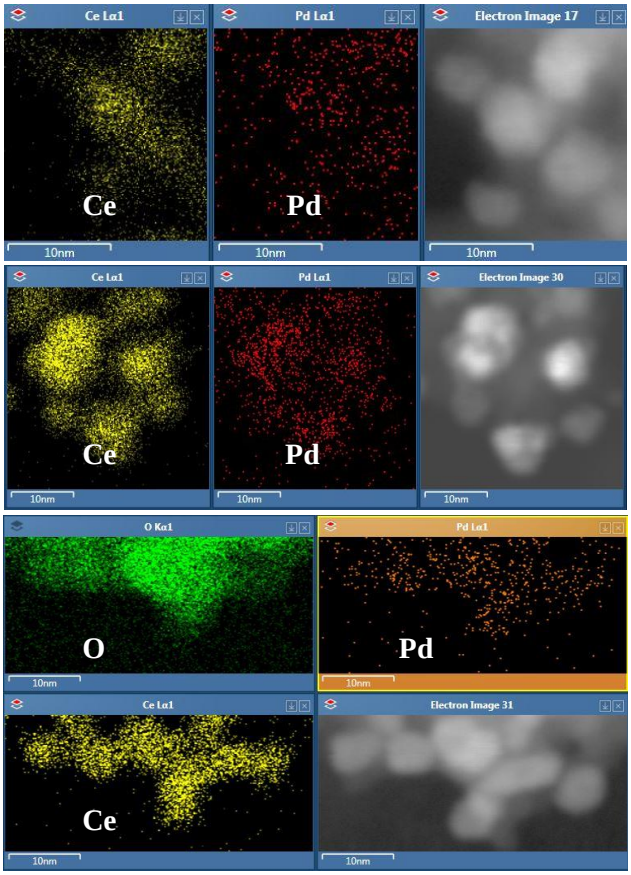

Figure 122. EDX mapping for Ce, Pd and O, and ADF images of 0.2 wt.% Pd-3.8 wt.% CeO_2 /SiO_2 calcined at 650 °C and reduced at 300 °C.

Figure 123 shows a line scan from the particle matrix support (SiO_2) to the carbon foil. It can be observed that the oxygen content is high on the support and on the particle, as expected. The Ce content was maximal on the particle observed on the ADF inset. Additionally, Pd was mainly detected on the particle as well, which permitted to assume that Pd decorated preferentially the CeO_2 nanoparticles.

Figure 123. EDX analysis of 0.2 wt.% Pd-3.8 wt.% CeO_2/SiO_2 calcined at 650 °C and reduced at 300 °C. Acquisition along the line scan indicated on the ADF image in the inset. Si and C have been omitted.

TEM images of the material after calcination at 650 °C and reduction at 300 °C are shown in Figure 124, in which macropores of ca. 100 nm are observed, in agreement with the latex template used.

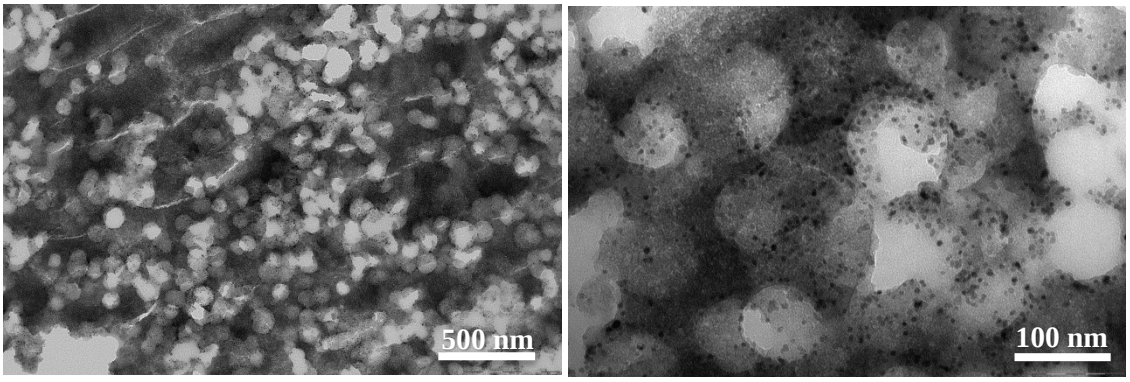

Figure 124. TEM images of 0.2 wt.% Pd-3.8 wt.% CeO_2 /SiO_2 calcined at 650 °C and reduced at 300 °C, sample prepared by microtomy.

The material texture was characterised by nitrogen physisorption. Figure 125 shows the isotherms for the 0.2 wt.% Pd-3.8 wt.% CeO_2/SiO_2 calcined at 650 °C and reduced at 300 °C. The hysteresis profile confirms the interconnected macro-mesoporous network. The specific surface area was 735 m^2/g and the total pore volume was 0.82 cm^3/g. These values are larger than those previously presented for the other here-in-prepared materials, which might be due to the modification of the sol-gel method used for this material preparation (acid step in the absence of the latex template, which was added with the base in the second step). However, as in the previous Pd-based materials, the mesopores size distribution was observed to be up to ca. 5 nm.

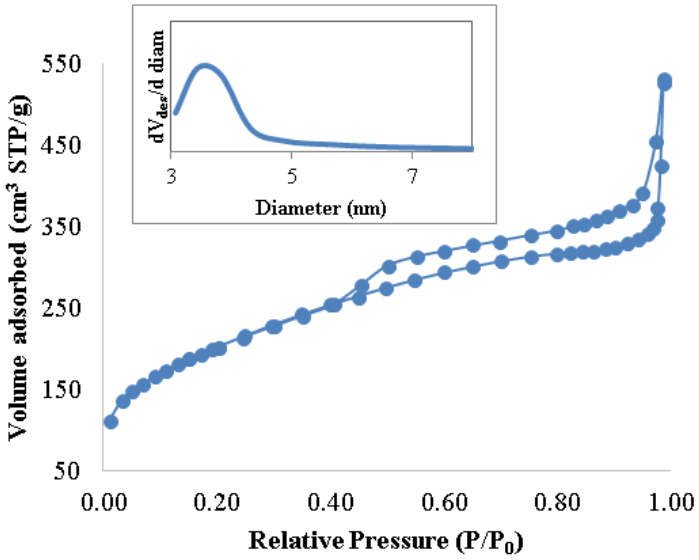

Figure 125. Nitrogen adsorption-desorption isotherms of the calcined and reduced 0.2 wt.% Pd-3.8 wt.% CeO_2 /SiO_2 catalyst. Mesopore size distribution is shown in the inset.

Wrapping up, the Pd sonochemical reduction at 205 kHz under 10 vol. % CO/Ar at 20 °C permitted to decorate a CeO_2-containing hybrid latex. Such template was successfully used in the preparation of a hierarchically porous Pd-CeO_2/SiO_2 material in which the Pd was selectively located on the CeO_2 nanoparticles. The Pd-CeO_2 particles exhibited a strong interaction that led to the formation of PdO_y-CeO_{2-x} species observed by H_2-TPR and XPS. These Pd-CeO_2 nanoparticles exhibited an average particle size of 4.8 ± 0.9 nm.

V.3.4- Hierarchically porous Pd/SiO_2 catalyst by a combination of miniemulsion polymerisation and sol-gel method

The aim of this work was to prepare meso- and macroporous silica matrix with Pd nanoparticles of a few nanometres in diameter mainly located in the macropores. As depicted on Figure 126, the catalyst was prepared in few steps, starting with the Pd-containing latex synthesis, then the silica matrix preparation, all these steps being carried out in water, and finally, the template removal by calcination. The main differences with the approach presented in Section V.3.1- *Hierarchically porous Pd/SiO2 catalyst via sol-gel synthesis with sonochemically decorated polystyrene latex template* are that in this case no sonochemical reduction takes place and the noble metal precursor is within the polymer spheres. While in the case of the sonochemical approach, Pd nanoparticles decorate the surface of the polymer beads.

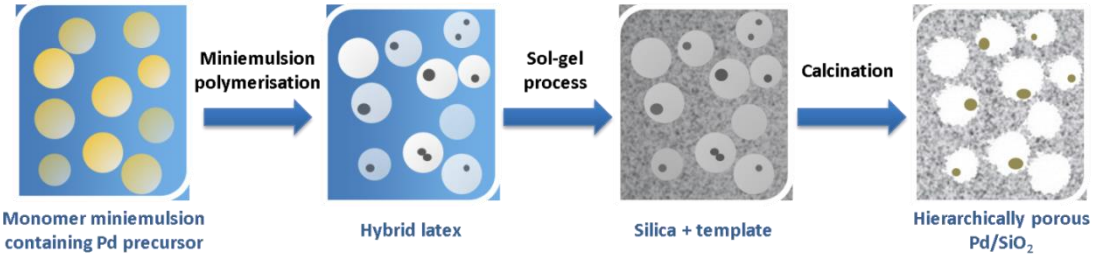

Figure 126. Pd-supported catalyst preparation by combination of miniemulsion polymerisation and sol-gel synthesis.

V.3.4.1- Pd-containing hybrid latex by miniemulsion polymerisation

The miniemulsion of styrene and $Pd(acac)_2$ in water was formed by sonication at 20 kHz, leading to oil-phase droplets of 118 nm (PDI: 0.45), as measured by DLS. After 2.5 h of polymerisation and 97 % of styrene conversion, the pH was 6.83, the solids content was 9.22 wt. %. The polymer particles exhibited an intensity-average particle size of 112 nm (PDI: 0.16) by DLS, in good agreement with the initial droplets size, which is expected in this kind of polymerisation [34]. In Figure 127, latex particles containing nanoaggregates of palladium can be observed. It is important to keep in mind that this image corresponds to a dry sample, so it explains why the polymer particles appear aggregated. However, in water, the polymer particles are well-dispersed and without sign of colloidal instability after 8 months of storage.

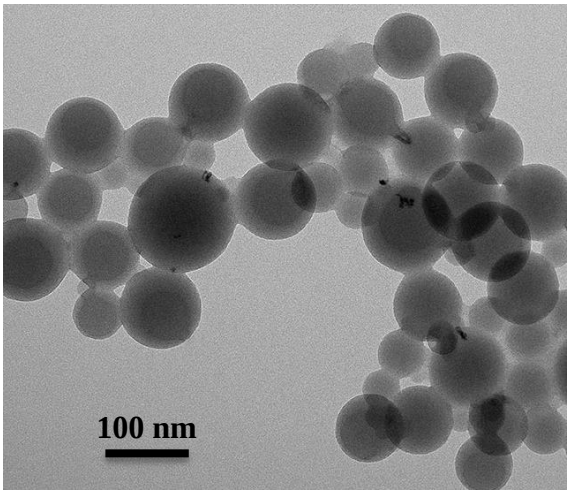

Figure 127. TEM image of the polystyrene latex containing 0.2 wt. % Pd.

V.3.4.2- Catalyst preparation and characterisation

The Pd-containing hybrid latex template was then used in the preparation of a hierarchically porous silica material by sol-gel synthesis, using a two-step acid-base catalysed sol-gel method as described in the experimental section. Then, the template was removed by a heat treatment in air at 650 °C, as previously determined for a Pd-containing polystyrene-silica composite material (Section V.3.1.2-*Catalyst preparation and characterisation*). Figure 128 shows a TEM image of the 0.2 wt. % Pd/SiO_2 catalyst after template removal by calcination. It is possible to see the macropores left by the polymer template containing Pd nanoparticles, as desired with this preparation method. The Pd nanoparticles were measured to have a number-average diameter (D_n) of 12.0 nm, a weight-average diameter (D_w) of 13.6 nm and dispersity (Đ) of 1.13 ($Đ = D_w/D_n$).

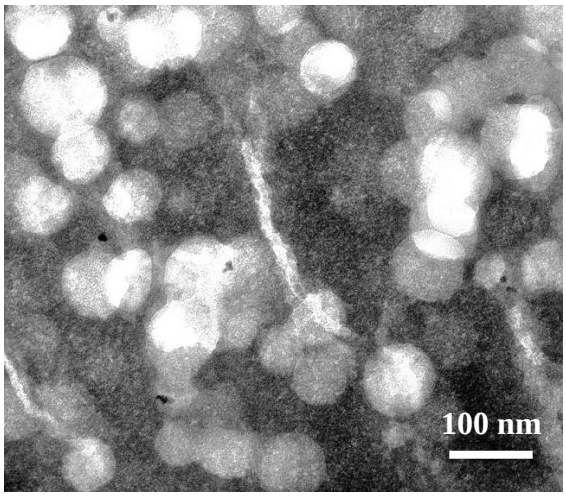

Figure 128. TEM image of the 0.2 wt. % Pd/SiO_2 catalyst (after removal of the polystyrene template by calcination at 650 °C).

A H_2-TPR analysis was carried out in the calcined material in order to evaluate the reduction temperature required to obtain metallic Pd species. Figure 129 shows the profile comparison of the Pd-containing silica with a Pd-free silica material. As expected, the silica does not show any reduction peak in the evaluated temperature range. However, the 0.2 wt. % Pd/SiO_2 prepared from the Pd-containing hybrid latex by mimiemulsion polymerisation exhibited a reduction peak centred at 75 °C, which is about 20 °C higher than the homologous material prepared using sonochemical decoration. Such difference could be due to a slightly stronger Pd-support interaction in this case.

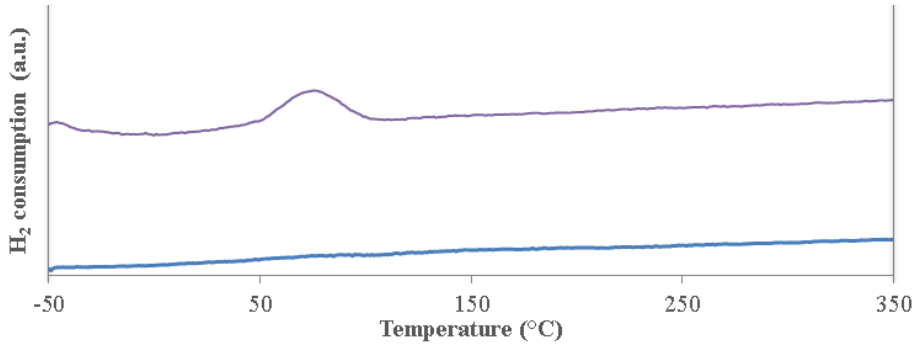

Figure 129. H_2-TPR profiles of 0.2 wt. % Pd/SiO_2 (violet, top) and Pd-free templated SiO_2 (blue, bottom), both calcined at 650 °C.

XPS analyses were carried out after each preparation step. The corresponding spectra are presented in Figure 130. The Pd3d core level spectrum for the hybrid latex after miniemulsion polymerisation shows a broad peak for Pd (Figure 130.a.), which was highly noisy due to the low Pd loading. The $Pd3d_{5/2}$ maximum was found at 338.6 eV, which does not correspond to pure $Pd(acac)_2$, whose $Pd3d_{5/2}$ signal has been reported to be at 336.4 eV [35]. This result suggests a close interaction of the Pd complex with the polystyrene formed *in-situ*. For instance, $Pd(acac)_2$ on active carbon cloth has exhibited binding energies around 338.4 eV upon impregnation, and such signal has been attributed to Pd(IV) species formed upon dissolution with ionic liquids [36]. After calcination at 650 °C, the Pd was mainly in the form of PdO (Figure 130.b.). After a hydrogen treatment at 300 °C, the Pd species got reduced to form mainly metallic Pd (Figure 130.c.).

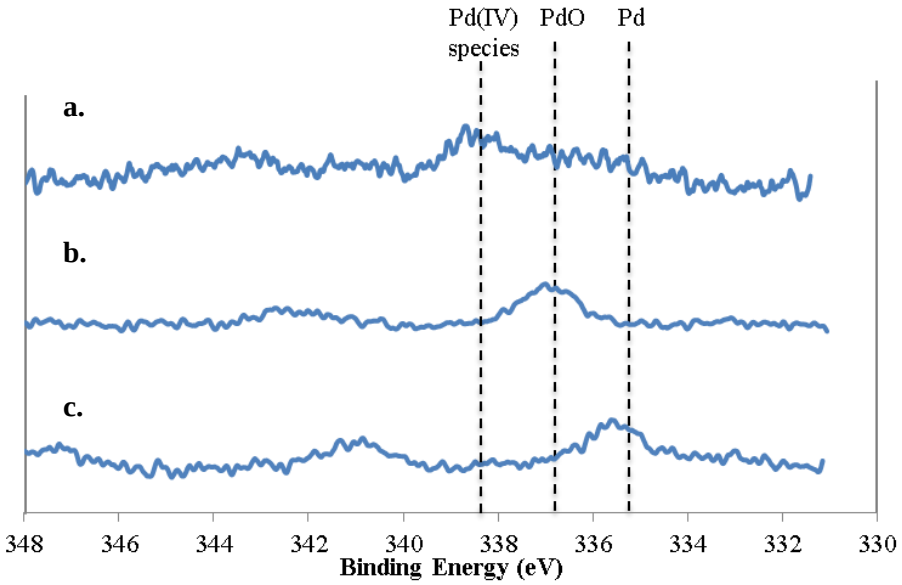

Figure 130. XPS spectra of: a. Polystyrene template with $Pd(acac)_2$, b. Silica composite with polymer template in a. after calcination at 650 °C, c. Silica material in b. after reduction at 300 °C.

After template removal and Pd reduction, as observed in Figure 131, the catalyst exhibited nitrogen physisorption isotherms characteristic of a hierarchically-porous material, which is expected considering the two-step acid-base catalysed sol-gel synthesis protocol used for the preparation of this silica-supported catalyst. In addition, a surface area of 711 m^2/g and a total pore volume of 0.93 cm^3/g were obtained. The mesopores size distribution was observed to be up to ca. 5 nm.

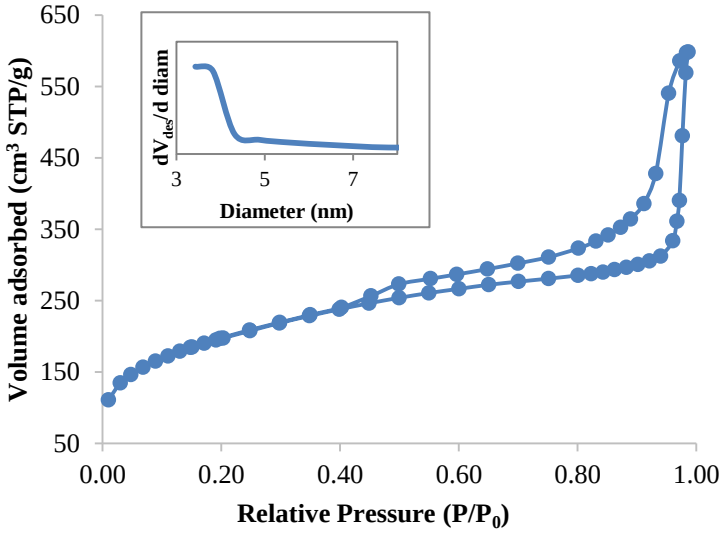

Figure 131. Nitrogen adsorption-desorption isotherms of the calcined and reduced 0.2 wt.% Pd/SiO_2 catalyst prepared with a miniemulsion-polymersiation-derived polymer template. Mesopore size distribution is shown in the inset.

In conclusion, it was possible to prepare a 0.2 wt. % Pd/polystyrene latex template by miniemulsion polymerisation. Such template was successfully used in the preparation of hierarchically porous 0.2 wt. % Pd/SiO_2 material. Despite of having 3-times lower Pd loading, it exhibited just slightly smaller Pd nanoparticles (12.0 ± 2.7 nm) than 0.7 wt.% Pd/SiO_2 prepared via a sonochemically decorated template (16.2 ± 4.6 nm). After the template removal by calcination at 650 °C, the Pd nanoparticles were mainly composed of and Pd(II), which were reduced to Pd(0) under hydrogen at 300 °C.

V.4- Conclusion

Four hierarchically porous materials were successfully prepared having different functionalities and exploring the versatility of the synthesis methodology proposed in this work. Their main characteristics are summarised in Table 21.

Table 21. Summary of the main characteristics of the prepared materials

	Pd/SiO_2	$Pt\text{-}Pd/SiO_2$	$Pd\text{-}CeO_2/SiO_2$	Pd/SiO_2 (miniemulsion approach)
Total surface area (m^2/g)	425	581	735	711
Total pore volume (cm^3/g)	0.47	0.64	0.82	0.93
Total porosity (%)	51	58	64	67
Active species	Pd	Bimetallic Pt-Pd	Pd/CeO_2 [b]	Pd
Loading	0.7 wt.% Pd	0.3 wt.% Pt 0.2 wt.% Pd	0.2 wt.% Pd 3.8 wt.% CeO_2	0.2 wt.% Pd
Metal particle size on template (nm) [a]	6.7 ± 2.7 nm ($Đ$ =1.59)	3.6 ± 1.3 nm ($Đ$ =1.39)	N.A. [b]	N.A. [c]
Metal particle size in final material (nm) [a]	16.2 ± 4.6 nm ($Đ$ = 1.23)	3.8 ± 1.4 nm ($Đ$ =1.54)	N.A. [b]	12.0 ± 2.7 nm ($Đ$ = 1.13)

[a] Number-average diameter (dispersity ($Đ = \overline{D_w/D_n}$) was calculated as the ratio of the weight-average diameter (D_w) over the number-average diameter (D_n)).
[b] Pd was finely dispersed on the CeO_2 nanoparticles, so it was not possible to measure the Pd particle size.
[c] The Pd precursor was mixed with the polymer beads.

In a first place, it was possible to demonstrate the preparation of hierarchically porous Pd-based catalysts by sol-gel method using a template of sonochemically decorated polystyrene latex (previously prepared by emulsion polymerisation). It permitted to demonstrate the feasibility of Pd sonochemical decoration, which was previously used in the preparation of Pt-based catalysts. Nevertheless, unlike in the case of Pt, the reduction atmosphere had an important impact on the successful latex decoration. Compared to pure Ar, the mixture 10 vol.% CO/Ar favoured the polymer homogeneous decoration with Pd nanoparticles, which were small enough to be stabilised at the surface of the polymer beads. Regarding sintering, an important increase of particle size was observed for these Pd nanoparticles, in comparison with the Pt-based materials. The Pt particle size previously obtained on the template was ca. 2.2 nm, which sintered to 4.6 nm or 6.5 nm when calcined at 450 °C or 650 °C, respectively. On the other hand, the synthesised Pd particles were of 6.7 nm, which reached 16.2 nm after calcination at 650 °C. Another important point to note is that macroscopic settlement of the Pd-decorated latex at 1 wt.% metal/polymer was an indication of the challenge to work with high Pd contents. Such a settlement was not observed in the case with Pt-decorated latexes.

The second approach demonstrated the versatility of the sonochemical latex decoration to prepare Pt-Pd bimetallic nanoparticles by a subsequent functionalisation of the polystyrene

beads. The bimetallic composition was successfully demonstrated by EDX mappings at high resolution. Additionally, the particles demonstrated a high thermal stability with a very limited sintering after calcination at 650 °C, going from an average particle diameter of D_n = 3.6 ± 1.3 nm after sonochemical preparation to D_n = 3.8 ± 1.4 nm, after calcination. Such nanoparticles were homogenously distributed on a hierarchically porous silica support.

The third material permitted to demonstrate the versatility of latex synthesis and its powerful coupling with sonochemical reduction to prepare Pd-CeO_2 nanoparticles. A CeO_2-containing hybrid latex was first prepared by emulsion polymerisation. Then, after Pd decoration by sonochemical means, the latex was used as template to prepare a hierarchically porous silica-supported catalyst. Even though, the sol-gel method was slightly modified since this hybrid latex was not stable at pH=2, a hierarchically porous support was successfully prepared by including a silica precursor pre-hydrolysis step. This was evidence of the versatility of the sol-gel method to work with latex templates that exhibit different colloidal behaviours. After the template removal by calcination, it was possible to observe a close interaction between Pd-CeO_2 on the EDX mappings, which led to the formation of stable PdO_y-CeO_{2-x} species, as observed by XPS.

A last approach permitted to demonstrate the possibility to prepare hybrid Pd/polystyrene latex template via miniemulsion polymerisation. This approach permitted to omit the sonochemical decoration in the preparation of monometallic Pd nanoparticles. However, this method gives very limited control on the nanoparticles synthesis: particle size, formation of bimetallic interactions, metal dispersion on the latex, etc.

These results permit to conclude that it is possible to prepare Pd-based catalysts by the combination of latex synthesis, sonochemistry and sol-gel method. The versatility of such preparation technique led to the successful preparation of hierarchically porous silica-supported catalysts with monometallic Pd, bimetallic Pt-Pd and mixed metallic-metal oxide Pd-CeO_2 functionalities. It is important to note that all the evaluated approaches were waterborne, contributing to a sustainable catalyst preparation.

The next chapter will be focused on the catalytic performances of these Pd-based materials for the direct synthesis of hydrogen peroxide from oxygen and hydrogen.

V.5- References

[1] C.H. Bartholomew, R.J. Farrauto, Fundamentals of Industrial Catalytic Processes, John Wiley & Sons, Inc., Hoboken, NJ, USA, 2005. doi:10.1002/9780471730071.

[2] T. Muroi, Role of Precious Metal Catalysts, Noble Metals, InTech, 2012.

[3] Y.H. Ng, M. Wang, H. Han, C.L.L. Chai, Organic polymer composites as robust, non-covalent supports of metal salts, Chem. Commun. (2009) 5530. doi:10.1039/b905283f.

[4] R. Rendon, S.K. Rendon-Lara, A.L. Fernandez-Osorio, V.M. Ugalde-Saldivar, Aerobic synthesis of palladium nanoparticles, Rev. Adv. Mater. Sci. 27 (2011) 31–42.

[5] T. Chihara, S. Teratani, M. Hasegawa-Ohotomo, T. Amemiya, K. Taya, Different behavior between Pt and Pd catalysts in the hydrogenolysis of cyclohexanediones and hydroxycyclohexanones, J. Catal. 90 (1984) 221–231. doi:10.1016/0021-9517(84)90250-1.

[6] J.M. Campos-Martin, G. Blanco-Brieva, J.L.G. Fierro, Hydrogen peroxide synthesis: an outlook beyond the anthraquinone process., Angew. Chem. Int. Ed. Engl. 45 (2006) 6962–84. doi:10.1002/anie.200503779.

[7] S. Okada, T. Kamegawa, K. Mori, H. Yamashita, An electroless deposition technique for the synthesis of highly active and nano-sized Pd particles on silica nanosphere, Catal. Today. 185 (2012) 109–112. doi:10.1016/j.cattod.2011.08.014.

[8] M.-O. Coppens, G. Wang, Optimal Design of Hierarchically Structured Porous Catalysts, in: U.S. Ozkan (Ed.), Des. Heterog. Catal., Wiley-VCH Verlag GmbH & Co. KGaA, Weinheim, Germany, 2009: pp. 25–58. doi:10.1002/9783527625321.

[9] J. Garnier, J. Warnant, P. Lacroix-Desmazes, P.-E. Dufils, J. Vinas, Y. Vanderveken, A.M. van Herk, An emulsifier-free RAFT-mediated process for the efficient synthesis of cerium oxide/polymer hybrid latexes., Macromol. Rapid Commun. 33 (2012) 1388–92. doi:10.1002/marc.201200093.

[10] ISO (International Organization for Standardization), ISO 13321, Particle size analysis—photon correlation spectroscopy, Geneva, 1996.

[11] J. Garnier, J. Warnant, P. Lacroix-Desmazes, P.-E. Dufils, J. Vinas, A. van Herk, Sulfonated macro-RAFT agents for the surfactant-free synthesis of cerium oxide-based hybrid latexes., J. Colloid Interface Sci. 407 (2013) 273–81. doi:10.1016/j.jcis.2013.06.037.

[12] J. Warnant, J. Garnier, A. Van Herk, P.-E. Dufils, J. Vinas, P. Lacroix-Desmazes, Synthesis of Complexing Copolymers by RAFT and Their Use in Emulsion Polymerization To Prepare CeO 2 /Polymer Hybrid Latexes, in: K. Matyjaszewski et al. (Ed.), Control. Radic. Polym. Mater., ACS Symposium Series, 2015: pp. 309–325. doi:10.1021/bk-2015-1188.ch019.

[13] S.I. Nikitenko, C. Le Naour, P. Moisy, Comparative study of sonochemical reactors with different geometry using thermal and chemical probes, Ultrason. Sonochem. 14 (2007) 330–336. doi:10.1016/j.ultsonch.2006.06.006.

[14] A. Manzke, C. Pfahler, O. Dubbers, A. Plettl, P. Ziemann, D. Crespy, E. Schreiber, U. Ziener, K. Landfester, Etching masks based on miniemulsions: A novel route towards ordered arrays of surface nanostructures, Adv. Mater. 19 (2007) 1337–1341. doi:10.1002/adma.200601945.

[15] A. Badalyan, P. Pendleton, Analysis of Uncertainties in Manometric Gas-Adsorption Measurements. I: Propagation of Uncertainties in BET Analyses, Langmuir. 19 (2003) 7919–7928. doi:10.1021/la020985t.

[16] R.W. Cranston, F.A. Inkley, Advances in Catalysis and Related Subjects, Academic Press, New York, 1955.

[17] P.A. Albouy, A. Ayral, Coupling x-ray scattering and nitrogen adsorption: An interesting approach for the characterization of ordered mesoporous materials. Application to hexagonal silica, Chem. Mater. 14 (2002) 3391–3397. doi:10.1021/cm0211453.

[18] N. Takeno, Atlas of Eh-pH diagrams Intercomparison of thermodynamic databases, 2005.

[19] M.J. Muñoz Portero, Características y usos de los diagramas de Pourbaix, Univ. Politécnica Val. (2011). https://riunet.upv.es/bitstream/handle/10251/13708/Características y usos.pdf (accessed November 10, 2015).

[20] P. Pfaffli, A. Zitting, H. Vainio, Thermal degradation products of homopolymer polystyrene in air, Scand. J. Work. Environ. Heal. 4 (1978) 22–27. doi:10.5271/sjweh.2744.

[21] M.A. Ver Meer, B. Narasimhan, B.H. Shanks, S.K. Mallapragada, Effect of mesoporosity on thermal and mechanical properties of polystyrene/silica composites, ACS Appl. Mater. Interfaces. 2 (2010) 41–47. doi:10.1021/am900540x.

[22] O. Bera, B. Pilić, J. Pavličević, M. Jovičić, B. Holló, K.M. Szécsényi, M. Špirkova, Preparation and thermal properties of polystyrene/silica nanocomposites, Thermochim. Acta. 515 (2011) 1–5. doi:10.1016/j.tca.2010.12.006.

[23] J.L. Gurman, L. Baier, B.C. Levin, Polystyrenes: A review of the literature on the products of thermal decomposition and toxicity, Fire Mater. 11 (1987) 109–130. doi:10.1002/fam.810110302.

[24] J.G. Firth, S.J. Gentry, A. Jones, Oxidation reactions on platinum catalysts, J. Catal. 34 (1974) 159–161. doi:10.1016/0021-9517(74)90023-2.

[25] K. Kamiya, T. Yoko, Synthesis of SiO2 glass fibres from Si(OC2H5)4-H2O-C2H5OH-

HCl solutions through sol-gel method, J. Mater. Sci. 21 (1986) 842–848. doi:10.1007/BF01117362.

[26] S. Ayyappan, R.S. Gopalan, G.N. Subbanna, C.N.R. Rao, Nanoparticles of Ag, Au, Pd, and Cu produced by alcohol reduction of the salts, J. Mater. Res. 12 (1997) 398–401. doi:10.1557/JMR.1997.0057.

[27] S.E. Skrabalak, B.J. Wiley, M. Kim, E. V. Formo, Y. Xia, On the Polyol Synthesis of Silver Nanostructures: Glycolaldehyde as a Reducing Agent, Nano Lett. 8 (2008) 2077–2081. doi:10.1021/nl800910d.

[28] K. McEleney, C.M. Crudden, J.H. Horton, X-ray Photoelectron Spectroscopy and the Auger Parameter As Tools for Characterization of Silica-Supported Pd Catalysts for the Suzuki?Miyaura Reaction, J. Phys. Chem. C. 113 (2009) 1901–1907. doi:10.1021/jp808837k.

[29] T. Zhang, Y. Nakagawa, T. Wakasugi, S. Isobe, Y. Wang, N. Hashimoto, S. Ohnuki, Hydrogen Absorption of Palladium Thin Films Observed by in Situ Transmission Electron Microscopy with an Environmental Cell, ACS Appl. Mater. Interfaces. 8 (2016) 14548–14551. doi:10.1021/acsami.6b02971.

[30] K. Cao, Q. Zhu, B. Shan, R. Chen, Controlled Synthesis of Pd/Pt Core Shell Nanoparticles Using Area-Selective Atomic Layer Deposition, Sci. Rep. 5 (2015) 8470. doi:10.1038/srep08470.

[31] Y. Zhou, N.J. Lawrence, T.S. Wu, J. Liu, P. Kent, Y.L. Soo, C.L. Cheung, Pd/CeO2-x nanorod catalysts for CO oxidation: Insights into the origin of their regenerative ability at room temperature, ChemCatChem. 6 (2014) 2937–2946. doi:10.1002/cctc.201402243.

[32] W.C. Conner, J.L. Falconer, Spillover in Heterogeneous Catalysis, Chem. Rev. 95 (1995) 759–788. doi:10.1021/cr00035a014.

[33] S. Phokha, S. Pinitsoontorn, P. Chirawatkul, Y. Poo-arporn, S. Maensiri, Synthesis, characterization, and magnetic properties of monodisperse CeO2 nanospheres prepared by PVP-assisted hydrothermal method, Nanoscale Res. Lett. 7 (2012) 425. doi:10.1186/1556-276X-7-425.

[34] E. Schreiber, U. Ziener, A. Manzke, A. Plettl, P. Ziemann, K. Landfester, Preparation of narrowly size distributed metal-containing polymer latexes by miniemulsion and other emulsion techniques: Applications for nanolithography, Chem. Mater. 21 (2009) 1750–1760. doi:10.1021/cm802796y.

[35] L. Huang, Y. Wang, Zhan Wang, Fengxi Chen, Heck Chemistry - a Highly Active Ligand-Free Metal Catalyst System in Situ Generated from PdII Supported on SiO2, Phys. Chem. 2 (2012) 27–34. doi:10.5923/j.pc.20120201.06.

[36] J.-P.T. Mikkola, P.P. Virtanen, K. Kordas, H. Karhu, T.O. Salmi, SILCA-Supported ionic liquid catalysts for fine chemicals, Appl. Catal. A Gen. 328 (2007) 68–76. doi:10.1016/j.apcata.2007.05.030.

VI. PALLADIUM-BASED CATALYSTS PERFORMANCE IN THE DIRECT SYNTHESIS OF HYDROGEN PEROXIDE

Contents

Some of the results described in this chapter have been published:

> A.F. Sierra Salazar, W.S.J. Li, M. Bathfield, A. Ayral, S. Abate, T. Chave, S. Nikitenko, V. Hulea, S. Perathoner, P. Lacroix-Desmazes. "Hierarchically porous Pd/SiO2 catalyst by combination of miniemulsion polymerisation and sol-gel method for the direct synthesis of H_2O_2". *Catalysis Today* (2016), DOI: 10.1016/j.cattod.2016.12.021.

VI.1- Introduction

Hydrogen peroxide (H_2O_2) is an important commodity compound with a forecasted global market of 4.67 million metric tons by 2017 [1]. It can be used in a very broad spectrum of applications: paper and textile bleaching, wastewater treatment, chemical synthesis, desulphurisation, metallurgy, electronics, propulsion and food industry among others [2]. H_2O_2 is considered to be a green oxidant since water is the only by-product [3]. However, it is currently produced by the anthraquinone process, which presents environmental challenges due to effluents treatment and complex use of large amounts of solvents [2,4,5]. A lot of industrial interest has appeared in the last few decades on the direct synthesis of H_2O_2 as a competitive alternative [2,6]. Indeed, it constitutes a real alternative for on-site, on-demand and small-scale hydrogen peroxide production (capacities less than 10 kt per year), avoiding additional costs such as transportation and storage [6–8]. The H_2O_2 direct synthesis by the oxidation of hydrogen on Pd catalysts is a greener option: cleaner and more atom-efficient, but it is challenged by the low selectivity or requirement of additives with most catalysts [9]. (Figure 132 presents the reaction pathway for the direct synthesis of hydrogen peroxide and the related side-reactions).

Nevertheless, this reaction is catalyst-structure sensitive [10,11], meaning that depending on the catalyst design, the selectivity can be optimised towards H_2O_2.

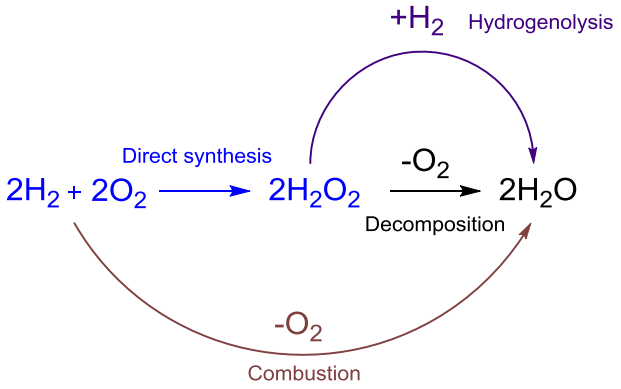

Figure 132. Reaction pathway of the direct synthesis of hydrogen peroxide (in blue) and the related undesired reactions leading to water [12].

The H_2O_2 direct synthesis is also challenged by safety issues: the reaction gas mixtures only have small regions out of the flammable range (e.g. below 1.1 vol.% H_2 or above 90.1 vol.% H_2 in air, at 21 °C and 4 bar) [13], such region become narrower when increasing pressure and temperature. Additionally, the solid catalyst must be in a liquid medium, otherwise dry catalyst could lead to explosions [6]; as a result a gas-liquid-solid system is required, which increases in complexity due to the three-phases mass transport phenomena. Considering these technical challenges, most of the efforts have focused on catalyst development in order to meet the several requirements needed to make of the direct synthesis of H_2O_2 an economically viable process at a large scale. Such requirements include H_2O_2 concentrations above 15% (aqueous) or 9% (alcohol), high H_2 conversion (> 99%) and selectivity towards H_2O_2 above 20% [6]. However, the selectivity and productivity vary largely depending on the operation conditions and type of reactor, which make difficult to compare catalysts performances from the literature [8]. Nevertheless, common trends can be identified. For instance, selectivity values have been reported up to 95 % at low H_2 conversion (< 10%), but at higher conversions, it drops to maximum selectivity values of 50-60% [6]. Such values of selectivity are often achieved with the help of promoters like halides that act as catalyst poisons to limit water production or acids that retard base-catalysed decomposition and hydrogenation of H_2O_2. In terms of operation conditions, low temperatures help limit the H_2O_2 decomposition, with a lower productivity as a drawback [14]. On the other hand, pressure has little effect on the selectivity, but improves the productivity by increasing the reagents concentration in the liquid phase; the drawback is the requirement of more expensive equipment that can stand high pressures [6] and the narrower safe hydrogen concentration range [13].

In order to have a base of comparison, a conservative performance for monometallic Pd is characterised by 20% selectivity and 64 $\frac{mol\ H_2O_2}{mol\ Pd \times h}$ productivity [6,15]. Regarding the productivity, it has been demonstrated on zeolite-supported metals that the best productivity is

achieved with Pd (284 $\frac{mol\ H_2O_2}{mol\ Pd \times h}$), followed by Pt (16 $\frac{mol\ H_2O_2}{mol\ Pt \times h}$) and Au (14 $\frac{mol\ H_2O_2}{mol\ Au \times h}$) [16]. However, alloys of Pd with Pt or Au have led to even better performances. For instance, Pd-Au catalyst has led to productivities of 298 $\frac{mol\ H_2O_2}{mol\ metal \times h}$ for a silica-supported catalyst [17] and 467 $\frac{mol\ H_2O_2}{mol\ metal \times h}$ for a zeolite-supported catalyst [18]. Considering the Pd-Pt system, the addition of 2.5 atom.% Pt has resulted in a 2.5-fold increase of the H_2O_2 productivity rate, without significantly affecting the selectivity [19]. Additionally, it has been shown that the addition of 0.1 wt.% Pt to a zirconia-supported Pd catalyst improved the productivity from 97 $\frac{mol\ H_2O_2}{mol\ metal \times h}$ to 122 $\frac{mol\ H_2O_2}{mol\ metal \times h}$. The same enhancement was achieved with a Pd-Au alloy, but requiring much more Au: 1.2 wt.% [20]. Other works have reported the use of Pd(II) and Pt(II) ions onto mesoporous ion-exchange resins, leading to productivities of 1070 $\frac{mol\ H_2O_2}{mol\ Pd \times h}$ and 1155 $\frac{mol\ H_2O_2}{mol\ metal \times h}$ for Pd and Pd-Pt systems[21]. Surprisingly, the Au-Pd combination has received much more attention from the academic community than the system Pt-Pd [6,8]. Even though, relevant Pt-Pd catalysts have been protected with several patents [2,22].

Catalyst design is an important tool to improve the performance of structure-sensitive reactions like this one. Control of the spatial distribution of active sites within the catalyst support, metal dispersion related to the particle size and catalyst texture are important parameters to tailor the catalyst design [23]. Several novel catalyst preparation methods have been recently reported for improving the selectivity of the direct synthesis of H_2O_2, such as: functionalised silica nanorattles containing Au nanoparticles [24], a yolk–shell structured Pd-void-ZrO_2 catalyst [25], a core–shell structured Pd/SiO_2–Al_2O_3 [26], single-crystal cubic [27] or octahedron [28] palladium supported on silica and Au-Pd nanoparticles on silica-coated capillary microchannels [29]. Concerning the support texture, silica-supported catalysts have been prepared with tailored hierarchical porosity in the presence of self-assembling molecules or polymer templates [30–37]. Metal-containing hybrid latex templates have also been prepared by miniemulsion polymerisation [38].

In Chapter III, we have discussed the preparation of hierarchically porous Pt/SiO_2 materials by a two-step acid-base catalysed sol-gel synthesis using a polystyrene latex template, where the polymer beads were sonochemically decorated with Pt nanoparticles. Chapter V has presented the versatility of such technique to prepare Pd-based catalysts, controlling the support hierarchical porosity and the preferential spatial location of the Pd nanoparticles within the macropores. Four materials were successfully prepared as schematised in Figure 133. Three of them were prepared using sonochemically decorated templates: monometallic Pd/SiO_2, bimetallic Pt-Pd/SiO_2 and mixed metallic-metal oxide Pd-CeO_2/SiO_2. The fourth one, monometallic Pd/SiO_2 was prepared with a template prepared via miniemulsion polymerisation. This chapter will be focused on the catalytic performance of these materials for the direct synthesis of H_2O_2, either after calcination or after calcination and reduction post-treatment.

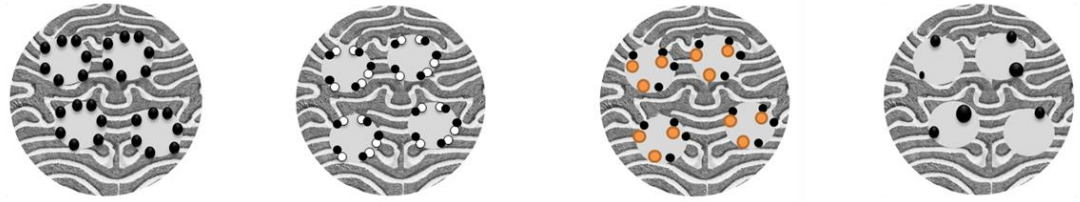

Hierarchically porous
0.7 wt.% Pd/SiO_2
Template via
emulsion polymerisation
and sonochemical reduction

Hierarchically porous
0.3 wt.% Pt - 0.2 wt.% Pd/SiO_2
Template via
emulsion polymerisation
and sonochemical reduction

Hierarchically porous
0.2 wt.% Pd - 3.8 wt.% CeO_2/SiO_2
Template via
controlled emulsion polymerisation
and sonochemical reduction

Hierarchically porous
0.2 wt.% Pd/SiO_2
Template via
miniemulsion polymerisation

Figure 133. Hierarchically porous Pd-based catalysts prepared in Chapter V.

VI.2- Experimental

VI.2.1- Materials

Anhydrous methanol (Carlo Erba, 99.9%) and sulphuric acid (H_2SO_4, Sigma Aldrich, 98%) were used as received. Catalysts as prepared in Chapter V.

VI.2.2- Catalytic test

The catalysts were either used after calcination or after a post-treatment with hydrogen at 40 mL/min and 300 °C for 2 hours in a vertical quartz tubular reactor (ex-situ reduction). The catalytic tests in batch were performed as previously described [39,40]. Typically, the catalysts were ground in a ceramic mortar to achieve a granulometry between 500 and 36 µm, with at least 70% between 500 and 250 µm, as measured in a set of mesh-sieves. The reactions were carried out at room temperature (30 °C) in a Parr 4843 stirred stainless-steel reactor coated with poly(tetrafluoroethylene) (PTFE) (capacity 300 mL, Figure 134.a.), which was equipped with 2 PTFE baffles and a PTFE gas entrainment impeller attached to a hollow PTFE stirring shaft to optimise gas-liquid mixing (Figure 134.b.). The reactor was loaded with 330 mg of catalyst with loading 0.2 wt.% Pd (or 60 mg when the loading was 0.7 wt.% Pd), 125 mL of methanol and 125 µL of H_2SO_4 to stabilise the produced H_2O_2. The reactor was purged with CO_2 for 15 minutes and with the reaction gas mixture ($H_2/O_2/CO_2$ = 9/63/28 vol.) for another 15 minutes. Then, the reactor was pressurised to 20 bars with the reaction mixture. The reaction began when stirring at 1300 rpm was started. The semibatch test was carried out in the same set-up with 60 mg of 0.2 wt.% Pd-3.8 wt.% CeO_2 /SiO_2 (granulometry between 250 and 36 µm), 125 mL of methanol and 125 µL of H_2SO_4. The reactor was purged with CO_2 for 15 minutes and with the reaction gas mixture ($H_2/O_2/CO_2$ = 9/63/28 vol.) for another 15 minutes. Then, the reactor was pressurised to 20 bars with the reaction mixture and subsequently, the outlet was carefully regulated to keep constant pressure. The total gas flow was ca. 420 N mL/min. The reaction began when stirring at 1300 rpm was started. All reactions proceeded for 3 hours with 2 mL-samples withdrawn periodically. Products concentration was monitored by potentiometric methods: H_2O in a Metrohm 831 KF Coulometer, and H_2O_2 in a Metrohm 794 Basic Trino.

After reaction, the catalysts were recovered by filtration through a cellulose filter paper, rinsed with methanol and dried at 50 °C overnight. A recycling catalytic test was performed as described above for batch reactions, using 250 mg of the recovered 0.2 wt.% Pd-3.8 wt.% CeO_2 /SiO_2 (initially used in a batch test).

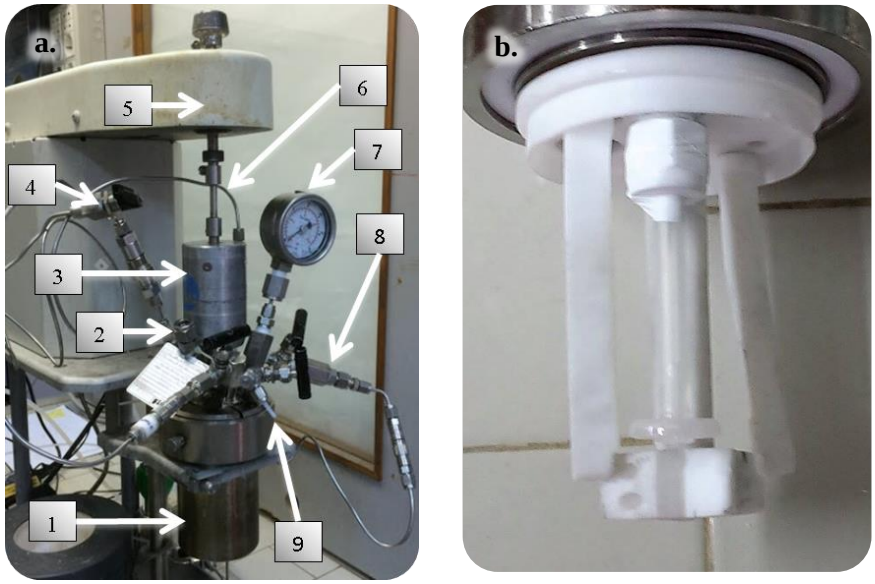

Figure 134. Set-up for the direct synthesis of H_2O_2: a. Parr 4843 stirred stainless-steel reactor (1. Reaction vessel with inner PTFE coating, 2. Safety rupture disc, 3. Magnetic drive, 4. H_2 and CO_2 mixture inlet line equipped with a valve and a quick connector, 5. Stirring unit, 6. O_2 inlet (valve and quick connector not visible in the picture), 7. Manometer, 8. Outlet equipped with a needle valve, a quick connector and a back-pressure valve (not visible in the picture). The outlet was bubbled through a water trap and then discharged outside), b. Stirring system with 2 PTFE baffles, a sampling tubing with a 0.2 µm PTFE filter and a PTFE gas entrainment impeller attached to a hollow PTFE stirring shaft.

VI.2.3- Characterisation

The catalysts were characterised before and after reaction as described in Chapter V.

VI.3- Results

The catalysts were tested in the direct synthesis of H_2O_2 from oxygen and hydrogen. Productivity $\left(\frac{mol\ H_2O_2}{mol\ Pd \times h}\right)$ and selectivity $\left(\frac{mol\ H_2O_2}{mol\ H_2O_2 + mol\ H_2O}\right)$ were calculated from the concentration monitoring data in order to investigate the catalytic performance of such materials. Structural and chemical stability were also evaluated.

VI.3.1- Hierarchically porous 0.7 wt. % Pd/SiO_2 catalyst via sol-gel synthesis with sonochemically decorated latex template

Two catalysts were derived from this material: directly after calcination, and after calcination and reduction treatment at 300 °C under hydrogen flow. All of them were tested in the direct synthesis of H_2O_2.

VI.3.1.1- Microstructure stability

Considering that the hydrogen treatment carried out to the catalyst after calcination was at 300 °C, which is 350 °C below the calcination temperature (650 °C), it is assumed that during such treatment, no significant structural modifications take place. Such an assumption is supported by the H_2-TPR profiles discussed in Chapter V that are evidence of no hydrogen consumption by the silica matrix below 350 °C. Consequently, only one of the samples will be discussed below in terms of stability under the reaction conditions. Figure 135 presents the nitrogen physisorption isotherms and Table 22 summarises the textural characteristic of the catalyst after calcination and reduction, both fresh and used.

The calcined and reduced catalyst exhibited a specific surface area of 425 m^2/g and a total pore volume of 0.47 cm^3/g. However, these values are below the expected characteristic observed on the silica matrix previously prepared under the same conditions: 615 m^2/g surface area and 0.74 cm^3/g total pore volume (Chapter III), and as discussed in Chapter V, this can be due to non-reduced Pd species (observed by XPS) that could interact with TEOS or with the ethanol produced *in-situ* during the sol-gel process. In addition, the textural characteristics degraded significantly after the catalytic test of direct synthesis of H_2O_2, as shown in Table 22. This means that the structure was not enough consolidated to stand the pressure (20 bars) used in the catalytic test. Such a condition led to densification of the catalyst, as observed by a decrease of total porosity from 51% to 43%. So there is still an opportunity for improving the structural stability of this material.

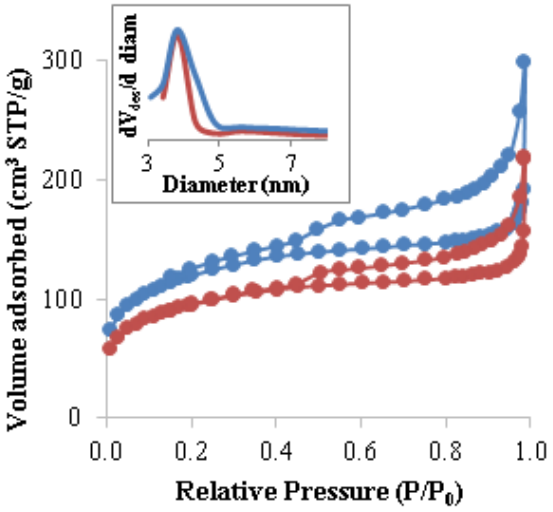

Figure 135. Nitrogen adsorption-desorption isotherms of calcined and reduced 0.7 wt.% Pd/SiO_2 catalyst. Mesopore size distributions are shown in the insets. Blue lines for fresh catalysts (—●—) and red lines for used catalysts (—●—).

Table 22. Textural characterisation from nitrogen physisorption analyses of 0.7 wt.% Pd/SiO_2 (calcined & reduced).

	Fresh	Used
Total surface area (m^2/g)	425	339
Total pore volume (cm^3/g)	0.47	0.34
Total porosity (%)	51	43

VI.3.1.2- Oxidation state and chemical environment of Pd by XPS characterisation

Figure 136 presents the XPS spectra of both catalysts, either fresh or after reaction. The $Pd3d_{5/2}$ binding energies expected for Pd, PdO, and PdO_2 are 335.1, 336.7 and 338.6 eV, respectively [4,39,41–44].

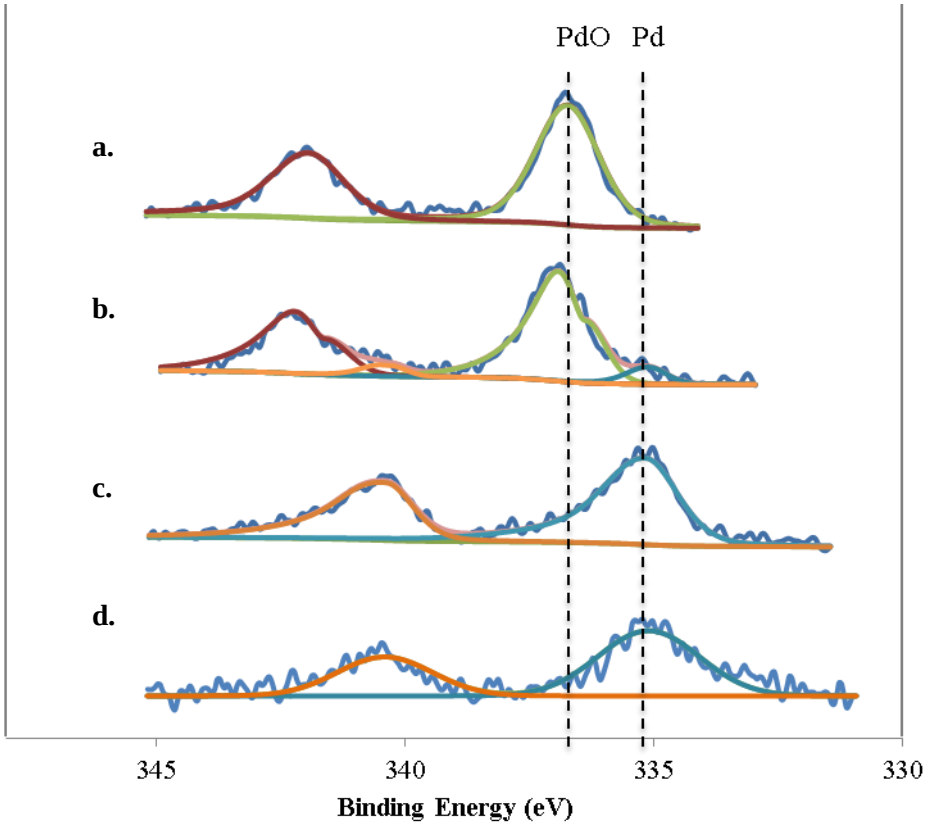

Figure 136. XPS signals of Pd3d core level: a. 0.7 wt.% Pd/SiO_2 catalyst calcined, fresh, b. 0.7 wt.% Pd/SiO_2 catalyst calcined, used, c. 0.7 wt.% Pd/SiO_2 catalyst calcined and reduced, fresh, d. 0.7 wt.% Pd/SiO_2 catalyst calcined and reduced, used. Dashed lines indicate $Pd3d_{5/2}$ binding energies for PdO and Pd.

It is important to note that these spectra are very noisy due to the low Pd concentration in the material (0.7 wt.% Pd), so it is difficult to precisely quantify the amount of species at each oxidation state. Nevertheless, it is possible to make a qualitative comparison of the oxidation state before and after reaction. The used catalyst after calcination (Figure 136.b.) exhibited a slight reduction at the reaction conditions, represented by a small component on the spectrum corresponding to Pd(0). Diversely, the reduced catalyst (Figure 136.c.) kept its oxidation state after reaction (Figure 136.d.), meaning that the Pd nanoparticles after the thermal treatment in hydrogen are chemically stable at the evaluated reaction conditions.

VI.3.1.3- Catalytic performance

The two materials (after calcination and after calcination and reduction) were active in the H_2O_2 direct synthesis, but they exhibited different performances (Figure 137). Catalysts 0.7 wt.% Pd/SiO_2 calcined and 0.7 wt.% Pd/SiO_2 calcined and reduced exhibited selectivity towards H_2O_2 of 54 ± 8 % and 49 ± 3 % at 180 min, respectively. Such values are slightly better than 40% selectivity reported elsewhere for a 0.3 wt.% Pd/K2621 in batch conditions, which was expected

to decrease when increasing the Pd loading on the catalyst [11]. This value is slightly better than 42% reported for 3.6 wt.% Pd/SiO_2 under slightly similar reaction conditions after 4 h of reaction [45]. Even though, the calcined and the reduced catalysts did not show a significant difference in selectivity, the reduced catalyst was more active, reaching a maximum productivity of 3460 $\frac{mol\ H_2O_2}{mol\ Pd \times h}$ at 10 min of reaction (it decreased due to reagents consumption), compared to a maximum of 840 $\frac{mol\ H_2O_2}{mol\ Pd \times h}$ at 120 min for the only calcined material. This lower activity can be attributed to the fact that an *in-situ* partial reduction took place at the beginning of the reaction for the only-calcined material. These productivity values are comparable to some of the highest results reported in the literature for monometallic Pd (under different reaction conditions): 1770$\frac{mol\ H_2O_2}{mol\ Pd \times h}$ and 5632$\frac{mol\ H_2O_2}{mol\ Pd \times h}$ in batch and semi-batch, respectively [11].

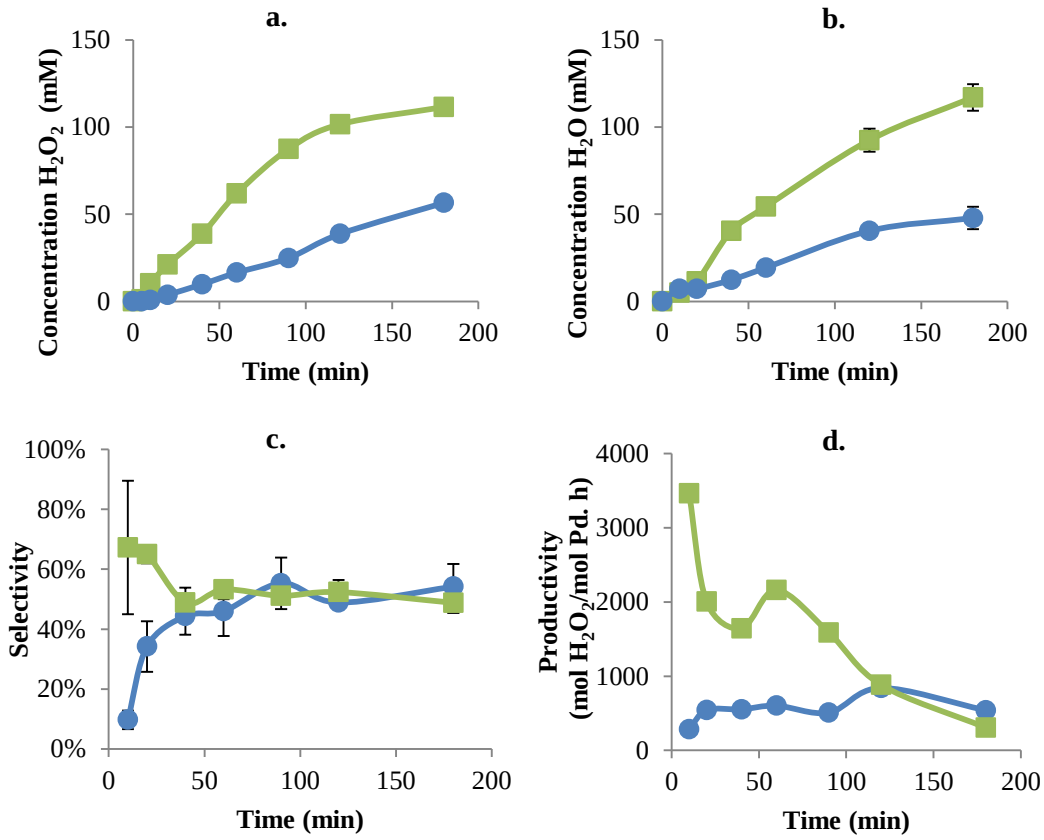

Figure 137. Profiles of: a. H_2O_2 concentration, b. H_2O concentration, c. H_2O_2 selectivity, and d. H_2O_2 productivity, using: 0.7 wt.% Pd/SiO_2 calcined (—●—) and 0.7 wt.% Pd/SiO_2 calcined and reduced (—■—). Please note that some of the error bars are not visible because they are smaller than the graph markers.

Generally, the productivity of H_2O_2 is expected to be higher with Pd(0) than with Pd(II), as observed here, but not necessarily more selective [46]. It has been reported that highly oxidised Pd catalysts are detrimental for the selectivity [11], as observed at the beginning of the reaction with the calcined catalysts (Figure 137.c). However, passivated surface Pd species with oxygen have shown to be better than non-passivated, exhibiting higher activities and selectivity values around 40 % [47]. Indeed, the ratio Pd(0)/Pd(II) has been reported to play an important role in the selectivity, being favoured with Pd(II) species at the surface [46]. Congruently, the calcined and reduced catalyst exhibited the best overall performance with the highest productivity. However, no statistically significant difference of selectivity at the end of the reaction was observed between the calcined and the reduced catalysts. It is then recommended to carry out semi-continuous and continuous tests in order to evaluate the selectivity in a longer run.

Additionally, it is important to note that the oxidation state of the reduced Pd nanoparticles was stable after reaction evidencing a good chemical stability. Conversely, the catalyst texture stability needs to be improved.

VI.3.1.4- Hydrogen consumption: limiting reagent

As an example, let's consider the concentration of products at 180 min achieved with 0.7 wt.% Pd/SiO_2 calcined and reduced:

$$[H_2O_2] = 0.112\ M$$

$$[H_2O] = 0.117\ M$$

At that time, the final volume of solvent could be approximated to 100 mL (after sampling). So the number of moles of H_2 consumed in H_2O_2 would be:

$$n_{H_2} = 0.112\ \frac{mol}{L} \times 0.100\ L = 0.0112\ mol\ H_2$$

And the number of moles of H_2 consumed in H_2O would be:

$$n_{H_2} = 0.117\ \frac{mol}{L} \times 0.100\ L = 0.0117\ mol\ H_2$$

So the total number of moles of H_2 consumed would be:

$$0.0112\ mol\ H_2 + 0.0160\ mol\ H_2 = \mathbf{0.0229\ mol\ H_2}$$

An estimation of the initial number of moles of H_2 can be calculated by:

$$n_{H_2} = \frac{P_{H_2} V_{H_2}}{RT}$$

The volume of gas is given by the volume of the reactor (ca. 300 mL) and the partial pressure of hydrogen is calculated from the initial pressure and the molar fraction:

$$P_{Total,i} = 22\ bar = 21.71\ atm$$

$$y_{H_2,i} = 0.09$$

$$P_{H_2,i} = P_{Total,i} \times y_{H_2,i} = 21.71\ atm \times 0.09 = 1.9539\ atm$$

So the initial number of moles of H_2 in the system would be:

$$n_{H_2,i} = \frac{1.9539\ atm \times 0.300\ L}{0.082\ \frac{atm\ L}{mol\ K} \times 303.15\ K} = \mathbf{0.0236\ mol\ H_2}$$

Since the estimation of the initial number of moles of H_2 (0.0236 mol) is very close to the total number of moles of H_2 consumed (0.0229 mol), it can be assumed that, in this case, most of the initial amount of hydrogen has been consumed at 180 min. It can be evidenced by a very low productivity at 180 min, in Figure 137.d. In the following catalytic test, it will be observed that most of the concentration profiles achieve a plateau at values close to 100 mM due to total conversion of hydrogen (the limiting reagent).

VI.3.2- Hierarchically porous Pt-Pd/SiO_2 catalyst by a combination of latex synthesis, sonochemistry and sol-gel process

It is known that bimetallic nanoparticles can exhibit unique catalytic behaviour [48]. Particularly, the system Pt-Pd has demonstrated to be more performant than monometallic Pd in the direct synthesis of hydrogen peroxide [49]. This motivated the evaluation of this material containing bimetallic Pt-Pd nanoparticles, both after calcination and after calcination and reduction. The textural and chemical stability was also considered.

VI.3.2.1- Microstructure stability

Figure 138 presents the nitrogen physisorption isotherms of the reduced and calcined catalyst both before and after reaction. It can be seen that the isotherms are very similar, as well as the mesopore size distributions shown in the inset.

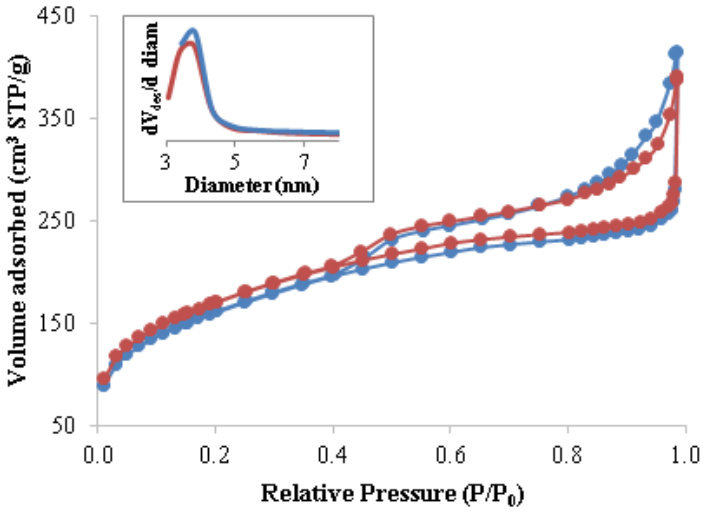

Figure 138. Nitrogen adsorption-desorption isotherms of the calcined and reduced 0.3 wt.% Pt - 0.2 wt.% Pd/SiO_2 catalyst. Mesopore size distributions are shown in the insets. Blue lines for the fresh catalyst (—●—) and red lines for the used catalyst (—●—).

Table 23. Textural characterisation of the calcined and reduced 0.3 wt.% Pt - 0.2 wt.% Pd/SiO_2 catalyst, before and after reaction.

	Fresh	Used
Total surface area (m^2/g)	581	614
Total pore volume (cm^3/g)	0.64	0.60
Total porosity (%)	58	57

Table 23 summarises the textural characterisation derived from the nitrogen physisorption analyses of these materials. The used catalyst exhibited a total pore volume of 0.64 ± 0.04 cm^3/g and a surface area of 581 ± 35 m^2/g, which are not significantly different to those of the fresh catalyst (0.60 ± 0.04 cm^3/g and 614 ± 37 m^2/g, respectively). The specific surface area and the total pore volume values of these materials are similar to those observed for single metal Pt-based catalysts prepared using the same method (632 ± 38 m^2/g and 0.64 ± 0.04 cm^3/g, 0.3cal450-205kHz characterised in Chapter III).

VI.3.2.2- Oxidation state and chemical environment of Pd and Pt by XPS characterisation

The fresh and used catalysts were characterised by XPS (Figure 139). Unfortunately, the metal loadings were too small to obtain low noise spectra, so reliable quantitative deconvolutions are not possible. Nevertheless, a noticeable shift was observed for the oxidation state of both Pt and Pd after reduction of the catalyst (Figure 139.c.), compared to the only calcined catalyst (Figure 139.a.). It means that after calcination, the predominant species are PdO and PtO, but after the heat treatment in hydrogen, metallic Pd(0) and Pt(0) became the predominant species. The binding energy peaks observed around 335.1 eV for $Pd3d_{5/2}$ and 71.2 eV for $Pt4f_{7/2}$ correspond to values previously reported for bimetallic nanoparticles [50]. Additionally, the oxidation state of either Pt or Pd was the same before and after reaction for both tested catalysts (oxidised and reduced). This implies chemical stability of the bimetallic nanoparticles at the evaluated reaction conditions.

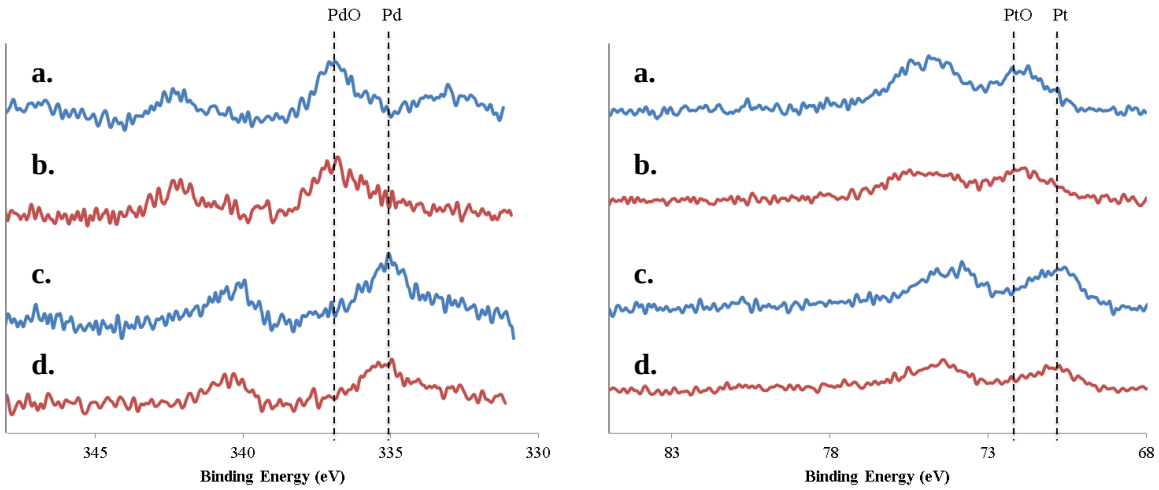

Figure 139. XPS spectra of Pd3d (left) and Pt4f (right) core levels of 0.3 wt.% Pt - 0.2 wt.% Pd/SiO_2: a. calcined, fresh, b. calcined, used, c. calcined and reduced, fresh, d. calcined and reduced, used. Dashed lines indicate $Pd3d_{5/2}$ binding energies for PdO, Pd, PtO and Pt. Blue lines for the fresh catalyst (—) and red lines for the used catalyst (—).

VI.3.2.3- Catalytic performance

The results of the catalytic tests of the calcined and the calcined and reduced materials are presented in Figure 140. It could be observed that the bimetallic nanoparticles were very active catalysts in the reaction between hydrogen and oxygen, since very high productivities of H_2O_2 were observed at 10 minutes of reaction: 24000 and 32500 $\frac{mol\ H_2O_2}{mol\ metal \times h}$ for the calcined and the calcined and reduced catalysts, respectively. In comparison with the literature, productivities up to 1155 $\frac{mol\ H_2O_2}{mol\ metal \times h}$ has been reported for other bimetallic Pd-Pt systems [21]. Unfortunately, a direct conclusion by comparison of these values is not possible since the reaction conditions were different.

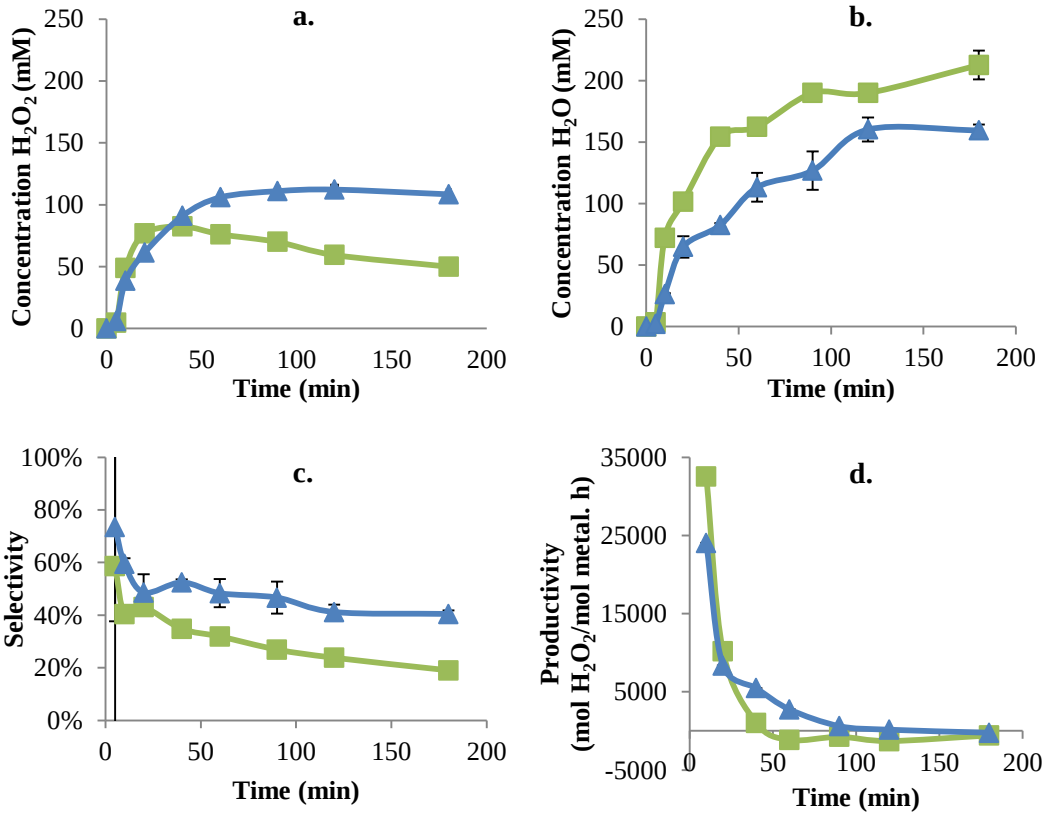

Figure 140. Profiles of: a. H_2O_2 concentration, b. H_2O concentration, c. H_2O_2 selectivity, and d. H_2O_2 productivity, using: 0.3 wt.% Pt - 0.2 wt.% Pd/SiO_2 calcined (—▲—) and 0.3 wt.% Pt - 0.2 wt.% Pd/SiO_2 calcined and reduced (—■—). Please note that some of the error bars are not visible because they are smaller than the graph markers.

Regarding the selectivity towards H_2O_2, a stable 40 ± 1 % was obtained after 2 hours of reaction with the only calcined catalyst. It was constant during the last hour of reaction. This value is comparable to 40% selectivity already reported for a monometallic 0.3 wt.% Pd/K2621 in batch conditions [11], but lower than 63% reported for $Pd_{16}Pt_1/SiO_2$ in semi-batch conditions [49]. On the other hand, the reduced catalysts showed a lower selectivity of 19 ± 1 % after 3 h, which is

due to the activity of the metallic nanoparticles in the hydrogenation of H_2O_2 in the presence of adsorbed H_2 [46], consuming the desired product and leading to water. This effect can be observed on the H_2O_2 concentration curve for this catalyst, where there is a maximum at 40 min (82 mM) and then it decreases continuously, while the water concentration increases.

The Pt effect on the H_2O_2 productivity has been proposed to be due to the modification of the Pd electronic structure that leads to the stabilisation of adsorbed dioxygen and intermediates species such as $OOH^{\bullet}$ and $OH^{\bullet}$ radicals. However an excess of Pt could destabilise the $OOH^{\bullet}$ radicals and decompose H_2O_2, decreasing the selectivity (the optimal atomic ratio has been found to be Pd/Pt = 16/1) [49]. This explains why a selectivity of 19 ± 1 % obtained with reduced Pt-Pd/SiO_2 (atomic ratio Pd/Pt = 10/9) was significantly lower than 49 ± 3 % obtained with reduced 0.7 wt. % Pd/SiO_2 (Section VI.3.1.3-*Catalytic performance*).

Consequently, it seems that an optimisation of Pt/Pd ratio would significantly improve the overall performance of this material. Moreover, the hierarchically porous 0.3 wt. % Pt - 0.2 wt. % Pd/SiO_2 catalyst exhibited chemical and structural stability at the reactions conditions. Although the selectivity towards H_2O_2 of the calcined and reduced catalyst was rather limited (19 ± 1 %), the non-reduced catalyst exhibited a good performance with a high productivity (24000 $\frac{mol\ H_2O_2}{mol\ metal \times h}$) and a stable selectivity (40 ± 1 %), already performing better than 0.7 wt.% Pd/SiO_2 described in the previous section (3460 $\frac{mol\ H_2O_2}{mol\ Pd \times h}$). Such performance could be explained by the presence of stable Pd(II) species as observed by XPS.

VI.3.3- Hierarchically porous Pd-CeO_2/SiO_2 catalyst by combination of latex synthesis, sonochemistry and sol-gel process

There is an interest to use hybrid latex containing inorganic nanoparticles such as cerium oxide [51]. For instance, in catalytic applications, a porous material synthesised with hybrid latex exhibited an important synergistic effect between platinum and cerium oxide: cerium oxide on its own has an oxygen storage capacity of 101 µmol O/g, but when it contains 1 % of platinum, the oxygen storage capacity increases to 505 µmol O/g [52]. The uses of cerium oxide in catalysis are diverse since it can be used in reactions catalysed on acid-base sites like dehydration and ketonisation, in reactions catalysed by redox centres like reduction and oxidation of organic compounds and in reactions catalysed by both like addition, substitution, isomerization and ring opening. The properties of the catalyst can be modulated by the composition of cerium-based mixed oxides [53].

In this particular work, a catalyst with mixed metallic-metal oxide Pd-CeO_2/SiO_2 was evaluated in the direct synthesis of hydrogen peroxide. It was tested after calcination and after calcination and reduction. The chemical and texture stability were evaluated, as well as the performance in batch and semi-batch operation conditions.

VI.3.3.1- Microstructure stability

The catalyst texture was characterised by nitrogen physisorption. Figure 141 shows the nitrogen isotherms for the 0.2 wt.% Pd-3.8 wt.% CeO_2 /SiO_2 calcined at 650 °C and reduced at 300 °C: before reaction, after reaction and after a recycle. In Table 24, it can be observed that the catalyst texture slightly degraded after the first reaction: surface area went from 735 ± 44 m^2/g to 654 ± 39 m^2/g and the structure became denser losing 6% of total porosity. However, the textural characteristics of the catalyst after the first reaction and after a recycle were very similar. This means that the initial catalyst texture was not stable at the reaction conditions, but during the first reaction, it adopted textural characteristics that remained stable for another catalyst reuse. The surface area and total pore volume after recycling were in agreement with the textural characteristics obtained in hierarchically porous Pt/SiO_2, discussed in Chapter III (632 ± 38 m^2/g and 0.64 ± 0.04 cm^3/g, for catalyst 0.3cal450-205kHz).

Table 24. Textural characterisation of 0.2 wt.% Pd-3.8 wt.% CeO_2 /SiO_2, calcined and reduced.

	Fresh	Used once	Recycled (used twice)
Total surface area (m^2/g)	735	654	635
Total pore volume (cm^3/g)	0.82	0.63	0.64
Total porosity (%)	64%	58%	58%

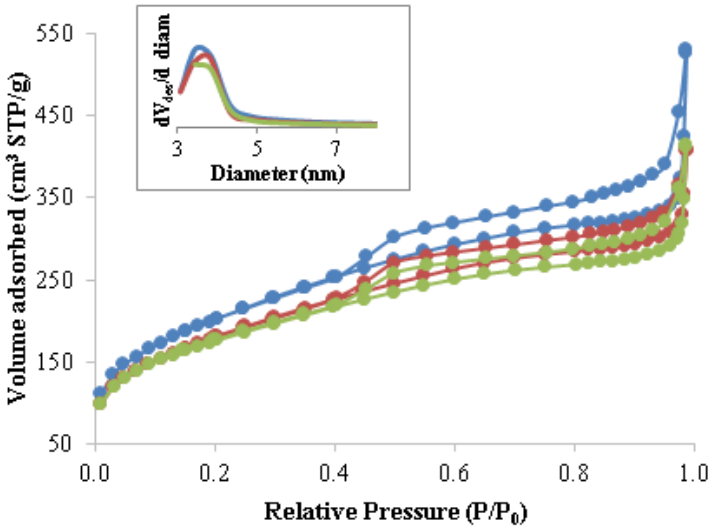

Figure 141. Nitrogen adsorption-desorption isotherms of the calcined and reduced 0.2 wt.% Pd-3.8 wt.% CeO_2 /SiO_2 catalyst. Mesopore size distributions are shown in the insets. Blue lines for the fresh catalyst (—●—), red lines for the used catalyst (—●—) and green for the recycled catalyst (—●—).

VI.3.3.2- Oxidation state and chemical environment of Pd and Ce by XPS characterisation

The $Pd3d_{5/2}$ binding energies expected for Pd and PdO are 335.1 and 337.9 eV, respectively [4,39,41–44]. After calcination at 650 °C, it is expected to observe a component around 338 eV, related to the interaction between Pd and CeO_2, corresponding to $Pd_xCe_{1-x}O_{2-x-\delta}$ $3d_{5/2}$ [54]. This is the main component on the spectrum corresponding to the calcined catalyst (Figure 142.a.), which remains the same after reaction (Figure 142.b.). This means that the oxidation state of the Pd does not change significantly at the reaction conditions. On the other hand, after a hydrogen treatment at 300 °C, there was certainly a new component between Pd and PdO binding energies. It is due to the Pd-support interaction that allows the formation of species with intermediate oxidation state in the presence of hydrogen [55]. It has been attributed to oxidised palladium clusters of the type PdO_x/Pd–O–Ce with a binding energy around 336 eV [54]. These species were also stable during the reaction in batch, as observed by comparing the spectra before (Figure 142.c) and after reaction (Figure 142.d.). However, in semi-batch operation, the PdO component was more pronounced (Figure 142.e.), probably due to the continuous flow of oxygen in excess that favoured the presence of oxidised Pd.

Regarding Ce, the binding energies expected for $Ce(IV)3d_{3/2}$ and $Ce(IV)3d_{5/2}$ are 916.9 and 898.3 eV, respectively. For $Ce(III)3d_{3/2}$ and $Ce(III)3d_{5/2}$, they are 901.2 and 882.6 eV, respectively [56]. However, the Ce spectrum presents other components, as evidenced on the least-squares fittings of a CeO_2 tablet published by Vercaemst *et al*. (Figure 143) [57]. It includes satellite lines due to the unpaired 4f electron in Ce(III): SU1, SU2 and SD at 904, 907, and 900 eV on the $Ce(III)d_{3/2}$ and at 886, 889, and 881 eV on the $Ce(III)3d_{5/2}$, respectively[56]. SU and SD stand for ‘shake-up’ (photoelectron energy loss) and ‘shake-down’ (photoelectron energy gain), respectively. Plasmon peaks (hatched components) and one Auger electron peak (A) can also be observed in Figure 143.

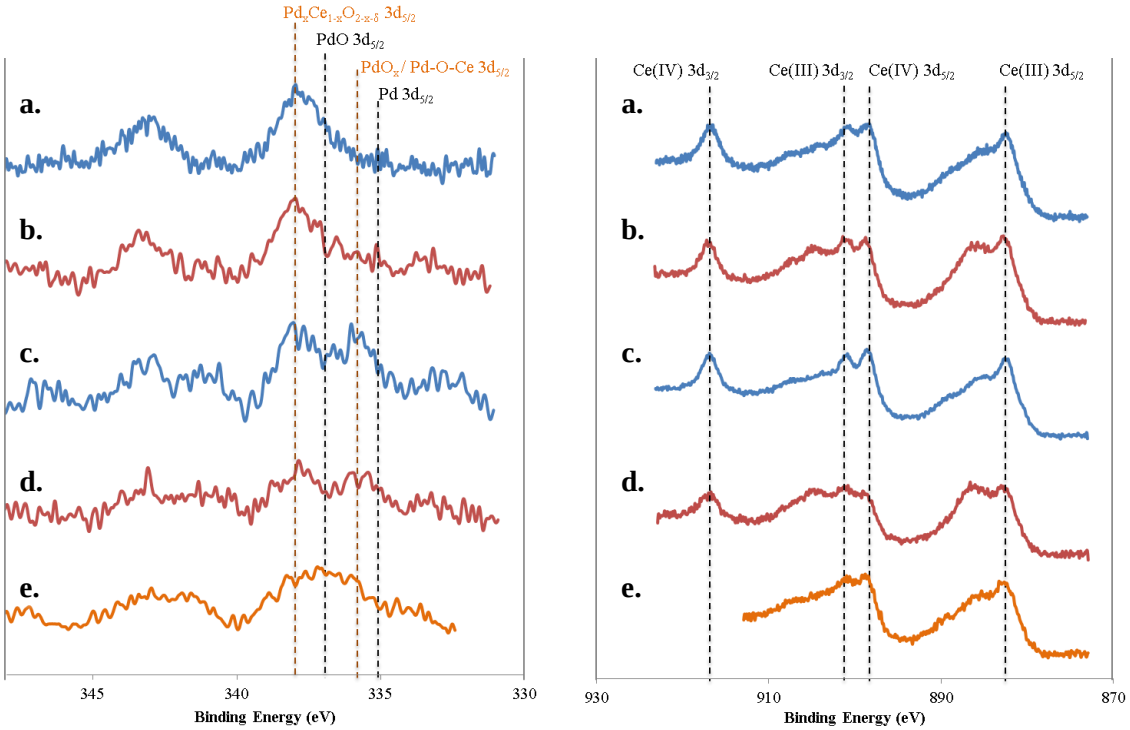

Figure 142. XPS spectra of Pd3d (left) and Ce3d (right) core levels of 0.2 wt.% Pd-3.8 wt.% CeO_2/SiO_2: a. calcined, fresh, b. calcined, used, c. calcined and reduced, fresh, d. calcined and reduced, used in batch, e. calcined and reduced, used in semi-batch. Blue lines for the fresh catalyst (—), red lines for the used catalyst in batch (—), orange lines for the used catalyst in semi-batch (—).

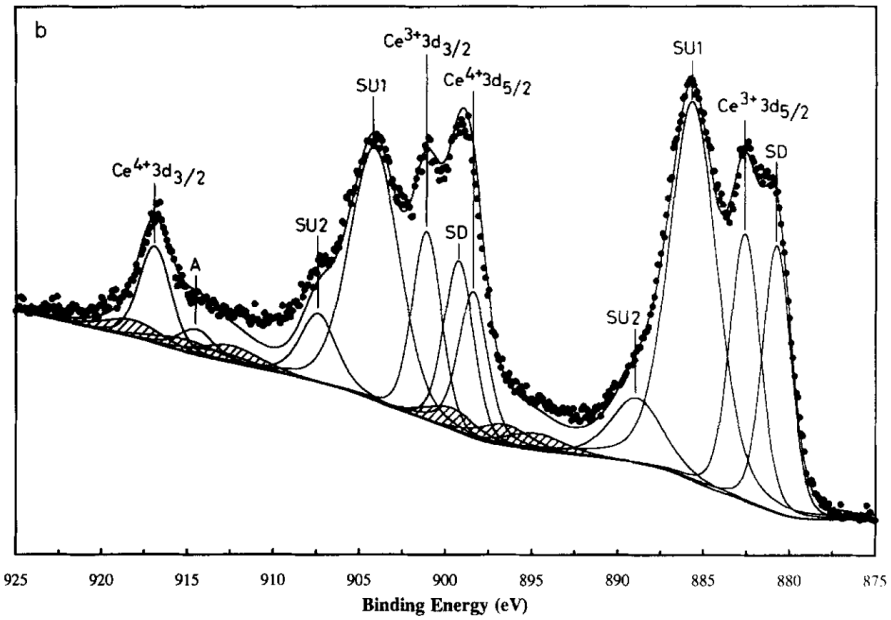

Figure 143. Typical XPS spectrum of Ce3d core level: example of a CeO_2 tablet [57]

By comparison of the Ce spectra in Figure 142, it can be seen that Ce(IV) and Ce(III) are present in all samples. Additionally, there is not an evident difference between the calcined fresh catalyst (Figure 142.a.) and the reduced fresh one (Figure 142.c.). However, used catalysts in batch presented bigger signals corresponding to the Ce(III) satellite components, and especially, in Figure 142.d., it can be seen that the peaks corresponding to Ce(IV) are smaller compare to the other spectra. This means that a partial reduction of ceria occurs in batch condition. On the other hand, in semi-batch operation, the Ce(III) satellite components were less intense than in the batch operation, and the overall spectrum was closer to the one of fresh catalyst. This means that the oxidation state of ceria was stable while operating in semi-batch.

Wrapping-up, in batch conditions, Pd oxidation state did not change after reaction. However, Ce was slightly reduced. On the other hand, after reaction in semi-batch, the PdO component became more important (compared to the other oxidised species), and the Ce(III) signals were less intense than in batch. In order to understand these differences, it is important to consider that in batch condition, the total pressure decreased over time, due to sampling and gas consumption in the reaction. Additionally, the gases partial pressures were not constant since oxygen and hydrogen were consumed over time. On the other hand, in semi-batch operation, the total pressure and gases molar fractions were constant during the whole reaction time. As a consequence, the concentration of gaseous species was higher in semi-batch condition than in batch (except at the very beginning of the reaction). This concentration difference, notably for CO_2, could explain an possible reoxidation of some Ce(III) species produced during the reaction [58]. Regarding the Pd oxidation state after semi-batch reaction, it is difficult to tell if an oxidation or a reduction took place in semi-batch condition given the low Pd loading to obtain reliable deconvolution results. However, what is certain is that the PdO component increased in comparison to the mixed oxidation states related to Pd-CeO_{2-x} interactions. On the whole, it could be concluded from this part that a mixture of Ce and Pd oxidation states were constantly present either after reaction in batch or in semi-batch operation, related to a certain chemical stability of the active species.

VI.3.3.3- Catalytic performance

A series of reactions were carried out to evaluate this material under different conditions. The catalyst was tested after template removal by calcination, and after calcination and reduction. Comparing these two materials (Figure 144), their performance was markedly different in the direct synthesis of H_2O_2. The only-calcined catalyst exhibited a very limited catalytic activity, with a maximum productivity of 260 $\frac{mol\ H_2O_2}{mol\ Pd \times h}$ after 120 minutes, compared to 3270 $\frac{mol\ H_2O_2}{mol\ Pd \times h}$ after just 10 minutes for the calcined and reduced catalyst. However, the only-calcined catalyst presented the highest selectivity after 3 h (68 ± 3 %), which can be attributed to a low activity in the H_2O_2 decomposition given the limited presence of metallic Pd(0) in the materials, as observed by XPS.

The catalysts were recovered by filtration and dried at 50 °C overnight. 76 wt. % of the reduced catalyst was reused in another reaction cycle (corresponding concentration profiles in Figure 144 were adjusted by a factor of 1/0.76=1.3 for comparison purposes). In such a test, the catalyst performance decreased, having a maximal productivity of 2400 $\frac{mol\ H_2O_2}{mol\ Pd \times h}$ at 10 minutes

compared to 3270 $\frac{mol\ H_2O_2}{mol\ Pd \times h}$ for the first test. In Figure 144, it can be seen that the concentration curves do not achieve a plateau for the recycle test, as it was the case for the first test. It can be due to the lower amount of catalyst in the reactor that was not enough to finish the hydrogen (limiting reagent) in the first hours. On the other hand, the selectivity at 180 minutes during the first and the recycle tests were not significantly different: 53 ± 2 % and 46 ± 6 %, respectively.

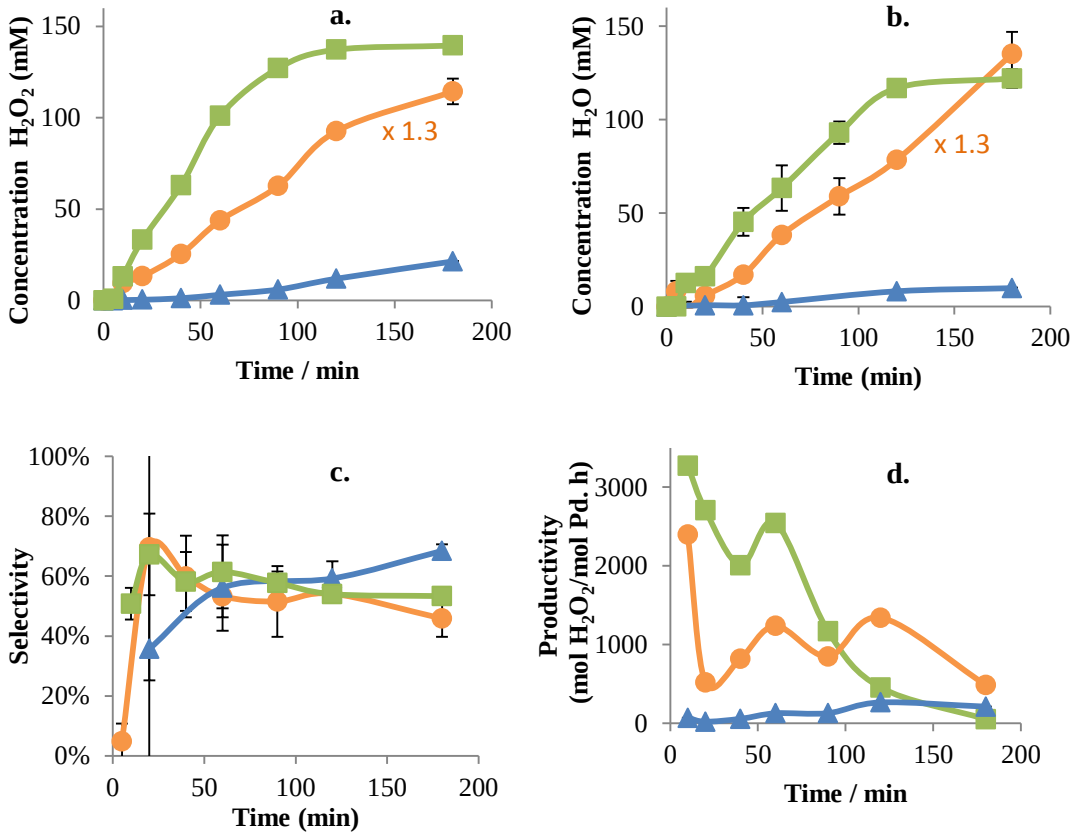

Figure 144. Profiles of: a. H_2O_2 concentration, b. H_2O concentration, c. H_2O_2 selectivity, and d. H_2O_2 productivity, using 0.2 wt.% Pd-3.8 wt.% CeO_2/SiO_2: calcined (—▲—), calcined and reduced (—■—) and recycled calcined and reduced (—●—). Please note that some of the error bars are not visible because they are smaller than the graph markers.

Considering the good selectivity obtained with the calcined and reduced catalyst, it was also tested in a semi-batch operation with a continuous flow of the gas reaction mixture. In order to challenge more the catalyst, 60 mg instead of 330 mg were used (consequently, the corresponding concentration curves in Figure 145 are scaled by a factor of 5.5 for comparison).

As shown in Figure 145, this catalyst exhibited a very good performance in semi-batch condition. The selectivity towards H_2O_2 was improved from 53 ± 2 % to 63 ± 2 %. Additionally, a high productivity was obtained at the beginning of the reaction with 4900 $\frac{mol\ H_2O_2}{mol\ Pd \times h}$ compared to 3270 $\frac{mol\ H_2O_2}{mol\ Pd \times h}$ for the batch operation. The average productivity for the semi-batch operation was ca. 2300$\frac{mol\ H_2O_2}{mol\ Pd \times h}$. Moreover, the selectivity was constant at the end of the test between 120

and 180 minutes (64 ± 2 % and 63 ± 2 %, respectively), which indicate a limited activity in the H_2O_2 decomposition. In addition, the concentration curves in Figure 145 do not reach a plateau for the semi-batch condition, which means that the catalyst was not deactivated at the reaction conditions after 3 h of operation.

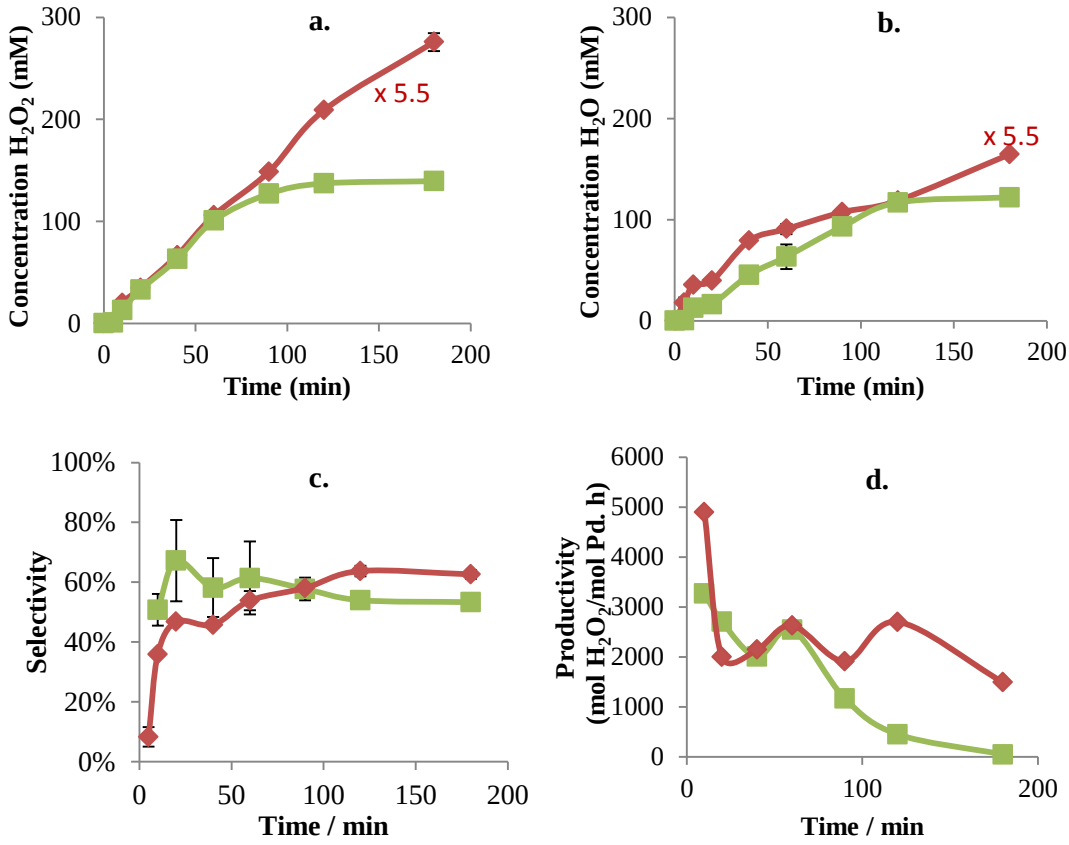

Figure 145. Profiles of: a. H_2O_2 concentration, b. H_2O concentration, c. H_2O_2 selectivity, and d. H_2O_2 productivity, using 0.2 wt.% Pd-3.8 wt.% CeO_2/SiO_2: in batch (—■—) and in semi-batch operation (—♦—).

It has been reported that for 2.5 wt. % Pd/CeO_2, the productivity has been 7 $\frac{mol\ H_2O_2}{mol\ Pd \times h}$ with less than 14% selectivity, in semi-batch operation at 1 bar and 20 °C. Such performance was doubled by doping the ceria with $(NH_4)_2SO_4$ to modify the surface acidity. However, a reduced Pd/CeO_2 catalyst, passivated in oxygen exhibited the best performance with 45 $\frac{mol\ H_2O_2}{mol\ Pd \times h}$ and 55% selectivity. The authors concluded that catalysts must be fully reduced to display their maximum activity and selectivity, but a surface Pd oxidation allows to increase both [59]. Having this basis set, the good catalytic performance of 0.2 wt.% Pd-3.8 wt.% CeO_2/SiO_2 after being activated in hydrogen could be attributed to the synergistic interaction between Pd and CeO_2, allowing the existence of Pd(II) species at the surface, as observed by XPS.

The reduced 0.2 wt.% Pd-3.8 wt.% CeO_2/SiO_2 catalyst exhibited a stable selectivity towards H_2O_2 in batch and in semi-batch conditions: 53 ± 2 % to 63 ± 2 %, respectively. Furthermore, it exhibited a high productivity at the beginning of the reaction: 3270 $\frac{mol\ H_2O_2}{mol\ Pd \times h}$ and 4900 $\frac{mol\ H_2O_2}{mol\ Pd \times h}$, for the batch and semi-batch conditions, respectively. The XPS analyses evidenced that ceria could stabilise oxidised palladium clusters of the type PdO_x/Pd–O–Ce throughout the reaction, leading to a mixture of Pd oxidation states that have been reported to be useful for achieving higher selectivity [11]. Indeed, this Pd-CeO_2/SiO_2 performed better than a monometallic Pd/SiO_2 that exhibited a selectivity of 49 ± 3 % and a maximum productivity of 3460 $\frac{mol\ H_2O_2}{mol\ Pd \times h}$, as described in Section V.3.1-*Hierarchically porous Pd/SiO2 catalyst via sol-gel synthesis with sonochemically decorated polystyrene latex template*.

Another advantage of using ceria is its acidic character. As mentioned in the introduction, acids are used to prevent the base-catalysed decomposition of H_2O_2. However, such additives must be then removed from the final product. The use of acidified supports has been reported as a greener option[6]. CeO_2 has acidic sites that can be tailored in strength depending on the synthesis and the calcination temperature[60], but also the dopants can have an effect on the concentration and strength of such acidic sites on ceria [61]. This motivates further investigations on the tailoring of the Pd/CeO_2/SiO_2 system to enhance synergistic interactions for achieving higher selectivity. Additionally, the textural characteristics of the material were stable enough to guarantee a recyclability of the catalyst.

VI.3.4- Hierarchically porous 0.2 wt.% Pd/SiO_2 catalyst by combination of miniemulsion polymerisation and sol-gel method

As in the previous cases, the material was tested after calcination or after calcination and reduction, and the structural and chemical stabilities were also investigated.

VI.3.4.1- Microstructure stability

As observed in Figure 146, the catalyst exhibited nitrogen physisorption isotherms characteristic of a hierarchically-porous material, which is expected considering the two-step acid-base catalysed sol-gel synthesis protocol used for the preparation of this silica-supported catalyst. In addition, a surface area of 711 m^2/g and a total pore volume of 0.93 cm^3/g were obtained in the calcined and reduced 0.2 wt.% Pd/SiO_2 fresh catalyst. Importantly, the textural characteristics did not change significantly after the catalytic test of direct synthesis of H_2O_2, as shown in

Table 25, and the isotherms and mesopore size distributions were almost identical before and after reaction. This allows concluding that this catalyst was structurally stable at the reaction conditions.

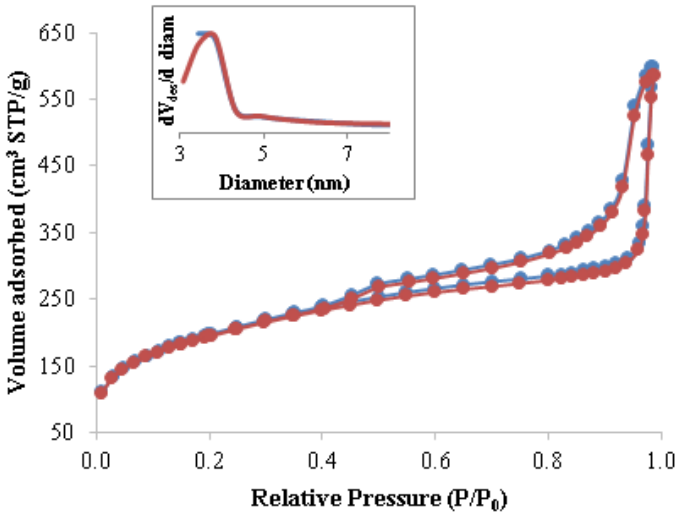

Figure 146. Nitrogen adsorption-desorption isotherms of the calcined and reduced 0.2 wt.% Pd/SiO_2 catalyst. Mesopore size distributions are shown in the insets. Blue lines for the fresh catalyst (—●—) and red lines for the used catalyst (—●—).

Table 25. Textural characterisation of the calcined and reduced 0.2 wt.% Pd/SiO_2 catalyst.

	Fresh	Used
Total surface area (m^2/g)	711	701
Total pore volume (cm^3/g)	0.93	0.91
Total porosity (%)	67	67

VI.3.4.2- Oxidation state and chemical environment of Pd by XPS characterisation

The complete XPS spectra for the 0.2 wt.% Pd/SiO_2 catalyst calcined and reduced, before and after reaction, are presented in Figure 147 (spectra for the non-reduced catalyst are similar). The Pd signals are not easily observable on Figure 147 because of the low Pd content in the sample. However, increasing the scanning time at the expected binding energies for Pd permitted to collect fairly useful spectra, as presented in Figure 148. It was observed that after reaction of H_2O_2 synthesis, the sample contained fluorine (BE 690 eV) [41], which is due to PTFE pollution coming from the reactor's stirrer and internal coating.

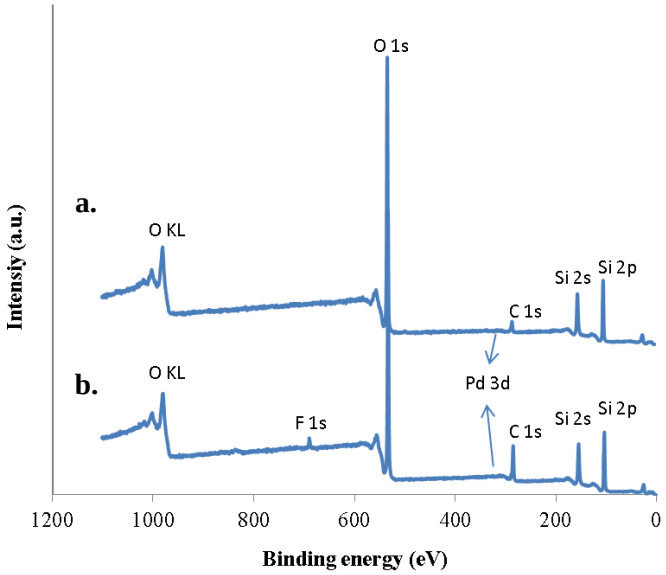

Figure 147. XPS survey spectra of the 0.2 wt.% Pd/SiO_2 catalyst calcined and reduced: a. fresh, b. used.

The binding energies expected for Pd(0) and Pd(II) are 335.1 and 336.7 eV, respectively [4,39,41,42]. In this material, the highest intensity on the $Pd3d_{5/2}$ binding energy peaks were observed between 335.6 and 337.0 eV, which means that in most of the cases, Pd is present in both oxidation states. These binding energies are consistent with other reports in the literature [11,42,62,63]. The deconvolution of the spectra was carried out taking as characteristic binding energies for Pd(0): $Pd3d_{5/2}A$ and $Pd3d_{3/2}A$, 335.1 and 340.2 eV, respectively, and for Pd(II): $Pd3d_{5/2}B$ and $Pd3d_{3/2}B$, 336.7 and 341.8 eV, respectively [39,41–43,64].

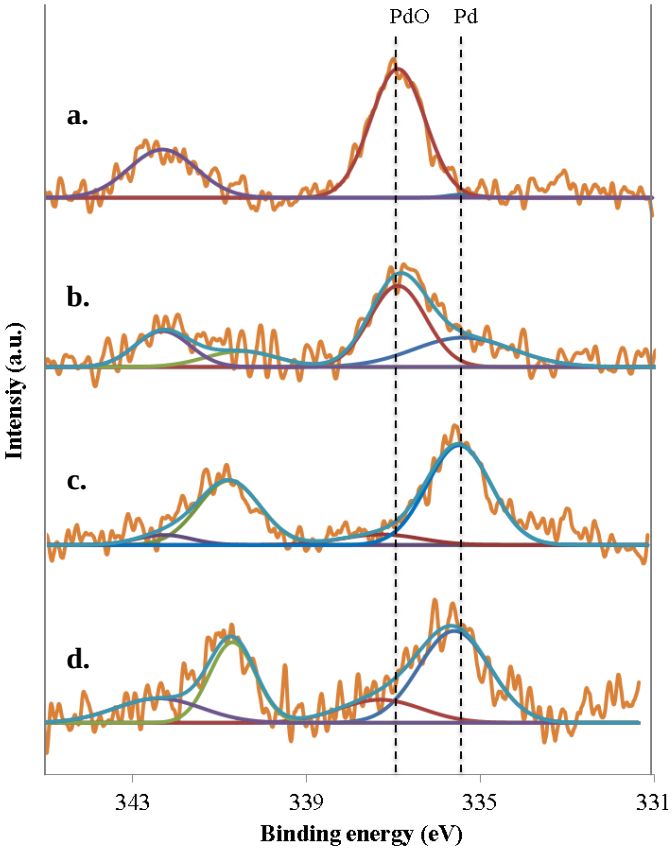

Figure 148. XPS signals of Pd3d core level of 0.2 wt.% Pd/SiO_2: a. calcined, fresh, b. calcined, used, c. calcined and reduced, fresh, d. calcined and reduced, used.

According to the XPS results, after removal of the polymer template by calcination at 650 °C, the palladium was only in Pd(II) oxidation state (Figure 148.a.). However, after its use in the direct synthesis of H_2O_2, a partial metal reduction was observed (Figure 148.b.), which occurred *in-situ* at the reaction conditions. This partial reduction was also observed in another work using 1.0 wt.% Pd/K2621 [11]. On the other hand, when the catalyst was reduced before the reaction, the predominant (88%) oxidation state was Pd(0) (Figure 148.c.). After reaction, this used catalyst exhibited the same $Pd3d_{5/2}$ binding energy peak as the fresh one: 335.6 eV. Even though the deconvolution results (Table 26) should be considered as approximate values because, due to the low Pd loading, the Pd signals collected by XPS were very noisy (Figure 148). A deconvolution of the spectra showed that the metallic Pd(0) oxidation state was still predominant in the used catalyst (Figure 148.d.), which is related to the stability of the Pd species on the support. Oxidation of Pd nanoparticles supported on silica has been observed to require temperatures above 350 °C in the presence of oxygen at atmospheric pressure [65]. In opposition to SiO_2, other supports like TiO_2 could assist the partial oxidation of the metallic Pd nanoparticles under air exposure at ambient conditions [66].

Table 26. XPS estimation of Pd(II) and Pd(0) composition in fresh and used catalysts.

Sample	Fresh			Used		
	$Pd3d_{5/2}$ binding energy (eV)	Pd(II) (%)	Pd(0) (%)	$Pd3d_{5/2}$ binding energy (eV)	Pd(II) (%)	Pd(0) (%)
0.2 wt.% Pd/SiO_2 calcined	337.0	100	-	336.8	61	39
0.2 wt.% Pd/SiO_2 calcined and reduced	335.6	12	88	335.6	23	77

VI.3.4.3- Catalytic performance

In agreement with the XPS results, the catalyst used directly after calcination was reduced *in-situ*. It can be evidenced on the concentration curves for H_2O and H_2O_2, in Figure 149, where a smaller initial slope is observed compared to the *ex-situ* reduced catalyst. This indicates that the only-calcined catalyst was less active due to a reduction process taking place at the beginning of the reaction. Additionally, the *ex-situ* reduced catalyst showed a very high instantaneous H_2O_2 productivity rate of 10390 $\frac{mol\ H_2O_2}{mol\ Pd \times h}$, just after 10 minutes. The reaction was almost finished after 60 minutes. On the other hand, the calcined catalyst presented a more or less stable productivity rate of 1700 ± 500 $\frac{mol\ H_2O_2}{mol\ Pd \times h}$ in average between 10 and 60 minutes, taking about 120 minutes to achieve complete hydrogen conversion. The marked H_2O_2 productivity peak observed in Figure 149 for the *ex-situ* reduced catalyst is due to high catalytic activity. Such a productivity profile relates to rapid reagents consumption, with hydrogen being the limiting reagent. As the hydrogen partial pressure in the medium decreased rapidly, a marked drop in the rate of the H_2O_2 productivity was observed. Similarly, the water productivity followed the same trend as hydrogen peroxide; so the selectivity did not exhibit any remarkable profile. This result could suggest that the catalyst texture equally allowed the reagents and products diffusion in and out of the catalysts, respectively, at the various rates that the reaction took place.

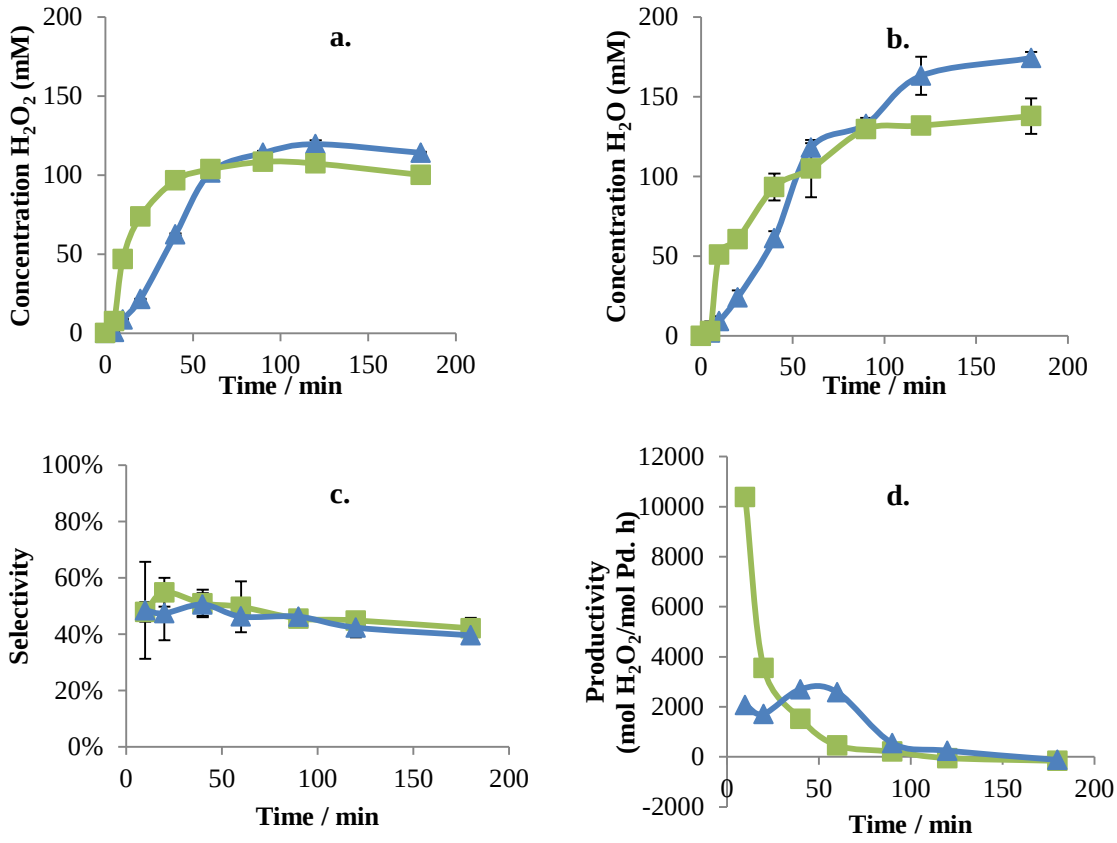

Figure 149. Profiles of: a. H_2O_2 concentration, b. H_2O concentration, c. H_2O_2 selectivity, and d. H_2O_2 productivity, using: 0.2 wt.% Pd/SiO_2 calcined (—▲—) and 0.2 wt.% Pd/SiO_2 calcined and reduced (—■—). Please note that some of the error bars are not visible because they are smaller than the graph markers.

Nonetheless, at these reaction conditions, there was not a significant difference in selectivity between the catalyst reduced *in-situ* or *ex-situ*. After 90 minutes, the calcined catalyst led to a selectivity of 46 ± 2 % compared with 46 ± 1 % for the *ex-situ* reduced catalyst. This is in agreement with the 40% selectivity reported elsewhere for a 0.3 wt.% Pd/K2621, which is expected to decrease when increasing the Pd loading on the catalyst [11]. Considering the concentrations in the medium, direct comparison is not possible in batch operation because, since both catalysts (*in-situ* reduced and *ex-situ* reduced) have different activities, the total pressure in the reactor decreases at different rates. Nevertheless, as an approximation, it is possible to scale both concentrations at 120 minutes to the same pressure (12.2 bars). In such a case, the H_2O_2 concentrations were found to be non-significantly different: 110.5 ± 2.3 mM and 107.3 ± 2.9 mM, for the *in-situ* and *ex-situ* reduced catalysts, respectively. In Figure 149, it can also be observed that at the end of the H_2O_2 direct synthesis, after 120 minutes, there is a very slight decrease in the H_2O_2 concentration, which is associated with the H_2O_2 conversion towards water. The related undesired reactions undergo at a very small rate (about 100 times slower) compared to the initial H_2O_2 production, as observed in previous studies [67,68].

Furthermore, since the *ex-situ* reduced catalyst was in general more active, it was also more active in the undesired consumption of H_2O_2. This is why at 180 min, there was a negative rate

of -159 ± 2 $\frac{mol\ H_2O_2}{mol\ Pd \times h}$ for the *ex-situ* reduced catalyst versus -120 ± 5 $\frac{mol\ H_2O_2}{mol\ Pd \times h}$ for the only-calcined one. This is in agreement with the literature regarding the role of Pd(0) in the hydrogenation of H_2O_2 in the presence of adsorbed H_2 [46], which is the predominant oxidation state in the *ex-situ* reduced catalyst.

The further reduced 0.2 wt.% Pd/SiO_2 catalyst (*ex-situ* reduced catalyst) exhibited a structural stability of the hierarchically porous silica matrix and chemical stability with mainly Pt(0) oxidation state at the reaction conditions. Furthermore it had a better overall performance in the H_2O_2 direct synthesis, with a remarkably higher instantaneous productivity in the early stage of the batch reaction: 10390 $\frac{mol\ H_2O_2}{mol\ Pd \times h}$, in comparison with the calcined catalyst (2700 $\frac{mol\ H_2O_2}{mol\ Pd \times h}$). Nonetheless, both materials exhibited similar selectivity values: 46 ± 1 % and 46 ± 2 % at 90 min, and 42 ± 4 % and 40 ± 1 % at 180 min, for the *ex-situ* reduced and the calcined catalysts, respectively.

VI.4- Conclusion

All the catalysts evaluated in this work were active in the direct synthesis of hydrogen peroxide. Table 27 summarises their performances.

Table 27. Summary of catalytic performances in the H_2O_2 direct synthesis

Catalyst	Pre-treatment	Final selectivity towards H_2O_2 (%)	Highest H_2O_2 productivity $\left(\frac{mol\ H_2O_2}{mol\ metal \times h}\right)$	Oxidation state	Stability
0.7 wt. % Pd/SiO_2 by sonochemical route	Calcination	54 ± 8	840 ± 10	PdO	Chemical stability, but structure densification
	Calcination &reduction	49 ± 3	3460 ± 20	Pd(0)	
0.3 wt.% Pt – 0.2 wt.% Pd / SiO_2	Calcination	40 ± 1	24000 ± 50	PdO+PtO	Chemical and structure stability
	Calcination &reduction	19 ± 1	32500 ± 50	Pd(0)-Pt(0)	
0.2 wt.% Pd-3.8 wt.% CeO_2 / SiO_2	Calcination	68 ± 3	260 ± 10	Pd(II)-CeO_{2-x} species	Chemical stability, but some structure densification
	Calcination &reduction	53 ± 2	3270 ± 20	Pd(II)-CeO_{2-x} species	
	Calcination &reduction *semi-batch*	63 ± 2	4900 ± 20	Pd(II)-CeO_{2-x} species	
0.2 wt.% Pd/SiO_2 by miniemulsion polymerisation	Calcination	40 ± 1	2700 ± 25	PdO	Partial reduction *in-situ* and structure stability
	Calcination &reduction	42 ± 4	10390 ± 20	Mostly Pd(0)	Chemical and structure stability

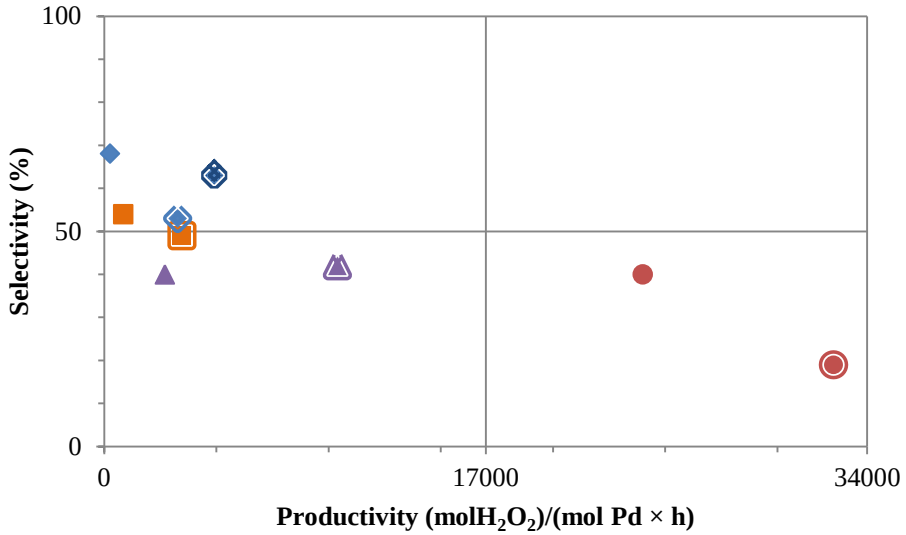

Figure 150. Selectivity vs. Productivity (catalyst - colour correspondence is given in Table 27)

It is not evident to determine which one of these was the best catalyst, since the best performance would imply to have high productivity at high selectivity. Figure 150 presents selectivity versus productivity graph with 4 quadrants. Unfortunately, the high selectivity-high productivity quadrant is empty.

The best productivity of H_2O_2 was obtained with the reduced bimetallic Pd-Pt catalyst with 32500 $\frac{mol\ H_2O_2}{mol\ metal \times h}$, unfortunately with a decreasing selectivity down to 19 ± 1 %. When non-reduced, the bimetallic catalyst achieved a better selectivity (40 ± 1 %), but decreased in productivity (24000$\frac{mol\ H_2O_2}{mol\ metal \times h}$). On the other hand, the best selectivity was obtained with the Pd-CeO_2/SiO_2 catalyst, reaching 68 ± 3 % when only calcined. After reduction, it reached 53 ± 2 % and 63 ± 2 %, in batch and semi-batch operation conditions, respectively.

Without reduction pre-treatment, the Pd catalyst prepared by sonochemistry exhibited a limited activity up to 840 $\frac{mol\ H_2O_2}{mol\ Pd \times h}$, with a selectivity of 54 ± 8 % at the end of the reaction, being better than with the bimetallic (40 ± 1 %) and miniemulsion (40 ± 1 %) strategies. But when reduced beforehand, the selectivity was not significantly different (49 ± 3 %) and the productivity increased to 3460$\frac{mol\ H_2O_2}{mol\ Pd \times h}$. In comparison with the literature, this selectivity was better than the 40% obtained with 0.3 wt.% Pd/K2621 [11] or than the 42% reported for 3.6 wt.% Pd/SiO_2 [45] under slightly similar reaction conditions.

Something remarkable about the bimetallic Pt-Pd catalyst tested here is that the 32500 $\frac{mol\ H_2O_2}{mol\ metal \times h}$ productivity corresponds to almost 10-fold increase compared with the catalyst 0.7 wt.% Pd/SiO_2, or 3-fold increase compared with the material 0.2 wt.% Pd/SiO_2 by miniemulsion. This productivity enhancement is very promising considering that in the literature, the enhancement of adding some Pt to Pd has been reported to result in a maximum 1.8-fold increase in productivity [49].

The selectivity variation is related to the Pd oxidation state, which is influenced by the metal-support interaction. An intermediate Pd oxidation state with mostly Pd(II) species at the surface improves the catalyst performance. In the materials tested with Pd alone, it was mostly present either as Pd(0) or Pd(II), leading to selectivity ranging from between 40 and 54 %. The interaction Pt-Pd after reduction favoured the metallic species, increasing the decomposition rate of H_2O_2, ultimately reducing the selectivity. In the presence of CeO_2, oxidised Pd species were favoured both after the calcination step and after a hydrogen treatment, leading to PdO_x/Pd–O–Ce species, which remained in the material after reaction due to the strong Pd-CeO_2 interaction. Such a peculiar Pd species in the catalyst, allowed reaching a stable selectivity up to 63 %. Such selectivity was better than the 55% reported for a Pd/CeO_2 catalyst in semi-batch conditions [59].

Regarding the chemical stability, the only-calcined monometallic Pd catalysts got partially reduced at the reaction conditions, which in a long run could affect the selectivity. In the other catalysts, the oxidation state was more or less stable at the evaluated reaction conditions.

Regarding the texture stability, the bimetallic Pt-Pd and the monometallic Pd prepared by miniemulsion were very stable at the reaction conditions, keeping the almost identical textural characteristics after reaction. Conversely, the monometallic Pd prepared by the sonochemical route presented some densification during the reaction. It could be due to influence of non reduced species during the sol-gel synthesis, leading to a weaker structure than expected. The Pd-CeO_2/SiO_2 catalyst also presented a slight densification after the first reaction, but it was stable when recycled. It is important to recall that the synthesis of this material was slightly different to the other materials due to colloidal stability limitations of the template (sol-gel acid step in the absence of the latex template, which was added with the base in the second step). This means that such a synthesis could still be optimised to achieve a more stable material since the very first use.

Concerning the application of these catalysts to larger scales, mass transport phenomena must be considered. In general, in the direct synthesis of hydrogen peroxide from oxygen and hydrogen in slurry batch reactors, there are no mass transfer limitations inside non-macroporous catalyst particles when they are small (under few hundred μm) [69]. So the presented materials with hierarchical porosity could potentially be used in bigger particles in fixed bed reactors or in thick coatings of Pd/SiO_2 on structured catalysts such as monoliths, for a continuous operation.

As a final remark, there is still opportunity for further development of catalysts for this reaction since the H_2O_2 direct synthesis is sensitive to the catalyst structure [11]. For instance, the Pd dispersion could be optimised with other loadings. Considering the outcome of this study that showed best productivities with the bimetallic Pt-Pd catalysts and best selectivity with the Pd-CeO_2 catalysts, it could be worth testing a catalyst Pt-Pd-CeO_2/SiO_2 that could take advantage of the productivity enhancement given by the Pt and the chemical stability provided by the ceria to achieve high selectivity. To my knowledge, such system has neither been reported in the literature nor claimed in patents.

VI.5- References

[1] Vocus PRW Holdings LLC, Global Hydrogen Peroxide Market, (2015). http://www.prweb.com/releases/hydrogen_peroxide/bleaching_pulp_paper/prweb9268178.htm (accessed September 28, 2016).

[2] G. Centi, S. Perathoner, S. Abate, Direct Synthesis of Hydrogen Peroxide: Recent Advances, in: Mod. Heterog. Oxid. Catal., Wiley-VCH Verlag GmbH & Co. KGaA, 2009: pp. 253–287. doi:10.1002/9783527627547.ch8.

[3] J.K. Edwards, S.J. Freakley, R.J. Lewis, J.C. Pritchard, G.J. Hutchings, Advances in the direct synthesis of hydrogen peroxide from hydrogen and oxygen, Catal. Today. 248 (2015) 3–9. doi:10.1016/j.cattod.2014.03.011.

[4] J.M. Campos-Martin, G. Blanco-Brieva, J.L.G. Fierro, Hydrogen peroxide synthesis: an outlook beyond the anthraquinone process., Angew. Chem. Int. Ed. Engl. 45 (2006) 6962–84. doi:10.1002/anie.200503779.

[5] V.R. Choudhary, A.G. Gaikwad, S.D. Sansare, Activation of supported Pd metal catalysts for selective oxidation of hydrogen to hydrogen peroxide, Catal. Letters. 83 (2002) 235–239. doi:10.1023/A:1021066904862.

[6] J. García-Serna, T. Moreno, P. Biasi, M.J. Cocero, J.-P. Mikkola, T.O. Salmi, Engineering in direct synthesis of hydrogen peroxide: targets, reactors and guidelines for operational conditions, Green Chem. 16 (2014) 2320–2343. doi:10.1039/c3gc41600c.

[7] A. Pashkova, R. Dittmeyer, Carbon dioxide as an alternative solvent for the direct synthesis of hydrogen peroxide: A review of recent activities, Catal. Today. 248 (2015) 128–137. doi:10.1016/j.cattod.2014.03.012.

[8] R. Dittmeyer, J.D. Grunwaldt, A. Pashkova, A review of catalyst performance and novel reaction engineering concepts in direct synthesis of hydrogen peroxide, Catal. Today. 248 (2015) 149–159. doi:10.1016/j.cattod.2014.03.055.

[9] J.K. Edwards, J. Pritchard, L. Lu, M. Piccinini, G. Shaw, A.F. Carley, D.J. Morgan, C.J. Kiely, G.J. Hutchings, The direct synthesis of hydrogen peroxide using platinum-promoted gold–palladium catalysts, Angew. Chemie (International Ed. (2014) 2381 – 2384. doi:10.1002/anie.201308067.

[10] S. Kim, D.-W. Lee, K.-Y. Lee, E.A. Cho, Effect of Pd Particle Size on the Direct Synthesis of Hydrogen Peroxide from Hydrogen and Oxygen over Pd Core–Porous SiO2 Shell Catalysts, Catal. Letters. 144 (2014) 905–911. doi:10.1007/s10562-014-1235-3.

[11] N. Gemo, S. Sterchele, P. Biasi, P. Centomo, P. Canu, M. Zecca, A. Shchukarev, K. Kordás, T.O. Salmi, J.-P. Mikkola, The influence of catalyst amount and Pd loading on the H2O2 synthesis from hydrogen and oxygen, Catal. Sci. Technol. 5 (2015) 3545–3555. doi:10.1039/C5CY00493D.

[12] S. Abate, K. Barbera, G. Centi, G. Giorgianni, S. Perathoner, Role of size and pretreatment of Pd particles on their behaviour in the direct synthesis of H2O2, J. Energy Chem. (2016). doi:10.1016/j.jechem.2016.01.008.

[13] X. Liu, Q. Zhang, Influence of initial pressure and temperature on flammability limits of hydrogen-air, Int. J. Hydrogen Energy. 39 (2014) 6774–6782. doi:10.1016/j.ijhydene.2014.02.001.

[14] N. Gemo, T. Salmi, P. Biasi, The use of modelling to understand the mechanism of hydrogen peroxide direct synthesis from batch, semibatch and continuous reactor points of view, React. Chem. Eng. 1 (2016) 23–29. doi:10.1039/C5RE00073D.

[15] J.K. Edwards, N.N. Edwin, A.F. Carley, A.A. Herzing, C.J. Kiely, G.J. Hutchings, Direct synthesis of H2O2 from H2 and O2 over gold, palladium, and gold-palladium catalysts supported on acid-pretreated TiO2, Angew. Chemie - Int. Ed. 48 (2009) 8512–8515. doi:10.1002/anie.200904115.

[16] G. Li, J. Edwards, A.F. Carley, G.J. Hutchings, Direct synthesis of hydrogen peroxide from H2 and O2 and in situ oxidation using zeolite-supported catalysts, Catal. Commun. 8 (2007) 247–250. doi:10.1016/j.catcom.2006.06.021.

[17] J.K. Edwards, A. Thomas, A.F. Carley, A.A. Herzing, C.J. Kiely, G.J. Hutchings, Au-Pd supported nanocrystals as catalysts for the direct synthesis of hydrogen peroxide from H2 and O2, Green Chem. 10 (2008) 388–394. doi:10.1039/B714553P.

[18] G. Li, J. Edwards, A.F. Carley, G.J. Hutchings, Direct synthesis of hydrogen peroxide from H2 and O2 using zeolite-supported Au-Pd catalysts, Catal. Today. 122 (2007) 361–364. doi:10.1016/j.cattod.2007.01.019.

[19] Q. Liu, J.C. Bauer, R.E. Schaak, J.H. Lunsford, Direct synthesis of H2O2 from H2 and O2 over Pd-Pt/SiO2 bimetallic catalysts in a H2SO4/ethanol system, Appl. Catal. A Gen. 339 (2008) 130–136. doi:10.1016/j.apcata.2008.01.026.

[20] G. Bernardotto, F. Menegazzo, F. Pinna, M. Signoretto, G. Cruciani, G. Strukul, New Pd–Pt and Pd–Au catalysts for an efficient synthesis of H2O2 from H2 and O2 under very mild conditions, Appl. Catal. A Gen. 358 (2009) 129–135. doi:10.1016/j.apcata.2009.02.010.

[21] G. Blanco-Brieva, E. Cano-Serrano, J.M. Campos-Martin, J.L.G.J.L.G. Fierro, Direct Synthesis of hydrogen peroxide solution with palladium-loaded sulfonic acid polystyrene

resins, Chem. Commun. (2004) 1184–1185. doi:10.1039/b402530j.

[22] S. Parasher, M.A. Rueter, B. Zhou, High temperature reduction of hydrogen peroxide catalyst for improved selectivity, US 2012/0020872 A1, 2012.

[23] C.M.A. Parlett, K. Wilson, A.F. Lee, Hierarchical porous materials: catalytic applications, Chem. Soc. Rev. 42 (2013) 3876–3893. doi:10.1039/c2cs35378d.

[24] L. Ouyang, L. Tan, J. Xu, P.F. Tian, G.J. Da, X.J. Yang, D. Chen, F. Tang, Y.F. Han, Functionalized silica nanorattles hosting Au nanocatalyst for direct synthesis of H2O2, Catal. Today. 248 (2015) 28–34. doi:10.1016/j.cattod.2014.05.010.

[25] M. Seo, S. Kim, H. Eun, D. Lee, K. Lee, A yolk–shell structured Pd@void@ZrO2 catalyst for direct synthesis of hydrogen peroxide from hydrogen and oxygen, J. Mol. Catal. A Chem. 413 (2016) 1–6. doi:10.1016/j.molcata.2015.12.004.

[26] M. Seo, S. Kim, D. Lee, H. Eun, K. Lee, Core – shell structured , nano-Pd-embedded SiO 2 – Al 2 O 3 catalyst (Pd @ SiO 2 – Al 2 O 3) for direct hydrogen peroxide synthesis from hydrogen and oxygen, Appl. Catal. A Gen. 511 (2016) 87–94. doi:10.1016/j.apcata.2015.11.040.

[27] S. Kim, D.W. Lee, K.Y. Lee, Direct synthesis of hydrogen peroxide from hydrogen and oxygen over single-crystal cubic palladium on silica catalysts, J. Mol. Catal. A Chem. 383-384 (2014) 64–69. doi:10.1016/j.molcata.2013.11.021.

[28] H.E. Jeong, S. Kim, M. Seo, D.-W. Lee, K.-Y. Lee, Catalytic activity of Pd octahedrons/SiO2 for the direct synthesis of hydrogen peroxide from hydrogen and oxygen, J. Mol. Catal. A Chem. 420 (2016) 88–95. doi:10.1016/j.molcata.2014.03.026.

[29] V. Paunovic, V. Ordomsky, M.F. Neira D'Angelo, J.C. Schouten, T.A. Nijhuis, Catalyst coating on prefabricated capillary microchannels for the direct synthesis of hydrogen peroxide, Ind. Eng. Chem. Res. 54 (2015) 2919–2929. doi:10.1021/ie504762y.

[30] D. Niu, Z. Ma, Y. Li, J. Shi, Synthesis of core−shell structured dual-mesoporous silica spheres with tunable pore size and controllable shell thickness, J. Am. Chem. Soc. 132 (2010) 15144–15147. doi:10.1021/ja1070653.

[31] A.B.D. Nandiyanto, N. Hagura, F. Iskandar, K. Okuyama, Design of a highly ordered and uniform porous structure with multisized pores in film and particle forms using a template-driven self-assembly technique, Acta Mater. 58 (2010) 282–289. doi:10.1016/j.actamat.2009.09.004.

[32] A.B.D. Nandiyanto, T. Ogi, F. Iskandar, K. Okuyama, Highly ordered porous monolayer generation by dual-speed spin-coating with colloidal templates, Chem. Eng. J. 167

(2011) 409–415. doi:10.1016/j.cej.2010.11.077.

[33] R. Balgis, T. Ogi, A.F. Arif, G.M. Anilkumar, T. Mori, K. Okuyama, Morphology control of hierarchical porous carbon particles from phenolic resin and polystyrene latex template via aerosol process, Carbon N. Y. 84 (2015) 281–289. doi:10.1016/j.carbon.2014.12.010.

[34] A.B.D. Nandiyanto, S.-G. Kim, F. Iskandar, K. Okuyama, Synthesis of spherical mesoporous silica nanoparticles with nanometer-size controllable pores and outer diameters, Microporous Mesoporous Mater. 120 (2009) 447–453. doi:10.1016/j.micromeso.2008.12.019.

[35] M. Bathfield, J. Warnant, C. Gérardin, P. Lacroix-Desmazes, Asymmetric neutral, cationic and anionic PEO-based double-hydrophilic block copolymers (DHBCs): synthesis and reversible micellization triggered by temperature or pH, Polym. Chem. 6 (2015) 1339–1349. doi:10.1039/C4PY01502A.

[36] C. Yacou, M.-L. Fontaine, A. Ayral, P. Lacroix-Desmazes, P.-A. Albouy, A. Julbe, One pot synthesis of hierarchical porous silica membrane material with dispersed Pt nanoparticles using a microwave-assisted sol–gel route, J. Mater. Chem. 18 (2008) 4274–4279. doi:10.1039/b807029f.

[37] T. Chave, A. Grunenwald, A. Ayral, P. Lacroix-Desmazes, S.I. Nikitenko, Sonochemical deposition of platinum nanoparticles on polymer beads and their transfer on the pore surface of a silica matrix, J. Colloid Interface Sci. 395 (2013) 81–84. doi:10.1016/j.jcis.2012.12.029.

[38] E. Schreiber, U. Ziener, A. Manzke, A. Plettl, P. Ziemann, K. Landfester, Preparation of narrowly size distributed metal-containing polymer latexes by miniemulsion and other emulsion techniques: Applications for nanolithography, Chem. Mater. 21 (2009) 1750–1760. doi:10.1021/cm802796y.

[39] R. Arrigo, M.E. Schuster, S. Abate, S. Wrabetz, K. Amakawa, D. Teschner, M. Freni, G. Centi, S. Perathoner, M. Havecker, R. Schlogl, Dynamics of palladium on nanocarbon in the direct synthesis of H2O2, ChemSusChem. 7 (2014) 179–194. doi:10.1002/cssc.201300616.

[40] S. Abate, S. Perathoner, G. Centi, Deactivation mechanism of Pd supported on ordered and non-ordered mesoporous silica in the direct H2O2 synthesis using CO2-expanded methanol, Catal. Today. 179 (2012) 170–177. doi:10.1016/j.cattod.2011.09.010.

[41] NIST, NIST Standard Reference Database 20, (2016).

[42] I.A. Witonska, M.J. Walock, M. Binczarski, M. Lesiak, A. V. Stanishevsky, S. Karski, Pd-Fe/SiO2 and Pd-Fe/Al2O3 catalysts for selective hydrodechlorination of 2,4-

dichlorophenol into phenol, J. Mol. Catal. A Chem. 393 (2014) 248–256. doi:10.1016/j.molcata.2014.06.022.

[43] L.S. Kibis, A.I. Stadnichenko, S. V. Koscheev, V.I. Zaikovskii, A.I. Boronin, Highly oxidized palladium nanoparticles comprising Pd 4+ species: Spectroscopic and structural aspects, thermal stability, and reactivity, J. Phys. Chem. C. 116 (2012) 19342–19348. doi:10.1021/jp305166k.

[44] M.M. Hyland, G.M. Bancroft, Palladium sorption and reduction on sulphide mineral surfaces: An XPS and AES study, Geochim. Cosmochim. Acta. 54 (1990) 117–130. doi:10.1016/0016-7037(90)90200-5.

[45] S. Abate, P. Lanzafame, S. Perathoner, G. Centi, SBA-15 as a support for palladium in the direct synthesis of H2O2 from H2 and O2, Catal. Today. 169 (2011) 167–174. doi:10.1016/j.cattod.2010.09.030.

[46] J.K. Edwards, J. Pritchard, M. Piccinini, G. Shaw, Q. He, A.F. Carley, C.J. Kiely, G.J. Hutchings, The effect of heat treatment on the performance and structure of carbon-supported Au-Pd catalysts for the direct synthesis of hydrogen peroxide, J. Catal. 292 (2012) 227–238. doi:10.1016/j.jcat.2012.05.018.

[47] S. Melada, R. Rioda, F. Menegazzo, F. Pinna, G. Strukul, Direct synthesis of hydrogen peroxide on zirconia-supported catalysts under mild conditions, J. Catal. 239 (2006) 422–430. doi:10.1016/j.jcat.2006.02.014.

[48] F. Zaera, New challenges in heterogeneous catalysis for the 21st century, Catal. Letters. 142 (2012) 501–516. doi:10.1007/s10562-012-0801-9.

[49] J. Xu, L. Ouyang, G.J. Da, Q.Q. Song, X.J. Yang, Y.F. Han, Pt promotional effects on Pd-Pt alloy catalysts for hydrogen peroxide synthesis directly from hydrogen and oxygen, J. Catal. 285 (2012) 74–82. doi:10.1016/j.jcat.2011.09.017.

[50] M. Martin-Martinez, L.M. Gómez-Sainero, J. Bedia, A. Arevalo-Bastante, J.J. Rodriguez, Enhanced activity of carbon-supported Pd-Pt catalysts in the hydrodechlorination of dichloromethane, Appl. Catal. B Environ. 184 (2016) 55–63. doi:10.1016/j.apcatb.2015.11.016.

[51] J. Garnier, J. Warnant, P. Lacroix-Desmazes, P.-E. Dufils, J. Vinas, A. van Herk, Sulfonated macro-RAFT agents for the surfactant-free synthesis of cerium oxide-based hybrid latexes., J. Colloid Interface Sci. 407 (2013) 273–81. doi:10.1016/j.jcis.2013.06.037.

[52] Z. He, X. Wang, Renewable energy and fuel production over transition metal oxides: The role of oxygen defects and acidity, Catal. Today. 240 (2015) 220–228. doi:10.1016/j.cattod.2014.04.023.

[53] L. Vivier, D. Duprez, Ceria-based solid catalysts for organic chemistry, ChemSusChem. 3 (2010) 654–78. doi:10.1002/cssc.201000054.

[54] E.M. Slavinskaya, T.Y. Kardash, O.A. Stonkus, R. V. Gulyaev, I.N. Lapin, V.A. Svetlichnyi, A.I. Boronin, Metal–support interaction in Pd/CeO2 model catalysts for CO oxidation: from pulsed laser-ablated nanoparticles to highly active state of the catalyst, Catal. Sci. Technol. 6 (2016) 6650–6666. doi:10.1039/C6CY00319B.

[55] G. Mattogno, G. Polsonetti, G.R. Tauszik, Characterization of palladium-on-alumina catalysts by X-ray photoelectron spectroscopy, J. Electron Spectros. Relat. Phenomena. 14 (1978) 237–243. doi:10.1016/0368-2048(78)85071-3.

[56] S. Tsunekawa, T. Fukuda, A. Kasuya, X-ray photoelectron spectroscopy of monodisperse CeO2−x nanoparticles, Surf. Sci. 457 (2000) L437–L440. doi:10.1016/S0039-6028(00)00470-2.

[57] R. Vercaemst, D. Poelman, R.L. Van Meirhaeghe, L. Fiermans, W.H. Laflère, F. Cardon, An XPS study of the dopants' valence states and the composition of CaS1 − xSex:Eu and SrS1 − xSex:Ce thin film electroluminescent devices, J. Lumin. 63 (1995) 19–30. doi:10.1016/0022-2313(94)00059-L.

[58] T. Staudt, Y. Lykhach, N. Tsud, T. Sk?la, K.C. Prince, V. Matol?n, J. Libuda, Ceria reoxidation by CO2: A model study, J. Catal. 275 (2010) 181–185. doi:10.1016/j.jcat.2010.07.032.

[59] F. Menegazzo, P. Burti, M. Signoretto, M. Manzoli, S. Vankova, F. Boccuzzi, F. Pinna, G. Strukul, Effect of the addition of Au in zirconia and ceria supported Pd catalysts for the direct synthesis of hydrogen peroxide, J. Catal. 257 (2008) 369–381. doi:10.1016/j.jcat.2008.05.019.

[60] M.I. Zaki, G.A.M. Hussein, S.A.A. Mansour, H.A. El-Ammawy, Adsorption and surface reactions of pyridine on pure and doped ceria catalysts as studied by infrared spectroscopy, J. Mol. Catal. 51 (1989) 209–220. doi:10.1016/0304-5102(89)80101-4.

[61] M.G. Cutrufello, I. Ferino, R. Monaci, E. Rombi, V. Solinas, Acid-base properties of zirconium, cerium and lanthanum oxides by calorimetric and catalytic investigation, Top. Catal. 19 (2002) 225–240. doi:10.1023/A:1015376409863.

[62] Y. Guo, C. Dai, Z. Lei, B. Chen, X. Fang, Synthesis of hydrogen peroxide over Pd/SiO2/COR monolith catalysts by anthraquinone method, Catal. Today. (2016). doi:10.1016/j.cattod.2016.03.023.

[63] G. Beketov, B. Heinrichs, J.P. Pirard, S. Chenakin, N. Kruse, XPS structural

characterization of Pd/SiO2 catalysts prepared by cogelation, Appl. Surf. Sci. 287 (2013) 293–298. doi:10.1016/j.apsusc.2013.09.145.

[64] G. Fu, X. Jiang, L. Tao, Y. Chen, J. Lin, Y. Zhou, Y. Tang, T. Lu, Polyallylamine functionalized palladium icosahedra: One-pot water-based synthesis and their superior electrocatalytic activity and ethanol tolerant ability in alkaline media, Langmuir. 29 (2013) 4413–4420. doi:10.1021/la304881m.

[65] S. Penner, D. Wang, B. Jenewein, H. Gabasch, B. Klötzer, A. Knop-Gericke, R. Schlögl, K. Hayek, Growth and decomposition of aligned and ordered PdO nanoparticles, J. Chem. Phys. 125 (2006). doi:10.1063/1.2338028.

[66] L. Ouyang, P. Tian, G. Da, X. Xu, C. Ao, T. Chen, R. Si, J. Xu, Y. Han, The origin of active sites for direct synthesis of H2O2 on Pd/TiO2 catalysts: Interfaces of Pd and PdO domains, J. Catal. 321 (2015) 70–80. doi:10.1016/j.jcat.2014.10.003.

[67] S. Abate, K. Barbera, G. Centi, G. Giorgianni, S. Perathoner, Role of size and pretreatment of Pd particles on their behaviour in the direct synthesis of H2O2, J. Energy Chem. 25 (2016) 297–305. doi:10.1016/j.jechem.2016.01.008.

[68] S. Abate, G. Centi, S. Perathoner, S. Melada, F. Pinna, G. Strukul, The issue of selectivity in the direct synthesis of H2O2 from H2 and O2: the role of the catalyst in relation to the kinetics of reaction, Top. Catal. 38 (2006) 181–193. doi:10.1007/s11244-006-0083-9.

[69] N. Gemo, P. Biasi, P. Canu, T.O. Salmi, Mass transfer and kinetics of H2O2 direct synthesis in a batch slurry reactor, Chem. Eng. J. 207-208 (2012) 539–551. doi:10.1016/j.cej.2012.07.015.

VII. GENERAL CONCLUSION AND PERSPECTIVES

Catalytic processes are present in about 90% of all industrial chemical transformations. Nevertheless, there is still a huge opportunity for improving catalysts performance in current processes as well as for developing new sustainable processes and products. This is why catalysis is one of the Green Chemistry Principles. Particularly, in 2015, heterogeneous catalysts were used extensively accounting for 73.6% of the global catalyst market volume due to their ease of handling, low price and easy market access. Such important market participation motivates the research on heterogeneous catalytic materials, and more specifically on supported metal catalysts, whose demand was 1,568.4 kilo tons in 2015 and is expected to grow in light of its increasing application in the organic synthesis of chemicals commodities.

In order to provide more performant catalysts, rational design approaches should be privileged. However, it requires the possibility of controlling the porous architecture of the material at different scales (from a few nanometres up to several centimetres) and the spatial distribution of individual functions. Unfortunately, the routes to control the spatial distribution of individual functions within porous solids are limited [1]. In order to address such a challenge, this study provides a novel waterborne preparation method for controlling the active sites distribution within hierarchically meso- and macroporous catalysts. Particularly, this method permits to preferentially locate the active sites within the macropores, with such macropores being surrounded by a mesoporous matrix.

In short, the proposed catalyst preparation consists of: first, the preparation of a polystyrene latex by emulsion polymerisation, followed by the latex decoration with Pt nanoparticles by sonochemical reduction of a water-soluble metal precursor. Subsequently, the metal-containing hybrid latex is used as template in the two-step acid-base catalysed sol-gel synthesis of a mesoporous silica matrix. This composite material is then calcined to remove the organic polymer template, leaving behind macropores decorated with Pt nanoparticles.

Furthermore, the morphology of the final material can be tuned based on the synthesis conditions at each preparation step. Some of the parameters that were considered in this study are highlighted in Figure 151.

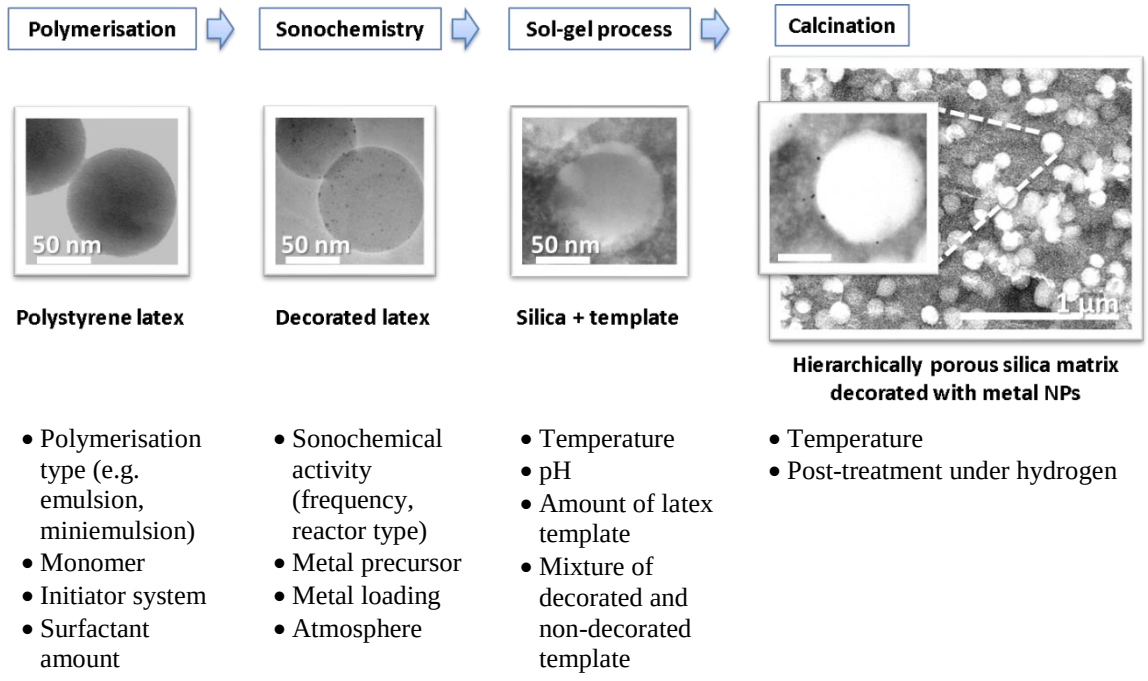

Figure 151. Some important synthesis parameters for the preparation of supported catalyst by combining emulsion polymerisation, sonochemistry and sol-gel route.

This study was tackled using two case studies in order to answer to the Research Question: "Is it possible to vary the morphology and catalytic performance of waterborne catalytic materials prepared by the combination of emulsion polymerisation, sonochemistry and sol-gel route by modifying the conditions of any of the preparation step?". The first case study was the selective hydrogenation of *p*-chloronitrobenzene to *p*-chloroaniline with hierarchically porous Pt-based catalysts (Figure 152) and the second was the direct synthesis of hydrogen peroxide from oxygen and hydrogen with hierarchically porous Pd-based catalysts (Figure 153).

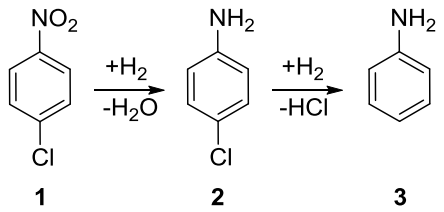

Figure 152. Simplified reaction pathway of the hydrogenation of *p*-chloronitrobenzene (1: *p*-chloronitrobenzene, 2: *p*-chloroaniline, 3: Aniline).

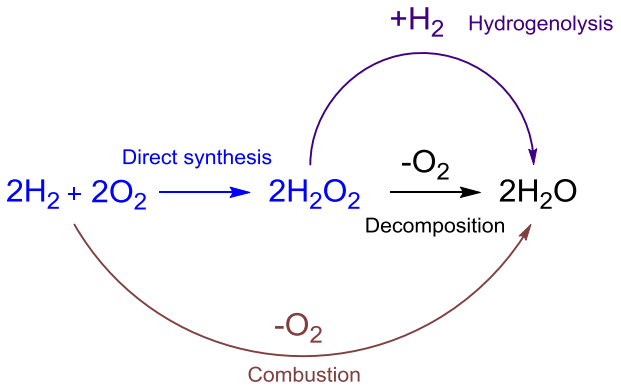

Figure 153. Reaction pathway of the direct synthesis of hydrogen peroxide (in blue) and the related undesired reactions leading to water.

VII.1- First case study: Selective hydrogenation of *p*-chloronitrobenzene to *p*-chloroaniline with hierarchically porous silica-supported Pt-based catalysts

It was possible to synthesise silica-supported platinum catalysts (as schematised in Figure 154) and evaluate them for the selective hydrogenation of *p*-chloronitrobenzene to *p*-chloroaniline.

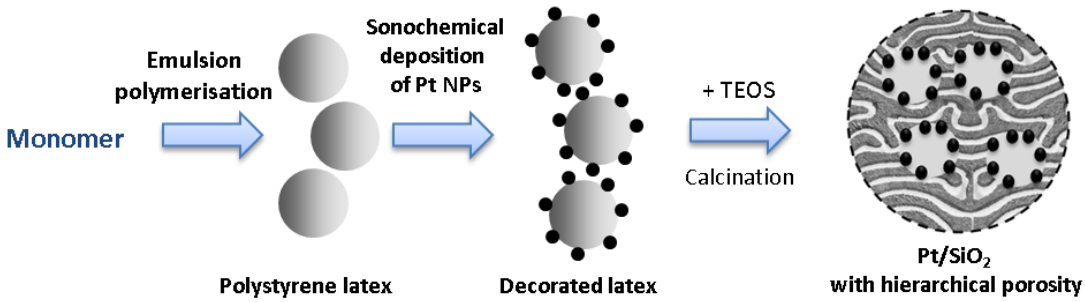

Figure 154. Schematic representation of the preparation of supported catalyst by combining emulsion polymerisation, sonochemistry and sol-gel route

Additionally, by varying the amount of decorated latex template during the sol-gel synthesis, it was possible to prepare materials with different macroporosities: 50%, 33%, 25% and 12.5% (% of macropore volume with respect to the total catalyst volume). Such variation, starting from the same decorated latex, permitted to vary the metal loading at the same time, as schematised in Figure 155.

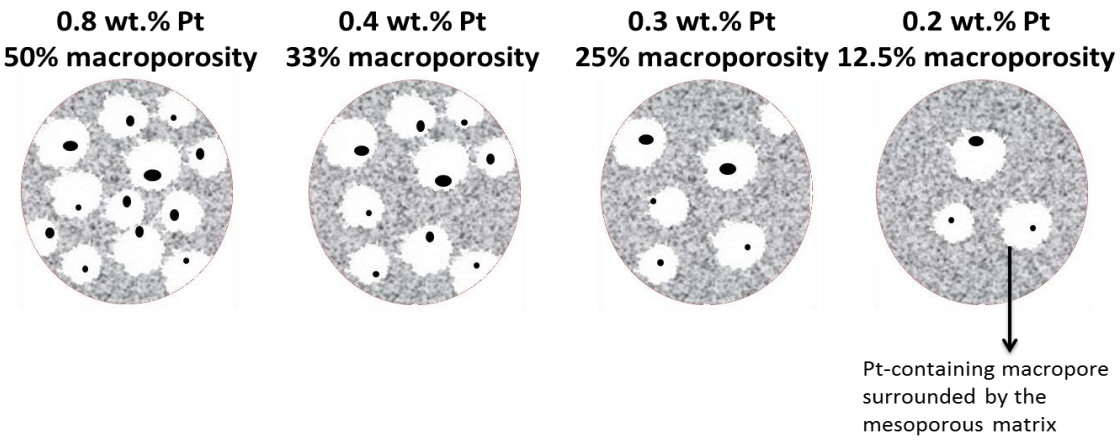

Figure 155. Schematic representation of the variation of the amount of active sites when decreasing the amount of decorated macropores.

Additionally, it was possible to decouple the amount of metal loading and the amount of macropores by using a combination of decorated and non-decorated latex template in the preparation of the catalyst, as depicted in Figure 156.

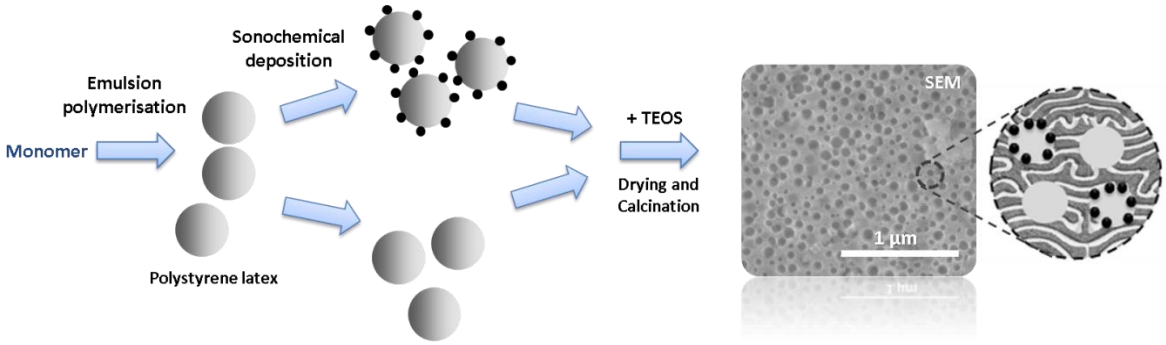

Figure 156. Schematic representation of the preparation of a 0.4 wt.% Pt catalyst with 50% macroporosity: 25% decorated and 25% non-decorated.

Moreover, it was demonstrated that the template removal in the presence of Pt can be carried out at 450 °C, instead of 650 °C without Pt, due to a polymer removal via a Pt catalytic oxidation. Furthermore, it was shown that no reduction pre-treatment was required after such calcination step (either at 450 °C or 650 °C), since the Pt nanoparticles were stable mostly in Pt(0) oxidation state.

Regarding the catalytic performance of these hierarchically porous silica-supported materials, they can be considered efficient catalysts for the selective hydrogenation of *p*-chloronitrobenzene (*p*-CNB) to *p*-chloroaniline (*p*-CAN), exhibiting better selectivity (up to 100% at 80% conversion) than a commercially-available reference catalyst (up to 92.5% at 80%

conversion). The main parameter that permitted to enhance the selectivity was the Pt particle size. The best size seemed to be *ca*. 7 nm. On these large metal particles the product *p*-CAN is adsorbed less strongly in comparison with the reactant *p*-CNB, decreasing the likelihood of *p*-CAN to be hydrogenated further towards aniline [2]. Such particle size was achieved either by calcination at high temperature (650 °C) or by adjusting the Pt loading on the hybrid polymer template (ca. 1 wt.% Pt/polystyrene). Catalysts with lower Pt loading, but similar Pt particle size (obtained by using less amount of Pt decorated latex template) also showed enhanced selectivity. For example, the sample 0.2 wt. % Pt/SiO_2 with 12.5% macroporosity (with particles of 6.7 ± 3.1 nm) exhibited 100% selectivity at 80% conversion.

In contrast, a catalyst prepared from the same type of hierarchically porous silica matrix but decorated with Pt via incipient wetness impregnation and subsequent reduction under hydrogen flow (Figure 157) exhibited very poor selectivity towards *p*-CAN (54.8% at 80% conversion), probably due to the lack of control to achieve narrow Pt particle size distributions (it exhibited Pt particles of size between 3 and 200 nm).

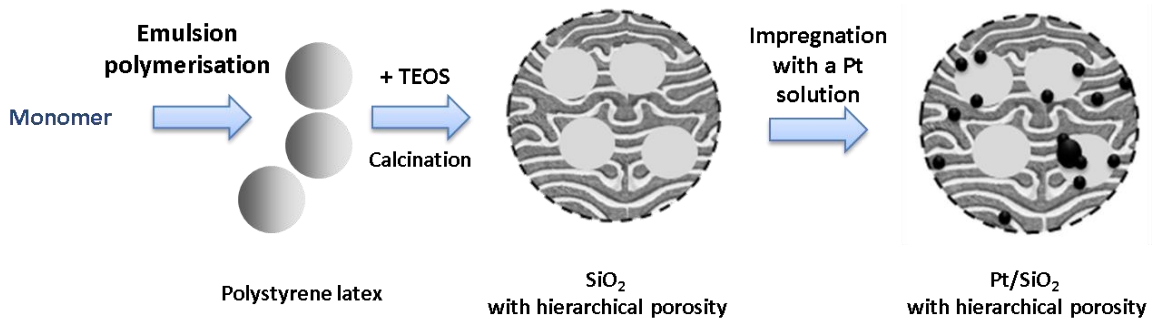

Figure 157. Schematic representation of the preparation of hierarchically porous catalyst via incipient wetness impregnation.

Regarding the hierarchically porous silica structure, it was also observed that for a given Pt loading and a mesoporous matrix with pores of 2-9 nm, an increase in the macroporosity slightly enhanced the initial reaction rate: 0.4 wt. % Pt/SiO_2 with 50% of total macroporosity (25% decorated and 25% non-decorated macroporosity) exhibited 31.0 ± 2.9 $mol_{CNB}/min\ mol_{Pt}$ versus 0.4 wt.% Pt/SiO_2 with 33% of total (decorated) macroporosity that exhibited 26.7 ± 2.9 $mol_{CNB}/min\ mol_{Pt}$. Such an improvement was attributed to the presence of more macropores (and thus, more directly connected macropores) at 50% of total macroporosity that enhanced the internal diffusion of products and reactants.

Furthermore, by widenning the mesopore size distribution to be in the range of 2-15 nm, it was possible to obtain an initial reaction rate of 91.7 ± 2.9 $mol_{CNB}/min\ mol_{Pt}$ (with 0.3 wt.% Pt/SiO_2 with 50% of total macroporosity), which was much higher than that obtained with the commercial catalyst (47.4 ± 2.9 $mol_{CNB}/min\ mol_{Pt}$). Such large mesoporous size (2-15 nm) was obtained by preparing the decorated template in a sonochemical set-up at 343 kHz (with moderate sonochemical activity that limits the modification of the latex pH and colloidal

stability). Nevertheless, very large mesoporosity could promote the Pt nanoparticles aggregation as in the case of the commercial catalyst, in which the mesopores of 11-28 nm permitted the aggregation of initial Pt particles of 2.9 ± 1.2 nm up to 14.1 ± 9.6 nm, compared with a hierarchically porous catalyst with mesopores of 2-15 nm, in which the initial Pt particles of 3.9 ± 1.0 nm only aggregated up to 8.8 ± 7.8 nm.

All the evaluated catalyst exhibited very good stability at the reaction conditions since no major changes of the textural characteristics were evidenced after reaction. For example, the specific surface area of 0.3 wt.% Pt/SiO_2 with 50% of total macroporosity went from 610 ± 37 m^2/g before reaction to 617 ± 37 m^2/g after reaction.

VII.1.1- Perspectives for the rational design of Pt-based silica-supported hierarchically porous catalysts for the selective hydrogenation *p*-chloronitrobenzene to *p*-chloroaniline.

As described, the modification of the catalyst morphology has an influence on the catalyst activity, being best when maximizing the macroporosity (50%) and when increasing the mesopore size range up to 2-15 nm. Additionally, the best selectivity values towards *p*-CAN were obtained with Pt nanoparticles of about 7 nm. However, further optimisation of these hierarchically porous materials is still possible. For instance, an optimisation of the Pt particle size can be carried out by only varying the Pt loading on the template and keeping constant all the other parameters. Furthermore, regarding the silica structure, surfactants such as poly(ethylene glycol)-block-poly(propylene glycol)-block-poly(ethylene glycol) could be used during the sol-gel synthesis in order to obtain larger and ordered mesopores arrays [3]. Such design might improve the effective diffusion within the catalyst by favouring less tortuous diffusion paths. However, the nanoparticles retention might also be less efficient.

VII.2- Second case study: direct synthesis of hydrogen peroxide from oxygen and hydrogen with hierarchically porous silica-supported Pd-based catalysts

It was possible to synthesise silica-supported palladium catalysts and evaluate them for the direct synthesis of hydrogen peroxide from oxygen and hydrogen. Taking into account the versatility of the investigated catalyst preparation method, four approaches were investigated to obtain active nanoparticles of different nature such as monometallic Pd, bimetallic Pt-Pd and mixed metallic-metal oxide Pd-CeO_2. The first approach was the preparation of Pd-based catalysts by a combination of polystyrene latex synthesis by emulsion polymerisation, functionalisation using sonochemistry (with Na_2PdCl_4 as precursor) and silica matrix synthesis by sol-gel method (Figure 158.a.). The second one utilised a subsequent functionalisation of the polystyrene beads by sonochemical reduction of Na_2PtCl_4 and Na_2PdCl_4 to create Pt-Pd bimetallic nanoparticles (Figure 158.b.). The third one comprised the synthesis of a hybrid latex template containing CeO_2 nanoparticles at the surface of the polymer beads. The template was then functionalised with Pd by sonochemical reduction of Na_2PdCl_4 and subsequently, the silica matrix was prepared via sol-gel method (Figure 158.c.). The last approach was the preparation of hybrid Pd/polystyrene latex template via miniemulsion polymerisation using an organo-soluble palladium precursor (palladium (II) acetylacetonate) (Figure 158.d.).

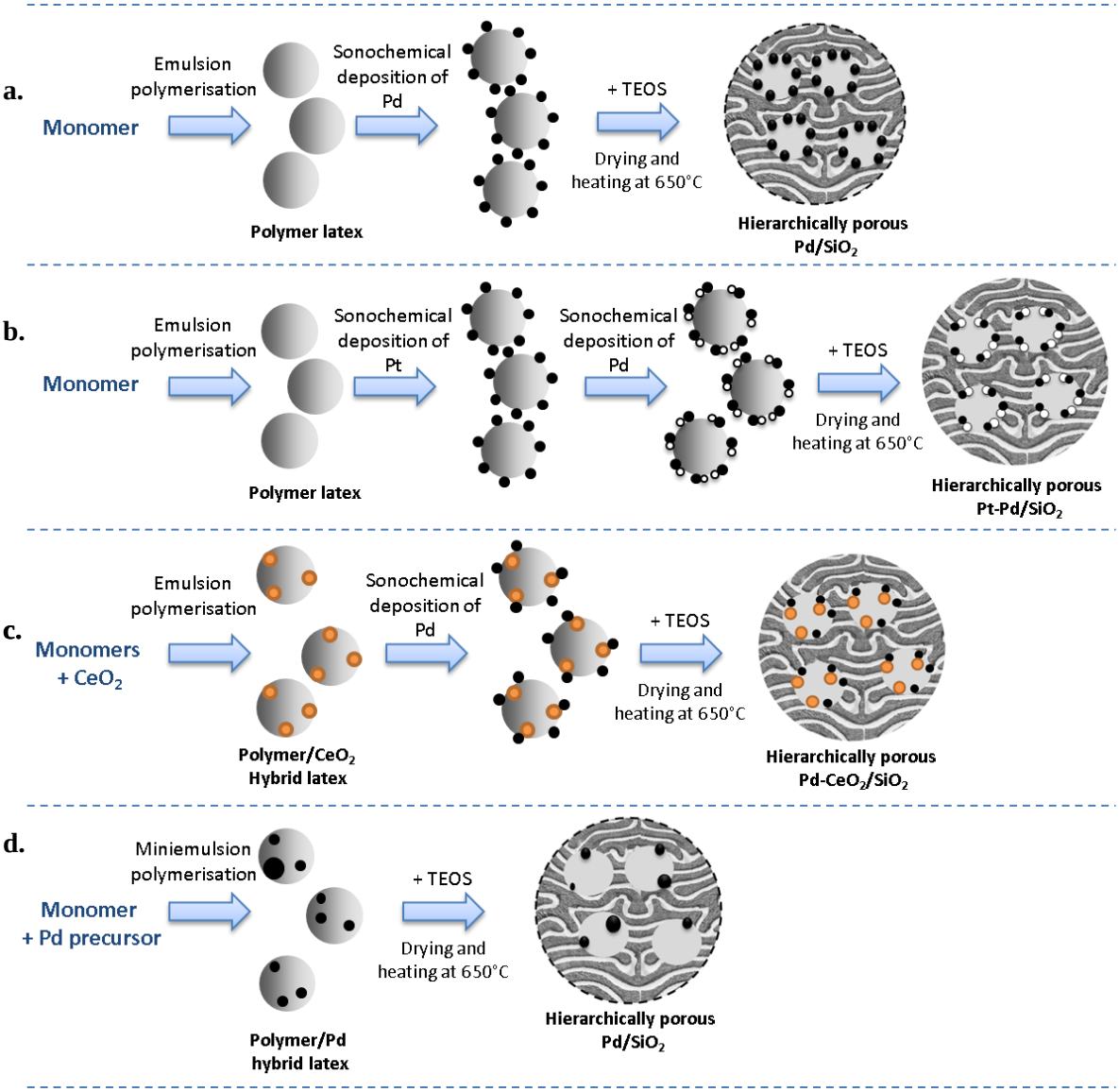

Figure 158. Strategies for the preparation of hierarchically porous Pd-based catalysts: a. Pd/SiO_2 via sol-gel synthesis with sonochemically decorated latex template, b. $Pt\text{-}Pd/SiO_2$ via sol-gel synthesis with sonochemically decorated latex template, c. $Pd\text{-}CeO_2/SiO_2$ via sol-gel synthesis with sonochemically decorated hybrid latex template and d.Pd/SiO_2 via sol-gel synthesis with hybrid latex template.

Contrarily to the Pt-based materials prepared in the first case study, the template removal needed to be carried out at 650 °C. Consequently, an important increase of particle size was observed for these Pd nanoparticles, in comparison with the Pt-based materials. The Pt particle size previously obtained on the template was ca. 2.2 nm, which sintered to 4.6 ± 1.1 nm or 6.5 ± 2.2 nm when calcined at 450 °C or 650 °C, respectively. On the other hand, the synthesised Pd nanoparticles were of 6.7 nm, which reached 16.2 nm after calcination at 650 °C. However, the bimetallic Pt-Pd particles demonstrated a high thermal stability with a very limited sintering after calcination at 650 °C, going from an average particle diameter of D_n = 3.6 ± 1.3 nm after sonochemical preparation to D_n = 3.8 ± 1.4 nm, after calcination.

The last approach using a hybrid Pd/polystyrene latex template prepared via miniemulsion polymerisation permitted to omit the sonochemical decoration in the preparation of monometallic Pd nanoparticles. However, this method gives very limited control on the nanoparticles synthesis: particle size, formation of bimetallic interactions, metal dispersion on the latex, etc.

Regarding the catalytic performances of these materials, the best productivity of H_2O_2 was obtained with the reduced bimetallic Pd-Pt catalyst with 32500 $mol_{H_2O_2}/(mol_{metal}.h)$, unfortunately with a decreasing selectivity down to 19 ± 1 %. When non-reduced, the bimetallic catalyst achieved a better selectivity (40 ± 1 %), but decreased in productivity (24000$mol_{H_2O_2}/(mol_{metal}.h)$). On the other hand, the best selectivity was obtained with the Pd-CeO_2/SiO_2 catalyst, reaching 68 ± 3 % when only calcined. After reduction, it reached 53 ± 2 % and 63 ± 2 %, in batch and semi-batch operation conditions, respectively. These selectivity values are better than 42 % reported elsewhere for 3.6 wt.% Pd/SiO_2 under slightly similar conditions [4].

Something remarkable about the bimetallic Pt-Pd catalyst tested here is that the 32500 $mol_{H_2O_2}/(mol_{metal}.h)$ productivity corresponds to almost 10-fold increase compared with the catalyst 0.7 wt.% Pd/SiO_2, or 3-fold increase compared with the material 0.2 wt.% Pd/SiO_2 by miniemulsion. This productivity enhancement is very promising considering that in the literature, the enhancement of adding some Pt to Pd has been reported to result in a maximum 1.8-fold increase in productivity [5].

Regarding the texture stability, the bimetallic Pt-Pd (specific surface area of ca. 600 m^2/g) and the monometallic Pd prepared by miniemulsion (specific surface area of ca. 700 m^2/g) were very stable at the reaction conditions, keeping the almost identical textural characteristics after reaction. Conversely, the monometallic Pd prepared by the sonochemical route presented some densification during the reaction (total porosity went from 51% to 43%) that could be attributed to influence of non-reduced Pd species during the sol-gel synthesis, leading to a weaker structure than expected. The Pd-CeO_2/SiO_2 catalyst also presented a slight densification after the first reaction (total porosity went from 64% to 58%), but it remained stable when recycled. This means that the synthesis of these two materials could still be optimised to achieve more stable textural characteristics since the very first use.

VII.2.1- Perspectives for the rational design of Pd-based silica-supported hierarchically porous catalysts for the direct synthesis of hydrogen peroxide from oxygen and hydrogen.

The selectivity variation is related to the Pd oxidation state, which is influenced by the metal-support interaction. An intermediate Pd oxidation state with mostly Pd(II) species at the surface improves the catalyst performance. In the materials tested with Pd alone, it was mostly present as Pd(0) after an *ex-situ* reduction treatment, leading to selectivity up to 49 ± 3 % (without any *ex-situ* reduction, the selectivity could go up to 54 ± 8 %, but with a much limited catalytic activity). The interaction Pt-Pd after reduction favoured the metallic species (Pd(0) and Pt(0)),

increasing the decomposition rate of H_2O_2, ultimately reducing the selectivity. In the presence of CeO_2, oxidised Pd species (PdO_x/Pd–O–Ce) were favoured, both after the calcination step and after a hydrogen treatment, and remained in the material after reaction due to the strong Pd-CeO_2 interaction. Such a peculiar Pd species in the catalyst allowed reaching a stable selectivity up to 63 %. Such selectivity was better than the 55% reported for a Pd/CeO_2 catalyst in semi-batch conditions [6]. So, considering the best productivities with the bimetallic Pt-Pd catalysts and best selectivity with the Pd-CeO_2 catalysts, it could be worth testing a catalyst Pt-Pd-CeO_2/SiO_2 that could take advantage of the productivity enhancement given by the Pt and the chemical stability provided by the ceria to achieve high selectivity.

VII.3- General perspectives

In the first case study (the selective hydrogenation of *p*-chloronitrobenzene to *p*-chloroaniline with hierarchically porous Pt-based catalysts), it was possible to confirm that this catalyst preparation method permits to tailor the catalyst hierarchical porosity and to control the metal distribution throughout the material. In the second case study (the direct synthesis of hydrogen peroxide from oxygen and hydrogen with hierarchically porous Pd-based catalysts), it was possible to show that this method permits to modify the nature of the active sites by playing with bimetallic and metal-metal oxide interactions. Consequently, these results permit to confirm that the modification of the preparation conditions defines the morphology and catalytic performance of hierarchically porous catalysts prepared by the combination of emulsion polymerisation, sonochemistry and sol-gel route.

Figure 159 summarises the type of Pt/SiO_2 catalysts evaluated in this work. Particularly, the catalysts prepared by the combination of latex synthesis, sonochemical reduction and sol-gel process permitted to achieve Pt nanoparticles between 4 and 10 nm, depending on the Pt loading and calcination temperature. The mesopores exhibited different ranges from 2-7 nm to 2-15 nm. Such difference was explained by slight variations of pH and latex stability during the sonochemical decoration. Furthermore, the macropore size varied between 110 and 400 nm depending on whether the polymer beads aggregated due to slight colloidal destabilisation. In order to study more in detail the effect of the sonochemical decoration on the final morphology, it would be recommended to decorate a polystyrene latex at various sonochemical activities, under CO/Ar in order to limit the side reactions that could occur with the *in-situ* generated H_2O_2. Similar experiments under Ar would permit to study the effect of $HO^{\bullet}$ radicals and *in-situ* generated H_2O_2 on the polymer beads surface, which could be characterised by titration of the surface functional groups [7–10] .

An additional perspective for catalyst morphology would be the decoration of a silica material with a non-decorated latex. After drying, the material could be impregnated with a Pt precursor solution and then calcined at 650 °C for template removal. This might allow the selective decoration of the mesoporous matrix around the macropores as suggested on Figure 159.d.

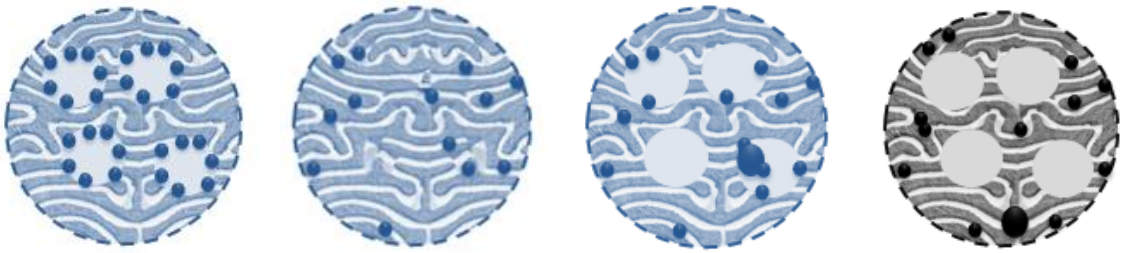

a. Via sonochemically decorated template	b. Mesoporous commercial catalyst	c. Via incipient wetness impregnation	d. Via incipient wetness impregnation before calcination (PERSPECTIVE)
NPs: 4 – 10 nm Mesopores: 2 – 15 nm Macropores:110–400nm	NPs: 3 nm Mesopores: 11 – 28 nm Macropores: N/A	NPs: 3 – 200 nm Mesopores: 2 – 15 nm Macropores:110–170nm	

Figure 159. Pt/SiO_2 catalysts with different morphology. (In blue, the catalysts tested for the selective hydrogenation of *p*-Chloronitrobenzene to *p*-Chloroaniline)

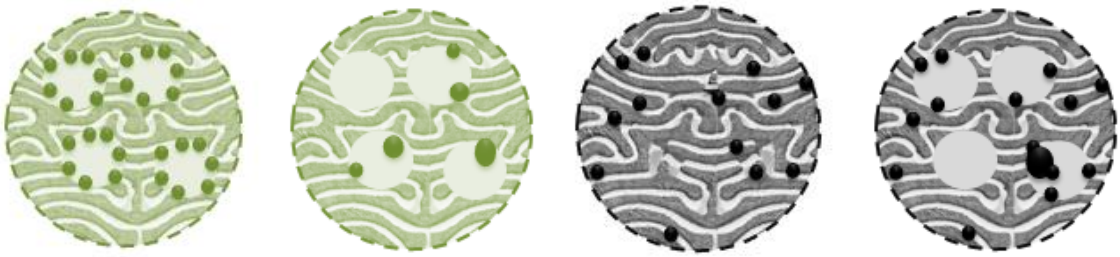

a. Via sonochemically decorated template

NPs: 16 nm
Mesopores: 2 – 5 nm
Macropores: ca. 130nm

b. Via miniemulsion polymerisation

NPs: 12 nm
Mesopores: 2 – 5 nm
Macropores: ca. 130nm

c. Mesoporous commercial catalyst (PERSPECTIVE)

d. Via incipient wetness impregnation (PERSPECTIVE)

Figure 160. Pd/SiO_2 catalysts prepared by different methods (In green, the catalysts tested for the direct synthesis of hydrogen peroxide from oxygen and hydrogen)

Figure 160 presents the Pd/SiO_2 catalysts evaluated in this work. The catalyst prepared by the combination of latex synthesis, sonochemical reduction and sol-gel process permitted to achieve Pd nanoparticles of ca. 16 nm, which was, on one hand, due to the large particle size obtained after Pd sonochemical reduction (7 nm) and on the other hand, due to the high calcination temperature required for template removal (650 °C). So a first perspective would be to prepare latex templates with a stronger interaction with Pd, for instance with thiol functional groups [11–13] and/or poly(vinylpyrrolidone) (PVP) at the surface of the polymer beads [14].. It would might favour a more even polymer surface decoration with smaller particles. A second perspective would imply the use of other polymer templates with lower degradation temperatures could be prepared like poly(methyl methacrylate) (PMMA), in order to limit the sintering of Pd nanoparticles during the calcination step at 650 °C. Indeed, it can be expected that the removal of a PMMA latex template could be carried out at lower temperature than in the case of polystyrene, since (when non included in a silica matrix) PMMA can be completely degraded at 215 °C [15], while polystyrene requires 425 °C [16]. A third perspective could be the removal of the polymer template using mild supercritical CO_2 conditions (as briefly explored in Annex III), which in addition potentially opens the way for the recycling of the polymer template.

Moreover, as in the first case study, it would be desirable to complete the study on the direct synthesis of hydrogen peroxide from oxygen and hydrogen by carrying out further experiments at the same reaction conditions in order to compare the performance of the hierarchically porous Pd-catalysts against a commercial Pd/SiO_2 material and against a Pd catalyst prepared by incipient wetness impregnation using a hierarchical macro- and mesoporous silica matrix.

a. Via sonochemically decorated template

NPs: 4 – 5 nm
Mesopores: 2 – 5 nm
Macropores: ca. 130nm

b. Via mixture of decorated templates (PERSPECTIVE)

c. Via mixture of decorated latex and functionalised micelles (PERSPECTIVE)

Figure 161. Catalysts with multiple functionalities supported on hierarchically porous SiO_2 (In green, the catalysts tested for the direct synthesis of hydrogen peroxide from oxygen and hydrogen)

Figure 161 presents some of the possible morphologies that can be achieved with multiple functionalities by combining latex synthesis, sonochemical reduction and sol-gel process. Two designs were already tested for the direct synthesis of hydrogen peroxide from oxygen and hydrogen: bimetallic Pd-Pt/SiO_2 and Pd-CeO_2/SiO_2. In both cases, the two functionalities were within the same macropore and exhibited a strong interaction. Moreover, other catalyst morphologies are possible. For instance, the combination of two decorated latex templates would lead to different active sites in independent macropores, as depicted in Figure 162. This could be particularly interesting for the design of catalysts for cascade reactions, in which a first step occurs at an active site, and a second step occurs in another active site within the same catalyst grain.

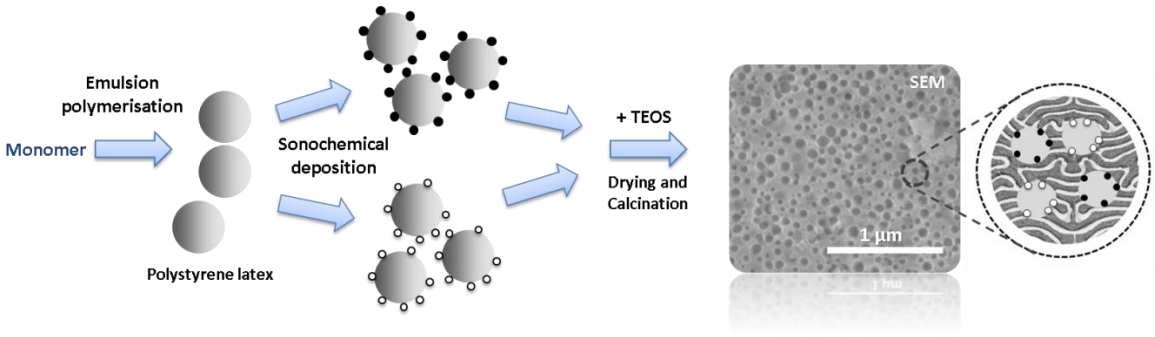

Figure 162. Schematic representation of the preparation of a catalyst with independent macropores decorated with different functionalities.

Furthermore, it could be possible to prepare a material with a certain functionality within the macropores and another within the mesopores (Figure 161.c). It could be done by a mixture of decorated latex and functionalised micelles. The latter can be prepared from triblock copolymers and a silica hybrid sol (where the Pt nanoparticles can be prepared, for instance, by microwave assisted polyol reduction) [17]. Another option for preparing functionalised micelles is the use of stimuli-responsive block copolymers to form PolyIon Complex (PIC) micelles. For instance double-hydrophilic block copolymers can exhibit a certain charge following a stimulus (such as a change of pH or of the ionic strength of the solution), so they can assemble with metal ions of the opposite charge by electrostatic complexation (e.g. Pt or Pd precursors). After the sol-gel synthesis, the resulting mesoporosity is ordered, containing the desired metal [18,19].

Regarding the synthesis of the latex template, additional perspective can be suggested. First, the polymer particle size can be decreased by the preparation of nanolatexes [20–22], in order to tailor macropores smaller than 100 nm. Such nanolatex templates could be combined with templates of a particle larger size in order to induce a macropore size hierarchy in the final material. Second, other functional groups than sulfonate or sulphate at the surface of the polymer beads can be used. For instance, in order to enhance the polymer-silica interaction, polyethylene oxide could be used to provide -OH terminations that could form Si-O bonds upon the sol-gel process. However, special attention must be given to the latex stability to avoid flocculation by hydrogen bonding in the presence of PEO [23]. Or in order to enhance the polymer-metal interaction, polyvinylpyrrolidone (PVP) could be used to stabilise metal nanoparticles at the surface of the polymer beads [14].

Furthermore, this study focused on hierarchically porous silica support. However, it could be extended to single or mixed oxide systems like TiO_2, Al_2O_3, SiO_2–TiO_2 or SiO_2–Al_2O_3 [17].

Regarding the operation conditions for catalyst testing, the catalytic reactions performed in this study were mainly performed in batch conditions, where no major mass transport limitations were expected. However, catalytic tests in dynamic flow conditions through a porous monolithic contactor would take advantage of the hierarchical porous characteristics of these materials, considering the higher mass transport limitations that a continuous-flow operation requires to overcome. For such operation conditions, this waterborne catalyst preparation method permits the preparation by dip-coating (during the sol-gel step before reaching the gel point) of monolithic pieces such as honeycomb structures or solid foams.

In conclusion, this catalyst preparation technique by the combination of latex synthesis, sonochemical reduction and sol-gel process provides a very powerful and versatile toolbox for catalyst tailoring and catalyst optimisation. In addition, there are plenty of perspectives for further developing this novel method that would permit to prepare catalysts with improved morphologies and controlled active sites distribution.

VII.4- References

[1] C.M.A. Parlett, M.A. Isaacs, S.K. Beaumont, L.M. Bingham, N.S. Hondow, K. Wilson, A.F. Lee, Spatially orthogonal chemical functionalization of a hierarchical pore network for catalytic cascade reactions, Nat. Mater. 15 (2016) 178–182. doi:10.1038/nmat4478.

[2] B. Coq, A. Tijani, R. Dutartre, F. Figuéras, Influence of support and metallic precursor on the hydrogenation of p-chloronitrobenzene over supported platinum catalysts, J. Mol. Catal. 79 (1993) 253–264. doi:10.1016/0304-5102(93)85106-4.

[3] P. Yang, T. Deng, D. Zhao, P. Feng, D. Pine, B.F. Chmelka, G.M. Whitesides, G.D. Stucky, Hierarchically Ordered Oxides, Science (80-.). 282 (1998) 2244–2246. doi:10.1126/science.282.5397.2244.

[4] S. Abate, P. Lanzafame, S. Perathoner, G. Centi, SBA-15 as a support for palladium in the direct synthesis of H2O2 from H2 and O2, Catal. Today. 169 (2011) 167–174. doi:10.1016/j.cattod.2010.09.030.

[5] J. Xu, L. Ouyang, G.J. Da, Q.Q. Song, X.J. Yang, Y.F. Han, Pt promotional effects on Pd-Pt alloy catalysts for hydrogen peroxide synthesis directly from hydrogen and oxygen, J. Catal. 285 (2012) 74–82. doi:10.1016/j.jcat.2011.09.017.

[6] F. Menegazzo, P. Burti, M. Signoretto, M. Manzoli, S. Vankova, F. Boccuzzi, F. Pinna, G. Strukul, Effect of the addition of Au in zirconia and ceria supported Pd catalysts for the direct synthesis of hydrogen peroxide, J. Catal. 257 (2008) 369–381. doi:10.1016/j.jcat.2008.05.019.

[7] S.M. Ahmed, M.S. El-Aasser, G.H. Pauli, G.W. Poehlein, J.W. Vanderhoff, Cleaning latexes for surface characterization by serum replacement, J. Colloid Interface Sci. 73 (1980) 388–405. doi:10.1016/0021-9797(80)90085-5.

[8] R.M. Fitch, W.T. McCarvill, Surface chemistry of polystyrene colloids prepared by mixed initiator/surfactant systems, J. Colloid Interface Sci. 66 (1978) 20–25. doi:10.1016/0021-9797(78)90179-0.

[9] Y. Gong, K. Nakashima, R. Xu, A Novel Method To Determine Effective Charge of Polystyrene Latex Particles in Aqueous Dispersion, Langmuir. 17 (2001) 2889–2892. doi:10.1021/la001483n.

[10] J.M. Stubbs, P. Roose, P. De Doncker, D.C. Sundberg, Probing the surface of polymer colloids by conductometric surfactant titration, Langmuir. 22 (2006) 2697–2705. doi:10.1021/la052721n.

[11] M. Cargnello, N.L. Wieder, P. Canton, T. Montini, G. Giambastiani, A. Benedetti, R.J. Gorte, P. Fornasiero, A Versatile Approach to the Synthesis of Functionalized Thiol-Protected Palladium Nanoparticles, Chem. Mater. 23 (2011) 3961–3969. doi:10.1021/cm2014658.

[12] W. Shi, Y. Sahoo, M.T. Swihart, P.N. Prasad, Gold nanoshells on polystyrene cores for control of surface plasmon resonance., Langmuir. 21 (2005) 1610–1617. doi:10.1021/la047628y.

[13] P. Carro, G. Corthey, A.A. Rubert, G.A. Benitez, M.H. Fonticelli, R.C. Salvarezza, The complex thiol-palladium interface: A theoretical and experimental study, Langmuir. 26 (2010) 14655–14662. doi:10.1021/la102505c.

[14] D. Crespy, K. Landfester, Synthesis of polyvinylpyrrolidone/silver nanoparticles hybrid latex in non-aqueous miniemulsion at high temperature, Polymer (Guildf). 50 (2009) 1616–1620. doi:10.1016/j.polymer.2009.02.003.

[15] C.G. Schäfer, S. Vowinkel, G.P. Hellmann, T. Herdt, C. Contiu, J.J. Schneider, M. Gallei, A polymer based and template-directed approach towards functional multidimensional micro-structured organic/inorganic hybrid materials, J. Mater. Chem. C. 2 (2014) 7960. doi:10.1039/C4TC00633J.

[16] P. Pfaffli, A. Zitting, H. Vainio, Thermal degradation products of homopolymer polystyrene in air, Scand. J. Work. Environ. Heal. 4 (1978) 22–27. doi:10.5271/sjweh.2744.

[17] C. Yacou, M.-L. Fontaine, A. Ayral, P. Lacroix-Desmazes, P.-A. Albouy, A. Julbe, One pot synthesis of hierarchical porous silica membrane material with dispersed Pt nanoparticles using a microwave-assisted sol–gel route, J. Mater. Chem. 18 (2008) 4274–4279. doi:10.1039/b807029f.

[18] C. Gérardin, J. Reboul, M. Bonne, B. Lebeau, Ecodesign of ordered mesoporous silica materials, Chem. Soc. Rev. 42 (2013) 4217. doi:10.1039/c3cs35451b.

[19] N. Baccile, J. Reboul, B. Blanc, B. Coq, P. Lacroix-Desmazes, M. In, C. Gérardin, Ecodesign of Ordered Mesoporous Materials Obtained with Switchable Micellar Assemblies, Angew. Chemie Int. Ed. 47 (2008) 8433–8437. doi:10.1002/anie.200802431.

[20] L. Yang, Y. Ke, Synthesis of polystyrene nanolatexes via emulsion polymerization using sodium dodecyl sulfonate as the emulsifier, High Perform. Polym. 26 (2014) 900–905. doi:10.1177/0954008314533979.

[21] S. Sajjadi, M. Yianneskis, Semibatch Emulsion Polymerization of Methyl Methacrylate with a Neat Monomer Feed, Polym. React. Eng. 11 (2003) 715–736. doi:10.1081/PRE-

120026371.

[22] Y. Zhang, Y. He, J. Zhao, Poly(methyl methacrylate) nanolatexes with high solid contents prepared by semi-continuous emulsion polymerization in the presence of oil-soluble initiators, Eur. Polym. J. 61 (2014) 316–325. doi:10.1016/j.eurpolymj.2014.11.004.

[23] R. Pelton, H. Xiao, M.A. Brook, A. Hamielec, Flocculation of Polystyrene Latex with Mixtures of Poly(p -vinylphenol) and Poly(ethylene oxide), Langmuir. 12 (1996) 5756–5762. doi:10.1021/la9506281.

VIII. ANNEX I. POROSITY IN CATALYTIC MATERIALS

Contents

Much effort has been put on the structuration of aluminophosphates, clays, hydroxides, metal organic frameworks and zeolites in order to improve their catalytic properties. This section aims to set a reference of pore sizes typically present in catalytic materials, highlighting the relevance of hierarchical zeolites, which constitute a well-recognised example of catalyst enhancement by porosity tailoring.

VIII.1- Aluminophosphates

Aluminophosphates ($AlPO_4$-n) are catalytic materials typically with formula $xR•Al_2O_3•1.0 \pm 0.2\ P_2O_5•yH_2O$, R being the organic template. These materials are prepared by hydrothermal treatment with alumina, phosphoric acid and an organic template of the type amine or quaternary ammonium salt. Similar materials are silicoaluminophosphate ($SAPO_4$-n), and their isomorphic substitution with metal ions: metal silicoaluminophosphate ($MeAPSO_4$-n) and metal aluminophosphates (Me-$AlPO_4$-n). The structure obtained in these materials is mostly microporous with pores ranging between 0.3 nm and 0.8 nm [1].

VIII.2- Pillared interlayered clays

Pillared interlayered clays (PILCs) are another type of porous material with pore size ranging between 0.4 nm and 2.0 nm. PILCs are prepared from clays that are negatively charged aluminosilicate sheets arranged in a sandwich-like structure with cations in between that counter balance the charge. These parent clays are swollen and the cations are ion exchanged with aluminium polyoxocations like $[AlO_4Al_{12}(OH)_{24}(H_2O)]^{7+}$, which, after calcination, lead to the formation of aluminium oxide pillars between the clay layers [1].

VIII.3- Porous clay heterostructures

Porous clay heterostructures (PCHs) are clay-based materials prepared with a surfactant template between the sheets, leading to pores between 1.4 nm and 2.2 nm. Particularly, a quaternary-ammonium salt (Q^+-FH) of the type $[C_{16}H_{33}N(CH_3)_3]^+$ was used with an neutral amine to swell the negatively charged clay layers. Tetraethylortosilicate (TEOS) was then added, which partially displaced the neutral amine. As a result, the silicate ions interacted with the surfactants forming rod-like micellar assemblies of Q^+ and neutral amine. As a the low water content was measured in the solvating amine, the water concentration out of the interlayer spaces was also low, leading to a faster base-catalysed hydrolysis of TEOS within the interlayer spaces than out of them. These micelles were then surrounded by hydrated silica structures, which after calcination permitted the formation of the porous structure depicted in Figure 163 [2].

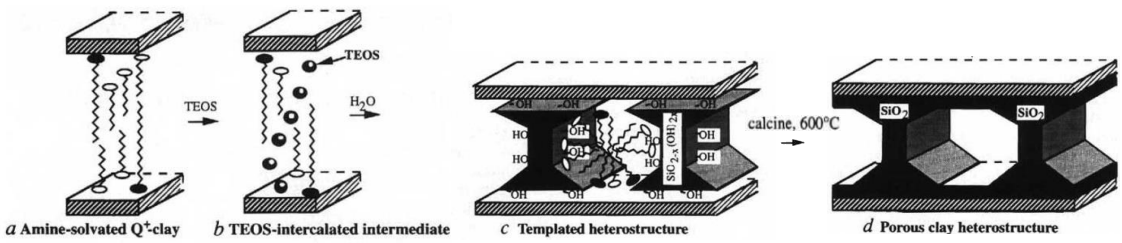

Figure 163. Formation of porous clay heterostructures [2]

VIII.4- Layered double hydroxydes

Layered double hydroxydes (LDHs) are hydrotalcite-like compounds consisting of positively charged hydroxide layers with anions and water molecules in between [1]. Their structure is like natural mineral brucite ($Mg(OH)_2$) with general formula $[M_{1-x}^{2+}M_x^{3+}(OH)_2]^{x+}[A^{n-}]_{x/n} \cdot mH_2O$, M^{2+} and M^{3+} being divalent and trivalent metal cations in the octahedral positions and A^{n-} being the interlayer exchangeable anions [3]. This kind of materials can be prepared by co-precipitation, ion exchange, calcination-rehydration and hydrothermal method. Sodium citrate assisted hydrothermal method has been tried in one pot process leading to NiAl-LDH with hierarchical porosity, with interlayer spacing of 0.73 nm, average mesoporous size ranging between 10 and 31 nm decreasing with the Ni/Al ratio as measured by N_2 physisorption, and macropores between 100 nm and 300 nm due to the macroscopic arrangement of layers as measured by SEM imaging [4]. An example of Ni_4Al-LDH is shown in Figure 164. Recently,

Mg-Al and Zn-Al LDHs have been assembled with commercial sepiolite ($Si_{12}O_{30}Mg_8(OH,F)_4(H_2O)_4 \cdot 8H_2O$) leading to LDH/sepiolite materials, which can be employed as intermediate phase in the development of highly dispersed metal oxide catalysts supported on sepiolite by thermal decomposition of the LDH component [5].

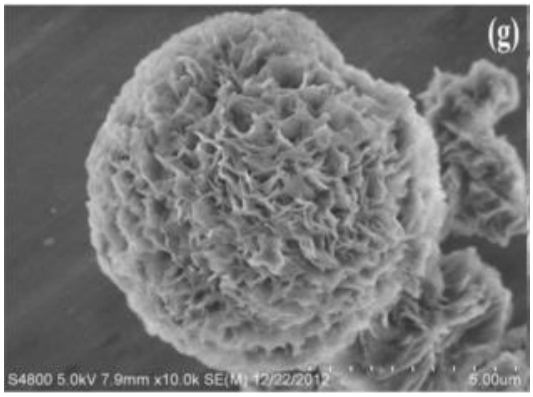

Figure 164. Hierarchically porous Ni_4Al-LDH

VIII.5- Metal organic frameworks

Metal organic frameworks (MOFs) are three-dimensional structures composed of inorganic and organic moieties self-assembled in such a way that the inorganic cationic systems act as nodes linked by polytopic organic linkers, as depicted in Figure 165 [6]. Examples of the inorganic part might be arsenates, silicates, sulphates, phosphates or phosphonates. The organic part can be branched carboxylic acids, amino complexes or others, which can have various lengths and volumes depending on their nature [1]. The great potential of MOFs over zeolites is that the former can be functionalised with organic moieties enabling enantioselective catalysis. Nevertheless, they required mild reaction conditions, since MOFs have low thermal, hydrothermal and chemical stability [6]. Depending on the organic moiety used on the MOF synthesis, the cavities or homogeneous periodic pores within the structure have been tuned between 0.38 nm and 2.88 nm [7]. This is the reason why MOFs have been claimed to fill the pore size gap between ultramicroporous (e.g. zeolites) and mesoporous materials [6]. Figure 166 shows a comparison of the cavity size of porous MOFs and standard zeolites and aluminophosphates. It can be seen that this materials have pores ranging between small mesopores and micropores.

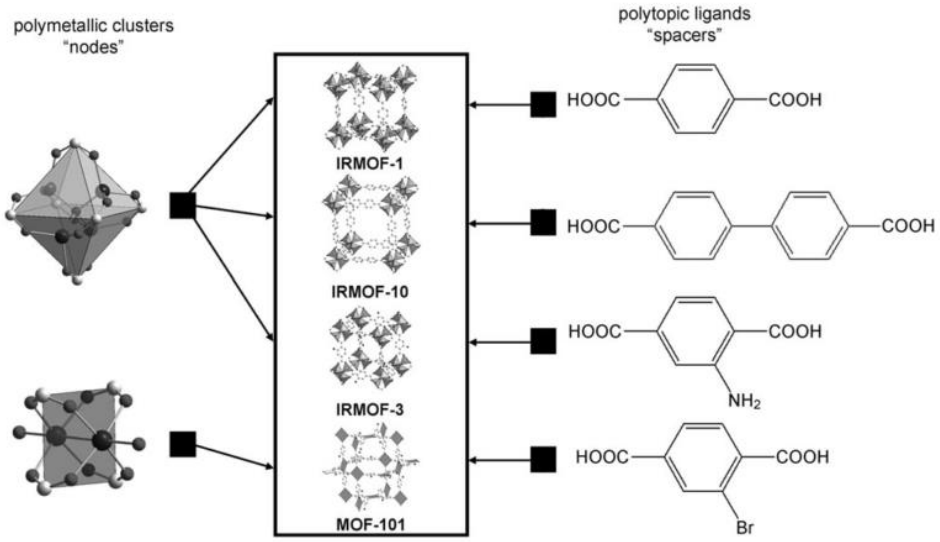

Figure 165. Self-assembly of metal–organic frameworks (centre) by combination of organic linkers (right) and polymetallic cluster nodes (left; top: μ^4-oxo $\{M_4O(-CO_2)_6\}$ and bottom: paddlewheel $\{M_2(-CO_2)_4\}$) [6–8].

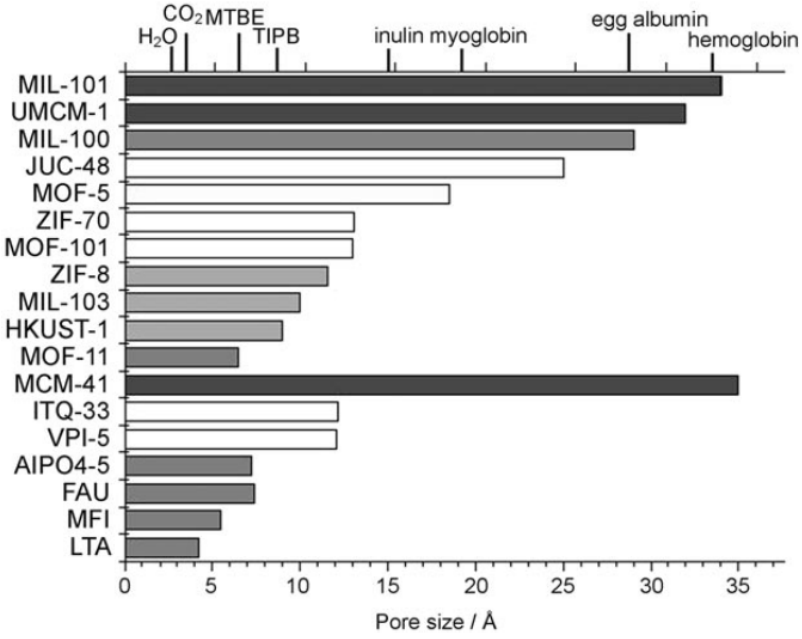

Figure 166. Pore sizes comparison between MOFs (MIL-101, UMCM-1, MIL-100, JUC-48, MOF-5, ZIF-70, MOF-101, ZIF-8, MIL-103, HKUST-1, MOF-11), standard mesoporous silicate (MCM-41), zeolites (ITQ-33, VPI-5, FAU, MFI, LTA) and aluminophosphates ($AlPO_4$-5). Potential guests molecules size is shown on the top axis: MTBE=methyl *tert*-butyl ether; TIPB=1,3,5-triisopropylbenzene [6].

VIII.6- Zeolites

Zeolites have a characteristic structure formed by three-dimensional TO_4 tetrahedra arrangements (where T can be Si^{4+} or Al^{3+} coordinated atoms). The tetrahedral subunits are assembled by sharing an oxygen atom (T-O-T bridges) to form an infinite lattice. Considering that aluminium atoms, present in the Si structure, only have 3+ valence, it leaves a negative charge in the framework that must be counterbalanced by the presence of cations [9]. The catalytic activity of zeolites is associated with the acid sites (Brønsted, Lewis) present in the framework, which can be tuned during and/or after the synthesis. The synthesis can be adapted to replace some of the tetrahedrally coordinated Si atoms by trivalent (Al, B, Fe, Cr, Sb, As, Ga) or tetravalent atoms (Ge, Ti, Zr, Hf). Post-synthesis procedures include steam treatment, chemical vapour deposition, ion exchange and reduction of exchanged metal ions [1].

The pore size of zeolites ranges from 0.41 nm, for the 10MR type (a ten member ring formed by eight SiO_4 tetrahedra), to 0.74 nm in the case of Y-Type zeolite [1]. Pore diameters of typical zeolites are summarised in Figure 167. These molecular-scale-sized pores allow the structure to act as a molecular sieve, leading to "shape selective catalysis", since some reactants and products are allowed entering and leaving the structure, respectively, while more bulky molecules cannot access the catalytic sites and large molecule products are retained within the pores [10]. The pores can also enhance the selectivity by limiting the formation of bulky transition-state intermediates [1,11].

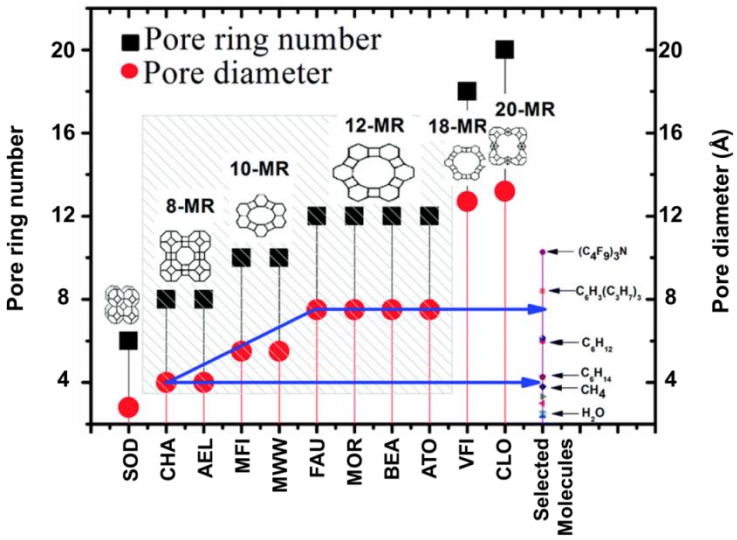

Figure 167. Typical zeolite pore sizes [12]

Zeolites have attracted the attention due to their unique properties such as crystallinity, large surface areas, acidity, ion-exchange capacity and shape-selective ability. However, these materials present a challenge: intracrystalline diffusion limitations due to their microporous structure. This has motivated the development of hierarchical zeolites, notably meso- and microporous [13]. Zeolites constitute an excellent example of the enhancement of catalytic performance by hierarchical structure tailoring, as it has been reviewed several times [12–16]. For instance, it has been observed that the vapour-phase benzene alkylation with ethylene to ethylbenzene was more active and more selective using mesoporous zeolite crystals than purely

microporous analogues. Such a better selectivity was due to a shorter diffusion path length that reduced the resident time of the product within the micropores, consequently, it limited successive alkylation reactions of the desired ethylbenzene to polyalkylbezenes [17].

VIII.6.1- Hierarchically porous zeolites

In order to achieve hierarchically porous structures with zeolite functionalities, several approaches have been explored such as post-synthesis chemical treatment (hydrothermal, acidic, basic, desilication, dealumination, etc.) [18], recrystallization or templating [13]. Figure 168 summarises some of the approaches that have been tried in the preparation of such hierarchically structured materials.

Regarding the use of surfactants in the preparation of hierarchical zeolites, there are not many successful examples of the primary surfactant-assisted method starting from purely molecular species, notably because the mesopore-templating molecules can be expelled out form the zeolite framework due to low affinity with the zeolite crystals [14,19] or because large surfactant molecules are not thermally stable at the high crystallisation temperatures [20]. Nevertheless, a composite material of microporous MFI zeolite with mesoporous MCM-41 has been synthesised by using two templates simultaneously: $C_6H_{13}(CH_3)_3NBr$ and $C_{14}H_{29}(CH_3)_3NBr$. The final structure exhibited MFI-type crystals partially embedded in aggregates or partially covered with thin surfaces of MCM-41[19]. Recently, a hierarchically porous ZSM-5 material (macropores, mesopores and micropores) was synthesized in the presence of n-hexyltrimethylammonium bromide (HTAB) and tetrapropylammonium hydroxide (TPAOH), leading to ZSM-5 samples with mesopores of diameter up to 32 nm. HTAB and TPAOH worked cooperatively in the assembly process: the role of TPA^+ was the templating of micropores, while the HTA^+ was the stabilisation of the zeolite nanocrystals [21]. More generally in this approach, tuneable organosilanes of the type $[(CH_3O)SiC_3H_6N(CH_3)_2C_nH_{2n+1}]Cl$ have been used as both a silica source and supramolecular template leading to mesopores in the range of 2-20 nm [22,23]. The other primary surfactant-assisted method consists of crystallising the zeolite inside the surfactant assembly. This approach requires the preparation of microemulsions or reverse micelles. The crystallisation takes place then within the droplets, which at the same time, control the zeolite crystal size [13]. For instance, water-in-oil microemulsions have been prepared with cetyltrimethylammonium bromide (CTAB) as surfactant and butanol as cosurfactant, containing the silicalite-1 synthesis gel within the aqueous droplets. Depending on the microemulsion composition, ,the silicalite-1 crystals morphology could be adjusted from coffin-shaped to rod-shaped or irregular-shaped nanoparticles [24].

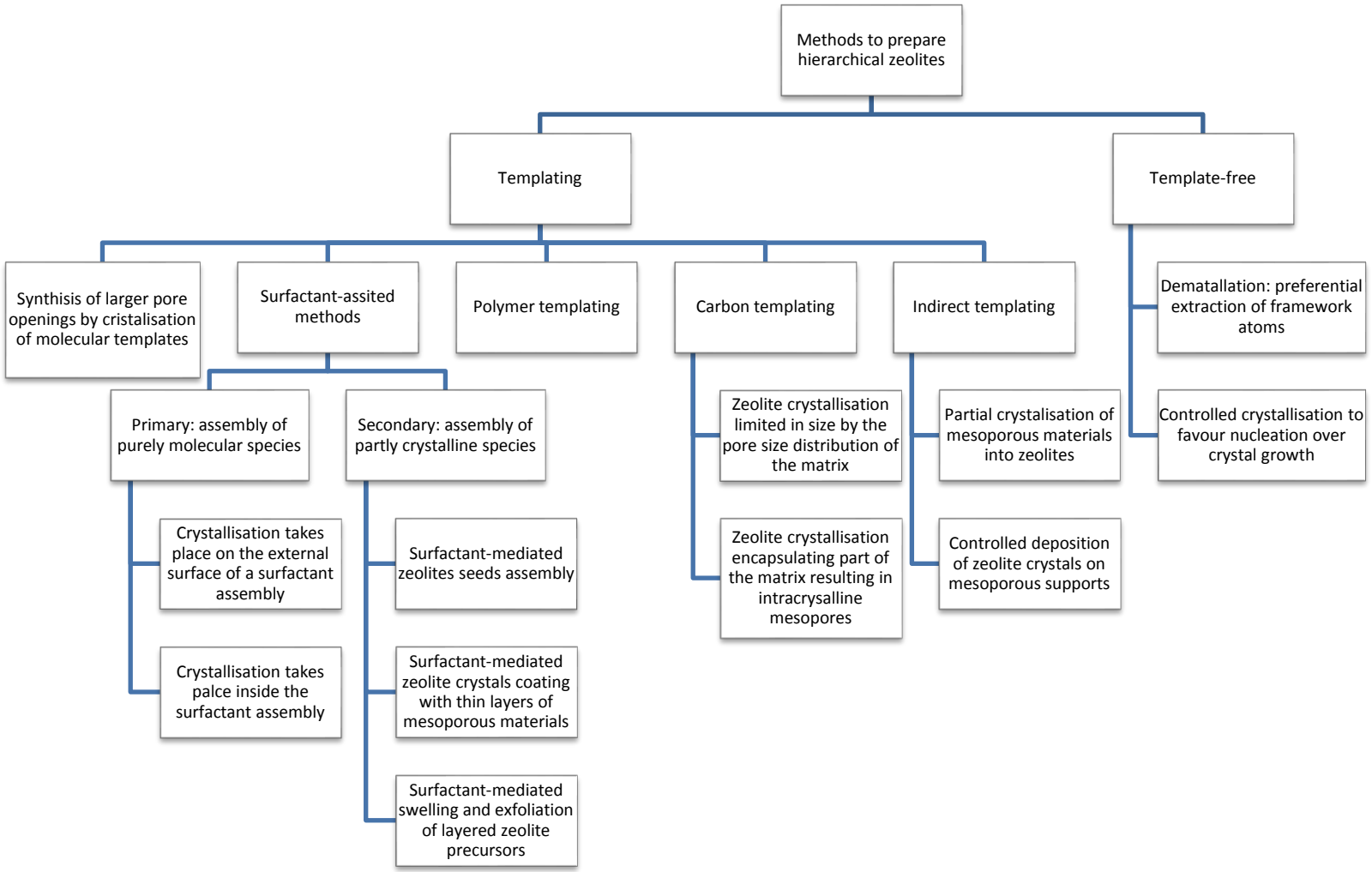

Figure 168. Concept map of hierarchical zeolite preparation methods [13].

An example of secondary surfactant-assisted method, i.e. assembly of partly crystalline species, is the synthesis of FAU/MCM-41 by a successive synthesis method or by the addition of FAU crystals to a MCM-41 synthesis gel. In both cases, a bimodal porous material was obtained; unfortunately, another independent MCM-41 phase was always formed [25].

In contrast, the use of carbon templates has been reported and reviewed several times [13,14,26]. It is a much promising technique in the preparation of hierarchical zeolites. The initial idea was to carry out the zeolite crystallisation within the porous carbonaceous matrix. That would prevent the crystal growing from being larger than the size of the pores. The hierarchically porous zeolite was obtained after carbon removal by calcination. This approach was successful in the preparation of MFI, BEA and ZSM-5 materials [13,27]. However, by slightly changing the crystallisation conditions, it is possible for the zeolite crystals to grow through the surrounding carbon pores in such a way that they encapsulate part of the carbon matrix. After calcination for carbon removal, the zeolite crystals exhibit intracrystalline mesopores, as depicted in Figure 169 [28]. Several materials have been prepared using this approach with carbon templates of different sizes and morphologies, including carbon nanotubes [13,26,29].

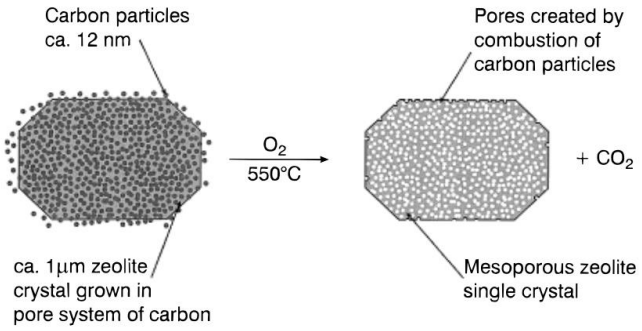

Figure 169. Representation of a zeolite crystal in the presence of a carbon template.

Considering polymer templates in the preparation of hierarchical zeolites, there are not many examples either. Nevertheless, some polystyrene-templated materials have been reported. For instance, a hierarchical micro- and macroporous β-zeolite was prepared by co-deposition of mono-disperse polystyrene beads (diameter: *ca*. 1200 nm or 600 nm) and nano β-zeolites particles (average diameter: 70 nm) in aqueous suspension, and subsequently the polystyrene was removed by calcination [30]. It has been reported other attempts to prepare FeZSM-5 hierarchical micro/macroporous material using polystyrene spheres (ranging from 280 to 1150 nm), unfortunately a large proportion of amorphous silica instead of zeolite was formed [31]. Another approach has been the preparation of a hard amorphous silica skeleton around the polymer beads (*ca*. 530 nm), which was then converted into silicalite in the presence of TPA^+ structure-directing agent at 130 °C under autogenous pressure for 40 h, leading to a micro-/mesoporous material after calcination [14]. More recently, MFI zeolite was successfully prepared in the presence of polystyrene latex, leading to a micro-, meso- and macroporous material [32].

A remarkable work using polymer templates is the fabrication of hollow zeolite spheres using a polystyrene beads template by a layer-by-layer technique based on electrostatic interaction [33]. In short, negatively charged nanocrystals of zeolite β and silicate-1 were deposited on positively charged polystyrene beads. The polystyrene latex template was prepared by disposition of five layers of polyelectrolytes of cationic polydiallyldimethylammonium chloride) (PDDA) and anionic poly(styrenesulfonate, sodium salt) (PSS) in the order of PDDA/PSS/PDDA/PSS/PDDA. Subsequently, the nanocrystals and PDDA were alternately deposited on the positively charged beads to form homogeneous nanozeolite/PDDA multilayers, as depicted in Figure 170. Finally, after calcination, hollow zeolite spheres were obtained.

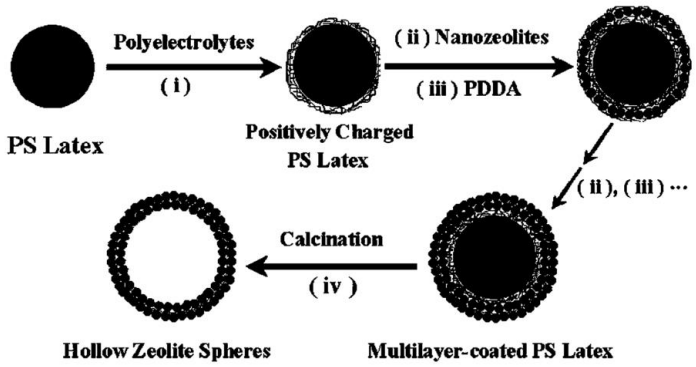

Figure 170. Hollow zeolite spheres preparation by layer-by-layer deposition [33].

VIII.7- Conclusion

Aluminophosphates, clays, hydroxides, metal organic frameworks and zeolites are typically microporous materials with pores of a few Angstroms. However their texture structuration to achieve hierarchically porous materials has permitted increase their catalytic performance. Hierarchical zeolites constitute a well-recognised example of catalyst enhancement by porosity tailoring. This has been possible by several techniques such as post-synthesis chemical treatment (hydrothermal, acidic, basic, desilication, dealumination, etc.), recrystallization or templating.

VIII.8- References

[1] I. Fechete, Y. Wang, J.C. Védrine, The past, present and future of heterogeneous catalysis, Catal. Today. 189 (2012) 2–27. doi:10.1016/j.cattod.2012.04.003.

[2] A. Galarneau, A. Barodawalla, T.J. Pinnavaia, Porous clay heterostructures formed by gallery-templated synthesis, Nature. 374 (1995) 529–531. doi:10.1038/374529a0.

[3] R.P. Bontchev, S. Liu, J.L. Krumhansl, J. Voigt, T.M. Nenoff, Synthesis, Characterization, and Ion Exchange Properties of Hydrotalcite Mg 6 Al 2 (OH) 16 (A) x (A‘) 2 - x ·4H 2 O (A, A‘ = Cl - , Br - , I - , and NO 3 - , 2 ≥ x ≥ 0) Derivatives, Chem. Mater. 15 (2003) 3669–3675. doi:10.1021/cm034231r.

[4] Y. Sun, J. Zhou, W. Cai, R. Zhao, J. Yuan, Hierarchically porous NiAl-LDH nanoparticles as highly efficient adsorbent for p-nitrophenol from water, Appl. Surf. Sci. 349 (2015) 897–903. doi:10.1016/j.apsusc.2015.05.041.

[5] A. Gómez-Avilés, P. Aranda, E. Ruiz-Hitzky, Layered double hydroxide/sepiolite heterostructured materials, Appl. Clay Sci. 130 (2016) 83–92. doi:10.1016/j.clay.2015.12.011.

[6] D. Farrusseng, S. Aguado, C. Pinel, Metal-Organic Frameworks: Opportunities for Catalysis, Angew. Chemie Int. Ed. 48 (2009) 7502–7513. doi:10.1002/anie.200806063.

[7] M. Eddaoudi, J. Kim, N. Rosi, D. Vodak, J. Wachter, M. O’Keeffe, O.M. Yaghi, Systematic Design of Pore Size and Functionality in Isoreticular MOFs and Their Application in Methane Storage, Science (80-.). 295 (2002) 469–472. doi:10.1126/science.1067208.

[8] M. Eddaoudi, J. Kim, M. O’Keeffe, O.M. Yaghi, Cu 2 [o -Br-C 6 H 3 (CO 2) 2] 2 (H 2 O) 2 ·(DMF) 8 (H 2 O) 2 : A Framework Deliberately Designed To Have the NbO Structure Type, J. Am. Chem. Soc. 124 (2002) 376–377. doi:10.1021/ja017154e.

[9] W. Hölderich, M. Hesse, F. Näumann, Zeolites: Catalysts for Organic Syntheses, Angew. Chemie Int. Ed. English. 27 (1988) 226–246. doi:10.1002/anie.198802261.

[10] N.Y. Chen, Industrial application of shape selective catalysis, Stud. Surf. Sci. Catal. 38 (1988) 153–163. doi:10.1016/S0167-2991(09)60652-2.

[11] E. Dumitriu, V. Hulea, Effects of channel structures and acid properties of large-pore zeolites in the liquid-phase tert-butylation of phenol, J. Catal. 218 (2003) 249–257. doi:10.1016/S0021-9517(03)00159-3.

[12] J. Shi, Y. Wang, W. Yang, Y. Tang, Z. Xie, Recent advances of pore system construction in zeolite-catalyzed chemical industry processes, Chem. Soc. Rev. 44 (2015) 8877–8903. doi:10.1039/C5CS00626K.

[13] J. Pérez-Ramírez, C.H. Christensen, K. Egeblad, C.H. Christensen, J.C. Groen, Hierarchical zeolites: Enhanced Utilisation of Microporous Crystals in Catalysis by Advances in Materials Design., Chem. Soc. Rev. 37 (2008) 2530–2542. doi:10.1039/b809030k.

[14] K. Na, M. Choi, R. Ryoo, Recent advances in the synthesis of hierarchically nanoporous zeolites, Microporous Mesoporous Mater. 166 (2013) 3–19. doi:10.1016/j.micromeso.2012.03.054.

[15] Y. Wei, T.E. Parmentier, K.P. de Jong, J. Zečević, Tailoring and visualizing the pore architecture of hierarchical zeolites, Chem. Soc. Rev. 44 (2015) 7234–7261. doi:10.1039/C5CS00155B.

[16] T.O. Drews, M. Tsapatsis, Progress in manipulating zeolite morphology and related applications, Curr. Opin. Colloid Interface Sci. 10 (2005) 233–238. doi:10.1016/j.cocis.2005.09.013.

[17] C.H. Christensen, K. Johannsen, I. Schmidt, C.H. Christensen, Catalytic Benzene Alkylation over Mesoporous Zeolite Single Crystals: Improving Activity and Selectivity with a New Family of Porous Materials, J. Am. Chem. Soc. 125 (2003) 13370–13371. doi:10.1021/ja037063c.

[18] A. Corma, From microporous to mesoporous molecular sieve materials and their use in catalysis, Chem. Rev. 97 (1997) 2373–2420. doi:10.1021/cr960406n.

[19] A. Karlsson, M. Stöcker, R. Schmidt, Composites of micro- and mesoporous materials: simultaneous syntheses of MFI/MCM-41 like phases by a mixed template approach, Microporous Mesoporous Mater. 27 (1999) 181–192. doi:10.1016/S1387-1811(98)00252-2.

[20] K. Na, M. Chol, W. Park, Y. Sakamoto, O. Terasakl, R. Ryoo, Pillared MFI zeolite nanosheets of a single-unit-cell thickness, J. Am. Chem. Soc. 132 (2010) 4169–4177. doi:10.1021/ja908382n.

[21] P. Bai, P. Wu, W. Xing, D. Liu, L. Zhao, Y. Wang, B. Xu, Z. Yan, X.S. Zhao, Synthesis and catalytic properties of ZSM-5 zeolite with hierarchical pores prepared in the presence of n-hexyltrimethylammonium bromide, J. Mater. Chem. A. 3 (2015) 18586–18597. doi:10.1039/C5TA05350A.

[22] M. Choi, R. Srivastava, R. Ryoo, Organosilane surfactant-directed synthesis of mesoporous aluminophosphates constructed with crystalline microporous frameworks, Chem. Commun. (2006) 4380. doi:10.1039/b612265e.

[23] M. Choi, H.S. Cho, R. Srivastava, C. Venkatesan, D.-H. Choi, R. Ryoo, Amphiphilic organosilane-directed synthesis of crystalline zeolite with tunable mesoporosity., Nat. Mater. 5 (2006) 718–723. doi:10.1038/nmat1705.

[24] J.-C. Lin, M.Z. Yates, Altering the Crystal Morphology of Silicalite-1 through Microemulsion-Based Synthesis, Langmuir. 21 (2005) 2117–2120. doi:10.1021/la0473456.

[25] K.R. Kloetstra, H.W. Zandbergen, J.C. Jansen, H. van Bekkum, Overgrowth of mesoporous MCM-41 on faujasite, Microporous Mater. 6 (1996) 287–293. doi:10.1016/0927-6513(96)00036-3.

[26] Y. Tao, H. Kanoh, L. Abrams, K. Kaneko, Mesopore-modified zeolites: Preparation, characterization, and applications, Chem. Rev. 106 (2006) 896–910. doi:10.1021/cr040204o.

[27] C.J.H. Jacobsen, C. Madsen, T.V.W. Janssens, H.J. Jakobsen, J. Skibsted, Zeolites by confined space synthesis - characterization of the acid sites in nanosized ZSM-5 by ammonia desorption and 27Al/29Si-MAS NMR spectroscopy, Microporous Mesoporous Mater. 39 (2000) 393–401. doi:10.1016/S1387-1811(00)00215-8.

[28] C.J.H. Jacobsen, C. Madsen, J. Houzvicka, I. Schmidt, A. Carlsson, Mesoporous Zeolite Single Crystals, J. Am. Chem. Soc. 122 (2000) 7116–7117. doi:10.1021/ja000744c.

[29] I. Schmidt, A. Boisen, E. Gustavsson, K. Ståhl, S. Pehrson, S. Dahl, A. Carlsson, C.J.H. Jacobsen, Carbon Nanotube Templated Growth of Mesoporous Zeolite Single Crystals, Chem. Mater. 13 (2001) 4416–4418. doi:10.1021/cm011206h.

[30] Q. Yanping, D. Peng, C. Shengli, W. Xiaodong, Fabrication of Macro-porous p-zeolite by Using Colloidal Polystyrene Spheres as a Template, Pet. Sci. 3 (2006) 85–88.

[31] K.A. Sashkina, V.S. Semeikina, V.S. Labko, N.A. Rudina, E. V Parkhomchuk, Template method for the synthesis of a heterogeneous fenton catalyst based on the hierarchical zeolite FeZSM-5, Kinet. Catal. 54 (2013) 638–643. doi:10.1134/S0023158413050145.

[32] E. V. Parkhomchuk, K.A. Sashkina, V.N. Parmon, New heterogeneous catalysts based on zeolites with hierarchical pore system, Pet. Chem. 56 (2016) 197–204. doi:10.1134/S0965544116030105.

[33] X.D. Wang, W.L. Yang, Y. Tang, Y.J. Wang, S.K. Fu, Z. Gao, Fabrication of hollow zeolite spheres, Chem. Commun. (2000) 2161–2162. doi:10.1039/b006539k.

IX. ANNEX II. SONOCHEMISTRY

Contents

This section intends to give a brief overview of sonochemistry, which is defined as the use of ultrasound to enhance or alter chemical reactions [1].

IX.1- Definition of ultrasound

Sound is created by the propagation of a mechanic wave in a medium. Such wave is characterised by its amplitude (p_{max} as the highest acoustic pressure) and frequency (f, which is the inverse of the period T), as depicted in Figure 171.

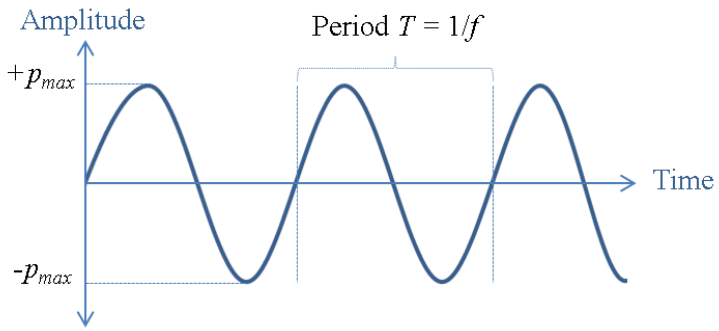

Figure 171. Planar representation of a sinusoidal sound wave [2]

The frequency can be calculated by:

$$f = \frac{c_{wave}}{\lambda}$$

Where f is the frequency (Hz), c_{wave} is the wave velocity (or wave propagation speed) (m/s) and λ is the corresponding wavelength (m) [3].

Ultrasound is associated with the frequencies above 18 kHz, i.e. above the audible frequencies to the human ear (between 16 Hz and 18 kHz). Depending on the frequency, the application of ultrasounds is different, as schematised in Figure 172

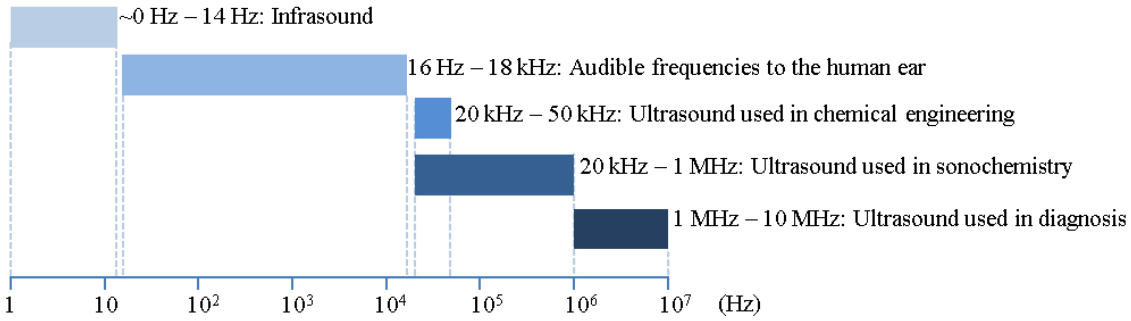

Figure 172. Classification of the acoustic waves based on their frequency [4]

The ultrasound domain can also be divided in three parts [4]:

- Low frequency ultrasound (20 – 100 kHz)
- High frequency ultrasound (100 – 1000 kHz)
- Very high frequency ultrasound (> 1 MHz)

IX.2- Acoustic cavitation

The first report of cavitation was published in 1895 by Thornycroft and Barnaby regarding the erosion of their submarine propeller. Nevertheless, the first use of ultrasound to enhance chemical reaction rates was reported by Richards and Loomis in 1927 [1]. The use of ultrasound relies on the chemical and mechanical effects of the implosive collapse of cavitation bubbles. Cavitation is defined as the formation, growth and collapse of bubbles containing vapour or gas within a moving liquid [3]. Such bubbles are formed by the effect of excessive constrains that break the medium continuity, so the cavitation can be of three types [5]:

- Optic cavitation: it is related to the formation of cavities by the incidence of a high energy laser into a light-absorbing liquid [6].
- Hydrodynamic cavitation: it occurs when a liquid is subjected to rapid changes of pressure, for instance a liquid flowing at high speed in the proximity of pump impellers [5].

- Acoustic cavitation: it results of ultrasound passing through a solution, which creates regions inside the solution with high and low pressure according to periodic compression and expansion stages. Through this oscillation, cavities are formed during the expansion stages. Then, during the compression, the volume of the cavities decreases and the concentration of gas inside increases, thus part of the gas is dissolved in the liquid and part of the vapour condenses at the interface. Contrarily, during the expansion stage, the size of the bubble increases by evaporation of the liquid and diffusion of the dissolved gas. Given that the exchange surface is smaller during the compression than during the expansion stages, the subsequent compression/expansion cycles induce the progressive bubble growth.
  These cavities can be of two types: stable or transient bubbles. The stable bubbles grow within the ultrasound field during several acoustic cycles. They can coalesce and escape from the medium due to buoyancy leading to the solution degassing. On the other hand, the transient bubbles last for one or a few acoustic cycles. They grow until they reach a critical bubble size that resonates with the ultrasound frequency, so they rapidly reach an unstable size, collapsing violently and fragmenting into microbubbles that will act as new sites of bubble nucleation. Stable and transient bubbles occur at small and high amplitude of pressure variation, respectively [2].
  The process of acoustic cavitation includes the formation, growth and collapse of acoustic bubble (e.g. at 20 kHz, these bubbles have a radius of ca. 150 µm) [7]. This phenomenon is schematised in Figure 173 [8].

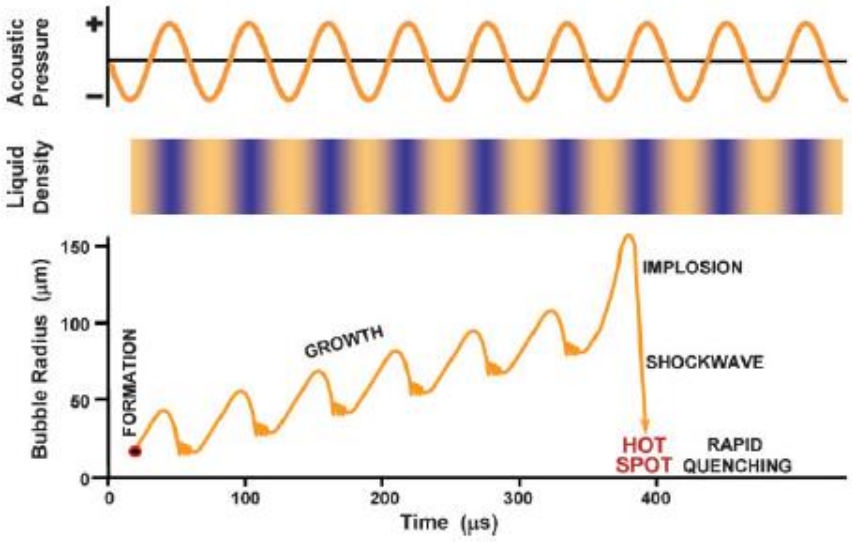

Figure 173. Scheme of the acoustic cavitation phenomenon [8].

IX.2.1- Effects of acoustic cavitation

Depending on the operating conditions, the acoustic cavitation phenomenon can lead to chemical and physical effects. These effects result from the sudden and violent collapse of the cavitation bubbles (within a few μs) releasing locally a high amount of energy [9,8].

Several theories have been proposed to explain the origin of the energy released during the bubble implosion, the "hot-spot" theory being the most used one. It considers that during the cavitation phenomenon, the bubble expands isothermally, while the implosion takes place adiabatically (since it occurs much faster than any possible heat exchange between the gas and the liquid). In this way, extreme conditions are achieved at the core of the cavitation bubble for a very brief period. The experimental study of these hot spots is very difficult given the very fast phenomenon, but theoretical models have permitted to approximatively estimate temperatures and pressures of roughly 5000 °C and 500 bars, respectively, localised at these spots [8,10]. According to this theory, three main regions can be observed when the cavitation phenomenon takes place: the interior of the bubble, the interface liquid/bubble and the solution, as depicted in Figure 174.

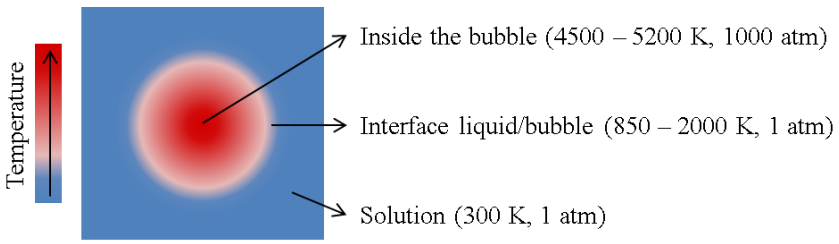

Figure 174. Cavitation bubble regions in aqueous medium under acoustic cavitation according to the "hot-spot" theory [2,4,10].

Nevertheless, the "hot-spot" theory has limitations regarding the explanation of some experimental observations such as the influence of dissolved gas (e.g. argon, krypton or xenon) or the formation of species like O_2^+, which cannot only be due to thermal excitation [11]. More recent studies have demonstrated the existence of plasma out of thermodynamic equilibrium, which permitted the development of a new model for the implosion phenomenon [12].

IX.2.1.1- Physical effects

A notable effect of the acoustic cavitation is a phenomenon known as sonoluminescence: when the cavitation bubbles contain high energy particles like excited $HO^{\bullet}$ radicals, they emit light (with wavelengths of 200–800 nm) for a very short time (about 100 ps). The analysis of the emitted light can give information about the conditions inside the acoustic bubble [7]. However, the real nature of sonoluminescence is still under investigation [12].

Regarding other physical effects that arise from the acoustic cavitation, it is important to note the agitation of the medium due to bubble implosion as well as the accelerated reaction kinetics due to enhanced mass transfer phenomena. Important mechanical effects can also take place as a result of the bubble collapse like the generation of shock waves of several giga Pascal (GPa). Additionally, when the bubble implosion that takes place in the vicinity of a surface, it occurs asymmetrically, inducing the formation of a microjet of liquid towards the material surface at a speed of ca. 150 m/s, resulting on the erosion of the surface, as illustrated in Figure 175 [3,7].

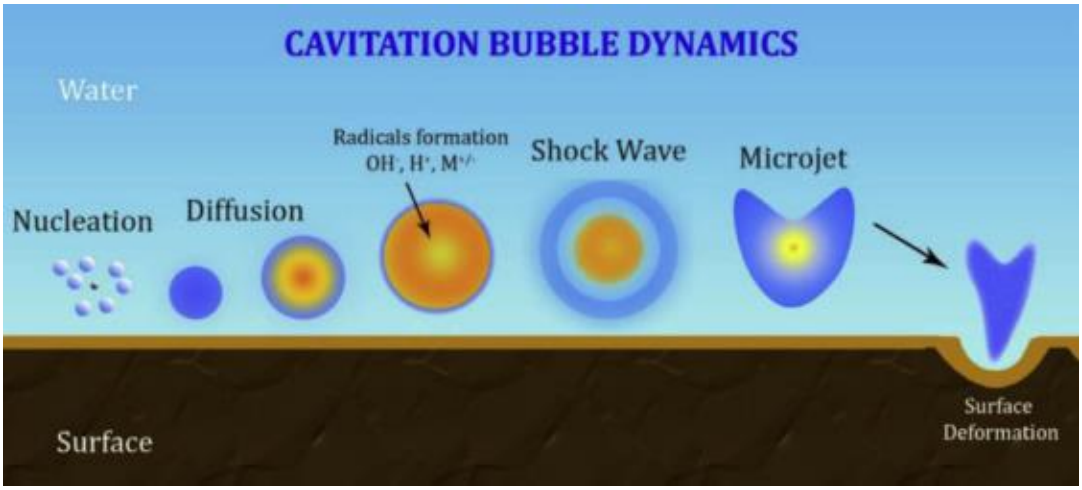

Figure 175. Schematic representation of the acoustic cavitation effects [7].

Several examples of the use of the physical effects of ultrasound are reported in the literature. For instance, it has been used in the preparation of bionanocomposites based on chitosan and vermiculite, whose synthesis has been enhanced using ultrasound irradiation for homogenisation of the reaction medium [13].

IX.2.1.2- Chemical effects

Three main types of reaction can occur as a result of the acoustic cavitation. The first one is the combustion or pyrolysis of organic molecules (with high vapour pressure and/or hydrophobic) present in the medium. It takes place within the cavitation bubble given the extreme condition already discussed. The second type is the degradation of non-volatile organic compounds at the interface liquid/bubble where hydrothermal conditions can be achieved. The third type regards redox reactions. Water molecules can be split into $H^{\bullet}$ and $OH^{\bullet}$ radicals within the cavitation bubble. Hydrogen (H_2) is generated by the recombination of $H^{\bullet}$ radicals within these bubbles. Similarly, hydrogen peroxide (H_2O_2) is generated by the recombination of $OH^{\bullet}$ radicals [12,14]. Such species can react with other molecules in the medium or at the boundary of the cavitation bubbles. In this way, the sonochemical activity can be estimated by measuring the hydrogen peroxide production rate. The concentration of H_2O_2 can be monitored by absorption spectrophotometry with a $TiOSO_4$ solution in 0.5 M H_2SO_4 (λ = 411 nm, ε = 707 L/mol.cm) [15,16].

A visible example of the sonochemical activity is the chemiluminescence of a luminol solution submitted to ultrasound, as shown in Figure 176. The luminol molecule reacts with $HO^{\bullet}$ radicals generated in the cavitation bubbles to give aminophthalate anions and a blue fluorescence [17].

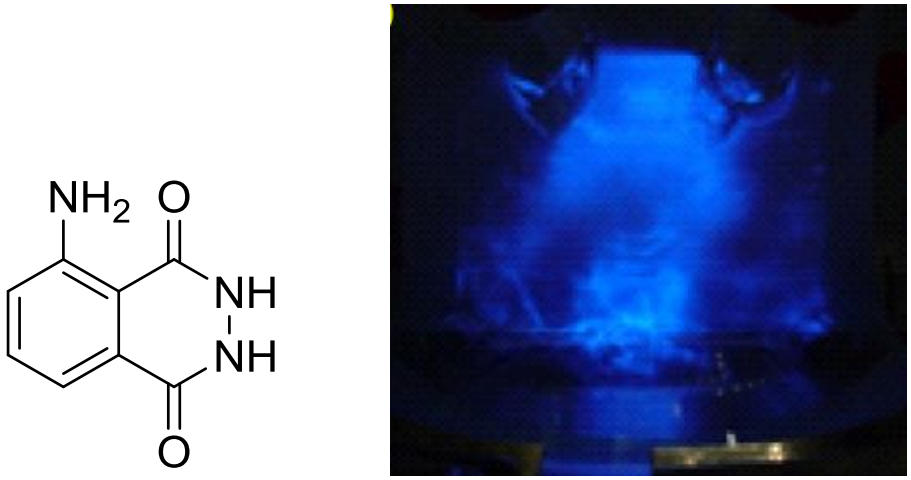

Figure 176. Left: Luminol structure and Right: Chemiluminescence of 0.01 M luminol solution (pH = 10.5 $NaHCO_3$) submitted to 204 kHz (P_{ac} = 32 W) ultrasound at 20 °C under 20 vol.% O_2/Ar bubbling at 80 mL/min with mechanical stirring at 370 rpm [15].

IX.3- Characterisation of a sonochemical system

In addition to the ultrasound frequency, the acoustic power transmitted to the medium (P_{ac} in W) and the acoustic intensity (I_{ac}, typically expressed in W/cm^2) are important physical values that characterise a given ultrasonic system.

The acoustic power is the amount of energy absorbed by the liquid medium during a given time under ultrasound irradiation. It is directly related to the electric power delivered by the generator [2]. The acoustic power can be determined experimentally using a calorimetry method. Indeed, the system can be considered as adiabatic during the first 60 seconds of ultrasound treatment independently of the solvent used [3]. Thus the acoustic power transmitted to the medium can be determined by the change in temperature over the first seconds of ultrasound treatment. So P_{ac} is given by:

$$P_{ac} = m\, C_p \left(\frac{\Delta T}{\Delta \tau}\right)$$

Where m is the mass of solvent (g), C_p is the solvent specific heat capacity (J/g.K), ΔT is the temperature variation (K) in a given duration of time of ultrasound irradiation, $\Delta \tau$ (s).

Regarding the acoustic intensity, it is the amount of energy transmitted to the system within a second by unit of area of the studied medium. It can be calculated by:

$$I_{ac} = \frac{{p_{max}}^2}{2\rho c_{wave}} = \frac{P_{ac}}{S}$$

Where I_{ac} is the acoustic intensity (W/m^2), p_{max} is the maximum acoustic pressure (N/m^2), ρ is medium density (kg/m^3), c_{wave} is the wave velocity (or wave propagation speed) (m/s), P_{ac} is the absorbed acoustic power (W) and S is the area of the ultrasound emitting surface (m^2).

IX.3.1- Influence of the operating conditions

The sonochemical effects depend on several operation conditions. Some of the key parameters are frequency, acoustic intensity, solvent, atmosphere, temperature and reactor geometry. Their effects are briefly described [1,3,18]:

- Frequency: The duration of the compression/expansion cycle is related to the characteristic period of the wave, which is the inverse of the frequency. So at higher frequencies, the duration of the cycle is shorter. With short compression/expansion cycles, the cavitation phenomenon becomes more difficult, requiring higher acoustic intensities to be observed (Figure 177).

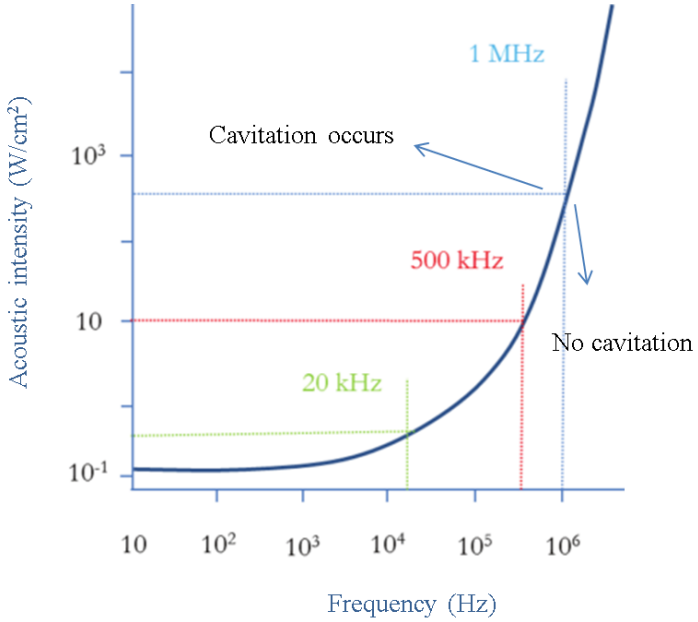

Figure 177. Variation of the acoustic intensity threshold with the frequency for water under air [4].

Another consequence of the short compression/expansion cycle is that the size of the cavitation bubble is also smaller. Thus, at 20 kHz, the bubble radius is of 178 µm, while at 513 kHz, it is of 7.1 µm [4]. Furthermore, at low frequencies (20 – 100 kHz), the number of transient bubbles formed in water is relatively low, but with a larger bubble size, resulting in predominant physical effects (shock waves, microjets, microconvection, etc.) over the chemical effects. Contrarily, at high frequencies (150 kHz – 1 MHz), several bubbles of smaller diameter are formed, favouring the formation of radicals (like HO$^{\bullet}$), resulting in more predominant chemical effects [2].

- Acoustic intensity: An increase of the acoustic intensity results in an increase of the acoustic pressure, finally enhancing the acoustic cavitation phenomenon. However, a very high acoustic intensity decreases the sonochemical activity by increasing the number of cavitation bubbles that coalesce, leading to liquid degassing and perturbation of the wave propagation [19].

- Solvent: The cavitation bubbles form more or less easily depending on the viscosity and vapour pressure of the liquid, which have an effect on the sonochemical activity. So, in liquids with high vapour pressure, the intensity of the cavitation phenomenon is limited. Contrarily, in liquids with low vapour pressure, the cavitation phenomenon occurs with more violence. Furthermore, high surface tension and high viscosity make difficult the formation of cavitation bubbles [2].

- Atmosphere: Dissolved gases in the solvent permit the creation of nucleation points, favouring the acoustic cavitation phenomenon. However, high concentration of dissolved gas favours the solution degassing, reducing the sonochemical effects.

Additionally, a gas with a high thermal conductivity reduces the sonochemical effects by enhancing the heat transfer out of the cavitation bubble. Furthermore, monoatomic gases like noble gases (e.g. Xe, Ar, Kr) favour the achievement of high temperatures, contrarily to diatomic gases like O_2 or N_2, which dissociate within the cavitation bubble, thus consuming part of the energy released during the implosion [2,4].

- Temperature: An increase in the temperature modifies the solvent properties by reducing the viscosity and increasing the vapour pressure, as well as the gas solubility in the liquid. This favours the formation of cavitation bubbles. However, the temperatures and pressures released during the bubble implosion decrease when increasing the temperature [4]. So a reasonable temperature range up to 80 °C can be appropriate in order to improve chemical reaction performances [2].

- Reactor geometry: the size, shape and position of the ultrasound emitting surface and even the solvent level are important geometry parameters that influence the wave propagation and reflexion, eventually modifying the sonochemical activity [20].

IX.4- Sonochemical reactors

Three main types of sonochemical reactors exist: ultrasounds bath, hydrodynamic continuous reactor and the sonotrode direct immersion reactor. They are schematised in Figure 178. The ultrasounds bath has been extensively used for cleaning lab glassware and to prepare dispersions. It usually works at 40 kHz. The immersed sonotrode horn set-up has particularly been used for synthesis at the lab scale, typically supplying acoustic powers in the range of 10 to 50 W/cm^2 at 20 kHz. Given the higher acoustic power supplied in this kind of reactor, the control of the temperature might be carried out with an external cooling fluid. There are commercially available reactors that provide different frequencies and powers. So it is important to optimise the reaction conditions and reactor volume depending on the desired application [3].

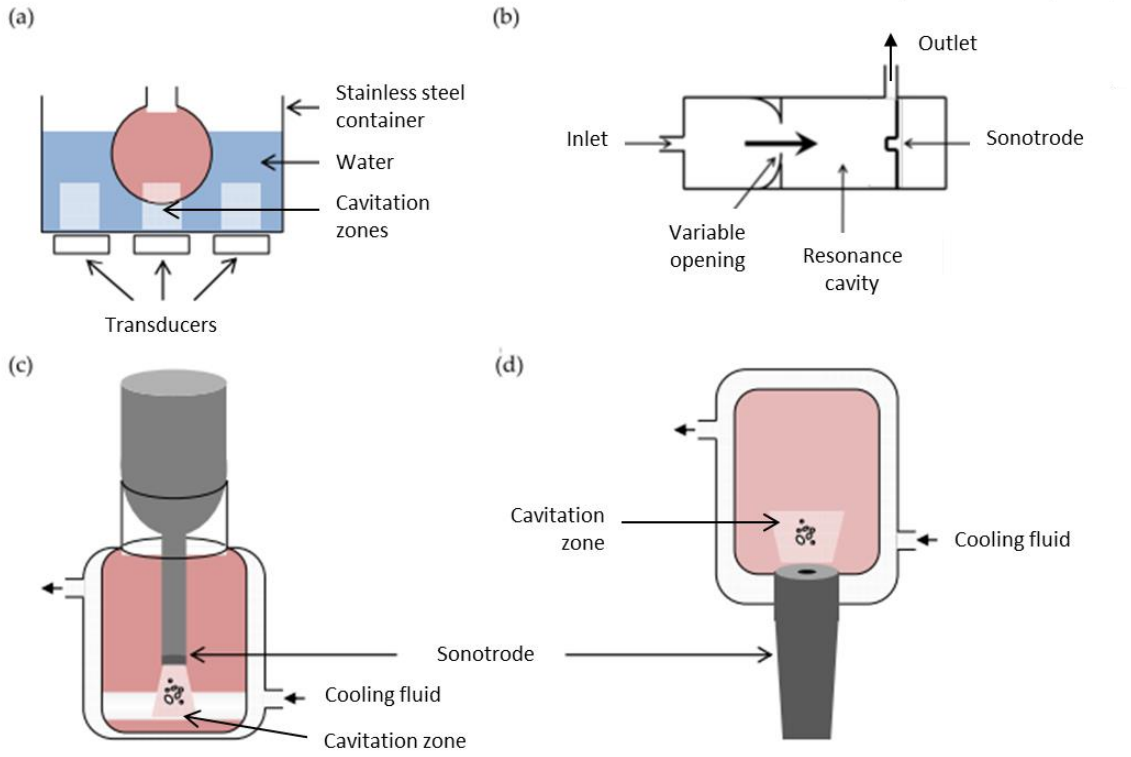

Figure 178. Schematic representation of: a. ultrasounds bath, b. hydrodynamic continuous reactor, c. downwards immersed sonotrode reactor and d. upwards immersed sonotrode reactor [3].

IX.5- Industrial applications

Ultrasounds are industrially interesting because they enable operation at milder operating conditions (lower temperatures and pressures), eliminate the need for extra costly solvents, and reduce the number of synthesis step. Additionally, ultrasounds increase end yields, permit the use of lower purity reagents and solvents, and/or increase the activity of existing catalysts [1].

Sonochemical processes are beginning to be used in industrial applications such as water treatment, mass transfer operations, emulsification, and leaching [21]. A couple of examples in the chemical industry are a pilot plant, funded by the Electricité de France, that uses ultrasound to oxidize cyclohexanol to cyclohexone, and a modular sonochemical reactor to produce up to 4 metric tons of Grignard reagent per year, designed at Clausthal Technical University (Germany) in collaboration with Hoechst and other companies. Such process was motivated by the increase in conversion by a factor of 5 and the reduction of the induction period from 24 h to 50 min with the application of ultrasounds [1].

Regarding other applications, a large-scale water treatment system from Ultrasonic Systems Gmbh, Thierhaupten, Germany has been used for water disinfection using the combination of ozone and ultrasound at 612 kHz at a flow rate of 35 L/min (67 L/min being the maximum system capacity), which was proven to be better than treatment using either method alone [22].

Large devices for precision cleaning applications with capacities up to 0.3 m^3 are also currently available and commercialised by companies such as Crest Ultrasonics Corporation in The United States.

The use of sonochemistry has a huge potential for the development of sustainable processes. Additionally, reactors of a few hundreds of litres are already available. Though, challenges in the reactor design as noise and erosion have to be overcome for a more widespread use of sonochemistry at the industrial scale [21].

IX.6- References

[1] L.H. Thompson, L.K. Doraiswamy, Sonochemistry: Science and Engineering, Ind. Eng. Chem. Res. 38 (1999) 1215–1249. doi:10.1021/ie9804172.

[2] R. Behling, N. Araji, G. Chatel, Qu'est-ce que la sonochimie ?, Actual. Chim. (2016) 11–20.

[3] C. Cau, Influence de la méthode de synthèse sur les propriétés structurales et catalytiques d'oxydes mixtes cérium-zirconium, Université de Montpellier II, 2013.

[4] N. Navarro, Dégradation sonocatalytique de composés organiques, Université Montpellier 2, 2012.

[5] F. Laugier, Les ultrasons en procédés polyphasiques: transfert gaz-liquide et réaction liquide-liquide, Institut National Polytechnique de Toulouse, 2007.

[6] E. Zwaan, S. Le Gac, K. Tsuji, C.-D. Ohl, Controlled cavitation in microfluidics, (2007). http://www1.spms.ntu.edu.sg/~cdohl/research_cavitation_microfluidics.html (accessed November 2, 2016).

[7] N. Pokhrel, P.K. Vabbina, N. Pala, Sonochemistry: Science and Engineering, Ultrason. Sonochem. 29 (2016) 104–128. doi:10.1016/j.ultsonch.2015.07.023.

[8] K.S. Suslick, Sonochemistry, Science. 247 (1990) 1439–1445. doi:10.1126/science.247.4949.1439.

[9] S.I. Nikitenko, R. Pflieger, Toward a new paradigm for sonochemistry: Short review on nonequilibrium plasma observations by means of MBSL spectroscopy in aqueous solutions, Ultrason. Sonochem. (2016). doi:10.1016/j.ultsonch.2016.02.003.

[10] K.S. Suslick, D.A. Hammerton, R.E. Cline, Sonochemical hot spot, J. Am. Chem. Soc. 108 (1986) 5641–5642. doi:10.1021/ja00278a055.

[11] D.J. Flannigan, K.S. Suslick, Plasma line emission during single-bubble cavitation, Phys.

Rev. Lett. 95 (2005). doi:10.1103/PhysRevLett.95.044301.

[12] A.A. Ndiaye, R. Pflieger, B. Siboulet, J. Molina, J.-F. Dufrêche, S.I. Nikitenko, Nonequilibrium vibrational excitation of OH radicals generated during multibubble cavitation in water., J. Phys. Chem. A. 116 (2012) 4860–7. doi:10.1021/jp301989b.

[13] E. Padilla-Ortega, M. Darder, P. Aranda, R. Figueredo Gouveia, R. Leyva-Ramos, E. Ruiz-Hitzky, Ultrasound assisted preparation of chitosan–vermiculite bionanocomposite foams for cadmium uptake, Appl. Clay Sci. 130 (2016) 40–49. doi:10.1016/j.clay.2015.11.024.

[14] J.H. Bang, K.S. Suslick, Applications of Ultrasound to the Synthesis of Nanostructured Materials, Adv. Mater. 22 (2010) 1039–1059. doi:10.1002/adma.200904093.

[15] R. Pflieger, T. Chave, G. Vite, L. Jouve, S.I. Nikitenko, Effect of operational conditions on sonoluminescence and kinetics of H2O2 formation during the sonolysis of water in the presence of Ar/O2 gas mixture, Ultrason. Sonochem. 26 (2015) 169–175. doi:10.1016/j.ultsonch.2015.02.005.

[16] T. Chave, N.M. Navarro, P. Pochon, N. Perkas, A. Gedanken, S.I. Nikitenko, Sonocatalytic degradation of oxalic acid in the presence of oxygen and Pt/TiO2, Catal. Today. 241 (2014) 55–62. doi:10.1016/j.cattod.2014.07.040.

[17] T. Tuziuti, K. Yasui, T. Kozuka, A. Towata, Y. Iida, Enhancement of Sonochemical Reaction Rate by Addition of Micrometer-Sized Air Bubbles, J. Phys. Chem. A. 110 (2006) 10720–10724. doi:10.1021/jp063373g.

[18] Y.G. Adewuyi, Sonochemistry: Environmental Science and Engineering Applications, Ind. Eng. Chem. Res. 40 (2001) 4681–4715. doi:10.1021/ie010096l.

[19] F. Nouaille, Développement d'un procédé innovant de conversion d'oxyde d'uranium en peroxyde d'uranium, Université de Lille 1, 2017.

[20] S.I. Nikitenko, C. Le Naour, P. Moisy, Comparative study of sonochemical reactors with different geometry using thermal and chemical probes, Ultrason. Sonochem. 14 (2007) 330–336. doi:10.1016/j.ultsonch.2006.06.006.

[21] F.J. Keil, K.M. Swamy, Reactors for sonochemical engineering - present status, Rev. Chem. Eng. 15 (1999). doi:10.1515/REVCE.1999.15.2.85.

[22] A.M. Al-Hashimi, T.J. Mason, E.M. Joyce, Combined Effect of Ultrasound and Ozone on Bacteria in Water, Environ. Sci. Technol. 49 (2015) 11697–11702. doi:10.1021/es5045437.

X. ANNEX III. EXPLORATION OF SOME POLYMER LATEX PERSPECTIVES FOR CATALYST TAILORING

Contents

The combination of latex synthesis, sonochemistry and sol-gel process has been demonstrated to be a powerful technique for the preparation of tailored catalysts, since it has been possible to modulate the catalyst hierarchical porosity and the active sites distribution throughout the material. Furthermore, there are other perspectives to make this catalyst preparation technique even more versatile. This short section is dedicated to the study of polymer latex perspectives for catalyst tailoring. The first perspective is related to the variation of latex template particle size by modifying the polymerisation conditions, in order to demonstrate the potential for macropore size modulation from the latex preparation step. The second perspective is related to an alternative procedure for latex template removal with organic solvents in order to propose an alternative to the template removal by calcination. Similarly, the third perspective is related to the polymer latex removal by extraction with supercritical carbon dioxide ($scCO_2$) in mild conditions of temperature and pressure (typically T<40 °C and P<250 bars), which requires the preparation of $scCO_2$ soluble polymer templates.

X.1- Experimental

X.1.1- Materials

1,1,2,2-Tetrahydroperfluorodecylacrylate (FDA, Elf Atochem) was vacuum-distilled, passed through activated basic alumina, and filtered through a 0.2 µm PTFE filter before use. 2-Methyl-2-propenoic acid, 3,3,4,4,5,5,6,6,7,7,8,8,8-tridecafluorooctyl ester (62-MA, DuPont™ Capstone™) was passed through activated basic alumina, and filtered through a 0.2 µm PTFE filter before use. Styrene (99.0%, Sigma Aldrich) was distilled prior to use. Potassium persulfate ($K_2S_2O_8$, KPS, 99%, Sigma Aldrich), sodium metabisulfite ($Na_2S_2O_5$, SMBS, 97%, Sigma Aldrich), sodium dodecyl benzene sulfonate ($C_{12}H_{25}C_6H_4SO_3Na$, SDBS, 99%, Aldrich), Zonyl® FSO fluorosurfactant (DuPont™), 2,2'-azobis(2,4-dimethylvaleronitrile) (V-65, Wako), α,α,α–trifluorotoluene (TFT, Aldrich, >99%), 1H,1H,2H,2H-perfluorodecanethiol ($C_8F_{17}C_2H_4SH$, Atochem), carbon dioxide (CO_2, SFE 5.2, Linde Gas SA, France, 99.9%), activated basic Brockmann I aluminum oxide (Aldrich), tetraethyl orthosilicate (TEOS, Aldrich, 98%) were used as received. Hydrochloric acid (HCl, 37%, Sigma Aldrich) and ammonium hydroxide (NH_4OH, 28%, Sigma Aldrich) were used to prepare acidic and basic solutions with deionised water (1 microS/cm, D8 ion exchange demineraliser A2E Affinage de L'Eau or 18.2 MΩ·cm at 25 °C, Milli-Q).

X.1.2- Polystyrene latex template synthesis

The polystyrene latex template was prepared by emulsion polymerisation of styrene in batch using a redox initiator system: KPS as oxidiser and SMBS as reducer. SDBS was used as surfactant. The polymerisation was carried out under argon atmosphere with a molar ratio styrene : water : KPS : SMBS : SDBS = 1 : 50 : 5×10^{-3} : 3.2×10^{-3} : 6.6×10^{-4}, in a 350 mL double-walled glass reactor with a glass stirring blade operating at 250 rpm. The temperature was regulated as follows: 1 h at 65 °C, 2 h at 72 °C and 3 h at 85 °C.

For the other latexes prepared in batch, the reaction conditions were the same, only the reagents formulation changed. When KPS was used as thermal initiator only, the reagents molar ratio was styrene : water : KPS : SDBS = 1 : 50 : 5×10^{-3} : 6.6×10^{-4}. When the SDBS was used at the critical micelle concentration (CMC), the reagents molar ratio was styrene : water : KPS : MBSS : SDBS = 1 : 50 : 5×10^{-3} : 3.2×10^{-3} : 1.5×10^{-3}. When SDBS was used in large excess (100 times the CMC), the reagents molar ratio was styrene : water : KPS : MBSS : SDBS = 1 : 50 : 5×10^{-3} : 3.2×10^{-3} : 1.4×10^{-1}.

For the latexes prepared in semi-batch conditions, the polymerisation was carried out under argon atmosphere in a 350 mL double-walled glass reactor with a glass stirring blade operating at 250 rpm. The reagents were added in semi-continuous mode using a KDS-100-CE syringe pump (KD Scientific Inc., USA). The temperature was regulated as follows: 3.5 h at 65 °C and 2 h at 85 °C. When KPS was fed semi-continuously, the molar ratio was styrene : water : KPS : MBSS : SDBS = 1 : 50 : 5×10^{-3} : 3.2×10^{-3} : 7×10^{-4}. A shot of 1/3 of the total KPS (solution at 10 g/L) was added at the very beginning, the other 2/3 were fed during 2.5 h. When KPS and styrene were fed semi-continuously, the molar ratio was styrene : water : KPS : MBSS : SDBS = 1 : 50 : 5×10^{-3} : 3.2×10^{-3} : 7×10^{-4} and a shot of 1/3 of the total KPS (solution at 10 g/L) was added at the very beginning of the reaction. The other 2/3 of KPS solution and the monomer were fed independently during 2.5 h. When KPS and styrene were fed semi-continuously in the presence of a large excess of surfactant, the procedure was the same, but the reagents molar ratio was styrene : water : KPS : MBSS : SDBS = 1 : 50 : 5×10^{-3} : 3.2×10^{-3} : 1.4×10^{-1}.

X.1.3- Polystyrene extraction with organic solvents

The first batch of trials were with 200 mg of catalysts (containing ca. 200 µL of polystyrene) after the sol-gel synthesis immersed in 5 mL of solvent (either tetrahydrofuran, chloroform or toluene) for 1 h under vigorous stirring. The second test was carried out with 200 mg of catalyst immersed in 5 mL of toluene for 30 min under vigorous stirring. Then the solid was removed by filtration and immersed in 5 mL of chloroform for 30 min under vigorous stirring. A third batch of trials was carried out by taking 1.3 g of catalyst and immersing it 25 mL of tetrahydrofuran for 30 min under vigorous stirring. Then, the solid was filtered out and put in 25 mL of fresh tetrahydrofuran for 30 min under vigorous stirring, this was done twice. Then all catalysts were dried at 120 °C for 2 h.

X.1.4- Latex synthesis of $scCO_2$ soluble polymer by miniemulsion polymerisation

The PFDA latex was prepared with FDA (20 g, 38.7 mmol), SDBS (0.4 g, 1.2 mmol), V-65 (0.2 g, 0.8 mmol) and deionised water (57 g). DIW and SDBS were combined in a 250 mL beaker and purged with argon for 30 min. FDA and V-65 were combined to form the organic phase and purged with argon for 15 min. In the case of PFDA with chain transfer agent, $C_8F_{17}C_2H_4SH$ (0.2 g, 0.4 mmol) was also added to the organic phase. The organic phase was then added to the

SDBS solution under vigorous stirring for 30 min under argon bubbling in an ice bath to form a macroemulsion. The macroemulsion was sonicated using a BioBlock Scientific Vibracell 75043 equipped with a CV33 probe (13 mm diameter) at 750 W, 20 kHz and 60% amplitude for 3 min. The miniemulsion was subsequently transferred into a 150 mL double-walled glass reactor under argon atmosphere equipped with a U-shaped glass stirring rod, pre-heated at 65 °C, in order to begin the reaction. The polymerisations proceeded for 5-6 hours. The P62MA latex was prepared with 62-MA (5.9 g, 13.5 mmol), $C_8F_{17}C_2H_4SH$ (0.3 g, 0.7 mmol), V-65 (0.1 g, 0.2 mmol), FSO (0.2 g) and deionised water (57 g) following the same procedure, but heating the reaction at 70 °C.

X.1.5- Silica-composite material synthesis

The silica matrix was prepared by a two-step acid-base catalysed sol-gel synthesis, as described elsewhere [1], except that for the cryogel, after reaching the gel point after the base addition, the gel was aged for 24 h at 40 °C and subsequently frozen with liquid nitrogen and freeze dried overnight. In all cases a polymer weight fraction polymer/(polymer + silica) of 50% was targeted.

X.1.6- Template removal by supercritical CO_2

A 16 mL high pressure cell equipped with two sapphire windows (Figure 179) (Top Industrie) was used for the removal of the PFDA template in the silica matrix. A liquid CO_2 delivery pump was used to regulate the flow of CO_2 into the cell (model PU-2080-CO_2, JASCO). Figure 179 shows a schematic representation of the set-up used for the extraction trials.

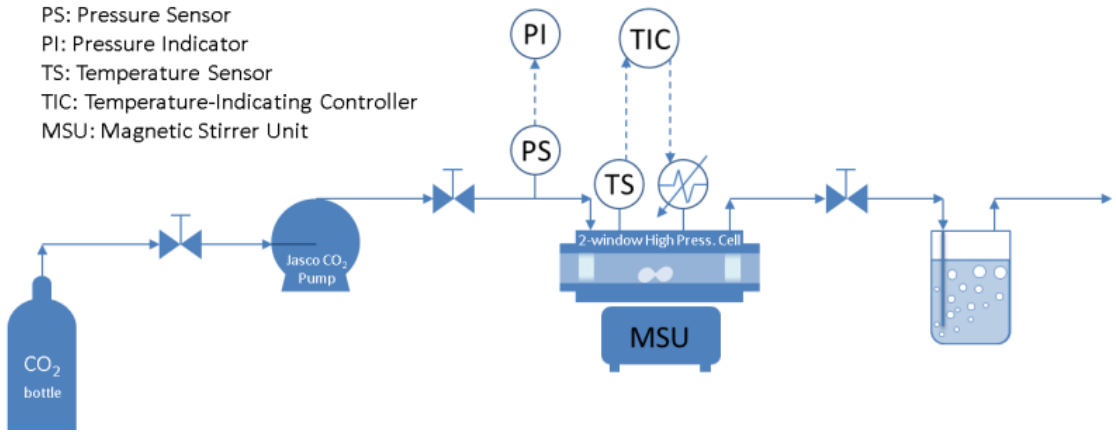

Figure 179. Process flow diagram of the double-window high pressure cell setup.

The cell was loaded with ca. 0.15 g of composite material in an Eppendorf support wrapped with perforated aluminium foil. The system was heated to 40°C using electric heating cartridges plugged into the cell and monitored by a temperature controller with a thermocouple type K inside the cell. Stirring of the magnetic bar was set to 150 rpm. Once the cell was at 40°C, CO_2 was pumped into the cell until 250 bars was attained. Once the cell was at 250 bars at 40°C (*i.e.* above the cloud point pressure of PFDA at 40°C) [2], the cell was kept under static conditions for 10 min before flushing the cell with scCO_2 at 5 mL/min for 35 min (approximately with 10

times the volume of the cell). The outlet valve was regulated during this procedure to keep the pressure of the cell around 220 bars. At the end of the CO_2 flush, the sample was carefully removed from the cell and weighed to check for the removal of the polymer template.

X.1.7- Characterisation

The latex percentage of solids was measured in a MLS moisture analyser (KERN). The materials were observed by transmission electron microscopy (TEM) using a 2200FS − 200 kV TEM (Jeol) and by scanning electron microscopy (SEM) with a high resolution microscope S-4800 (Hitachi) operating at 2 kV. Thermogravimetric analyses (TGA) were performed on a Q50 TGA (TA Instruments) using a temperature ramp of 20 °C/min in synthetic air from 25°C to 900°C. The latex dispersity (Đ) was calculated as the ratio of the weight-average diameter (D_w) over the number-average diameter (D_n).

X.2- Modulation of the latex particle size: effect of the polymerisation conditions

The modification of the experimental conditions during the free radical polymerisation of a styrene by emulsion polymerisation can have an effect on the polymer particle size. The effect of three parameters was studied: the radical initiator system, the surfactant concentration and the feeding conditions (batch or semi-batch) for the monomer and/or the initiator.

X.2.1- Effect of the radical initiator

The polystyrene latex described in Chapter III was prepared by free radical aqueous emulsion polymerisation with a redox system: KPS and SMBS. With this redox couple, the initiator is mostly a sulfonate radical $^{\bullet}SO_3H$ [3]:

$$S_2O_5^{2-} + H_2O \longrightarrow 2\,HSO_3^-$$

$$S_2O_8^{2-} + HSO_3^- \longrightarrow SO_4^{2-} + \dot{S}O_4^- + \dot{S}O_3H$$

$$\dot{S}O_4^- + HSO_3^- \longrightarrow SO_4^{2-} + \dot{S}O_3H$$

But KPS can be an initiator by itself as well because it can be thermally decomposed into sulphate radicals $^{\bullet}O\text{-}SO_3^-$:

$$S_2O_8^{2-} \xrightarrow{\Delta} 2\,\dot{S}O_4^-$$

It should be also noticed that the sulphate radicals bind the monomer creating a **-C-O-S**O_3^- sulphate bond, which could be more easily hydrolysable than a **-C-S**O_3H sulfonate bond that would be created by the sulfonate radicals (Figure 180). The problem with a possible hydrolysis is that the polymer particles are stabilised in suspension by the charges provided by the deprotonated sulphate and sulfonate groups (in addition to the SDBS surfactant contribution). If they are removed from the polymer, the polystyrene beads would be less colloidally stable and could coagulate. So using the KPS – SMBS couple, the obtained latex should stand longer in time.

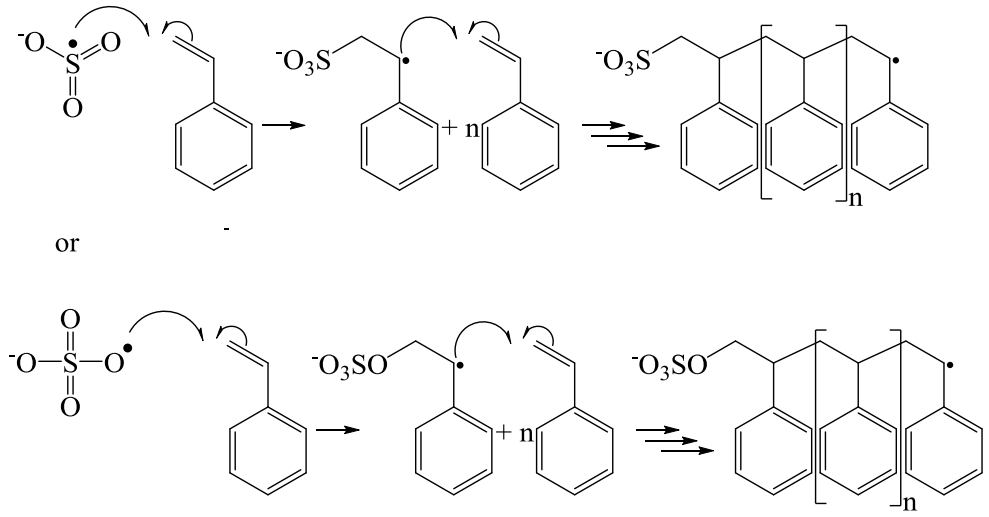

Figure 180. Initiation and propagation stages of styrene polymerisation with sulfonate (top) or sulphate (bottom) radical initiators

KPS was used to carry out a latex synthesis following the same procedure as described in Chapter III for the redox system, but without SMBS. As a result, the polystyrene particles that were obtained only with KPS were larger (194 nm) than those obtained with the redox system (134 nm) (Figure 181). This can be explained by a slower radical generation rate for KPS alone, so fewer particles are created in the nucleation step and as a result they grow more. This is given by the Smith−Ewart equation:

$$\boldsymbol{N_P} = k \times (\boldsymbol{\rho}/\mu)^{0.4} \times (a_S S)^{0.6}$$

Where N_P is the number of particles, k is a proportionality constant, ρ is the rate of radical generation, μ the rate of particle volume growth, a_S the area occupied by one surfactant molecule and S the amount of surfactant present in the system per volume unit [3–5]. So when keeping all parameters constant and decreasing the rate of radical generation, the number of polymer particles decreases, which results in larger particles.

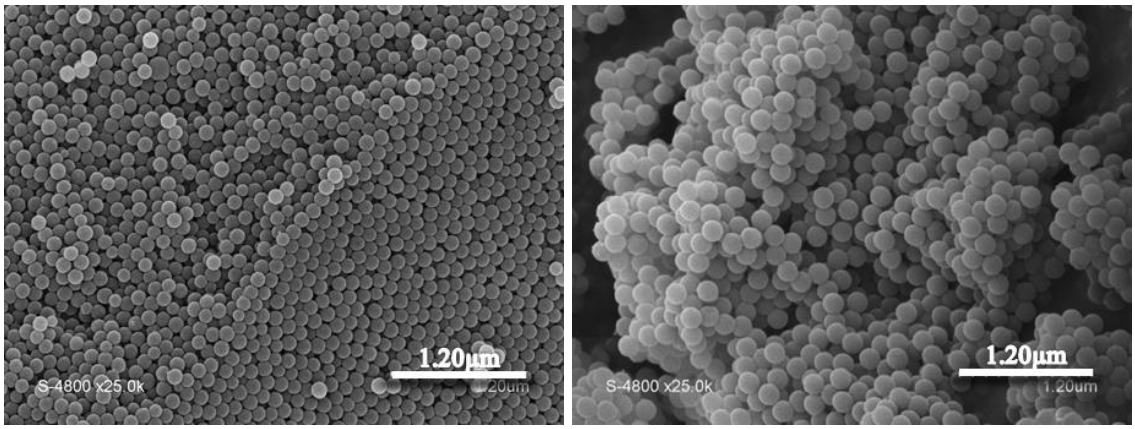

a. **b.**

Figure 181. SEM images of polystyrene latex synthesised with: a. redox couple KPS and SMBS (D_n: 134 nm, D_w: 140 nm, Đ: 1.04) and b. KPS (D_n: 194 nm, D_w: 195 nm, Đ: 1.00).

In conclusion, the redox couple KPS-SMBS as initiator system permitted to obtain smaller polystyrene particles (134 nm) by emulsion polymerisation than only KPS as a thermal initiator (194 nm). Additionally, the surface composition of the particles obtained with the redox initiator system are expected to be more stable in time than those with the thermal initiator due to the presence of sulfonate groups at the surface of the polymer beads (which are less likely to be hydrolysed than sulphate groups). A corollary will be a better colloidal stability of the latex prepared by the redox system.

X.2.2- Effect of the surfactant concentration

Other latex experiments were carried out using the redox couple KPS-SMBS as initiator system and varying the surfactant (SDBS) concentration. The first experiment was using an SDBS concentration at the critical micelle concentration (CMC) which is 2.3 times the SDBS concentration used in the previous latex syntheses. The second experiment was carried out using a large excess of surfactant (100 times the CMC). The SEM images of the obtained latexes are shown in Figure 182. However, it can be noticed that large amounts of surfactant tend to form big masses covering the polystyrene beads as shown in Figure 182.b, making difficult to measure the particle size reliably. Other techniques such as STEM and TEM were tried with this type of latex, but the images were not better.

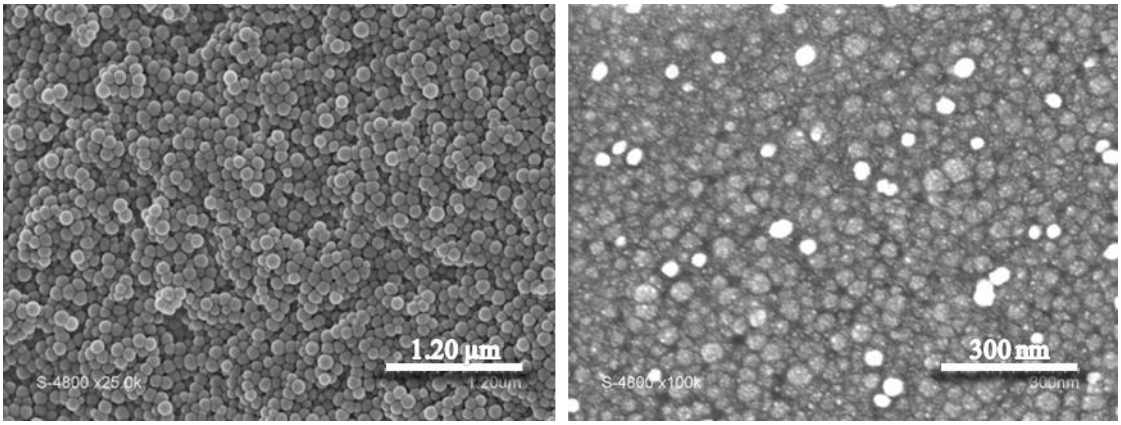

a. **b.**

Figure 182. SEM images of polystyrene latex synthesised with additional SDBS: a. at CMC, D_n: 119 nm, D_w: 127 nm, Đ: 1.06. b. with a large excess of SDBS, D_n: 46 nm, D_w: 50 nm, Đ: 1.09.

In general, the increase of 2.3 times the SDBS concentration to reach the critical micelle concentration (CMC) only decreased slightly the latex particle size, going from 134 nm to 119 nm. On the other hand, a larger excess of SDBS decreased the particle size to 46 nm. This particle size behaviour with the variation of surfactant concentration is expected since increasing the amount of surfactant in the medium, it increases the number of particles in the nucleation step according to the Smith−Ewart equation:

$$\boldsymbol{N_P} = k \times (\rho/\mu)^{0.4} \times (a_S \boldsymbol{S})^{0.6}$$

Where N_P is the number of particles, k is a proportionality constant, ρ is the rate of radical generation, μ the rate of particle volume growth, a_S the area occupied by one surfactant molecule and S the amount of surfactant present in the system per volume unit [3–5]. So when keeping all parameters constant and increasing the amount of surfactant, the number of polymer particles increases, which results in smaller particles.

Unfortunately, the challenge to be able to use a latex with large amounts of surfactant in the sonochemical step is related to the formation of foam due to the required Ar bubbling to remove the dissolved oxygen from the medium, even using a dilution factor of 10, as shown in Figure 183. The partial removal of surfactant was tried with a dialysis membrane of 10k Dalton (40 mL of latex against 2.5 L of deionised water, in three cycles). After the process, the dialysed latex was so thick that it was impossible to use it in the sonochemistry set-up. This probably was due to the removal of salts that increased the thickness of the counterions double layer of the polymer particles, so the mobility of the system was reduced and the viscosity was increased. In the sol-gel synthesis, the excess of surfactant would lead to the formation of micelles that would induce an additional undesired porosity.

Figure 183. Foam formation in the sonochemical reactor due to surfactant excess

As a conclusion, an increase of the surfactant concentration can reduce the particle size of the polymer latex, going from 134 nm at 0.44 times the CMC down to 46 nm at 100 times the CMC, but at such surfactant concentration, it is not possible to carry out the subsequent steps of

sonochemical reduction and sol-gel synthesis as desired. Therefore additional efforts should be done to prepare nanolatexes and remove the excess of surfactants prior to sonochemical reduction while keeping the colloidal stability of the latex. As a perspective, it could be considered to remove the surfactant excess by ultrafiltration of the latex with an aqueous solution of surfactant at low concentration in order to keep the latex colloidal stability.

X.2.3- Effect of the formulation feeding conditions

The Smith−Ewart[6] theory was developed for batch systems. Fortunately, Sajjadi[7,8] extended it to semi-continuous polymerisation processes, proposing that:

$$\boldsymbol{N_P} \; \alpha \; \left(\frac{R_I}{\boldsymbol{R_a}}\right)^{\frac{2}{3}} (a_S S)$$

Where N_P is the number of particles, R_I is the rate of radicals generation, R_a is the rate of monomer addition, a_S the area occupied by one surfactant molecule and S the amount of surfactant present in the system per volume unit. This equation assumes that the rate of volumetric growth of the particles is proportional to the polymerisation rate and that the processes occurred under completely starved conditions (i.e. the polymerisation is equal to the rate of monomer addition) [4]. In agreement with this equation, when decreasing the rate of monomer addition, the number of polymer particles increase, resulting in smaller particles.

So in order to work at starved conditions, it is important to guarantee the availability of radicals along the whole polymerisation reaction. This is solved by adding part of the initiator in semi-continuous mode while the monomer is added. It is also important to define the monomer inlet flow depending on the kinetics of monomer polymerisation. So in order to find out the average monomer reaction rate, an experiment with KPS added in semi-continuous mode was carried out (using a surfactant concentration at 44% the CMC). As a result, it was found that the average monomer consumption rate was 1×10^{-4} mol/L.s and the resulting latex exhibited nanoparticles of 193 nm in average (Figure 184.a.). This larger particle size in comparison with the batch polymerisation with redox initiator system (134 nm) is related to a slower rate of radical generation R_I due to slow feeding of the oxidant, which results in a smaller number of particles and, thus, larger particles.

Subsequently, an experiment with semi-continuous feeding of monomer and KPS was carried out. Styrene and KPS were fed independently during the same time (2.5 h), assuring a monomer inlet flow at the average monomer consumption rate. The resulting latex exhibited a particle size of 110 nm (Figure 184.b.), which is significantly smaller than the polymerisation in semi-continuous feeding of KPS (193 nm) and the batch reaction (134 nm).

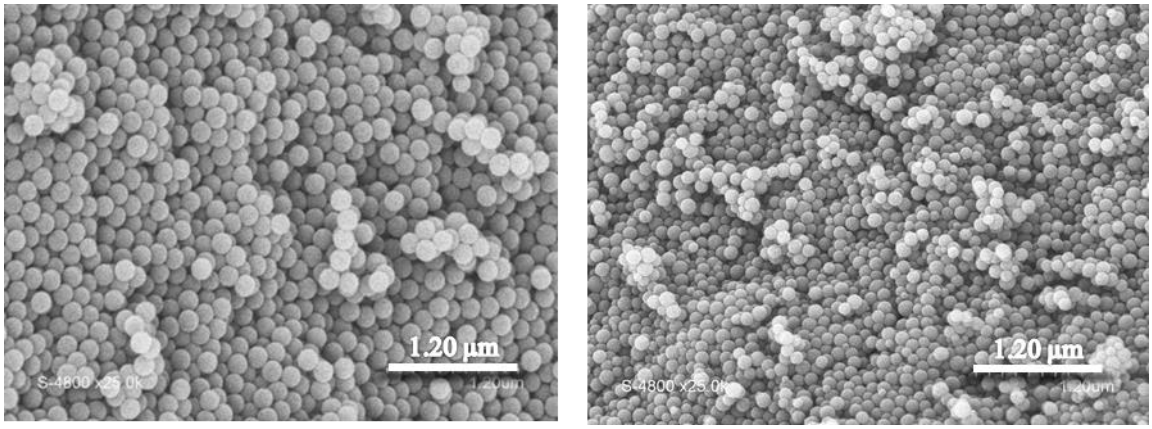

a. **b.**

Figure 184. SEM images of polystyrene latex synthesised with semi-continuous feeding of: a. KPS (D_n: 192 nm, D_w: 193 nm, Đ: 1.00), and b. KPS and styrene (D_n: 110 nm, D_w: 120 nm, Đ: 1.09).

However, having a closer look at the monomer consumption during the initial experiment of KPS semi-continuous feeding, it can be seen that at the beginning of the reaction, the monomer consumption is slower than the average (as shown in Figure 185). This means that in the second experiment, the monomer was not fed under starved conditions at the beginning of the polymerisation, which is when most of the particle nucleation occurs. So new experiments either with an extra amount of initiator (to increase the monomer consumption rate) or with a slower monomer addition rate appear as suitable perspectives for further decrease the polymer particle size in order to operate at actual starved conditions all along the polymerisation reaction.

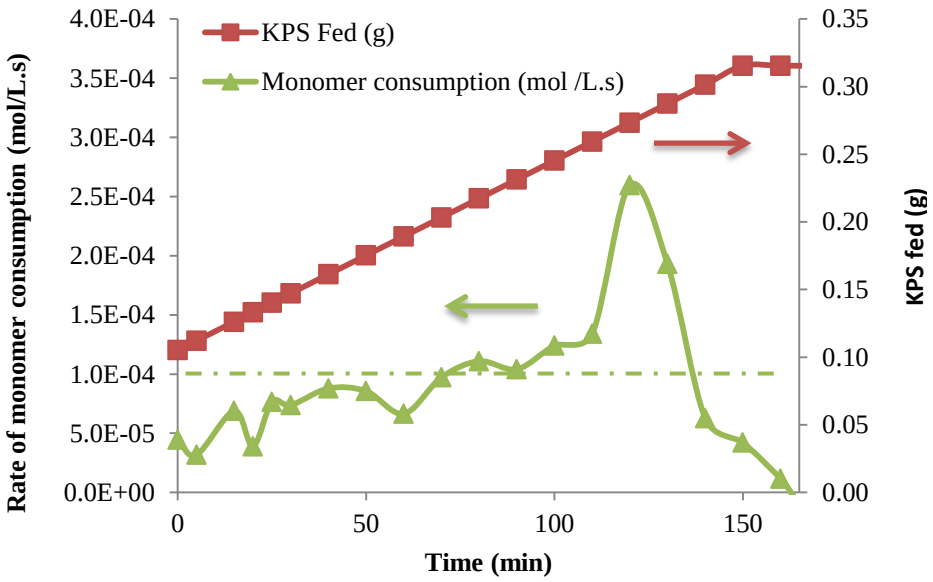

Figure 185. Rate of monomer consumption during the semi-continuous feeding of KPS

The semi-continuous feeding of KPS increases the polystyrene particle size to 192 nm. However, when KPS and styrene were fed simultaneously in semi-continuous mode, the particle size decreased to 110 nm (in semi-batch mode), which is also smaller than 134 nm in batch mode. This means that varying the operation conditions; it is possible to modify the polymer particle size at a given latex formulation. More experiments in actual starved feed conditions of styrene would probably lead to a more significant decrease of the particle size [9–12].

X.3- Alternative latex template removal with organic solvents

Within the scope of preparing hierarchically porous catalysts, polymer templating is a useful tool to achieve a large variety of pore sizes. In addition to pore generation, the polymer template can act as carrier of catalytically active nanoparticles (ex. Pd, Pt) in order to place them at controlled locations within the catalyst, such as the macropores [1,13]. However, the polymer template must be removed in order to generate the desired porosity. It is usually done by calcination at high temperature, making the polymer recycling impossible and oxidising the active metal nanoparticles, partially or totally, which might create the requirement of a subsequent reduction post-treatment (as it was observed with Pd nanoparticles). Several solvents such as benzene, xylene, chloroform, toluene and tetrahydrofuran have been evaluated in a dissolution recycling process for polystyrene wastes, being tetrahydrofuran and chloroform the solvents in which the polystyrene solubility is higher. At the end of the process, the solvent can be recovered by distillation [14]. Toluene and chloroform have been used to remove polystyrene templates from thin membranes [15]. In this section, the polymer template extraction from the composite silica-polymer materials is explored with organic solvents.

Several tests were carried out. The first batch of trials was performed with one step extraction either with tetrahydrofuran, chloroform or toluene for 1 h under vigorous stirring. A second test was carried out in two steps: 30 min under vigorous stirring in toluene, and then, after filtration, 30 minutes in chloroform. A third extraction test was carried out in three steps: each step of 30 min of vigorous stirring in tetrahydrofuran (the solid was recovered by filtration before replacing the solvent). Unfortunately, none of these procedures led to satisfying results. In all cases, only a fraction of polymer was removed as shown in Figure 186. This is because the solvent had to diffuse through the mesopores of the silica matrix, solvate the polymer, dissolve it and then, the polymer chain had to diffuse out of the material through the mesopores. This problem arises due to mass transport limitations that are not sorted until the hierarchical porosity is achieved after the polymer template removal. Additionally, the solvent swells the polymer beads breaking the internal structure of the silica matrix and reducing the granulometry of the material (it was considerably finer after the extraction with solvents).

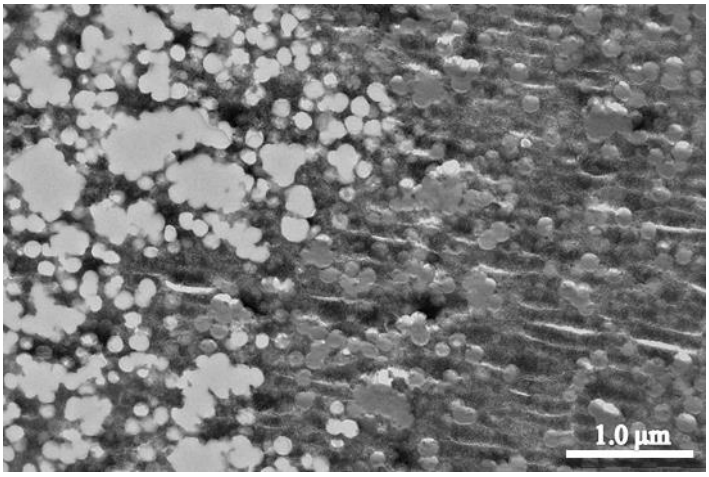

Figure 186. TEM image of the partial polystyrene template removal with tetrahydrofuran after three extraction cycles

In conclusion, the removal of the polystyrene template from the silica matrix with tetrahydrofuran, chloroform or toluene was not successful probably due to mass transport limitations through the composite material that is only mesoporous before the template removal. Additionally, the polymer swelling with such solvents affected the structure stability of the material.

X.4- Alternative latex template removal by extraction with supercritical CO_2

The preparation of hierarchically porous silica catalyst via polymer templating requires the polymer removal, usually by calcination. As an alternative, we proposed the polymer template extraction by the use of supercritical CO_2 ($scCO_2$). For this to work, a polymer soluble in $scCO_2$ must be used. One such polymer is PFDA, which is soluble in $scCO_2$ at relatively mild conditions (typically T<40 °C and P<250 bars) [2]. A PFDA latex was therefore synthesised by miniemulsion polymerisation as detailed in the experimental section. The latex was then used in two-step acid-base catalysed sol-gel synthesis to obtain a silica material containing the PFDA template.

In a first trial, a PFDA latex was obtained with a number-average diameter (D_n) of 127 nm, a weight-average diameter (D_w) of 241 nm and a dispersity (Đ) of 1.90 ($Đ = D_w/D_n$), as shown in Figure 187.a. This latex exhibited a good colloidal stability, which allowed the preparation of a silica-composite material with the polymer template properly dispersed within the material, as shown in Figure 187.b. Some pores were observed on this material prior to extraction, which must be an artefact due to sample grinding for SEM imaging.

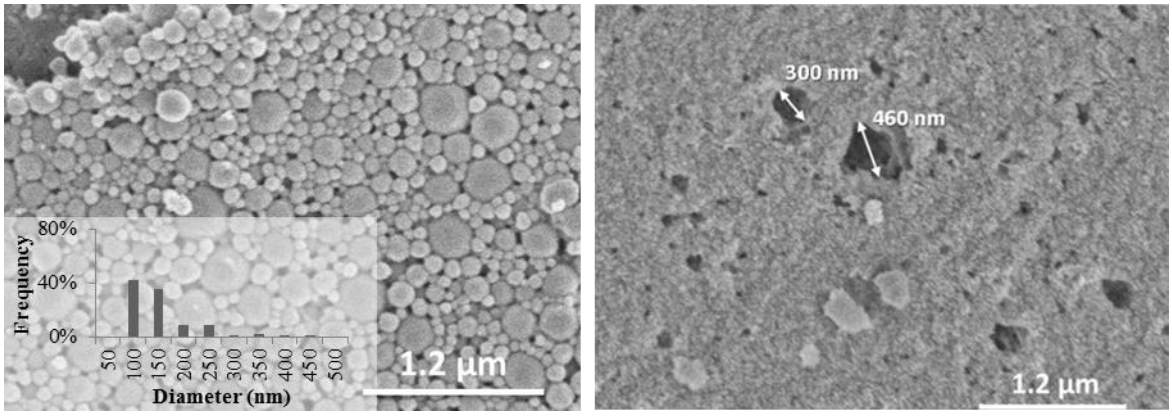

a. **b.**

Figure 187. a. SEM image of PFDA without chain transfer agent (the particle size distribution is presented in the insert) and b. SEM image of the corresponding silica-composite material.

Subsequently, the PFDA latex was intended to be removed by $scCO_2$ in the high pressure cell. It was held at 40 °C and 250 bars for 10 min, followed by a flush of $scCO_2$ at 40 °C and 220 bars at a rate of 5 mL/min for 35 min. Unfortunately, a difference of mass before and after this treatment was not obtained and therefore the removal of the PFDA from the silica matrix could not be confirmed. A second trial was performed, but this time the $scCO_2$ was flushed at 5 mL/min for 60 min to ensure the removal of the PFDA template. Unfortunately, the difference in mass was only 1% (compared to a maximum theoretical value of about 50% mass loss), which can be assumed to be negligible and it was likely that none of the PFDA was removed. The reason for this was due to the insolubility of the synthesised PFDA in $scCO_2$. If the molecular weight of the PFDA is high and/or polymer chains are crosslinked (gel content), it could significantly reduce the solubility of PFDA in $scCO_2$. Since PFDA is only soluble in a select range of solvents, gel permeation chromatography could not be used to determine the molecular weight. The solubility of the dried PFDA latex was hence tested in trifluorotoluene (TFT), a solvent in which PFDA is soluble under ambient conditions. If the PFDA is soluble in $scCO_2$ under our experimental conditions, it should dissolve instantly in TFT under ambient conditions. Upon the addition of few milligrams of the dried latex in approximately 3 mL of TFT, it was evident that the dried PFDA was not soluble in TFT and hence this was the reason why the PFDA template was not removed under $scCO_2$. This meant that the molecular weight of the polymer needed to be decreased in order to avoid the formation of a gel. A new PFDA latex was thus synthesised with the addition of 1 mol.% of a chain transfer agent (1H,1H,2H,2H-perfluorodecanethiol) with respect to FDA monomer. The resulting latex was confirmed to be more soluble in TFT than PFDA without chain transfer agent. However, it was still not completely soluble as the TFT solution was cloudy.

The PFDA latex with chain transfer agent exhibited a number-average diameter (D_n) of 107 nm, a weight-average diameter (D_w) of 229 nm and a dispersity (Đ) of 2.12 ($Đ = D_w/D_n$), as shown in Figure 188.a. It was then used in sol-gel synthesis to make a silica material with this template (Figure 188.b.). The elimination of the PFDA template was tested again under $scCO_2$ conditions. An extracted mass of 7.5% was observed and thermogravimetric analyses (TGA) of the materials before and after extraction permitted to confirm a polymer removal of 15% of the total PFDA content. These results showed that removal of the PFDA template was successful to

a certain extent, but the molecular weight of the PFDA needed to be decreased even further in order to increase its solubility in $scCO_2$. Additionally, after a few months of storage, this latex was partially irreversibly decanted, indicating that its colloidal stability should be improved.

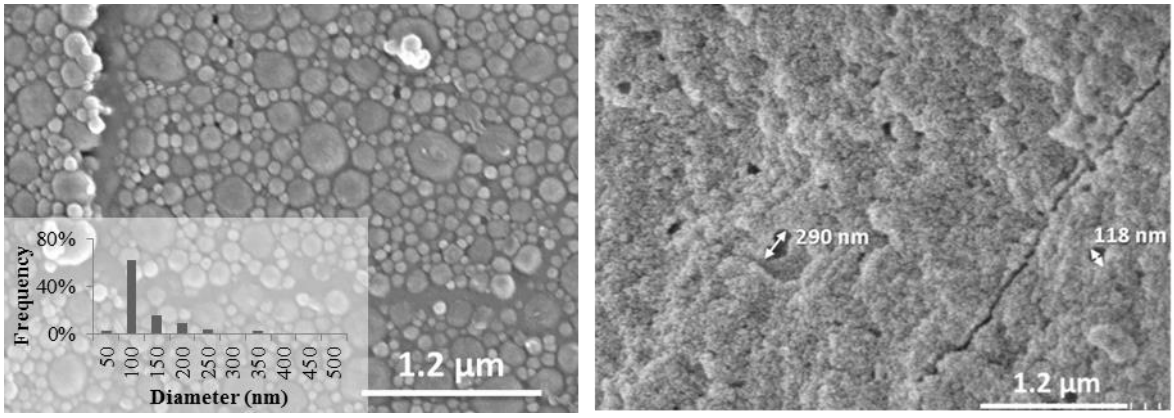

a. **b.**

Figure 188. a. SEM image of PFDA with chain transfer agent (the particle size distribution is presented in the insert) and b. SEM image of the corresponding silica-composite material.

Alternatively, a methacrylate (instead of acrylate) fluorinated polymer was synthesised to reduce gel content (since acrylates are known to be prone to transfer to polymer, leading to crosslinking, whereas methacrylates are much less prone to transfer to polymer). A P62MA latex was thus prepared by miniemulsion polymerisation as described above, including a chain transfer agent to keep the molecular weight low and a fluorinated surfactant to guarantee the colloidal stability. Figure 189.a. shows a SEM image of such polymer but the polymer beads are hardly seen. TEM imaging was also performed giving slightly better results (Figure 189.b.). However, the polymer beads did not have sharp edges. Difficulties for SEM and TEM observations are probably due to the low glass transition temperature of this polymer (below 30 °C, as measured by differential scanning calorimetry – DSC). This latex exhibited a D_n of 624 nm (D_w = 842 nm and Đ = 1.35).

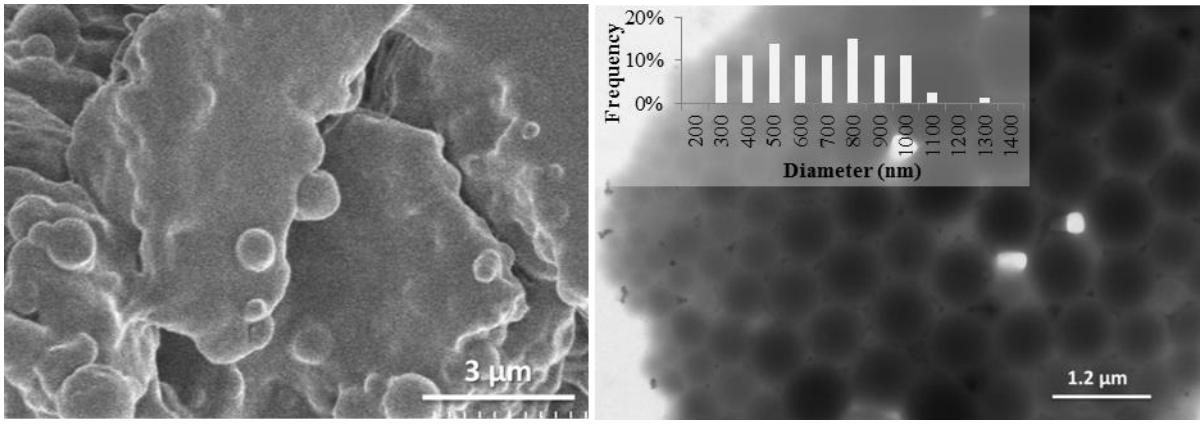

a. **b.**

Figure 189.. Images of P62MA by: **a.** SEM and **b.** TEM

P62MA latex was then used in sol-gel synthesis to make a silica composite material at 40 °C with a subsequent drying in a ventilated oven at 80 °C. Figure 190.a. shows such material before extraction. Empty pores can be observed on this figure, which are probably due to polymer flowing (due to its low glass transition temperature) and the shear forces during the sample grinding. The elimination of the P62MA template was tested again under $scCO_2$ conditions; the corresponding material is shown in Figure 190.b. An extracted mass of 8.8% was observed and thermogravimetric analyses (TGA) of the materials before and after extraction permitted to confirm a polymer removal of 18% of the total P62MA content.

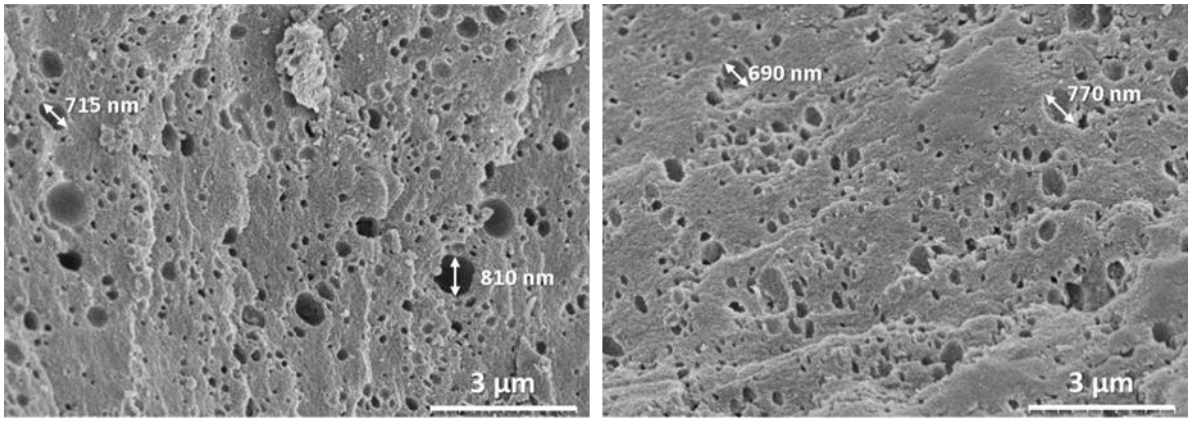

a. **b.**

Figure 190. SEM images of hierarchically porous silica prepared via conventional drying: a. before and b. after P62MA template removal.

Considering that the matrix porosity (mesopores connecting the latex particles entrapped in the silica matrix) could constrain the polymer extraction, the silica synthesis was modified. After the gel point, the gel was aged for 24 h at 40 °C and subsequently frozen with liquid nitrogen and freeze dried overnight. The water crystals formation increased the silica porosity as the water density decreases when frozen. Figure 191.a. presents the composite material before polymer extraction. It can be seen that the matrix shows a more open microstructure. Figure 191.b. shows a silica material after polymer removal. 11.4% of mass was extracted, which corresponds to a polymer removal of 24% of the total P62MA content as confirmed by thermogravimetric analyses (TGA).

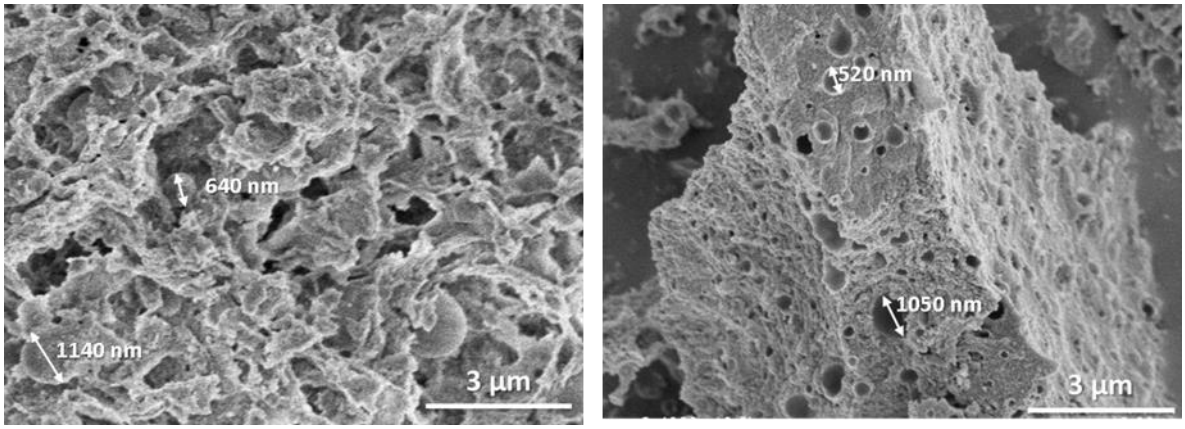

a. **b.**

Figure 191. SEM images of hierarchically porous silica prepared via cryogel synthesis: a. before and b. after P62MA template removal.

This work shows that the removal of PFDA from the silica matrix and revealing a hierarchical porosity due to the polymer template is possible under mild supercritical CO_2 conditions, as long as the molecular weight of the polymer is kept low enough to avoid crosslinking of the polymer chains. Under such conditions, P62MA was also removed by $scCO_2$ until a certain extent. However, in order to increase the efficiency of the polymer extraction, it could be envisaged to reduce the polymer chain lengths, increase the silica-matrix mesopore size and reduce the polymer-silica interaction. Future studies will also be needed to determine how to decorate these latexes with platinum or palladium nanoparticles to be transferred to the silica matrix. Moreover, this strategy potentially allows recycling of the polymer template.

X.5- Conclusion

The combination of latex synthesis, sonochemistry and sol-gel process is a versatile catalyst preparation technique. The exploration of further perspectives in the latex synthesis step highlights the potential to modulate the catalyst hierarchical porosity. Furthermore, the template removal by alternative processes other than calcination would potentially allow the template reuse and limit the sintering phenomena inherent to high temperature treatments.

The modification of the experimental conditions during the free radical polymerisation of a styrene by emulsion polymerisation led to different particle sizes. It was observed that a redox couple KPS-SMBS as initiator system permitted to obtain smaller polystyrene particles (134 nm) than only KPS as a thermal initiator (194 nm). Additionally, the particles obtained with such redox initiator couple are expected to be more stable in time than those with the thermal initiator due to the presence of sulfonate groups (less likely to be hydrolysed). An increase of the surfactant concentration can also reduce the particle size of the polymer latex, going from 134 nm at 0.44 times the critical micelle concentration (CMC) to 119 nm at the CMC. Furthermore, a very large surfactant excess could help reduce the particle size down to 46

nm, but at such surfactant concentration, it was not possible to carry out the subsequent steps of sonochemical reduction and sol-gel synthesis. Additionally, varying the operation conditions, it was possible to modify the polymer particle size at a given latex formulation. For instance, when KPS and styrene were fed simultaneously in semi-continuous mode, the particle size was 110 nm compared with 134 nm in batch mode.

Regarding the polystyrene template extraction from the silica matrix with tetrahydrofuran, chloroform or toluene, it was incomplete and the polymer swelling with such solvents affected the structure stability of the material. Conversely, the exploration of polymer template extraction with supercritical CO_2 led to promising results as long as the polymer molecular weight is kept low enough to avoid crosslinking of the polymer chains. This approach permitted to remove up 24% of the total CO_2-phile P62MA template and revealed the hierarchical porosity of the matrix. In order to increase the efficiency of the polymer extraction, it is recommended to reduce the polymer chain lengths, increase the silica-matrix mesopore size and reduce the polymer-silica interaction. Moreover, this strategy potentially allows recycling of the polymer template.

X.6- References

[1] A.F. Sierra Salazar, T. Chave, A. Ayral, S.I. Nikitenko, V. Hulea, P.J. Kooyman, F.D. Tichelaar, S. Perathoner, P. Lacroix-Desmazes, Engineering of silica-supported platinum catalysts with hierarchical porosity combining latex synthesis, sonochemistry and sol-gel process – I. Material preparation, Microporous Mesoporous Mater. (2016) 207–214. doi:10.1016/j.micromeso.2016.07.009.

[2] P. Lacroix-Desmazes, P. André, J.M. Desimone, A.-V. Ruzette, B. Boutevin, Macromolecular Surfactants for Supercritical Carbon Dioxide Applications : Synthesis and Characterization of Fluorinated Block Copolymers Prepared by Nitroxide- Mediated Radical Polymerization, J. Polym. Sci. Part A Polym. Chem. 42 (2004) 3537–3552. doi:10.1002/pola.20193.

[3] J. Garnier, P.-E. Dufils, J. Vinas, Y. Vanderveken, A. van Herk, P. Lacroix-Desmazes, Synthesis of poly (vinylidene chloride)-based composite latexes by emulsion polymerization from epoxy functional seeds for improved thermal stability, Polym. Degrad. Stab. 97 (2012) 170–177. http://www.sciencedirect.com/science/article/pii/S0141391011003600 (accessed November 17, 2014).

[4] J. de S. Nunes, J.M. Asua, Theory-Guided Strategy for Nanolatex Synthesis, Langmuir. 28 (2012) 7333–7342. doi:10.1021/la3006647.

[5] W. V. Smith, R.H. Ewart, Kinetics of Emulsion Polymerization, J. Chem. Phys. 16 (1948) 592–599. doi:10.1063/1.1746951.

[6] W. V Smith, R.H. Ewart, Kinetics of Emulsion Polymerization Kinetics of Emulsion Polymerization, J. Chem. Phys. 16 (1948) 592. doi:10.1063/1.1746951.

[7] S. Sajjadi, M. Yianneskis, Semibatch Emulsion Polymerization of Methyl Methacrylate with a Neat Monomer Feed, Polym. React. Eng. 11 (2003) 715–736. doi:10.1081/PRE-120026371.

[8] S. Sajjadi, Particle formation under monomer-starved conditions in the semibatch emulsion polymerisation of styrene. Part II. Mathematical modelling, Polymer (Guildf). 44 (2003) 223–237. doi:10.1016/S0032-3861(02)00735-8.

[9] J. Aguilar, M. Rabelero, S.M. Nuño-Donlucas, E. Mendizábal, A. Martínez-Richa, R.G. López, M. Arellano, J.E. Puig, Narrow size-distribution poly(methyl methacrylate) nanoparticles made by semicontinuous heterophase polymerization, J. Appl. Polym. Sci. 119 (2011) 1827–1834. doi:10.1002/app.32886.

[10] Y. Chen, F. Jahanzad, S. Sajjadi, Semicontinuous Monomer-Starved Emulsion Polymerization as a Means to Produce Nanolatexes: Analysis of Nucleation Stage, Langmuir. 29 (2013) 5650–5658. doi:10.1021/la4000654.

[11] R. Ledezma, M. Esther Treviño, L.E. Elizalde, L.A. Pérez-Carrillo, E. Mendizábal, J.E. Puig, R.G. López, Semicontinuous heterophase polymerization under monomer starved conditions to prepare nanoparticles with narrow size distribution, J. Polym. Sci. Part A Polym. Chem. 45 (2007) 1463–1473. doi:10.1002/pola.21916.

[12] Y. Zhang, Y. He, J. Zhao, Poly(methyl methacrylate) nanolatexes with high solid contents prepared by semi-continuous emulsion polymerization in the presence of oil-soluble initiators, Eur. Polym. J. 61 (2014) 316–325. doi:10.1016/j.eurpolymj.2014.11.004.

[13] A.F. Sierra-Salazar, W.S.J. Li, M. Bathfield, A. Ayral, S. Abate, T. Chave, S.I. Nikitenko, V. Hulea, S. Perathoner, P. Lacroix-Desmazes, Hierarchically porous Pd/SiO2 catalyst by combination of miniemulsion polymerisation and sol-gel method for the direct synthesis of H2O2, Catal. Today. (2016). doi:10.1016/j.cattod.2016.12.021.

[14] M.T. García, I. Gracia, G. Duque, A. De Lucas, J.F. Rodríguez, Study of the solubility and stability of polystyrene wastes in a dissolution recycling process, Waste Manag. 29 (2009) 1814–1818. doi:10.1016/j.wasman.2009.01.001.

[15] H. Kuroki, C. Islam, I. Tokarev, H. Hu, G. Liu, S. Minko, Tunable Ultrathin Membranes with Non-Volatile Pore Shape Memory, ACS Appl. Mater. Interfaces. (2015) 150427003748006. doi:10.1021/acsami.5b01416.

XI. ANNEX IV. ADDITIONAL REACTION PATHWAY IN THE HYDROGENATION OF *P*-CNB

The reactions of hydrogenation of *p*-CNB are described in Chapter IV. Typically, when hierarchically porous catalysts prepared by the combination of latex synthesis, sonochemical decoration and sol-gel process were used, only traces of chloronitroso benzene and chlorophenyl hydroxyl amine were observed, especially at the beginning of the reaction, following the reaction pathway presented in Figure 192.

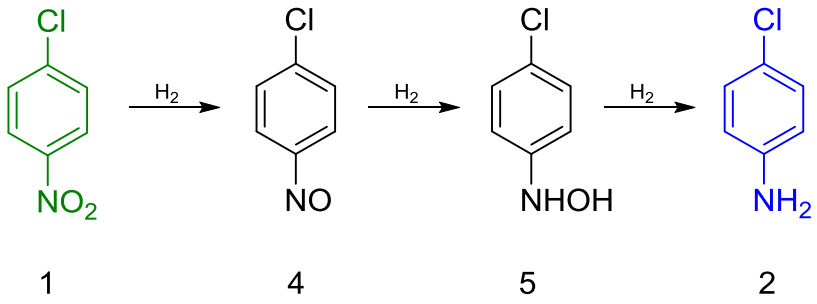

Figure 192. Reaction pathway of the hydrogenation of *p*-CNB (1: *p*-CNB, 2: *p*-CAN, 4: chloronitroso benzene, 5: chlorophenyl hydroxyl amine).

However, when the catalyst prepared by incipient wetness impregnation was used (1cal650-50%-IWI), the material balance curve decreased continuously, indicating that not all products were quantified, as shown in Figure 193 (the corresponding raw GC-FID data is presented in Figure 194).

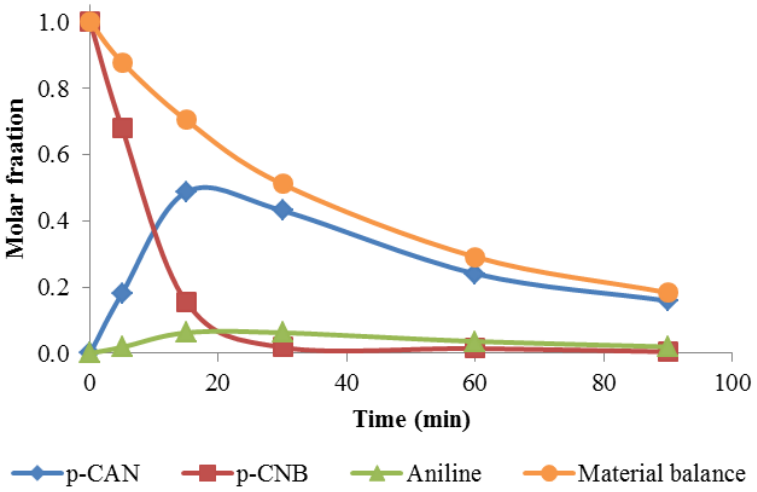

Figure 193. Evolution of the reaction medium composition by GC-FID using 1cal650-50%-IWI

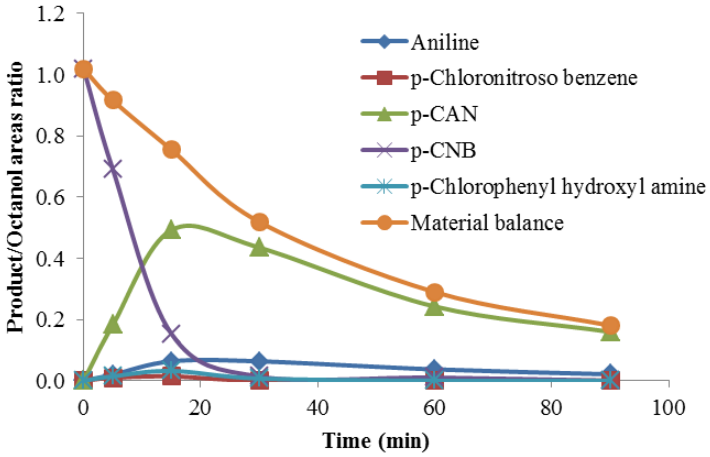

Figure 194. Evolution of the GC-FID product/octanol areas ratio using 1cal650-50%-IWI

A first hypothesis could be the formation of polyaniline[1] that could have been trapped within the catalyst. However thermogravimetric analyses (TGA), collected for the catalysts where the polymer was expected, did not show significant mass loss difference before and after reaction, ruling out this hypothesis. Secondly, it could be thought of the formation of dimers or soluble polymer chains that would not be visible by GC-FID due to a positive charge by protonation of the amine and/or too high boiling point, precluding elution in the GC column. In order to investigate this, ^{1}H-NMR spectra where collected of the reaction media of 0.4cal650-25/25% (where no polymer is expected), and 1cal650-50%-IWI, as shown in Figure 195.

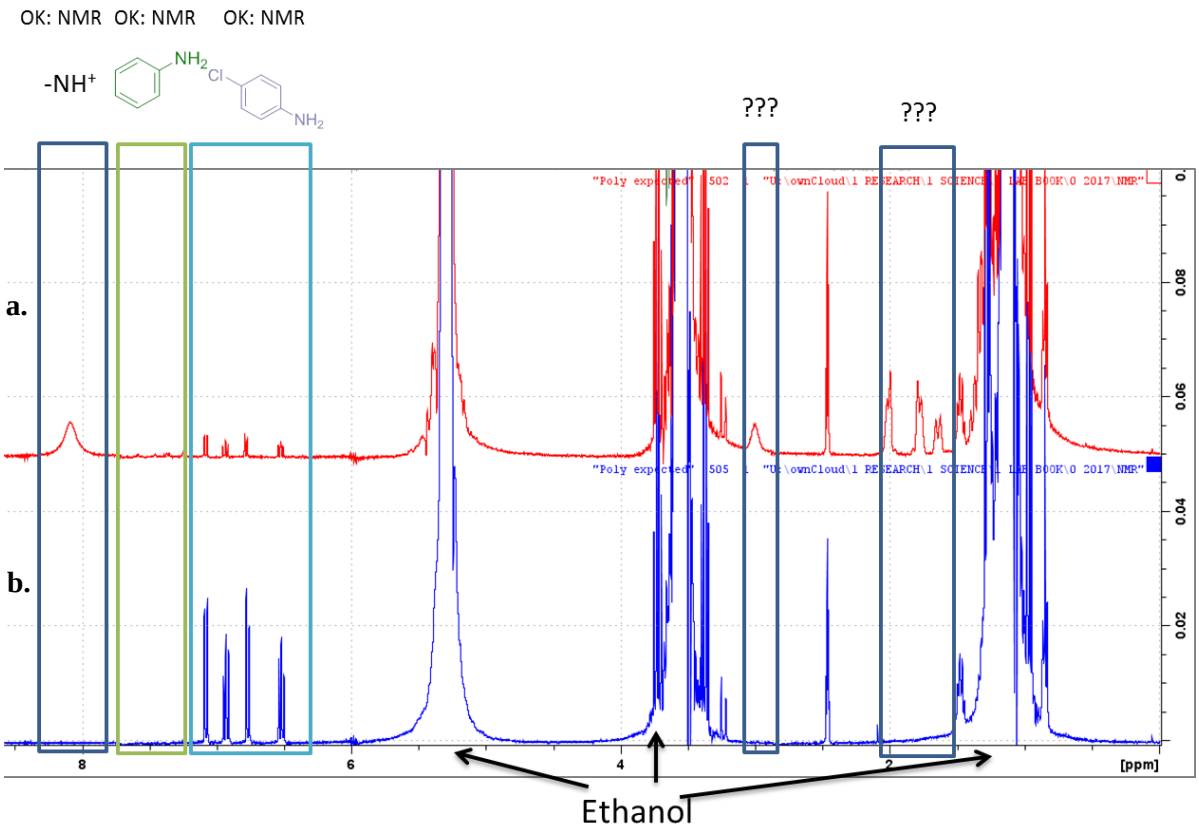

Figure 195. ^{1}H-NMR spectra of the reaction media of: a. 1cal650-50%-IWI and b. 0.4cal650-25/25%.

The signals between 6.0 and 7.9 ppm correspond to the aromatic groups of aniline and *p*-CAN, which was confirmed by analysis of the commercial products. The signal at 8.1 ppm corresponds to a protonated amine [2,3]. The unknown signals present in 1cal650-50%-IWI and absent in 0.4cal650-25/25% are between 1.5 and 3.0 ppm. However, the ^{1}H-NMR spectrum of the first expected adduct (N-(4-chlorophenyl)-1,2-phenylenediamine, Figure 196) did not exhibit any signal within this range, so the hypothesis of polymer formation was rejected.

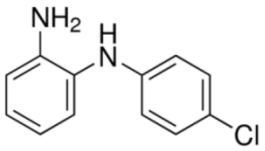

Figure 196. N-(4-chlorophenyl)-1,2-phenylenediamine)

Subsequently, by analysing the reaction medium of 1cal650-50%-IWI after concentrating the medium by partial evaporation of ethanol and making a liquid-liquid extraction with benzene-D and water, it was possible to obtain a better ^{1}H-NMR spectrum of the investigated molecule in the aqueous phase, as shown in Figure 197.

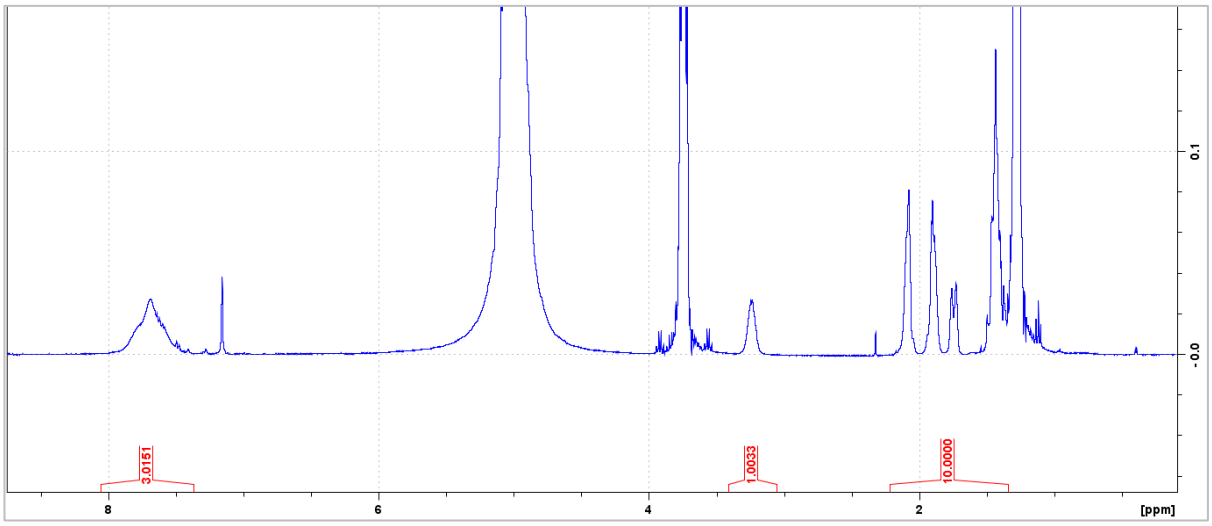

Figure 197. ^{1}H-NMR spectrum of the aqueous fraction after extraction from 1cal650-50%-IWI reaction medium.

In order to confirm the structure of the molecule, ^{13}C NMR, DEPT ^{13}C NMR, COSY and HMQC analyses were carried out. ^{15}N NMR was not successful due to the low concentration of product within this sample and the low natural abundance of ^{15}N. Alternatively, an extracted fraction with D_2O provided more resolved NMR spectra. Compiling the information from all the spectra: 6 carbons, of which 1 was a CH and 14 protons, the proposed structure is cyclohexylammonium.

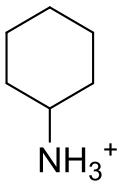

Figure 198. Cyclohexylammonium structure

It is important to notice that cyclohexylamine (pKa = 10.64) is a stronger base than aniline (pKa = 4.6) or *p*-CAN (pKa = 4.0). This explains why cyclohexylamine was protonated forming cyclohexylammonium chloride, which being a salt was not observable by GC-FID. In order to confirm the presence of cyclohexylammonium chloride in solution, cyclohexylamine and the stoichiometric amount of HCl were added to the aqueous fraction after extraction from 1cal650-50%-IWI reaction medium. In Figure 199, it can be seen that the ^{1}H-NMR spectra before and after addition of these two compounds are identical (just more intense when cyclohexylamine was added), confirming that the product in solution is cyclohexylammonium chloride (Figure 200).

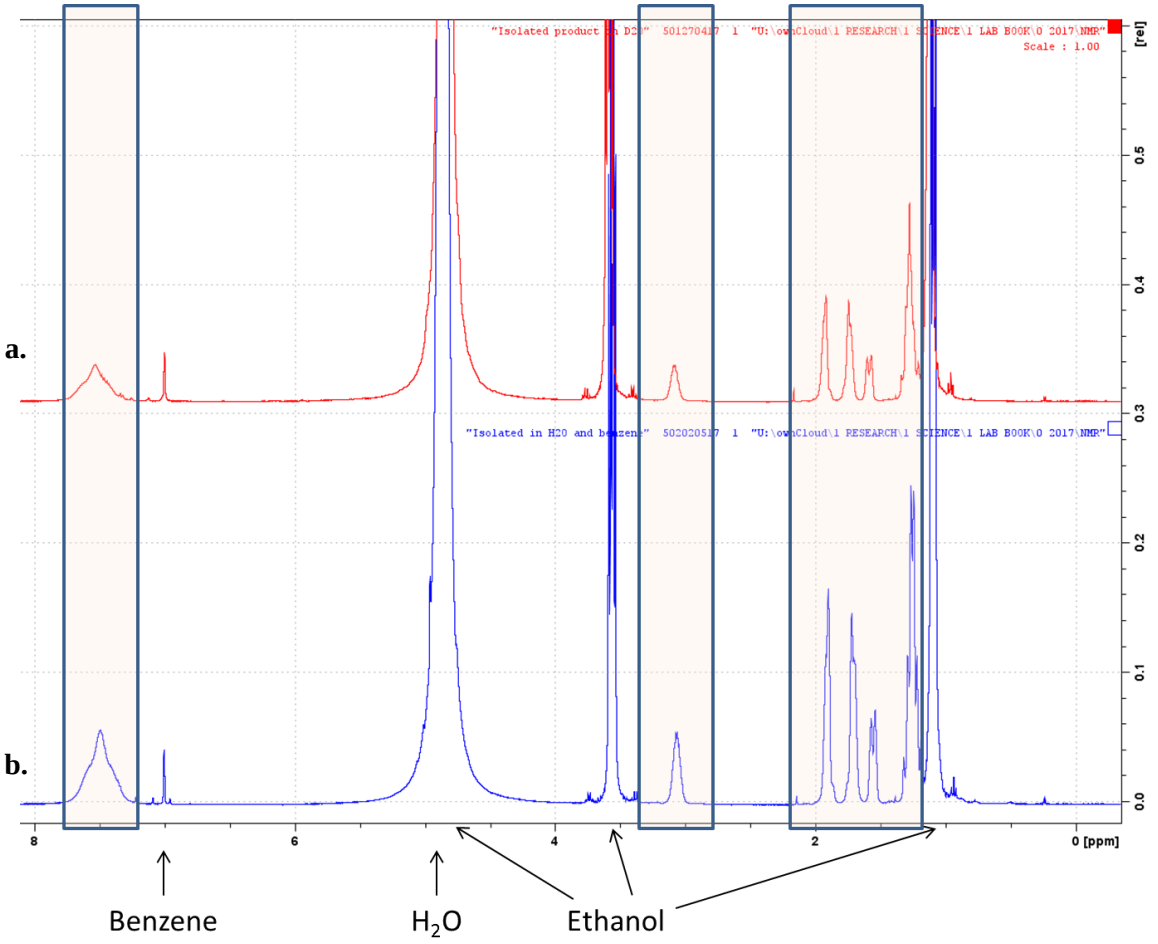

Figure 199. ^{1}H-NMR spectrum of: a. the aqueous fraction after extraction from 1cal650-50%-IWI reaction medium, b. same as a plus cyclohexylamine and stoichiometric amount of HCl. (Benzene-D capillaries were used to collect the ^{1}H-NMR spectrum)

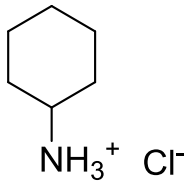

Figure 200. Cyclohexylammonium chloride structure

Considering the concentration profiles and the additional identified product, the proposed reaction pathway for the hydrogenation of *p*-CNB that leads to cyclohexylammonium chloride is presented in Figure 201.

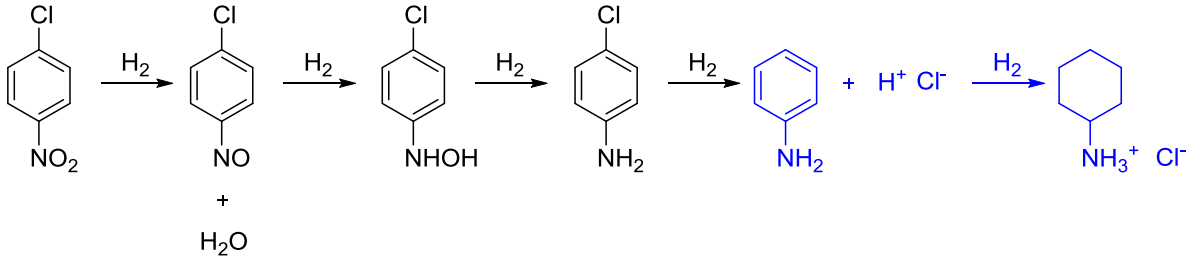

Figure 201. Hydrogenation pathway of *p*-CNB towards cyclohexylammonium chloride.

In this case the selectivity was calculated as:

$$Selectivity = \frac{[p-CAN]}{[p-CNB]_0 - [p-CNB]} \times 100$$

Where $[p-CNB]_0$ is the initial concentration of *p*-CNB, $[p-CNB]$ and $[p-CAN]$ are the concentration of *p*-CNB and *p*-CAN at any time, respectively. The concentrations are expressed in molarity. So it was found that at 80% conversion of *p*-CNB, the selectivity towards *p*-CAN was only 54.8% (compared with up to 100% with other catalysts reported in Chapter IV).

It can be then concluded that 1cal650-50%-IWI was the least selective catalyst to produce *p*-CAN (as discussed in Chapter IV) because it continued catalysing the hydrogenation beyond aniline, favouring the hydrogenation of the aromatic ring. This hierarchically porous catalyst prepared by incipient wetness impregnation could be a promising catalyst for the one-step hydrogenation of nitrobenzene to cyclohexylamine, which has not been largely studied in the literature [4], despite the very few catalyst patents for this process [5]. However, it would be challenging giving the lack of control in the narrow Pt particle size distribution.

XI.1- References

[1] A.M. Arzymanyan, A.A. Matnishyan, M.I. Fedorov, S.H.R. Melkonian, Homopolycondensation of aniline halides: synthesis of a regular structured polyaniline, Polym. Sci. 33 (1991) 714–720. doi:10.1016/0032-3950(91)90128-D.

[2] R. Abdelkader, H. Amine, B. Mohammed, Thermally stable forms of pure polyaniline catalyzed by an acid-exchanged montmorillonite clay called maghnite- H+ as an effective catalyst, Int. J. Polym. Sci. 2012 (2012). doi:10.1155/2012/846710.

[3] X. Wang, T. Sun, C. Wang, C. Wang, W. Zhang, Y. Wei, 1H NMR determination of the doping level of doped polyaniline, Macromol. Chem. Phys. 211 (2010) 1814–1819. doi:10.1002/macp.201000194.

[4] X. Lu, Y. Chen, Z. Zhao, H. Deng, D. Zhou, C. Wei, R. Nie, Q. Xia, Highly selective one-step hydrogenation of nitrobenzene to cyclohexylamine over the supported 10% Ni/carbon catalysts doped with 3‰ Rh, RSC Adv. 6 (2016) 15354–15361. doi:10.1039/C5RA27202E.

[5] A.J. T., C.N. J., Hydrogenation of nitrobenzene, US 3.678.108, 1972.

XII. ANNEX V: RÉSUMÉ ÉTENDU

Les procédés catalytiques sont d'une importance capitale dans le développement industriel de notre société [1]. En effet, les procédés catalytiques actuels représentent environ 90% de toutes les transformations chimiques industrielles [2]. Les catalyseurs hétérogènes sont largement utilisés (73,6% du volume mondial du marché des catalyseurs en 2015) en raison de leur facilité d'utilisation et de leur faible coût. Cette forte contribution au marché motive la recherche et le développement des matériaux catalytiques hétérogènes, et particulièrement, des catalyseurs métalliques supportés, dont la demande a été de 1 568,4 kilo tonnes en 2015 et qui devrait augmenter en raison de leur application croissante en synthèse organique. Parmi eux, des procédés catalytiques impliquant des nanoparticules supportées de métaux précieux tels que le platine, le palladium et l'or sont actuellement utilisés pour produire des carburants et d'autres molécules d'intérêt industriel [3,4].

En outre, la catalyse est l'un des 12 Principes de la Chimie Verte [5] en raison de son potentiel à contribuer au développement de produits et de procédés durables. La catalyse hétérogène est généralement préférée par rapport à la catalyse homogène en raison de la facilité de récupération des catalyseurs solides dans les milieux réactionnels, de sorte qu'ils peuvent être recyclés et réutilisés plusieurs fois avant leur désactivation [6]. Néanmoins, il est toujours nécessaire de développer des matériaux catalytiques hétérogènes encore plus performants.

La conception rationnelle des catalyseurs est un sujet qui a été activement discuté comme une opportunité pour accélérer le développement de matériaux sur mesure répondant à des besoins spécifiques, en établissant des relations structure-propriété et en évitant l'approche d'essai-erreur [7]. Ainsi, du point de vue expérimental, des outils pour la modulation de la texture du catalyseur (porosité interne et interconnexion des pores) et pour la préparation sur mesure de sites actifs sont essentiels à la préparation rationnelle de catalyseurs. Cependant, actuellement, il existe une disponibilité très limitée de méthodes pour contrôler la répartition spatiale des sites actifs de métaux dans des matériaux poreux [8].

Le but de ce travail est de développer une nouvelle méthode de synthèse pour la préparation de catalyseurs afin d'améliorer la distribution des sites actifs (métaux nobles) à faible taux de charge, tout en contrôlant la porosité hiérarchique du matériau de support. Une structure à porosité hiérarchique combine des pores de différentes tailles (micropores : < 2 nm, mésopores : 2-50 nm et macropores : > 50 nm). L'importance de la porosité hiérarchique en catalyse réside dans les pores interconnectés de différentes tailles qui permettent aux réactifs et aux produits d'atteindre tous les sites actifs [9].

La méthode proposée consiste en la synthèse d'une empreinte porogène (*template* en anglais) décorée avec des nanoparticules métalliques, lesquelles sont transférées à une matrice de silice mésoporeuse issue du procédé de sol-gel. Une représentation schématique est donnée dans la Figure 202. La première étape est la synthèse d'une empreinte porogène de billes de polystyrène (latex) obtenues par polymérisation en émulsion aqueuse. La deuxième étape est la synthèse et le dépôt de nanoparticules de métaux nobles sur la surface des billes de polymère par voie sonochimique dans l'eau. La troisième étape est la synthèse du support par un procédé sol-gel

en milieu aqueux en utilisant le latex décoré et l'orthosilicate de tétraéthyle (TEOS) dans des conditions contrôlées pour moduler la porosité finale de la matrice de silice (mésoporeuse). Il est important de noter que toutes les étapes de cette approche sont effectuées dans l'eau, ce qui limite les impacts environnementaux de la préparation du catalyseur. L'élimination du porogène organique (latex) par calcination génère les macropores. Le matériau résultant possède alors une morphologie inédite pour un catalyseur, avec des macropores fonctionnalisés par des nanoparticules métalliques, dans une matrice de silice mésoporeuse.

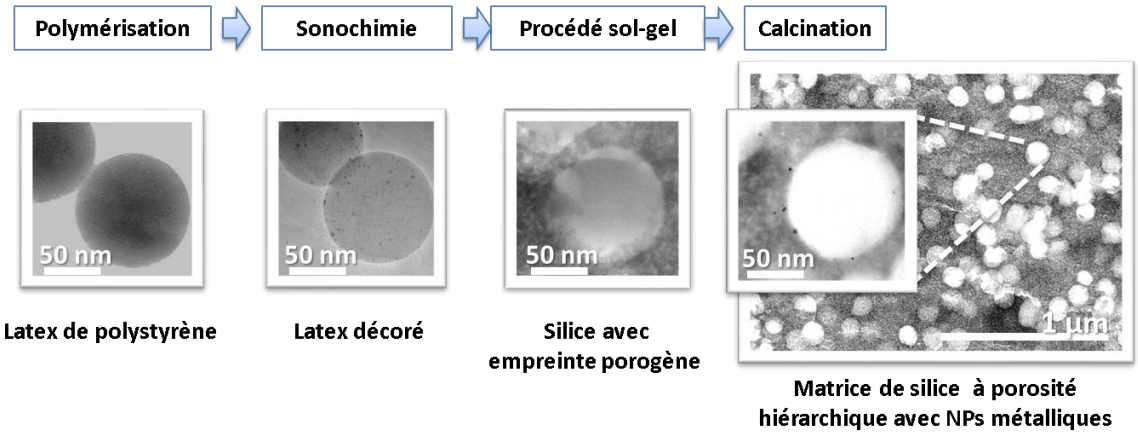

Figure 202. Préparation du catalyseur supporté en combinant la polymérisation en émulsion, la sonochimie et le procédé de sol-gel (les trois étapes sont conduites en milieu aqueux).

Ce projet a été abordé à l'aide de deux cas d'étude d'intérêt industriel, afin de répondre à la question de recherche: « Est-il possible de modifier la morphologie et les performances catalytiques des matériaux catalytiques préparés par la combinaison de la polymérisation en émulsion, la sonochimie et le procédé de sol-gel en modifiant les conditions de chaque étape de préparation? ». Le premier cas d'étude a été l'hydrogénation sélective du *p*-chloronitrobenzene pour produire la *p*-chloroaniline avec des catalyseurs à porosité hiérarchique à base de Pt (Figure 203). Le second cas d'étude a été la synthèse directe du peroxyde d'hydrogène à partir d'oxygène et d'hydrogène avec des catalyseurs à porosité hiérarchique à base de Pd (Figure 204).

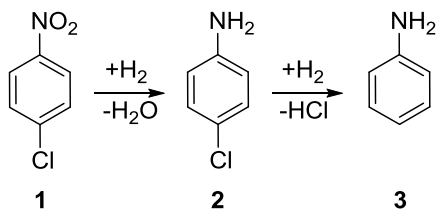

Figure 203. Schéma simplifié de la réaction de l'hydrogénation of *p*-chloronitrobenzene (1: *p*-chloronitrobenzene, 2: *p*-chloroaniline, 3: Aniline).

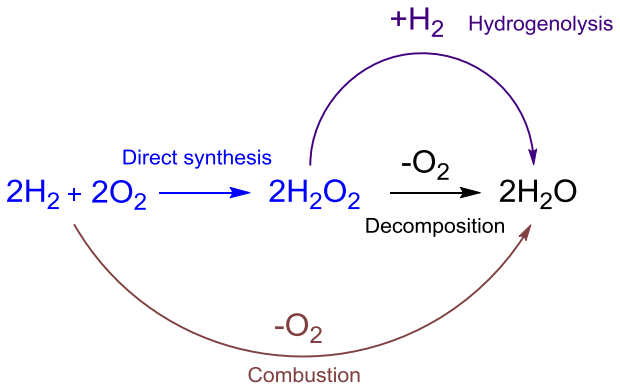

Figure 204. Schéma de la réaction de la synthèse directe de peroxyde d'hydrogène à partir d'oxygène et d'hydrogène (en bleu).

Ce travail de thèse a été possible grâce à la participation de plusieurs collaborateurs dans 7 laboratoires répartis dans 4 pays :

- En France :
  - Dr. Patrick Lacroix-Desmazes, MSc. Jennifer Li et Dr. Maël Bathfield au laboratoire d'Ingénierie et Architectures Macromoléculaires - Institut Charles Gerhardt Montpellier,
  - Prof. André Ayral à l'Institut Européen de Membranes,
  - Dr. Tony Chave et Dr. Sergey Nikitenko à l'Institut de Chimie Séparative de Marcoule – CEA, et
  - Prof. Vasile Hulea au laboratoire des Matériaux Avancés pour la Catalyse et la Santé - Institut Charles Gerhardt Montpellier.
- En Italie : Prof. Siglinda Perathoner et Dr. Salvatore Abate à *Università di Messina*
- En Afrique du Sud : Prof. Patricia J. Kooyman à *University of Cape Town*
- Aux Pays-Bas : Dr. Frans D. Tichelaar à *Delft University of Technology*

Cette collaboration s'est déroulée dans le cadre européen du programme de doctorat en chimie industrielle durable (SINCHEM – Sustainable Industrial Chemistry) financé par la Commission européenne (http://www.sinchem.eu/).

XII.1- Premier cas d'étude: L'hydrogénation sélective du *p*-chloronitrobenzene pour produire la *p*-chloroaniline avec des catalyseurs à base de Pt supporté sur de la silice à porosité hiérarchique

Il a été possible de synthétiser des catalyseurs de platine sur un support de silice (comme schématisé dans la Figure 205) et de les évaluer pour l'hydrogénation sélective du *p*-chloronitrobenzene afin de produire la *p*-chloroaniline.

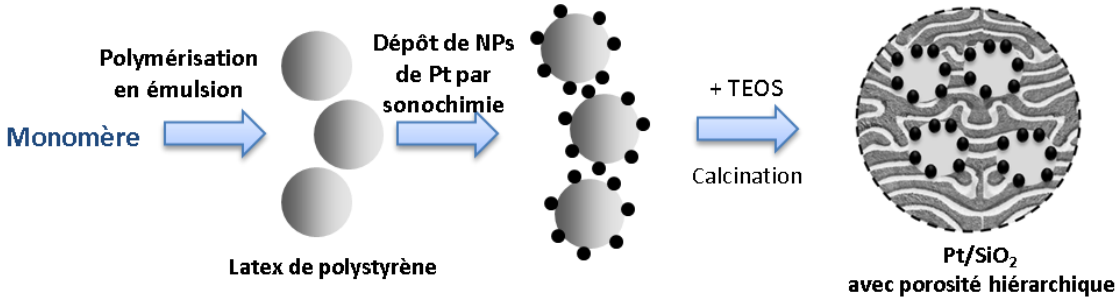

Figure 205. Représentation schématique de la préparation d'un catalyseur à porosité hiérarchique en combinant la polymérisation en émulsion, la sonochimie et le procédé de sol-gel.

De plus, en faisant varier la quantité de latex décoré lors de la synthèse sol-gel, nous avons pu préparer des matériaux avec des macroporosités différentes: 50 %, 33 %, 25 % et 12,5 % (% de volume macropore par rapport au volume total de catalyseur). Une telle variation, à partir du même latex décoré, a permis de faire varier simultanément le taux de macropores et le taux de charge métallique, comme schématisé dans la Figure 206.

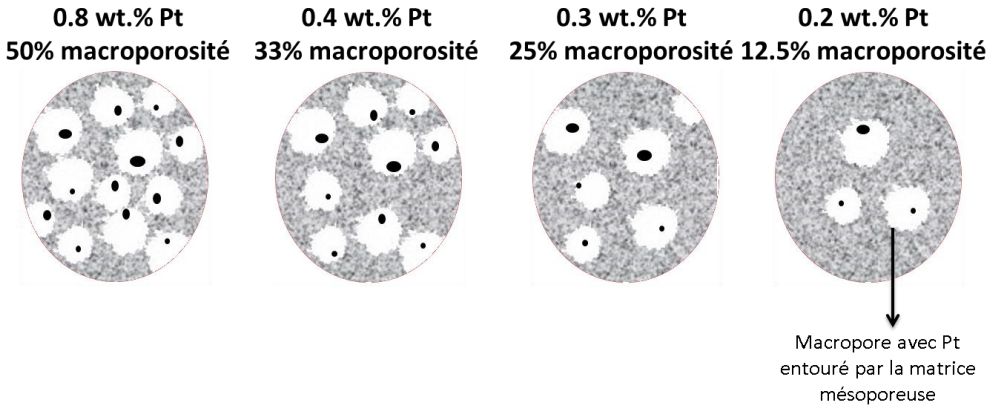

Figure 206. Représentation schématique de la variation de la quantité de sites actifs lors de la diminution de la quantité de macropores décorés.

En outre, il a été possible de dé-corréler la quantité de métal et la quantité de macropores en utilisant une combinaison de latex décoré et de latex non décoré dans la préparation du catalyseur, comme représenté dans la Figure 207.

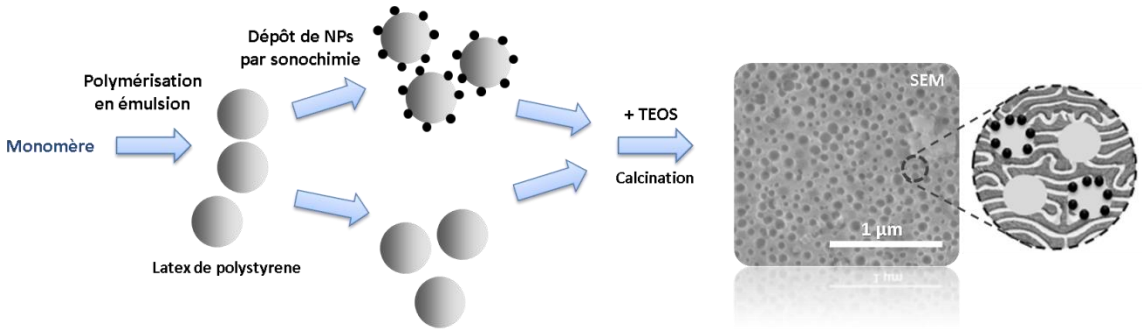

Figure 207. Représentation schématique de la préparation d'un catalyseur avec 0,4% en masse de Pt et 50% de macroporosité: 25% décoré et 25% non décoré.

Il a aussi été démontré que l'élimination du porogène en présence de Pt peut être effectuée à 450 °C, au lieu de 650 °C en absence de Pt, en raison de l'élimination du polymère par oxydation catalysée par le Pt. En outre, aucun post-traitement de réduction n'est nécessaire après l'étape de calcination (à 450 ° C ou 650 ° C) car les nanoparticules de Pt restent stables principalement dans l'état d'oxydation Pt(0).

En ce qui concerne les performances catalytiques de ces matériaux supportés sur de la silice à porosité hiérarchique, ils peuvent être considérés comme des catalyseurs efficaces pour l'hydrogénation sélective du *p*-chloronitrobenzene (*p*-CNB) pour produire la *p*-chloroaniline (*p*-CAN), présentant une meilleure sélectivité (jusqu'à 100% à 80% de conversion du *p*-CNB, avec les catalyseurs avec 0,2% en masse de Pt et 12.5% de macroporosité et avec 0,4% en masse de Pt et 50% de macroporosité dont 25% décoré et 25% non décoré) qu'un catalyseur commercial de référence (jusqu'à 92,5% à 80% de conversion). Le paramètre principal qui a permis d'améliorer la sélectivité a été la taille des nanoparticules de Pt : la taille d'environ 7 nm a conduit aux meilleurs résultats en termes de sélectivité. Sur ces nanoparticules métalliques de taille relativement élevée, le produit *p*-CAN est moins fortement adsorbé en comparaison avec le réactif *p*-CNB, ce qui diminue la probabilité du produit *p*-CAN d'être hydrogéné en l'aniline [10]. Une telle taille de nanoparticule a été obtenue soit par calcination à haute température (650 °C), soit par ajustement du taux de charge de Pt sur le latex hybride (environ 1% en masse Pt/polystyrène pour obtenir environ 0,8% en masse Pt/ SiO_2). Les catalyseurs avec un taux de Pt inférieur, mais une taille de nanoparticules de Pt similaire (obtenus en utilisant moins de latex décoré) ont également montré une sélectivité améliorée. Par exemple, l'échantillon 0,2% en poids de Pt/SiO_2 avec 12,5% macroporosité (avec des particules de 6,7 ± 3,1 nm) a présenté une sélectivité de 100% à 80% de conversion.

Au contraire, un catalyseur préparé à partir du même type de matrice de silice à porosité hiérarchique, mais décoré avec du Pt par imprégnation suivie d'une réduction sous flux d'hydrogène (Figure 208), a montré une sélectivité très faible envers le *p*-CAN (54,8% à une conversion de 80%), probablement en raison du contrôle limité de la taille des nanoparticules par imprégnation (des nanoparticules de Pt de taille comprise entre 3 nm et 200 nm ont été mesurées).

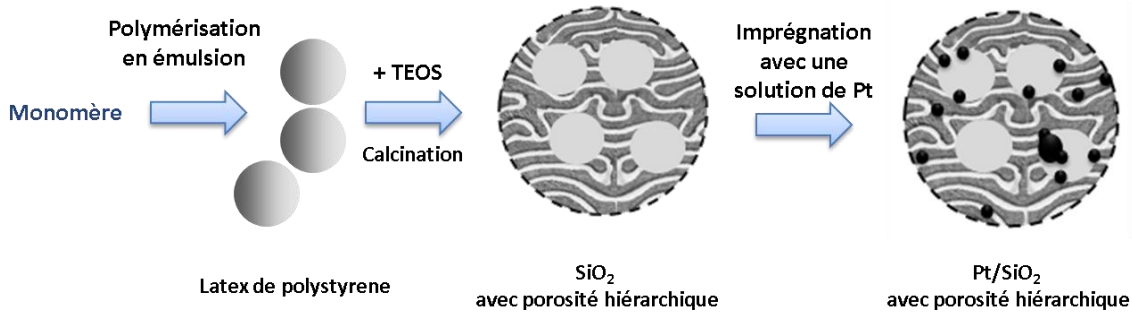

Figure 208. Représentation schématique de la préparation d'un catalyseur à porosité hiérarchique par imprégnation.

En ce qui concerne la structure de la silice à porosité hiérarchique, il a été observé que pour un taux de charge de Pt donné et une matrice mésoporeuse avec des pores de 2-9 nm, la vitesse initiale de réaction augmente légèrement en augmentant le taux de macropores. Ainsi, le catalyseur à 0,4% en masse Pt/SiO_2 avec 50% de macroporosité totale (25% décorée et 25% non décoré) a présenté une vitesse initiale de réaction de 31,0 ± 2,9 $mol_{CNB}/min.mol_{Pt}$, tandis que le catalyseur à 0,4% en masse Pt/SiO_2 avec 33% de macroporosité totale (décoré) a montré une vitesse de 26,7 ± 2,9 $mol_{CNB}/min.mol_{Pt.}$ Cette accélération de la vitesse de réaction a été attribuée à la présence de plus de macropores à 50% de macroporosité totale, ce qui a amélioré la diffusion interne des produits et des réactifs.

De plus, en élargissant la distribution de taille des mésopores pour être dans la gamme de 2 à 15 nm, il a été possible d'augmenter la vitesse initiale de réaction jusqu'à 91,7 ± 2,9 $mol_{CNB}/min.mol_{Pt}$ (avec 0,3% en masse Pt/SiO_2 avec 50 % de macroporosité totale), ce qui est une valeur beaucoup plus élevée que celle obtenue avec le catalyseur commercial (47,4 ± 2,9 $mol_{CNB}/min.mol_{Pt}$). Cette distribution en taille des mésopores (2-15 nm) a été obtenue en préparant le latex décoré dans un réacteur sonochimique à 343 kHz (avec une activité sonochimique modérée qui limite la modification du pH et garantit la stabilité colloïdale du latex). Néanmoins, une plus grande taille de mésopores risquerait de conduire à l'agrégation des nanoparticules de Pt comme dans le cas du catalyseur commercial, dans lequel les mésopores de 11 à 28 nm ont permis l'agrégation des particules de Pt initialement de 2,9 ± 1,2 nm jusqu'à 14,1 ± 9,6 nm. En comparaison, dans un catalyseur à porosité hiérarchique avec des mésopores de 2 à 15 nm, les particules de Pt initialement de 3,9 ± 1,0 nm se sont agrégées seulement jusqu'à 8,8 ± 7,8 nm.

Tous les catalyseurs évalués ont présenté une très bonne stabilité aux conditions réactionnelles : aucun changement majeur des caractéristiques de leur texture n'a été observé après réaction. Par exemple, on conserve la surface spécifique élevée du catalyseur à 0,3% en masse. Pt/SiO_2 avec 50% de macroporosité totale : 610 ± 37 m²/g avant réaction à 617 ± 37 m²/g après réaction.

XII.2- Second cas d'étude: synthèse directe du peroxyde d'hydrogène à partir d'oxygène et d'hydrogène avec des catalyseurs à base de Pd supporté sur de la silice à porosité hiérarchique

Il a été possible de synthétiser des catalyseurs de Pd supporté sur de la silice à porosité hiérarchique et de les évaluer pour la synthèse directe du peroxyde d'hydrogène à partir d'oxygène et d'hydrogène. Grâce à la souplesse du procédé étudié pour la préparation des catalyseurs, quatre approches ont pu être explorées pour obtenir des nanoparticules actives de différentes natures : monométalliques (Pd), bimétalliques (Pt-Pd) et métalliques-oxyde métallique (Pd-CeO_2). La première approche a consisté en la préparation de catalyseurs à base de Pd par une combinaison de la synthèse de latex de polystyrène par polymérisation en émulsion, la fonctionnalisation par voie sonochimique (à partir de Na_2PdCl_4) et la synthèse de la matrice de silice par un procédé sol-gel (Figure 209.a.). La deuxième approche a inclus la fonctionnalisation des billes de polystyrène par réductions sonochimiques consécutives du Pt puis du Pd (en utilisant Na_2PtCl_4 et Na_2PdCl_4) pour créer des nanoparticules bimétalliques Pt-Pd (Figure 209.b.). La troisième approche a consisté en la synthèse d'un latex hybride contenant des nanoparticules de CeO_2 à la surface des billes de polymère, par polymérisation en émulsion. Ce latex polymère/CeO_2 a ensuite été fonctionnalisé avec du Pd par réduction sonochimique de Na_2PdCl_4, puis la matrice de silice a été préparée par la méthode sol-gel (Figure 209.c.). La dernière approche a été la préparation de la matrice de silice en présence d'un latex hybride Pd/polystyrène préparé par polymérisation en miniémulsion à partir d'un précurseur palladié organosoluble (palladium (II) acetylacetonate) (Figure 209.d.).

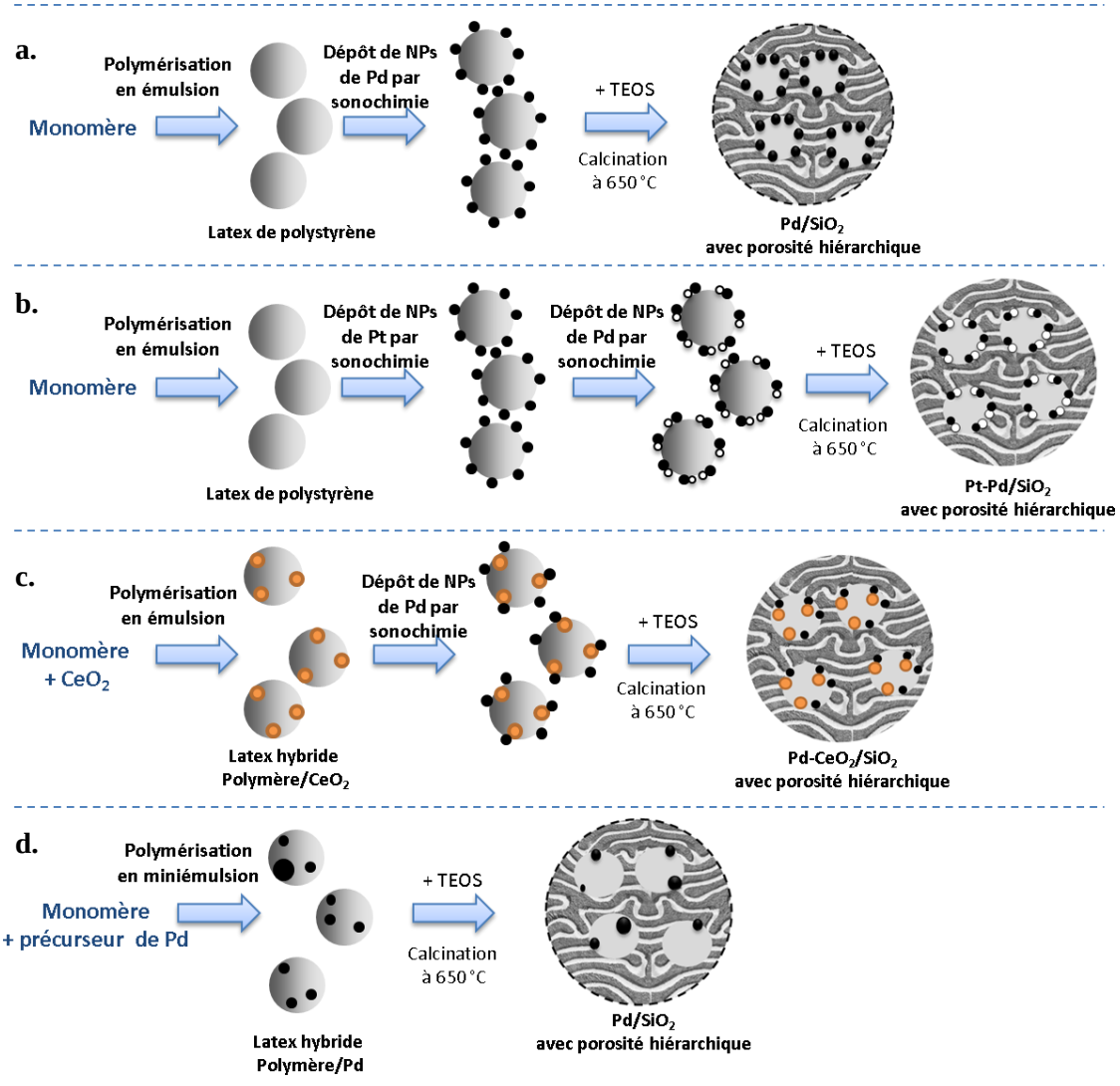

Figure 209. Stratégies pour la préparation de catalyseurs à base de Pd avec porosité hiérarchique: a. Pd/SiO_2 par synthèse de la matrice de silice par le procédé de sol-gel en présence d'un latex préparé par polymérisation en émulsion et décoré par voie sonochimique (réduction du Pd), b. $Pt\text{-}Pd/SiO_2$ par synthèse de la matrice de silice par le procédé de sol-gel en présence d'un latex préparé par polymérisation en émulsion et décoré par voie sonochimique (réductions consécutives du Pt puis du Pd), c. $Pd\text{-}CeO_2/SiO_2$ par synthèse de la matrice de silice par le procédé de sol-gel en présence d'un latex hybride polymère/CeO_2 préparé par polymérisation en émulsion et décoré par voie sonochimique (réduction du Pd) et d. Pd/SiO_2 par synthèse de la matrice de silice par le procédé de sol-gel en présence d'un latex hybride préparé par polymérisation en miniémulsion.

Contrairement aux matériaux à base de Pt préparés dans le premier cas d'étude, l'élimination du polymère a dû être effectuée à 650 °C car l'oxydation du porogène organique en présence de Pd n'est pas complète à plus basse température. Par conséquent, une augmentation importante de la taille des nanoparticules de Pd a été observée par rapport aux matériaux à base de Pt. Les nanoparticules de Pd obtenues sur le latex étaient de 6,7 ± 2.7 nm, mais elles ont atteint 16.2 ± 4.6 nm après la calcination à 650 °C. D'autre part, la taille des nanoparticules de Pt

précédemment obtenue sur le latex était d'environ 2,2 nm, lesquelles ont respectivement augmenté à 4,6 ± 1.1 nm ou 6,5 ± 2.2 nm lors de la calcination à 450 °C ou à 650 °C. Au contraire, les particules bimétalliques de Pt-Pd ont quant à elles montré une stabilité thermique élevée avec un frittage très limité après calcination à 650 °C, allant d'une taille moyenne de nanoparticule de 3,6 ± 1,3 nm après préparation sonochimique jusqu'à seulement 3,8 ± 1,4 nm, après calcination.

La dernière approche à l'aide d'un latex hybride Pd/polystyrène préparé par polymérisation en miniémulsion aqueuse a permis de s'affranchir de l'étape de réduction sonochimique dans la préparation des nanoparticules monométalliques de Pd. Cependant, cette méthode restreint le contrôle et la versatilité de la synthèse des nanoparticules qu'offre la sonochimie: contrôle de la taille et distribution en taille des nanoparticules, formation d'interactions bimétalliques Pt-Pd, dispersion du métal à la surface du latex, etc.

En ce qui concerne les performances catalytiques de ces matériaux, la meilleure productivité de H_2O_2 a été 32500 $mol_{H_2O_2}/(mol_{metal}.h)$, obtenue avec le catalyseur Pt-Pd bimétallique préalablement réduit, malheureusement, avec une sélectivité de seulement 19 ± 1%, avec tendance à la baisse quand la conversion augmente. Lorsqu'il est non réduit, le catalyseur bimétallique a présenté une meilleure sélectivité (40 ± 1%), mais sa productivité a diminué (24000 $mol_{H_2O_2}/(mol_{metal}.h)$). D'autre part, la meilleure sélectivité a été obtenue avec le catalyseur Pd-CeO_2/SiO_2, atteignant 68 ± 3% lorsqu'il est seulement calciné. Et avec réduction préalable, le catalyseur Pd-CeO_2/SiO_2 a respectivement atteint une sélectivité de 53 ± 2% et 63 ± 2%, dans des conditions batch et semi-continu.

Un fait remarquable sur le catalyseur bimétallique Pt-Pd testé ici est que sa productivité de 32500 $mol_{H_2O_2}/(mol_{metal}.h)$ est environ 10 fois plus élevé que celle du catalyseur à 0,7% en masse Pd/SiO_2, ou 3 fois plus élevée que celle du catalyseur à 0,2% en masse Pd/SiO_2 obtenu par miniémulsion. Cette amélioration de la productivité est très prometteuse étant donné que, dans la littérature, l'amélioration par l'ajout de Pt au Pd a entraîné une augmentation maximale de la productivité de 1,8 fois [11].

Compte-tenu des meilleures productivités obtenues avec le catalyseur bimétallique Pt-Pd/SiO_2 et de la meilleure sélectivité obtenue avec le catalyseur Pd-CeO_2/SiO_2, il pourrait être intéressant de tester un catalyseur Pt-Pd-CeO_2/SiO_2 qui pourrait tirer profit de l'amélioration de la productivité apportée par le couple Pt-Pd et de la sélectivité plus élevée due a la stabilité des espèces oxydées de Pd par interaction avec l'oxyde de cérium.

En ce qui concerne la stabilité de la texture poreuse, le catalyseur bimétallique (Pt-Pd/SiO_2, avec surface spécifique d'environ 600 m^2/g) et le catalyseur de Pd monométallique préparé par miniémulsion (avec surface spécifique d'environ 700 m^2/g) se sont révélés être très stables dans les conditions de réaction catalytique : ils ont conservé des caractéristiques de texture presque identiques après réaction. Au contraire, le catalyseur de Pd monométallique préparé par voie sonochimique a présenté une certaine densification au cours de la réaction (la porosité totale est passée de 51% à 43%). Cette densification pourrait être attribuée à l'influence sur le procédé sol-gel des espèces de Pd non-réduites par sonochimie, entraînant la formation d'un réseau silicique moins résistant. Le catalyseur Pd-CeO_2/SiO_2 a aussi présenté une légère densification après une première utilisation (la porosité totale est passée de 64% à 58%), mais il est

néanmoins resté stable lors du recyclage. Cela signifie que la synthèse de ces deux derniers matériaux pourrait être encore optimisée pour obtenir des caractéristiques de texture plus stables lors d'une toute première utilisation.

XII.3- Bilan et perspectives générales

Dans le premier cas d'étude (hydrogénation sélective du *p*-chloronitrobenzene pour produire la *p*-chloroaniline avec des catalyseurs à base de Pt supporté sur de la silice à porosité hiérarchique), nous avons démontré que notre procédé de préparation du catalyseur en milieu aqueux permet de moduler de manière simultanée et indépendante la porosité hiérarchique méso-macro du catalyseur et sa teneur en métal, et de contrôler la distribution en taille des nanoparticules de métal ainsi que la distribution spatiale du métal dans le matériau (nanoparticules de métal situées dans les macropores).

Dans le deuxième cas d'étude (synthèse directe du peroxyde d'hydrogène à partir d'oxygène et d'hydrogène avec des catalyseurs à base de Pd supporté sur de la silice à porosité hiérarchique), il a été possible de montrer que notre méthode de préparation du catalyseur en milieu aqueux permet d'introduire des sites actifs de natures différentes en jouant avec des interactions bimétalliques (Pt-Pd) et d'oxyde métallique-métal (CeO_2-Pd).

Ainsi, nos résultats concernant ces deux cas d'étude permettent d'affirmer que la modification des conditions expérimentales de préparation des catalyseurs en milieu aqueux, que ce soit lors de l'étape de synthèse du porogène (latex) par polymérisation en (mini)émulsion, de l'étape de synthèse des nanoparticules métalliques par réduction des précurseurs métalliques par sonochimie, de l'étape de synthèse du support silicique par procédé sol-gel ou encore lors de l'étape de la calcination du matériau final, permet de moduler les caractéristiques morphologiques et texturales qui déterminent les performances catalytiques de ces catalyseurs à porosité hiérarchique.

La Figure 210 résume le type de catalyseurs de Pt/SiO_2 évalués dans ce travail. En particulier, les catalyseurs préparés par la combinaison de la synthèse du latex, la réduction sonochimique et le procédé sol-gel ont été obtenus avec des nanoparticules de Pt entre 4 et 10 nm, en fonction de la température de calcination et le taux de charge de Pt. La gamme de tailles des mésopores formés pendant l'étape du procédé sol-gel a varié de 2-7 nm à 2-15 nm. Une telle différence a été expliquée par des légères variations de pH et de stabilité du latex lors de la décoration du porogène (latex) par réduction sonochimique de précurseurs métalliques. En outre, la taille des macropores a varié entre 110 nm et 400 nm en raison de l'agrégation de billes de polymère à cause d'une légère déstabilisation colloïdale lors de l'étape de sonochimie et/ou de l'étape du procédé sol-gel. Afin d'étudier plus en détail les effets de la décoration sonochimique du latex (création de nanoparticules métalliques en surface du latex) sur la morphologie finale du catalyseur, il serait recommandé d'effectuer une étude en décorant un latex de polystyrène à diverses activités sonochimiques sous CO/Ar ce qui permettrait évaluer les effets sonochimiques sur le latex en limitant les réactions secondaires qui pourraient se produire avec le H_2O_2 généré *in-situ*. Des expériences similaires sous Ar permettraient d'étudier l'effet sur la surface des billes de polymère (et l'effet sur le tensioactif présent dans la formulation du latex)

des radicaux hydroxyl HO· et du peroxyde d'hydrogène H_2O_2 générés *in-situ*. Cette surface peut être caractérisée par un titrage des groupes fonctionnels [12–15].

Une perspective supplémentaire pour varier la morphologie du catalyseur serait la préparation d'un matériau de silice avec un latex non décoré. Après séchage, le matériau peut être imprégné d'une solution de précurseur de Pt puis calciné à 650 °C pour l'élimination du porogène (latex). Cela pourrait permettre l'introduction sélective du métal dans les mésopores (au lieu d'introduire le métal dans les macropores), comme suggéré dans la Figure 210.

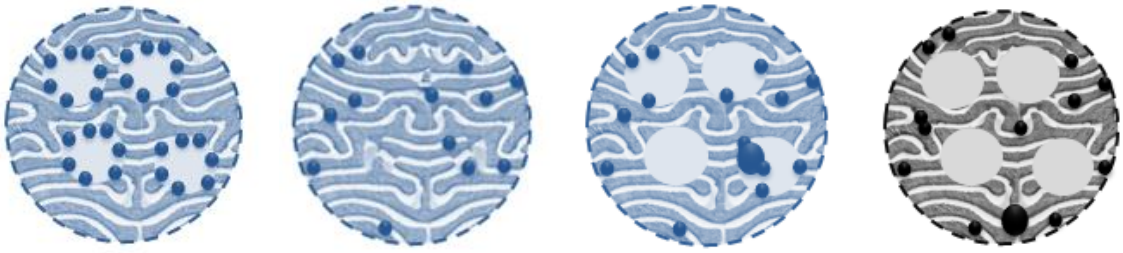

a. Porogène décoré par voie sonochimique	b. Catalyseur mésoporeux commercial	c. Par voie d'imprégnation à sec	d. Par voie d'imprégnation à sec avant calcination (PERSPECTIVE)
NPs : 4 – 10 nm Mésopores : 2 – 15 nm Macropores:110–400nm	NPs : 3 nm Mésopores: 11 – 28 nm Macropores : N/A	NPs : 3 – 200 nm Mésopores : 2 – 15 nm Macropores :110–170nm	

Figure 210. Pt/SiO_2 catalyseurs avec différentes morphologies. (En bleu, les catalyseurs testés dans notre travail pour l'hydrogénation sélective du *p*-chloronitrobenzene pour produire la *p*-chloroaniline)

La Figure 211 présente les catalyseurs de Pd/SiO_2 évalués dans notre travail. Le catalyseur préparé par la combinaison de la synthèse du latex, de la réduction sonochimique et du procédé sol-gel est constitué de nanoparticules de Pd d'environ 16 nm. Cette taille relativement élevée des nanoparticules métalliques résulte, d'une part, de la taille des nanoparticules obtenues après réduction sonochimique (~ 7 nm), et d'autre part, du frittage des nanoparticules lors de la calcination à température élevée requise pour l'élimination du porogène polymère (650 °C). Ainsi, une première perspective serait la préparation de latex qui puissent avoir une interaction plus forte avec le Pd pour stabiliser ces nanoparticules métalliques et limiter leur croissance, par exemple en incluant des fonctions thiols à la surface des billes de polymère [16–18] et/ou en incluant des chaînes poly(oxyde d'éthylène) ou poly(vinyl pyrrolidone) à la surface des billes polymères [19]. Cela pourrait favoriser une décoration de surface plus uniforme des billes de polymère, conduisant donc à des nanoparticules métalliques plus petites. Une deuxième perspective impliquerait l'utilisation d'autres polymères porogènes avec des températures de dégradation plus faibles, comme par exemple, à base de poly(méthacrylate de méthyle) (PMMA), afin de limiter le frittage des nanoparticules de Pd pendant l'étape de calcination. En effet, on peut s'attendre à ce que l'élimination d'un latex de PMMA puisse être effectuée à une température plus basse que dans le cas du polystyrène, car (lorsqu'il n'est pas inclus dans une

matrice de silice) le PMMA peut être complètement dégradé dès 215 °C [20], tandis que le polystyrène nécessite 425 °C [21]. Une troisième perspective serait l'extraction du polymère en utilisant du CO_2 supercritique sous conditions douces (typiquement 40 °C et 250 bars) (alternative succinctement explorée dans l'Annexe III). En plus de limiter le frittage des nanoparticules métalliques grâce à la faible température utilisée en CO_2 supercritique par rapport à la méthode par calcination, cela ouvrirait potentiellement la voie au recyclage du polymère porogène. Ceci rendrait encore plus pertinent le procédé de synthèse du catalyseur en termes de développement durable (procédé en milieux aqueux et CO_2 supercritique, deux solvants verts, et recyclage du polymère porogène).

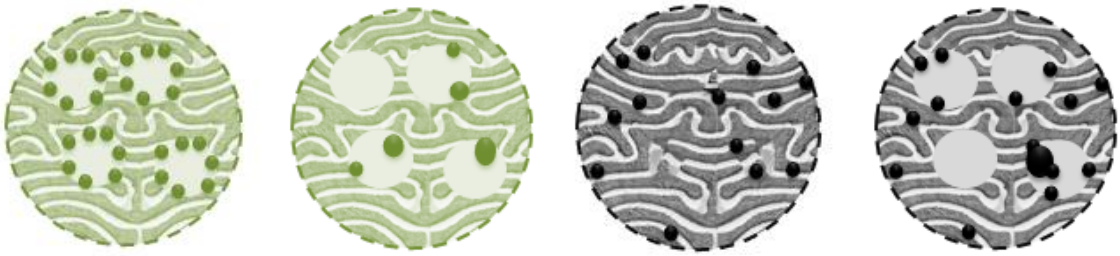

a. Porogène décoré par voie sonochimique	b. Porogène préparé par polymérisation en miniemulsion	c. Catalyseur mésoporeux commercial (PERSPECTIVE)	d. Par voie d'imprégnation à sec (PERSPECTIVE)
NPs : 16 nm Mésopores : 2 – 5 nm Macropores : ~ 130nm	NPs : 12 nm Mésopores : 2 – 5 nm Macropores : ~ 130nm		

Figure 211. Catalyseurs Pd/SiO_2 préparés par des méthodes différentes (en vert, les catalyseurs testés dans notre travail pour la synthèse directe du peroxyde d'hydrogène à partir d'oxygène et d'hydrogène)

Egalement, comme dans le premier cas d'étude, il serait souhaitable de compléter l'étude sur la synthèse directe du peroxyde d'hydrogène en effectuant d'autres expériences dans les mêmes conditions de réaction afin de comparer les performances de nos catalyseur de Pd/SiO_2 à porosité hiérarchique obtenus par voie sonochimique, en comparaison à un matériau commercial de Pd/SiO_2 et en comparaison à un catalyseur de Pd préparé par imprégnation à sec d'une matrice de silice à porosité hiérarchique.

a. Porogène décoré par voie sonochimique

NPs : 4 – 5 nm
Mésopores : 2 – 5 nm
Macropores : ~ 130nm

b. Par mélange de différents porogènes décorés (PERSPECTIVE)

c. Par mélange d'un porogène de type macro (latex décoré) et d'un porogène de type méso (micelles fonctionnalisées) (PERSPECTIVE)

Figure 212. Des catalyseurs avec de multiples fonctionnalités supportés sur de la silice à porosité hiérarchique (en vert, les catalyseurs testés dans notre travail pour la synthèse directe du peroxyde d'hydrogène à partir d'oxygène et d'hydrogène)

La Figure 212 présente quelques morphologies possibles qui peuvent être obtenues avec des fonctionnalités multiples en combinant la synthèse du latex, la réduction sonochimique et procédé sol-gel. Deux modèles ont déjà été testés pour la synthèse directe de peroxyde d'hydrogène : bimétalliques Pd-Pt/SiO_2 et Pd-CeO_2/SiO_2. Dans les deux cas, les deux fonctionnalités (Pd-Pt ou Pd-CeO_2) étaient introduites dans le même macropore et présentaient une forte interaction entre elles. Cependant, d'autres morphologies de catalyseur sont possibles. Par exemple, la combinaison de deux latex décorés différemment conduirait à différents sites actifs localisés dans des macropores indépendants, comme le montre la Figure 213. Cela pourrait être particulièrement intéressant pour la conception de catalyseurs en vue de réactions en cascade, pour lesquelles une première étape se produit sur un site actif dans un macropore, et une deuxième étape se produit sur un autre type de site actif dans un autre macropore au sein du même grain de catalyseur.

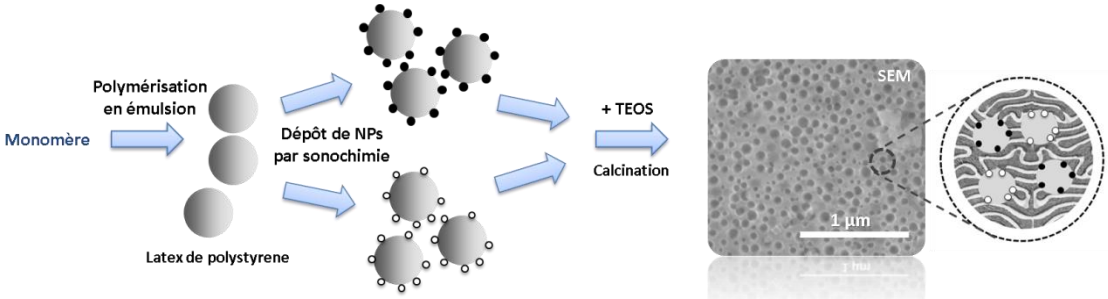

Figure 213. Représentation schématique de la préparation d'un catalyseur avec des macropores décorés avec différentes fonctionnalités.

Par ailleurs, il serait possible de préparer un matériau avec une certaine fonctionnalité introduite dans les macropores et une autre fonctionnalité introduite dans les mésopores (Figure 212.c). Cela pourrait se faire par un mélange de latex décoré et de micelles fonctionnalisées. Les micelles fonctionnalisées peuvent par exemple être préparées à partir de copolymères à blocs (des nanoparticules de Pt peuvent être préparées, par exemple, par réduction avec des polyols assistée par micro-ondes) [22]. Une autre option très séduisante pour préparer des micelles fonctionnalisées est l'utilisation de copolymères à blocs sensibles aux stimuli pour former des micelles constituées de complexes de polyions (PIC micelles en anglais : PolyIon Complex micelles). Par exemple, des copolymères à blocs double hydrophiles peuvent présenter des charges suite à un stimulus (comme un changement de pH pour un copolymère à blocs poly(oxyde d'éthylène)-*b*-poly(acide acrylique) qui présentera donc des charges négatives de type carboxylates $-CO_2^-,Z^+$). Cela leur permet de se co-assembler avec des polyions métalliques de charge opposée (par exemple charges cationiques de M^{n+} pour MX_n) par complexation électrostatique (par exemple : Pt(II) ou Pt(IV), ou Pd(II) ou Pd(IV)) gouvernée par le gain entropique lié au relargage des contre-ions Z^+ et X^-. Après la synthèse sol-gel, la mésoporosité résultante serait ordonnée et contiendrait le métal désiré [23,24].

En ce qui concerne la synthèse du latex porogène, une perspective supplémentaire peut être suggérée. Tout d'abord, la taille des particules de polymère peut être diminuée par la préparation de nanolatex [25–27] afin d'obtenir des macropores inférieurs à 100 nm (par exemple, pour limiter l'agrégation des nanoparticules métalliques dans un même macropore). Ces nanolatex pourraient être combinés avec des latex d'une taille plus grande afin d'induire une hiérarchie de taille des macropores dans le matériau final (pour améliorer le phénomène de diffusion dans le grain de catalyseur). Une deuxième perspective serait d'introduire d'autres groupes fonctionnels que des sulfates et sulfonates à la surface des billes de polymère. Par exemple, pour améliorer l'interaction polymère-silice, le poly(oxyde d'éthylène) (POE) pourrait être utilisé car il se forme des liaisons hydrogène entre les silanols Si-OH de la silice et les unités oxyde d'éthylène du POE lors du procédé sol-gel. De la même manière et aussi pour améliorer l'interaction entre le polymère et les nanoparticules métalliques, la polyvinylpyrrolidone (PVP) pourrait être utilisée pour à la fois assurer une interaction forte entre le latex et la matrice silicique mais aussi pour stabiliser les nanoparticules métalliques à la surface des billes de polymère [19].

De plus, notre étude a été effectuée sur un support de silice à porosité hiérarchique. Toutefois, elle pourrait être étendue à d'autres systèmes d'oxydes simples ou mixtes comme TiO_2, Al_2O_3, SiO_2-TiO_2 ou SiO_2-Al_2O_3 [22].

En ce qui concerne les conditions de fonctionnement pour le test du catalyseur, les réactions catalytiques effectuées dans notre étude ont été principalement effectuées dans des conditions de batch, où aucune limitation majeure du transport de matière n'était attendue. Cependant, les essais catalytiques dans des conditions d'écoulement dynamiques à travers un contacteur monolithique poreux profiteraient davantage des caractéristiques de nos matériaux à porosité hiérarchique, compte tenu des limitations de transport de masse plus élevées en opération en continu. Pour de telles conditions de fonctionnement, notre procédé de préparation de catalyseurs en milieu aqueux devrait permettre la préparation, par simple immersion (lors de l'étape sol-gel avant d'atteindre le point de gel), de pièces monolithiques telles que des structures en nid d'abeilles ou des mousses solides.

En conclusion, notre technique de préparation du catalyseur en milieu aqueux par la combinaison de synthèse du latex, réduction sonochimique et procédé sol-gel fournit une boîte à outils très puissante et polyvalente pour la préparation et l'optimisation des catalyseurs. Notre travail ouvre la voie à de nombreuses perspectives pour développer davantage cette nouvelle méthode qui permettrait de préparer des catalyseurs avec des morphologies améliorées et avec une distribution contrôlée de sites actifs de natures différentes au sein de la porosité hiérarchique méso et macro.

XII.4- Références

[1] S. George, Introduction: heterogeneous catalysis, Chem. Rev. 95 (1995) 475–476. http://pubs.acs.org/doi/abs/10.1021/cr00035a001 (accessed January 15, 2015).

[2] American Chemical Society, Technology Vision 2020 The U.S. Chemical Industry, Washington, DC, 1996. https://energy.gov/sites/prod/files/2013/11/f4/chem_vision.pdf.

[3] C.H. Bartholomew, R.J. Farrauto, Fundamentals of Industrial Catalytic Processes, John Wiley & Sons, Inc., Hoboken, NJ, USA, 2005. doi:10.1002/9780471730071.

[4] T. Muroi, Role of Precious Metal Catalysts, Noble Metals, InTech, 2012.

[5] P.T. Anastas, J.C. Warner, Green Chemistry: Theory and Practice, Oxford University Press, New York, 1998.

[6] M.-O. Coppens, G. Wang, Optimal Design of Hierarchically Structured Porous Catalysts, in: U.S. Ozkan (Ed.), Des. Heterog. Catal., Wiley-VCH Verlag GmbH & Co. KGaA, Weinheim, Germany, 2009: pp. 25–58. doi:10.1002/9783527625321.

[7] 2013 AIChE Annual Meeting, Rational Catalyst Design, (2013). https://aiche.confex.com/aiche/2013/webprogram/Session24747.html (accessed November 15, 2014).

[8] C.M.A. Parlett, M.A. Isaacs, S.K. Beaumont, L.M. Bingham, N.S. Hondow, K. Wilson, A.F. Lee, Spatially orthogonal chemical functionalization of a hierarchical pore network for catalytic cascade reactions, Nat. Mater. 15 (2016) 178–182. doi:10.1038/nmat4478.

[9] A. Corma, From microporous to mesoporous molecular sieve materials and their use in catalysis, Chem. Rev. 97 (1997) 2373–2420. doi:10.1021/cr960406n.

[10] B. Coq, A. Tijani, R. Dutartre, F. Figuéras, Influence of support and metallic precursor on the hydrogenation of p-chloronitrobenzene over supported platinum catalysts, J. Mol.

Catal. 79 (1993) 253–264. doi:10.1016/0304-5102(93)85106-4.

[11] J. Xu, L. Ouyang, G.J. Da, Q.Q. Song, X.J. Yang, Y.F. Han, Pt promotional effects on Pd-Pt alloy catalysts for hydrogen peroxide synthesis directly from hydrogen and oxygen, J. Catal. 285 (2012) 74–82. doi:10.1016/j.jcat.2011.09.017.

[12] S.M. Ahmed, M.S. El-Aasser, G.H. Pauli, G.W. Poehlein, J.W. Vanderhoff, Cleaning latexes for surface characterization by serum replacement, J. Colloid Interface Sci. 73 (1980) 388–405. doi:10.1016/0021-9797(80)90085-5.

[13] R.M. Fitch, W.T. McCarvill, Surface chemistry of polystyrene colloids prepared by mixed initiator/surfactant systems, J. Colloid Interface Sci. 66 (1978) 20–25. doi:10.1016/0021-9797(78)90179-0.

[14] Y. Gong, K. Nakashima, R. Xu, A Novel Method To Determine Effective Charge of Polystyrene Latex Particles in Aqueous Dispersion, Langmuir. 17 (2001) 2889–2892. doi:10.1021/la001483n.

[15] J.M. Stubbs, P. Roose, P. De Doncker, D.C. Sundberg, Probing the surface of polymer colloids by conductometric surfactant titration, Langmuir. 22 (2006) 2697–2705. doi:10.1021/la052721n.

[16] M. Cargnello, N.L. Wieder, P. Canton, T. Montini, G. Giambastiani, A. Benedetti, R.J. Gorte, P. Fornasiero, A Versatile Approach to the Synthesis of Functionalized Thiol-Protected Palladium Nanoparticles, Chem. Mater. 23 (2011) 3961–3969. doi:10.1021/cm2014658.

[17] W. Shi, Y. Sahoo, M.T. Swihart, P.N. Prasad, Gold nanoshells on polystyrene cores for control of surface plasmon resonance., Langmuir. 21 (2005) 1610–1617. doi:10.1021/la047628y.

[18] P. Carro, G. Corthey, A.A. Rubert, G.A. Benitez, M.H. Fonticelli, R.C. Salvarezza, The complex thiol-palladium interface: A theoretical and experimental study, Langmuir. 26 (2010) 14655–14662. doi:10.1021/la102505c.

[19] D. Crespy, K. Landfester, Synthesis of polyvinylpyrrolidone/silver nanoparticles hybrid latex in non-aqueous miniemulsion at high temperature, Polymer (Guildf). 50 (2009) 1616–1620. doi:10.1016/j.polymer.2009.02.003.

[20] C.G. Schäfer, S. Vowinkel, G.P. Hellmann, T. Herdt, C. Contiu, J.J. Schneider, M. Gallei, A polymer based and template-directed approach towards functional multidimensional micro-structured organic/inorganic hybrid materials, J. Mater. Chem. C. 2 (2014) 7960. doi:10.1039/C4TC00633J.

[21] P. Pfaffli, A. Zitting, H. Vainio, Thermal degradation products of homopolymer polystyrene in air, Scand. J. Work. Environ. Heal. 4 (1978) 22–27. doi:10.5271/sjweh.2744.

[22] C. Yacou, M.-L. Fontaine, A. Ayral, P. Lacroix-Desmazes, P.-A. Albouy, A. Julbe, One pot synthesis of hierarchical porous silica membrane material with dispersed Pt nanoparticles using a microwave-assisted sol–gel route, J. Mater. Chem. 18 (2008) 4274–4279. doi:10.1039/b807029f.

[23] C. Gérardin, J. Reboul, M. Bonne, B. Lebeau, Ecodesign of ordered mesoporous silica materials, Chem. Soc. Rev. 42 (2013) 4217. doi:10.1039/c3cs35451b.

[24] N. Baccile, J. Reboul, B. Blanc, B. Coq, P. Lacroix-Desmazes, M. In, C. Gérardin, Ecodesign of Ordered Mesoporous Materials Obtained with Switchable Micellar Assemblies, Angew. Chemie Int. Ed. 47 (2008) 8433–8437. doi:10.1002/anie.200802431.

[25] L. Yang, Y. Ke, Synthesis of polystyrene nanolatexes via emulsion polymerization using sodium dodecyl sulfonate as the emulsifier, High Perform. Polym. 26 (2014) 900–905. doi:10.1177/0954008314533979.

[26] S. Sajjadi, M. Yianneskis, Semibatch Emulsion Polymerization of Methyl Methacrylate with a Neat Monomer Feed, Polym. React. Eng. 11 (2003) 715–736. doi:10.1081/PRE-120026371.

[27] Y. Zhang, Y. He, J. Zhao, Poly(methyl methacrylate) nanolatexes with high solid contents prepared by semi-continuous emulsion polymerization in the presence of oil-soluble initiators, Eur. Polym. J. 61 (2014) 316–325. doi:10.1016/j.eurpolymj.2014.11.004.

ABSTRACT

Catalysis is one of the Green Chemistry Principles given its importance for limiting environmental impacts and improving current processes, as well as for developing new sustainable processes and products. In order to provide more performant catalysts, this study provides a novel preparation method for controlling the distribution of metal nanoparticles (NPs) within hierarchically meso- and macroporous catalysts. It consists of the combination of latex synthesis, sonochemistry and sol-gel process. All these steps can be carried out in water, reducing environmental impact. The first step is the synthesis of latex, typically polystyrene. The second step is the sonochemical synthesis and deposition of noble metal NPs on the surface of the latex polymer. The third step is the synthesis of the support by sol-gel process using tetraethyl orthosilicate (TEOS) under controlled conditions to modulate the porosity of the final silica matrix. As a result, an original catalyst morphology is obtained with active sites preferentially located within the macropores, which are surrounded by a mesoporous matrix. Using this approach, a monodisperse polystyrene latex (~130 nm) was prepared by emulsion polymerisation and then decorated with Pt NPs (~2.3 nm) by sonochemical reduction. The mesoporous silica support was prepared by sol-gel synthesis in the presence of the decorated latex. After calcination, the organic template left behind macropores with the Pt NPs within the generated macropores. Mesopores (2-15 nm) connecting these macropores (110-400 nm) were tuned by varying the synthesis conditions. Typically, specific surface areas of 615 m^2/g and total pore volumes of 0.74 cm^3/g were obtained. In a first case study, hierarchically porous Pt/SiO_2 catalysts were evaluated in the selective hydrogenation of *p*-chloronitrobenzene (*p*-CNB) to produce *p*-chloroaniline. They exhibited activities up to 91.7 ± 2.9 $mol_{CNB}/(min\ mol_{Pt})$ and selectivity values up to 100 ± 2% at 80% of conversion, in comparison with 47.7 ± 2.9 $mol_{CNB}/(min\ mol_{Pt})$ and 91 ± 2%, respectively, obtained with a commercial catalyst under the same conditions. Moreover, in a second case study, it was possible to prepare silica-supported Pd, Pd-Pt and $Pd\text{-}CeO_2$ catalysts with hierarchical porosity (meso and macro). These materials were tested in the direct synthesis of hydrogen peroxide from hydrogen and oxygen. The best productivity of H_2O_2 was obtained with the bimetallic Pd-Pt catalyst with 32500 $mol_{H2O2}/(h\ mol_{metal})$ in batch, and the best selectivity was obtained with $Pd\text{-}CeO_2/SiO_2$ catalyst (63 ± 2%) in semi-batch. In summary, this thesis proposes a new aqueous preparation method for hierarchically porous functional materials by the combination of latex synthesis, sonochemical reduction and sol-gel process. It has been demonstrated that this preparation technique provides a very powerful and versatile toolbox for catalyst tailoring and optimisation. Further perspectives to achieve improved morphologies and controlled active sites distribution are also proposed.

KEY WORDS: LATEX • SONOCHEMISTRY • SOL-GEL • CATALYST CHARACTERISATION • CATALYSIS

RESUME

La catalyse est l'un des piliers pour le développement de procédés durables, car elle permet d'utiliser moins de ressources en accélérant les réactions chimiques. Afin de fournir des catalyseurs plus performants, cette étude propose une nouvelle méthode de préparation de catalyseurs pour contrôler la distribution de nanoparticules (NPs) métalliques au sein des catalyseurs hiérarchiquement poreux (méso et macro) en combinant la synthèse de latex, la réduction sonochimique et le procédé sol-gel. La première étape est la synthèse d'une empreinte porogène de billes de polystyrène (latex) obtenues par polymérisation en émulsion aqueuse. La deuxième étape est la synthèse et le dépôt de NPs de métaux nobles sur la surface des billes de polymère par voie sonochimique dans l'eau. La troisième étape est la synthèse du support catalytique par un procédé sol-gel en milieu aqueux en utilisant le latex décoré et l'orthosilicate de tétraéthyle (TEOS) dans des conditions contrôlées pour moduler la porosité finale de la matrice de silice (mésoporeuse). Toutes les étapes de cette approche sont effectuées dans l'eau, ce qui limite les impacts environnementaux de la préparation du catalyseur. L'élimination du porogène (latex) par calcination génère les macropores. Le matériau résultant possède alors une morphologie inédite pour un catalyseur, avec des macropores fonctionnalisés par des NPs métalliques, dans une matrice de silice mésoporeuse. Ainsi, il a été possible de synthétiser un latex monodisperse de polystyrène (~130 nm), lequel a été décoré avec des NPs de Pt (~2.3 nm) par réduction sonochimique. Le matériau final de silice a présenté des mésopores (2-15 nm) reliant les macropores (110-400 nm) contenant les NPs de Pt. Il a été possible d'obtenir des surfaces spécifiques et des volumes poreux totaux de 615 m^2/g et 0,74 cm^3/g, respectivement. Dans un premier cas d'étude, des catalyseurs de Pt/SiO_2 à porosité hiérarchique ont été évalués dans l'hydrogénation sélective du *p*-chloronitrobenzene (*p*-CNB) pour produire la *p*-chloroaniline. Ils ont présenté des activités catalytiques allant jusqu'à 91,7 ± 2,9 $mol_{CNB}/(min\ mol_{Pt})$ et des sélectivités jusqu'à 100 ± 2% à 80% de conversion, par rapport à 47,7 ± 2,9 $mol_{CNB}/(min\ mol_{Pt})$ et 91 ± 2%, respectivement, obtenus dans les mêmes conditions avec un catalyseur commercial. Dans un deuxième cas d'étude, des catalyseurs à base de Pd, Pd-Pt et $Pd\text{-}CeO_2$ supportés sur de la silice à porosité hiérarchique ont été préparés et testés dans la synthèse directe du peroxyde d'hydrogène. La meilleure productivité a été obtenue avec le catalyseur bimétallique Pd-Pt avec 32500 $mol_{H2O2}/(h\ mol_{métal})$ en batch, et la meilleure sélectivité a été obtenue avec le catalyseur $Pd\text{-}CeO_2/SiO_2$ (63 ± 2%) en semi-continu. En résumé, cette thèse propose une nouvelle méthode de préparation dans l'eau de matériaux fonctionnels à porosité hiérarchique en combinant la synthèse de latex, la réduction sonochimique et le procédé sol-gel. Il a été démontré que cette technique de préparation fournit une boîte à outils très puissante et polyvalente pour la préparation et l'optimisation des catalyseurs. Des perspectives pour améliorer davantage les morphologies et la distribution contrôlée des sites actifs sont également proposées.

MOTS CLES: LATEX • SONOCHIMIE • SOL-GEL • CARACTERISATION DE CATALYSEUR • CATALYSE